Characterisation of Atypical Human GTPases: Elucidation of Molecular Functions and Interactors

LJ KAY

PhD

2016

Characterisation of Atypical Human GTPases: Elucidation of Molecular Functions and Interactors

LAURA JAYNE KAY

A thesis submitted in partial fulfilment of the requirements of the University of Northumbria at Newcastle for the degree of Doctor of Philosophy

Research undertaken in the Faculty of Health and Life Sciences and in collaboration with the University of Newcastle, Newcastle upon Tyne

October 2016

In loving memory of

Donald Kay (1937 – 2015)

Abstract

Emerging evidence suggests that several atypical Rho GTPases participate in the development of serious human pathologies such as chronic lymphocytic leukaemia and neurodegeneration. However, these GTPases remain poorly characterised at the functional, structural and biochemical level. Furthermore, the interactors and signalling pathways associated with these enzymes remain obscure. This study aimed to elucidate the molecular functions and interactors of three highly atypical human GTPases for the first time: hMiro1, hMiro2 and RhoH.

Using PCR-based cloning and molecular biology techniques, full-length and truncated versions of these highly unusual human GTPases were successfully expressed, purified and characterised. Colorimetric assays were utilised to assess the GTPase hydrolytic activity of the human Miros *in vitro*, while PC3 cell migration assays and fluorescent microscopy allowed for an evaluation of Miro GTPase influence in live cancer cells. Biophysical characterisation of the Miros and RhoH was performed using dynamic light scattering (DLS) and circular dichroism (CD) thermal denaturation, while label-free proteomics allowed for the identification of several novel putative Miro interaction partners. Meanwhile, RhoH association with the death-associated kinase DRAK2 was assessed *in vitro* using anti-phosphoserine/phosphothreonine assays.

The results show, for the first time, that individual domains of the human Miros are capable of intrinsic hydrolytic activity against GTP. Biophysical assessment by DLS suggests the Miros exist monomerically and exhibit average thermal stability. Knockdown of the human Miros produced a significant reduction in cell proliferation, with knockdown phenotypes associated with mitochondrial perinuclear aggregation under fluorescent microscopy. 37 novel putative signalling interactors for the human Miros were identified by mass spectrometry. Meanwhile, assessment of RhoH-DRAK2 interaction showed a novel association between these proteins *in vitro*, indicating that DRAK2 directly phosphorylates RhoH.

The results improve current understanding of these important and unusual human GTPases and the molecular functions they engage in. The novel interactors identified may also prove clinically relevant in the future, particularly to the understanding and treatment of neurodegenerative disorders and chronic lymphocytic leukaemia.

Table of Contents

Chapter 1: Introduction 1

1.1 The Ras superfamily of small GTPases 1

1.1.1 The Ras superfamily: a brief overview 1

1.1.2 An overview of classical Ras superfamily regulation 2

1.1.3 An overview of classical Ras superfamily structure 4

1.2 Structure and function of classical Ras superfamily enzymes 8

1.2.1 Conserved regions of classical Ras superfamily enzymes 8

1.2.2 Residues participating in nucleotide binding 12

1.2.3 The GTP hydrolysis mechanism employed by classical Ras superfamily enzymes 15

1.3 Atypical members of the Ras superfamily 19

1.3.1 Atypical members of the Ras superfamily: an overview 19

1.3.2 Known example of atypical Ras superfamily GTPases: the RhoBTB proteins 26

1.4 Miro GTPases 30

1.4.1 The Miro GTPases at a glance 30

1.4.2 Molecular structure of Miro GTPases 30

1.4.3 Evolution and function of the Miro GTPases 31

1.4.4 Miro as a facilitator of mitochondrial transport 35

1.4.5 Miro as a facilitator of mitochondrial transport: the influence of Ca^{2+} 39

1.4.6 Miro in mitochondrial morphology 41

1.4.7 Influences on ATP homeostasis and apoptosis 43

1.4.8 Miro GTPases in health and pathology 45

Chapter 2: Materials and Methods 52

2.1 Materials 52

2.1.1 Chemicals, enzymes and kits 52
2.1.2 Bacterial strains and vectors 55
2.1.3 Oligonucleotides 57
2.1.4 Media 59
2.1.5 Buffers 61
2.2 Methods 69
2.2.1 General practice 69
2.2.2 Microbiological Methods 70
2.2.3 DNA methods 73
2.2.4 Protein methods 78
2.2.5 *In vitro* characterisation methods 83
2.2.6 Mammalian cell culture methods 86
2.2.7 Omics methods 94
Chapter 3: Cloning, expression and purification of the human Miro GTPases 98
3.1 Introduction 98
3.2 Cloning, expression and purification of full-length wildtype hMiro1 and hMiro2 98
3.3 Cloning, expression and purification of hMiro1 and hMiro2 domains of interest 107
3.3.1 Cloning, expression and purification of the hMiro1 and hMiro2 C-terminal GTPase domains 110
3.3.2. Cloning, expression and purification of hMiro1 and hMiro2 ‘crystal’ truncates 123
3.3.3. Cloning, expression and purification of hMiro1 and hMiro2 N-terminal GTPase domains 134
Chapter 4 reμsults: *in vitro* characterisation of the human Miros 143
4.1 Introduction 143
4.1.1 Objectives 143

4.2 Analysis of the GTP hydrolytic activity of hMiro1, hMiro2 and isolated hMiro GTPase domains 143

4.2.1 Fluorometric detection using novel phosphate sensor method 144

4.2.2 Colorimetric detection using the malachite green assay 144

4.2.3 Colorimetric detection using the PiColourLock™ Gold assay kit 145

4.2.4 Generation of phosphate standard curve 145

4.2.4.2 For PiColourLock™ Gold assay kit 146

4.2.5. hMiro1 and hMiro2 N-terminal GTPase domains are capable of hydrolysing GTP in the presence of $MgCl_2$, $CaCl_2$ or both cations 146

4.2.6. hMiro1 and hMiro2 C-terminal GTPase domains exhibit hydrolytic activity against GTP in the presence of $MgCl_2$, $CaCl_2$ or both cations 149

4.2.6. hMiro1 and hMiro2 'crystal constructs' show hydrolytic activity against GTP in the presence of $MgCl_2$, $CaCl_2$ or both cations 152

4.2.7 The hMiro1 and hMiro2 C-terminal GTPase domains display substrate promiscuity, showing hydrolytic activity against ATP and UTP 155

4.2.8 hMiro1 and hMiro2 GTPase domains: assessment of enzymatic kinetic parameters 160

4.3 Function of the human Miro GTPases in mammalian cell lines: knock-down studies 166

4.3.1 Migration assays using PC3 cells 166

4.3.2 Fluorescent microscopy 167

4.4 Biophysical characterisation of the Miro GTPases 171

4.5 Discussion 183

4.5.1 Hydrolytic activity of hMiro1 and hMiro2 GTPase domains 183

4.5.2. Knockdown studies 190

4.5.3 Biophysical characterisation of hMiro1 and hMiro2 190

4.5.4 Conclusions 193

Chapter 5: Investigating Miro GTPase signalling pathways using proteomics and computer-based prediction software 194

5.1 Introduction 194

5.1.1 Objectives 194
5.1.2 Overview of proteomics applications 194
5.2 Biological samples: hMiro overexpression and knockdown 197
5.2.1 hMiro overexpression studies 197
5.2.2 Biological samples: hMiro knockdown samples 204
5.3 Discussion 221
5.3.1 Summary of results 221
5.3.2 Indicated differences between hMiro1 and hMiro2 signalling 222
5.3.3 Identified proteins of particular note 223
5.4 Conclusions 227
Chapter 6: characterisation of the atypical GTPase human RhoH 228
6.1 Introduction 228
6.1.1 Objectives 228
6.1.2 RhoH at a glance 228
6.1.3 RhoH domain architecture 229
6.1.4 RhoH function 235
6.1.5 DRAK2 as a putative interactor of RhoH 243
6.1.6 RhoH and DRAK2: convergence of functional roles and potential clinical relevance 246
6.2 Results 247
6.2.1 Cloning of full length and truncated versions of human RhoH 247
6.2.2 Expression trials 250
6.2.3 Confirmation of target protein expression 254
6.2.4 Expression up-scale and purification 258
6.2.5 *In vitro* characterisation 264
6.2.6 Phosphorylation assays 272
6.3 Conclusions and discussion 286
6.3.1 RhoH characteristics *in vitro* 286

6.3.4 DRAK2 as a regulator of RhoH 287

7: Concluding remarks 289

7.1 Summary 289

7.2 Perspectives and future directions 289

8: References 292

Appendices 324

Appendix 1: General laboratory equipment use 324

Appendix 2: Gel filtration calibration curve 326

Appendix 3: PCR protocols 327

Appendix 4: Mutant primers for site-directed mutagenesis (SDM) 331

Appendix 5: Cell line data 332

Appendix 6: Additional growth components for VSMCs 334

Appendix 7: X!Tandem search parameters 335

Appendix 8: MASCOT search parameters 336

Appendix 9: Kinetic assays calculations 337

Appendix 10: Further xCELLigence information 338

Appendix 11: STRING data example 340

Appendix 12: Proteomics data examples 341

Appendix 13: RhoH DLS data 346

Appendix 14: Further LOMETS results 349

Table of Figures

Figure 1.1 The Ras Superfamily of small GTPases. 1
Figure 1.2 Schematic illustration of classical Ras superfamily GTPase regulation between active and inactive states. 3
Figure 1.3 Typical structural aspects of a classical Ras superfamily GTPase. 5
Figure 1.4 Typical structure of a 'classical' Rho sub-family member. 7
Figure 1.5 Differences between GTP- and GDP- bound versions of the classical Ras GTPase, HRas 11
Figure 1.6. Residues participating in nucleotide binding in the classical Ras and Rho GTPase (a) H-Ras and (b) Cdc42 14
Figure 1.7 Mechanism of GTP hydrolysis employed by the Giα1 G domain 17
Figure 1.8. Mechanism of GAP-mediated GTP hydrolysis in classical Ras and Rho enzymes 18
Figure 1.9. GTPases of the Rho sub-family, with atypical members highlighted. 20
Figure 1.10. Schematic representation of a selection of atypical GTPases of the Ras superfamily 22
Figure 1.11. Amino acid sequence alignment showing differences between select classical Ras superfamily GTPases and the atypical Rho GTPases studied herein. 23
Figure 1.12. Schematic representation of Miro GTPase structure 30
Figure 1.13. Schematic representation of neurone structure and axonal transport 36
Figure 1.14. Schematic diagram of the mitochondrial motor/adaptor complex thought to be necessary for mitochondrial transport 38
Figure 1.15. Schematic representation of models of Ca^{2+}-mediated mitochondrial arrest 40
Figure 3.1. Analytical restriction digest results showing full-length hMiro1 sequence liberated from pET-28a 99
Figure 3.2. Analytical restriction digest results displaying full-length hMiro2 sequence separated from pET-28a. 100
Figure 3.3. Coomassie-stained 12% SDS-PAGE gel showing IMAC purification of over-expressed (a) hMiro1 and (b) hMiro 104
Figure 3.4. Anti-hMiro1 (a) and anti-hMiro2 (b) Western blots 105

Figure 3.5. Size analysis of over-expressed full-length hMiro1 and hMiro2 samples based on SDS-PAGE and Western blotting 106
Figure 3.6. Schematic illustration of Miro domain architecture, displaying the GTPase domains in addition to the cut-off areas for the 'xtal' constructs 108
Figure 3.7 Comparison of amino acid sequences: dMiro, hMiro1 and hMiro2..... 109
Figure 3.8. 1% agarose gel showing hMiro C-terminal GTPase domain PCR products…… 111
Figure 3.9. 1% agarose gel showing target hMiro1 and hMiro2 N-terminal GTPase sequences following restriction digest of constructed plasmids 112
Figure 3.10. 12% SDS PAGE gel showing expression trial data for the C-terminal GTPase domain of Miro1 (Coomassie stained) 113
Figure 3.11. Further expression trial results for the C-terminal GTPase domain of Miro1 and Miro2 114
Figure 3.12. 12% Coomassie-stained SDS-PAGE gel showing expression trial results for the C-terminal GTPase domain of Miro2 115
Figure 3.13. Further expression trial data for the C-terminal GTPase domain of Miro2 116
Figure 3.14. MASCOT MS/MS Ions Score Histogram and analysis, indicating the presence of peptides in the hMiro1 C-terminal GTPase domain in the digested sample 118
Figure 3.15. Successful purification of the hMiro1 C-terminal construct (Q415 – P580) by ion-metal affinity chromatography (IMAC) 119
Figure 3.16. Purification of the hMiro2 C-terminal construct (Q413–F589) by ionmetal affinity chromatography (IMAC)..... 120
Figure 3.17. Concentrated C-terminal GTPase domains of (a) hMiro1 and (b) hMiro2 following IMAC purification 121
Figure 3.18. Western blotting of the hMiro1 (a) and hMiro2 (b) C-terminal GTPase domains 122
Figure 3.19. Successful PCR-based amplification of the nucleotide sequences encoding the 'crystal construct' domains of hMiro1 and hMiro2, respectively..... 124
Figure 3.20. 1% agarose gels showing results of analytical restriction digest to screen for hMiroXTAL inserts into pET15bTEV 125
Figure 3.21. 12% Coomassie-stained SDS-PAGE gel showing expression trial data for the hMiro1 'crystal construct' 126

Figure 3.22. 12% SDS-PAGe gel showing further expression trial results for the hMiro1 'crystal construct' 127
Figure 3.23. 12% SDS-PAGe gel displaying expression trial data for the hMiro2 'crystal construct'. 128
Figure 3.24. 12% SDS-PAGE gel showing further expression trial data for the hMiro2 'crystal construct'. 129
Figure 3.25. Purification of the hMiro1 xtal construct (E177–R590) by ion-metal affinity chromatography (IMAC). 131
Figure 3.26. Purification of the hMiro2 xtal construct (E177–P586) by ion-metal affinity chromatography (IMAC). 132
Figure 3.27. Western blot of hMiro1 (a) and hMiro2 (b) IMAC-purified 'crystal construct samples. 133
Figure 3.28. Successful PCR-based amplification of the nucleotide sequences encoding the N-terminal GTPase domain of (a) hMiro1 and (b) hMiro2 135
Figure 3.29. Analytical restriction digest of plasmid DNA extracted from TOP10 E.coli transformants after ligation of pET15b-TEV/hMiro1 3–169 PCR products (lanes 1–6) and pET15b-TEV/hMiro2 3–169 products (lanes 8–13), respectively. 136
Figure 3.30. 12% SDS-PAGE gel showing expression trial data hMiro1 N-terminal GTPase domain. 137
Figure 3.31. 12% SDS-PAGE gel showing expression trial data hMiro1 N-terminal GTPase domain 138
Figure 3.32 12% SDS-PAGE gel displaying expression trial data hMiro2 N-terminal GTPase domain. 139
Figure 3.33 12% SDS-PAGE gel showing expression trial data hMiro2 N-terminal GTPase domain. 140
Figure 3.34. Western blotting of hMiro1 and hMiro2 N-terminal GTPase domains 142
Figure 4.1. Malachite green reaction 144
Figure 4.2. Standard curve for phosphate signal using the Malachite Green assay kit. 145
Figure 4.3. Standard curve for phosphate signal using the PiColourLock™ Gold assay kit 146
Figure 4.4. GTP hydrolytic activity of the hMiro1 N-terminal GTPase domain. 147
Figure 4.5. GTP hydrolytic activity of the hMiro2 N-terminal GTPase domain 148
Figure 4.6. GTP hydrolytic activity of the hMiro1 C-terminal GTPase domain. 150
Figure 4.7. GTP hydrolytic activity of the hMiro2 C-terminal GTPase domain 151
Figure 4.8. GTP hydrolytic activity of the hMiro1 xtal construct. 153

Figure 4.9. GTP hydrolytic activity of the hMiro2 xtal construct 154
Figure 4.10. The hMiro1 N-terminal GTPase domain cannot hydrolyse ATP, UTP or CTP 156
Figure 4.11. The hMiro2 N-terminal GTPase domain displays an absence of hydrolytic activity towards ATP, UTP and CTP 157
Figure 4.12. The hMiro1 C-terminal GTPase domain shows hydrolytic activity against ATP and UTP but not CTP 158
Figure 4.13. The hMiro2 C-terminal GTPase domain displays hydrolytic activity against ATP and UTP but not CTP 159
Figure 4.14. Hydrolytic activity of hMiro1 and 2 individual GTPase domains using varying substrate concentrations 161
Figure 4.15. Lineweaver-Burke plot for hMiro1 N-terminal GTPase domain against GTP 162
Figure 4.16. Lineweaver-Burke plot for hMiro2 N-terminal GTPase domain against GTP 162
Figure 4.17. Lineweaver-Burke plot for hMiro1 C-terminal GTPase domain against GTP 163
Figure 4.18. Lineweaver-Burke plot for hMiro2 C-terminal GTPase domain against GTP 163
Figure 4.19. Lineweaver-Burke plot for hMiro1 C-terminal GTPase domain against ATP 164
Figure 4.20. Lineweaver-Burke plot for hMiro2 C-terminal GTPase domain against ATP 164
Figure 4.21. Knockdown of hMiro1, hMiro2 or both hMiros in PC3 cells reduces cell migration relative to controls 166
Figure 4.22. Fluorescent microscopy analysis of control PC3 cells versus hMiro1, hMiro2 or dual (hMiro1 and hMiro2) knockdown cells. 20x objective lens utilised 168
Figure 4.23. Fluorescent microscopy analysis of control PC3 cells versus hMiro1, hMiro2 or dual (hMiro1 and hMiro2) knockdown cells 169
Figure 4.24. Fluorescent microscopy analysis of control PC3 cells versus hMiro1, hMiro2 or dual (hMiro1 and hMiro2) knockdown cells 170
Figure 4.25. Both hMiro1 and hMiro2 exhibit monomeric behaviour *in vitro* 172
Figure 4.26. Thermal denaturation of hMiro1XTAL 182
Figure 4.27. Thermal denaturation of hMiro2XTAL 182
Figure 5.1. Schematic of a general ‘shotgun’ proteomics approach 195

Figure 5.2. Sequence trace sections for hMiro1-encoding mutants, with relevant codons highlighted 201
Figure 5.3. Sequence trace sections for hMiro2-encoding mutants, with relevant codons highlighted. 202
Figure 5.4. Immunoblot displaying successful overexpression of both wildtype and mutant hMiros 203
Figure 5.5. Basic results from the STRING online tool for (A) hMiro1 and (B) hMiro2 206
Figure 5.6. Number of proteins identified for each condition from the raw proteomics results, following hit filtering and conflict resolution in Progenesis 211
Figure 5.7. Number of hMiro1 proteins identified through proteomics endeavours, cross-checked against putative interactors identified by STRING, homology and literature searches 212
Figure 5.8. Number of hMiro2 proteins identified through proteomics endeavours, cross-checked against putative interactors identified by STRING, homology and literature searches 215
Figure 5.9. Major biological functions of the identified proteins of interest, shown as a percentage of the overall number of proteins for either hMiro1 or hMiro2 219
Figure 5.10 Summary of biological function(s) associated with the identified proteins of interest 220
Figure 6.1 Schematic diagram of putative RhoH domain architecture 229
Figure 6.2 Comparison of RhoH secondary structure against the canonical Rho GTPases Rac1, RhoA and Cdc42 230
Figure 6.3. Substitution of Glycine-12 in Rho and Ras superfamily enzymes results in steric hindrance of GAP 232
Figure 6.4. The role of Ras/Rho Glutamine-61 and the GAP arginine finger in GAPmediated GTP hydrolysis 233
Figure 6.5 RhoH acts upstream of Zap70 to mediate T-cell function 237
Figure 6.6. Summary of known RhoH interactions in T-cell biology 239
Figure 6.7. Molecular structure of the DAPK family of serine/threonine kinases 244
Figure 6.8. RhoH amino acid sequence, showing cut-off points for the $RhoH_{T1}$ and $RhoH_{T2}$ truncates 247
Figure 6.9 PCR products yielded from the PCR-based amplification of RhoH full length, RhoH truncation 1 (S4-SA174) and RhoH truncation 2 (V10-S184) 249

Figure 6.10 Analytical restriction digest for confirmation of the presence of RhoH-encoding sequences into pET15b-TEV 250
Figure 6.11 Expression trials show promising expression for $RhoH_{FL}$ and $RhoH_{T1}$ 243
Figure 6.12 Anti-RhoH Western blot of RhoH samples obtained from expression trials 255
Figure 6.13 LC-MS results indicating the presence of RhoH in the excised $RhoH_{FL}$ SDS-PAGE band 256
Figure 6.14 LC-MS results indicating the presence of RhoH in the excised $RhoH_{T1}$ SDS-PAGE band 257
Figure 6.15 IMAC purified fractions of $RhoH_{FL}$ obtained from lysed recombinant C43 (DE3*) E.coli* extract 259
Figure 6.16 Successful size exclusion purification of $RhoH_{FL}$ from lysed recombinant C43 (DE3) *E.coli* extract 260
Figure 6.17 Succesful IMAC purification of $RhoH_{T1}$ from lysed recombinant C43 (DE3) *E.coli* extract 261
Figure 6.18 Gel filtration leading to successful size exclusion purification of $RhoH_{T1}$ from lysed recombinant C43 (DE3) *E.coli* extract 262
Figure 6.19 Anti-RhoH immunoblots showing presence of RhoH in purified $RhoH_{FL}$ and $RhoH_{T1}$ samples 263
Figure 6.20. *In silico* model of $RhoH_{FL}$ 3D structure 268
Figure 6.21. *In silico* model of $RhoH_{T1}$ 3D structure 269
Figure 6.22. Visualisation of a 3D model of $RhoH_{T1}$ (blue) superimposed with the known 3D crystallographic structure of Cdc42 (red) 270
Figure 6.23. Superimposition of a 3D model of $RhoH_{FL}$ (blue) against the known 3D crystallographic structure of Cdc42 (red) 271
Figure 6.24 Successful IMAC purification of $DRAK2_{FL}$ from lysed recombinant C43 (DE3) *E.coli* extract 273
Figure 6.25 Successful size exclusion purification of $DRAK2_{FL}$ from lysed recombinant C43 (DE3) *E.coli* extract 274
Figure 6.26 IMAC purification of $DRAK2_{XTAL}$ from lysed recombinant C43 (DE3) *E.coli* extract 275
Figure 6.27 Successful size exclusion purification of $DRAK2_{XTAL}$ from lysed recombinant C43 (DE3) *E.coli* extract 276
Figure 6.28 20µM $DRAK2_{FL}$ phosphorylates $RhoH_{FL}$ and appears capable of autophosphorylation 277

Figure 6.29 10µM DRAK2$_{FL}$ phosphorylates RhoH$_{FL}$ and appears to undergo autophosphorylation.....278
Figure 6.30 20µM DRAK2$_{FL}$ phosphorylates RhoH$_{T1}$ and appears to undergo autophosphorylation.....279
Figure 6.31 10µM DRAK2$_{FL}$ appears to autophosphorylate in the presence of magnesium and ATP, and is able to phosphorylate DRAK2$_{FL}$.....280
Figure 6.32 Phosphorylation of RhoH$_{FL}$ by 20µM DRAK2$_{XTAL}$ in the presence of magnesium and ATP.....281
Figure 6.33 RhoHFL is phosphorylated by 10µM DRAK2$_{XTAL}$ in the presence of magnesium and ATP.....282
Figure 6.34 Phosphorylation of RhoH$_{T1}$ by 20µM DRAK2$_{XTAL}$ in the presence of magnesium and ATP.....283
Figure 6.35 10µM DRAK2$_{XTAL}$ phosphorylates RhoH$_{T1}$ in the presence of magnesium and ATP.....284

Table of Tables

Table 1.1 Commonly conserved residues participating in nucleotide binding amongst Ras superfamily enzymes (residue positions correspond to H-Ras) 13
Table 1.2 Differences in the G domain loop regions: classical versus atypical Ras superfamily enzymes 24
Table 1.3 Differences in the switch regions and CaaX box: classical versus atypical Ras superfamily enzymes 25
Table 1.4 Differences in the Rho insert domain: classical versus atypical Ras superfamily enzymes 25
Table 1.5. Miro functions and interactors across species 33
Table 2.1 Stock and working concentrations of antibiotics in media. 52
Table 2.2 Enzymes, buffers and reaction co-constituents. 53
Table 2.3 Kits utilised throughout project. 53
Table 2.4 List of primary antibodies. 54
Table 2.5 List of secondary antibodies. 54
Table 2.6 E.coli strains used throughout this project. 55
Table 2.7 Vectors used throughout this study. 56
Table 2.8 Components in 1 litre of LB-broth. 59
Table 2.9 Components in 1 litre of TB-broth. 59
Table 2.10 Components of 6x bromophenol blue DNA loading dye. 61
Table 2.11 Components of 6x xylene cyanol DNA loading dye. 61
Table 2.12 Components of 50x TAE running buffer for agarose gel electrophoresis. 62
Table 2.13 Components of 10x SDS-PAGE running buffer. 63
Table 2.14 6x SDS-PAGE loading buffer components. 63
Table 2.15 12% (w/v) acrylamide resolving gel components. 64
Table 2.16 Components used to make up 100 mL of Buffer B for use in making SDS-PAGE resolving gels. 64
Table 2.17 SDS-PAGE stacking gel components. 65
Table 2.18 Components used to make up 100 mL of Buffer C, used when producing SDS-PAGE stacking gels. 65
Table 2.19 Components required to make up 1 litre of coomassie stain. 65
Table 2.20 Components required to make up 1 litre of destain solution. 66
Table 2.21 Components of a typical ligation reaction. 77
Table 2.22 LC-MS/MS eluent programme 96

Table 3.1. Expression optimisation of hMiros using auto-induction trials and the C43 expression host 102
Table 3.2. hMiro bacterial expression optimisation using IPTG induction and the C43 expression host 103
Table 3.3. Percentage identity matrix illustrating amino acid identity between the hMiros and dMiro. 108
Table 3.4. Details of each designed construct. 108
Table 3.5. Expression optimisation of hMiros C-terminal GTPase domains using IPTG induction 117
Table 3.6. Expression optimisation of hMiro 'crystal construct' polypeptides using IPTG induction 129
Table 3.7. Expression optimisation of hMiros N-terminal GTPase domains using IPTG induction 141
Table 4.1. Kinetic parameters for intrinsic hydrolysis of the hMiro constructs and typical Ras superfamily enzymes. 165
Table 4.2 Primary observations of fluorescent microscopy of control and knockdown PC3 cells 167
Table 4.3. G_4 motif residues exhibited by classical Ras superfamily enzymes in comparison to those shown by hMiro GTPase domains 186
Table 4.4 Differences in the G domain loop regions: classical versus atypical Ras superfamily enzymes 188
Table 5.1. Panel of hMiro1 plasmids intended for use in proteomics investigations ... 199
Table 5.2. Panel of hMiro2 plasmids designed for use in proteomics investigations. .. 200
Table 5.3. Pathways predicted to be associated with hMiro1 207
Table 5.4. Pathways predicted to be associated with hMiro2 208
Table 5.5. Number of proteins identified for each condition (mean across duplicates), showing MASCOT versus X! Tandem 210
Table 5.6. Identification of 13 proteins of interest associated with hMiro1 mutants 213
Table 5.7. Identification of 24 proteins of interest related to hMiro2 signalling through cross-referencing of experimental proteomics data with computerbased prediction methods 216
Table 6.1. Main differences between RhoH and its closest classical Rho GTPase homologue, Cdc42 231
Table 6.3. Involvement of aberrant RhoH in lymphomas and leukaemias 242
Table 6.4. Expression optimisation of recombinant human RhoH constructs 252

Table 6.5 Top-scoring models for the prediction of $RhoH_{FL}$ and $RhoH_{T1}$ 3D structure 267

Acknowledgements

The completion of this work would not have been possible without the support, guidance and friendship of many people. First, I wish to thank my supervisor Dr Meera Soundararajan for her immeasurable guidance and advice throughout this work. I also extend my thanks and gratitude to Prof Gary Black, who originally encouraged me to pursue a PhD and has been a great source of knowledge, guidance and support throughout my time at Northumbria University. A sincere thank you must go to Prof Jeremey Lakey and his group at Newcastle University, who have supported the project through their insight, practical input and encouragement. I particularly owe thanks to Dr Peter Daniels of this group for contributions and support during biophysical characterisation experiments.

The Graduate School at Northumbria University has been paramount to this project, providing funding, encouragement and guidance. I must extend particular gratitude to Dr Lynn Dover and Prof John Dean for their advice during annual progression discussions. I would also like to express sincere gratitude to Dr Nick Caplan and Paul Agnew, both of whom have been invaluable in their efforts to deliver guidance and advice during more difficult periods.

I have been extremely fortunate to work with many inspiring and enthusiastic individuals throughout my PhD, many of whom have become true friends. I am immensely grateful towards Dr Victoria Barlow for helping me stay positive, inquisitive and caffeinated throughout this project. My years as a PhD student would certainly have been much less enjoyable without the friendship of Dr Francesca Everest, Dr Hayley Tsang, Miss Hazel Ingram and Miss Kathryn Gray. I would also like to express my gratitude to Dr Nicola Brown, Dr Graeme Turnbull and particularly Dr Andrew Nelson for their insight and advice. Special recognition must be given to Dr Rosemary Bass for her assistance during cell migration studies.

The laboratories I have worked in throughout this project are inhabited by some of the most enthusiastic and engaging individuals I have ever met. Although there are far too many people to acknowledge by name, I extend my gratitude to all of my friends and colleagues in Ellison Building. In particular, I would like to thank the members of A321. My appreciation also must go to the Ellison Building third and fourth floor technical staff, with a special mention for Dr Steven Reed and Miss Robyn Graham-Wilkinson.

I am greatly indebted to my best friend Cheryl Guthrie. Cheryl has been an amazing friend to me for over 15 years, celebrating with me during the good times and comforting me during the most difficult of times. I cannot thank Cheryl enough for her friendship, her support, and crucially, her excellent tea-making skills. I must also extend my gratitude to her partner, Phillip Scott. Thank you both for being there for me. Thank you both for believing in me.

I owe a vast amount of gratitude towards Alesis Novik, who has encouraged me more than almost anyone else to complete this work. I would like to thank him for his faith in me, for his encouragement, and for the countless times he reassured me throughout the final months of my studies. Alesis has proved a wonderful source of comfort during tough times, and I will never be able to thank him enough for his support.

Finally, I would like to thank the most important people in my life: my family. The completion of this thesis would not have been feasible without their enduring support, love and encouragement. My mother Christina is the most loyal, resilient and optimistic person I have ever encountered. I cannot thank her enough for her unwavering positivity and love. I must also extend deep gratitude towards my father David for his encouragement and wisdom. Thank you both for loving and supporting me throughout the years, and particularly throughout my doctoral studies. To my brothers Anthony and Stephen, thank you for many happy times throughout the years and for inspiring me with your own achievements. Special acknowledgement must also go to my grandparents on my mother's side, Connie and John: these two wonderful people are simply inspirational. I cannot thank them enough for their endless love, support and optimism. I must also thank my grandmother of my father's side, Dorothy, and my grandfather Donald who sadly passed away during the course of my doctoral studies. I feel endlessly fortunate to have known my grandfather Donald, and dedicate this thesis to him, knowing he was proud of the achievements of his grandchildren. To Heather, Geoff, Adam, Peter and everyone else in my family who has helped and encouraged me throughout this journey, thank you. Thank you for your love and support. Thank you for helping me become the person I am today.

Declaration

I declare that the work contained in this thesis has not been submitted for any other award and that it is all my own work. I also confirm that this work fully acknowledges opinions, ideas and contributions from the work of others. The work was done in collaboration with Newcastle University, Newcastle upon Tyne.

Any ethical clearance for the research presented in this thesis has been approved. Approval has been sought and granted by the Faculty Ethics Committee on 22/10/2012.

I declare that the word count of this thesis is 44,789 words.

Name: LAURA JAYNE KAY

Signature:

Date: 28/08/2016

List of Abbreviations

ACN	Acetonitrile
ADP	Adenosine diphosphate
APS	Amonium per sulphate
ATP	Adenosine triphosphate
ATPase	Adenosine triphosphatase
BLAST	Basic local alignment and search tool
BPB	Bromophenolblue
BSA	Bovine serum albumin
Ca^{2+}	Calcium divalent cation
CT	C-terminal or C-terminal GTPase domain
C-terminal	Carboxy terminal
EDTA	Ethylenediaminetetraacetic acid
ESI	Electrospray ionisation
g	Gram(s)
GAP	GTPase activating protein
GDI	Guanine dissociation inhibitor
GDP	Guanosine diphosphate

GEF	Guanine nucleotide exchange factor
GTP	Guanosine triphosphate
GTPase	Guanosine triphosphatase
h	Hour(s)
HEPES	(4-(2-hydroxyethyl)-1-piperazineethanesulfonic acid)
HMW	High molecular weight
kbp	Kilo base pair(s)
K_{cat}	substrate molecules turned over per enzyme molecule per unit time
kDa	Kilo Dalton
K_m	Substrate concentration required for ½ maximal velocity
L	Litre(s)
LB	Luria Bertani broth or Lineweaver-Burke
LC-MS	Liquid chromatography mass spectrometry
LMW	Low molecular weight
Mg^{2+}	Magnesium divalent cation
NT	N-terminal or N-terminal GTPase domain
PAGE	Polyacrylamide gel electrophoresis
pBLAST	Protein basic local alignment and search tool
PBS	Phosphate buffered saline

PCR	Polymerase chain reaction
RPM	Rotations per minute
s	Second(s)
SDM	Site directed mutagenesis
SDS	Sodium dodecyl sulphate
SDS-PAGE	Sodium dodecyl sulphate polyacrylamide gel electrophoresis
TEMED	Tetramethylethylenediamine
TFA	Trifluoroacetic acid
Tris	Trisaminomethane
UTP	Uridine triphosphate
UV	Ultraviolet
V	Volt(s)
v/v	Volume per volume
V_{max}	Maximal velocity
w/v	Weight per volume
xg	Times gravity
XTAL	Crystal
α	Alpha
β	Beta

Δ	Delta
µg	Micro gram(s)
µL	Micro litre(s)
µM	Micro molar
Σ	Sum
^{o}C	Degrees celcius
18.2 MΩ H20	18 mega ohm water

Chapter 1: Introduction

1.1 The Ras superfamily of small GTPases

1.1.1 The Ras superfamily: a brief overview

The Ras superfamily of small guanosine triphosphatases (GTPases), named after one of the most extensively studied oncogenes in human carcinogenesis, Ras, comprises over 150 distinct human members across six sub-families: Ras, Rho, Rab, Ran, Arf and Miro (Figure 1.1). Typically, these so-called 'small' GTPases are monomeric in nature, containing a canonical ~21 kDa catalytic 'G domain' (1,2). This G domain enables the hydrolytic degradation of GTP to GDP and is central to the function of Ras superfamily GTPases, enabling these enzymes to act as binary molecular switches within a diverse range of signalling pathways (3,4). While features of this G domain are strongly conserved throughout the sub-families of the Ras superfamily, delineation of the sub-classes is afforded by further differences in protein regulation, post-transcriptional modifications, function, structure and downstream interactors (5-9).

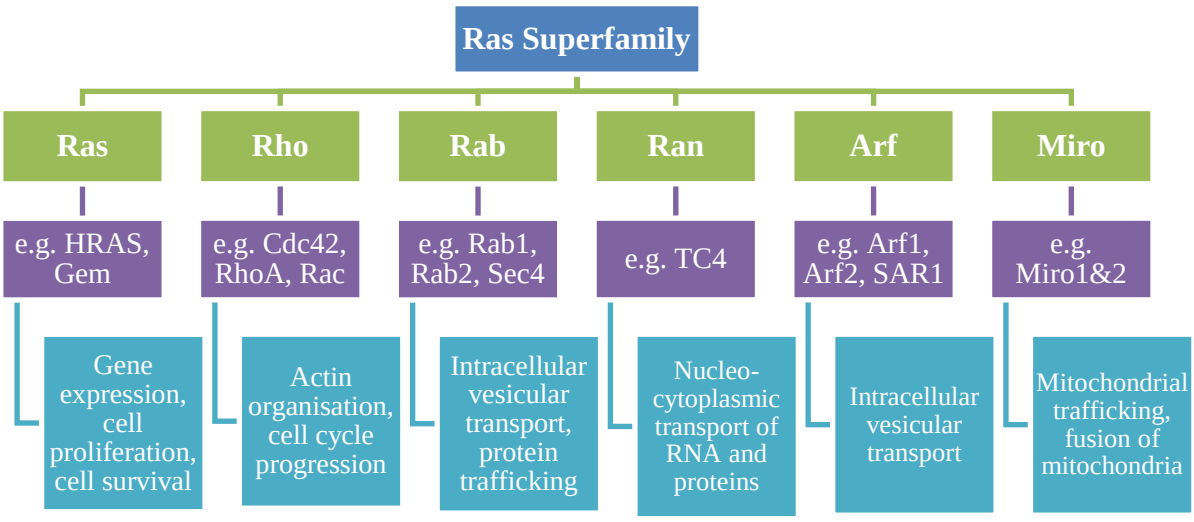

Figure 1.1 The Ras Superfamily of small GTPases. The Ras superfamily and comprising sub-families, with examples of members of each sub-family displayed. Typical functions associated with each sub-family are also shown.

Several members of the Ras superfamily are medically relevant (10-17), driving the study of their structure, function and binding partners. For example, approximately 30% of all tumours screened contain at least one mutation in a Ras superfamily encoding gene (18). Furthermore, germline mutations in members of the Ras superfamily or their regulatory proteins have been associated with several inherited developmental syndromes such as Costello syndrome (19), Cardiofaciocutaneous syndrome (20) and Noonan syndrome (21), amongst others (22). Furthermore, dysregulation of some members of the Ras superfamily has been associated with such diverse disorders as dementia (23,24), diabetes (25,26) and cardiovascular disease (27,28). More recently, several highly 'atypical' proteins of the Ras superfamily have been identified (29), the majority of which appear to reside within the Rho sub-family (30). As further discussed in section 1.3, these proteins exhibit traits that make them highly unusual relative to 'classical' members of the Ras superfamily. Nonetheless, these 'atypical' GTPases have been implicated in a range of pathologies when absent or dysregulated, such as leukaemias (31-33), amyotrophic lateral sclerosis (ALS) (34) and Parkinson's (35,36). Thus, an understanding of the structure, function and regulation of these atypical proteins is highly desirable.

1.1.2 An overview of classical Ras superfamily regulation

Classically, proteins of the Ras superfamily cycle between an active GTP-bound state and an inactive GDP-bound state (37). In their active state, they typically bind effector proteins and activate downstream signalling pathways (38,39). While Ras superfamily GTPases typically possess intrinsic GTPase activity (2,37), their activity tends to be regulated by three types of regulatory protein: Guanine nucleotide exchange factors (GEFs) (40,41), GTPase activating proteins (GAPs) (41,42) and guanine nucleotide dissociation inhibitors (GDIs) (41,43,44), as shown in Figure 1.2 and discussed further in 1.2.4. It should be noted, however, that atypical members of the Ras superfamily may partly or completely elude this scheme of regulation (43).

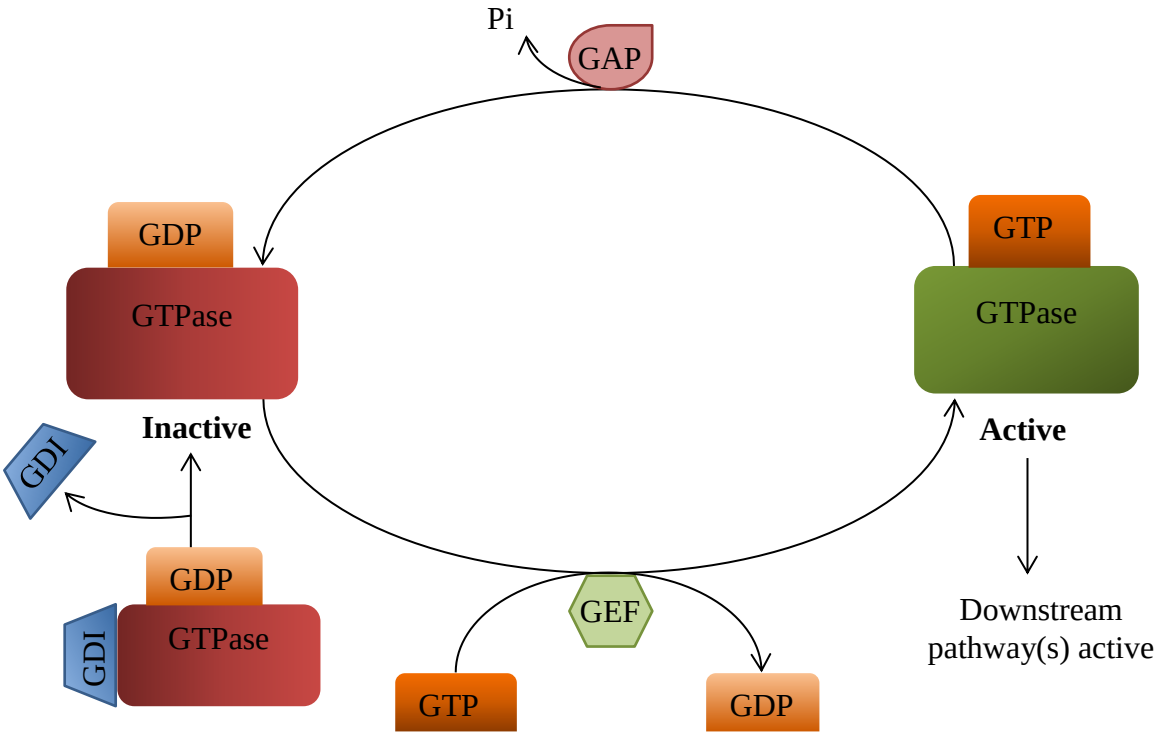

Figure 1.2. Schematic illustration of classical Ras superfamily GTPase regulation between active and inactive states. Schematic diagram illustrating the quintessential regulation of a classical Ras GTPase by GAPs, GEFs and GDIs.

As illustrated in Figure 1.2, classical activation of Ras superfamily GTPases to their GTP-bound state is facilitated by guanine nucleotide exchange factor proteins (GEFs), which stimulate the exchange of GDP for GTP (37). Alternatively, deactivation is typically undertaken by activity of GAP regulatory proteins, which promote GTP hydrolysis and henceforth return the Ras superfamily protein to the inactive GDP-bound state (42). A more detailed description of the mechanism of GTP hydrolysis in Ras superfamily enzymes is provided in section 1.2.3. GTPases within a branch are often targeted by shared and distinct GEFs and GAPs. Across different branches of the Ras superfamily, GTPases are often targeted by structurally distinct GEFs and GAPs which act by similar mechanisms (2,37,42).

Some members of the Ras superfamily are also modulated by a third class of regulatory proteins: GDIs (2,37,43,44). Rho, Rab and some Ras family members undergo post-translational prenylation at their C-terminus, facilitating their attachment to endomembranes and allowing them to perform at their appropriate sites of action. GDIs facilitate the extraction of these prenylated proteins from endomembranes, preventing exchange of GDP for GTP and

promoting cytosolic sequesteration of these proteins away from their sites of action (37). The term GDI itself was coined upon discovery of RhoGDI, classified as an inhibitor of GDP dissociation (45). However, the primary function of Rho and Rab GDIs is now thought to centre around the maintenance of their target GTPases in inactive complexes in the cytoplasm (37). In mammals, only a small number of GDIs have been identified. RhoGDIs and RabGDIs target gernaylgeranylated Rho and Rab GTPases, respectively. Meanwhile, the GDI PDEδ favours farnesylated GTPases (41).

1.1.3 An overview of classical Ras superfamily structure

The canonical feature of Ras superfamily proteins is their ability to bind and hydrolyse GTP by virtue of a ~21 kDa G-domain. As illustrated in Figure 1.3, the classical G-domain model is comprised of six β-sheets (β_1-β_6) and five α-helices in addition to four to five conserved G-box 'loop' elements referred to as G_1-G_5 (2). Two domains, known as the switch I and switch II domains, are integral to the binding of ɣ-phosphate oxygens of GTP and are involved in fundamental conformational changes between the GDP-bound (state 1) and GTP-bound (state 2) states of these GTPases (37,46). Following GTP hydrolysis and the release of ɣ-phosphate, the switch domains relax into GDP-specific conformation (37). In addition to the G-domain, some small GTPases (primarily of the Ras and Rho sub-families) possess a C-terminal tetrapeptide CaaX motif ('CaaX box') required for localisation of these proteins to the plasma membrane (47,48).

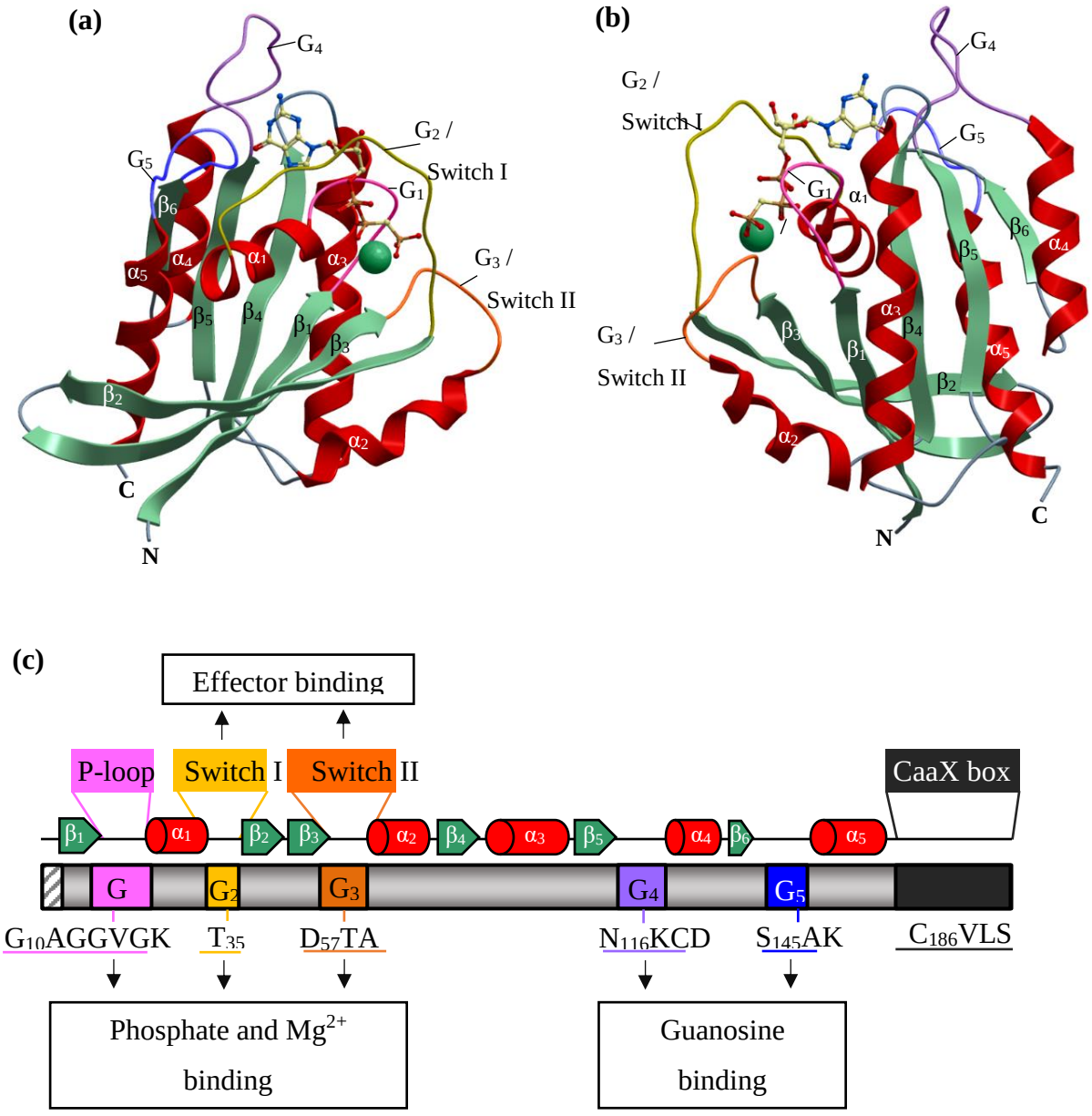

Figure 1.3. Typical structural aspects of a classical Ras superfamily GTPase. Anterior **(a)** and posterior **(b)** three-dimensional model of human H-Ras, a classical GTPase of the Ras family, with **(c)** additional schematic diagram displaying the G loops, switch regions, CaaX box, beta strands and alpha helices. In **a–b**, H-Ras is shown bound to Mg^{2+} and the GTP analogue GCP. Critical areas are labelled accordingly, with beta strands displayed in green and alpha helices shown in red. Note that the ligands adhere to the CPK chemical element colouring scheme as follows: Nitrogen (blue), Oxygen (red), Phosphorous (yellow). Model generated in MolSoft MolBrowser version 3.8 (MolSoft L.L.C) from entry 121P of the RCSB PDB (49). In **(c)**, an identical colour coding system has been adopted from the 3D structures **(a)** and **(b)**, while the G domain as a whole is delineated as grey; the amino acid residues shown apply to H-Ras specifically.

The features of the G-domain shown in Figure 1.3 are generally well-conserved across classical members of the Ras superfamily (with the exception of the Miros, which are highly atypical and discussed in detail in section 1.4). However, each sub-family within the Ras superfamily may exhibit unique structural aspects conserved within that particular sub-family only (50). With respect to the high number of atypical GTPases seen within the Rho-subfamily, it is pertinent to discuss classical structural aspects of this sub-family, including aspects unique to the Rhos alone. From a three-dimensional model of the classical Rho family member RhoA (Figure 1.4), it can be seen that classical Rho members contain several structural aspects that are also common to the Ras superfamily as a whole. Classical Rho GTPases possess a G-domain encompassing the typical six β-sheets and five α-helices, along with the aforementioned conserved G-box G_1-G_5 loops. Two other important classical aspects, the switch I and switch II regions, are also present. Canonical members of the Rho sub-family also possess the C-terminal CaaX box. A distinguishing aspect of classical Rho proteins, however, is the presence of a surface-exposed alpha helical 'Rho insert' domain between the fourth α-helix and fifth β-sheet (5). This domain is thought to be involved in Rho-specific signalling events (51) and has been shown to be necessary for some Rho-specific regulatory events; for example, the insert region of RhoA is essential for Rho kinase activation and subsequent cellular transformation events (52).

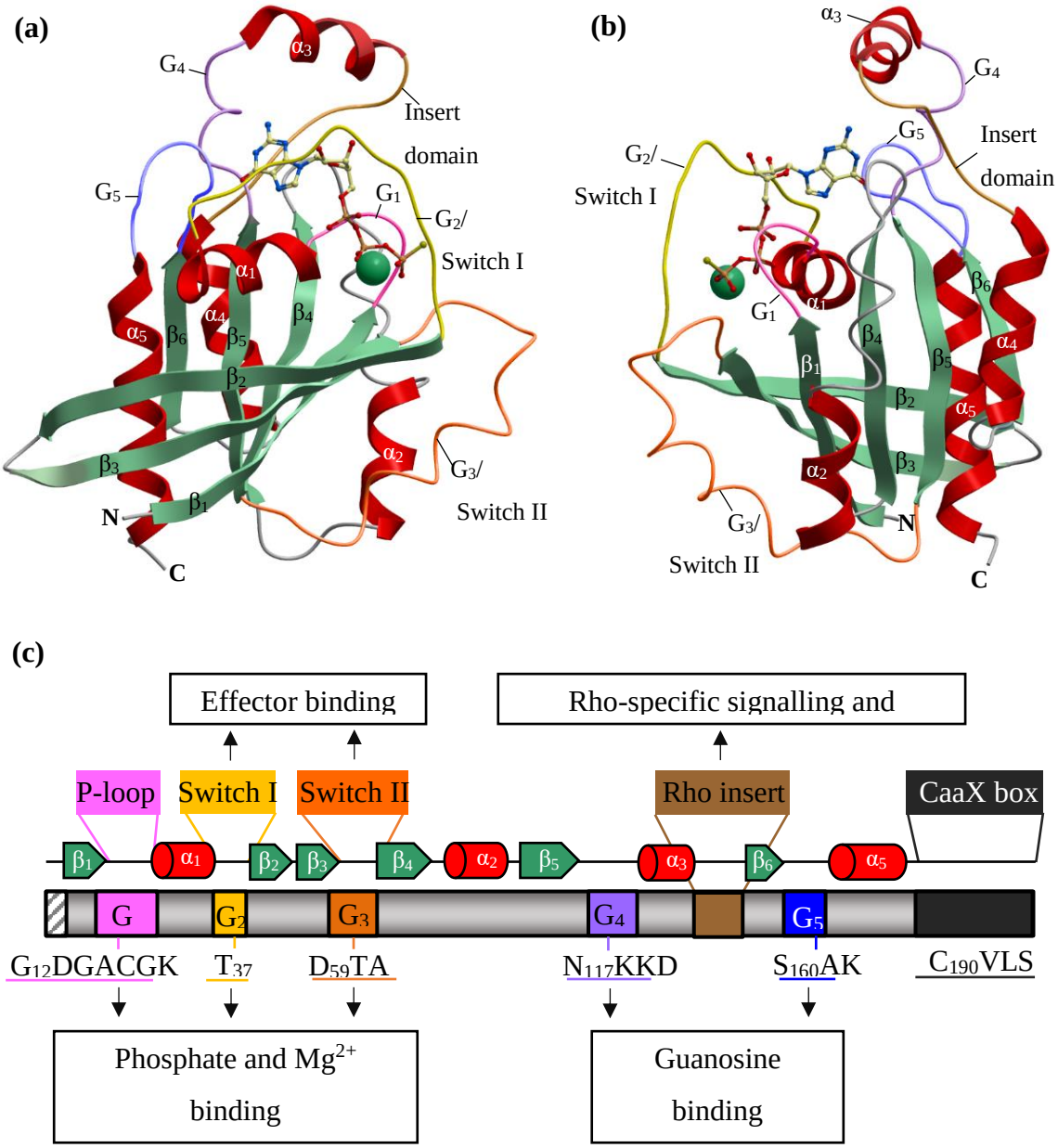

Figure 1.4. Typical structure of a 'classical' Rho sub-family member. Anterior **(a)** and posterior **(b)** three-dimensional model of human RhoA, a classical GTPase of the Rho sub-family, followed by a corresponding schematic diagram **(c)**. In (a) and (b), RhoA is bound to Mg^{2+} (green sphere) and the GTP analogue GSP. The GSP ligand adheres to the CPK chemical element colouring scheme as follows: Nitrogen (blue), Oxygen (red), Phosphorous (yellow). Critical areas are labelled accordingly, with beta strands displayed in green and alpha helices shown in red. Model generated in MolSoft MolBrowser version 3.8 (MolSoft L.L.C) from entry 1A2B of the RCSB PDB (53). In (c), an identical colour coding system has been adopted from the 3D structures (a) and (b), while the G domain as a whole is delineated as grey; the amino acid residues shown apply to H-Ras specifically.

1.2 Structure and function of classical Ras superfamily enzymes

1.2.1 Conserved regions of classical Ras superfamily enzymes

When comparing classical members of the Ras superfamily with atypical members, it is important to understand the conserved regions of the classical enzymes in some detail. As such, specific conserved regions will be examined in turn. Due to the presence of several atypical small GTPases within the Rho sub-family, the Rho-insert domain (unique to members of the Rho sub-family), will also be discussed here in further detail.

1.2.1.1 The G_1 loop (P loop)

The G_1 region, also known as the phosphate binding loop (or P loop), is composed of the following consensus sequence: GxxxxGK[S/T] (54). This loop region is vital for its role in the correct positioning and binding of alpha and beta phosphates in the guanine nucleotide, and is able to essentially 'wrap around' the guanine nucleotide phosphates, allowing nitrogen atoms of the main chain to interact with the negatively charged phosphates (55). Meanwhile, the lysine (K) of this motif exhibits a critical role in nucleotide binding *via* its ability to directly interact with the beta and gamma phosphate oxygens (55,56). The hydroxyl group of the serine or threonine located at the end of the motif is also involved with binding to the beta phosphate oxygen and the magnesium ion co-factor (55-57).

The initial glycine residue in this motif is classically located at position 12 (G12) and is commonly mutated to a valine in mutant oncogenic Ras proteins (58), rendering these mutants constitutively active (GTP-bound) (59). Due to the high conservation of certain residues in this motif (notably the initial glycine), the G_1 region is sometimes referred to as an identifying 'fingerprint' region (55).

1.2.1.2 The G_2 loop

The G_2 loop, also referred to as the switch I region or effector binding loop (60), contains a highly conserved threonine that is essential for binding divalent magnesium (55,61), a common co-factor for members of the Ras superfamily (61,62). In HRAS and several other Ras members, the G_2 motif is comprised of the following sequence: YDPTIEDSY (2,63). However, the G_2 motif shows a great degree of variation across the Ras superfamily, with some residues shared within sub-families but only the threonine (T) exhibiting strong conservation across the superfamily (2,37,55). The G_2 motif connects the α_1-helix to the β_2-strand of the classical G

domain (60) and mutations in the G_2 region of HRAS have been demonstrated to disrupt HRAS binding to downstream effectors (64-66).

1.2.1.3 The G_3 loop

Within the Ras superfamily, the consensus residue sequence for the G_3 motif is: DxxG (2,54,55). The aspartic acid (D) residue here is invariant amongst members of the Ras superfamily, playing a role in the binding of the co-factor magnesium (63). The G_3 motif glycine forms a hydrogen bond with the gamma-phosphate of GTP, securing nucleotide binding alongside residues of the G_1 motif (55,60,67).

1.2.1.4 The G_4 loop

The G_4 region (consensus sequence: [N/T]KxD) is primarily involved in recognising the non-phosphate areas of the guanine nucleotide (63). The conserved [N/T]KxD motif within this region, for example, interacts with the nucleotide guanine ring *via* the formation of hydrogen bonds; this confers specificity for GTP as a substrate, rather than ATP, and stabilises interactions with residues of the G_1 motif (55,63). This [N/T]KxD motif plays crucial roles in binding the guanine nucleotide ring (68). X-ray crystallographic structures of Ras (69) and the GTP-binding domains of other proteins (70-72) show that the asparagine (N) residue of this motif forms a hydrogen bond with the N7 atom of the guanine moiety, while the aspartic acid (D) residue forms hydrogen bonds with the N1 and N2 atoms. The lysine (K) residue is also known to directly bind to the guanine nucleotide (55). As such, the G_4 loop encompasses a critical region for the binding of the guanine nucleotide specifically, rather than other nucleotides.

1.2.1.5 The G_5 loop

The G_5 region, also known as the G_5 loop, contains the consensus sequence [S/C]A[K/L/T] in Ras and acts as a recognition site for the guanine base (61). The residues of this region are thought, mostly, to produce electrostatic or hydrophobic associations with the guanine nucleotide and are generally not well conserved across the Ras superfamily (55,61). Despite low sequence conservation amongst members of the Ras superfamily, however, previous studies have demonstrated an important role for the G_5 motif in influencing the intrinsic rate of GDP release from the G domain (73). The typically conserved alanine (A) within the G_5 domain appears critical in this sense and is thought to form hydrogen bonds with the 6-keto group of the guanine moiety (74), with substitutions of this residue producing an increased rate of guanine nucleotide exchange (75) and contributing to increased rates of neoplastic

transformation in somatic cells (76-78) or the manifestation of Costello syndrome in germline A146 HRAS mutants (79). Further to this, the threonine (T) residue observed in many G_5 regions appears to directly bind the guanine nucleotide (61), with substitution mutations in this residue shown to produce an accelerated rate of GDP release from the G domain (73).

1.2.1.6 The switch I and switch II regions

The switch I (Ras residues 30–38) and switch II (Ras residues 59–67) regions of the Ras superfamily exhibit significant conformational changes when a typical small GTPase transitions from the GDP-bound state to the GTP-bound state (2,46,63). Indeed, the switch regions typically demonstrate an increased general flexibility in x-ray structures and nuclear magnetic resonance (NMR) studies (46,69,80,81). As shown in Figures 1.3 and 1.4, the G_2 and G_3 regions comprise part of the switch I and II regions, respectively.

Interestingly, GDP-bound proteins often exhibit a much greater degree of structural diversity than GTP-bound proteins (55). In the GTP-bound form, two hydrogen bonds form between the gamma-phosphate oxygens to main chain NH groups of the highly conserved threonine (T) and glycine (G) present in switch I and switch II, respectively (Figure 1.5). This is sometimes referred to as the universal 'loaded spring' mechanism, where gamma-phosphate release following GTP hydrolysis allows the two switch regions to relax into the GDP-bound conformation (37). The extent of the conformational change between GTP and GDP-bound forms can vary significantly across the Ras superfamily (2,55). For some GTPases, additional elements may be involved. For example, Ran GTPases frequently exhibit a large conformational change in the switch I region involving the unravelling of an extra β-strand and the relocation of the COOH-terminal extension (sometimes referred to as the C-terminal switch) (82,83). Regardless of the extent of the conformational change, however, all conformational changes shown in classical small GTPases when transitioning between the GTP-bound and GDP-bound state are thought to be a consequence of the loaded spring mechanism (2,6,37,55).

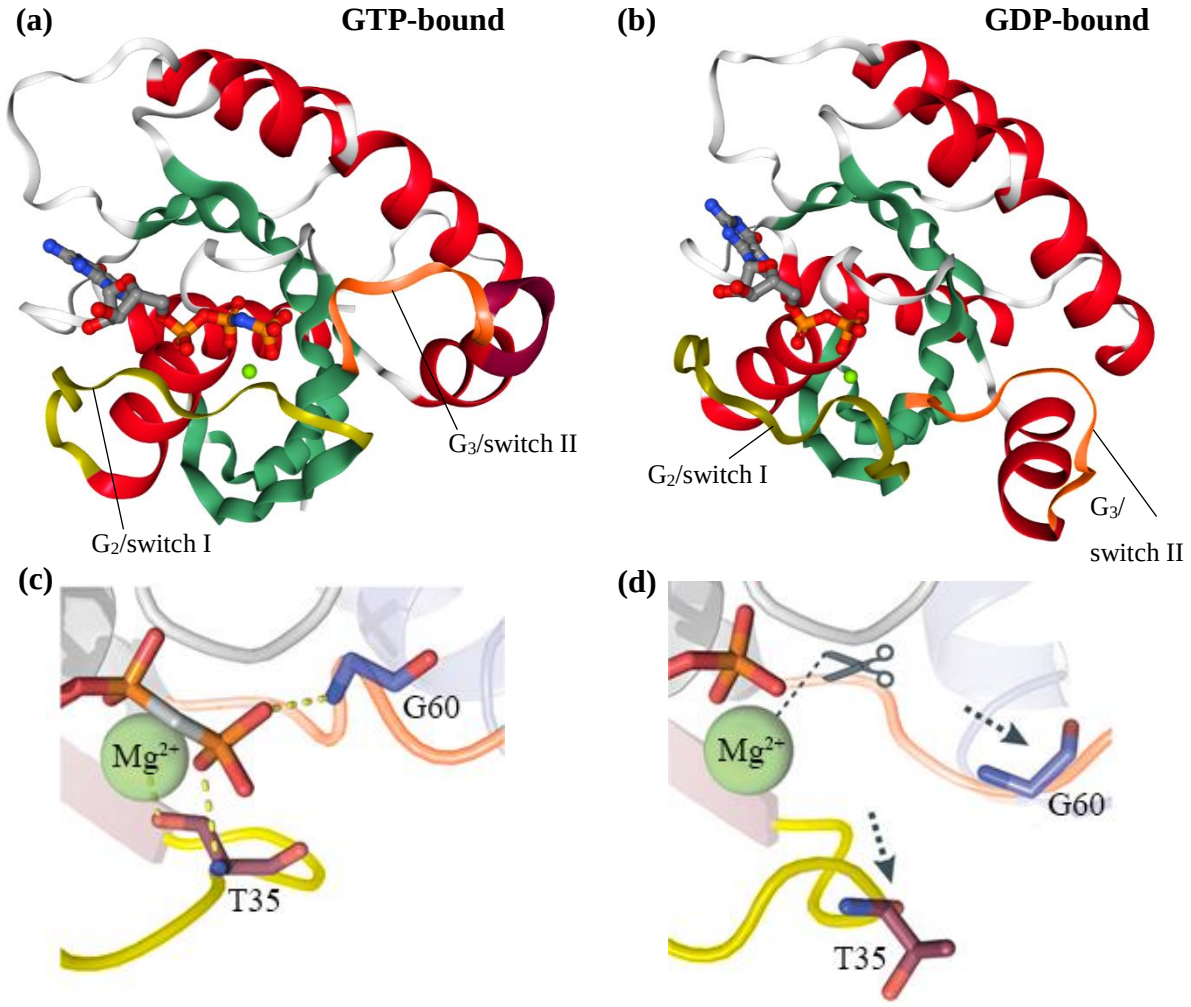

Figure 1.5. Differences between GTP- and GDP- bound versions of the classical Ras GTPase, HRas. 3D representations of **(a)** GTP-bound HRas (PDB: 5P21) and **(b)** GDP-bound HRas (PDB: 4Q21), where alpha helices are displayed in red and beta sheets shown in teal green. Close-ups of the interactions between key residues of the Switch I and II regions of a canonical Ras superfamily GTPase and the gamma phosphate of GTP are shown in **(c)** (GTP-bound GTPase) and **(d)** (GDP-bound GTPase). The switch I and II regions bind to the gamma phosphate *via* the main chain NH groups of the invariant threonine and glycine residues, producing a "loaded spring". Release of the gamma phosphate following hydrolysis of GTP enables the switch regions to relax into an alternative conformation. In all images, Mg^{2+} is shown as a green sphere, while the Switch I and Switch II regions are shown in yellow and orange, respectively. Not that (c) and (d) were adopted from (84).

1.2.1.7 Magnesium co-factor

Divalent magnesium (Mg^{2+}) has been well-established as a vital cofactor for many GTP-binding proteins, necessary for both GTP hydrolysis and guanine nucleotide binding (62,85). In the presence of Mg^{2+}, Ras shows a high binding affinity to the guanine nucleotides, exhibiting a dissociation constant on the order of sub-nanomolar concentrations (85-87). In some cases, EDTA-mediated removal of Mg^{2+} completely abrogates GTPγS binding capability (88,89) and intrinsic rates of GTP hydrolysis become undetectable in the absence of Mg^{2+} (86,88), indicating that Mg^{2+} is crucially required for the process of GTP hydrolysis by these GTPases. Indeed, the GEFs ARNO and Sos appear to stimulate GDP dissociation at least partially through destabilisation of bound Mg^{2+} from their respective GTPases (90-92).

1.2.1.8 The C-terminal CaaX box

The C-terminal CaaX box (or CaaX domain) represents a vital feature of many proteins of the Ras superfamily and particularly those of the Ras and Rho sub-families, allowing for the targeting of these enzymes to their site of action at the plasma membrane. This tetrapeptide sequence is recognised by farnesyltransferase and/or geranylgeranyltransferase I, and post-translationally modified by covalent addition of a farnesyl or geranylgeranyl isoprenoid to the CaaX cysteine, respective of the transferase in question. Other proteins of the Ras superfamily are modified for targeting to their site of action by alternative means.

1.2.2 Residues participating in nucleotide binding

Across classical members of the Ras superfamily, several highly conserved residues participating in nucleotide binding have been observed; for clarity, these are shown in Table 1.1, below. Additionally, an illustration of residues of the classical Rho GTPase Cdc42 involved in binding GCP (a non-hydrolysable analogue of GTP) is provided (Figure 1.6). Further discussion regarding these residues in the GTP hydrolysis mechanism employed by classical Ras superfamily GTPases is provided in 1.2.3. Note that some highly conserved residues, such as G12, play important roles in enabling GTP hydrolysis but may not directly engage in nucleotide binding (for instance, the oncogenic G12V mutation in Ras hinders the correct orientation of a water molecule required for hydrolysis, rendering the GTPase constitutively active).

Table 1.1. Commonly conserved residues participating in nucleotide binding amongst Ras superfamily enzymes (residue positions correspond to H-Ras).

Conserved residue (Ras)	Location	Role in nucleotide binding	Reference(s)
K16	G_1 loop	Interacts with β and γ phosphate oxygens	(55,69)
[S/T]17	G_1 loop	Interacts with β phosphate oxygens	(55-57)
F28	Switch I region	Stabilises nucleotide base	(93)
T35	G_2 loop /switch I region	Forms a hydrogen bond with the nucleotide γ phosphate	(37,55)
G60	G_3 loop/switch II region	Forms a hydrogen bond with the nucleotide γ phosphate	(94,95)
N116	G_4 loop	Forms hydrogen bond with N7 atom of guanine moiety	(55,69)
K117	G_4 loop	directly binds to guanine nucleotide	(55)
D119	G_4 loop	Hydrogen bonds with N1 and N2 atoms	(96,97)
A146	G_5 loop	Forms hydrogen bonds with 6-keto group of guanine moiety	(45,98)

(a) H-Ras

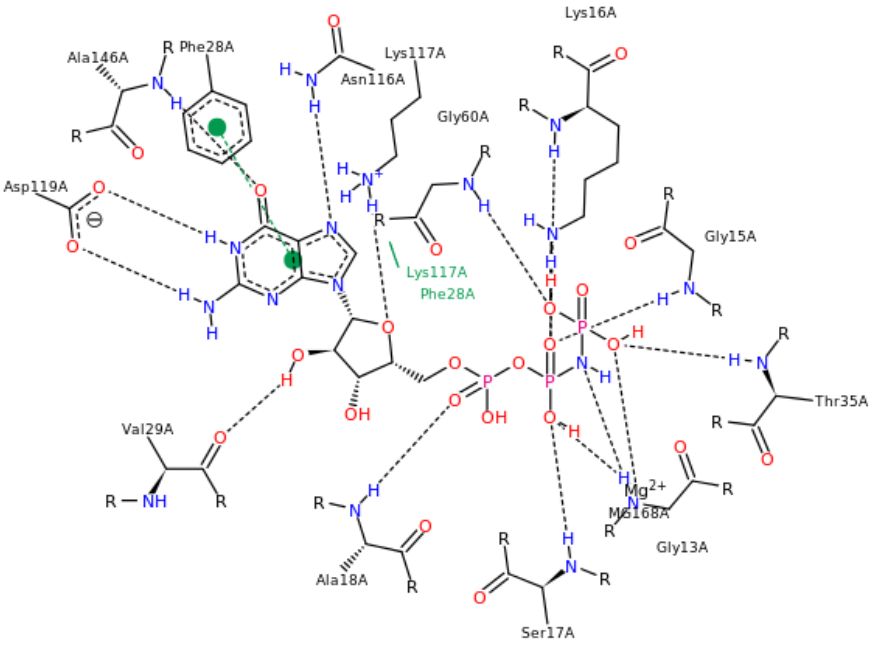

(b) Cdc42

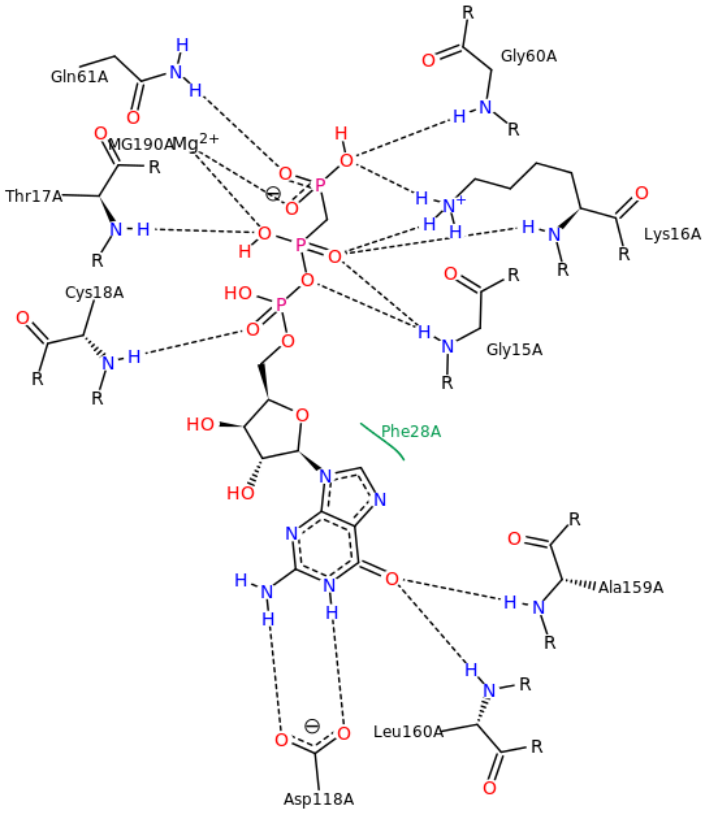

Figure 1.6. Residues participating in nucleotide binding in the classical Ras and Rho GTPase (a) H-Ras and (b) Cdc42. Note that black dashed lines indicate hydrogen bonds, salt bridges, and metal interactions. Green solid line show hydrophobic interactions and green dashed lines show π-π and π-cation interactions. Image derived from 2D interaction diagrams provided on the Protein Database (PDB) deposit for H-Ras (3TGP) and CdC42 (2QRZ) bound to non-hydrolysable analogues of GTP (GNP for H-Ras; GCP for Cdc42).

1.2.3 The GTP hydrolysis mechanism employed by classical Ras superfamily enzymes

Analysis of relevant crystal structures, alongside mutagenesis studies and computational modelling, have provided clarity on the mechanism of GTP hydrolysis employed by enzymes of the Ras superfamily (61,99). A number of key residues have been identified in the active site of Ras superfamily GTPases that directly or indirectly participate in GTP hydrolysis, including: G61, K16, T35 and G60 (100-102). Further comprehension of the Ras GTPase hydrolytic reaction has been made possible by elucidation of crystal structures in the presence of aluminium or magnesium trifluoride, which imitate the hydrolysed γ-phosphate before dissociation and therefore model the reaction transition state (102-104). Taken together, the abundance of data available enables a deeper understanding of the GTP hydrolysis mechanism employed by Ras superfamily enzymes. However, some controversies remain (54,61,99,105,106). It should also be noted that the intrinsic hydrolytic activity of Ras superfamily GTPases is highly inefficient (54,61), exhibiting about 1% of the average reaction rate of heterotrimeric G proteins (54). Consequently, small GTPases typically require interaction with a GAP enzyme to undergo efficient hydrolysis (41,42).

In canonical Ras enzymes, GTP hydrolysis is believed to occur through direct transfer of the GTP γ-phosphate group to H_2O, with a significant role in catalysis undertaken by a glutamine (Q) in the switch II loop, directly adjacent to the G_3 loop (typically present at position 61 in classical Ras and Rho GTPases), which acts as a catalytic base to activate a H_2O molecule for nucleophilic attack (61). Analysis of relevant crystal structures show that the H_2O molecule is located no further than 4 Å from the γ-phosphate group of GTP and is oriented for the nucleophilic attack *via* hydrogen bonding with the γ-phosphate and carbonyl of the invariant threonine (typically at position 35) of the G_2 loop (107). Indeed, analysis of the Ras-RasGAP complex indicates that RasGAP acts to catalyse GTP hydrolysis by stabilising the position of glutamine 61 of Ras (104), and mutations of this glutamine residue are known to significantly impair GTP hydrolysis (105). However, this glutamine residue appears too weak a base to accept a proton (61); indeed, while this residue is capable of stabilising the pentavalent intermediate state in the GTP hydrolysis reaction (105,108), it is generally accepted that the γ-phosphate group of GTP itself accepts the proton in a mechanism known as ‘substrate-assisted catalysis’ (106), with the reaction proceeding as an associative in-line transfer of the phosphate group with a pentavalent intermediate

and an inversion of configuration of stereochemistry (99). In this associative transfer, a negative charge accumulates on the γ-phosphate, an event that is directly followed by hydrolysis of the bond between the β and γ-phosphate with a charge transition to the β-phosphate (61). However, a dissociative mechanism has also been previously suggested, assuming that the first catalytic step is the disruption of the bond between β- and γ-phosphate (61,99).

As previously mentioned, $GDP{\cdot}Mg^{2+}{\cdot}AlF4^{-}$ (or AlF_3OH^{-}) complexes are stable transition state analogues that preserve the ability for sustained interaction with GAP enzymes and are identical to the pentacoordinate intermediate state (109,110). Crystal structures of these complexes indicate that the carboxyamide group of the switch II glutamine (typically present at position 61 in canonical ras and Rho proteins) is capable of polarising and orienting the nucleophilic H_2O molecule in the transition state for GTP hydrolysis (70). The presence of the 'arginine finger' in Ras and Rho GAP enzymes stabilises the transition state by neutralising the developing negative charge at the γ-phosphate (111). Further analysis by *in silico* methods have additionally revealed that, upon GTP binding, re-orientation of the lysine (K), glycine (G) and valine (V) amides of the p-loop (typically at positions 16, 15 and 14, respectively) forces the GTP molecule into a strained, inflexible conformation (112). This leads to a charge redistribution, with the negative charge of the γ-phosphate transferred to the β-phosphate group, decreasing the energy of transition activation barrier for the intermediate state of the reaction (113). According to comparisons of crystal structures and mutagenesis studies, the scheme of GTP hydrolysis employed by the G protein Giα1 appears to be highly similar to that utilised by many canonical enzymes of the Ras superfamily (61,70,99,102,107,109,110,112); this scheme has been displayed as Figure 1.7. For ease of understanding, an additional schematic illustration (Figure 1.7) is provided; Figure 1.8 displays GAP-mediated hydrolysis in Ras superfamily enzymes specifically.

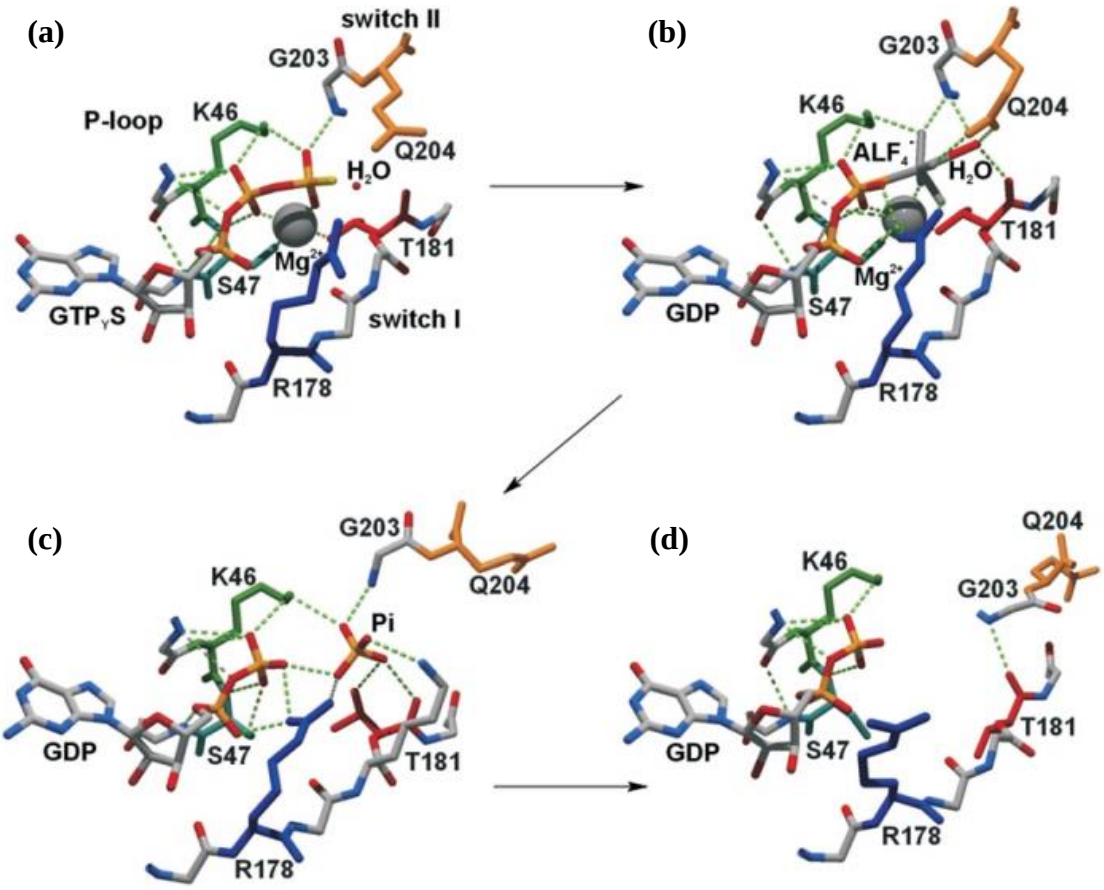

Figure 1.7 Mechanism of GTP hydrolysis employed by the Giα1 G domain. The mechanism of GTP hydrolysis employed by canonical Ras and Rho enzymes is thought to follow the general scheme displayed above, albeit with the R178 residue supplied by Ras and Rho GAP enzymes. In **(a)**, the Giα1 enzyme is in the 'on' (GTP-bound) conformation (Giα1·GTPγ·Mg^{2+} enzyme-substrate complex; PDB 1gia). Here, a H_20 molecule is located merely 3.8Å from the γ-phosphate of GTP and oriented for a nucleophilic attack. In **(b)**, a Giα1·GDP·AlF_4^-·Mg^{2+} intermediate state model is shown (PDB 1gfi), with the AlF_4^- forming an octahedral complex where the γ-phosphate and a H_20 molecule are placed in transaxial positions. In this figure, an arginine (donated by GAP proteins in Ras and Rho reactions) forms hydrogen bonds with the pentacoordinate intermediate and the oxygen bridging the phosphates, while the switch II glutamine and switch I threonine (Q61 and T35 in canonical Ras and Rho enzymes) are placed so that the attacking H_2O molecule is polarised and well-oriented. In **(c)**, the Giα1·GDP·Pi enzyme-products complex is shown (PDB 1git). The switch II glutamine is displaced and the Mg^{2+} coordination sphere disrupted. Meanwhile, an arginine (donated by GAP in Ras and Rho reactions) forms hydrogen bonds with β-phosphate and Pi. The threonine of G_2 and its preceding lysine (not marked) re-orient and form hydrogen bonds with Pi. Conformational changes occur in switch I and switch II. In **(d)**, the Giα1·GDP complex is shown (PDB 1gg2). Switch II is disordered and switch I moves away from the nucleotide due to loss of the Mg^{2+} ligand. The catalytic site is disrupted. Figure adopted from Paduch and colleagues (61).

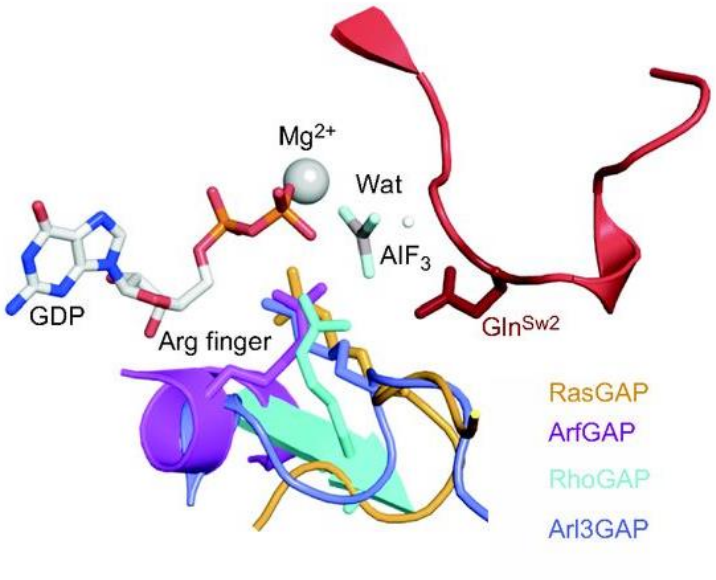

Figure 1.8. Mechanism of GAP-mediated GTP hydrolysis in classical Ras and Rho enzymes. The canonical arginine finger/switch II glutamine mechanism is shown. GAP provides an arginine (the arginine finger) to stabilise the partial negative charges that develop at the transition state and positions the conserved glutamine at position one to activate a water molecule (wat) for nucleophilic attack of the GTP γ-phosphate. The arginine fingers from representative structures of RasGAP, ArfGAP, RhoGAP, and Arl3GAP in complexes with their corresponding GTPase are overlaid. For clarity, the conserved glutamine from the DTAGQ motif of the G_3 loop/switch II region (in red) is shown only for Ras. The term 'wat' represents the nucleophilic water molecule. Figure derived from Cherfils and Zeghouf (41).

1.3 Atypical members of the Ras superfamily

Classical GTPases of the Ras superfamily, such as the Rho subfamily proteins Cdc42, Rac and RhoA, follow the canonical GEF/GAP/GDI scheme of regulation (Figure 1.2) and largely retain the classical structural characteristics described in section 1.1. Many of these – particularly the former three – have been extensively studied, with structures defined by x-ray crystallography (104,114-116) and NMR (117-120). However, while classical GTPases are distinguished by the characteristics described above, several 'atypical' small GTPases exist that exhibit structural deviation from archetypical small GTPases and may follow alternative schemes of regulation (30). The atypical members will be discussed in the following sub-sections.

1.3.1 Atypical members of the Ras superfamily: an overview

As aforementioned, some GTPases of the Ras superfamily exhibit unique structural or functional features relative to their classical counterparts, making it appropriate to classify them as 'atypical'. The majority of these atypical proteins reside in the Rho subfamily (30). Rho GTPases are archetypically considered critical regulators of the actin filament system and therefore heavily involved in cell migration and morphology (2,30). As shown in Figure 1.9, the Rho subfamily is comprised of 20 members classified into 8 further sub-families. Out of these 8 sub-families, Rnd, Wrch-1/Chp, RhoH and RhoBTB are considered atypical relative to the Rho, Rac, Cdc42 and RhoD/RhoF subfamilies. Additionally, two atypical proteins previously regarded as Rho GTPases have been allocated to their own sub-family: the Miro sub-family (see section 1.4). Beyond atypical Rho proteins, other small GTPases that may be regarded as atypical include the Rad/Gem/Kir (RGK) families of the Ras sub-family (121) and the centaurins, which are not typically included as members of the Ras superfamily but contain GTPase domains (60,122).

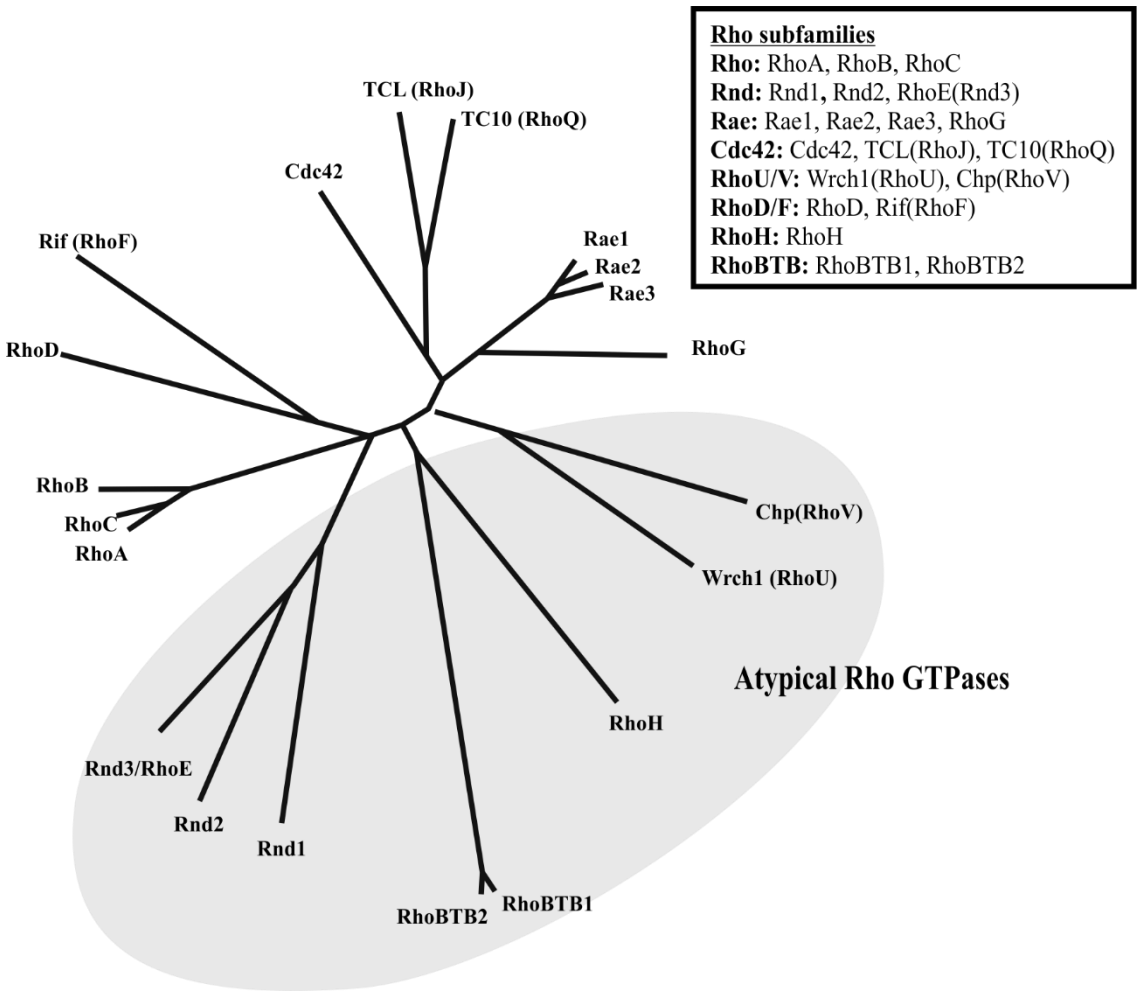

Figure 1.9. GTPases of the Rho sub-family, with atypical members highlighted. Unrooted dendritic-tree representation of the human Rho GTPases. The atypical Rho GTPases are distinguished by the grey circled area. The Rho GTPases can be further sub-dividied into 8 additional sub-families or divisions (as shown in the boxed area at the top left). Figure adopted from Aspenstrom *et al*., 2007 (30).

Atypical GTPases of the Ras superfamily may be distinguished from classical small GTPases in a number of ways (30,60). For example, GTP cycling is sometimes completely inapplicable to atypical GTPases. The atypical Rnd proteins and RhoH are GTPase deficient, remaining constitutively in the GTP-bound state (123,124). It is currently thought that this GTPase deficiency may also be associated with the RhoBTB GTPases (125), though RhoBTB2 has been shown to bind GTP (126) and RhoBTB3 appears to bind ATP rather than GTP (127). Too, Wrch-1 and the Rac1 splice variant Rac1b appear to exist primarily in the GTP-bound conformation, bypassing the classical scheme of GTPase activation and deactivation (30). In fact, the regulation of atypical GTPases rarely adheres to the simple GAP/GEF/GDI scheme described in Figure 1.2 (section 1.1). Very few GAPs, GEFs and GDIs have been identified which interact with

atypical GTPases of the Ras superfamily (30,60,128). Instead, these GTPases may be regulated by alternative means, such as protein:protein interactions involving domains not present in classical Ras superfamily members (30). Several of these proteins are also known to be regulated at the level of transcription (123,124), or through targeted destruction (7,124,129,130).

In addition to this, atypical small GTPases often exhibit functional deviations from their classical counterparts; they are often involved in dissimilar signalling pathways to classical small GTPases and may interact with unique binding partners (17,30,124). Perhaps most strikingly, some atypical GTPases of the Ras superfamily exhibit unusual domains not seen amongst classical member (Figure 1.10). For example, the atypical Miro GTPases contain two GTPase domains, in addition to calcium-binding EF hand domains (131). Furthermore, several residues normally strongly conserved in classical Ras superfamily GTPases (such as those in the G_1–G_5 loops and switch regions) may be substituted or absent in atypical Rho GTPases (see Figure 1.10 and correspondingly, Table 1.2 – Table 1.4). For example, Figure 1.11 indicates that the invariant T35 in the G_2 region is absent in the GTPase domains of both hMiro1 and hMiro2. Furthermore, G60 is replaced by a glutamic acid residue in the hMiro1 GTPase domains and the hMiro2 N-terminal GTPase domain. The Q61 residue required for crucial re-orientation of H_2O (see section 1.2.3) is also substituted in all atypical Rho proteins shown in Figure 1.11. Despite stark differences between the atypical and classical Rho GTPases, however, the unusual 'atypical' proteins appear to engage in crucial cellular functions and are implicated in serious human pathologies such as myeloproliferative disorders (31-33) and neurodegeneration (34,129,132). Further understanding of these proteins and their cellular functions is therefore highly medically relevant.

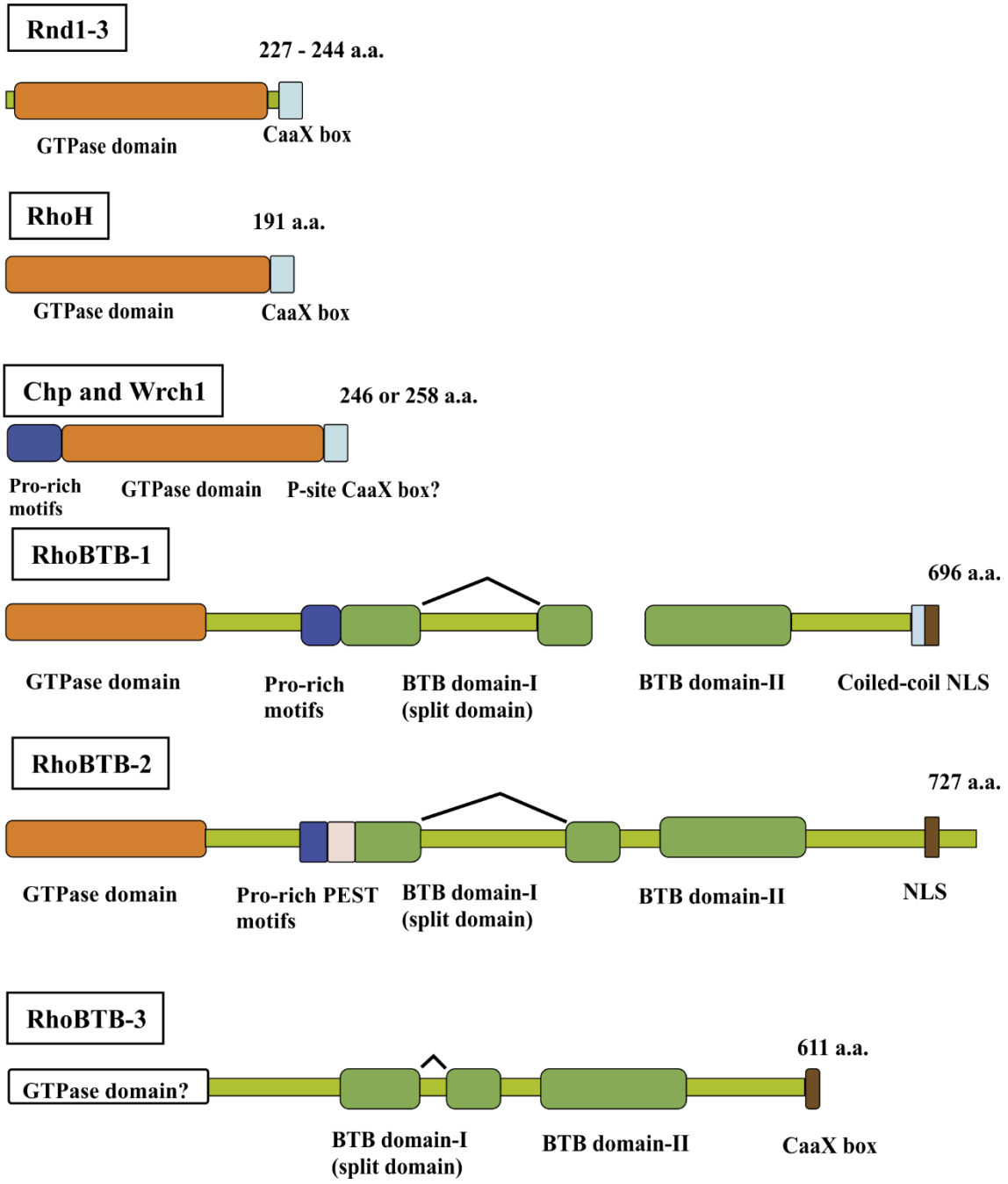

Figure 1.10. Schematic representation of a selection of atypical GTPases of the Ras superfamily. Schematic diagrams of the atypical Rho GTPases are shown. The CAAX (Cystein–Aliphatic–Aliphatic–Any amino acid) box is targeted by post-translational modification for targeting to the plasma membrane. However, the CAAX box of Wrch-1 may not be functional. The term 'P-site' denotes palmitoylation site, whereas 'BTB' domain represents what is known as the Broad complex/Tramtrack/Bric-a-brac domain. The term 'NLS' denotes nuclear localisation site. PEST (Proline–Glutamic acid–Serine–Threonine) is a motif associated with protein stability. The abbreviation 'a.a.' denotes amino acid residues. Figure adopted from a review by Aspenstrom and colleagues (30).

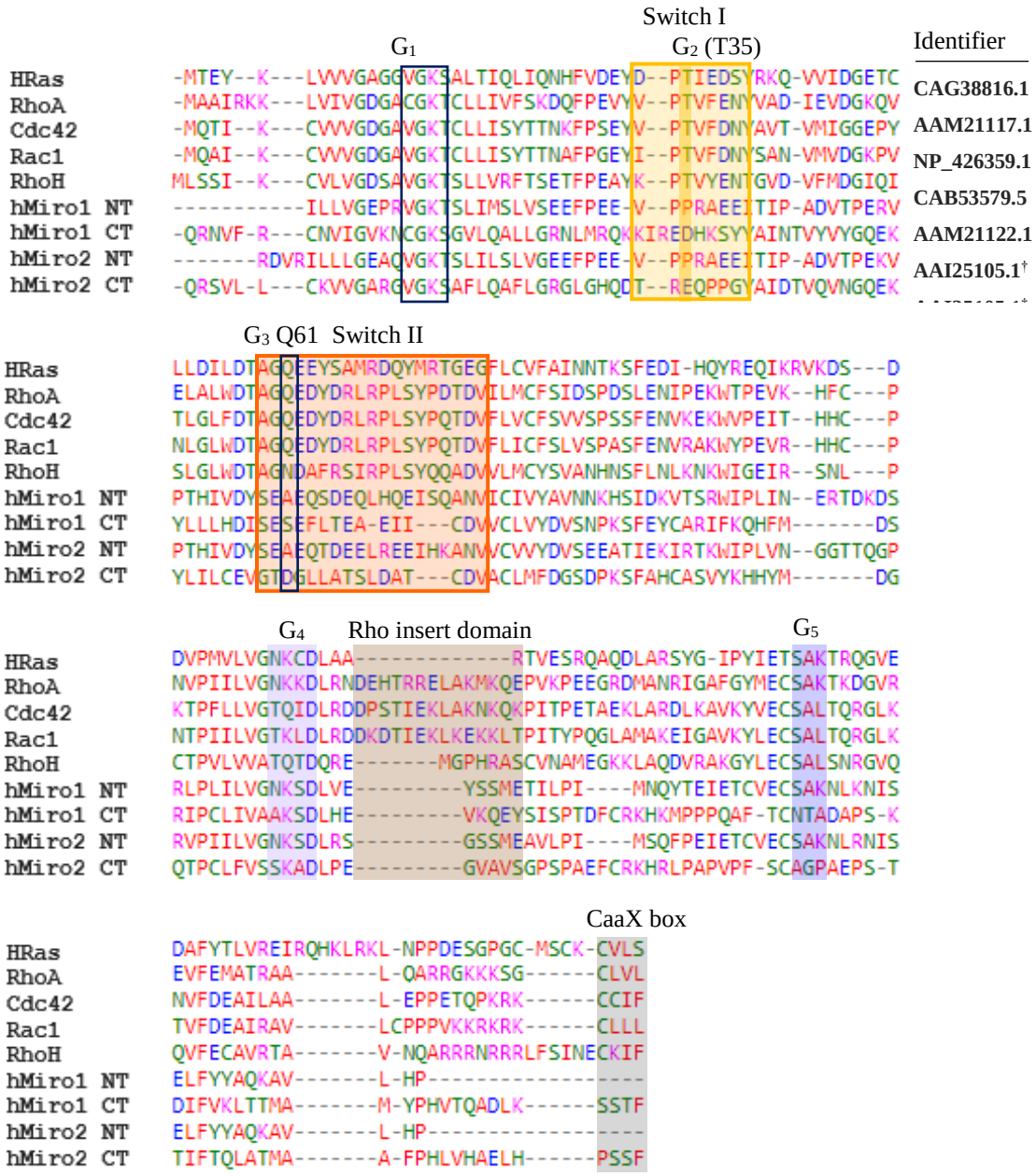

Figure 1.11. Amino acid sequence alignment showing differences between select classical Ras superfamily GTPases and the atypical Rho GTPases studied herein. NCBI identifiers are shown for each protein. Residue colouring specifies the following: red indicates small and hydrophobic residues, blue represents acidic residues, magenta marks basic residues and green shows residues bearing hydroxyl, sulphydryl or amine groups. * Residues V14, K16 and [S/T]17, as dicussed in section 1.2.3; †Residues 7–169 of hMiro1, representing the N-terminal GTPase domain; ‡Residues 415–592 of hMiro1, representing the C-terminal GTPase domain; §Residues 3–169 of hMiro2, representing the N-terminal GTPase domain; ‖ Residues 413–589 of hMiro2, representing the C-terminal GTPase domain.

Table 1.2 Differences in the G domain loop regions: classical versus atypical Ras superfamily enzymes.

Protein	Identifier	G_1	G_2	G_3	G_4	G_5
----	Consensus sequence	GxxxxGK[S/T]	T	DxxG	[N/T]KxD	[S/C]A [L/T/K]
HRas	CAG38816.1	GAGGVGKS	T	DTAG	NKCD	SAK
RhoA	AAM21117.1	GDGACGKT	T	DTAG	NKKS	SAK
Cdc42	NP_426359.1	GDGAVGKT	T	DTAG	TQID	SAL
Rac1	CAB53579.5	GDGAVGKT	T	DTAG	TKLD	SAL
RhoH	AAM21122.1	GDSAVGKT	T	DTAG	TQTD	SAL
hMiro1 NT	AAI25105.1: 7-169	GEPRVGKT	P	DYSE	NKSD	SAK
hMiro1 CT	AAI25105.1: 415-592	GVKNCGKS	D	DISE	AKSD	NTA
hMiro2 NT	AAI25105.1: 3-169	GEAQVGKT	P	DYSE	NKSD	SAK
hMiro2 CT	AAI25105.1: 413-589	GARGVGKS	E	CEVG	SKAD	AGP

Table 1.3 Differences in the switch regions and CaaX box: classical versus atypical Ras superfamily enzymes.

Protein	Identifier	Switch I	Switch II	CAAX box
HRas	CAG38816.1	D--PTIEDSY	AGQEEYSAMRDQYMRTGEG	CVLS
RhoA	AAM21117.1	V--PTVFENY	AGQEDYDRLRPLYSPDTDV	CLVL
Cdc42	NP_426359.1	V--PTVFENY	AGQEDYDRLRPLSYPQTDV	CCIF
Rac1	CAB53579.5	I--PTVFENY	AGQEDYDRLRPLSYPQTDV	CLLL
RhoH	AAM21122.1	K--PTVYENT	AGNDAFRSIRPLSYQQADV	CKIF
hMiro1 NT	AAI25105.1: 7-169	V--PPRAEEI	SEAEQSDEQLHQEISQANV	----
hMiro1 CT	AAI25105.1: 415-592	KIREDHKSYY	SESEFLTEA-EII---CDV	SSTF
hMiro2 NT	AAI25105.1: 3-169	V--PPRAEEI	SEAEQTDEELREEIHKANV	----
hMiro2 CT	AAI25105.1: 413-589	T--REQPPGY	GTDGLLATSLDAT---CDV	PSSF

Table 1.4 Differences in the Rho insert domain: classical versus atypical Ras superfamily enzymes

Protein	Identifier	Rho insert domain
HRas	CAG38816.1	--------------
RhoA	AAM21117.1	DEHTRRELAKMKQE
Cdc42	NP_426359.1	DPSTIEKLAKNKQK
Rac1	CAB53579.5	DKDTIEKLKEKKLT
RhoH	AAM21122.1	-------MGPHRAS
hMiro1 NT	AAI25105.1: 7-169	---------YSSME
hMiro1 CT	AAI25105.1: 415-592	---------VKQEY
hMiro2 NT	AAI25105.1: 3-169	---------GSSME
hMiro2 CT	AAI25105.1: 413-589	---------GVAVS

Before proceeding, it is noteworthy to mention that some members of the Ras superfamily appear to act somewhat atypically, but retain classification as typical small GTPases. An example is the SRβ sub-unit of the eukaryotic signal recognition particle receptor that targets ribosome-nascent polypeptide chain complexes to the endoplasmic reticulum (133). SRβ forms the eukaryotic signal particle receptor alongside SRα (134). Although both SRα and SRβ are GTPases, SRα belongs to the SIMBI ('SRP, MinD, BioD') class of GTPases (135), while SRβ is classified as a member of the Arf sub-family of the Ras superfamily (133). SRβ may be mistakenly regarded as atypical for three main reasons. Firstly, SRβ is the only member of the Arf family that is permanently membrane-anchored by an N-terminal membrane anchor (136); meanwhile, other Sar1 and Arf proteins are transiently attached to the membrane in their GTP-bound state (137). Secondly, in contrast to the majority of Ras superfamily GTPases, which act monomerically, SRβ is active only as a heterodimer with SRα (133), and may form self-regulatory homodimers which are unable to bind SRα (138). Thirdly, the GTPase switch cycle mechanism of SRβ varies somewhat from that seen in other Arf members (133).

Despite the characteristics outlined above, SRβ is considered a classical small GTPase because it retains many classical characteristics seen in other members of its sub-family, including structural similarities and a partly-shared switch cycle mechanism. Indeed, akin to classical Ras superfamily GTPases, SRβ cycles between active GTP-bound and inactive GDP-bound conformations (139,140). Furthermore, the function of SRβ does not diverge from that of other Arf proteins (targeting of macromolecular complexes to secretory membranes) and the regulation of SRβ does not differ significantly from other Arf proteins (133). Moreover, inherent variances exist within the Arf sub-family that are believed to correlate with the specific roles of each Arf member in targeting macromolecular complexes to secretory membranes; this provides an explanation for many of the peculiarities observed in SRβ (133). In short, while SRβ does exhibit some atypical features, it is not sufficiently unusual with regards to structure, function and regulation relative to other members of its sub-family. Meanwhile, the atypical Rho GTPases discussed above display highly unusual structural, functional or regulatory features relative to classical GTPases of the Rho sub-family.

1.3.2 Known example of atypical Ras superfamily GTPases: the RhoBTB proteins

The RhoBTB proteins comprise a subfamily of three known atypical Rho GTPases in humans: RhoBTB1, RhoBTB2 and RhoBTB3 (128,141). Identified in 2001 by Rivero

and colleagues (125), the RhoBTB family are large (~80 kDa) and comprised of an N-terminal GTPase domain followed by a proline rich region, a tandem of two broadcomplex, tramtrack, bric-a-brac (BTB) domains, and a conserved C-terminal region (128,142). In humans, RhoBTB1 and RhoBTB2 exhibit a high degree of amino acid sequence identity, while RhoBTB3 is considerably diverse (128).

The RhoBTB proteins may be distinguished as truly atypical Rho GTPases for three reasons. Firstly, the RhoBTB proteins possess a highly atypical domain architecture, featuring domains that are quite distinct from anything else seen within the Ras superfamily (128,142). Secondly, the cellular roles of the RhoBTB proteins are distinct from the roles typically adopted by Rho GTPases (namely, reorganisation of the actin cytoskeleton) (127,143-147). Thirdly, regulation of RhoBTB activity may evade the classical scheme of Ras superfamily regulation altogether; current evidence suggests that the RhoBTB proteins exist in an auto-inhibitory state, and that regulation may not involve interaction with specific GEFs and GAPs, but rather with other proteins that relieve the RhoBTB auto-inhibited conformation, followed by auto-ubiquitination and destruction by the proteasome (128,148).

As aforementioned, the structure of the RhoBTB proteins is highly atypical relative to classical Rho GTPases (Figure 1.10) (128). The BTB domains exhibited by these proteins are not typically observed in classical Rho GTPases (128). In humans, nearly 200 different proteins contain BTB domains, usually in combination with other domains. The BTB domain is a protein:protein interaction domain engaging in homomeric and heteromeric associations with other BTB domains (149), and RhoBTB proteins are also capable of forming both homodimers and heterodimers (148). However, the BTB domains found within the RhoBTBs exhibit unique features: a tandem of two BTB domains is not found elsewhere within the BTB protein family (150). Furthermore, the first BTB domain observed in the RhoBTB proteins is bipartite, being disrupted by an extension of unknown function that is rich in charged residues (128).

The C-terminal region of RhoBTB1, RhoBTB2 and RhoBTB3 are also unusual compared with canonical Rho GTPases (128,150). This region may constitute a novel domain altogether, as it has not been identified in any other human proteins beyond the RhoBTB subfamily (128,150). The core of this unusual C-terminal domain comprises approximately 80 amino acid residues folding as four consecutive α-helices. In RhoBTB1 and RhoBTB2, this region is predicted to end in a β-strand (151). Neither RhoBTB1 nor

RhoBTB2 contains a CaaX box, as typically observed in classical Rho GTPases (2,128). However, the C-terminal region of RhoBTB3 appears to end with a CaaX motif, suggested that it may be targeted for post-translational modification in a similar manner to classical Rho GTPases (148,152).

The GTPase domains of RhoBTB1 and RhoBTB2 are Rho-related, but comprise atypical features, including: an unusually long Rho insert region compared with classical Rho GTPases, two insertions placed one immediately prior to switch I, and a two-residue deletion affecting switch II phosphate/magnesium binding (128). Additionally, the glycine residue at position G12 in Ras appears substituted by asparagine (128). These alterations do not appear to prevent GTP binding in RhoBTB1 and RhoBTB2 (126). Intriguingly, however, the GTPase domain of RhoBTB3 varies considerably from the other RhoBTBs, exhibiting the capability to bind ATP by virtue of some crucial amino acid substitutions in the G_4 and G_5 loops (127). Notably, despite the differences between RhoBTB3 and the other RhoBTB proteins, phylogenetic studies indicate that RhoBTB3 should indeed reside within the RhoBTB subfamily (128,142).

Several cellular roles have been proposed for the RhoBTB proteins. As aforementioned, however, these roles are distinct from what would typically be observed in classical Rho GTPases (128). Indeed, no interaction was observed between the RhoBTB proteins and the GTPase-binding domains of WASP, PAK1 or Rhotekin, three well-established effectors of many typical Rho GTPases (143). Furthermore, the RhoBTB proteins do not appear to play a major role in reorganisation of the actin cytoskeleton (143). Instead, interest in the RhoBTBs as potential tumour suppressors emerged when RHOBTB2 (also known as DBC2, deleted in breast cancer 2), was identified as the gene homozygously deleted in breast cancer samples (153). Subsequent investigations reinforced the association of RhoBTB proteins in tumorigenesis (154,155), though recent studies have also implicated the RhoBTBs in cell growth (145,147,153,156), apoptosis (157), chemokine expression (146) and vesicular transport (127,144). The first BTB domain of all three RhoBTB proteins is now also known to interact specifically with cullin 3, forming cullin-3 dependent ubiquitin ligase complexes capable of targeting proteins for ubiquitination and subsequent proteasomal degradation (148).

Regulation of the RhoBTB proteins does not appear to occur through the GAP/GEF/GDI scheme utilised by typical members of the Ras superfamily. Indeed, an autoregulatory model for RhoBTB proteins has been proposed (148), stipulating that RhoBTB proteins

exist in an inactive state through an intramolecular interaction of the first BTB domain with the GTPase domain, preventing binding to cullin 3 and the formation of a ubiquitin ligase complex (148). The model suggests that interaction of RhoBTB with other proteins (including potential substrates) leads to alleviation of the autoinhibitory state and facilitates binding to cullin-3 (148).

To conclude, while the RhoBTB proteins each contain a GTPase domain exhibiting similarities to the classical Rho GTPases (therefore qualifying them as Rho proteins), the RhoBTBs are highly unusual relative to classical Rho proteins with regards to domain architecture, function and regulation: consequently, the RhoBTB proteins can be regarded as atypical Rho GTPases.

1.4 Miro GTPases

1.4.1 The Miro GTPases at a glance

Initially characterised as atypical Rho GTPases (29), the Miro GTPases ('mitochondrial Rho GTPases') are so unusual that it is now considered appropriate to classify them into a separate sub-family: the Miro sub-family (142,158,159). Two genes encoding Miro GTPases are present in humans: Miro1 and Miro2 (also referred to as RhoT1 and RhoT2). Both human Miros consist of 618 amino acid residues, sharing 60% amino acid identity (29). As schematically illustrated in Figure 1.12, the Miro GTPases are comprised of two GTPase domains flanked by a pair of Ca^{2+} binding EF hand domains (29,131,132,158,160,161). Anchored to the mitochondrial outer membrane (MOM) by means of a C-terminal transmembrane sequence (162), the Miro proteins are accessible to the cytoplasm, where they appear to be involved in a variety of mitochondrial-related processes including the transportation, motility, morphology and homeostasis of mitochondria (97,132,163-166). Considering the importance of healthy mitochondria in neuronal function, in addition to the strong implication of dysfunctional mitochondria in neurodegenerative and psychiatric disorders such as Alzheimer's disease (AD), Parkinson's disease (PD) and schizophrenia (167-171), a comprehensive understanding of the Miro proteins is of great medical relevance.

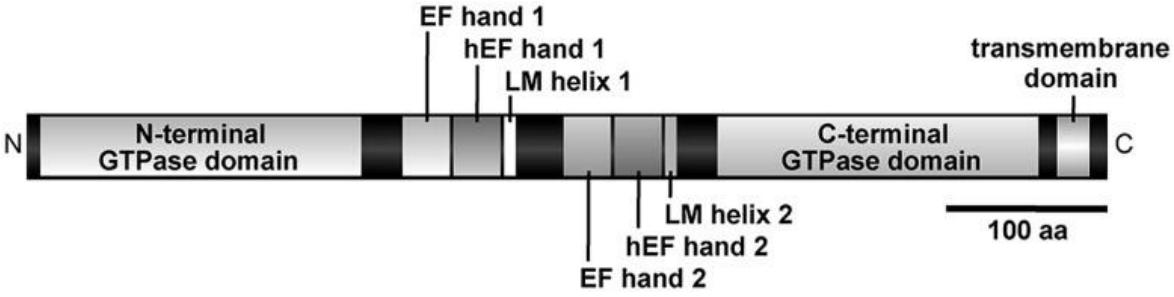

Figure 1.12. Schematic representation of Miro GTPase structure. Schematic illustration of the molecular structure of Miro GTPases according to findings on the structure of Drosophila Miro (131).

1.4.2 Molecular structure of Miro GTPases

As shown in Figure 1.12, the Miro GTPases contain a C-terminal transmembrane domain required for targeting to the mitochondrial outer-membrane (MOM), where they are anchored at the C-terminus with the majority of the protein accessible to the cytoplasm

(159,162). The cytoplasmic region of these proteins comprises two structurally distinct GTPase domains, flanked by a pair of calcium-binding EF-hands. Of these GTPase domains, the N-terminal GTPase domain is the most well-studied, and structurally most similar to Rho GTPases (29). Conversely, the C-terminal GTPase domain appears most structurally similar to Rheb, a protein of the Ras sub-family (131,172). Despite the N-terminal GTPase domain's similarity to Rho GTPases, initial classification of the Miro GTPases as members of the Rho sub-family was disregarded when both GTP domains were found to lack the conserved Rho G3 DxxG motif (54,173) and Rho-specific insert helix (29,162), a surface-exposed alpha-helical domain unique to the Rho GTPases (174,175). A dot blot overlay assay confirmed that the two EF hand domains of Miro are able to bind Ca^{2+} (164) and the bordering regions of these EF hand domains appear to be highly conserved amongst eukaryotes (131,160). A recent crystallographic study showed that these bordering regions contain non-canonical 'hidden' EF hands (hEF hands) proceeded by single helices (LM helices 1 and 2) in the single Drosophila Miro orthologue, dMiro (131). In dMiro, these hEF hands exhibit a helix-loop-helix structure capable of stabilising local EF hands *via* formation of an anti-parallel EF hand β-scaffold. The structure of the LM helices, however, is similar to that of extrinsic ligands bound to EF hand proteins, as described for the protein complexes of moluscan myosin heavy chain and light chain (131,176), as well as Troponin I and Troponin C (177). This combination of EF-hEF hands followed by an LM helix has been observed in a variety of other Ca^{2+} binding proteins, including the retinal protein recoverin (178,179), the pollen protein polcalcin (180) and GCAP3, a human guanylate cyclase-activating protein (181). Similar to other EF-hand containing proteins, it has been suggested that the Miros may require interaction partners in order to undergo conformational changes.

1.4.3 Evolution and function of the Miro GTPases

Prior phylogenetic analysis has revealed the presence of at least one homologue of Miro in the genome of almost every eukaryotic organism, with no clear homologues apparent in prokaryotes (160). Exceptions include eukaryotes possessing hydrogenosomes and mitosomes in lieu of typical aerobic mitochondria, in addition to a minority of eukaryotes exhibiting aerobic mitochondria, such as the phylum Apicomplexa (160). Interestingly, the N-terminal GTPase domain is absent in Miro homologues of the order Trypanosomatid (160,173). Instead, this GTPase domain is replaced by a novel domain containing a sequence unique to any currently defined domain sequences. Additionally, Miro homologues present in this order lack functional versions of the second EF hand

domain. This is in contrast to Miro homologues present in Stramenopiles and Amoebozoa, which contain a non-functional C-terminal GTPase domain absent of typically well-conserved residues (160,173). The C-terminal GTPase domains of Miro homologues in the class Oligohymenophorea are also unusual. In this class, the C-terminal GTPase domain sequences are not conserved, even within the class itself (160). Such discrepancies in structure across eukaryotic lineages implies that the functional demands of Miro can differ significantly amongst eukaryotes, and that Miro proteins have been independently modified to address this.

The notion of functional discrepancy across eukaryotic Miros is also implied when current literature on the topic of Miro functionality is surveyed. As summarised in table 1.5, Miro function across species can be diverse, though some conserved functions are also apparent. In virtually all organisms studied, at least one expressed Miro protein appeared to significantly affect mitochondrial morphology. Miro involvement in mitochondrial transport and homeostasis is also widely seen. Interestingly, very recent research suggests that human Miro1 and 2 bind together as one complex, and that functional ablation of both Miros is required to produce the classical Miro1 ablation phenotype previously reported (83). This perhaps indicates that Miro2 function is dependent on cell type or context, and exhibits a degree of redundancy in some circumstances.

Table 1.5. Miro functions and interactors across species.

Organism(s)	Protein name(s)	Function(s)	Confirmed interactor(s)	Reference(s)
Mammals (including Homo sapiens, *Mus musculus* and *Rattus norvegicus*)	Miro-1 and Miro-2	Mitochondrial transport/ trafficking	GRIF-1 /OIP98/huMilt2/ TRAK2	(163)
			OIP106/huMilt1/ TRAK1	(163)
			Kinesin	(164)
			Dynein	(182)
			DISC1/ DISC1-Boymaw	(183)
			Alex3 (in Eutherians)	(184)
			HUMMR (in neurones)	(185)
		Mitophagy	PINK1	(186)
			Parkin	(186)
		Mitochondrial morphology	Mitofusin 1/2	(187)

Organism(s)	Protein name(s)	Function(s)	Confirmed interactor(s)	Reference(s)
		Mitochondrial distribution during cytokinesis	Cenp-F	(83)
Drosophila melanogaster	dMiro	Mitochondrial transport	Milton	(188)
		Mitochondrial morphology		
Saccharomyces cerevisiae	Gem1p	Mitochondria-ER interaction	Mdm34p Mmm1p Mdm10p Mdm12p	(189)
		Mitochondrial morphology	-	
		Inheritance of mitochondria	-	
Dictyostelium discoideum	gemA	Mitochondrial homeostasis	-	(173,190)
Arabidopis thaliana	Miro-1, Miro-2 and Miro-3	Inheritance of mitochondria	-	(161,173)
		Mitochondrial morphology	-	

1.4.4 Miro as a facilitator of mitochondrial transport

Perhaps the most well-documented function of the Miros is the transport of mitochondria (17,83,97,132,159,162-165). Mitochondrial transport is facilitated by the action of kinesins and dyneins, acting as anterograde and retrograde motors, respectively (191,192). In this context, the term ‘anterograde’ refers to the movement of mitochondria away from the nucleus and towards synapses in neurones. Conversely, the term ‘retrograde’ denotes the movement of mitochondria back towards the nucleus or cell body. In axons, this movement of mitochondria occurs along linear arrays of uniformly polarised microtubules, with the ends of these microtubules located at the cell body referred to as the ‘minus’ ends and the ends situated at distal areas regarded as ‘plus’ ends (Figure 1.13). Deficiencies in mitochondrial transport are most striking in neuronal cells, where efficient transport of mitochondria from the cell body to areas of high energy demand, such as synaptic terminals, is critical for cell function and survival (193). However, retrograde mitochondrial movement also appears crucial in neuronal health: transgenic mice with retrograde transport exhibited motor neuron degeneration and loss, denervation of muscle and marked decline in strength and endurance (98).

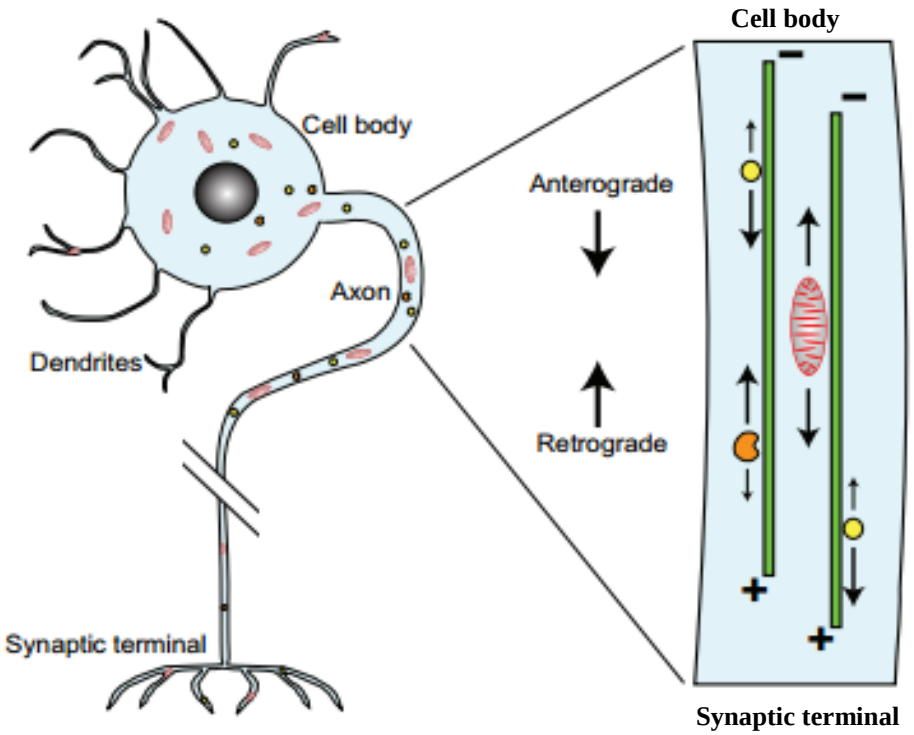

Figure 1.13. Schematic representation of neurone structure and axonal transport. A peripheral neurone containing a cell body that obtains signals from presynaptic neurons and an axon that carries action potentials from the cell body to the synaptic terminal, which repsonds by releasing neurotransmitters to a post-synaptic neurone or muscle cell. Normal neurone development and function is dependent upon the long-distance transport of cytoplasmic components including vesicles (yellow), mitochondria (red) and endocytic organlles (orange) along the axon. This enables organlles and other newly-synthesised materials to be transported from cell body to distal areas, and also for aged materials to be transported back to the cell body for recyling. Both forms of transport require motor proteins that attach to 'cargo' and pull it along microtubules (green) towards either the microtubule plus (distal) ends or minus (towards cell body) ends. Diagram adopted from (194).

Indeed, a search for previously unidentified genes necessary for axonal and synaptic function in *Drosophila melanogaster* revealed key roles for Drosophila Miro (dMiro) in the transport of mitochondria from the neuronal cell body to distal areas. Most closely related to Miro-1 in humans, dMiro represents the single Miro protein expressed in Drosophila. Distribution of mitochondria in mutant dMiro neurones was significantly altered relative to wildtype controls, with neat clustering of mitochondria observed towards the soma of mutant larval neurones and an absence of mitochondria noted at distal regions, including neuromuscular junctions (NMJs). This apparent inability to transport mitochondria produced larvae with slim body, small muscle size and

progressive locomotive defects with ascending paralysis, culminating in death at the larval or early-pupal stage. This phenotype was rescued by the induction of wild-type *dMiro* expression in neurones but not muscle cells, suggesting a critical role for dMiro in neurones (132).

Further studies in Drosophila implied the formation of a protein complex comprised of dMiro and the kinesin-associated protein Milton, enabling the anterograde transport of mitochondria *via* apparent recruitment of kinesins (188). Two mammalian homologues of Milton, TRAK1 (also known as OIP106) and TRAK2 (also known as OIP98/Grif-1), which can form complexes with mammalian Miro1 and Miro2 and with microtubule motors, have also been shown to co-localise with the hMiros (163), indicating that these proteins act as a component of a conserved protein complex necessary for the transport of mitochondria (Figure 1.14). Within this complex, Milton/TRAK acts as an adaptor protein, connecting the motor proteins to Miro, which is bound to the mitochondrial outer member by virtue of the Miro C-terminal localisation sequence. Both TRAK1 and TRAK2 are necessary for axonal and dendritic mitochondrial transport, although they appear to engage differing transport machineries to achieve this. TRAK1 binds to both kinesin-1 and dynein/dynactin and is predominantly localised in axons, while TRAK2 preferentially binds dynein/dynactin and exhibits dendritic localisation (195). The interaction of TRAK1 with both the kinesin (anterograde) and dynein (retrograde) motors may enable movement in both directions in the axon while TRAK2's more favourable interactions with dynein may encourage retrograde movement at distal ends. It is presently unknown whether Milton is able to bind both the kinesin and dynein motors in Drosophila.

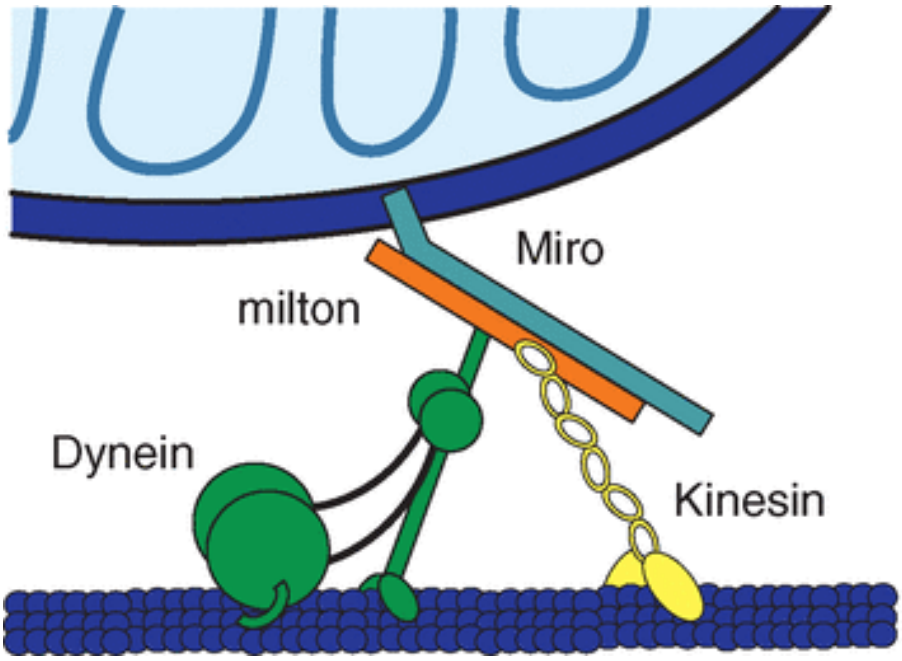

Figure 1.14. Schematic diagram of the mitochondrial motor/adaptor complex thought to be necessary for mitochondrial transport. The anterograde motor Kinesin-1 (also referred to as kinesin heavy chain or Kif5) and the retrograde motor (the dynein/dynactin complex) facilitate the transport of many cellular cargoes but are bound to mitochondria by their interactions with two mitochondrion-specific proteins: Miro and milton (or the milton homologues TRAK1 and TRAK2 in mammals). Miro is anchored to the mitochondrial outer membrane while Milton serves as an adaptor protein, linking the motor proteins to Miro and therefore the mitochondria. Adopted from (191).

Interestingly, while the Miro/Milton(TRAK) transport complex shown in Figure 1.12 is widely accepted, the direct Ca^{2+}-dependent binding of hMiro1 to kinesin motor Kif5 has been demonstrated, indicating that a degree of redundancy for a Milton-like adaptor protein (164). In contrast to this, however, TRAK2 and hMiro1 have been shown to directly form a protein complex and co-localise with mitochondria in mammalian brain tissue extracts (163). Furthermore, the GTPase state of the hMiro1 N-terminal GTPase domain appears to recruit TRAK2 to mitochondria in mammalian cell lines, producing downstream effects on anterograde mitochondrial movement (163). Indeed, over-expression of hMiro1 appears to increase TRAK2 recruitment to mitochondria and encourage anterograde mitochondrial transport. Correspondingly, abolishing the kinesin-binding domain in TRAK2 impairs anterograde movement of mitochondria (163). This suggests that mitochondrial transport in mammals is mediated by a mechanism dependent on the N-terminal GTPase domain for recruitment of TRAK to the mitochondria, and that the resulting Miro-TRAK-kinesin protein complex is required for anterograde movement

of mitochondria along microtubules. It should be noted, however, that although initial studies exclusively documented the effect of Miro on anterograde transport, live-imaging of GFP-tagged mitochondria in Drosophila later suggested that dysfunctional dMiro results in the impairment of both anterograde and retrograde mitochondrial transport (165). A more recent study found that retrograde mitochondrial transport was mediated by action of the Miro C-terminal GTPase domain (196), despite prior suggestions that this domain was merely an artefact (159).

Despite the indication that a Milton/TRAK adaptor may be redundant in some contexts due to direct Miro-kinesin motor binding (164), both TRAK1 and TRAK2 have been directly linked to mitochondrial motility. Indeed, recent studies implicate a link between neuronal nutrient availability and mitochondrial motility through glucose signalling and the subsequent modification of TRAK1 and 2. Extracellular glucose was shown to activate O-GlcNAc transferase (OGT), an enzyme catalysing post-translational O-glycosylation of target proteins (197). Proteomic investigations suggest that activated OGT targets TRAK1 and 2 for GlcNAcylation (198), leading to the arrest of mitochondrial motility (199). Taken together, the present literature suggests a Miro/Milton(TRAK)/motor transport complex engaged in the transportation and motility of mitochondria that is sensitive to signalling both from within the complex (163), from intracellular components (164) or from external factors such as extracellular glucose (199).

1.4.5 Miro as a facilitator of mitochondrial transport: the influence of Ca^{2+}

While the necessity of the Miro/TRAK/motor complex in mitochondrial transport is now commonly accepted, the role of cytosolic Ca^{2+} in this complex remains disputed. Cytosolic Ca^{2+} is required for mitochondrial transport, with transport of mitochondria arrested in the presence of increased intracellular Ca^{2+} (200). Interestingly, Miro has also been implicated in Ca^{2+} regulation (201,202). However, various hypotheses exist on the link between Miro, Ca^{2+} and mitochondrial transport (Figure 1.15). One model stipulates that increased cytosolic Ca^{2+} results in dissociation of the kinesin motor from microtubules and the subsequent interaction of kinesin with Miro on the mitochondrion, resulting in the dissociation of motors from the microtubules (166) (Figure 1.15a). An alternative model indicates that Miro binds directly to kinesin without the need for the Milton adaptor, and that increased cytosolic Ca^{2+} inhibits Miro's interaction with kinesin, leading to the direct uncoupling of Miro from kinesin (164), (Figure 1.15b). However,

the arrest of mitochondrial transport in neurones has also been linked to the mitochondrial tethering protein syntaphilin (SNPH), resulting in a third model. In this model, the so-called "Engine-Switch and Brake" model, increased cytoplasmic Ca^{2+} is thought to dissociate kinesin from Miro (203) (Figure 1.15c). Following dissociation, kinesin interacts with SNPH, disrupting the ATPase activity of kinesin and resulting in the arrest of mitochondrial motility. Thus, SNPH performs as an engine-off switch by detecting the Ca^{2+}-induced arrest of mitochondria, and as a brake by securing static mitochondria to the MT.

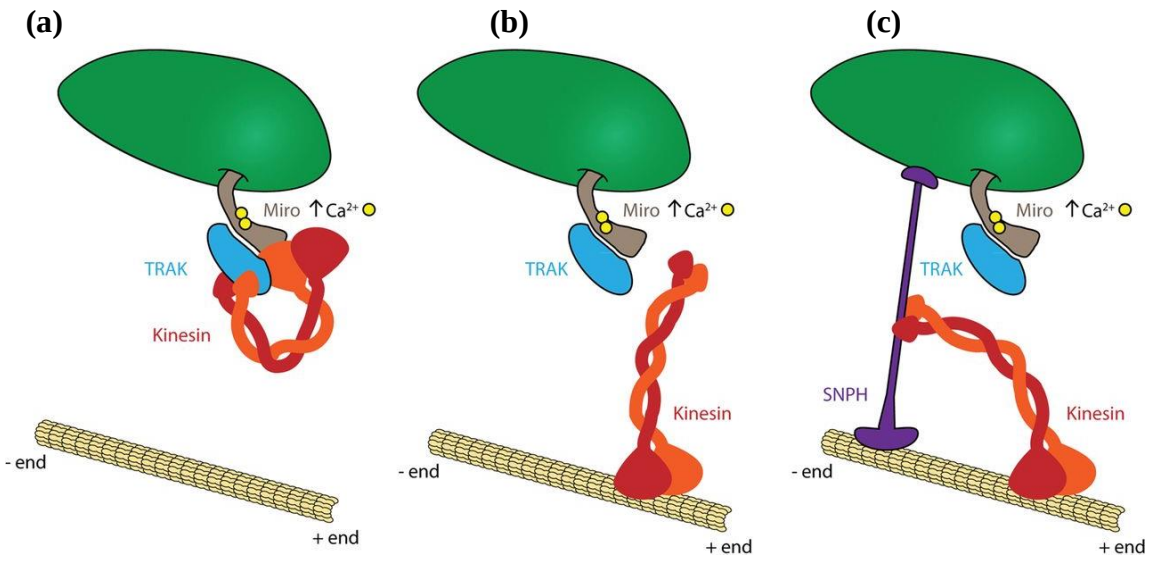

Figure 1.15. Schematic representation of models of Ca^{2+}-mediated mitochondrial arrest. (**a**) Increased cytosolic Ca2+ promotes the detachment of kinesin from the microtubules and results in interaction of the kinesin motor domains with Miro, leading to mitochondrial arrest. (**b**) Increased cytosolic calcium leads to dissociation of Miro from the kinesin motors, resulting in detachment of the mitochondrion from the microtubule. (**c**) An alternative model implicates the detachment of kinesin from Miro and the subsequent interaction of kinesin with SNPH. Figure adopted from Birsa *et al.* (204).

A third proposition is that intramitochondrial $Ca^{2+,}$ rather than cytoplasmic Ca^{2+}, plays a critical role in mediating mitochondrial transport, and that Miro is involved in orchestrating intramitochondrial Ca^{2+} levels in the matrix (201). Mitochondria are able to buffer cytoplasmic Ca^{2+} via uptake of Ca^{2+} through the mitochondrial calcium uniporter (MCU). The uptake of Ca^{2+} through the MCU has been shown to be inversely related to mitochondrial velocity in axons, thus illuminating a mechanism by which cytoplasmic Ca^{2+} influences mitochondrial trafficking. Two independent studies have demonstrated

that expression of Miro1 at the mitochondrial outer membrane affects the concentration of Ca^{2+} in the mitochondrial matrix (97,201). However, the importance of Ca^{2+} sensing in Miro proteins has not yet been fully established. As elevated intramitochondrial Ca^{2+} has been associated with slower movement or stopping of mitochondria and a subsequent increase in ATP production, these results taken as a whole indicate a previously hypothesised link between mitochondrial motor machinery, mitochondrial trafficking and the mediation of bioenergetic efficiency in mitochondria (205,206).

1.4.6 Miro in mitochondrial morphology

In addition to facilitating mitochondrial transport, the Miro GTPases may modulate mitochondrial morphology. Mitochondria are dynamic organelles that continually move, fuse and divide; indeed, the dynamic balance of mitochondrial fission and fusion events is a major factor in determining mitochondrial morphology (207,208). However, the exact roles the Miro GTPases play in mitochondrial morphology remain unclear. Initial functional studies in mammalian cells showed perinuclear aggregation of mitochondria when a mutant of hMiro1 bearing a constitutively active N-terminal GTPase domain was over-expressed. A similar effect was obtained from over-expression of a mutant of hMiro1 harbouring a dominant-negative N-terminal GTPase domain, though to a lesser extent. These results imply that a balanced level of Miro activity in the N-terminal GTPase domain of hMiros is necessary for the maintenance of normal mitochondrial morphology (29).

Despite aforementioned structural differences in the Miros of earlier eukaryotes, the influence of Miro on mitochondrial morphology appears strongly conserved. In *Arabidopsis thaliana*, a flowering plant, three Miro homologues are expressed: MIRO1 (At5g27540), MIRO2 (At3g63150) and MIRO3 (At3g05310) (161). Although Miro3 is expressed exclusively in the endosperm (209,210), Miro1 and Miro2 in this species appear to be ubiquitously expressed and have been shown to co-localise with mitochondria (161). An insertational mutation of Arabidopsis Miro1 resulted in impaired pollen tube growth and early embryonic lethality (161,211) This phenotype was enhanced when the Miro2 gene was mutated in a similar fashion, though defective female gameogenesis with delayed polar nuclear fusion was also noted with Miro2 mutants (211). Separate to Miro2 mutation, Miro1 mutants impaired mitochondrial inheritance during cell division, though mutant mitochondria appeared to remain influenced by protoplasmic streaming in an actin-dependent manner. Interestingly, bloated

mitochondria were observed with the Miro1 mutant phenotype. However, these bloated mitochondria possessed normal inner membrane structures. In light of the evidence obtained and the absence of an obvious Milton homologue in the Arabidopsis genome, it has been suggested that the predominant role of the Miros in Arabidopsis is the maintenance of mitochondrial morphology rather than mitochondrial transport (161,212).

The single Miro protein in *Saccharomyces cerevisiae*, Gem1p, appears to require both GTPase domains and functional EF hands for the maintenance of normal mitochondrial morphology (158). This is in disagreement with many later reports regarding the apparent lack of functionality in the C-terminal GTPase domain of the human Miros. A 662-amino acid protein, Gem1p shares 30% amino acid identity with the human Miros . When Gem1p was ablated in *S.cerevisiae* (*Gem1p*Δ cells), mitochondria exhibited both abnormal distribution and abnormal morphology, with a collapsed, globular or 'grape-like' appearance observed amongst mitochondria (158). However, mitochondria displaying abnormal morphology retained inner cristae structures when viewed under TEM. Although these results indicate a conserved role for Miro in regulating mitochondrial morphology, Gem1p does not appear to be integral to mitochondrial fusion and fission (158,213). Of additional note, Gem1p did not appear to influence the actin cytoskeleton directly, and the endoplasmic reticulum and nuclei of *Gem1p*Δ cells appeared normal relative to controls.

A role for Miro in mitochondrial morphology has also been observed in *Drosophila*, with overexpression of wildtype dMiro producing significant aggregation of mitochondria in dopaminergic neurones (129) and abnormally elongated mitochondria in larval motor neurones (165). *In vivo*, however, the effects of dMiro on mitochondrial morphology appear to be dependent on context and cell-type, suggesting that dMiro is not directly involved in modulating mitochondrial morphology but perhaps that one or more binding partners are necessary to exert the effects on mitochondrial morphology observed previously. Indeed, a recent effort to identify regulators of Miro showed that Vimar in Drosophila, and its mammalian homologue RAP1GDS1, is involved in the regulation of mitochondrial morphology (214). Vimar and its homologues function as GEF proteins, regulating mitochondrial fission in response to intracellular Ca^{2+} (214). Prior reports indicated that under normal cellular conditions, Miro was capable of increasing mitochondrial size through inhibition of the dynamin-related protein Drp1 (129,215); however, it now appears that Miro interacts directly with Vimar homologues and promotes mitochondrial fission when intracellular Ca^{2+} increases (214). Furthermore,

mitochondrial enlargement observed in a Drosophila model of Parkinson's disease was rescued through ablation of Vimar expression (214). The function of Vimar appears to be conserved in RAP1GDS, its mammalian homologue (214).

1.4.7 Influences on ATP homeostasis and apoptosis

According to northern blot analysis on human tissue, both Miro 1 and Miro 2 appear to be ubiquitously expressed in humans (29). However, while Miro 1 appears abundantly expressed in heart and skeletal muscle, Miro 2 expression is most prominent in heart, liver, kidney, pancreas and skeletal muscle tissue. This is particularly interesting with regards to the high energy demand these cell types commandeer, suggesting perhaps that the Miro GTPases may be involved in ATP homeostasis or cellular bioenergy homeostasis. In *S.cerevisiae,* the Gem1p abrogation strain grew significantly slower on glycerol minimal media relative to wildtype cells, suggesting that Gem1p is necessary for correct mitochondrial respiration (158). Too, the single Miro homologue GemA in *Dictyostelium discoideum* appears to play a role in mitochondrial respiration, with gemA knockout mutants exhibiting impaired cell growth on nutrient media alongside reduced ATP content and increased oxygen consumption. However, glucose consumption, mitochondrial membrane potential and the production of ROS in *gemA* knockout mutants remained unaltered (160).

As previously discussed, mitochondria are involved in the buffering of intracellular Ca^{2+}, with the Miro GTPases appearing to play a role. Further to this, Miro sub-cellular localisation in some species has been demonstrated at mitochondrial-endoplasmic reticulum (ER) contact sites (189,216). In yeast, mitochondria are connected to the ER-mitochondria encounter structure (ERMES) tethering complex believed to consist of an ER membrane protein (Mmm1), two outer mitochondrial membrane proteins (Mdm10 and Mdm34) and a cytosolic protein (Mdm12), all of which collectively form a bridge between mitochondria and the ER, with the Miro homologue Gem1 presenting as a discretionary sub-unit (189,216). The ERMES complex has been implicated in phospholipid exchange between mitochondria and the ER, although also appears to be involved in orchestrating mitochondrial protein import, mitochondrial DNA replication and some mitochondrial dynamics. A 2013 study conducted by Murley *et al.* demonstrated a spatial and functional link between ERMES, the yeast Miro Gem1 and ER-associated mitochondrial division (217). This study indicated that Gem1 performed as a negative regulator of ER-mitochondrial contact, aiding in mitochondrial dissociation

from the ER and thus facilitating in the spatial resolution and distribution of newly generated mitochondrial tips subsequent to mitochondrial division. Taken together, these results are indicative of a role for yeast Miro and the ERMES complex in mediating mitochondrial division, biogenesis and distribution. Whether this function role is conserved in higher organisms remains unknown. However, it is notable that mammalian Miro1 has also been shown to localise to ER-mitochondrial contact sites, implying a role for mammalian Miro in a putative mammalian version of the ERMES complex.

One suggested function of Miros localised at mitochondria-ER contact sites is the orchestration of mitocondria-ER Ca^{2+} signalling. At mitochondria-ER contact sites, Ca^{2+} is released from the ER to mitochondria, aiding in normal mitochondrial function (218). Intramitochondrial Ca^{2+} is required for ATP production via the activation of TCA cycle enzymes and the enhancement of electron chain complexes and the ATP synthase complex (219). Transfer of Ca^{2+} from the ER to the mitochondria is proposed to occur through the following proteins: the Ca^{2+} channel inositol 1,4,5-trisphosphate receptor $Ins(1,4,5)P_3R$ on the ER, the voltage-dependent anion-selective channel protein 1 (VDAC1) on the mitochondrial outer membrane and the mitochondrial Ca^{2+} uniporter (MCU) on the mitochondrial inner membrane (220). Mitochondria-ER contact sites may provide a critical supply of Ca^{2+} for mitochondrial membrane proteins that are dependent on Ca^{2+} binding for their functions but are unable to bind Ca^{2+} under normal cytoplasmic concentrations of Ca^{2+} (220). As aforementioned, Miro has been implicated in the modulation of intramitochondrial Ca^{2+} levels with overexpression of Miro1 linked to increased mitochondrial Ca^{2+} uptake while overexpression of Miro1 mutants harbouring defective EF-hands negatively influenced this uptake (164). Thus, one may hypothesise that Miro is able to influence ATP production in mitochondria through mediation of intramitochondrial Ca^{2+} content, particularly at mitochondria-ER contact sites. Interestingly, the mitochondrial GTPase mitofusin-2 (Mfn2), known to interact with Miro, is a recognised constituent of the mitochondria-ER contact sites in mammalian cells (221). It may therefore be postulated that Miro-Mfn2 interaction is involved with mitochondria-ER communication.

Overload of Ca^{2+} due to a local influx can stimulate apoptosis *via* opening of the mitochondrial permeability transition pore (MPTP), resulting in cytochrome c release and propagation of the caspase cascade (222). It has therefore been proposed that the function of Miro in mediating homeostasis of intramitochondrial Ca^{2+} may be associated with some pro-apoptotic effects linked to the Miros. Early research on the human Miros (29)

concentrated on the creation of Miro mutants containing amino acid substitutions in the N-terminal GTPase domain, making this GTPase domain either constitutively active (G13V) or dominant negative (S18N) with respect to GTP/GDP-bound status. Ectopic expression of Miro1 mutants bearing the constitutively active N-terminal GTPase domain (Miro1 V13) induced a collapse of the mitochondrial network in non-neuronal cells, with mitochondria exhibiting perinuclear aggregation. Too, ectopic expression of this mutant was associated with increased presence of the apoptotic marker M30 (recognising caspase-cleaved cytoskeleton-18) relative to both control cells and cells ectopically expressing S18N Miro mutants. Correspondingly, the introduction of caspase inhibitors reduced this increase in M30, suggesting a role for the GTP/GDP-bound status of the Miro1 N terminal GTPase domain in apoptosis. However, while overexpression of Miro in other organisms has produced a similar pattern of mitochondrial aggregation, other studies have failed to demonstrate a clear link between Miro overexpression and apoptosis (29). At present this link therefore remains obscure.

1.4.8 Miro GTPases in health and pathology

1.4.8.1 The Miro GTPases in the health and pathology non-neuronal cells

Mitochondria comprise crucial organelles within a cell, and particularly those with high energy demands or the need to supply distal areas of the cell with energy at an alternative rate to other areas (for example, neuronal cells). It is not surprising, therefore, that the Miro proteins have been implicated in both neurodegenerative diseases and certain cancers when dysregulated. With regards to the latter, neoplastic cells typically demand greater energy supplies to support high proliferation and consequently often exhibit mitochondrially-induced metabolic changes (223,224). Interestingly, a recent study on the effect of Ca^{2+} uptake into mitochondria at mitochondria-ER contact sites has shown an apparent fundamental need for basal mitochondrial Ca^{2+} in the survival of transformed primary human fibroblasts (225) this is remarkable given the implied function of Miro in mediating intramitochondrial Ca^{2+} uptake at mitochondria-ER sites. Other than metabolic changes in neoplastic cells and the apparent importance of Ca^{2+} uptake at mitochondria-ER sites, knockdown of the Miro1-facilitated movement of mitochondria has been shown to decrease the velocity and directional persistence of epithelial cancer cells (96). The velocity and persistence in direction of neoplastic cells is a critical factor in tumorigenesis and particularly metastasis, the latter of which is a major marker of advanced pathology in cancer patients and the cause of 90% of cancer patient deaths (226). Despite emerging

evidence, however, further data is required to clarify the potential roles for the Miro GTPases in the development and progression of cancers.

Intriguingly, the Miros may also play a role in simple infection-related pathology. It is now thought that effector proteins from pathogens may specifically target the Miros due to their involvement in mitochondrial movement (94). Effective mitochondrial transport is believed to be a component of innate immune responses, therefore the Miros may present a suitable target for the disruption of mitochondrial-related innate immune responses. The *Vibrio cholerae* protein VopE was recently demonstrated to co-localise with mitochondria during *Vibrio* infection of mammalian cells, and appears to bind to the N-terminal GTPase domain of the mammalian Miros directly (94). The authors of this study propose that VopE acts as a Miro-specific GTPase-activating protein (GAP), disrupting the movement of mitochondria and therefore disrupting mitochondrial-related innate immunity. Hence, dysfunctional Miro activity has not only been implicated in cancer, but also with defective mitochondrial innate immunity.

Beyond the manipulation and involvement of Miro GTPases in this manner, however, a study by Ahmad *et al.* (2014) implicated Miro in a far more beneficial role for the maintenance of cell health, through mediating the transfer of mitochondria from mesenchymal stem cells (MSC) to epithelial cells (EC) (227). This form of mitochondrial transfer is thought to help rejuvenate damaged cells during times of stress. In this study, overexpression of Miro1 increased the velocity of mitochondrial transfer to ECs and enhanced rescue of epithelial injury, while Miro1 knockdown reduced these positive effects. Indeed, recent mammalian cell studies indicate important roles for Miro in microtubule dynamics and cytokinesis. Here, the N-terminal GTPase domain and EF-hands of hMiro1 and 2 were shown to recruit the centromere-kinetochore complex associating protein Centromere protein F (Cenp-F), enabling the management of intracellular mitochondrial distribution through mitochondrially-influenced control of microtubules dynamics (83). The C-terminal region of Cenp-F appears to bind Miro, with Cenp-F ablation displaying the same phenotype as abrogation of both human Miros. Interestingly, ablation of both hMiro1 and hMiro2 function was required to achieve phenotypes previously reported to occur with abolishment of Miro1 alone. Thus, it may be that Miro2 retains a degree of redundancy in some cellular contexts, while appearing functionally important in other situations. The authors postulated that interaction between Cenp-F and the Miros allowed for connections to occur between mirochondria and the tips of growing microtubules, enabling mitochondria to track microtubule tips, perhaps in

a manner previously described for ER tip-tracking (95). Hence, the Miro GTPases appear to be involved in numerous intracellular processes in non-neuronal cells, through their involvement in mitochondrial transport and their apparent influence on microtubule dynamics when functioning alongside interactors.

1.4.8.2 Miro GTPases in neuronal pathology

The Miro GTPases appear to play a critical role in the maintenance of neuronal health. This is perhaps unsurprising when one considers the crucial role the Miros appear to play in mitochondrial transport (discussed previously) coupled with the need for mitochondria to travel vast distances in neuronal cells down axons (sometimes 1 meter long) from the cell body towards distal regions for nervous transmission (228,229). Indeed, altered Miro function has been associated with such neurological pathologies as Parkinson's Disease (129,186), amyotrophic lateral sclerosis (ALS) (230), and schizophrenia (231).

1.4.8.3 Animal models of Miro abrogation

As previously discussed, this link between neuropathology and impaired Miro function was first indicated by Guo *et al.* (2005), with dMiro$^{-/-}$ Drosophila larvae exhibiting a slim body, small muscle size, progressive locomotor defects and early death in a manner reminiscent of severe neurodegenerative disease (132). This remarkable phenotype was rescued when WT dMiro was introduced to neuronal cells but not muscle cells, and the effect was believed to be a consequence of defective mitochondrial anterograde transport in dMiro$^{-/-}$ neuronal cells. Notably, the authors of this study also investigated the presence of abnormal pre-synaptic vesicle accumulation in dMiro$^{-/-}$ neuronal cells and found an impairment but not absolute blockage of vesicular transport in dMiro mutants. Interestingly, mutations affecting axonal transport often present with abnormal pre-synaptic vesicle accumulation, and typically this state of accumulation is a marker of neuropathology (232-234). While vesicular transport appeared impaired in dMiro mutant neurones, however, this effect was qualitatively and quantitatively diverse from the significant defects in mitochondrial transport observed. Thus, while the impairment of vesicular transport in this respect may contribute in a lesser regard to the dMiro mutant phenotype, it would appear unlikely that both transport defects were the consequence of a shared mechanism.

Other than the dMiro mutant flies, recent global and neurone-specific Miro1 mouse knockouts were developed with striking results (235). Mice globally deficient of Miro1

were cyanotic and died shortly following birth, with fetal ultrasound revealing no cardiac abnormalities prior to birth, but post-mortem autopsy demonstrating unexpanded lungs, suggesting death due to an inability to breathe (235). Despite this, Miro1 global knockout mice lung tissue appeared histologically normal, with no abnormalities in lung morphology observed. This indicates that Miro1 may play a crucial role in embryonic lung development (235). Indeed, defects in neuronal respiratory control pathways were noted in the global Miro1 knockout mouse, with the nucleus ambiguus notably absent and impaired phrenic nerve innervation of the diaphragm muscle, alongside reduced axonal branching of the phrenic nerve (235). Taken together, this suggests that Miro1 plays a key role in the embryonic development of respiratory neurology. The Miro1 neurone-specific knockout mouse phenotype was also striking, exhibiting rapidly progressing upper motor neuron disease symptoms and early death after approximately 4 weeks. At birth, the neurone-specific Miro1$^{-/-}$ mice appeared indistinguishable from WT littermates. However, by 2 weeks Miro1$^{-/-}$ mice exhibited hind-limb clasping, a known early marker for neuronal impairment. These mice failed to gain weight as they matured and developed a stiff tail, spinal curvature (kyphosis), hind-limb spasticity and progressive locomotive defects (235). This phenotype was reflective of the development of upper human amyotrophic lateral sclerosis (AML), with symptoms becoming progressively worse and premature death occurring at approximately 35 days (235). Interestingly, the researchers of this study implicated impaired retrograde transport of mitochondria in the development of this phenotype, rather than the anterograde transport impairment strongly implicated in earlier studies. However, the previously observed perinuclear aggregation of mitochondria was shown in mouse embryonic fibroblasts obtained from Miro1$^{-/-}$ mice (235). No significant differences were reported in mitochondrial respiration or mitochondrial membrane potential in Miro1$^{-/-}$ cells relative to controls, indicating that defective transport is the main culprit in developing the phenotype shown but that this transport is not influenced by defective mitochondrial respiration or membrane potential. In contrast to other research, this study indicated that Miro1 is not essential for mitochondrial uptake of Ca^{2+} or the Ca^{2+}-related inhibition of mitochondrial motility (235).

1.4.8.4 Implications in Parkinson's Disease pathways

Overexpression of dMiro in Drosophila has been demonstrated as toxic, producing an age-dependent loss of dopaminergic (DA) neurones, the neurones specifically affected in Parkinson's Disease (PD) patients (129). The exact process by which this dMiro overexpression produces toxicity remains obscure. However, Miro GTPases are known to be associated with proteins involved with PD when dysfunctional: the mitochondria-localized Pten-induced kinase 1 (PINK1) and Parkin, an E3 ubiquitin ligase usually localised in the cytoplasm. Under normal circumstances, PINK1 and Parkin proteins form crucial components of a mitochondrial quality control system aimed at targeting damaged mitochondria for isolation and mitophagy, in order to sustain cellular metabolic requirements and prevent damage caused by defective mitochondria. Loss-of-function mutations in PINK1 and Parkin are associated with rare recessive forms of PD. Mitochondrial damage results in PINK1 accumulation on the outer mitochondrial membrane (OMM) and recruitment of Parkin from the cytosol to mitochondria. Upon recruitment, Parkin ubiquitinates various substrates on the OMM [VDAC1, Drp1 (dynamin-related protein 1), Mfns, TOM20 (translocase of outer mitochondrial membrane 20) and TOM40], allowing for initiation of mitophagy by the ubiquitin/proteasome pathway (236). Interestingly, Miro appears to interact with PINK1 and Parkin and is ultimately targeted for ubiquitination by Parkin when mitochondrial damage occurs (186). In a Drosophila PD model involving loss of PINK1 function, reduced dMiro function improved the degenerative phenotype shown in PINK1 mutant DA neurones (129). This suggests a role for mitochondrial transport and Miro in PINK1-related PD pathogenesis (129), a notion further supported by the profound effects seen in altered PINK1 function on the transportation of axonal mitochondria in Drosophila larval motor neurones or mammalian hippocampal neurones. Indeed, Miro appears to be specifically targeted for degradation by PINK1 and Parkin *in vivo* in Drosophila or in cultured mammalian cells treated with the mitochondrial toxin CCCP (129,186). Whether Miro is a direct substrate of PINK1-mediated phosphorylation or whether this phosphorylation is a perquisite for the regulation of Miro stability by PINK1 and Parkin, however, remains unknown (129,186,204). Miro has been previously shown to undergo PINK1-mediated phosphorylation at Ser-156 and that phosphorylation at this site is necessary for degradation of Miro by Parkin (186). However, more recent studies disagree with this finding, suggesting that this serine residue is not necessary for Miro stability and that parkin forms a lone target for PINK1 phosphorylation (129). Whatever the case, loss

of hMiro in HeLa cells resulted in the perinuclear aggregation of mitochondria and facilitated in increased mitophagy, a phenotype previously associated with activation of the PINK1/parkin pathway (129). It has also been postulated that Miro may form a constituent of the Parkin receptor complex, as hMiro1 appears capable of stabilising phosphor-mutant versions of Parkin on the OMM (36). The regulation of Miro stability and turnover by PINK1 and parkin could perhaps act to isolate damaged mitochondria from the network, promoting their transport to the cell body and subsequent degradation. However, further studies are required to elucidate the relationship between Miro, PINK1 and Parkin.

1.4.8.5 Miro in other neurological disorders

Beyond Parkinson's, altered Miro function has been implicated in the pathogenesis of other neurological disorders featuring abnormal mitochondrial distribution, morphology or function. Inhibition of dMiro has been shown to activate the PAR-1/MARK family kinases, for example, subsequently promoting the pathological phosphorylation of tau (23). Abnormal phosphorylation of tau has been broadly associated with neurodegenerative disorders known as tauopathies (237), such as: Alzheimer's (238), frontotemporal dementia (239) and progressive suprenuclear palsy (240). In fact, activation of the PAR-1/MARK-tau pathway has been demonstrated in animal models of Alzheimers in addition to patient samples (23,241-243). Other than this, Miro and TRAK1 have been shown to interact with DISCI (Disrupted in Schizophrenia 1) to increase axonal mitochondrial transport (231). DISCI function is presently unclear but appears to play roles in neuronal development and has been identified as a possible risk factor for schizophrenia, bipolar disorder and depression when dysregulated (231). A sequence variant of DISCI, 37W, showed impaired ability to promote mitochondrial anterograde transport, dysregulated coupling of mitochondria to the transport machinery complex and perinuclear aggregation of mitochondria. Interestingly this variant is able to associate with Miro1, akin to WT DISCI. Although further research is required, this study illuminates a potential link between Miro1 functionality and signalling complexes associated with severe psychiatric or neurological disorders. Furthermore, an ALS-related variant of the vesicle-associated membrane protein associated protein B (VAPB) has been demonstrated to decrease Miro association with tubulin *via* Ca^{2+} level increase in the cytoplasm, producing the overall result of impaired mitochondrial anterograde transport. This effect was rescued when a Ca^{2+} insensitive mutant of Miro1 was overexpressed (230). Another research paper found that Miro1 and Miro2 interact with hypoxia up-regulated

mitochondrial movement regulator (HUMMR), which appears to play a critical role in maintaining mitochondrial anterograde transport in cells exposed to hypoxia (185). As cerebrovascular events leading to transient hypoxia have been previously linked to psychiatric (244-246) and neurodenegenerative disorders (247,248). This may, again, illuminate a link between the Miros and neurological pathology

Chapter 2: Materials and Methods

2.1 Materials

2.1.1 Chemicals, enzymes and kits

2.1.1.1 Antibiotics

Kanamycin and ampicillin were dissolved in sterile deionised water and filtered using a 0.2 µm Minisart® filter unit (Sartorius) attached to a sterile syringe of appropriate volume (Plastipak®, Becton Dickinson) before use. Penicillin-streptomycin was provided as a concentrated solution by the supplier. All antibiotics were diluted with appropriate media to the working concentrations displayed in Table 2.1.

Table 2.1 Stock and working concentrations of antibiotics in media.

Antibiotic	Stock concentration	Working concentration	Supplier
Ampicillin	100 mg/mL	200 µg/mL	Sigma
Kanamycin	50 mg/mL	50 µg/mL	Melford
Penicillin	10, 000 U/mL	10 U/mL	Life Technologies
Streptomycin	10, 000 µg/mL	10 µg/mL	Life Technologies

2.1.1.2 Enzymes

All enzymes, buffers and reaction co-constituents used are shown in Table 2.2; these were stored at -20ºC, with buffers and components maintained in 20µL aliquots to avoid damage from repeat free-thaw cycles.

Table 2.2 Enzymes, buffers and reaction co-constituents.

Enzyme	Co-constituents	Supplier
KOD Polymerase	$MgCl_2$, dNTPs, reaction buffer	Toboyo Global
XhoI	Reaction buffer	New England Biolabs
NdeI	Reaction buffer	New England Biolabs
Bam HI	Reaction buffer	New England Biolabs
T4 DNA Ligase	Reaction buffer	New England Biolabs

2.1.1.3. Kits

With the exception of the miniprep cell re-suspension buffer, all kits and components were stored at room temperature. These kits and corresponding suppliers are listed in Table 2.3, below.

Table 2.3. Kits utilised throughout project.

Kit	Supplier	Catalogue identifier
QIAprep Spin Miniprep Kit	Qiagen	Cat No./ID 27104
QIAquick Gel Extraction Kit	Qiagen	Cat No./ID 28704
QIAquick PCR Purification Kit	Qiagen	Cat No./ID 28104
Malachite Green Assay Kit	Cayman Chemical	Item #10009325
PiColorLock™ Phosphate Detection Kit	Innova Biosciences	Product #303

2.1.1.4 Antibodies

To prevent damage from recurrent freeze-thaw cycles, all antibodies were stored at -20^{o}C in 5-10 µL aliquots. Unless otherwise indicated, all antibodies were diluted in 1 x PBS. The primary antibodies utilised throughout this project are detailed in Table 2.4, while Table 2.5 lists the secondary antibodies used. Each antibody shown in Table 2.4 arrived with a certificate of quality and specificity from the respective supplier. However, to ensure the suitability of the antibodies, positive and negative controls were utilised for antibody-related experiments wherever possible. Typically, a positive control comprised a sample of the target protein previously confirmed by other methods, such as LC-MS.

Negative controls were quintessentially samples wherein the target protein was absent but a similar protein (for example, another GTPase) was present; this assisted in assessing the specificity of each antibody for its respective target protein.

Table 2.4. List of primary antibodies.

Primary Antibody (1º Ab)	Origin	Dilution	Supplier	Catalogue identifier
Anti-RhoT1 monoclonal	Mouse	1:1000	AbCam	ab55035
Anti-RhoT2 polyclonal	Rabbit	1:2000	ProteinTech	11237-1-AP
Anti-RhoH polyclonal	Rabbit	1:1500	AbCam	ab138123
Anti-Hexahistidine monoclonal	Mouse	1:2000	BioRad	620-0203
Anti-Myc polyclonal	Rabbit	1:1000	Cell Signalling	2272
Anti-phosphoSer/phosphoThr polyclonal	Rabbit	1:1500	AbCam	ab17464
Anti-GAPDH	Rabbit	1:1000	Cell Signalling	#2118

Table 2.5 List of secondary antibodies.

Seconday Antibody (2º Ab)	Origin	Dilution	Supplier	Catalogue number
Anti-mouse HRP-linked polyclonal	Rabbit	1:1000	AbCam	ab97046
Anti-rabbit HRP-linked polyclonal	Goat	1:1500	Dako	D048701-2

2.1.2 Bacterial strains and vectors

2.1.2.1 Bacterial strains

The bacterial strains used throughout this project are enumerated in Table 2.6. All bacterial strains were stored at -80^{o}C in 20% (v/v) glycerol.

Table 2.6 *E.coli* strains used throughout this project.

Bacterial strain	Application
E.coli TOP10	Cloning host
E.coli BL21 (DE3)	Target protein over-expression
E.coli Tuner (DE3)	Target protein over-expression
E.coli C41 (DE3)	Target protein over-expression
E.coli C43 (DE3)	Target protein over-expression

Various strains were trialled in order to obtain suitable amounts of soluble target protein. For example, while BL21 (DE3) is regarded as a robust 'workhorse' strain for protein over-expression (249,250), C41 (DE3) and C43 (DE3) cells have been previously demonstrated to enhance over-expression of difficult-to-express or toxic target proteins (251,252). Alternatively, Tuner cells may be utilised when tight adjustment of expression levels are required in all cells within a culture (253). Specifically, DE3 strains were used owing to the fact they contain the λDE3 lysogen in the host chromosome; the λDE3 lysogen carries the gene for T7 RNA polymerase, allowing for the expression of recombinant proteins using the pET expression as further described in 2.1.2.2.

2.1.2.2. Vectors

A pEGFP-C vector encoding GFP-tagged RhoH was supplied by the Rajat Varma Lab (National Institute of Health, USA). Meanwhile, the Pontus Aspenström Group (Karolinska Institutet, Sweden) donated pRK5-Myc vectors encoding full-length human Miro1 and 2. Vectors encoding full-length and truncated DRAK2 were purchased from Addgene. These vectors had been previously sequenced and were either utilised outright or used as template DNA for PCR reactions, depending on context. The empty expression vectors pET28a and pET15b-TEV were utilised for cloning purposes to enable

subsequent expression of DNA segments encoding constructs of interest. Table 2.7 enumerates all of the vectors used throughout this study.

Table 2.7 Vectors used throughout this study. Relevant properties of each plasmid, including whether it possesses a multiple cloning site (MCS) or the capacity for ligation independent cloning (LIC) are also given.

Vector	Relevant Properties	Supplier
pET-28a	His-tag (N, C), Kan^r, T7 lac, $lacI^q$, thrombin cleavage site, MCS	Novagen
pET15b-TEV	His-tag (N),Amp^r, T7 lac, $lacI^q$, TEVcleavage site, MCS	NIGMS Protein Structure Initiative Site
pNIC28-Bsa4	His-tag (N), Kan^r, T7, lac, $lacI^q$, TEVcleavage site, MCS, LIC	Oxford University Structural Genomics Consortium
pRK5-Myc	Myc-tag, Amp^r, MCS, mammalian	Karolinska Institutet
pEGFP-C	GFP-tag, MCS, mammalian	Rajat Varma Lab

The pET-28a, pET15b-TEV and pNIC28-Bsa4 vectors each made use of the pET expression system pioneered by Studier and Moffatt (254). This system is renowned as a simple and powerful tool, enabling the controlled overexpression of target proteins in transformed bacterial cells (254,255). Vectors exploiting the pET system contain a T7 promoter upstream of a multiple cloning site (MCS) into which the gene encoding the target protein is inserted. Typically, an antibiotic resistance gene is also present in the pET vector to assist in the selection of transformed bacterial cells.

For the pET vectors used throughout this project, a *lac* operator sequence was present immediately downstream of the T7 promoter, carrying the natural promoter and coding sequence for the *lac* repressor (*lacI*). When expressed, the *lac* repressor acts at the *lac* promoter on the pET vector and at the *lacUV5* promoter in the host chromosome of DE3 strains, repressing transcription of both the target gene in the vector and the T7 RNA polymerase gene in the host chromosome, respectively. Allolactose, or a suitable analogue, such as IPTG, is able to bind to the *lac* repressor, causing a conformational change in the *lac* repressor and its dissociation from the *lac* operator. In this way, expression of target proteins throughout this project could be easily controlled by addition of IPTG to media containing the transformed DE3 expression host of choice.

2.1.3 Oligonucleotides

2.1.3.1. Oligonucleotide primers for amplification of full length hMiro1

Forward: 5'-TGCCATAGCATATGAAGAAAGACGTGCGGAT-3'

Reverse: 5'-TGCCATAGCTCGAGTCATCGCTGTTTCAATAATGC-3'

2.1.3.2. Oligonucleotide primers for amplification of full length hMiro2

Forward: 5'- TGCCATAGCATATGAGGCGGGACGTGCGCATCCTGTTACT-3'

Reverse:

5'- TGCCATAGCTCGAGTCACTGGCTCTTCACCAGGACCCTGTAGAGTG-3'

2.1.3.3. Oligonucleotide primers for amplification of the hMiro1 N-terminal GTPase domain (K3-P169)

Forward: 5'-TGCCATAGCATATGAAGAAAGACGTGCGGAT-3'

Reverse: 5'-TGCCATAGCTCGAGTCAAGGATGAAGAACAGCTTTCTGTG-3'

2.1.3.4. Oligonucleotide primers for amplification of the hMiro1 C-terminal GTPase domain (Q415-P580)

Forward: 5'-TGCCATAGCATATGCAAAGAAATGTGTTCAGATGTAATG-3'

Reverse: 5'-TGCCATAGCTCGAGTCACGGATACATGGCCATTGTT-3'

2.1.3.5. Oligonucleotide primers for amplification of the hMiro1 'xtal' construct (E177-R590)

Forward: 5'-TGCCATAGCATATGGAGGAGAAGGAGATGAAACCA-3'

Reverse: 5'- TGCCATAGCTCGAGTCAAGCTCTTGGGGTCAGCTTGT-3'

2.1.3.6. Oligonucleotide primers for amplification of the hMiro2 N-terminal GTPase domain (R3-P169)

Forward: 5'-TGCCATAGCATATGCGGGACGTGCGCATCCTGTTA-3'

Reverse: 5'-TGCCATAGCTCGAGTCATGGGATGCAGGACGGCCTT-3'

2.1.3.7. Oligonucleotide primers for amplification of the hMiro2 C-terminal GTPase domain (Q413-F589)

Forward: 5'-TGCCATAGCATATGCAGCGGAGCGTCCTCCTGT-3'

Reverse: 5'-TGCCATAGCTCGAGTCAGAAGGAAGAGGGATGCAGCTCT-3'

2.1.3.8. Oligonucleotide primers for amplification of the hMiro2 'xtal' construct (E177-P586)

Forward: 5'- TGCCATAGCATATGGAGGCCAAGCAGTTGAGG -3'

Reverse: 5'-TGCCATAGCTCGAGTCAGGGATGCAGCTCTGCGTG -3'

2.1.3.9. Oligonucleotide primers for amplification of RhoH full length wildtype

Forward: 5'-TGCCATAGCATATGCTGAGTTCCATCAAGTGCGT-3'

Reverse:

5'- TGCCATAGCTCGAGTCATTAGAAGATCTTGCACTCATTGATGGAG-3'

2.1.3.10. Oligonucleotide primers for amplification of RhoH S4-A174

Forward: 5'-TGCCATAGCATATGTCCATCAAGTGCGTGTTGGTG-3'

Reverse: 5'-TGCCATAGCTCGAGTCATGGCCTGGTTGACGGCAGTT-3'

2.1.3.11. Oligonucleotide primers for amplification of RhoH V10-S184

Forward: 5'- TGCCATAGCATATGGTGGGCGACTCTGCTGTG-3'

Reverse: 5'- TGCCATAGCTCGAGTCAGGAGAAGAGCCTCCTTCTGTT-3'

2.1.4 Media

2.1.4.1 Luria Bertani (LB) media for culturing *E.coli*

The components for the creation of 1 litre of LB media are shown in Table 2.8, below. Note that the components were dissolved in distilled water and the media brought to a pH of 7.0. Prior to use, the completed media was autoclaved as discussed in Appendix 1 and subsequently allowed to cool.

Table 2.8. Components in 1 litre of LB-broth.

LB broth component	Amount in 1 litre
Tryptone	10 g
Yeast extract	5 g
Sodium chloride	10 g

2.1.4.2 Modified terrific broth (TB media) for culturing *E.coli*

To produce 1 litre of TB media, the components shown in Table 2.10 were fully dissolved in distilled water and the resulting media brought to a pH of 7.0 prior to autoclaving (Appendix 1). Before inoculation with *E.coli*, the media was allowed to cool to room temperature.

Table 2.9. Components in 1 litre of TB-broth.

LB broth component	Amount in 1 litre
Tryptone	12 g
Yeast extract	24 g
Glycerol	4 mL

2.1.4.2 Solid media for culturing *E.coli*

To prepare agar plates, LB media was supplemented with 2% bacterial agar N^{o}1. The LB-agar was subsequently autoclaved (Appendix 1) and allowed to cool to approximately

50ºC prior to addition of any required selective antibiotics. Then, while still in liquid form, the LB-agar was poured into Petri dishes and allowed to solidify.

2.1.4.3 Media for culturing mammalian cells

COS7, PC3 and MCF-7 cells were cultured in Dulbecco's Modified Eagle Medium (DMEM) supplemented with 10% fetal bovine serum (FBS), 2 mM L-glutamine, 100 I.U/mL penicillin and 100 μg/mL streptomycin. During growth of mammalian cells for transfection purposes, DMEM supplemented with FBS and L-glutamine was used as described above, but with the absence of penicillin-streptomycin.

2.1.4.4 Opti-MEM® Reduced Serum Media for transfection or siRNAi

During transfection procedures, plasmid DNA or siRNA were incubated in Opti-MEM® Reduced Serum Media (Life Technologies), a modified form of DMEM buffered with HEPES and sodium bicarbonate and supplemented with sodium pyruvate, thymidine, L-glutamine, hypoxanthine, trace elements and growth factors.

2.1.5 Buffers

2.1.5.1 For agarose gel electrophoresis

2.1.5.1.1 6x DNA loading buffer (bromophenol blue)

The components of the 6x bromophenol blue DNA loading buffer are shown in Table 2.10, below. The 6x bromophenol blue DNA loading buffer was made up in sterile deionised water.

Table 2.10. Components of 6x bromophenol blue DNA loading dye.

6x bromophenol blue DNA loading buffer component	Amount required
Glycerol	30%
Bromophenol blue	0.25%

The bromophenol blue loading buffer was utilised during analytical agarose gel electrophoresis or when target fragment size was suspected to run significantly higher than 300 bp; this was a precaution to prevent contamination of bromophenol blue when performing agarose gel purification, as bromophenol blue is known to run at approximately the same rate as a 300 bp DNA fragment through a 1% agarose gel.

2.1.5.1.2 6x DNA loading buffer (xylene cyanol)

The components of the 6x xylene cyanol DNA loading buffer are shown in Table 2.11. 6x xylene cyanol DNA loading buffer was made up in sterile deionised water.

Table 2.11. Components of 6x xylene cyanol DNA loading dye.

6x xylene cyanol DNA loading buffer component	Amount required
Glycerol	30%
Xylene cyanol	0.25%

The xylene cyanol loading buffer was used when agarose gels were desired for agarose gel purification and the target fragment size was suspected to run significantly lower than 3000 bp (xylene cyanol runs at the same rate as a DNA fragment of approximately 3000 bp when a 1% agarose gel is utilised).

2.1.5.1.3 Tris-Acetate-EDTA (TAE) running buffer (50x)

Tris-Acetate-EDTA (TAE) running buffer was produced in 50x stocks, and diluted to 1x in distilled water when required. The recipe for producing 1 litre of 50x Tris-Acetate-EDTA (TAE) running buffer is shown in Table 2.12, below.

Table 2.12. Components of 50x TAE running buffer for agarose gel electrophoresis.

50x TAE running buffer (1L)	Amount required
Tris-base	242 g
Glacial acetic acid	57.1 mL
0.5 M EDTA, pH 8	100 mL

2.1.5.2 For SDS-PAGE electrophoresis and staining

2.1.5.2.1 SDS-PAGE running buffer (10x)

Running buffer for SDS-PAGE electrophoresis was produced in 10x stocks and stored at 4ºC. When required, a 1x solution was made up by diluting the stock in distilled water. The recipe for producing 1 litre of 10x SDS-PAGE running buffer is shown in Table 2.13, below. When producing 10x stock, each component was dissolved separately in deionised water in the order shown in Table 2.13. Prior to addition of SDS, the buffer was brought to approximately 900 mL and the pH adjusted to 8.8.

Table 2.13. Components of 10x SDS-PAGE running buffer.

10x SDS-PAGE running buffer (1L)	Amount required
Tris-base	30.3 g
Glycine	144 g
SDS	10 g

2.1.5.2.2 6x SDS-PAGE loading buffer

To produce 10 mL of 6x SDS-PAGE loading buffer, the components shown in Table 2.14 were dissolved in sterile deionised water. 6x SDS-PAGE loading buffer was stored at 4ºC until required.

Table 2.14 6x SDS-PAGE loading buffer components.

6x SDS-PAGE loading buffer (10 mL)	Amount required
1 M Tris-HCl pH 6.8	0.6 mL
50% glycerol	5 mL
10% SDS	2 mL
B-mercaptoethanol	0.5 mL
1% bromophenol blue	1 mL
Sterile deionised water	0.9 mL

2.1.5.2.3 12% (w/v) Acrylamide resolving gel components

The components required for standard 12% (w/v) acrylamide SDS-PAGE resolving gels are shown in Table 2.15, below. Note that this recipe is sufficient to produce two 0.75 mm gels. The components of Buffer B are additionally supplied in Table 2.16.

Table 2.15 12% (w/v) acrylamide resolving gel components.

12% (w/v) acrylamide resolving gel solution	Amount required for 2 0.75mm gels
40% (v/v) 37.5:1 acrylamide: bisacrylamide solution	3 mL
Buffer B	2.5 mL
Deionised water	4.5 mL
Ammonium persulphate (APS)	100 µL
TEMED	20 µL

Table 2.16 Components used to make up 100 mL of Buffer B for use in making SDS-PAGE resolving gels.

Buffer B (100mL)	Amount required for 100mL
2M Tris-HCl pH 8.8	75 mL
10% SDS	4 mL
Deionised water	21 mL

2.1.5.2.4 12% (w/v) Acrylamide stacking gel components

The components for producing standard SDS-PAGE stacking gels is shown in Table 2.17. This recipe is sufficient to produce two 0.75mm gels. The components of Buffer C are exhibited in Table 2.18. Bromophenol blue was an optional addition, aiding in visualisation of the stacking gel wells by producing a blue colour contrasting to the transparent wells.

Table 2.17 SDS-PAGE stacking gel components.

SDS-PAGE stacking gel solution	Amount required for 2 gels
40% (v/v) 37.5:1 acrylamide: bisacrylamide solution	0.5 mL
Buffer B	1 mL
Deionised water	2.5 mL
1% Bromophenol blue	30 µL
Ammonium persulphate (APS)	60 µL
TEMED	20 µL

Table 2.18 Components used to make up 100 mL of Buffer C, used when producing SDS-PAGE stacking gels.

Buffer B (100mL)	Amount required
1M Tris-HCl pH 6.8	50 mL
10% SDS	4 mL
Deionised water	46 mL

2.1.5.2.5 Coomassie stain for SDS-PAGE gels

The components required for production of 1 litre of coomassie stain are shown in Table 2.19.

Table 2.19 Components required to make up 1 litre of coomassie stain.

Coomassie stain (1L)	Amount required
Coomassie brilliant blue R250	1 g
Glacial acetic acid	100 mL
Methanol	300 mL
Deionised water	600 mL

2.1.5.2.6 Destain for SDS-PAGE gels

The components required for production of 1 litre of destain solution are provided in Table 2.20, below.

Table 2.20 Components required to make up 1 litre of destain solution.

Destain solution (1L)	Amount required
Glacial acetic acid	100 mL
Methanol	100 mL
Deionised water	800 mL

2.1.5.3 For protein purification

2.1.5.3.1 Lysis (“start”) buffer for IMAC purification of His-tagged proteins

Lysis (“start”) buffer for the IMAC purification of His-tagged proteins consisted of:

- 50 mM HEPES (pH 7.4)
- 500 mM NaCl
- 5 mM imidazole
- 5% glycerol

2.1.5.3.2 Elution buffer for IMAC purification of His-tagged proteins

Standard final elution buffer for the IMAC purification of His-tagged proteins was composed of the following:

- 50 mM HEPES (pH 7.4)
- 500 mM NaCl
- 500 mM imidazole
- 5% glycerol

2.1.5.3.3 Gel filtration buffer

Gel filtration buffer consisted of the following components:

- 50 mM HEPES (pH 7.4)
- 500 mM NaCl
- 5 mM DTT
- 2% glycerol

2.1.5.4 For further protein work

2.1.5.4.1 Bradford assay reagents

Bovine serum albumin (BSA) was made to a concentration of 2 mg/mL and stored at -20^{o}C for subsequent dilution to produce defined BSA standards. Bradford Reagent (Brilliant blue G in phosphoric acid and methanol) was stored at 4^{o}C and allowed to warm to room temperature prior to each use.

2.1.5.4.2 Protein crystallisation screens

All crystallisation buffers utilised are shown in Appendix 2.

2.1.5.4.3 Phosphate buffered saline (PBS)

All phosphate buffered saline (PBS) was made up in 18.2Ω water and autoclaved prior to use. A 1x PBS solution comprised the following: 1.1 mM KH_2PO_4, 155.2 mM NaCl and 3mM Na_2HPO_4-7·H_2O. Generally, a 10x PBS stock was generated, autoclaved and diluted to 1x on a purpose-by-purpose basis. To maintain sterility, PBS diluted from stock was diluted in 18.2Ω water and autoclaved.

2.1.5.4.4 Semi-dry transfer buffer for Western blotting

Transfer buffer for the transfer of proteins from SDS-PAGE gel to a blotting membrane through the semi-dry method was achieved via use of the following buffer: 25 mM Tris, 192 mM glycine, 20% (v/v) methanol adjusted to a pH 8.3.

2.1.5.4.5 Blocking solution for Western blotting

Blocking solution for all Western blots contained 5% (w/v) skimmed milk powder (Marvel) in 1 x PBS with 0.025% (v/v) Tween-20.

2.1.5.4.6 Radioimmunoprecipitation assay (RIPA) buffer

Radioimmunoprecipitation assay (RIPA) buffer was freshly prepared for each use in sterile 18.2Ω H_20 and filter-sterilised (2.2.1.1) prior to application. At all times, this buffer was kept on ice or at 4^{o}C. Standard RIPA buffer was composed of: 50 mM Tris pH 7.4, 150 mM NaCl, 1% sodium deoxycholate, 1% Triton X-100 and 0.1% SDS. Before use, P8340 protease inhibitor cocktail (Sigma Aldrich, UK) was added to a final 1 x concentration according to manufacturer's instructions.

2.2 Methods

2.2.1 General practice

Guidelines for good laboratory practice were adhered to wherever possible, with laboratory equipment utilised according to manufacturer's recommendations and advice from senior laboratory members. Where necessary, aseptic technique was applied (all microbiological techniques, for example).

2.2.1.1 Sterilisation

Unless otherwise stated, all solutions and apparatus were sterilised by autoclaving at 121^{o}C for 20 minutes at 1.05 bar pressure. Where it was not possible to autoclave, solutions were filter sterilised using a 0.2 µm Minisart® filter unit (Sartorius) attached to a sterile syinge of appropriate volume (Plastipak®, Becton Dickinson).

2.2.2 Microbiological Methods

2.2.2.1 Preparation of chemically competent *E.coli* cells

Competent cells of the necessary *E.coli* strains were prepared by an altered version of the $CaCl_2$ method described by Cohen *et al.* (256). A single colony of the desired *E.coli* strain was aseptically transferred from an LB-agar plate into 100 mL of LB broth. The inoculated broth was incubated at 37^{o}C with 200 RPM shaking. When an OD_{600} of 0.6 was obtained, the culture was transferred into 50 mL Falcon tubes and incubated on ice for 10 minutes. The culture was pelleted by centrifugation at 4000 x g for 10 minutes at 4^{o}C and the supernatant discarded. The cell pellet was then re-suspended by gentle pipetting in 10 mL of ice-cold $CaCl_2$ (100 mM) and incubated on ice for a further 10 minutes prior to re-centrifugation at 4000 x g for 10 minutes (4^{o}C). The supernatant was discarded and the pellet re-suspended in 2mL ice-cold $CaCl_2$ (100 mM). The cells were incubated on ice for at least 2 hours, after which they were dispensed into 100 µL aliquots in pre-frozen Eppendorf tubes and stored at -80^{o}C until required.

2.2.2.2 Transformation of chemically competent *E.coli* cells

Transformation of the required *E.coli* strains was accomplished by an altered version of the heat shock procedure described by (257). Aliquots of the necessary competent cells were retrieved from -80^{o}C storage and thawed on ice for 10 minutes. 20 - 100 ng of the desired plasmid DNA (1-2 µL) was transferred to each appropriate aliquot of competent cells and allowed to incubate on ice for 20 minutes. Following incubation, the cells were rapidly transferred to a 42^{o}C water bath for 90 seconds and immediately placed back on ice for 2 minutes. 200 µL LB broth was added to each aliquot and the cells were incubated at 37^{o}C for 45-60 minutes, after which they were plated out onto LB agar plates containing an appropriate concentration of the necessary antibiotic. Plates were incubated at 37^{o}C in a static incubator overnight (approximately 16 hours) and subsequently assessed for the presence of colonies. All transformation procedures occurred alongside negative controls, involving the heat shock of competent cells in the absence of vector; this ensured that the cells had not developed resistance to the selective antibiotic in the absence of the antibiotic-resistance marker conferred by the chosen plasmid.

2.2.2.3 Plating bacteria

2% agar plates were prepared by addition of 2 g agar to 100 mL LB-broth, followed by autoclaving at 120^{o}C. Autoclaved LB-agar was allowed to cool to approximately 45^{o}C before addition of the necessary antibiotic (if required). The warm LB-agar was subsequently poured into sterile petri dishes and left to solidify at room temperature. The plates were surface dried in an oven at 65^{o}C for 5-10 minutes and allowed to cool to room temperature. Bacterial suspensions were dispensed evenly across the surface of the agar using sterile disposable plastic spreader. When all of the bacterial suspension had been absorbed into the agar, the plate was inverted and incubated at 37^{o}C for approximately 16 hours.

2.2.2.4 Growth of bacteria for plasmid extraction

To obtain a high copy number of the desired plasmid DNA, TOP10 *E.coli* transformed with the necessary plasmid transferred into 5-10 mL LB media containing the appropriate antibiotic and grown overnight at 37^{o}C with 200 RPM orbital shaking. The LB media was inoculated from an agar plate, glycerol stock or liquid culture using a sterile wire loop.

2.2.2.5 Growth of bacteria for start cultures in protein expression experiments

The necessary *E.coli* strain harbouring the plasmid of choice was grown overnight in LB supplemented with the selective antibiotic (37^{o}C with 200 RPM orbital shaking). Cultures were inoculated from an agar plate, glycerol stock or liquid culture using a sterile wire loop or pipette tip. Cultures were grown either in sterile 28 mL glass universals or small glass conical flasks.

2.2.2.6 Growth of bacteria for expression trials

Following the transformation of one or more suitable expression strains with the plasmid DNA of choice, small scale expression trials were conducted to assess optimal conditions for recombinant protein over-expression. Expression trials required the production of a starter culture containing the transformed bacteria of choice (section 2.2.2.5). Initial expression tests involved inoculation of 50 mL growth media with 500 µL of the appropriate start culture, where either LB, TB or autoinduction media was utilised depending on requirements. All bacterial growth media was supplemented with the appropriate antibiotic. For cells grown in LB or TB media, the recombinant *E.coli* strains were grown at 37^{o}C with 200 RPM shaking in baffled flasks until mid-exponential phase

(OD_{600} 0.6-0.8), at which point they were cooled to the desired temperature and IPTG added to a final concentration of 0.1, 0.5 or 1.0 mM. Cultures were subsequently incubated at 18ºC, 25ºC or 37ºC for a suitable amount of time. Autoinduction was based on the Terrific Broth formulation from 'ForMedium', wherein induction occurs as a result of the uptake of lactose from bacteria after glucose (preferentially uptaken by bacteria for energy metabolism) is depleted in the medium. The amount of glucose present in auto-induction media is formulated to become depleted at a high cell density, leaving only lactose available for bacterial energy metabolism and therefore resulting in induction of target protein expression. Where autoinduction media was concerned, cells were incubated at 18ºC, 25ºC or 37ºC for up to three days. Samples from autoinduction cultures were harvested every 6 hours. In all cases, induced cultures were harvested by centrifugation at 4000 x g for 20 minutes. Subsequent re-suspension of the pellet was undertaken in lysis buffer (25 mM HEPES pH 7.5, 500 mM NaCl, 5 mM imidazole and 5% glycerol), and the resulting suspension of cells either immediately processed (section 2.2.4.3) or frozen for later use. For preps exhibiting proteasomal degradation, such as the Miro full-length preps, the commercial protease inhibitor cocktail P8849 (Sigma-Aldrich, UK) was added according to the manufacturer's instructions immediately following cell resuspension.

2.2.3 DNA methods

2.2.3.1 Preparation of donated plasmid DNA

In all cases, donated plasmid DNA was provided as a blot on filter paper. To extract pDNA from the filter paper, the paper was cut into small fragments using a sterile scalpel and transferred to clean Eppendorf tube. 30 µL of QIAPrep elution buffer was added to each tube of blotted DNA and incubated at 50^{o}C for 30 minutes, followed by a further incubation at room temperature for 30 minutes. 10 µL of the elution buffer was subsequently transferred to a sterile Eppendorf tube and incubated on ice for 10 minutes prior to incubation with TOP10 competent cells for heat shock transformation (2.2.2.2). Transformation of TOP cells with donated plasmid DNA was as previously described (2.2.2.2) with slight alterations: TB media was used as the recovery medium following heat shock, and the cells incubated at 37^{o}C for at least 1 hour to ensure suitable recovery of transformed bacteria.

2.2.3.2 Plasmid DNA extraction and purification from recombinant *E.coli* cells

A single colony from a freshly streaked plate was aseptically transferred to 5 mL LB medium in a sterile 28 mL glass universal, where both the plate and LB medium contained the antibiotic to which recombinant cells harbouring the desired plasmid were resistant. The inoculated medium was subsequently incubated at 37^{o}C with orbital shaking at 200 RPM. Following incubation, the bacterial cells were harvested by centrifugation at 5400 x g for 15 minutes (4^{o}C).

2.2.3.3 Polymerase Chain Reaction (PCR)

Numerous different protocols were used (see Appendix 3 for detailed information regarding each protocol). In each case, PCR success was assessed by agarose gel electrophoresis using 10 µL of the completed PCR reaction.

2.2.3.4 PCR clean-up

Purification of PCR products was accomplished by use of the QIAquick PCR Purification Kit (Qiagen, UK), where all centrifugation steps occurred at 17, 900 x g in a conventional table-top microcentrifuge at room temperature. 5 volumes of Buffer PB were added to 1 volume of the PCR reaction and mixed by pipetting, with the resulting solution transferred to an unused QIAquick column attached to a 2 mL collection tube and centrifuged for 60

seconds. The flow through was discarded. 750 µL Buffer PE was subsequently added to the QIAquick column and the column centrifuged for 60 seconds. Again, the flow-through was discarded. The QIAquick column was then centrifuged for a further 60 seconds to remove latent Buffer PE. Elution of DNA from the column was then achieved by addition of 30 µL Buffer EB to the column, which was subsequently placed in a sterile Eppendorf tube and incubated for 1 minute at room temperature prior to 60 seconds centrifugation. To determine the success of the purification, 5 µL of the eluted sample was subjected to agarose gel electrophoresis as described in section 2.2.3.7.

2.2.3.5 Quantification of DNA

DNA was quantified spectroscopically at 260 nm using the NanoDrop 2000 spectrophotometer (Thermo Fisher Scientific, UK) connected to a laptop containing the NanoDrop 2000/2000c software package. Between each use, the NanoDrop 2000 sample pedestal (lower optical surface) was gently wiped clean with a lens tissue to remove residual sample, blank or water. Liquid measured spectroscopically by the NanoDrop 2000 was dispensed at 1 µL onto the lower optical surface (sample pedestal) and the instrument lever arm (containing the upper optical surface) lowered to produce a liquid column between the optical surfaces. To initiate the apparatus, sterile deionised water was first dispensed onto the sample pedestal. Subsequently, QIAprep Buffer EB was dispensed onto the sample pedestal and a blank measurement taken. Sample DNA could then be dispensed onto the sample pedestal for spectrophotometric quantification, with DNA concentration calculated by the NanoDrop 2000 software and provided in µg/mL.

2.2.3.6 Restriction digestions

Typically, restriction digests occurred in a volume of 30 µL, where 3 µL of a suitable 10x buffer provided by NEB was utilised in addition to 2 µL of each enzyme. DNA concentrations differed from digest to digest depending on context, with up to 5 µg DNA digested. Digestions were conducted at 37^{o}C for 1-4 hours.

2.2.3.7 Agarose gel electrophoresis

1% (w/v) agarose gels were prepared by heating agarose in 1 x TAE buffer (2.1.5.1.3) until fully dissolved. Following heating, the agarose solution was allowed to cool to approximately 60^{o}C and poured into a gel casting tray of the necessary size. Bubbles were avoided by slow pouring and the use of a sterile pipette tip to remove bubbles immediately after pouring. An appropriately sized comb was inserted into the solution and the gel

allowed to set for approximately 15 minutes. Set gels were placed into agarose gel electrophoresis tanks and submerged in 1 x TAE buffer prior to removal of the gel comb by hand. Samples were prepared by the addition of 2 µL of an appropriate 6 x DNA loading buffer per 10 µL of sample. Appropriate loading buffer was defined as a buffer containing a dye that would run much faster or slower during electrophoresis than the expected DNA sample bp size; this was to aid visualisation of DNA and to avoid contamination of dye substances during gel purification procedures. Either bromophenol blue 6x loading buffer (2.1.5.1.1) or xylene cyanol 6x loading buffer (2.1.5.1.2) was used. Samples were mixed and loaded carefully into wells using a micropipette. In addition to loading samples, 10 µL of suitable side standard was loaded into an empty well in order to determine the size of DNA fragments post-electrophoresis. The electrophoresis apparatus was attached to a power pack and electrophoresis initiated at 120 volts until a suitable separation of DNA had been obtained.

2.2.3.8 Visualisation of DNA and photography of agarose gels

Following electrophoresis, agarose gels were stained by submersion in 10 µg/mL ethidium bromide solution for 15 minutes. An ethidium bromide solution was repeatedly used for analytical gels until staining appeared diminished, at which point a new solution was created. For gels required for agarose gel purification, however, ethidium bromide was freshly prepared in sterile deionised water and used each time. Following staining, DNA fragments were visualised by the ultraviolet (UV) source emitted by the Bio-Rad Gel Doc 2000 gel documentation system, accompanied by Quantity One software. Physical copies of gel visualisations were obtained using a Mitsubishi Video Copy Processor (Model P91) attached to the gel documentation device, fed with Mitsubishi thermal paper (K65HM-E/High density type, 110 mm x 21 mm). Soft copies of images were maintained on an external hard-drive.

2.2.3.9 Agarose gel purification

Agarose gel purification is a technique in which a DNA band is excised from an agarose gel following agarose gel electrophoresis (2.2.3.7), in order to isolate a DNA fragment of a desired size. All agarose gel purifications were implemented via aid of the QIAquick Gel Extraction Kit (Qiagen), with every centrifugation occurring at 17,900 x g in a benchtop micro-centrifuge for 60 seconds. First, the sample to be purified is subjected to agarose gel electrophoresis. The gel is then visualised under low intensity 'prep' UV light, to locate the fragment of interest and liberate the gel segment containing the fragment by

use of a clean scalpel. The gel segment of interest was placed into a pre-weighed micro-centrifuge tube and subsequently re-weighed to obtain the weight of the gel slice. For every 100 mg of agarose gel, 300 µL of QG buffer was added to the tube. The gel was then dissolved by incubation of 50^{o}C for 10 minutes with brief vortexing every 2-3 minutes. Once fully dissolved, 100 µL of isopropanol was added for every 100 mg of gel, and the sample loaded into a QIAprep spin filter tube placed in a 2 mL collection tube. The sample was centrifuged and the resulting flow through discarded. Subsequently, 500 µL of QG buffer was added to the spin filter column and centrifuged for one minute, with the flow-through again discarded. 750 µL buffer PE was then added to the spin filter column, which was again centrifuged and the flow-through discarded. After another centrifugation to remove residual ethanol from the PE buffer, the spin filter column was placed into a sterile 1.5 mL Eppendorf tube and 30 µL of EB buffer added to the centre of the spin filter column. The column was allowed to sit at room temperature for 1 minute and subsequently centrifuged to elute the gel purified sample into the sterile Eppendorf tube. The filter was discarded and the purified sample retained for use. Purification was assessed by removing 2 µL of purified sample and diluting it in a separate tube with 8 µL of sterile distilled water. The sample was then assessed by agarose gel electrophoresis as described previously. Verified purified samples were either used immediately or stored at -20^{o}C.

2.2.3.10 Ligation

All ligations were performed at a 3:1, 5:1 and 8:1 insert to vector ratio, with concentrations determined by use of the NanoDrop 2000 spectrophotometer (Thermo Fisher Scientific), as described in 2.2.3.5. The components of a typical ligation are shown in Table 2.21. The components were added to a target volume of 10 – 25 µL, with the lowest possible volume used in each case. The components were added together in a sterile 1.5 mL Eppendorf tube, mixed by tapping and pulse spun before incubation at room temperature for 25 minutes. Following incubation, 2 µL of each reaction was added to an aliquot of competent TOP10 cells on ice in order to perform the heat shock procedure described in 2.2.2.2. The remaining ligation reaction mixture was frozen for further use if necessary.

Table 2.21 Components of a typical ligation reaction. Where the amount of DNA fragment added was dependent on the desired ratio, length of fragment (bp) and concentration (ng/µL).

Component	Amount
Desired plasmid (vector) cut with appropriate restriction enzymes	100 ng (~5 µL)
10 x ligation buffer	2 µL
DNA fragment cut with appropriate restriction enzymes	7 µL
Sterile deionised water	5 µL
T4 DNA Ligase (3 U/µL)	1 µL

2.2.3.11 Site-directed mutagenesis (SDM) procedure

Site-directed mutagenesis (SDM) was performed with reference to the Stratagene instruction manual for the QuickChange: Site-Directed Mutagenesis Kit, though the kit itself was not utilised. Mutant primers (Appendix 4) with a length of 25-45 bases and GC content of ≥ 40% were designed with the target mutation at the centre of the primer and a Tm (melting temperature) of ≥ 78ºC. The Tm for each primer was determined as follows:

Tm = 81.5 + 0.41 (%GC) - 675/ N - % mismatch

Where N = primer length in bases

%GC = percentage of guanine and cytosine residues in the primer

%mismatch = percentage of the primer non-complementary at the point of the mutation

To aid in primer design, the online program PrimerX was utilised (258), available at: http://www.bioinformatics.org/primerx/index.htm

Mutant plasmids were subsequently generated by PCR, using the target plasmid to mutate as PCR template. The subsequent PCR products were then digested with 1 µL of DpnI (10 U/µL) restriction enzyme for 1 hour at 37ºC. Chemically competent TOP10 *E.coli* cells were then transformed with the DpnI treated DNA as described in 2.2.2.2.

Components of all SDM reactions and exact details of the PCR programs used to produce mutant plasmids by SDM can be found in Appendix 4.

2.2.4 Protein methods

2.2.4.1 SDS-PAGE electrophoresis

12% SDS-PAGE gels were used as standard throughout this project. All gels were produced manually in-house. Gels were poured between two clean glass plates of 10.1 x 7.2 cm and 10.1 x 8.2 cm dimensions, with a 1 mm spacer ridge present on the larger plate. Prior to pouring, the plates were clamped together, ensuring that the lower sections were aligned. The plates were then secured with vertical downward pressure in a casting stand with rubber cushioning. The components for the resolving gel (section 2.1.5.1.6) were dispensed into a Falcon tube and poured into the space between the two plates, leaving a gap of approximately 1-2 cm below the top of the smallest plate. Water or isopropanol was then layered over the top of the resolving gel to ensure a straight gel and prevent drying out during polymerisation. The resolving gel was allowed to set for approximately 15 minutes and the water layered on top removed by filter paper absorption. The components of the stacking gel (section 2.1.5.2.4) were then added together separately into a Falcon tube and mixed prior to pouring between the SDS-PAGE plates. To produce wells, a 10-toothed comb was then immediately placed between the plates to the top. The stacking gel was allowed to set for approximately 20 minutes and the comb subsequently removed, leaving defined wells which were rinsed with distilled water prior to securing the gel vertically into electrophoresis apparatus. The electrophoresis apparatus was placed into an SDS-PAGE tank which was then filled with SDS-PAGE 1 x running buffer (secion 2.1.5.1.4). Samples were prepared by addition of 5 µL of SDS-PAGE loading buffer (section 2.1.5.1.5) to 20 µL of sample, with all separate samples loaded into a unique well. 4 µL of BioRad Precision Plus All Blue was also loaded into an empty well as a molecular weight side standard for each gel. Prior to loading with a micropipette, all samples were boiled for 5 minutes at 120^{o}C and subsequently pulse spun in a micro centrifuge. Samples and side standards were loaded with a P20 Gilson pipette using an appropriately sized tip. Electrophoresis was undertaken by connecting the SDS-PAGE electrophoresis equipment to a BioRad powerpack (BioRad, UK) and applying an electric field at 200 volts, 120 milliamps until the visible dye front surpassed the bottom of the gel (approximately 60 minutes). Each gel was then liberated from between the plates and stained (2.2.4.2).

2.2.4.2 Visualisation of protein bands and photography of SDS-PAGE gels

After electrophoresis, the SDS-PAGE gels were removed from the plates and placed into Coomassie blue stain for 60 minutes with 50 RPM shaking followed by immersion in de-staining buffer overnight at room temperature with 100 RPM shaking until bands were visible and the background was significantly de-stained. Gels were subsequently photographed via use of the Bio-Rad Gel Doc 2000 gel documentation system connected to Quantity One software. Hard copies of gels were produced using a Mitsubishi Video Copy Processor (Model P91) connected to the Gel Doc system, which printed onto Mitsubishi thermal paper (K65HM-E/High density type, 100 mm x 21 mm).

2.2.4.3 Isolation of intracellular proteins from recombinant *E.coli*

Cultured expression strains were centrifuged in 450 mL centrifuge tubes for 20 min at 4,000 xg. The supernatant was discarded and the cells re-suspended in 10 mL lysis buffer. Subsequently, the cells were lysed by sonication through 10 cycles of 30 second pulses at an amplitude of 14, with 15 second rest intervals between each pulse. The resulting lysate was decanted into a sterile 50 mL centrifuge tube and centrifuged at 4°C for 60 min at 16,000 x g. The soluble fraction was retained in a sterile plastic universal and on ice until purification (2.2.4.4) was performed.

2.2.4.4 Ion metal affinity chromatography for His-tagged Protein purification

For high yield protein purification, an automated FPLC system (AKTA PRIME, GE Lifesciences) was utilised, connected to two consecutively attached 1 mL Ni Sepharose HisTrap columns (GE Lifesciences). The columns were stored in 20% ethanol at 4^{o}C prior to use, with 30 mL double distilled water pumped through the columns at 0.5 mL/min to remove the ethanol. Before storage, the columns were stripped with 100 mM EDTA at 1.5 mL/min for 10 column volumes. 18.2 Ω distiller water was then pumped through the columns at 1.5 mL/min for 5 column volumes prior to recharging the columns with 10 volumn volumes of 500 mM $NiSO_4$ at 1.5 mL/min. Another 5 column volumes of 18.2 Ω distilled water was then pumped through the columns at a rate of 1.5 mL/min prior to equilibration of the columns with 10 column volumes of start buffer (section 2.1.5.1.9) at a rate of 1 mL/min. The sample to be IMAC-purified was then loaded onto the columns at 1 mL/min through a sample inlet tube attached to the automated FPLC system. Once all of the sample had been loaded, 20 mL of lysis (“start”) buffer was then loaded through the sample inlet tube at 1 mL/min to ensure that the entirety of the sample

was loaded onto the columns. Finally, the protein was eluted at a flow rate of 1.5 mL/min using a linear gradient of imidazole (elution buffer; 2.1.5.10) extending from 5 mM to 500 mM. The location of the target protein was assessed by monitoring A280 using a UV spectrometer attached to the FPLC, and samples collected in 2 mL fractions using an automated fraction collector. Purity of eluted protein samples was assessed by SDS-PAGE electrophoresis of appropriate fractions.

2.2.4.5 Gel filtration chromatography

Gel filtration represents a simple chromatographic method for separating molecules according to size. A variety of gels are available, comprised of porous beads suspended in an eluent. The gels are available with pores of a controlled range of sizes, serving as a molecular sieve for separating molecules by size. The largest molecules are unable to fit through the pores in the gel matrix, and thus are eluted first, while the smaller molecules access the pores and are retained in the gel matrix for a longer time period.

A sephacryl™ S-200 HR HiPrep™ 16/60 column (GE Lifesciences) attached to an automated FPLC system (AKTA PRIME, GE Lifesciences) was utilised for gel filtration purposes. Prior to each use, this column was stored in 20% ethanol at room temperature. Removal of storage ethanol occurred at 0.5 mL/min with 60 mL double distilled water initially. Another 30mL of double distilled water was subsequently pumped through the column at 1mL/min. The column was then equilibrated with 60mL gel filtration buffer (section 2.1.5.11) at 1 mL/min. Once equilibrated, purified protein from an affinity column was concentrated to 2 mL and pre-loaded into a 2 mL superloop connected to AKTA PRIME sample input port. A syringe filled with gel filtration buffer was then attached to the sample input port, the system set manually to “inject” and the sample within the loop injected onto the column at 0.5 mL/min according to AKTA PRIME manufacturer’s instructions. As per manufacturer’s recommendations, the entirety of the sample was injected and the system reset to “load” position before removal of the syringe at the sample input port. Each gel filtration was then performed at 1 mL/min until a length of 180 mL had passed through the column, with 3 mL fractions collected via the automated sample collection carousel. All results obtained were compared against a gel filtration calibration curve prepared using the low molecular weight calibration set from GE Healthcare, United Kingdom (see Appendix 6).

2.2.4.6 Concentration of target protein

Concentration of proteins was undertaken at 10^{o}C by centrifugation at 4000 x g in 15 mL concentrators of the appropriate kDa cut-off. After concentrating all fractions containing the desired protein to approximately 1 mL, protein concentration was quantified by Bradford's assay (2.2.4.7) and the protein retained for downstream processing.

2.2.4.7 Determination of protein concentration

Bradford reagent (Sigma Aldrich, UK) was performed to estimate protein concentration. The Bradford method involved the production of BSA standards (diluted in target buffer) with concentrations ranging from 1 - 10 µg/mL. After warming the Bradford reagent to room temperature, 5 µL of protein standards were added in triplicate to separate wells in a sterile 96 well plate. 5 µL of the target buffer was then added in triplicate to separate wells. Finally, 5 µL of the sample was added in triplicate to separate wells. Additionally, 1:10 and 1:50 sample:buffer versions of the sample were dispensed in triplicate in separate wells. 250 µL of Bradford reagent was added to each well and mixed on a shaker for ~30 seconds. The samples were incubated at room temperature for 5 minutes and the absorbance of each well read at 595 nm. The production of a standard curve of BSA concentration was then used to estimate the protein concentration of the desired sample.

2.2.4.8 Semi-dry Western blotting

Throughout this project, Western blotting was applied as a method for the detection of specific target proteins in recombinant *E.coli* lysate, purified protein samples and lysate obtained from COS7 cells. First, samples, controls and visible marker (BioRad Precision Plus All Blue) of interest were subjected to SDS-PAGE gel electrophoresis as described in 2.2.4.1. Following electrophoresis, the gel was submerged in semi-dry transfer buffer (2.1.5.4.4) in a clean container. The blotting paper and blotting membrane to be used were also placed in the same transfer buffer, in separate clean containers. However, if a PVDF membrane was to be used, the membrane was first placed briefly in methanol before submersion into transfer buffer. The gel, blotting paper and membrane were incubated in transfer buffer at room temperature for 10 minutes and subsequently placed on a horizontal semi-dry transfer block in the following order: blotting paper, membrane, gel, blotting paper. A sterile pipette was used to flatten the assembled blotting items, ensuring the removal of bubbles and excess buffer. The transfer block was then connected to a powerpack and the protein bands allowed to transfer from gel to membrane for 30 minutes

at 20 volts. Success of the transfer was evaluated by the extent of transfer of the visible marker from SDS-PAGE gel to membrane. Following a successful transfer, the blotting membrane was placed into blocking solution (2.1.5.4.5) and blocked either for 30 minutes at room temperature with moderate shaking or at 4^{o}C overnight. The membrane was subsequently washed with 2 washes of 1 x PBS (2.1.5.4.3) prior to incubation with the primary antibody of choice in 0.05% blocking solution 2.1.5.4.5). The blot was left to incubate with primary antibody either for 2 hours at room temperature with moderate shaking or overnight at 4^{o}C with mild shaking, the latter of which was preferred if the quality of antibody had yet to be determined. Incubation with the primary antibody was followed by five washes implemented under moderate shaking of five minutes each of the following: PBS, PBST, PBST, PBST, PBS. The secondary antibody (diluted in PBS) was then added and left to incubate for 90 minutes at room temperature with moderate shaking. Finally, the five washes were repeated and enhanced chemiluminescence (ECL) solution (BioRad, UK) prepared by mixing the luminol and peroxidase components in equal quantities. The membrane was incubated with ECL for 5 minutes in the dark with moderate shaking prior to visualisation with a G:BOX Chemi XT4 chemiluminescent visualisation device (Syngene, UK) using GeneSys Software v 1.01 (Syngene, UK).

2.2.4.9 Protein crystallisation

Crystallisation attempts were executed according to the vapour diffusion method using 24-multi well plates (Falcon® Mutltiwell^{TM} 24 well, Becton Dickinson, UK). The rim of each well was coated in vacuum grease and 500 µL of appropriate crystallisation buffer (Appendix 2) aliquoted into each well. Pre-silanised cover slips were polished with silk scarf and 1 µL protein solution at 5mg/mL or higher concentrated added with 1 µL of the appropriate crystallisation buffer (taken from the corresponding well) to form a 2 µL drop. The cover slip containing the 1:1 (v/v), and 2:1 protein:precipitant was subsequently inverted and sealed above the appropriate well. This method was utilised for all crystallisation buffers. The plates were labelled appropriately and incubated at 22^{o}C. The incubated plates were monitored for crystal growth every day for 4 weeks, then subsequently every 3 days for week for 12 weeks.

2.2.5 *In vitro* characterisation methods

2.2.5.1 Malachite green assessment of phosphate release

The malachite green colorimetric method is typically regarded as the gold standard in analysing the release of phosphate by hydrolytic enzyme activity. The assay works on the principle of a colour change when malachite green molybdate and free orthophosphate complex under acidic conditions. The absorbance of the green molybdophosphoric acid complex at 620-640 nm is directly indicative of free organic phosphate concentration. Thus, a malachite green assay kit (Cayman Chemicals Ltd.) was utilised to assess nucleotide hydrolytic activity of enzymes, with the absorbance of phosphate standards provided by the manufacturer assessed in triplicate to generate a standard curve for phosphate concentration. This enabled the absorbance values obtained from nucleotide hydrolysis assays to be converted into amount of phosphate generated. All assays were performed according to the manufacturer's instructions, with absorbance values read at 635 nm on a FLUOStar Omega plate reader maintained at 25^{o}C. 2 mM of $MgCl_2$, $CaCl_2$ or both was added to each reaction as a co-factor, accordingly. Assays were performed with either 0.25 mM, 0.5 mM or 1 mM nucleotide substrate (ATP, GTP, UTP or CTP), depending on context. Assay buffer with substrate added was used as a blank control to assess acid hydrolysis of nucleotides in the absence of GTPase.

2.2.5.2 PiColourLock™ assessment of phosphate generation

PiColourLock™ Gold, a modified form of the standard malachite green assay kit (Innova Biosciences) was utilised as a secondary means of verifying the hydrolytic capacity of target enzymes. As with 2.2.5.1, a standard curve for phosphate concentration with this kit was generated based on the manufacturer's instructions. This standard curve was used to assess phosphate generation by target enzymes when assays were performed according to standard operating procedure advertised by the manufacturer. Assays were performed in triplicate in 96-well plates at 25^{o}C or 37^{o}C. A typical reaction mixture comprised the following: the enzyme of choice, GTP and one of more cations ($MgCl_2$, $CaCl_2$ or both cations). After 30 or 60 minutes, the reaction was stopped by addition of the 'PiColourLock™ Gold Mix'. This plate was shaken gently and incubated for 5 minutes at room temperature prior to addition of the PiColourLock™ stabiliser compound. After 15 minutes, the absorbance of each well was read at 635 nm on a FLUOStar Omega plate reader maintained at 20^{o}C. Assay buffer containing GTP was utilised as a control.

Absorbance values were generated by subtracting blank absorbance from each raw value, and mean values used to generate bar charts.

2.2.5.3 Phosphorylation assays to assess kinase activity on target proteins

The kinases (DRAK2 constructs) and their putative protein targets (RhoH constructs) were bacterially expressed in C43 (DE3) or BL21 (DE3) *E.coli* as described previously (2.2.2.5 – 2.2.2.6). All kinases and targets harboured hexahistidine tags and, as such, were isolated from their expression hosts (2.2.4.3) and subject to IMAC purification (2.2.4.4) followed by gel filtration (2.2.4.5) to achieve sufficient purification and remove imidazole. Confirmation of the identity of each protein was performed by Western blotting (2.2.4.8) using antibodies specific to the target, or by single-band LC-MS analysis (2.2.6.2).

To perform each phosphorylation assay, a reaction mixture for each condition was created in triplicate. Typically, a reaction mixture consisted of a set concentration of a specific kinase (10µM or 20µM) in combination with either 5 times or 10 times a specified putative target, with the reaction occurring in gel filtration buffer (2.1.5.3.3) supplemented with 2 mM $MgCl_2$ and 1 mM ATP. ATP was the final component added to the reaction mixture. Samples were taken at 0 minutes, 10 minutes and 45 minutes following the addition of ATP and frozen immediately at -80^{o}C in 1.5 mL sterile Eppendorfs.

To analyse the success of each reaction, samples were later thawed and an appropriate amount of SDS-PAGE buffer (2.1.5.2.2) added. The samples were then subjected to SDS-PAGE electrophoresis (2.2.4.1) and Western blotting performed (2.2.4.8) using the ab17464 Anti-phosphoSer/phosphoThr polyclonal (AbCam) in the dilutions shown in Table 2.4 (2.1.1.4). To ensure loading consistency for Western blotting and confirm the presence of RhoH and DRAK2 constructs on the blotting membrane, select blots were stripped and re-probed with either an anti-RhoH or anti-DRAK2 primary antibody in the dilutions shown in Table 2.4 (section 2.1.1.4). Additionally, all SDS-PAGE gels used in Western blotting were dyed in Coomassie blue (section 2.2.4.2) post-transfer to further assess Western blotting loading efficiency.

2.2.5.4 Dynamic light scattering (DLS) for determination of oligomeric state

Dynamic light scattering (DLS) is a technique for measuring particle size within the sub-micron region and has been previously established as a method of determining oligomeric

state. DLS measurements are based on Brownian motion (pedesis), the random motion of particles in solution as a result of collisions with the surrounding medium.

DLS experiments were performed using a Zetasizer Nano S dynamic light scattering instrument (Malvern, UK) at the Institute for Cell and Molecular Bio Sciences (ICamB), Newcastle University. A solution of 0.5 mg/mL protein suspended in an appropriate buffer (50 mM HEPEs pH 7.4, 500 mM NaCl, 5mM DTT, 2% glycerol) was centrifuged at 4°C, 16900 x g for 5 minutes. 60 µL was then added to a 45 µL quartz glass cuvette (Hellma; 10.5.251-QS), which had been extensively cleaned with 2% (v/v) Hellmanex, deionised water and 100% Ethanol and air-dried before use. Four replicate runs were performed for each sample in addition to a blank run with buffer alone. Samples were subjected to a 633 nm laser and light scattering detected at 173^{o} by an avalanche photodiode. Size measurements and analysis were performed using Zetasizer software version 4 (Malvern, UK) and results plotted using Excel (Microsoft) and SigmaPlot (Systat).

2.2.5.5 Analysis of protein stability by circular dichroism (CD) thermal denaturation

Circular dichroism (CD) thermal deanturation experiments were performed using a J-810 spectropolarimeter (Jasco). 400 µL of 0.5 mg/mL protein in a solution containing 50 mM HEPES pH 7.4, 500 mM NaCl, 5mM DTT and 2% glycerol was added to a 0.1 cm quartz glass cuvette (Hellma; 110-1-40 QS) that had been extensively cleaned with 2% (v/v) Hellmanex, deionised water and 100% Ethanol and air dried before use. The temperature was increased from 20°C to 95°C at a rate of 2°C/min using a Peltier temperature control device. CD absorbance was measured at a wavelength of 220 nm every 0.2°C. A sensitivity of 100 mdeg was used, with a slit width of 2 nm. T_m values were determined by examining the peak minima of the first order derivative plot of each melting curve. For presentation, units were converted to fraction folded using the absorption values at 25°C and 95°C to represent fully folded and fully unfolded protein respectively. Due to limitations on the amount of sample, each sample was only measured once.

2.2.6 Mammalian cell culture methods

2.2.6.1 General conduct

All mammalian cell culture techniques were performed aseptically under laminar flow in a class II biological safety cabinet. 70% ethanol was utilised to sterilise the cabinet prior to use. Additionally, all items placed into the safety cabinet were sterilised with 70% ethanol before use. Enhanced cleanliness was observed in the laboratory under which mammalian culture methods were implemented, with lab coats and other items from microbiological laboratories prohibited.

2.2.6.2 Culture of mammalian cells

Several adherent cell lines were sampled for protocol optimisation and initial mammalian cell experiment set-up, namely: COS7, MCF-7, hVSMC, PC3 and HEK-293 (see Appendix 5 for further information). Cells were maintained at 37ºC/5% CO_2 in complete DMEM media as described previously (2.1.4.3). hVSMCs required additionally components for growth (Appendix 6). Mammalian cells were permitted to grow until 70-90% confluent prior to passaging (2.2.5.2).

2.2.6.2 Mammalian cell passage

Adherent mammalian cells were subject to passage when 70-90% confluent. Passage involved the removal of media from confluent cells under sterile conditions, followed by the washing of the cell monolayer twice with phosphate buffered saline (PBS). PBS was removed and 0.25% trypsin-EDTA added at a volume able to cover the monolayer. The cells were allowed to incubate with trypsin-EDTA at 37ºC for 5 minutes until cellular adherence to the culture vessel was visibly disrupted under a microscope. To stop the trypsinisation reaction, complete media was added at an excess volume to the trypsin-EDTA present. The resulting solution containing the target mammalian cells was spun at 1200 x g for 5 minutes, producing a pellet comprised of the target mammalian cells. Supernatant was removed from this pellet, and the pellet re-suspended in 1 mL complete media. A fraction of this re-suspended pellet, typically 200 µL, was transferred to a new culture flask containing the fresh complete media of choice. Complete media for the target mammalian cells and 0.25% trypsin-EDTA were warmed to 37ºC in a water bath prior to use.

2.2.6.3 Counting cells

Cell counting was performed using a glass haemocytometer, plastic coverslip and trypan blue to assess cell viability. Prior to use, the haemocytometer and coverslip were sterilised with 70% ethanol. The coverslip to be used was moistened and affixed to the haemocytometer, with Newton's refraction rings observed to indicate correct adhesion of the coverslip. The haemocytometer was placed under laminar flow and the cell suspension to be assessed swirled gently and 100 µL transferred into a sterile 1.5 mL Eppendorf. 400 µL 0.4% trypan blue solution was added to the 100 µL cell suspension and mixed gently. 100 µL of the resulting solution of trypan blue and cells was applied to the haemocytometer and unstained (live) cells counted with a hand tally counter under 10x objective under a microscope, with four 16 corner squares of cells assessed in this manner. The average cell count was multiplied by 10^4 and further multiplied by five to correct for the trypan blue dilution. The final value obtained represented the number of viable cells per mL of original cell suspension.

2.2.6.4 Plasmid DNA transfection of mammalian cells

Lipofectamine™ 2000 reagent was utilised for the transfection of exogenous plasmid DNA (pDNA) into mammalian cells, according to method optimisation based initially on the manufacturer's instructions. 250,000 cells were plated into each well of a 6-well plate using the appropriate complete media and allowed to grow at 37ºC/5% CO_2 until 65-70% confluent (approximately 20 hours for COS7 cells). When sufficiently confluent, this complete media was removed from each well and the mammalian cell monolayer washed twice with PBS. 2mL of the usual basal media for the target cells was added to each well; this media contained 10% FBS and 2 mM L-glutamine albeit was devoid of antibiotics. For each well, 1000 ng of the pDNA of choice was diluted in a separate, sterile Eppendorf containing 125 µL Opti-MEM® media. For each well, 6.25 µL Lipofectamine™ 2000 reagent was also diluted in 125 µL Opti-MEM® media in a separate sterile Eppendorf. The diluted pDNA for each well was then added to the corresponding diluted Lipofectamine™ 2000 reagent and incubated for 25 minutes. The pDNA-lipid complexes were then added to each well accordingly. Typically, cells were allowed to incubate for 24–48 hours prior to lysis and extraction of proteins for downstream analysis.

2.2.6.5 Reverse siRNA transfection of mammalian cells

The reverse transfection technique for siRNA was utilised to transfect MCF-7 and PC3 cells in 24-well plates, allowing for completion of sets of siRNA-mediated knockdown in a shorter timeframe. Within each well, 3 pmol desired siRNA was diluted in 100 µL Opti-MEM® media and mixed gently. 1 µL of Lipofectamine™ RNAiMAX was subsequently added to each well containing diluted siRNA and allowed to incubate for 20 minutes at room temperature. During this 20 minute incubation, cells were trypsinised and pelleted as previously described (2.2.6.2). The pelleted cells were re-suspended in the typical complete media for these cells, though without antibiotics present. The cells were re-suspended so that 100, 000 cells were present per mL, and 500 µL of this re-suspended solution added to each well (50, 000 cells per well). The plate was then rocked gently back and forth and incubated at 37^{o}C/5% CO_2 for 36 hours prior to downstream processing as described in 2.2.5.6.

2.2.6.6 Lysis of mammalian cells for downstream processing

Following transfection of pDNA or reverse transfection of siRNA, target cells were lysed and subject to protein extraction. This first involved removal of growth media and washing the cell monolayer twice with 5-10 mL ice-cold PBS. The cells were then trypsinised and pelleted in 1.5 mL Eppendorfs using the method described in 2.2.6.2. The resulting cell pellets were re-suspended on ice in 30 µL of radioimmunoprecipitation assay buffer (RIPA buffer) supplemented with the P8340 protease inhibitor cocktail (Sigma Aldrich, UK), allowing for cell lysis to occur. Incubation was permitted for 30 minutes with occasional mixing by tapping. Each Eppendorf was then spun at 15,000 x g for 18 minutes (4^{o}C) and the subsequent supernatant retained on ice in a fresh sterile Eppendorf. The protein concentration of each resulting supernatant was determined using the Bradford method (2.2.4.7), and 20 µg of each sample loaded onto a separate well of an SDS-PAGE gel for subsequent downstream SDS-PAGE electrophoresis (2.2.4.1). This was then utilised for assessing knockdown or overexpression efficiency using Western blotting (2.2.4.8) or proteomic studies through geLC/MS (2.2.7.2).

2.2.6.7 Assessment of mammalian cell migration

Migration experiments were performed using an xCELLigence RTCA DP instrument (Roche Diagnostics GmbH, Germany) placed in a humidified incubator maintained at 37°C and 5% CO_2. For each experiment, a CIM-Plate 16 (ACEA Biosciences Inc., China)

was used, comprised of an upper and lower chamber separated by a microporous membrane containing randomly distributed pores of median 8 µm diameter. Cells were maintained in low serum (0.1% FBS) medium for 24 hours prior to each migration experiment. 190 µL complete RPMI media (containing 10% FBS) were added to the lower chambers and 50 µL serum-free media added to each upper chamber. The CIM-Plate 16 was placed in the RTCA DP device at 37°C and 5% CO_2 and allowed to equilibrate for 15 minutes. During this time, a baseline measurement was performed to establish background signal produced by serum-free media. Cells to be used (control cells or cells subjected to siRNA knockdown by reverse transfection as described previously)were trypsinised, pelleted and resuspended in serum-free RPMI media, the cells were subsequently counted and $2x10^4$ cells from each necessary sample seeded in the upper chamber. Each condition was performed in duplicate or triplicate, depending on the experiment and signal was detected on a schedule of every 15 minutes for 24 hours.

All data were recorded by RTCA software (v 1.2.1.1002) and raw data exported to MS Excel for analysis, with each set of replicates assessed and any unsatisfactory replicates excluded from analysis. Mean values were derived from each set of replicates and graphs produced showing cell index versus time in hours, where cell index may be defined as impedence versus baseline reading. Subsequently, the area under the curve of each mean value set was used to produce overall comparisons between control and knockdown samples.

2.2.6.8 Preparation of cells for fluorescent microscopy

Cells were grown on glass coverslips in 6-well plates using complete media until 70-90% confluent. Subsequently, the media was removed and the cells washed with PBS. A stock (1 mM) solution of Mitotracker Red FM (Life Technologies, UK) in DMSO was diluted to a final concentration of 250 nM in fresh complete RPMI media warmed to 37ºC. This solution was added to the cells and allowed to incubate at 37ºC/5% CO_2 for 30 minutes. The MitoTracker Red FM dye is a cationic fluorophore readily sequestered into the matrix space of polarised mitochondria. Unlike other cationic fluorophores such as rhodamine 123 and tetramethylrhodamine methylester (TMRM), Mitotracker Red FM contains a reactive chloromethyl group capable of forming covalent bonds with thiol groups of mitochondrial membrane proteins; this enables the Mitotracker to be retained within mitochondria even upon loss of mitochondrial membrane potential (259).

The coverslips bearing the cells were washed twice in ice-cold PBS and the cells fixed in methanol for 10 minutes at -20^{o}C. Following fixation, the cells were washed three times in ice-cold PBS. A drop of VECTASHIELD® mounting medium with DAPI (Vector Laboratories, UK) was added to the cells. The coverslip inverted and placed onto a Polysine® adhesion slide (VWR, UK) so that the cells and mounting medium were directly touching the slide. Processed samples were assessed under a Leica DM 5000 fluorescent microscope (Leica Microsystems, UK) at magnifications varying from 20x to 100x using differential interference contrast (DIC) and fluorescent filters to assess DAPI and Mitotracker-associated fluorescence. Areas non-uniformly stained or otherwise anomalous were disregarded and excluded from further analysis. Images were captured at 20x, 40x, 63x and 100x using a Leica DFC 310 FX digital camera attached to the fluorescent microscope (Leica, Milton Keynes, UK).

2.2.7 Omics methods

2.2.7.1 General practice for omics sample collection and processing

A common issue in the processing of samples for proteomics is contamination by human keratin from those undertaking the processing and handling of samples. To prevent contamination and any unintentional impact on results, gloves were worn at all times (including preparation of tubes and tips for autoclave sterilisation) and samples processed under laminar flow as much as possible. Long hair was kept beneath a hair net and 70% ethanol utilised to sterilise all surfaces and equipment prior to use. Additionally, sample preparation was undertaken as efficiently as possible, with all samples and reagents kept on ice in the presence of the aforementioned P8340 protease inhibitor cocktail. When running SDS-PAGE gels for later band or fragment excision, empty lanes were run between samples to minimise sample cross-contamination.

2.2.7.2 Proteomics processing of single SDS-PAGE bands of interest

When analytical SDS-PAGE electrophoresis indicated the presence of an interesting protein, the band representing this protein was excised from the gel using a sterile scalpel under laminar flow. The excised gel segment was further cut into small pieces and added to a sterile 1.5 mL Eppendorf. Subsequent pulse centrifugation ensured the gel fragments were located at the bottom of the tube. Removal of Coomassie blue (an inhibitor of later trypsin digestion) was performed *via* 3-5 washes of 100 µL of 100mM ammonium bicarbonate/acetonitrile (1:1, vol/vol) with shaking. This solution was removed and reduction performed in 200 µL 10 mM DTT (made in 50 mM ammonium bicarbonate) at 56^{o}C for 60 minutes in a closed water bath. The gel fragments were allowed to cool, reduction solution removed and alkylation performed in the dark for 30 minutes using 200 µL 54 mM iodoacetamide (prepared in 50 mM ammonium bicarbonate). 50 µL 100% acetonitrile was added to the gel fragments and allowed to incubate at room temperature until the gel pieces became white and shrunken. The acetonitrile was removed and the samples subjected to drying in a centrifugal evaporator (speedvac) for 15 minutes to encourage dissipation of latent acetonitrile. The gel fragments were then pre-incubated on ice for 60 minutes with 5 µg Typsin Gold (Promega) solution prepared in 50mM acetic acid. 20 µL ammonium bicarbonate was then added to each tube to cover gel pieces and maintain moisture during trypsin digestion. The trypsin digestion itself was performed overnight at 37^{o}C in a water bath with occasional gentle shaking. After at least 12 hours,

the digestion was arrested by addition of 100 µl 1:2 (vol/vol) 5% formic acid/acetonitrile to each tube. The tubes were then incubated with shaking for 30 min at room temperature and the supernatant retained due to the presence of extracted peptides. The addition of 30 µl of 0.1% (vol/vol) trifluoroacetic acid to each sample followed by 5 minutes incubation ensured further peptide extraction, the supernatant retained once again due to the presence of peptides within it. The resulting pooled liquid was subjected to freeze-drying overnight in a Christ Alpha 1-2 LD Freeze Dryer, and the resulting lyophilised samples each re-suspended in 30 µL of LC-MS Buffer A (5% acetonitrile and 0.1% formic acid in LCMS-grade water). 6 µL of sample was loaded into a vial and 3 µL injected for LC-MS.

2.2.7.3 Proteomics processing for complex protein mixtures

Complex protein mixtures were subject to Bradford's assay to determine protein concentration (2.2.4.7). 20 µg of each sample was then loaded onto a separate lane of a 12% SDS-PAGE gel (2.2.4.1). SDS-PAGE electrophoresis was performed at 200V, albeit for only 20-30 minutes, until the samples had run approximately half way down the gel. The gel was stained in Coomassie blue and destained as previously described (2.2.4.2). Once sufficiently destained, the gel was then placed on a sterile surface in a laminar flow hood and each lane slice horizontally into 8 separate fractions. Each separate fraction was sliced into smaller segments and placed into a tube onto which the sample details and fraction number were recorded (1 denoting highest molecular weight, 8 denoting lowest molecular weight). Each fraction was then subjected to the same process described in 2.2.7.2.

2.2.7.4 Liquid chromatography mass spectrometry

Separation of peptides was performed by an Ultimate 3000 nano LC-MS/MS system (Dionex LC packings, Amsterdam, The Netherlands) in combination with an Ultimate 3000 RS autosampler. The autosampler was held at 4^{o}C and utilised to inject 3 µL of sample onto the column. Separation of peptides was accomplished with an EasySpray column (PepMap C18, 2 µm 100 A, 75 µm x 50 cm) maintained at 45^{o}C. The eluent profile utilised for each sample is detailed in Table 2.22.

Table 2.22. LC-MS/MS eluent programme

Time (min)	Buffer A	Buffer B	Flow Rate (µL/min)
0.0	95%	5%	0.2
0.1	95%	5%	0.2
120.0	60%	40%	0.2
120.1	10%	90%	0.2
128.0	10%	90%	0.2
128.1	95%	5%	0.2
140.0	95%	5%	0.2

Analysis was undertaken with a Q Exactive™ hybrid quadrupole-orbitrap™ mass spectrometer (Thermo Fisher Scientific Inc.) equipped with a nanoelectrospray ionization source operated at 2.3 kV. The ion transfer tube was held at 280°C throughout analysis and positive ion mode selected for ion production. Data were obtained using a data dependent Top 10 methodology, with scans acquired in the Orbitrap mass analyser over a range of 150-1500 m/z, mass resolution set to 70,000 and target value set to 1.00E+06. The ten most intense peaks with a charge state of ≥2 were subsequently fragmented in the HCD collision cell and tandem mass spectra obtained in the Orbitrap with mass resolution set to 17,500 and target value set to was 1.00E+05. Maximum ion accumulation times were 100 ms for the full MS scan and 50 ms for the tandem mass spectra. The mass spectrometery system was linked to a high performance personal computer harbouring corresponding Exactive Tune software (Thermo Fisher Scientific Inc.). This software enabled real-time assessment of each LC/MS run as it occurred. Samples were analysed in random order to minimise bias, and data automatically saved in the Thermo Fisher .RAW data format. Prior to any use of LC/MS for peptide analysis, all necessary components of the Q Exactive system were washed and equilibrating using the NUOmics standard operating procedure.

2.2.7.5 Analysis of data using Progenesis software

Thermo Fisher .RAW data files were retained and loaded onto Progenesis 64 (Nonlinera Dynamics) software for analysis, with any unsatisfactory runs removed from analysis. Areas during the wash and prior to the time taken for the sample to reach the electrospray port were excluded. Alignment was performed using the automatically assigned alignment tool and further validated using a manually assigned reference. Upon alignment review, manual vectors were implemented where necessary to improve alignment. Peptides were reviewed and those with a charge state <2 or >8 were excluded from subsequent analysis. The 'between group' comparison was selected for experimental design. Peak picking was executed and reviewed. The identification of peptides and generation of suggested identities was then accomplished by exporting MS/MS MGF files to Mascot or X!Tandem. Parameters utilised for X!Tandem and Mascot searches are provided in Appendix 7 And 8, respectively. Subsequently, Mascot-derived files were imported back into Progenesis where conflicts were resolved and identities refined. Confidence in the identification of a given protein was based on the number of peptides matched to any one protein. PCA plots were generated from the data and a report comparing sample groups versus control groups generated by the Progenesis software.

Chapter 3: Cloning, expression and purification of the human Miro GTPases

3.1 Introduction

Although preliminary gene functions for the hMiros were described more than a decade ago , the biochemical and signalling characteristics of these enzymes remains obscure. Only limited three dimensional structures of truncated versions of Miros have been demonstrated (131), while biochemical characterisation has been limited to the confirmation of EF-hand calcium-binding ability using dot blot overlay assays (164). The hydrolytic activity of the N-terminal and C-terminal GTPase domains has not been reported, with the C-terminal GTPase domain frequently under-studied relative to the N-terminal GTPase domain. In light of this, the primary objective of the work undertaken in this chapter was to obtain yields of pure hMiro1 and hMiro2 appropriate for structural studies (elucidation of protein three dimensional structure through crystallisation) and *in vitro* biochemical characterisation.

The results demonstrate the successful sub-cloning of full-length wildtype hMiro1 and hMiro2 into the bacterial expression vector pET-28a. Additionally, the successful cloning of truncated versions of hMiro1 and 2 into an engineered version of pET15b is shown, using PCR-based amplification of target sequences. The successful purification of both full-length wildtype and truncated versions of hMiro1 and hMiro2 for functional and structural characterisation is shown, in addition to subsequent identification of target proteins by Western blotting and mass spectrometry.

3.2 Cloning, expression and purification of full-length wildtype hMiro1 and hMiro2

First, the cloning, expression and purification of full-length wildtype hMiro1 and hMiro2 was attempted. PRK5-Myc mammalian expression vectors encoding full-length wildtype versions of hMiro1 and 2 were kindly donated by the Pontus Aspenström Group at the Karolinska Institutet, Sweden (29). These vectors were used to sub-clone hMiro1 and hMiro2 separately into the bacterial expression vector pET-28a. The pET-28a vector allows for the expression of recombinant proteins containing an N-terminal hexahistidine tag (His-tag). In each instance, undigested pET-28a was subjected to an overnight restriction digest with NdeI/XhoI restriction enzymes (section 2.2.3.6), followed by gel

purification (2.2.3.9). The pRK5-Myc vectors encoding hMiro1 and hMiro2 were subjected to NdeI/XhoI restriction digest in parallel, with the genes encoding hMiro1 or hMiro2 isolated and purified using an identical gel purification procedure. Gel purified products were subjected to a standard ligation procedure at room temperature (section 2.2.3.10). Products of ligation were transformed into chemically competent TOP10 *E.coli*, yielding transformants on kanamycin plates. Plasmid DNA (pDNA) from up to five transformants was subsequently assessed for the presence of a correctly-sized insert by means of an analytical restriction digests (Figures 3.1 and 3.2; section 2.2.3.6). Plasmid DNA from one clone each of hMiro1 and hMiro2 in pET-28a was confirmed by sequencing using the T7 promoter and T7 terminator sequencing primers, with no mutations detected.

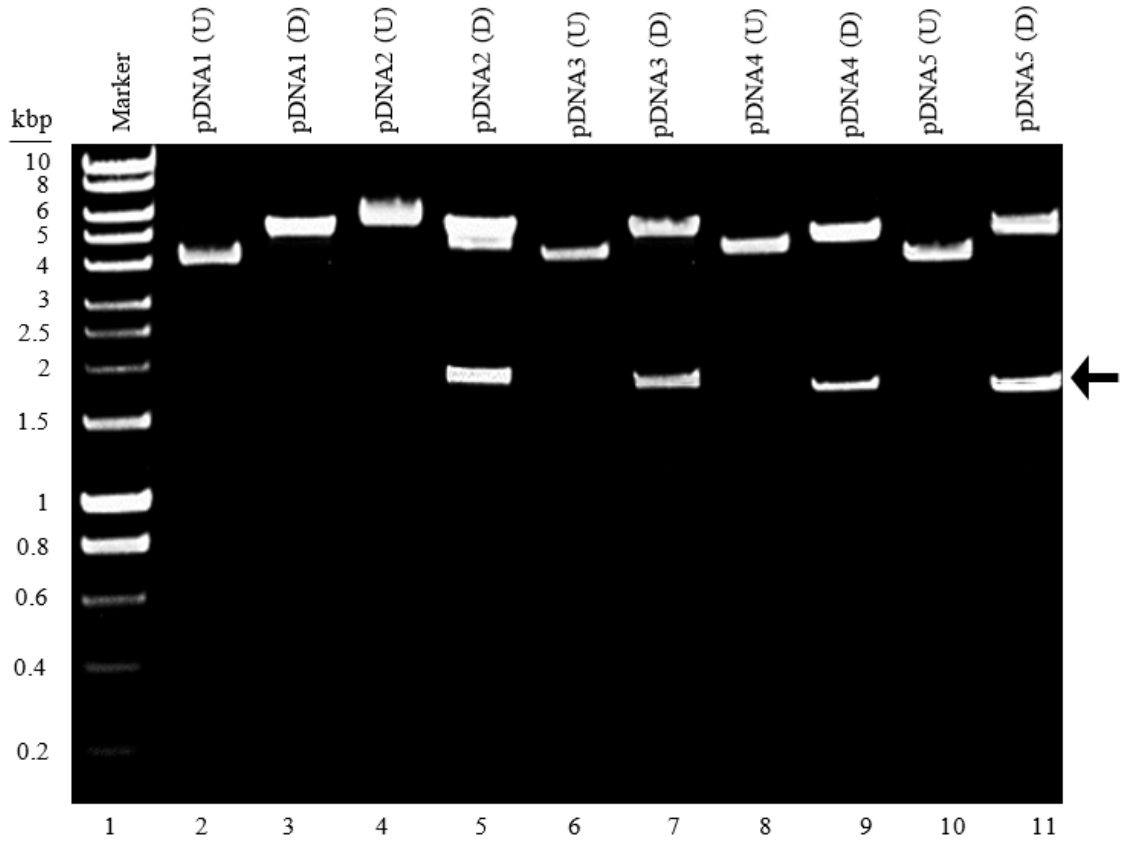

Figure 3.1. Analytical restriction digest results showing full-length hMiro1 sequence liberated from pET-28a. 1% agarose gel showing the presence of the Miro1 encoding sequence (indicated by arrow) in a vector isolated from TOP10 *E.coli* transformants. Undigested (U) vector versus NdeI/XhoI restriction digested (D) pDNA from five transformed TOP10 colonies is shown (lanes 2-11). Bioline Hyperladder I marker is indicated as 'marker' in lane 1.

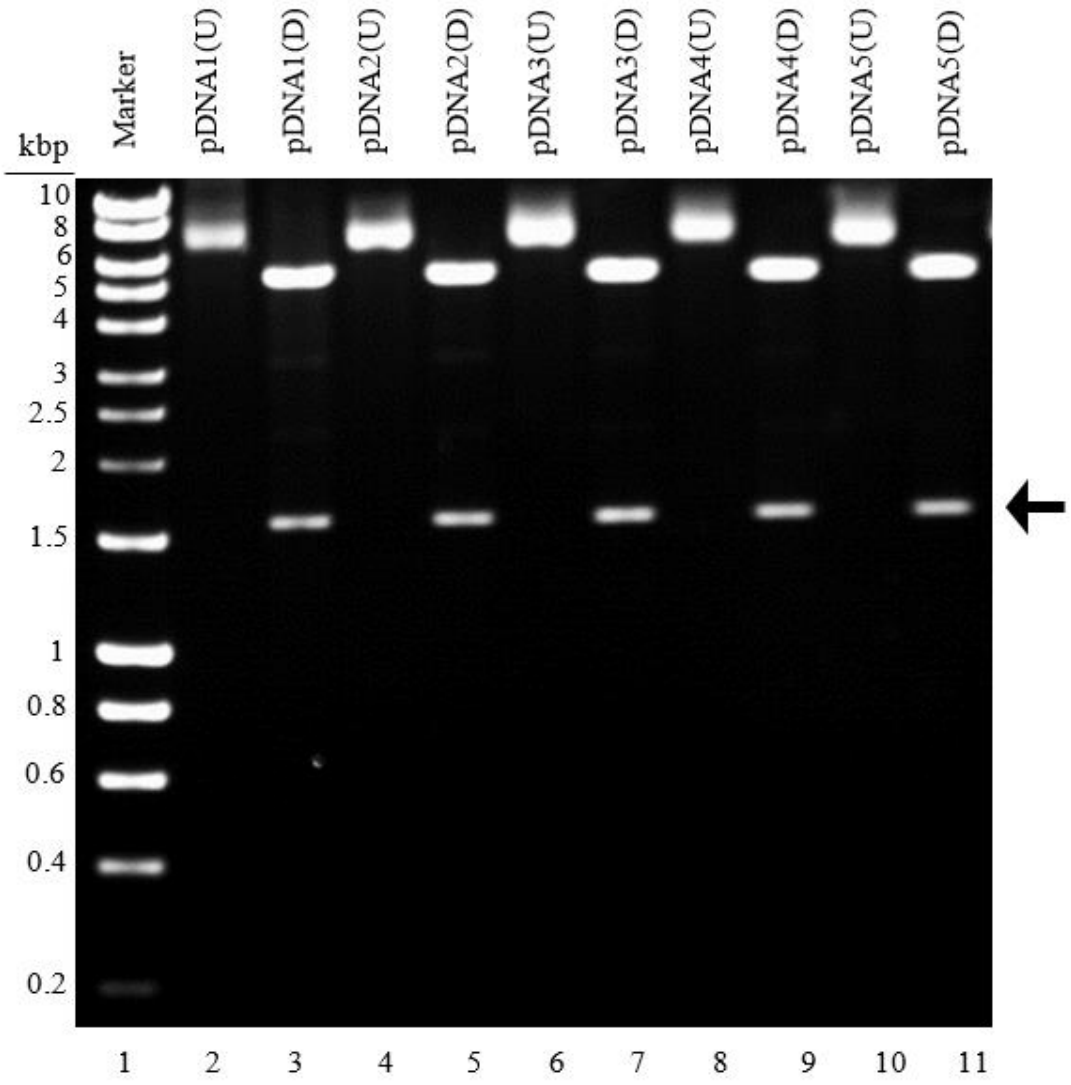

Figure 3.2. Analytical restriction digest results displaying full-length hMiro2 sequence separated from pET-28a. 1% agarose gel showing Miro2 encoding sequences in pDNA isolated from TOP10 *E.coli* transformants. Undigested (U) pDNA versus NdeI/XhoI restriction digested (D) pDNA isolated from five transformed colonies (lanes 2-11). Lane 1 displays marker (Hyperladder I, BioLine).

BL21 (DE3), C41 (DE3) and C43 (DE3) chemically competent *E.coli* cells were transformed with the pDNA for each successful hMiro clone. The recombinant *E.coli* strains were grown and subjected to auto-induction (Table 3.1) based on the Terrific Broth formulation from ForMedium, United Kingdom. This broth contains both glucose and lactose, with the amount of glucose formulated to become depleted at a high cell density, leaving only lactose available for bacterial energy metabolism and therefore resulting in

induction of target protein expression when a specific cell density is reached. Auto-induction trials suggested an optimum induction temperature of 18^{o}C using C43 (DE3) cells. Further experiments were conducted by inducing over-expression at this temperature using either 0.1mM, 0.5mM or 1mM IPTG after the recombinant *E.coli* reached mid-exponential growth phase (2.2.2.6). These IPTG-mediated induction experiments indicated that the optimum expression conditions for both hMiro1 and hMiro2 was 18^{o}C overnight in C43 (DE3) cells using a final concentration of 1mM IPTG (Table 3.2). For all expression experiments, cells were harvested and sonicated as previously described (2.2.4.3). Cell debris was removed by centrifugation and both human Miros were purified initially by immobilised metal affinity chromatography (IMAC) (Figure 3.3 a and b; method described in 2.2.4.4). However, both recombinant proteins appeared to elute from the IMAC column at the same imidazole concentration as a number of contaminants. Thus, further purification *via* gel purification was attempted, producing pure versions of hMiro1 and hMiro2.

Table 3.1. Expression optimisation of hMiros using auto-induction trials and the C43 expression host. Expression of hMiro1 and hMiro2 using auto-induction LB broth, where - indicates no visible expression, + indicates some visible expression, ++ indicates notable expression and +++ indicates maximum over-expression.

		Miro1 over-expression				Miro2 over-expression		
		37°C	25°C	18°C		37°C	25°C	18°C
Time (hours)	6	-	-	-		-	-	-
	12	-	-	-		-	-	-
	18	+	-	-		++	+	-
	24	+	+	++		++	++	+
	32	+	++	+++		++	++	++
	36	+	++	++		++	++	+++
	40	+	++	++		+	++	++
	44	+	++	+		+	++	++
	48	+	+	+		+	++	+
	52	-	+	+		+	+	+
	56	-	+	+		-	+	+
	60	-	-	-		-	-	-

Table 3.2. hMiro bacterial expression optimisation using IPTG induction and the C43 expression host. Expression of hMiro1 and hMiro2 using IPTG induction (0.1mM, 0.5mM or 1mM) in LB broth, where - indicates no visible expression, + indicates some visible expression, ++ indicates notable expression and +++ indicates maximum over-expression.

Miro1 over-expression (18^{o}C overnight)				**Miro2 over-expression (18^{o}C overnight)**		
0.1mM IPTG	**0.5 mM IPTG**	**1mM IPTG**		**0.1mM IPTG**	**0.5 mM IPTG**	**1mM IPTG**
++	++	+++		+	+	+++

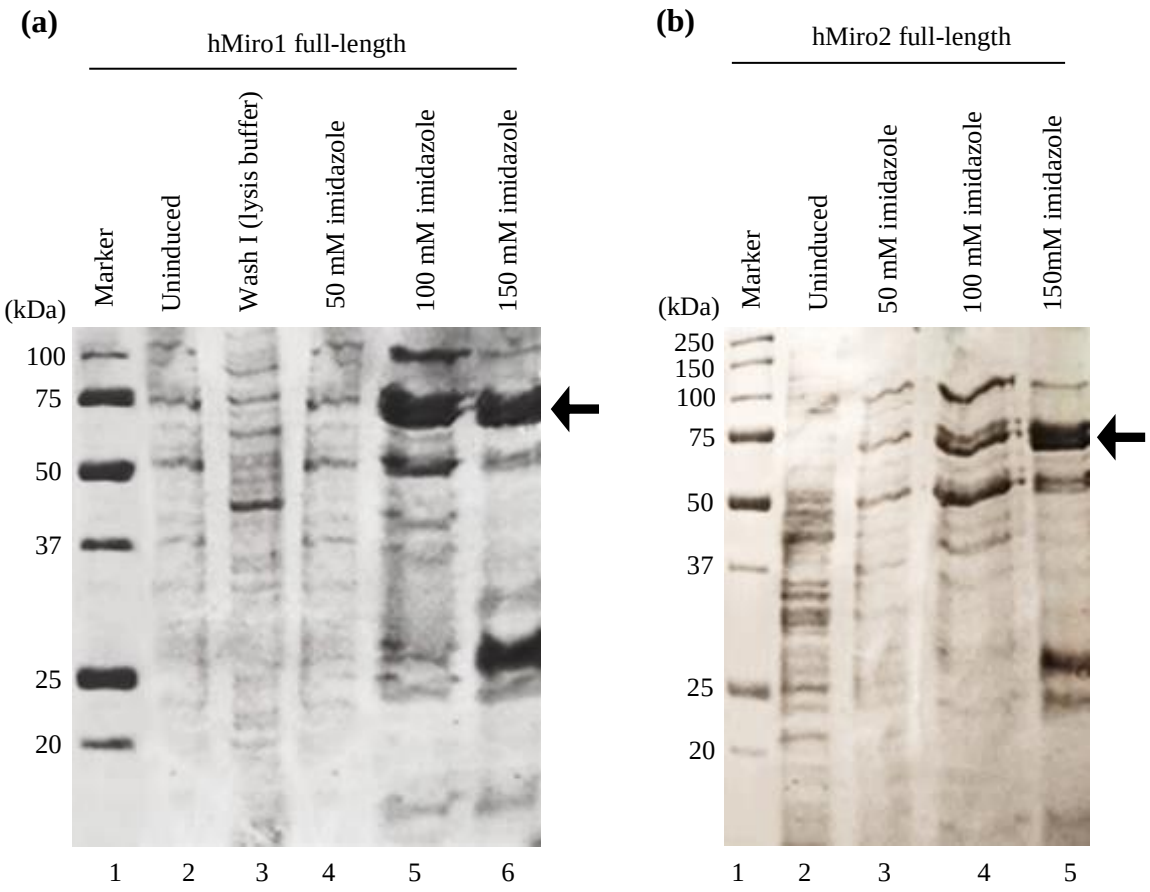

Figure 3.3. Coomassie-stained 12% SDS-PAGE gel showing IMAC purification of over-expressed (a) hMiro1 and (b) hMiro. N-terminally His-tagged, full-length hMiro1 was purified from BL21 (DE3) *E.coli* cells by IMAC. For both gels (a) and (b), BioRad Precision Plus marker is shown in lane 1. Lanes 2 and 3 respectively show uninduced and induced samples in both (a) and (b).

The presence of hMiro1 and hMiro2 in purified samples was confirmed by Western blotting (Figure 3.4 a and b; Figure 3.5 b and c). Gel filtration was subsequently used to further purify hMiro1 and hMiro2 in Western-confirmed samples (see 2.2.4.5), where a sephacryl™ S-200 HR HiPrep™ 16/60 column attached to an ÄKTA PRIME FPLC system was used with appropriate gel filtration buffer (50 mM HEPES 7.4, 500 mM NaCl, 5 mM DTT, 2% glycerol) to successfully isolate both hMiro GTPases from contaminants (Figure 3.5 a). Pure fractions of the full-length recombinant proteins were subsequently concentrated to 1–1.5 mg/mL (2.2.4.6), with Bradford's assay utilised to determine protein concentration (section 2.2.4.7). Concentrated samples were intended for use in structural studies and *in vitro* characterisation. However, attempted concentration of the full-length hMiro proteins proved problematic, predominantly due to the propensity for these expressed, purified proteins to aggregate in all buffers tested. Furthermore, the

purity and yield were unreproducible in subsequent preps. Consequently, an alternative approach to studying structure and *in vitro* biochemical properties was adopted: the cloning, expression and purification of separate hMiro domains of interest, as discussed in section 3.3.

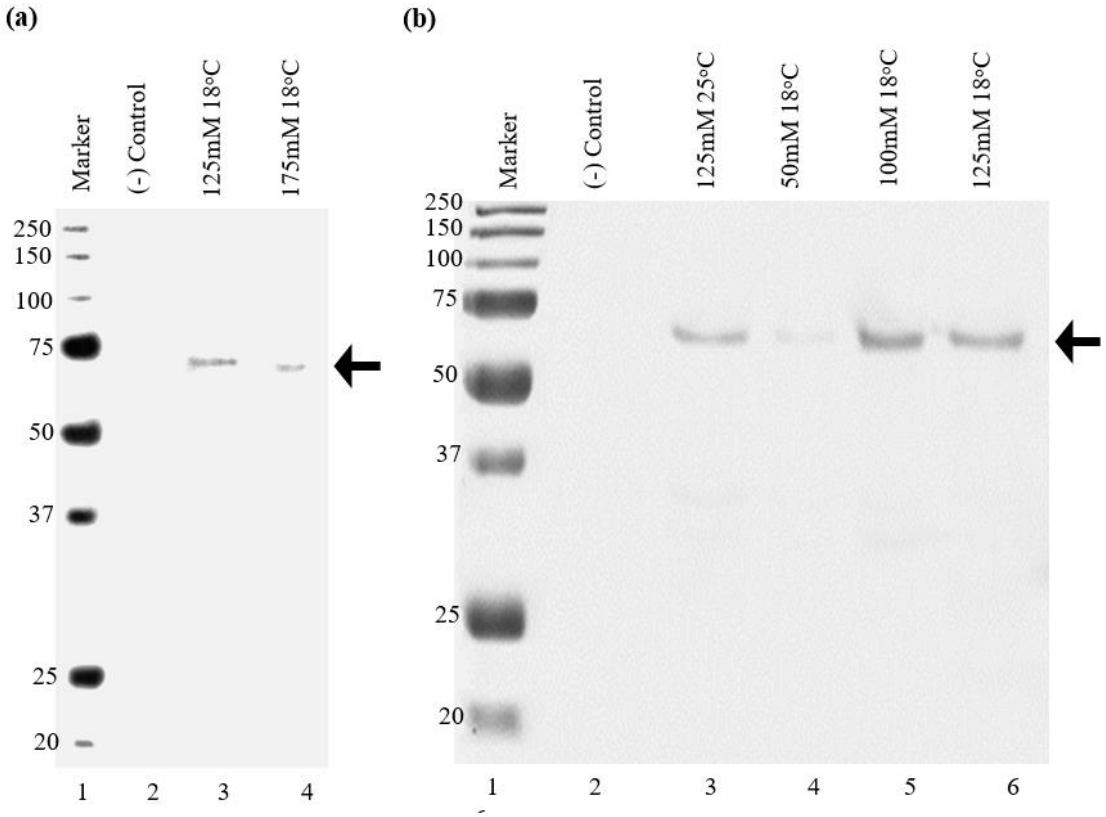

Figure 3.4. Anti-hMiro1 (a) and Anti-hMiro2 (b) Western blots. Western blot of IMAC-purified hMiro1 (a) and hMiro2 (b) samples, where '125mM' and '175mM' correspond to the concentration of imidazole at which samples eluted from the column, and '18°C' and '25°C' refer to the temperatures used during IPTG-induced over-expression.

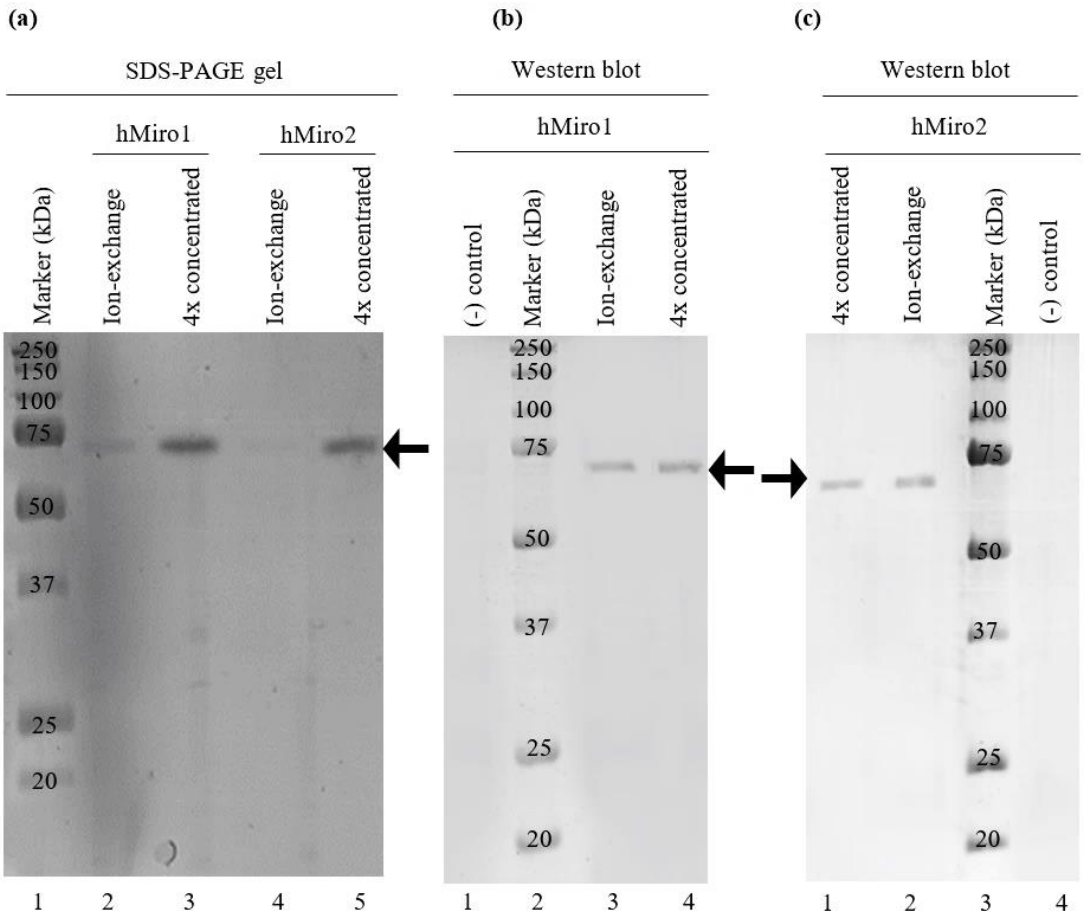

Figure 3.5. Size analysis of over-expressed full-length hMiro1 and hMiro2 samples based on SDS-PAGE and Western blotting. (a) Successfully ion-exchange purified samples run on a 12% SDS-PAGE gel. **(b)** Anti-hMiro1 immunoblot. **(c)** anti-hMiro2 immunoblot. Concentrated samples were approximately 1–1.5 mg/mL.

3.3 Cloning, expression and purification of hMiro1 and hMiro2 domains of interest

Due to the issues associated with expression and purification of full-length hMiro1 and hMiro2, an alternative approach to studying the structure and function of hMiro1 and 2 was adopted: the division of each protein into domains of interest for individual study. As previously discussed, the putative C-terminal 'GTPase' domains of both hMiro1 and hMiro2 are highly novel, being only distantly related to the Ras superfamily and largely uncharacterised . With this novelty in mind, the elucidation of the structure and function of these hitherto uncharacterised C-terminal 'GTPase' domains was sought (hMiro1 and hMiro2 CT), beginning with PCR-based amplification of the nucleotide sequences encoding these regions (2.2.3.3, Appendix 3). The N-terminal domains of both hMiro1 and hMiro2 (hMiro1 and hMiro2 NT), displaying approximately 30% amino acid identity with RhoA , were also separately cloned and expressed, allowing for comparative analysis to their C-terminal GTPase counterparts. While the N-terminal GTPase domain of the hMiros is considered less novel in the literature, cloning the ordered GTPase region of the hMiro N terminus was hoped to provide a more complete understanding of the hMiros when characterised. While cloning of these separate domains was in process, a truncated version of the Drosophila Miro (dMiro) was successfully crystallised by Klosowiak and colleagues. The portion of dMiro crystallised comprised the EF-domains and C-terminal GTPase domain. As shown in Table 3.3, each hMiro shares around ~50% amino acid identity with dMiro. Considering this, an attempt to mimic the successful crystallisation of the dMiro construct was attempted: constructs of hMiro1 and hMiro2 were engineered with similar domain cut-off points to the successfully crystallised dMiro construct (see schematic illustration, Figure 3.6), based on an amino acid sequence alignment of dMiro compared with hMiro1 and hMiro2 (Figure 3.7); the resulting engineered constructs were named the 'xtal' constructs. The cloning, expression and purification of the GTPase domains and crystal constructs of hMiro1 and hMiro2 is discussed separately in the following sections of this chapter. The cut-off values selected for each hMiro1 and hMiro2 construct are provided in Table 3.4 (following page).

Table 3.3. Percentage identity matrix illustrating amino acid identity between the hMiros and dMiro.

	hMiro1	hMiro2	dMiro
hMiro1	100%	60.3%	52.3%
hMiro2	60.3%	100%	49.6%
dMiro	52.3%	49.6%	100%

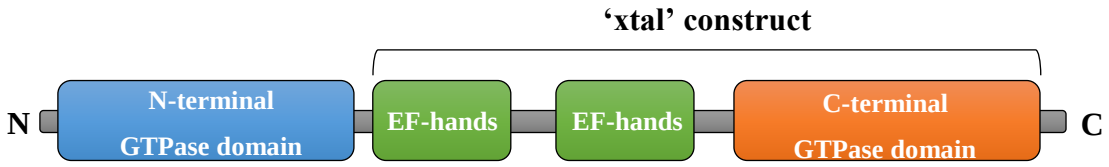

Figure 3.6. Schematic illustration of Miro domain architecture, displaying the GTPase domains in addition to the cut-off areas for the 'xtal' constructs.

Table 3.4. Details of each designed construct.

	NT construct	CT construct	Xtal construct
hMiro1	K3–P169	Q415–P580	E177–R590
hMiro2	R3–P169	Q413–F589	E177–P586

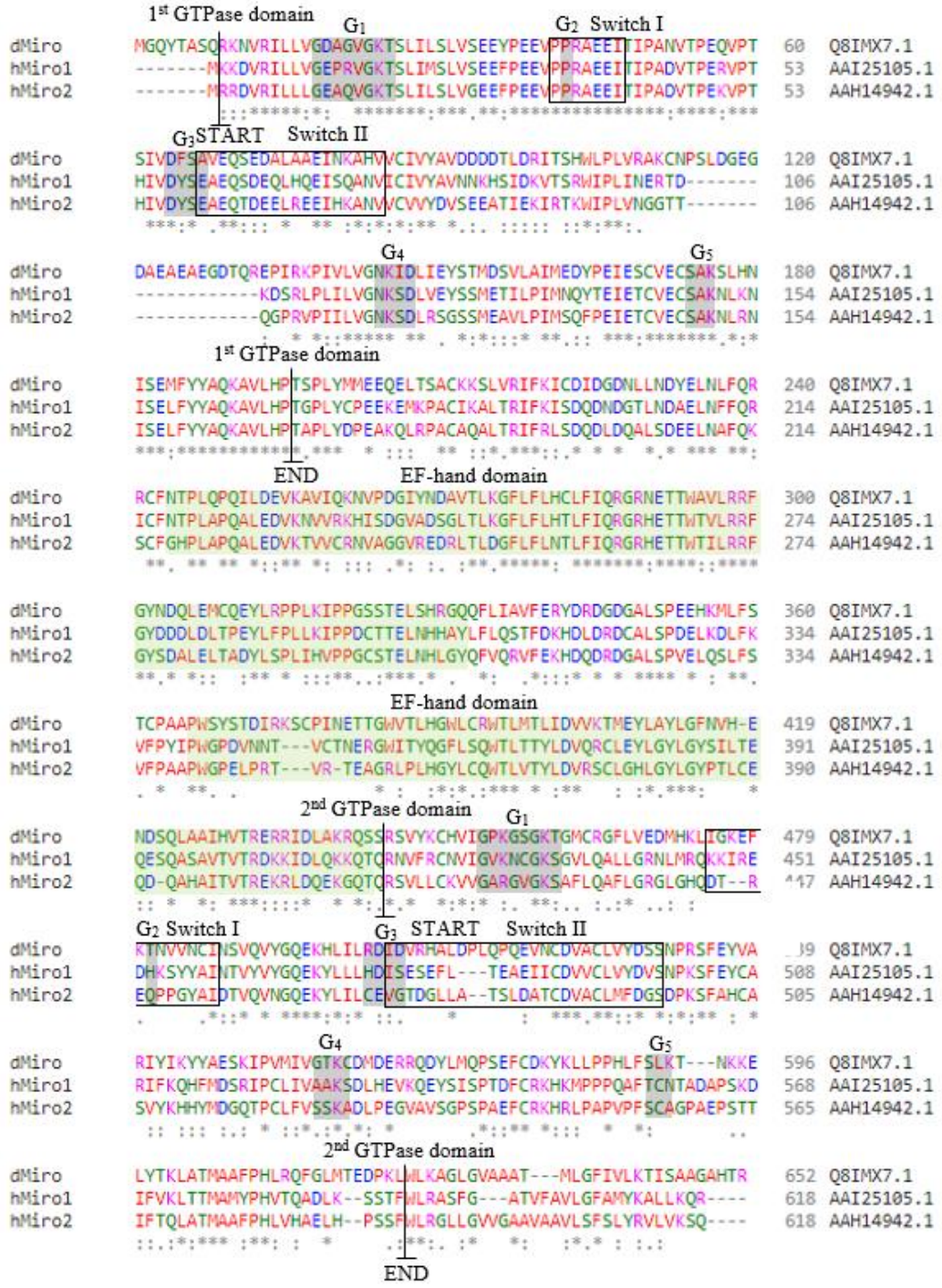

Figure 3.7 Comparison of amino acid sequences: dMiro, hMiro1 and hMiro2. Annotated CLUSTAL OMEGA alignment of the amino acid composition of dMiro, hMiro1 and hMiro2, with identifiers provided to the right. Asterisks (*) specify positions in which single, fully conserved residues are present, while colons (:) denote the conservation of residues with strongly similar properties. Periods (.) specify conservation of residues with weakly similar properties. Colour coding is used to represent the properties of each residue (red, small and hydrophobic residues; blue, acidic residues; magenta, basic residues; green, residues bearing hydroxyl, sulphydryl or amine groups; grey, unusual amino acid residues). G loops are shaded in grey and EF-hand domains shaded green. The

switch boxes are delineated in black-outlined boxes. The beginning and end of each GTPase domain is indicated.

3.3.1 Cloning, expression and purification of the hMiro1 and hMiro2 C-terminal GTPase domains

3.3.1.1 Cloning of the hMiro1 and hMiro2 C-terminal GTPase domains

The previously described pRK5-Myc vectors encoding full-length hMiro1 and 2 were utilised as DNA templates in separate PCR reactions, using primers designed to amplify the nucleotide sequences encoding the C-terminal GTPase domains of hMiro1 and hMiro2, respectively (section 2.1.3). Primers were designed so that appropriate, compatible restriction enzyme sites were incorporated at the ends of each hybridisation sequence (NdeI/XhoI in all cases). These sequences were successfully amplified *via* PCR using as described in 2.2.3.3 and shown in figure 3.8.

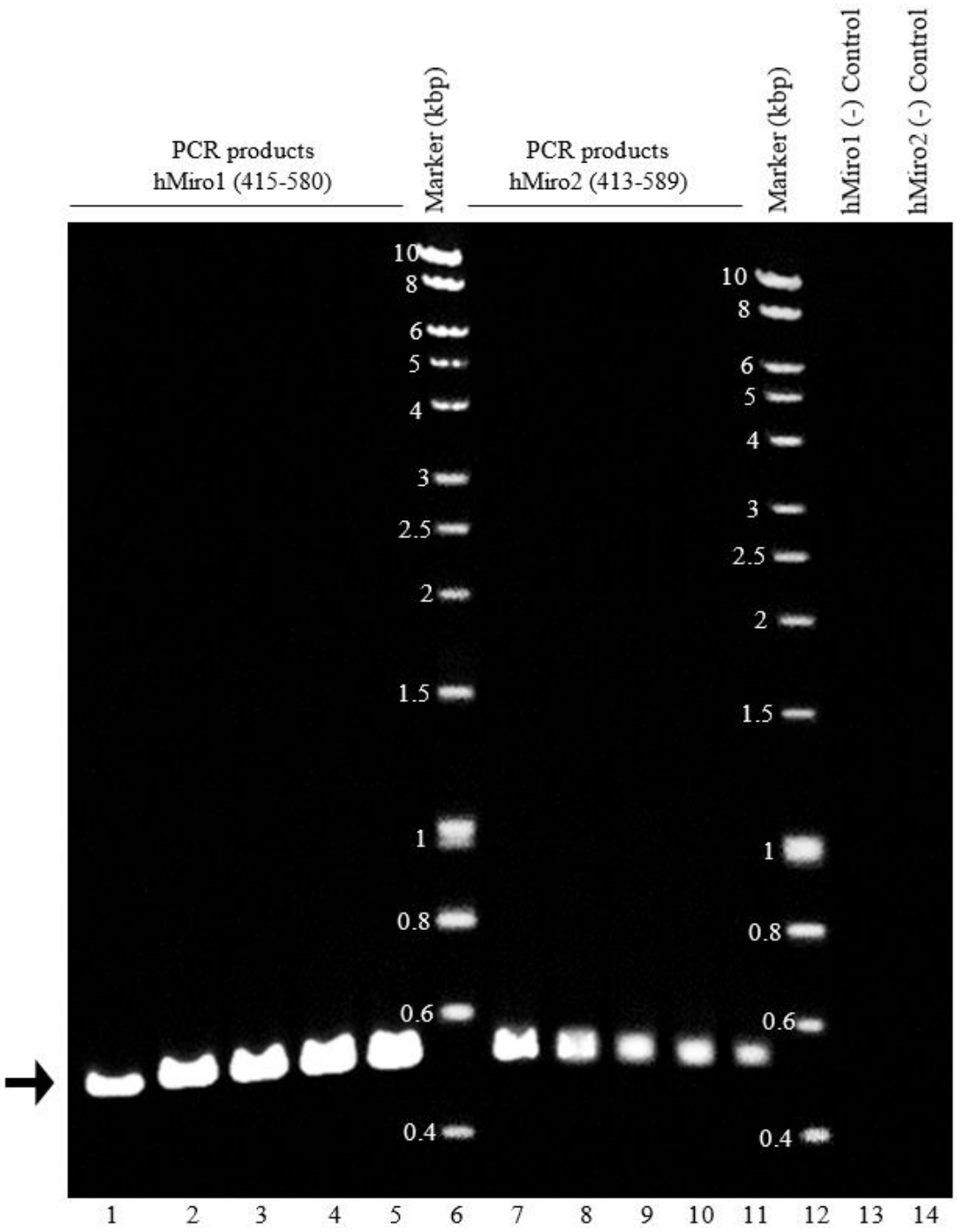

Figure 3.8. 1% agarose gel showing hMiro C-terminal GTPase domain PCR products. PCR-based amplification of the gene sequences encoding hMiro 1 415-580 (lanes 1-5) and hMiro2 413-589 (lanes 7-11), respectively. Lanes 6 and 12 contain marker (Bioline Hyperladder I). Lanes 13 and 14 correspond to negative controls containing all components of the optimised reaction except the DNA template.

Successfully amplified nucleotide sequences were subjected to PCR clean-up as previously described (section 2.2.3.4). Subsequently, a typical overnight restriction digest procedure was performed on purified PCR products, using restriction enzymes

(NdeI/XhoI) targeting the sites incorporated into the initial primers (section 2.2.3.6). Digested nucleotide sequences were gel-purified (2.2.3.9) and ligated into pET15b-TEV (method described in 2.3.10) to generate a set of plasmids separately encoding the truncated mutants of interest. The products of ligation were transformed into chemically competent TOP10 *E.coli* cells and pDNA isolated from transformants. Each isolated aliquot of pDNA was screened in an analytical restriction digest (NdeI/XhoI) to check for correctly-sized inserts (Figure 3.9; 2.2.3.6). pDNA was then sent for sequencing using the standard sequencing primers T7 promoter and T7 terminator, with no unwanted mutations identified.

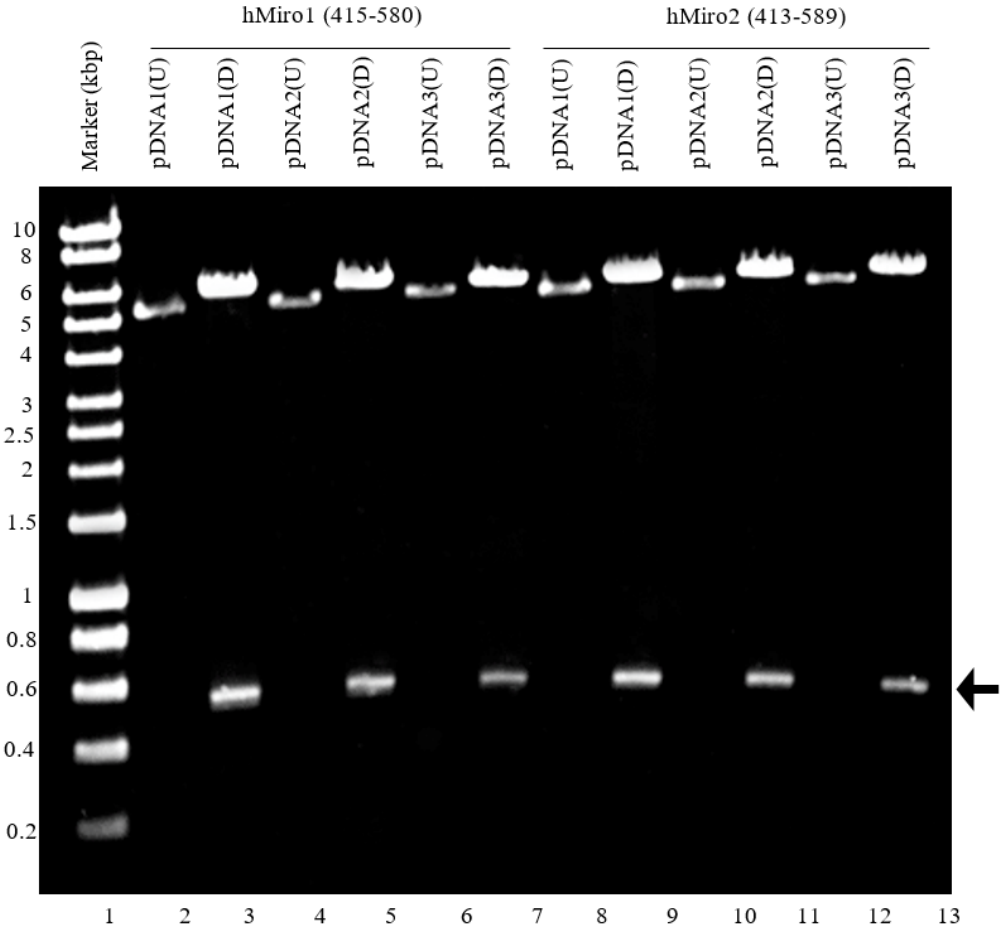

Figure 3.9. 1% agarose gel showing target hMiro1 and hMiro2 N-terminal GTPase sequences following restriction digest of constructed plasmids. Analytical restriction digest of pDNA extracted from TOP10 *E.coli* transformants after ligation of pET15b-TEV/hMiro1 415-580 PCR products (lanes 2-7) and pET15b-TEV/hMiro2 413-589 products (lanes 8-13), respectively. Lane 1 contains Hyperladder I (BioLine). For each lane in which plasmid is shown, 'U' represents undigested plasmid and 'D' represents plasmid that has undergone a double restriction digest with the specify the restriction enzymes.

3.3.1.2. Expression trials: hMiro1 and hMiro2 C-terminal GTPase domains

The pDNA for each clone was transformed into separate aliquots of chemically competent C43 or BL21 *E.coli* cells. Recombinant *E.coli* strains were grown until mid-exponential phase (section 2.2.2.6), followed by IPTG induction at a final concentration of 0.1mM, 0.5 mM or 1 mM and incubation either at 37ºC for 4 hours, 25ºC overnight or 18ºC overnight. Appropriate final IPTG concentrations and induction temperatures were determined by initial small-scale expression trials (figures 3.11-3.14).

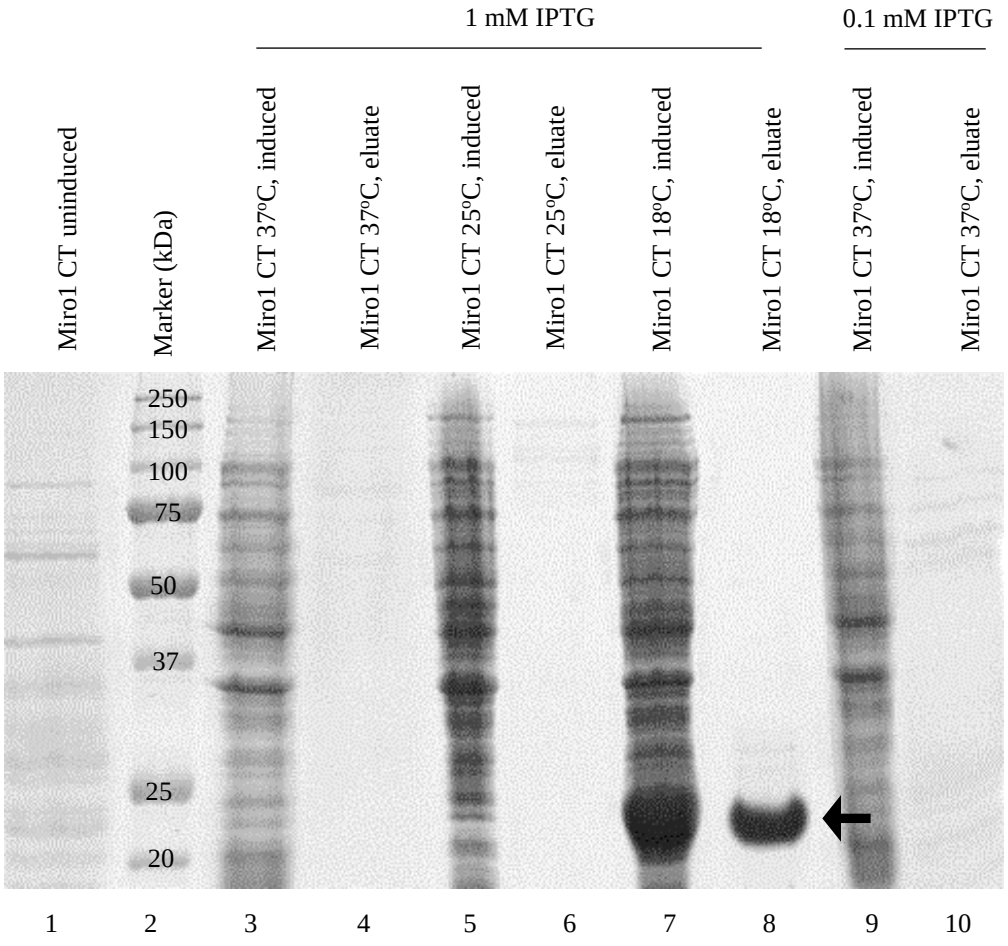

Figure 3.10. 12% SDS PAGE gel showing expression trial data for the C-terminal GTPase domain of Miro1 (Coomassie stained).

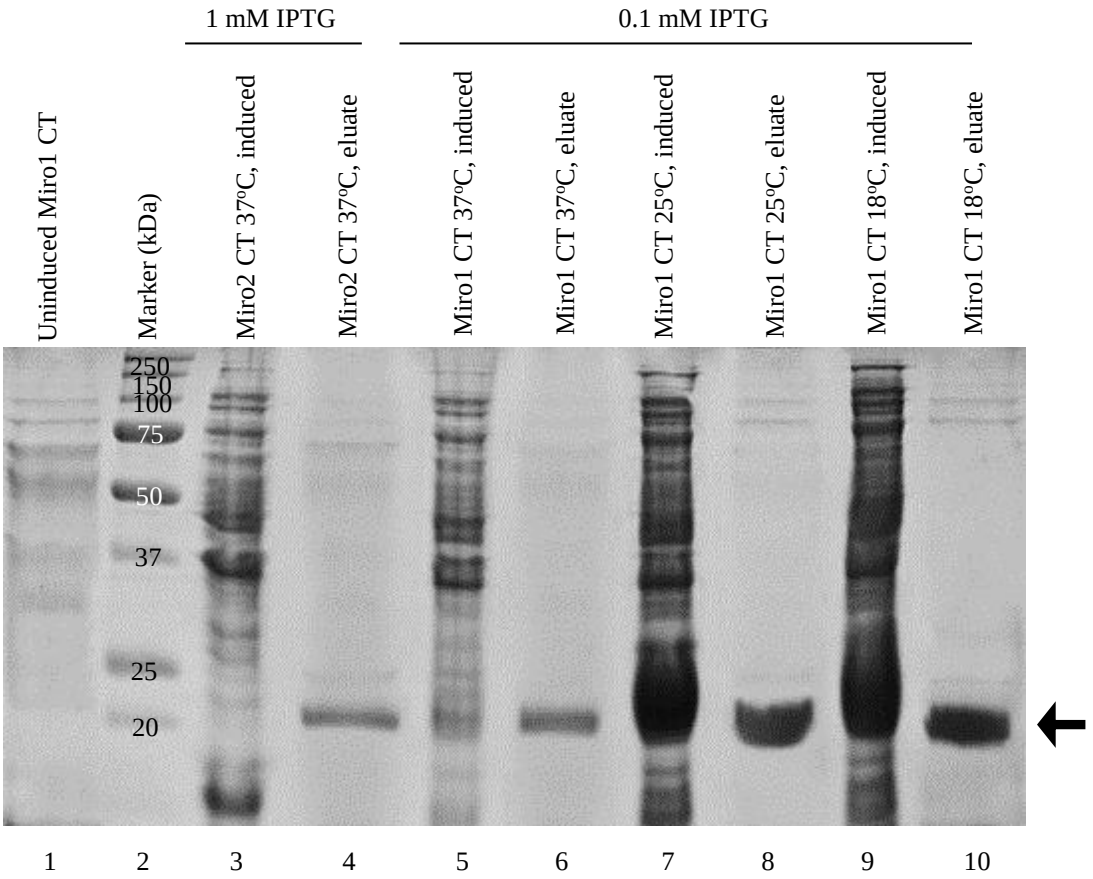

Figure 3.11. Further expression trial results for the C-terminal GTPase domain of Miro1 and Miro2. 12% Coomassie-stained SDS-PAGE gel showing expression trial data for the C-terminal GTPase domain of Miro1 and Miro2.

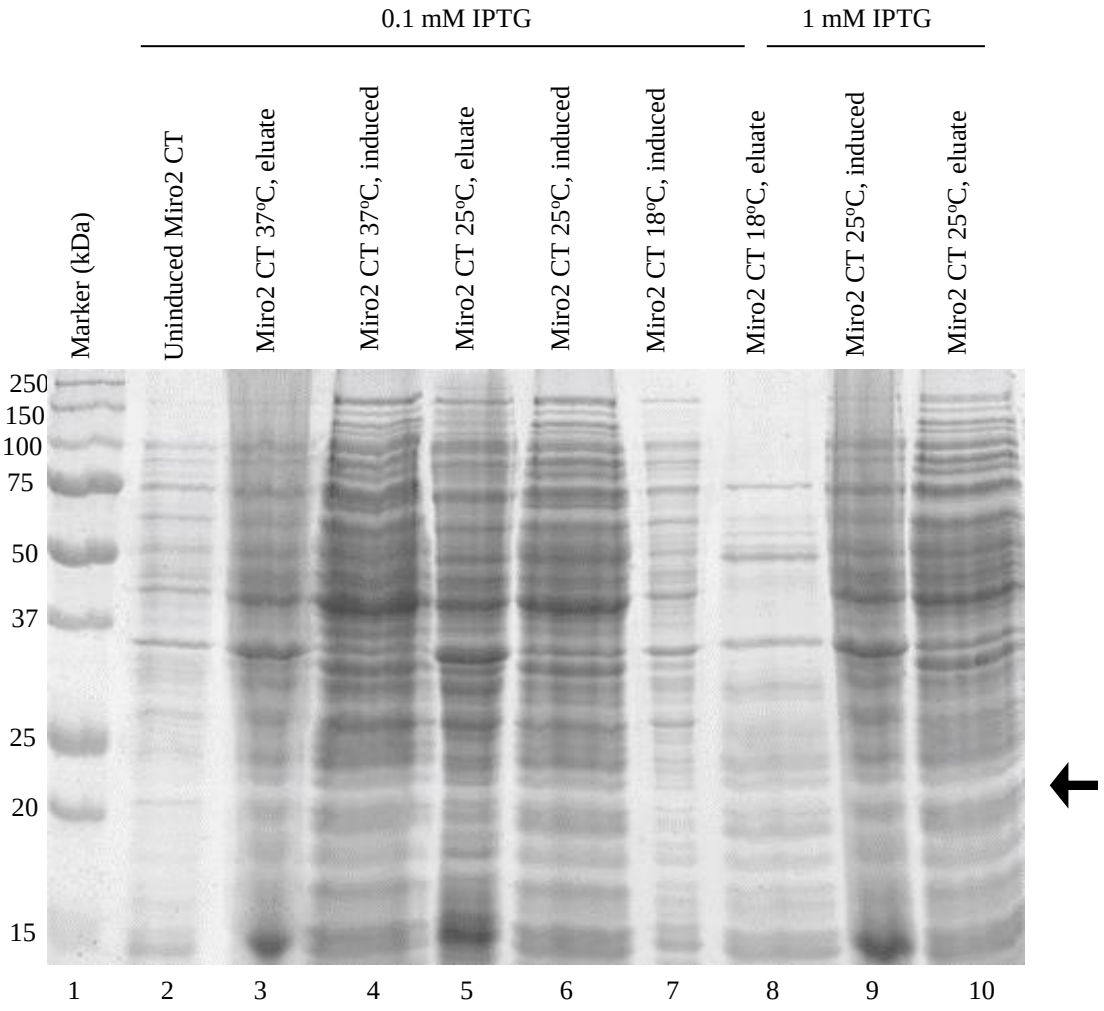

Figure 3.12. 12% Coomassie-stained SDS-PAGE gel showing expression trial results for the C-terminal GTPase domain of Miro2.

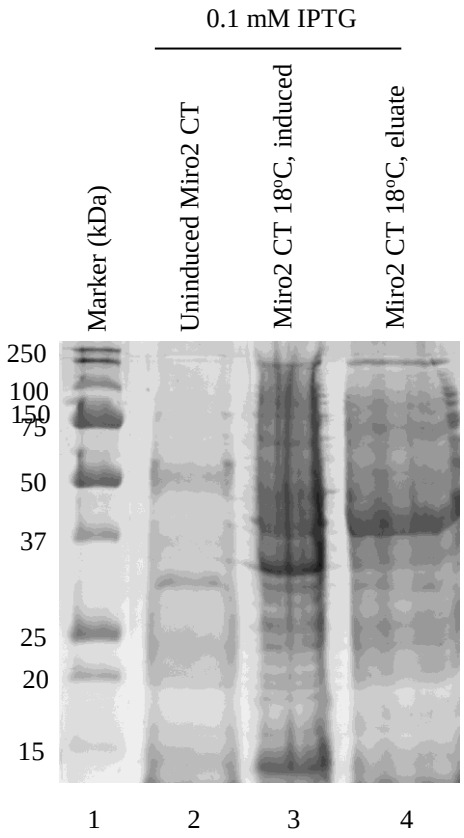

Figure 3.13. Further expression trial data for the C-terminal GTPase domain of Miro2. 12% Coomassie-stained SDS-PAGE gel utilised. Uninduced and induced culture lysate was compated to partially IMAC-purified lysate (eluate).

From these initial expression trials, over-expression of the C-terminal 'GTPase' domain of hMiro1 was strongly indicated at several conditions. Over-expression of the hMiro2 'GTPase' domain was not immediately indicated by expression trials, though bands consistently appeared at around 37 kDa, suggesting possible dimerisation. As shown in figures 3.13–3.14 and indicated in table 3.5 (below), over-expression of the C-terminal 'GTPase' domain of hMiro1 appeared optimal at 18ºC, using 0.1 mM–0.5 mM IPTG.

Table 3.5. Expression optimisation of hMiros C-terminal GTPase domains using IPTG induction. Expression of hMiro1 and hMiro2 using IPTG induction (0.1mM or 1mM) in 50 mL LB broth, where - indicates no visible expression, + indicates some visible expression, ++ indicates notable expression and +++ indicates maximum over-expression.

		hMiro1 CT Over-expression				hMiro2 CT Over-expression		
		37°C	25°C	18°C		37°C	25°C	18°C
[IPTG] (mM)	0.1	-	-	+++		-	-	-
	1	-	++	+++		-	-	-

Confirmation of over-expression of the hMiro1 C-terminal GTPase domain was undertaken by LC-MS analysis of excised SDS-PAGE bands, using a previously demonstrated method (260) in conjunction with the Bruker Daltonics HCT system (section 2.2.7.4). Analysis of LC-MS data using the MASCOT MS/MS Ions Search tool (261) was indicative of over-expression of the desired polypeptide (Figure 3.12), with the top score identified as 'hypothetical protein' EAW80247.1 matching the hMiro1 amino acid sequence on the National Centre for Biotechnology Information (NCBI) database. This analysis showed 21% sequence coverage when corrected for the C-terminal GTPase domain alone, with all peptides matching against the amino acid composition of the hMiro C-terminal 'GTPase' domain provided in NCBI.

Mascot Score Histogram

Ions score is -10*Log(P), where P is the probability that the observed match is a random event.
Individual ions scores > 52 indicate identity or extensive homology (p<0.05).
Protein scores are derived from ions scores as a non-probabilistic basis for ranking protein hits.

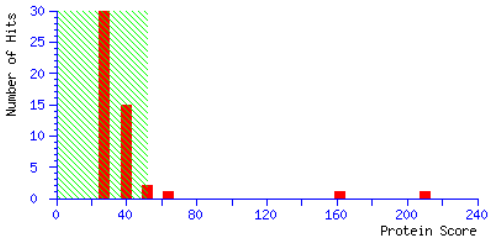

Peptide Summary Report

Format As: Peptide Summary — Help
Significance threshold p< 0.05 — Max. number of hits AUTO — Show Percolator scores
Standard scoring / MudPIT scoring — Ions score or expect cut-off 0 — Show sub-sets 0
Show pop-ups / Suppress pop-ups — Sort unassigned Decreasing Score — Require bold red
Preferred taxonomy: All entries

Select All | Select None | Search Selected | Error tolerant

1. gi|12053353 Mass: 67543 Score: 210 Matches: 7(4) Sequences: 4(2) emPAI: 0.10
hypothetical protein [Homo sapiens]
Check to include this hit in error tolerant search

Query	Observed	Mr(expt)	Mr(calc)	Delta	Miss	Score	Expect	Rank	Unique	Peptide
15	827.4680	826.4607	826.4185	0.0423	0	(19)	1.5e+02	4	U	K.SDLHEVK.Q
☑ 16	414.3910	826.7674	826.4185	0.3490	0	38	1.9	1	U	K.SDLHEVK.Q
☑ 36	480.2940	958.5734	958.4140	0.1595	0	19	1.8e+02	1	U	K.LTTMAMYP.- + 2 Oxidation (M)
☑ 41	507.4230	1012.8314	1012.6029	0.2285	0	(68)	0.0017	1	U	K.SGVLQALLGR.N
☑ 42	507.4660	1012.9174	1012.6029	0.3145	0	78	0.00019	1	U	K.SGVLQALLGR.N
☑ 101	899.5700	1797.1254	1796.8621	0.2634	0	76	0.00022	1	U	K.SYYAINTVYVYGQEK.Y
☑ 102	899.5980	1797.1814	1796.8621	0.3194	0	(67)	0.0016	1	U	K.SYYAINTVYVYGQEK.Y

Figure 3.14. MASCOT MS/MS Ions Score Histogram and analysis, indicating the presence of peptides in the hMiro1 C-terminal GTPase domain in the digested sample. Screenshot of the Mascot Score Histogram and Peptide Summary Report.

3.3.1.3. Expression up-scale: hMiro1 and hMiro2 C-terminal GTPase domains

The most promising conditions from the expression trials were scaled up. For the C-terminal 'GTPase' domain of hMiro2, 2 litre cultures induced with 0.5 mM IPTG at 18ºC were utilised, as expression trials were inconclusive. Cells were harvested, broken open and cell-free supernatant obtained as discussed in section 2.2.4.3. Subsequently, the recombinant polypeptides were purified by IMAC using a Nickel NTA column attached to an ÄKTA Prime fast protein liquid chromatography (FPLC) system (section 2.2.4.4). Figures 3.15 (hMiro1) and 3.16 (hMiro2) indicate the successful purification of these over-expressed recombinant polypeptides.

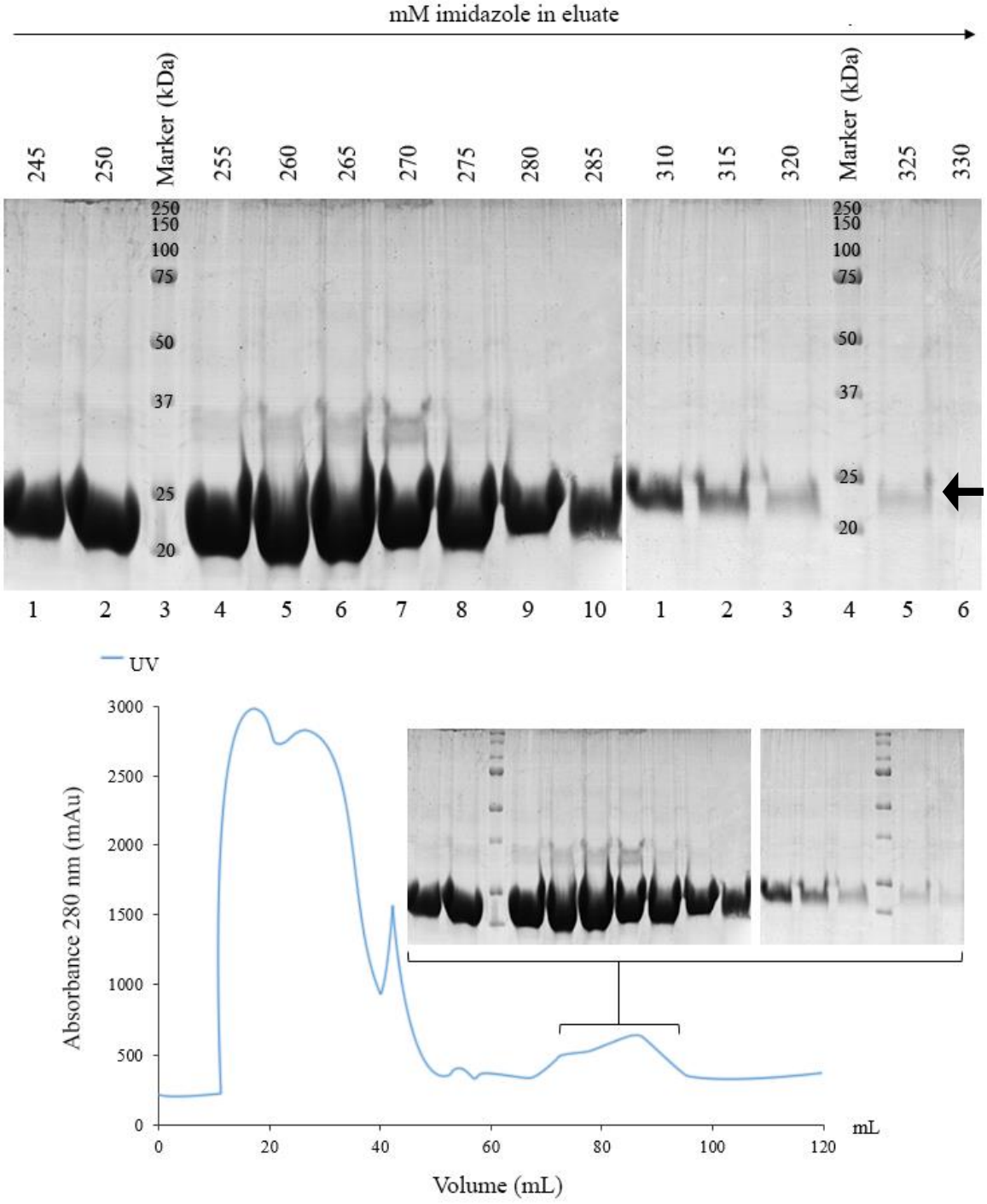

Figure 3.15. Successful purification of the hMiro1 C-terminal construct (Q415 – P580) by ion-metal affinity chromatography (IMAC). Chromatogram obtained from the ÄKTA PRIME automated FPLC system shown, alongside 12% SDS-PAGE gels of samples of the fractions from the purification process containing the purified hMiro1 C-terminal construct. Coomassie staining was utilised for SDS-PAGE gels.

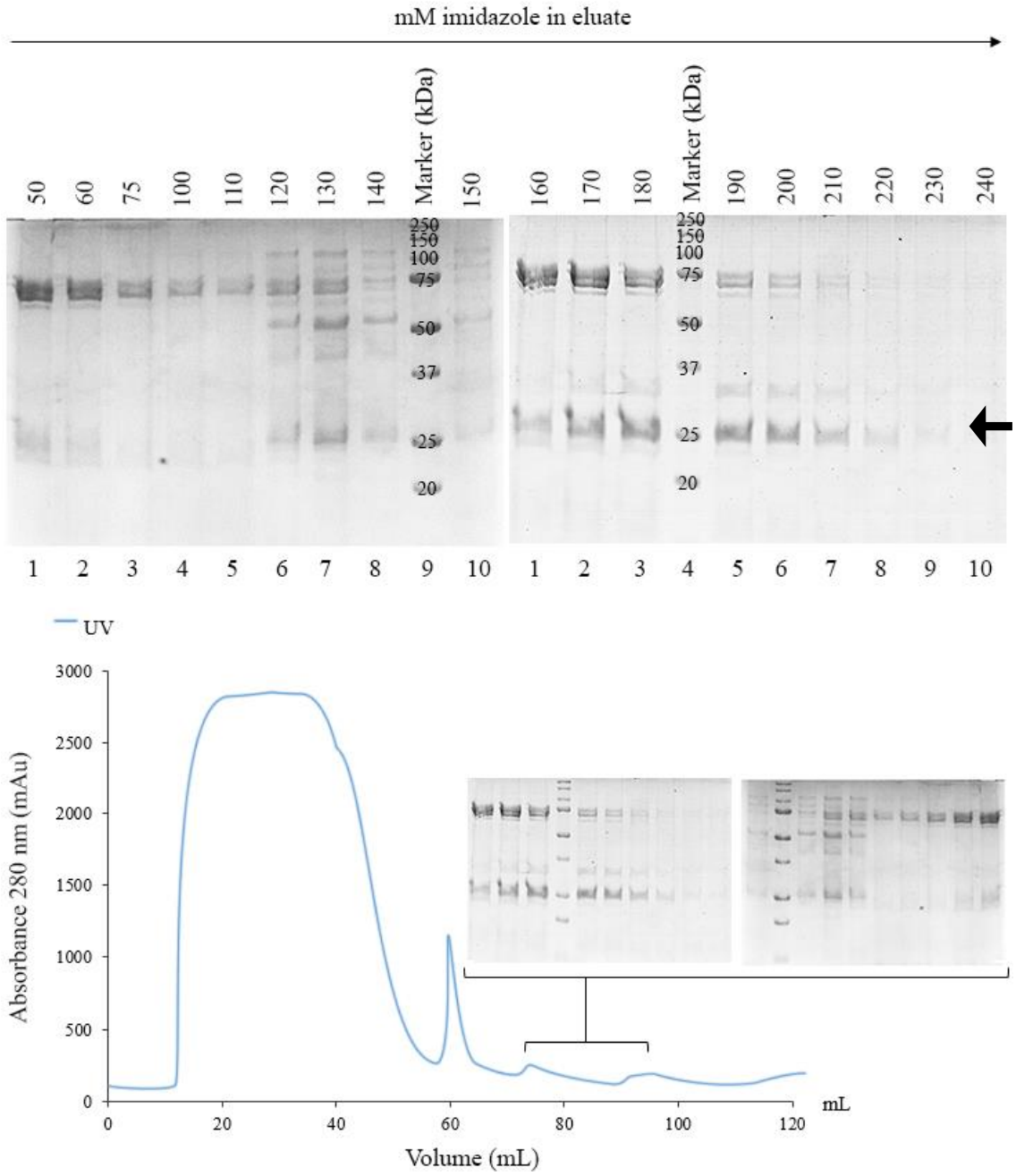

Figure 3.16. Purification of the hMiro2 C-terminal construct (Q413–F589) by ion-metal affinity chromatography (IMAC). Chromatogram obtained from the ÄKTA PRIME automated FPLC system shown, alongside 12% SDS-PAGE gels of samples of the fractions from the purification process containing the purified hMiro2 C-terminal construct. Coomassie staining was utilised for SDS-PAGE gels.

Suitably IMAC-pure fractions of apparent hMiro1 and hMiro2 C-terminal 'GTPase' domain were concentrated (figure 3.22a; section 2.2.4.6) and buffer-exchanged (section 2.2.4.6) into gel filtration buffer (2.1.5.3.3). For hMiro2, it was necessary to perform size exclusion using centrifugal concentrators to remove high molecular weight contaminants prior to concentration and buffer exchange (figure 3.22 b). To confirm the identity of the concentrated and buffer-exchanged polypeptides, Western blotting was performed (2.2.4.8), using monoclonal antibodies raised against hMiro1 (Figure 3.23a) and hMiro2 (Figure 3.23b). Bands on these blots indicated that hMiro-like polypeptides had been successfully over-expressed.

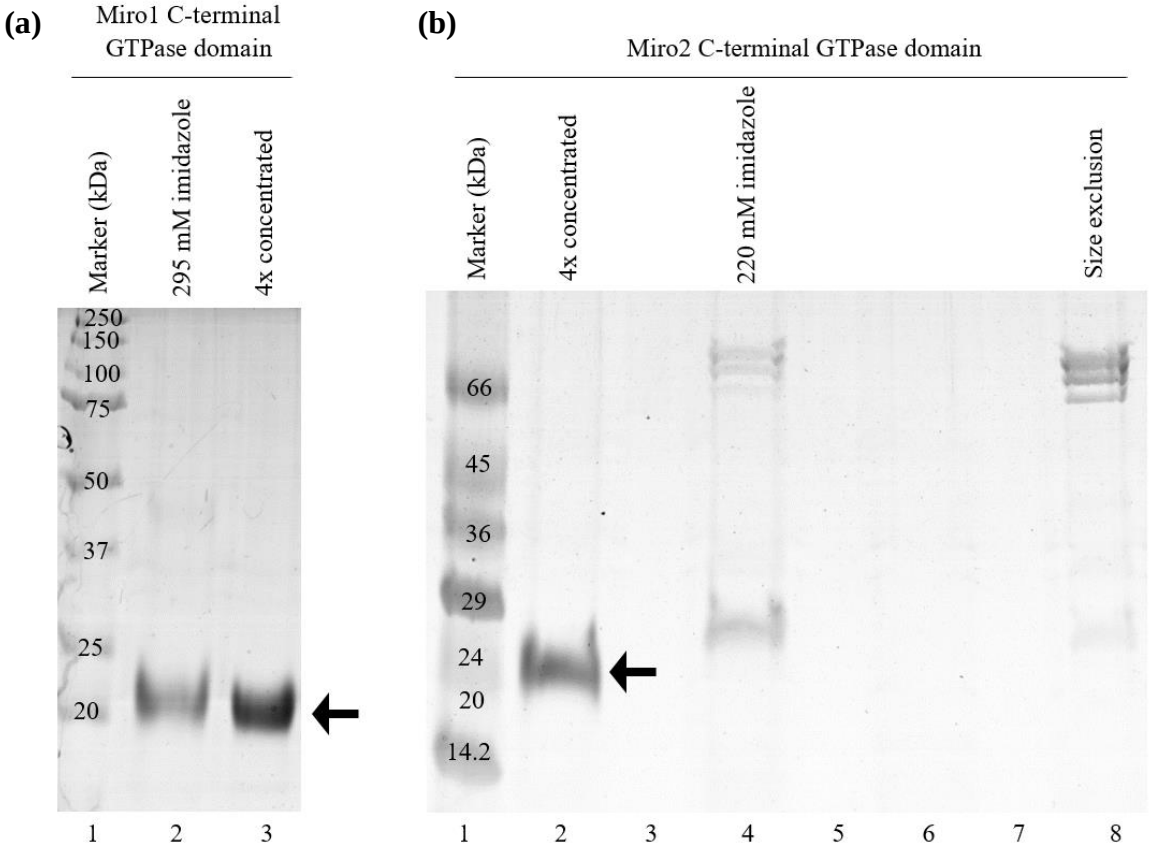

Figure 3.17. Concentrated C-terminal GTPase domains of (a) hMiro1 and (b) hMiro2 following IMAC purification. 12% SDS-PAGE gels stained in Coomassie, showing the (a) hMiro1 and (b) hMiro2 C-terminal GTPase domains.

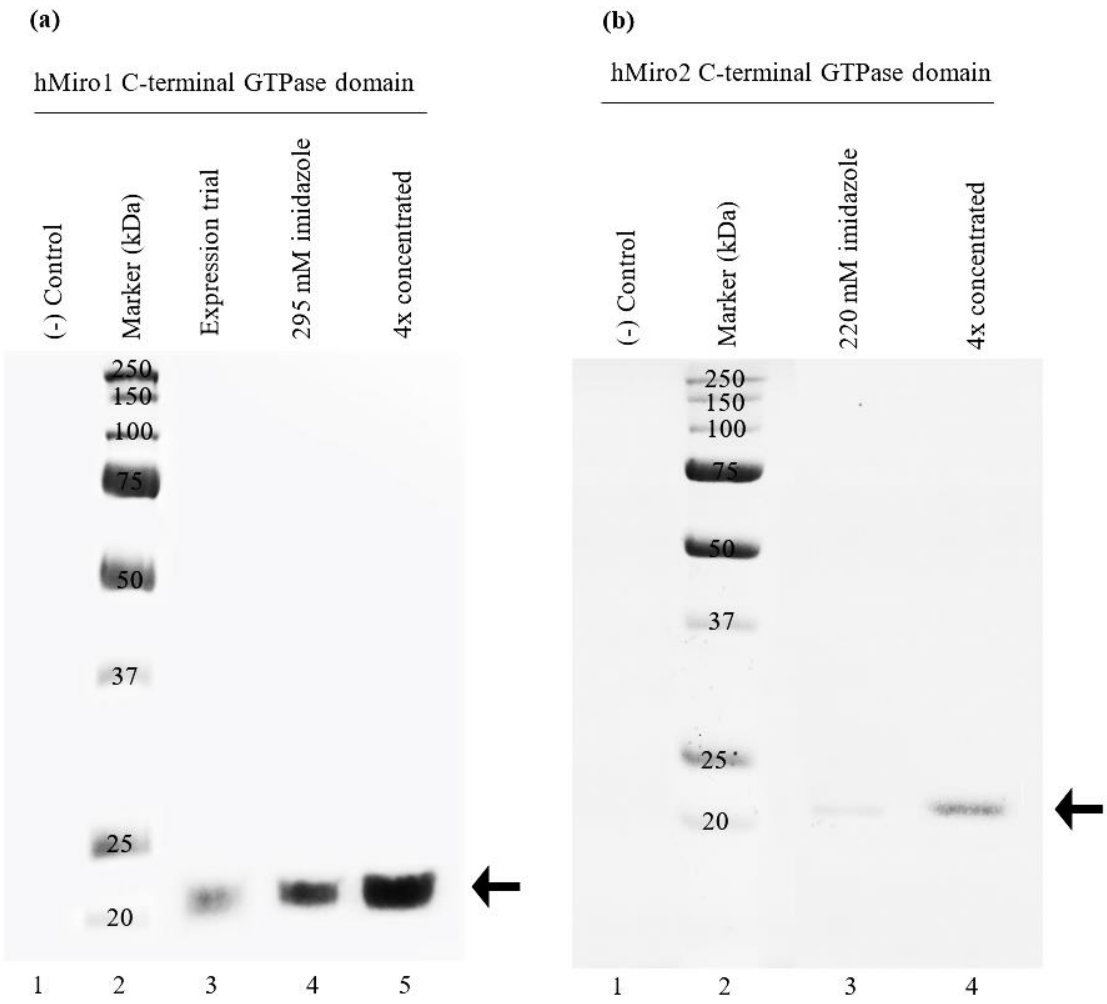

Figure 3.18. Western blotting of the hMiro1 (a) and hMiro2 (b) C-terminal GTPase domains. Immunoblots showing detection of (a) hMiro1 and (b) hMiro2 using chemiluminescent detection.

3.3.2. Cloning, expression and purification of hMiro1 and hMiro2 'crystal' truncates

As previously mentioned, a truncated version of the Dropsophila Miro, dMiro, was successfully crystallised (131) whilst cloning of the C-terminal GTPases of hMiro1 and hMiro2 was in process. In the hope of producing successful crystals of hMiros truncated in a similar manner, 'xtal constructs' of hMiro1 and hMiro2 were engineered for cloning and expression purposes. The 'xtal' constructs comprised the EF-hands and C-terminal GTPase domain of each hMiro, as discussed in 3.2.

3.3.2.1. Cloning of the hMiro1 and hMiro2 'crystal' truncates

Following the successful cloning, expression and purification of the hMiro1 and hMiro2 C-terminal 'GTPase' domains, the 'crystal constructs' were subject to the same process and methodology as described in section 3.2. Primers were designed for cloning of the nucleotide sequences encoding the hMiro1 and hMiro2 'crystal constructs' (residues 177-589 for hMiro1 and residues 177-586 for hMiro2; section 2.1.3) into the bacterial expression vector pET15b-TEV. PCR-based amplification of the desired domains was successfully accomplished using previously described mammalian vectors donated by the Pontus Aspenström group as template (figure 3.19 a and b).

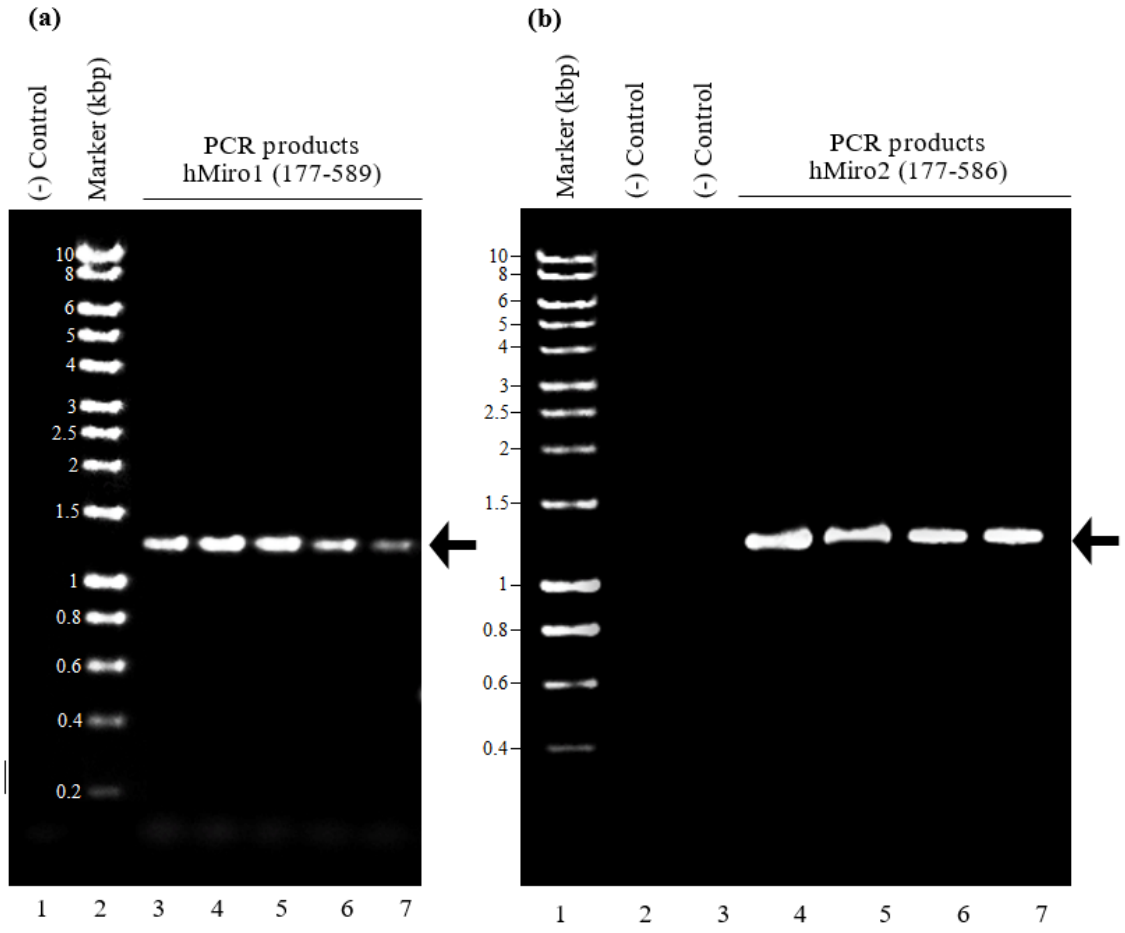

Figure 3.19. Successful PCR-based amplification of the nucleotide sequences encoding the 'crystal construct' domains of hMiro1 and hMiro2, respectively. 1% agarose gels showing successful PCR-based amplification of the gene sequences encoding hMiro 1 177–590 (a, lanes 3-7) and hMiro2 177–586 (b, lanes 4–11), respectively. Lanes 1 (a) and 2–3 (b) contain negative control reactions. Marker (Bioline Hyperladder I) is shown in lane 2 of gel (a) and 1 of gel (b).

Amplified sequences were subjected to PCR-clean up procedures prior to restriction digest and ligation into pET15bTEV. Products of ligation were transformed into TOP10 *E.coli* cells, with at least 3 transformed colonies screened for the presence of the hMiro sequences of interest as an insert. Following confirmation of insert presence (figure 3.20 a and b), one suitable clone for each construct was transformed into C43 *E.coli* and expression trials initiated.

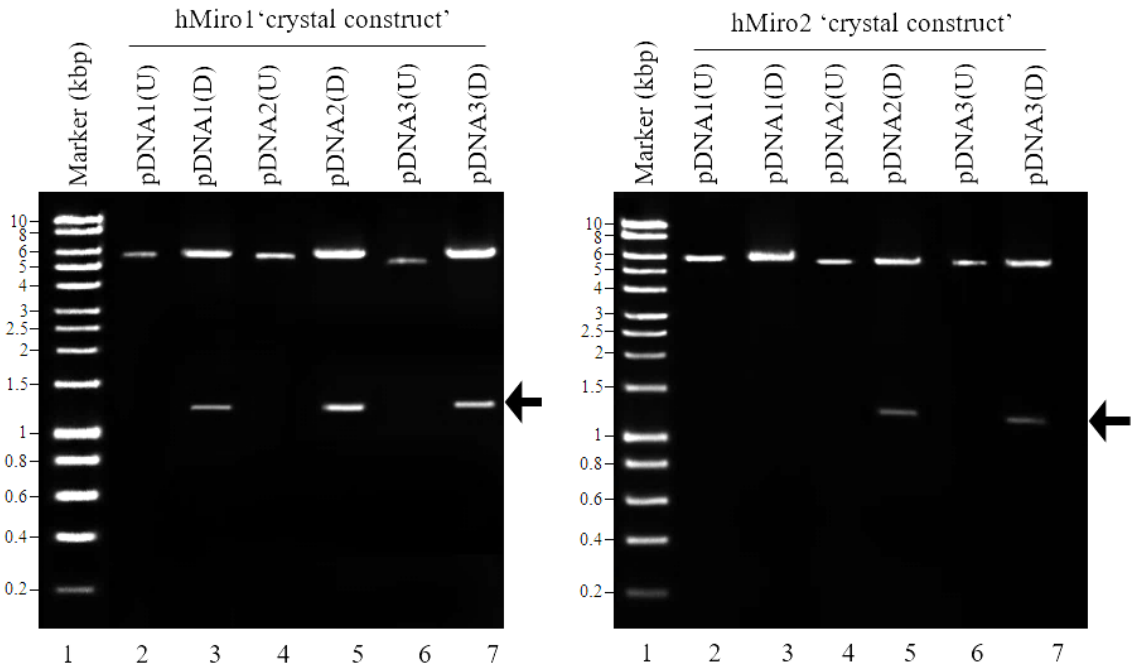

Figure 3.20. 1% agarose gels showing results of analytical restriction digest to screen for hMiroXTAL inserts into pET15bTEV. Analytical restriction digest of plasmid DNA extracted from TOP10 *E.coli* transformants after ligation of pET15b-TEV/hMiro1 177-589 PCR products (lanes 2-7, a) and pET15b-TEV/hMiro2 177-586 products (lanes 2-7, b), respectively. Lane 1 of both (a) and (b) contains Hyperladder I (BioLine). For each lane in which plasmid is shown, 'U' represents undigested plasmid and 'D' represents plasmid that has undergone a double restriction digest with the appropriate restriction enzymes (NdeI/XhoI).

3.3.2.2. Expression trials: of hMiro1 and hMiro2 'crystal' truncates

Expression trials for expression of the hMiro 'crystal constructs' was undertaken as previously indicated (section 3.2). However, as a final IPTG concentration of 0.5 mM appeared largely successful in previous cultures, a constant IPTG concentration of 0.5 mM was implemented in these trials, with temperature variables assessed (18^{o}C, 25^{o}C and 37^{o}C). As shown in figures 3.21–3.34 and summarised in table 3.6, expression trials were suggestive of the successful expression and purification of the target hMiro1 recombinant polypeptide. Expression of hMiro2 was suggested by the presence of a band in the induced sample, though expression trial data yielded no obvious bands in IMAC column eluates. The most successful conditions indicated by the expression trials were correspondingly up-scaled.

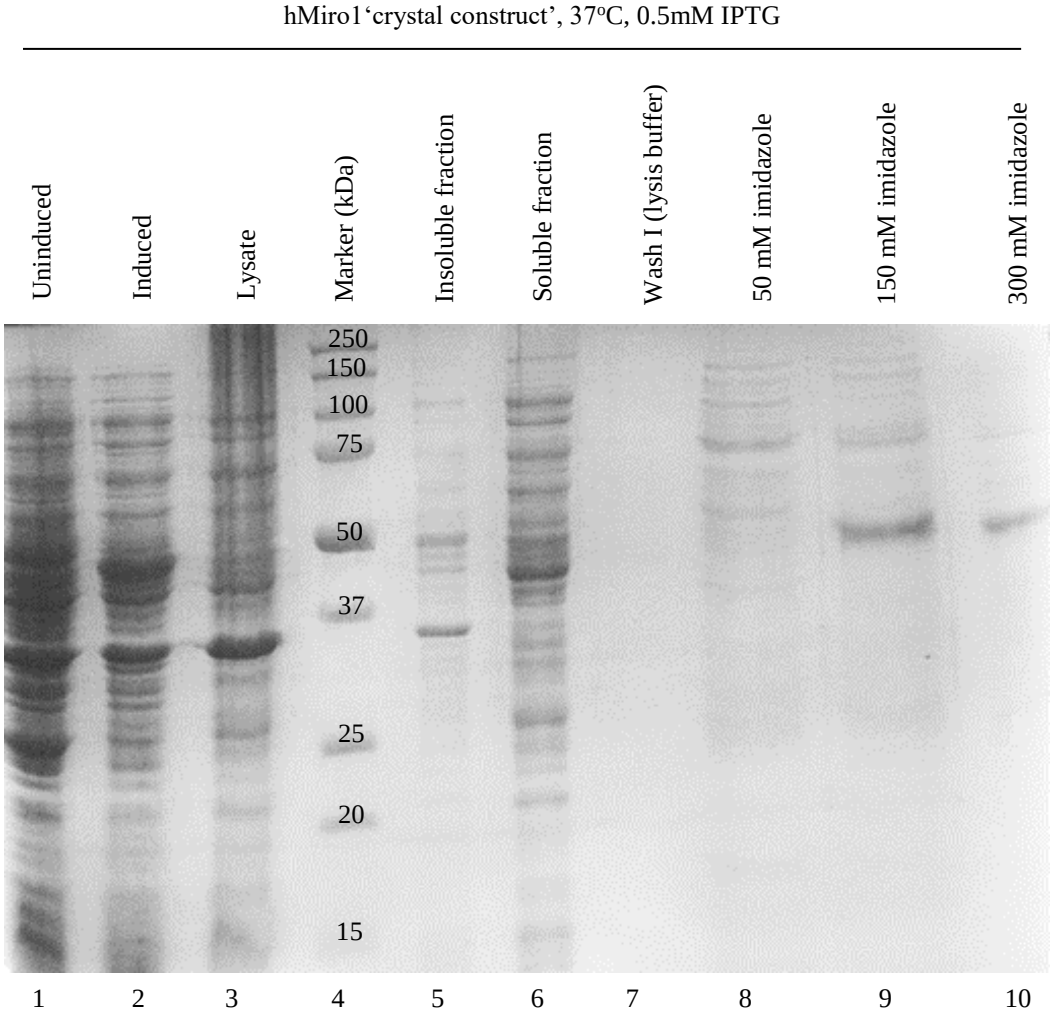

Figure 3.21. 12% Coomassie-stained SDS-PAGE gel showing expression trial data for the hMiro1 ‘crystal construct’. 50mL culture induced at 37ºC for 4 hours to a final IPTG concentration of 0.5mM. Note the presence of bands of around the expected molecular weight for the target recombinant polypeptide (~47.6 kDa) in eluates containing 150 mM and 300 mM imidazole.

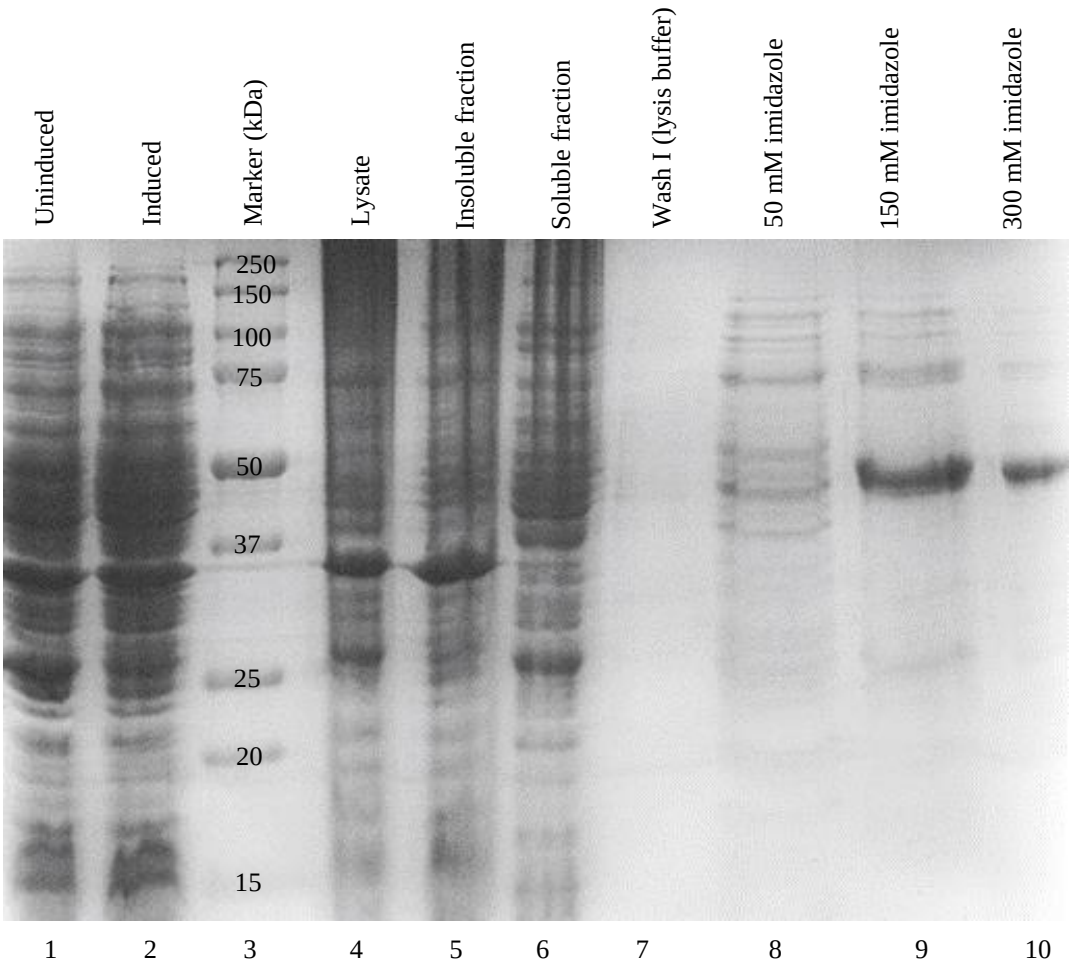

Figure 3.22. 12% SDS-PAGe gel showing further expression trial results for the hMiro1 ‘crystal construct’. 50mL culture induced at 18ºC overnight (16 hours) to a final IPTG concentration of 0.5mM. Note the presence of bands of around the expected molecular weight for the target recombinant polypeptide (~47.6 kDa) in eluates containing 150 mM and 300 mM imidazole. Gel stained in Coomassie blue.

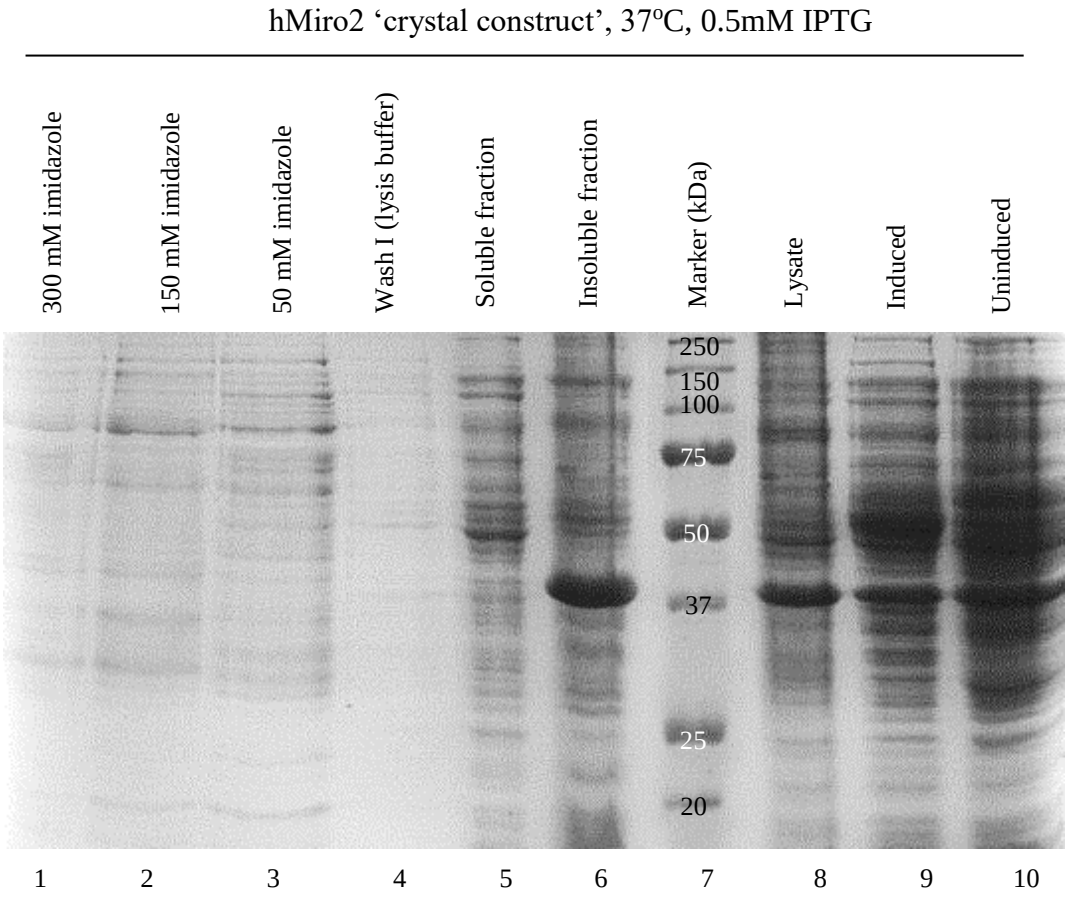

Figure 3.23. 12% SDS-PAGe gel displaying expression trial data for the hMiro2 'crystal construct'. 50mL culture induced at 37ºC for 4 hours to a final IPTG concentration of 0.5mM. Note the presence of bands of around the expected molecular weight for the target recombinant polypeptide (~47.6 kDa) in eluates containing 150 mM and 300 mM imidazole. Coomassie staining utilised.

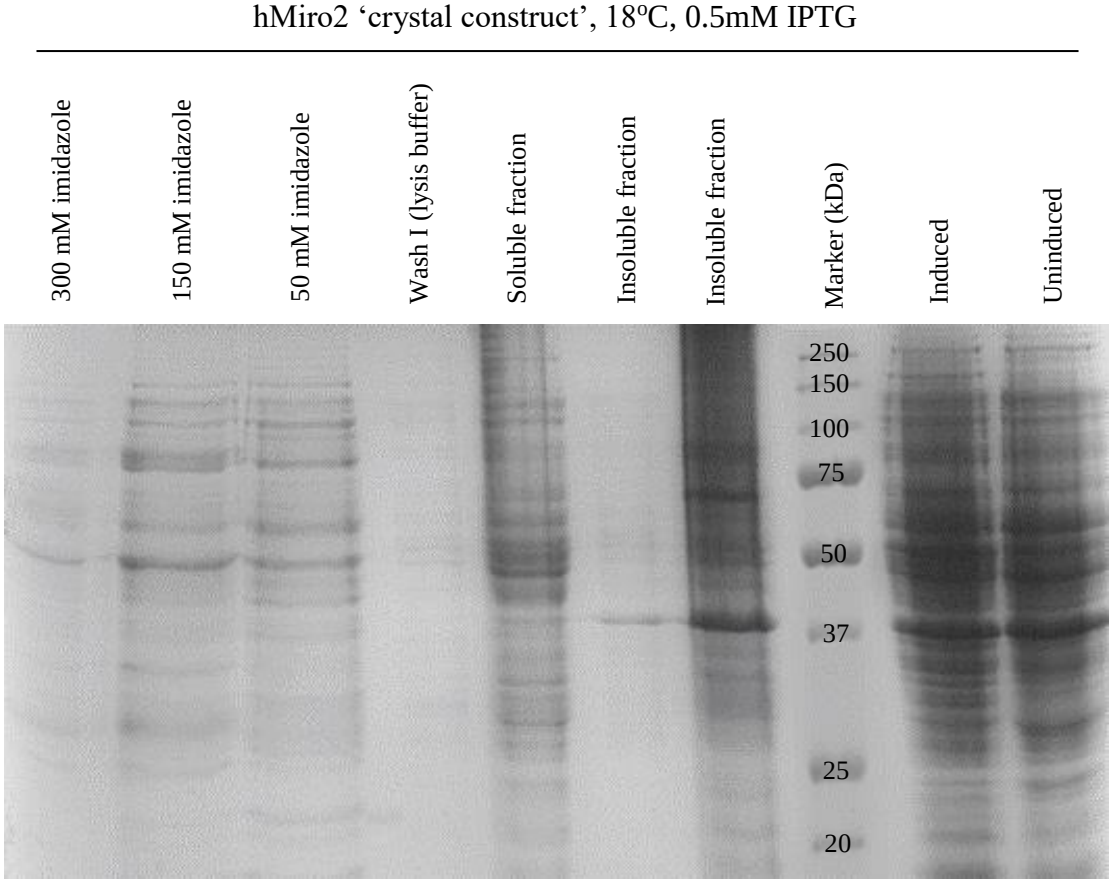

Figure 3.24. 12% SDS-PAGE gel showing further expression trial data for the hMiro2 'crystal construct'. 50mL culture induced at 18°C overnight (16 hours) to a final IPTG concentration of 0.5mM. Note the presence of bands of around the expected molecular weight for the target recombinant polypeptide (~47.6 kDa) in eluates containing 150 mM and 300 mM imidazole. Coomassie staining applied to gel.

Table 3.6. Expression optimisation of hMiro 'crystal construct' polypeptides using IPTG induction. Expression of hMiro1 and hMiro2 using IPTG induction (0.5 mM) in 50 mL LB broth, where - indicates no visible expression, + indicates some visible expression, ++ indicates notable expression and +++ indicates maximum over-expression.

hMiro1 'crystal construct'		**hMiro2 'crystal construct'**	
18°C	37°C	18°C	37°C
+++	++	+	+

3.3.2.3. Expression up-scale: hMiro1 and hMiro2 ‘crystal’ truncates

The most promising conditions from the ‘crystal construct’ expression trials were scaled up, using 2L cultures in LB broth for each construct. Cells were harvested, broken open and cell-free supernatant obtained as discussed previously (section 2.2.4.3). For protein purification, the ÄKTA Prime IMAC approach was utilised (section 2.2.4.4). As illustrated in Figure 3.25 (hMiro1) and Figure 3.26 (hMiro2), up-scale of expression and purification appeared to produce pure fractions of both the hMiro1 and hMiro2 target polypeptides. IMAC-purified samples were assessed for the presence of the target polypeptides by both Western blotting (Figure 3.27 a and b) and in-gel trypsinisation followed by LC-MS analysis (see section 2.2.7.4); these approaches indicated the presence of the hMiro1 and 2 ‘crystal construct’ polypeptides in IMAC-purified samples.

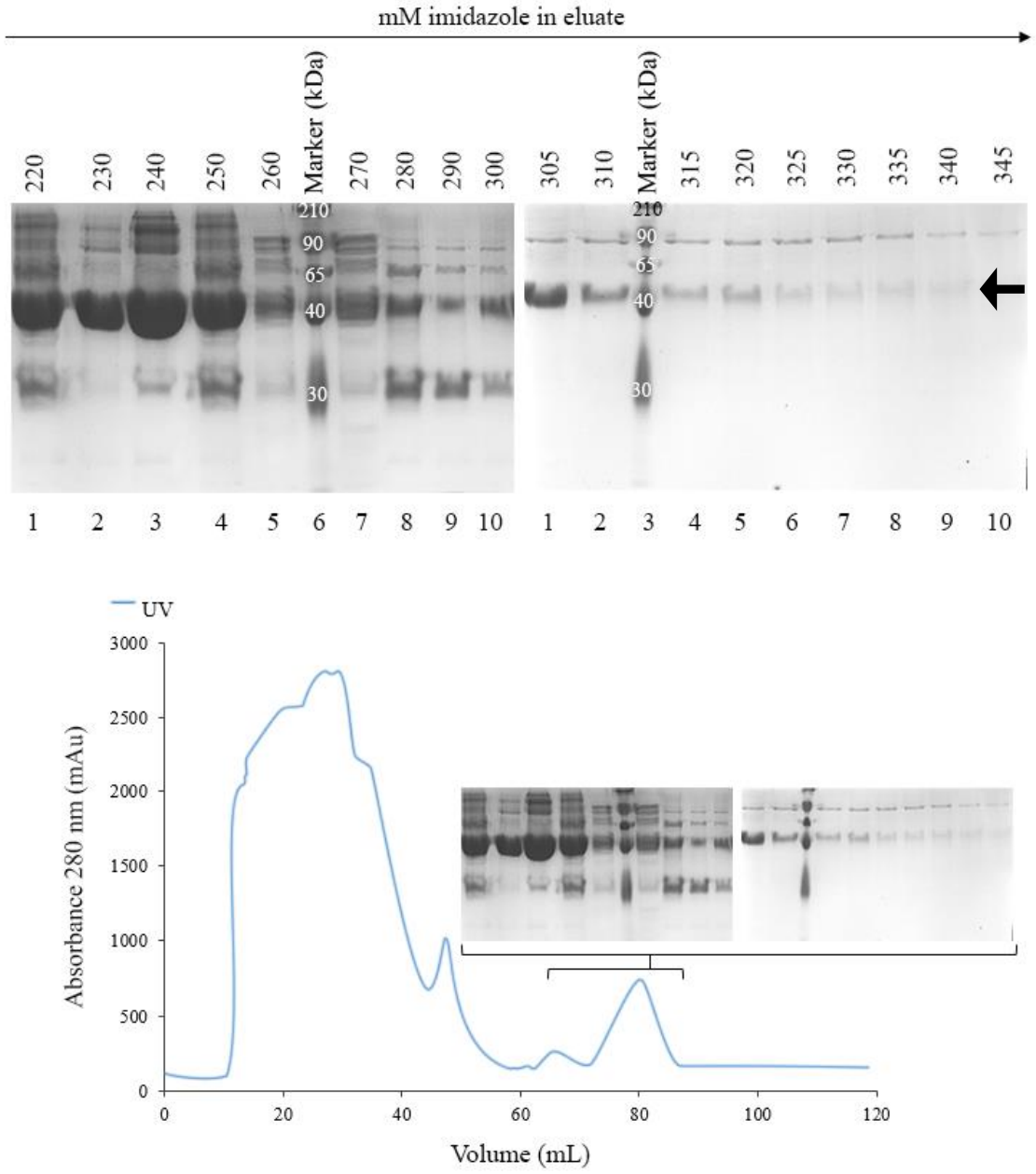

Figure 3.25. Purification of the hMiro1 xtal construct (E177–R590) by ion-metal affinity chromatography (IMAC). Chromatogram obtained from the ÄKTA PRIME automated FPLC system shown, alongside 12% SDS-PAGE gels of samples of the fractions from the purification process containing the purified xtal construct. Coomassie staining used for SDS-PAGE gels.

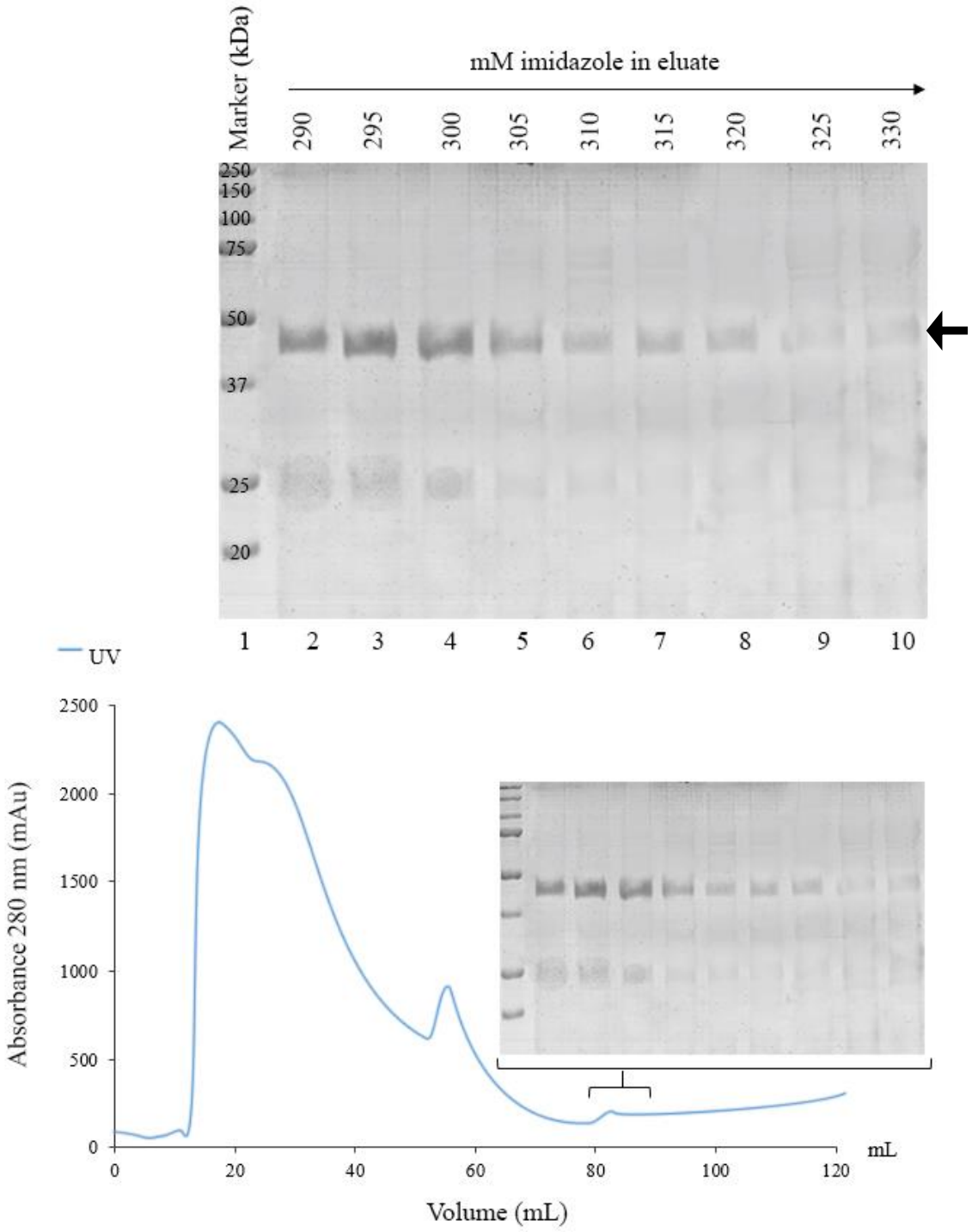

Figure 3.26. Purification of the hMiro2 xtal construct (E177–P586) by ion-metal affinity chromatography (IMAC). Chromatogram obtained from the ÄKTA PRIME automated FPLC system shown, alongside 12% SDS-PAGE gels of samples of the fractions from the purification process containing the purified hMiro2 xtal construct. SDS-PAGE gels shown are Coomassie-stained.

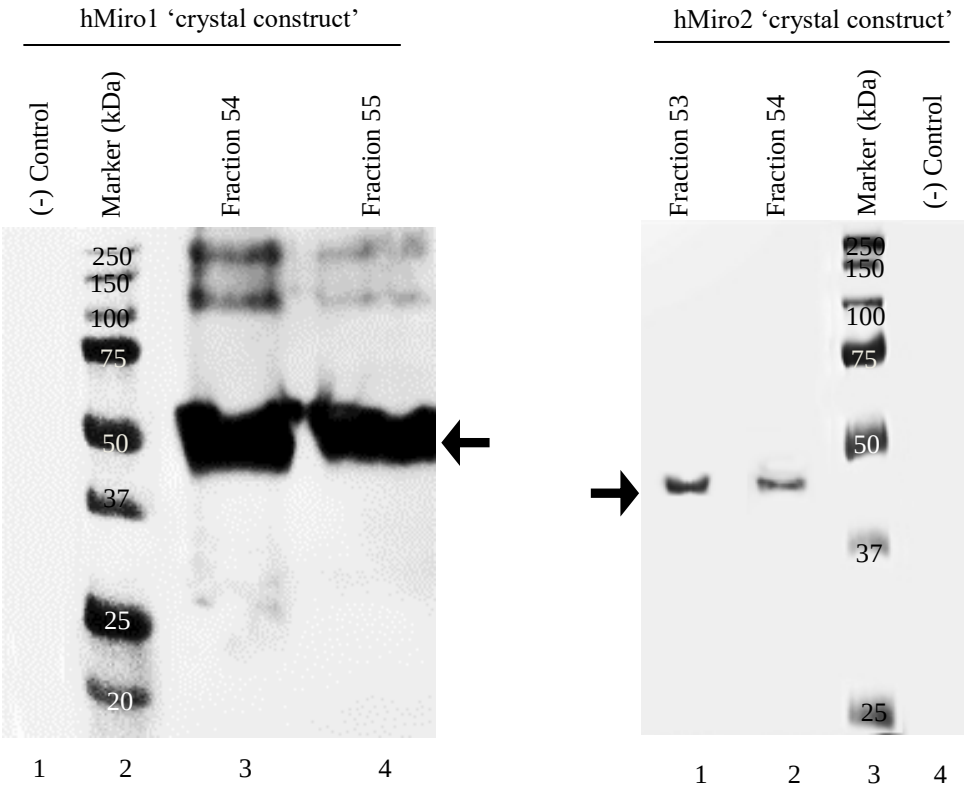

Figure 3.27. Western blot of hMiro1 (a) and hMiro2 (b) IMAC-purified 'crystal construct samples. Chemilumiscent visualisation of Western blots using antibodies raised against **(a)** hMiro1 and **(b)** hMiro2.

3.3.3. Cloning, expression and purification of hMiro1 and hMiro2 N-terminal GTPase domains

3.3.3.1. Cloning of the hMiro1 and hMiro2 N-terminal GTPase domains

Following the successful cloning, expression and purification of the hMiro1 and hMiro2 C-terminal GTPase domains and 'crystal constructs', the N-terminal GTPase domains of both hMiros were subject to the same process and methodology described above. Primers were designed for cloning of the nucleotide sequences encoding the hMiro1 and hMiro2 N-terminal GTPase domains into the bacterial expression vector pET15b-TEV. PCR-based amplification of the hMiro N-terminal GTPase domains was successfully accomplished using vectors encoding the full-length, wildtype versions of hMiro1 and hMiro2 as template (Figure 3.28 a and b). Ligation of PCR products into pET15b (2.2.3.10), followed by transformation into TOP10 (2.2.2.2) and screening of extracted pDNA was performed as previously described (2.2.3.6). As shown in figure 3.29, all transformants screened contained a gene sequence of the expected size following analytical restriction digest.

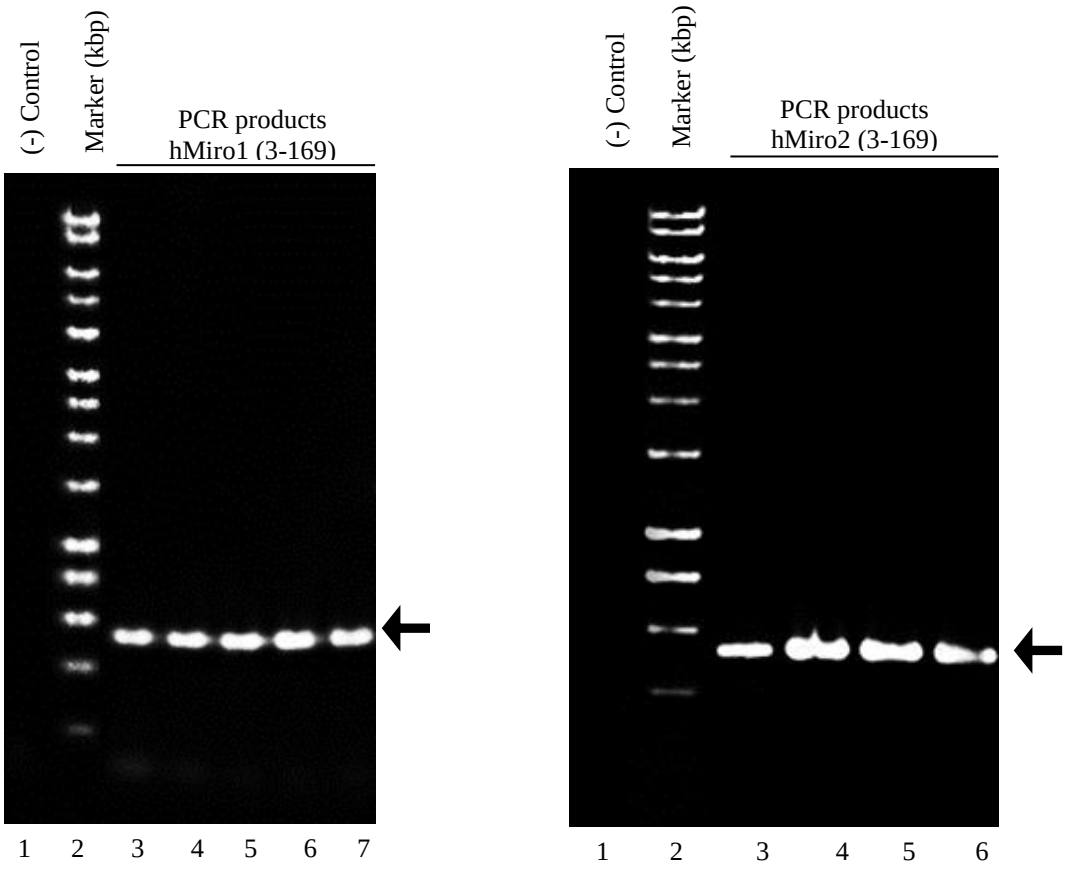

Figure 3.28. Successful PCR-based amplification of the nucleotide sequences encoding the N-terminal GTPase domain of (a) hMiro1 and (b) hMiro2. 1% agarose gels showing PCR-based amplification of the gene sequences encoding hMiro1 3–169 (lanes 3 –7, a) and hMiro2 3 –169 (lanes 3 –6, b). Lane 2 (a) and 2 (b) contain marker (Bioline Hyperladder I). Lanes 1 (a) and 1 (b) show negative controls containing all components of the optimised reaction except the DNA template.

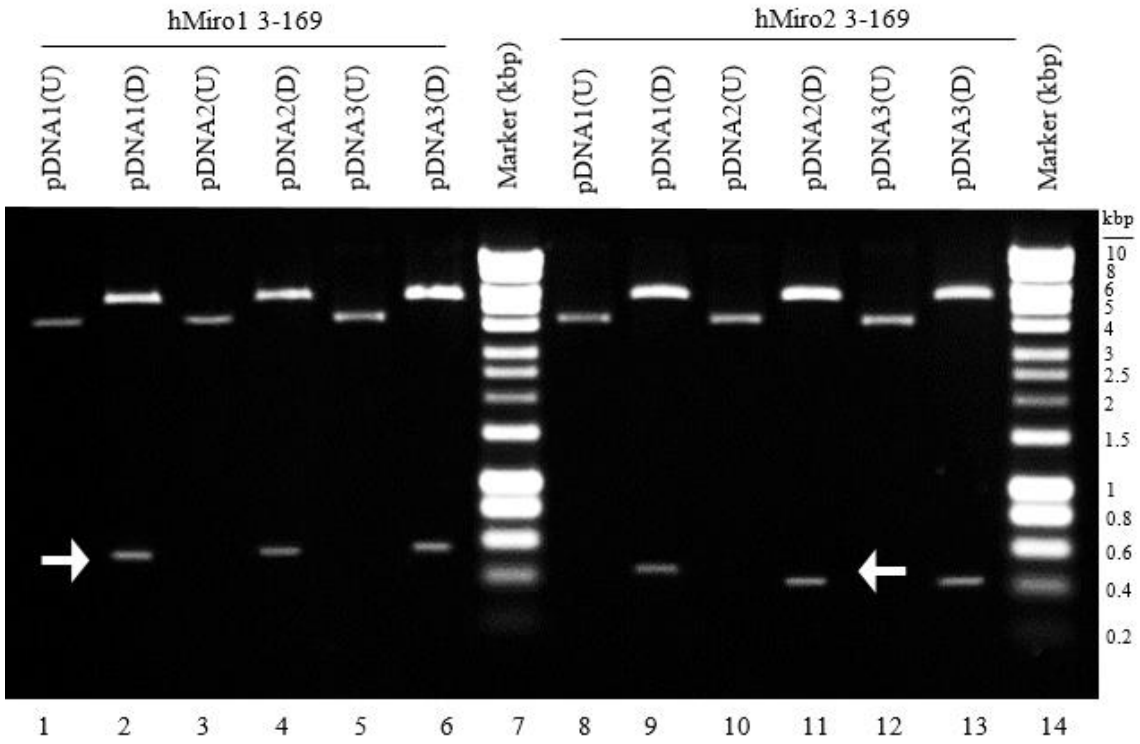

Figure 3.29. Analytical restriction digest of plasmid DNA extracted from TOP10 *E.coli* transformants after ligation of pET15b-TEV/hMiro1 3–169 PCR products (lanes 1–6) and pET15b-TEV/hMiro2 3–169 products (lanes 8–13), respectively. Lanes 7 and 14 contain Hyperladder I (BioLine). For each lane in which plasmid is shown, 'U' represents undigested plasmid and 'D' represents plasmid that has undergone a double restriction digest with the appropriate restriction enzymes. 1% agarose gel.

3.2.3.2. Expression trials: hMiro1 and hMiro2 N-terminal GTPase domains

The hMiro1 and hMiro2 N-terminal GTPase domain expression trials were undertaken as previously discussed (section 2.2.2.6), though with varying temperature conditions utilised and a constant IPTG concentration of 0.5 mM applied. All trials were attempted in the C43 *E.coli* strain. Figures 3.30–3.33 illustrate the results obtained at each tested condition, with a summary of results shown in the form of Table 3.7.

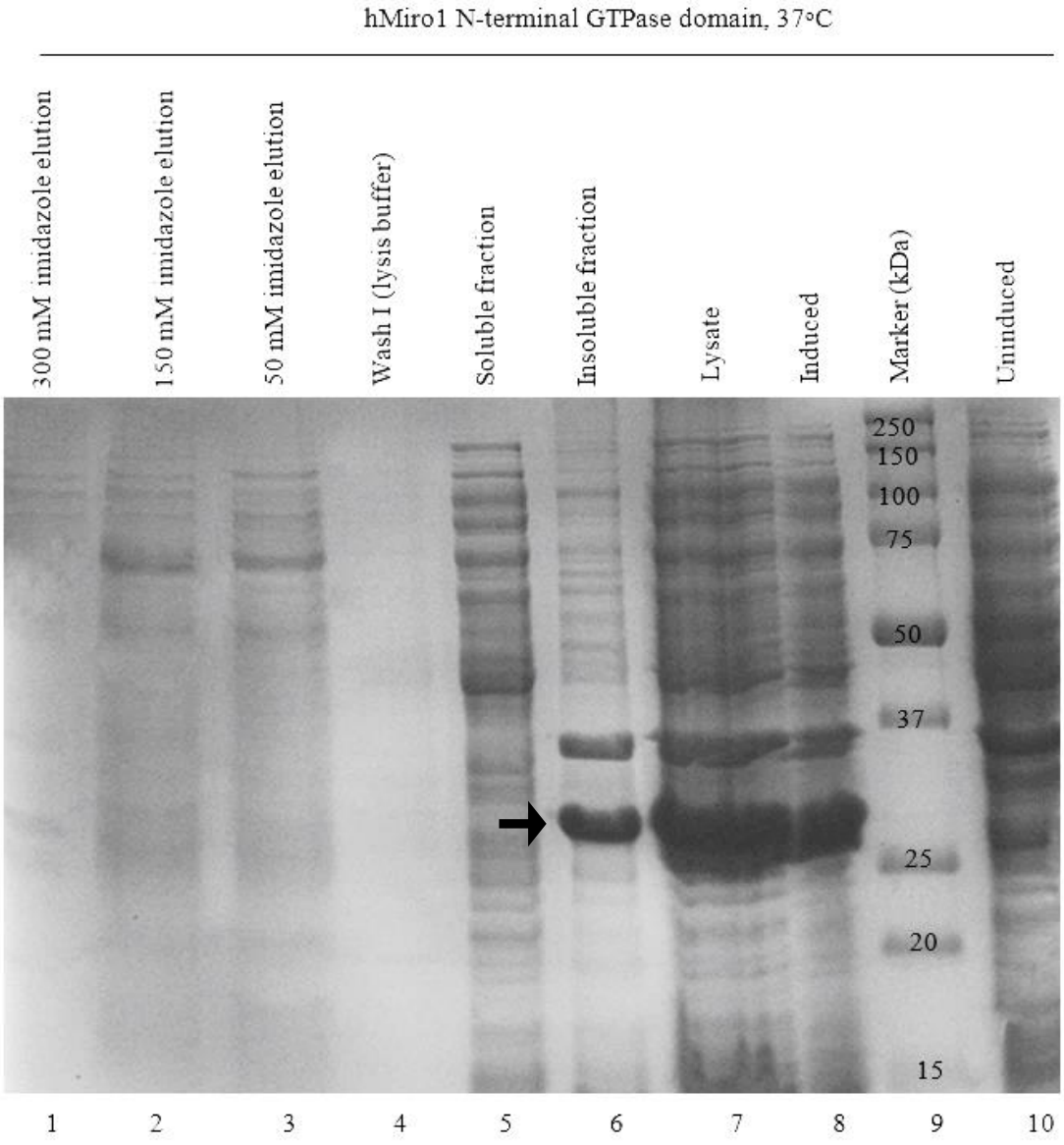

Figure 3.30. 12% SDS-PAGE gel showing expression trial data hMiro1 N-terminal GTPase domain. 50 mL culture induced at 37ºC for 4 hours to a final IPTG concentration of 0.5 mM. Note the apparent presence of over-expressed protein in the lysate, and largely in the insoluble fraction.

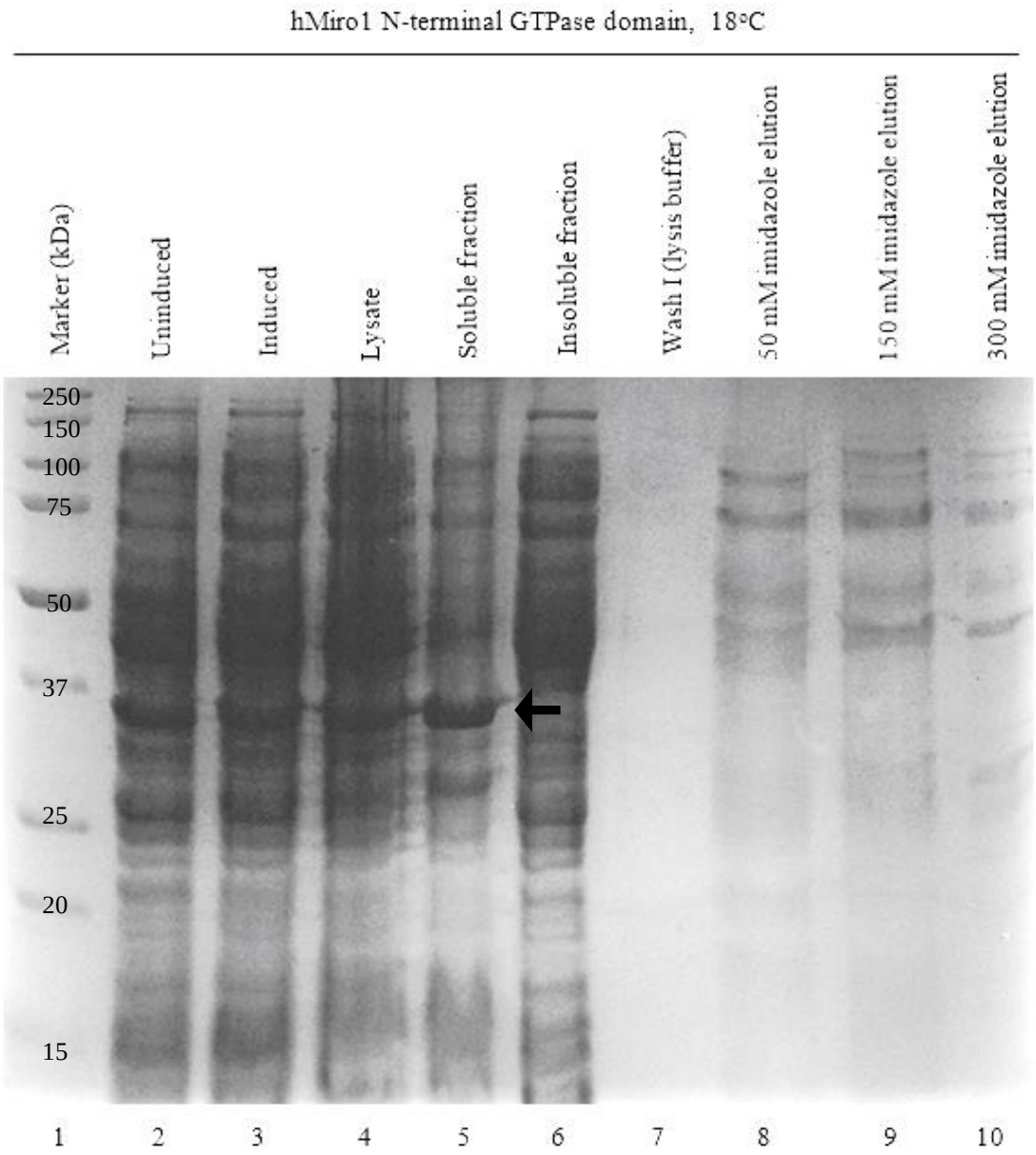

Figure 3.31. 12% SDS-PAGE gel showing expression trial data hMiro1 N-terminal GTPase domain. 50 mL culture induced at 18ºC for 16 hours to a final IPTG concentration of 0.5 mM. The presence of the target polypeptide is not strongly indicated. Gel stained in Coomassie blue.

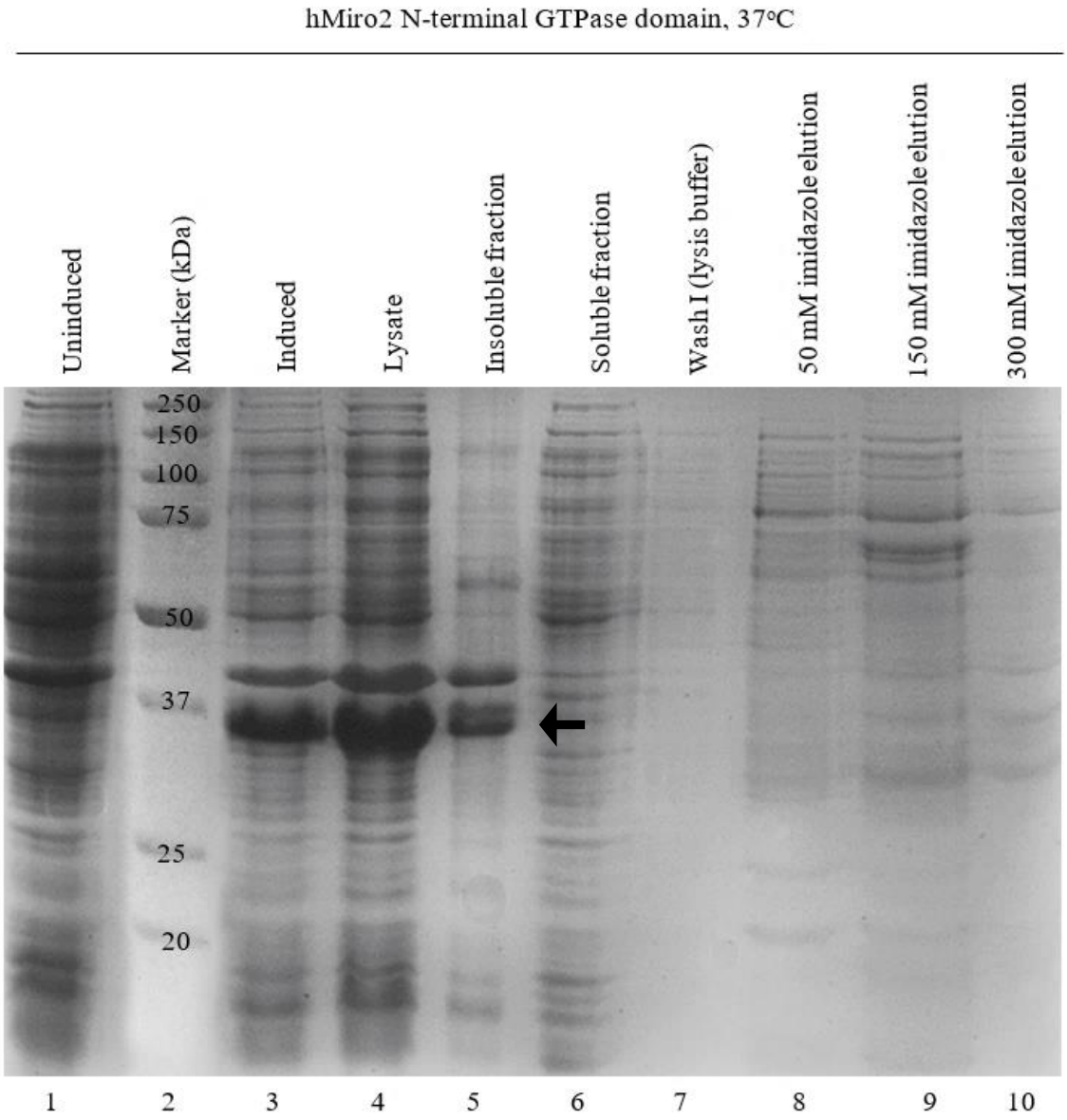

Figure 3.32 12% SDS-PAGE gel displaying expression trial data hMiro2 N-terminal GTPase domain. 50 mL culture induced at 37°C for 4 hours to a final IPTG concentration of 0.5 mM. Note the apparent presence of over-expressed protein in the induced culture (lane 3), lysate (lane 4) and insoluble fraction (lane 5) at around double the expected molecular weight for the hMiro2 N-terminal GTPase domain. Coomassie staining utilised.

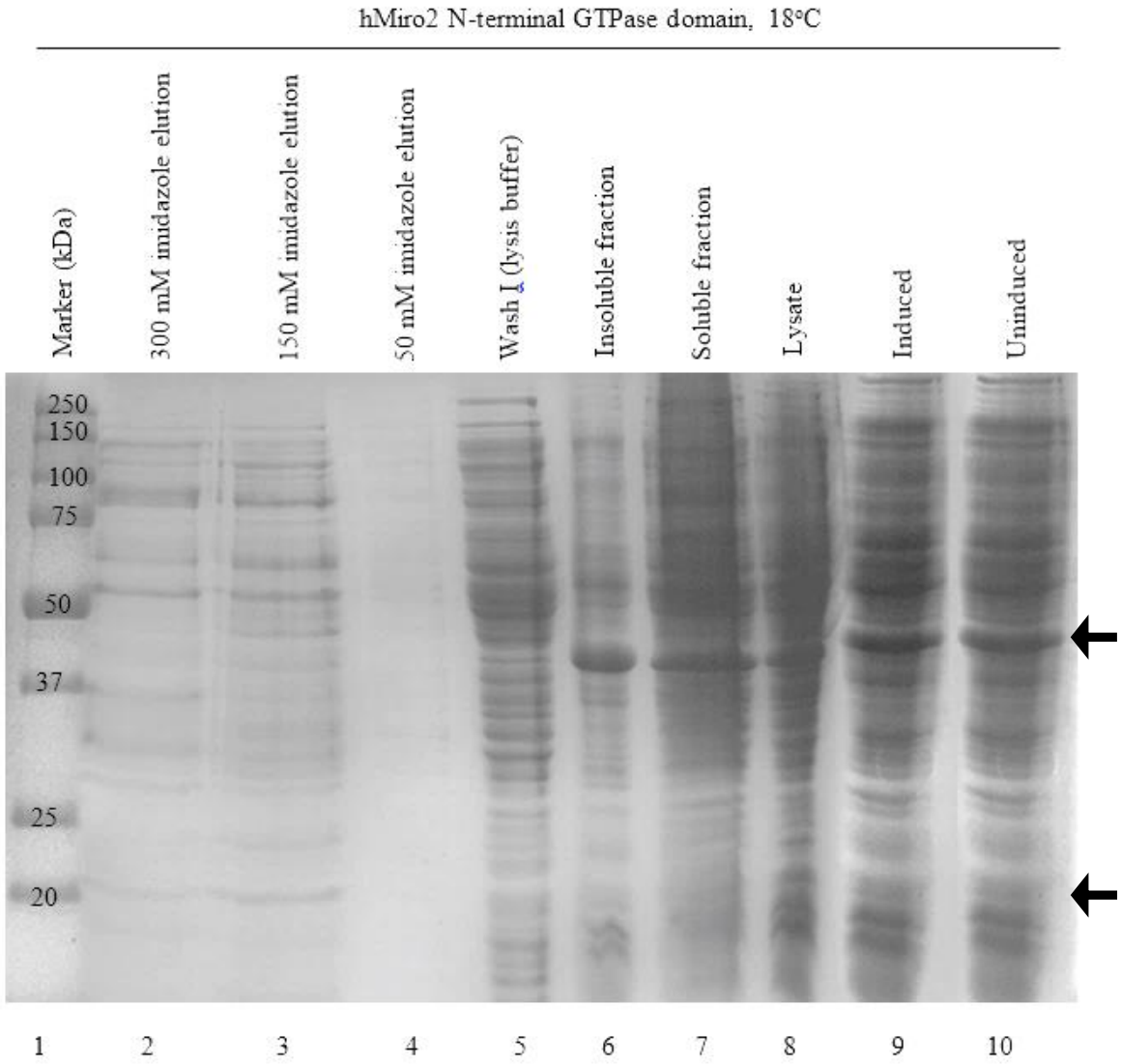

Figure 3.33 12% SDS-PAGE gel showing expression trial data hMiro2 N-terminal GTPase domain. 50 mL culture induced at 37ºC for 4 hours to a final IPTG concentration of 0.5 mM. Note the apparent presence of over-expressed protein in the induced culture (lane 3), lysate (lane 4) and insoluble fraction (lane 5) at around double the expected molecular weight for the hMiro2 N-terminal GTPase domain. Arrows point to expected molecular weight (~20 kDa) and the bands showing roughly double the expected molecular weight. Coomassie staining used.

Table 3.7. Expression optimisation of hMiros N-terminal GTPase domains using IPTG induction. Expression of hMiro1 and hMiro2 using IPTG induction (0.1mM or 1mM) in 50 mL LB broth, where - indicates no visible expression, + indicates some visible expression, ++ indicates notable expression and +++ indicates maximum over-expression.

hMiro1 N-terminal GTPase domain		**hMiro2 N-terminal GTPase domain**	
18ºC	37ºC	18ºC	37ºC
+	+	+	+

Although some over-expression was indicated in the SDS-PAGE gels, bands were of around twice the molecular weight expected. It was unclear whether these bands were mere contaminants or whether the target recombinant polypeptides may have been forming dimers. Thus, Western blotting was applied to samples. As shown in Figure 3. 44, the blots indicated the presence of a hMiro2 polypeptide of double the molecular weight of the expected recombinant N-terminal GTPase domain, suggesting that this domain is indeed liable to dimerization. However, no indication of a hMiro1 polypeptide was shown using anti-hMiro1. As the antibodies utilised were raised against full-length versions of hMiro1 and hMiro2, this negative result may be a consequence of lack of epitopes in the single hMiro1 N-terminal GTPase domain. Trypsinisation of the excised gel fragment and analysis by LC-MS was therefore performed, with results indicating that the correct recombinant protein had been over-expressed (Figure 3.34).

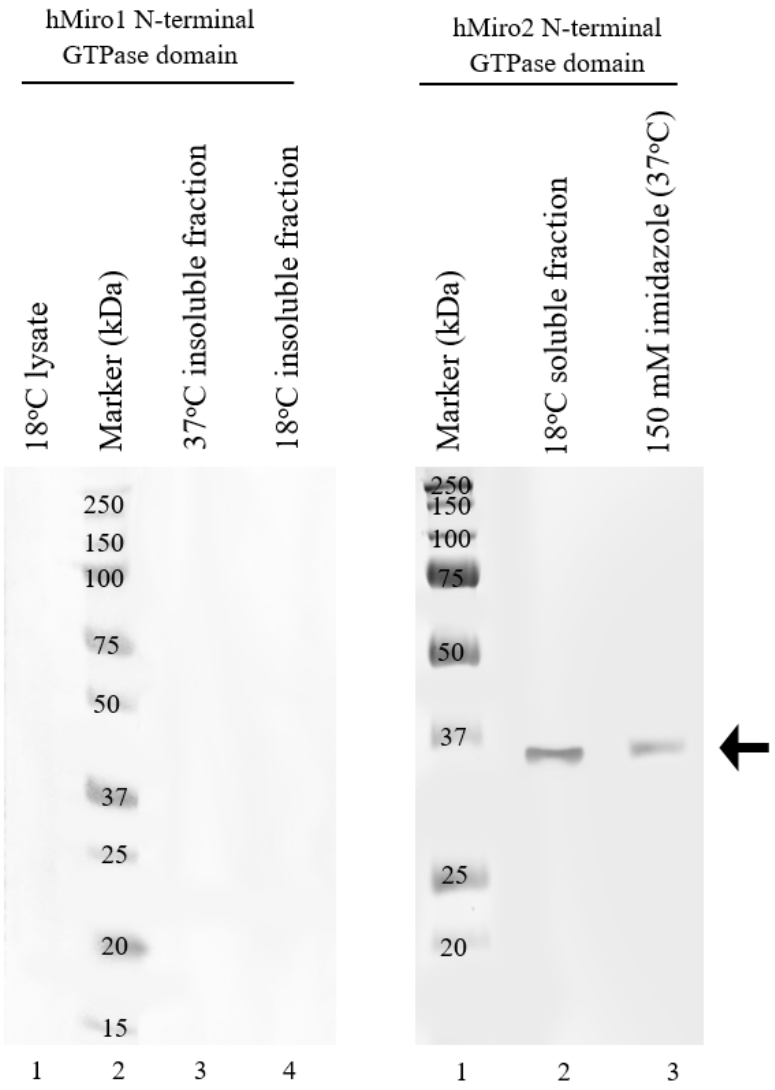

Figure 3.34. Western blotting of hMiro1 and hMiro2 N-terminal GTPase domains. Anti-hMiro1 and anti-hMiro2 antibodies raised in mouse were utilised for the chemiluminescent detection of hMiro1 and hMiro2 domains using a secondary anti-mouse antibody conjugated to HRP.

Chapter 4 reµsults: *in vitro* characterisation of the human Miros

4.1 Introduction

4.1.1 Objectives

In recent years, an increasing body of work has been performed with the aim of elucidating Miro function *in vivo,* using a variety of model organisms (132,165,235,262). Although these studies have enriched our understanding of Miro function, many biochemical and biophysical properties of these enzymes remain obscure. As such, the work implemented in this chapter sought to characterise the human Miros *in vitro*. Primary objectives encompassed, firstly, an assessment of the hydrolytic capabilities of the human Miros, including an assessment of each individual GTPase domain. In particular, an evaluation of the C-terminal "GTPase" domain of each human Miro was pertinent, as these domains are poorly represented in the literature and are often disregarded as artefacts. Secondly, knockdown studies were undertaken with the objective of filling knowledge gaps currently present in the literature and assessing the functional consequences of dual hMiro1 and hMiro2 knockdown in fast-growing PC3 cancer cells. Thirdly, the oligomeric state of the human Miros was evaluated by biophysical assessments. Canonical Ras and Rho proteins are quintessentially monomeric, thus an appraisal of the oligomeric state of these highly unusual enzymes was desirable. Finally, thermal stability of the hMiro1 and hMiro2 'crystal' constructs was undertaken in an attempt to further characterise the biophysical properties of these enzymes.

4.2 Analysis of the GTP hydrolytic activity of hMiro1, hMiro2 and isolated hMiro GTPase domains

The hydrolytic capacity and catalytic efficiency of the hMiro1 and hMiro2 N-terminal GTPase domains remained unknown prior to this study, despite the exhibition of strong primary structure similarity between these domains and the G domains of Ras, and particularly Rho, enzymes. Furthermore, a complete lack of understanding regarding the function and biochemical properties of the hMiro C-terminal GTPase domains existed. To elucidate the hydrolytic activity of hMiro1 and hMiro2, the purified truncated proteins discussed in chapter 3 were buffer-exchanged into gel filtration buffer (2.1.5.3.3). Protein concentration was estimated using the Bradford assay (section 2.2.4.7) and molarity calculated using the estimated amount of protein per mL and computed molecular weight.

Several different assay methods were attempted for measuring GTP hydrolytic activity, all of which operated on the principle of measuring inorganic phosphate release either through fluorescent or colorimetric detection. In the presence of GTP, an enzyme capable of GTP hydrolysis should yield GDP and free inorganic phosphate. These methods therefore provided a means for measuring substrate turnover and product generation.

4.2.1 Fluorometric detection using novel phosphate sensor method

Initially, a novel fluorescent detection method was used. This method was centred around conformational changes in a pure, recombinant *E.coli* 'Phosphate Sensor' protein (Life Technologies, United Kingdom) labelled with the fluorophore MDCC and was advertised as a novel, highly sensitive method capable of detecting picomolar concentrations of free inorganic phosphate. Upon binding inorganic phosphate, the Phosphate Sensor undergoes a conformational change resulting in a large increase in fluorescence (263). As the hMiro GTPase domains remained completely uncharacterised *in vitro* prior to this study, a sensitive method of phosphate detection was highly desirable. However, due to technical incompatibilities, it was not feasible to fully apply this method and instead, the 'gold standard' malachite green method was utilised (4.2.2).

4.2.2 Colorimetric detection using the malachite green assay

As the Phosphate Sensor fluorometric method proved unusable in context, a standard Malachite Green colorimetric assay kit was attempted (Cayman Chemical). The Malachite Green method is based on the formation of a complex between free orthophosphate and malachite green molybdate under acidic conditions, absorbing at 620-640nm (Figure 4.1).

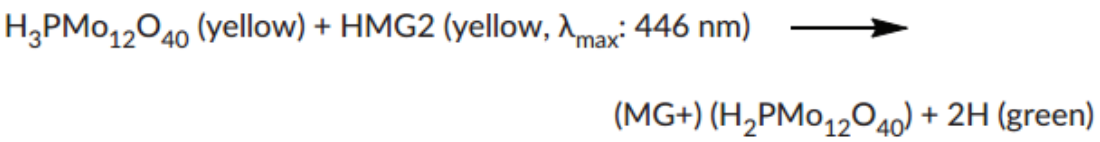

Figure 4.1. Malachite green reaction. Overview of the malachite green colorimetric reaction.

With the Malachite Green method, it was possible to utilise a 96-well plate method and henceforth monitor multiple kinetic assays simultaneously.

4.2.3 Colorimetric detection using the PiColourLock™ Gold assay kit

A second kit was utilised to validate results from the standard malachite green kit. Although still considered the gold standard, the malachite green assay can result in precipitation when used for a substantial amount of time, resulting in an unstable end-point signal. The PiColourLock™ Gold kit (Innova Biosciences, United Kingdom) is advertised as an improved colorimetric detection method based on the malachite green detection of phosphate, albeit producing an enhanced stability end-point signal less prone to precipitation. Furthermore, this kit contains a patented stabiliser to reduce acid hydrolysis of substrates and further improve end-point stability.

4.2.4 Generation of phosphate standard curve

4.2.4.1 For Cayman Chemicals Malachite Green Kit

For assessment of the amount of phosphate generated by the Miro GTPase domains, it was necessary to create a standard curve for absorbance of phosphate at varying concentrations, using the chosen assay buffer (Figure 4.2). This was performed using phosphate standards provided by the manufacturer, according to the instructions provided. Later calculation of µM phosphate produced under each condition was undertaken *via* the method described in 2.2.5.1, Chapter 2.

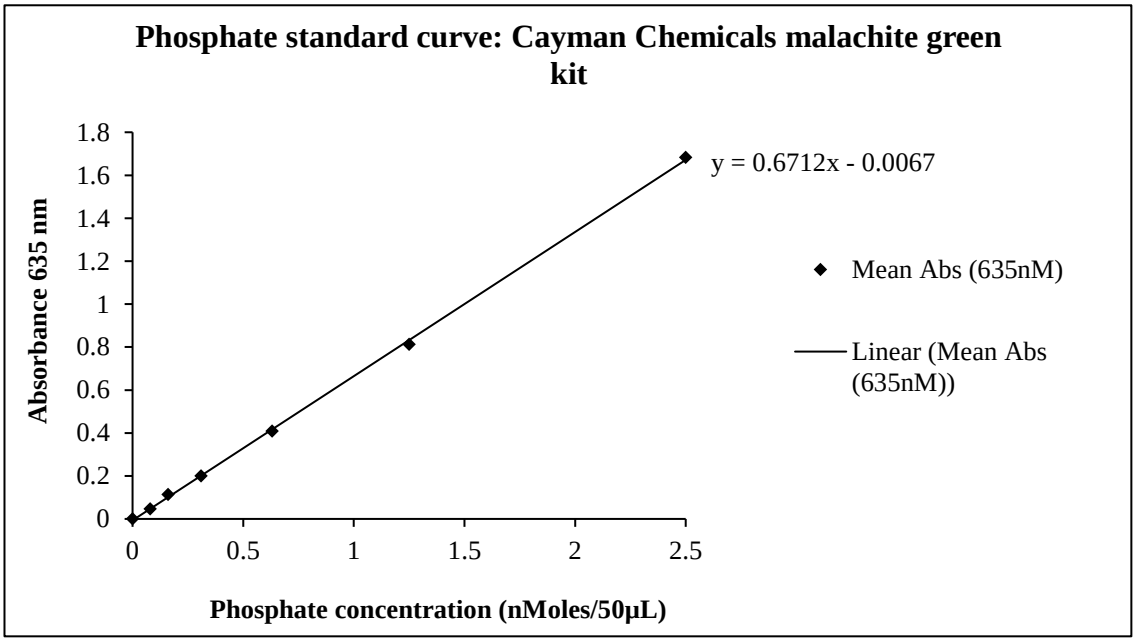

Figure 4.2. Standard curve for phosphate signal using the Malachite Green assay kit. Phosphate samples were prepared in triplicate according to the guidelines of the Cayman Chemicals Malachite Green assay kit. The samples were prepared, incubated and read according to manufacturer's guidelines.

4.2.4.2 For PiColourLock™ Gold assay kit

The PiColourLock™ Gold kit obtained from Innova Biosciences also required the creation of a phosphate standard curve in assay buffer. Standard curve generation was undertaken according to the manufacturer's instructions, using phosphate standards provided as part of the kit. The curve obtained is shown as Figure 4.3, below. Subsequent calculation of µM phosphate produced under each test condition was calculated using this standard curve and the method described in Appendix 9.

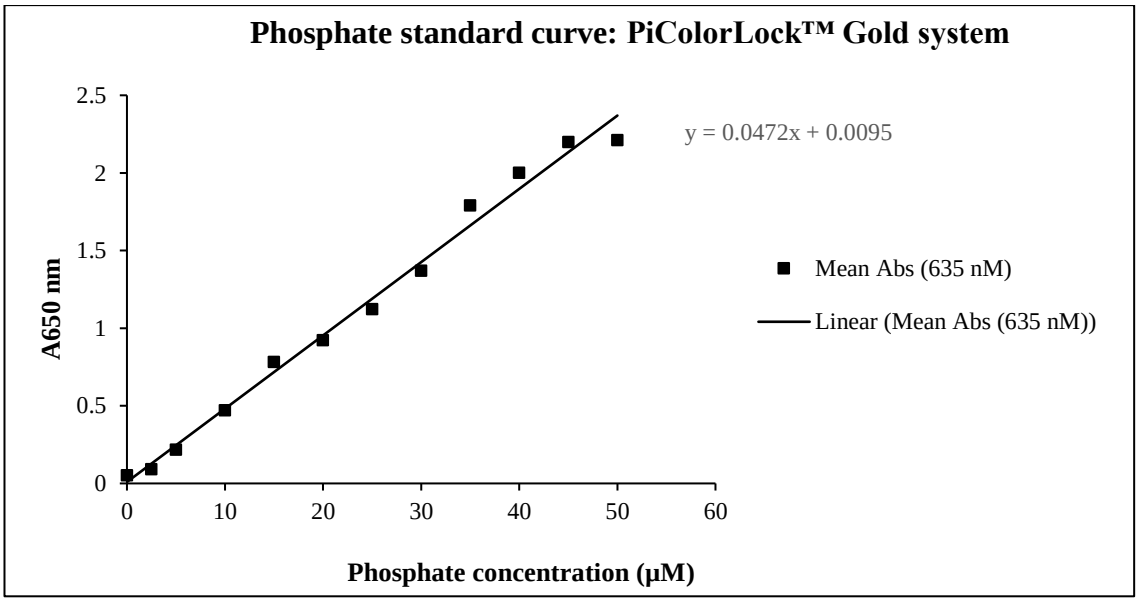

Figure 4.3. Standard curve for phosphate signal using the PiColourLock™ Gold assay kit. Phosphate standards were prepared, incubated and read according to manufacturer's guidelines.

4.2.5. hMiro1 and hMiro2 N-terminal GTPase domains are capable of hydrolysing GTP in the presence of $MgCl_2$, $CaCl_2$ or both cations

The N-terminal GTPase domains of both hMiro1 and hMiro2 resembles the G domains of many classical Ras superfamily proteins, but particularly canonical Rho proteins. As such, this domain was expected to hydrolyse GTP in the presence of Mg^{2+}, a quintessential cofactor of Ras superfamily proteins (62,86,89,90). However, some GTPases are known to bind Ca^{2+} or calmodulin (264-266). Indeed, the Rho GTPases often act within Ca^{2+} signalling pathways (267). Correspondingly, phosphate detection assays were performed for the N-terminal GTPase constructs of hMiro1 and hMiro2 in the presence of either Mg^{2+}, Ca^{2+} or both divalent cations. The results show that both Miro1 (Figure 4.3) and 2 N-terminal GTPase domains (Figure 4.4) are capable of hydrolysing GTP in the presence of either Mg^{2+}, Ca^{2+} or both cations. All reactions were undertaken at 25ºC, using 50 µM protein.

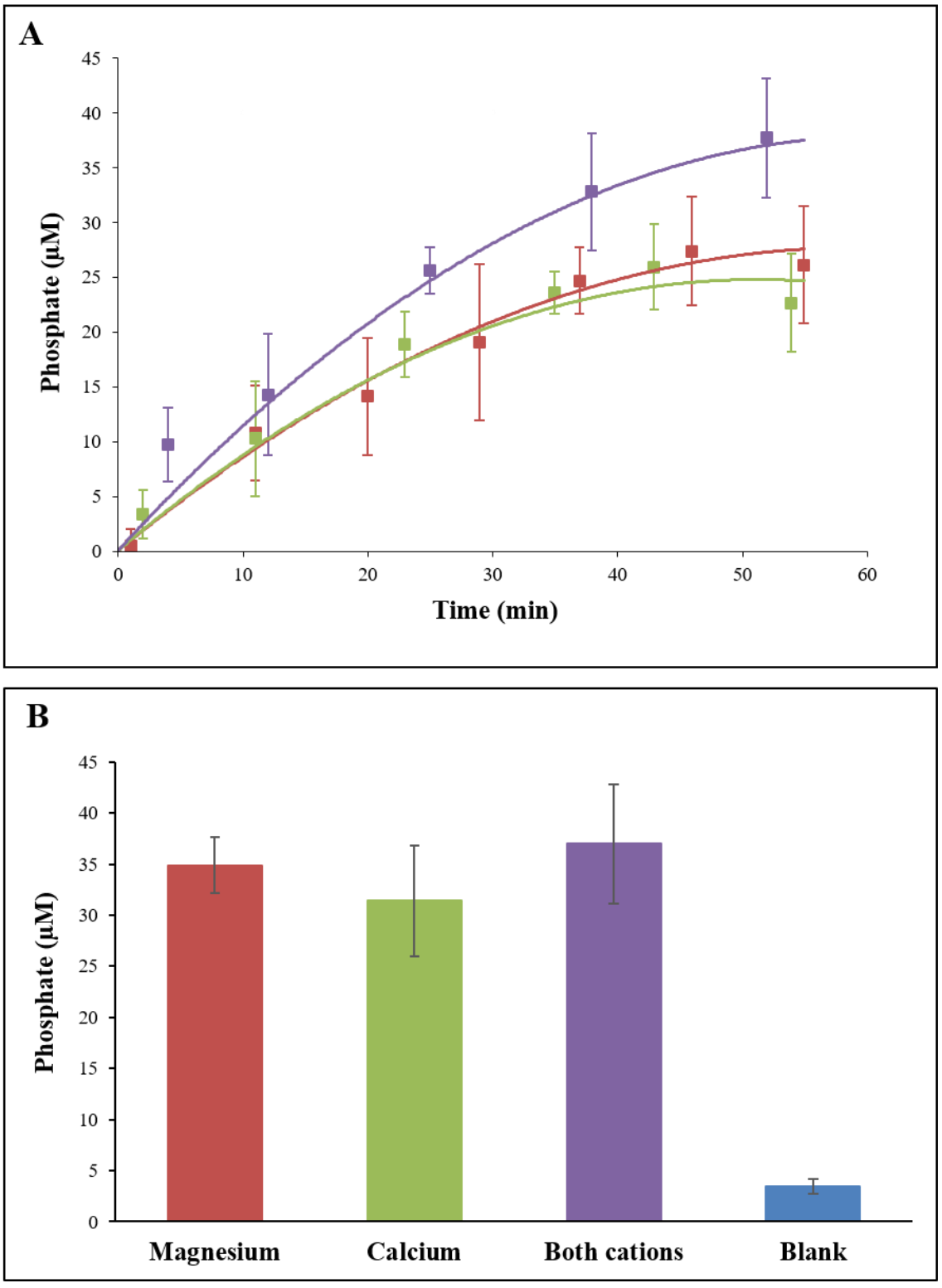

Figure 4.4. GTP hydrolytic activity of the hMiro1 N-terminal GTPase domain. (A) Plot of time in minutes against phosphate generation as detected by the standard malachite green assay (Cayman Chemicals, USA). **(B)** Total phosphate generation after 45 minutes using the PiColorLock™Gold system (Innova Biosciences, UK). Blank readings comprised assay buffer, both cations and GTP to assess for phosphate released by acid hydrolysis. Error bars represent standard error of the mean.

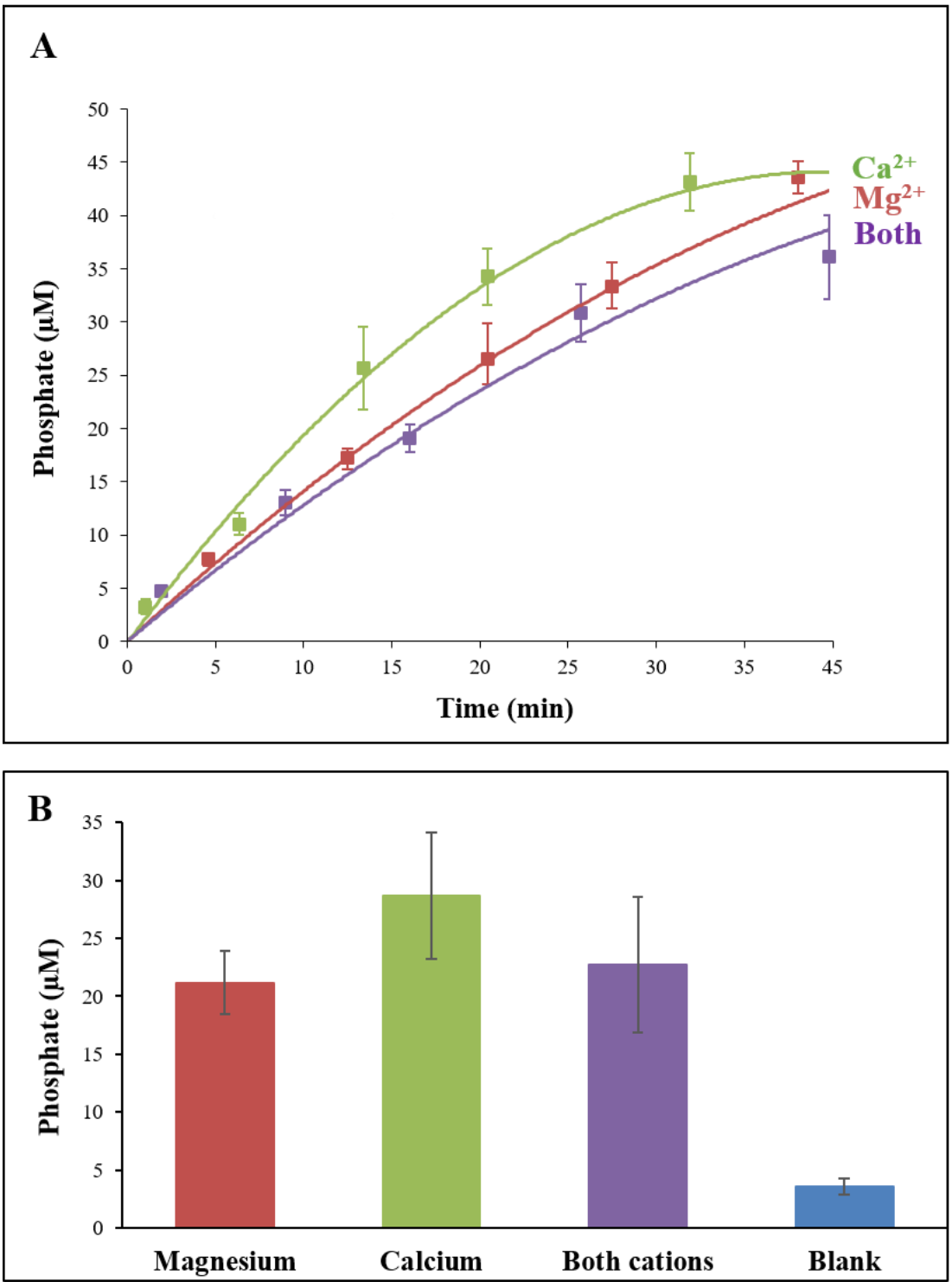

Figure 4.5. GTP hydrolytic activity of the hMiro2 N-terminal GTPase domain. (A) Kinetic assay using the malachite green assay kit (Cayman Chemicals, USA), with µM phosphate plotted against time in minutes. **(B)** Total phosphate generation after 45 minutes using the PiColorLock™Gold kit (Innova Biosciences, UK). Blank readings comprised assay buffer, both cations and GTP to assess for phosphate released by acid hydrolysis. Error bars represent standard error of the mean.

4.2.6. hMiro1 and hMiro2 C-terminal GTPase domains exhibit hydrolytic activity against GTP in the presence of $MgCl_2$, $CaCl_2$ or both cations

The C-terminal domains of the human Miros are highly unusual (17,29). Indeed, these domains have been previously questioned as relic domains in the literature (268,269). However, prior to this work, biochemical assays had not been performed to definitively assess the hydrolytic capacity of these domains. Thus, Malachite Green assays were performed with both the isolated Miro C-terminal GTPase domains. As shown in Figure 4.5 for hMiro1 and Figure 4.6 for hMiro2, both of the C-terminal GTPase domains for these enzymes are, remarkably, able to hydrolyse GTP in the presence of $MgCl_2$, $CaCl_2$ or both cations.

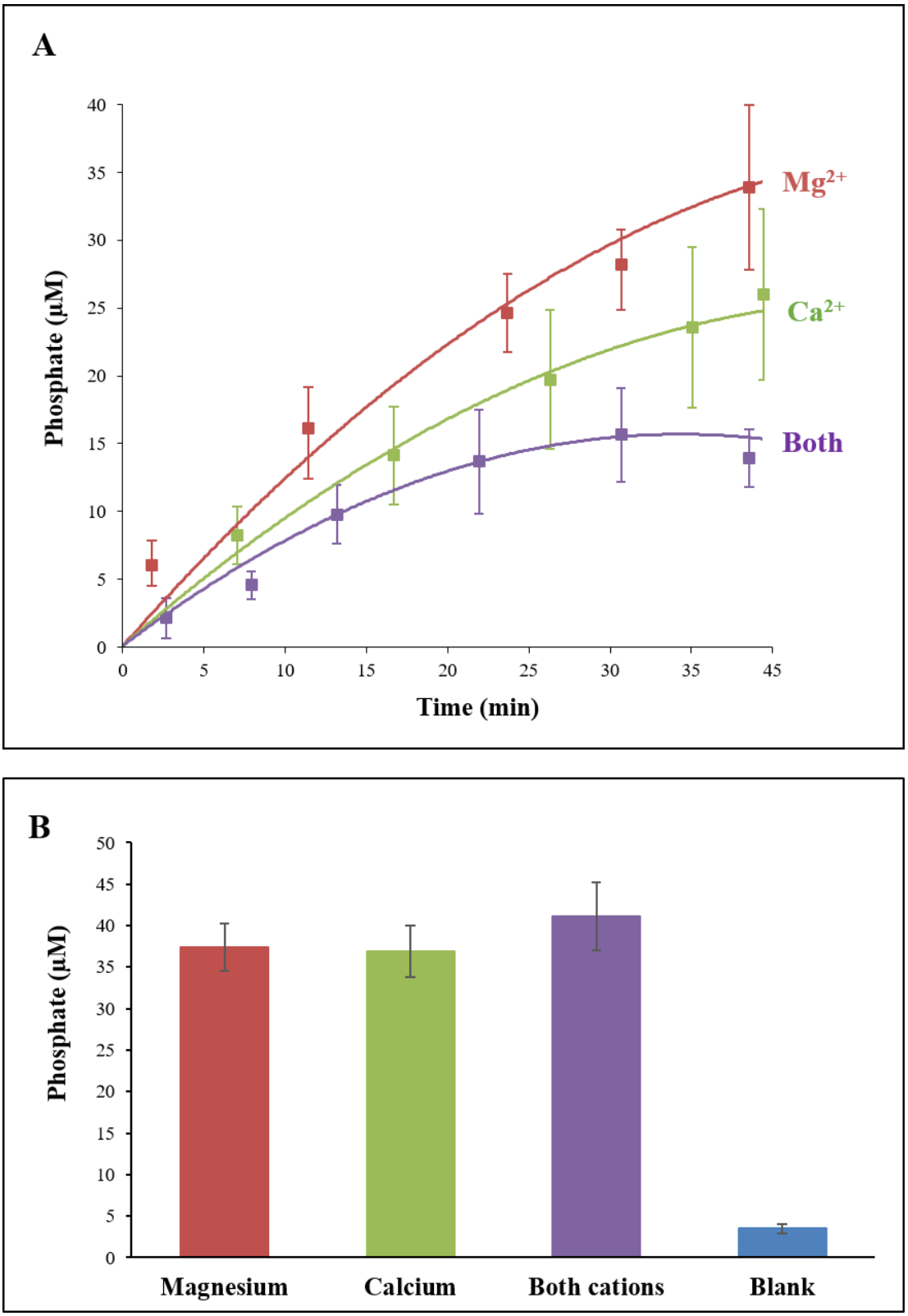

Figure 4.6. GTP hydrolytic activity of the hMiro1 C-terminal GTPase domain. (A) Kinetic assay using the malachite green assay kit (Cayman Chemicals, USA), with µM phosphate plotted against time in minutes. **(B)** Total phosphate generation after 45 minutes using the PiColorLock™Gold kit (Innova Biosciences, UK). Blank readings comprised assay buffer, both cations and GTP to assess for phosphate released by acid hydrolysis. Error bars represent standard error of the mean.

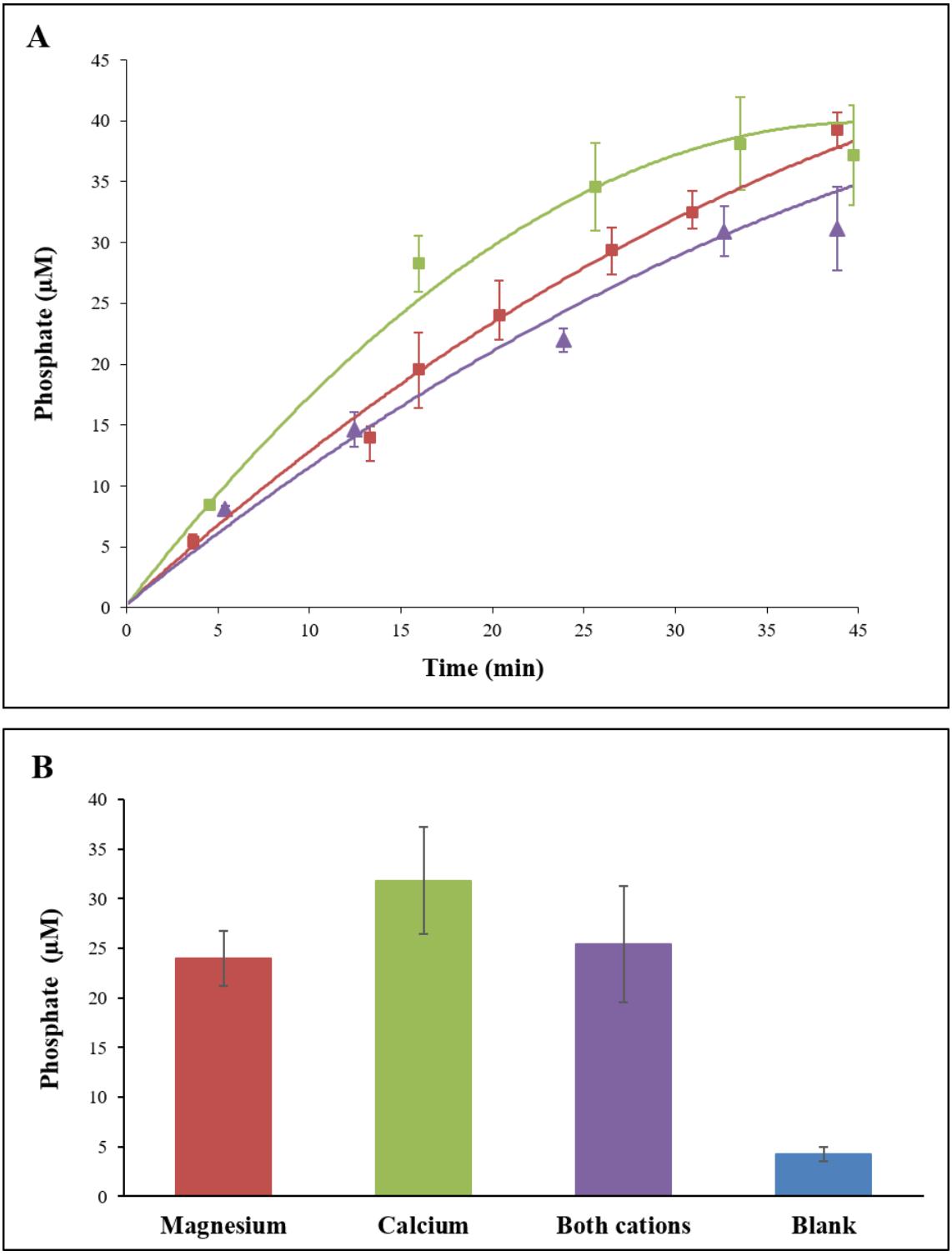

Figure 4.7. GTP hydrolytic activity of the hMiro2 C-terminal GTPase domain. (A) Kinetic assay using the malachite green assay kit (Cayman Chemicals, USA), with µM phosphate plotted against time in minutes. **(B)** Total phosphate generation after 45 minutes using the PiColorLock™Gold kit (Innova Biosciences, UK). Blank readings comprised assay buffer, both cations and GTP to assess for phosphate released by acid hydrolysis. Error bars represent standard error of the mean.

4.2.6. hMiro1 and hMiro2 'crystal constructs' show hydrolytic activity against GTP in the presence of $MgCl_2$, $CaCl_2$ or both cations

The hMiro1 and hMiro2 'crystal' constructs each contained the EF-hand regions of each hMiro, plus the C-terminal GTPase domain. Although these constructs were engineered in the hopes of producing crystals for x-ray crystallography, they also represented the longest hMiro constructs engineered that showed appropriate and reproducible expression and purification. These constructs were tested for hydrolytic activity against GTP for numerous reasons: to evaluate hydrolytic activity in the longest constructs available, and to assess whether the EF-hand regions held regulatory roles for the C-terminal GTPase domain (for example, through auto-inhibition or structural obstruction). The results shown in Figures 4.7 and 4.8 indicate that the C-terminal domains of hMiro1 and hMiro2 are capable of hydrolysing GTP in the presence of $MgCl_2$, $CaCl_2$ or both cations, regardless of the presence or absence of the EF-hand domains. Interestingly, the presence of $CaCl_2$ appeared to mildly increase GTPase activity, with a greater amount of phosphate generally produced in the presence of either $CaCl_2$ or both cations. However, this was statistically significant across replicates relative to GTP hydrolytic activity in the presence of $MgCl_2$ alone.

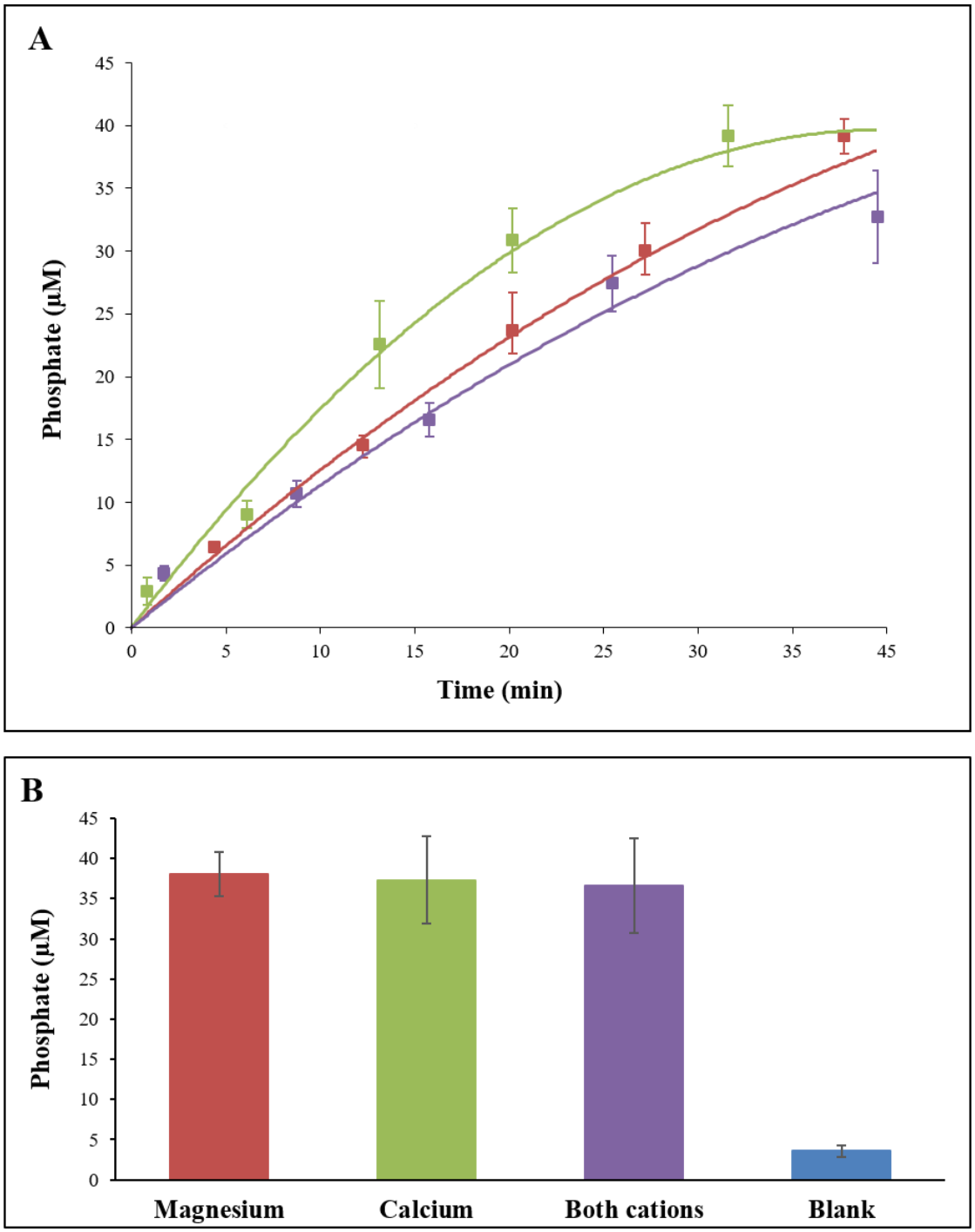

Figure 4.8. GTP hydrolytic activity of the hMiro1 xtal construct. (A) Kinetic assay using the malachite green assay kit (Cayman Chemicals, USA), with µM phosphate plotted against time in minutes. **(B)** Total phosphate generation after 45 minutes using the PiColorLock™Gold kit (Innova Biosciences, UK). Blank readings comprised assay buffer, both cations and GTP to assess for phosphate released by acid hydrolysis. Error bars represent standard error of the mean.

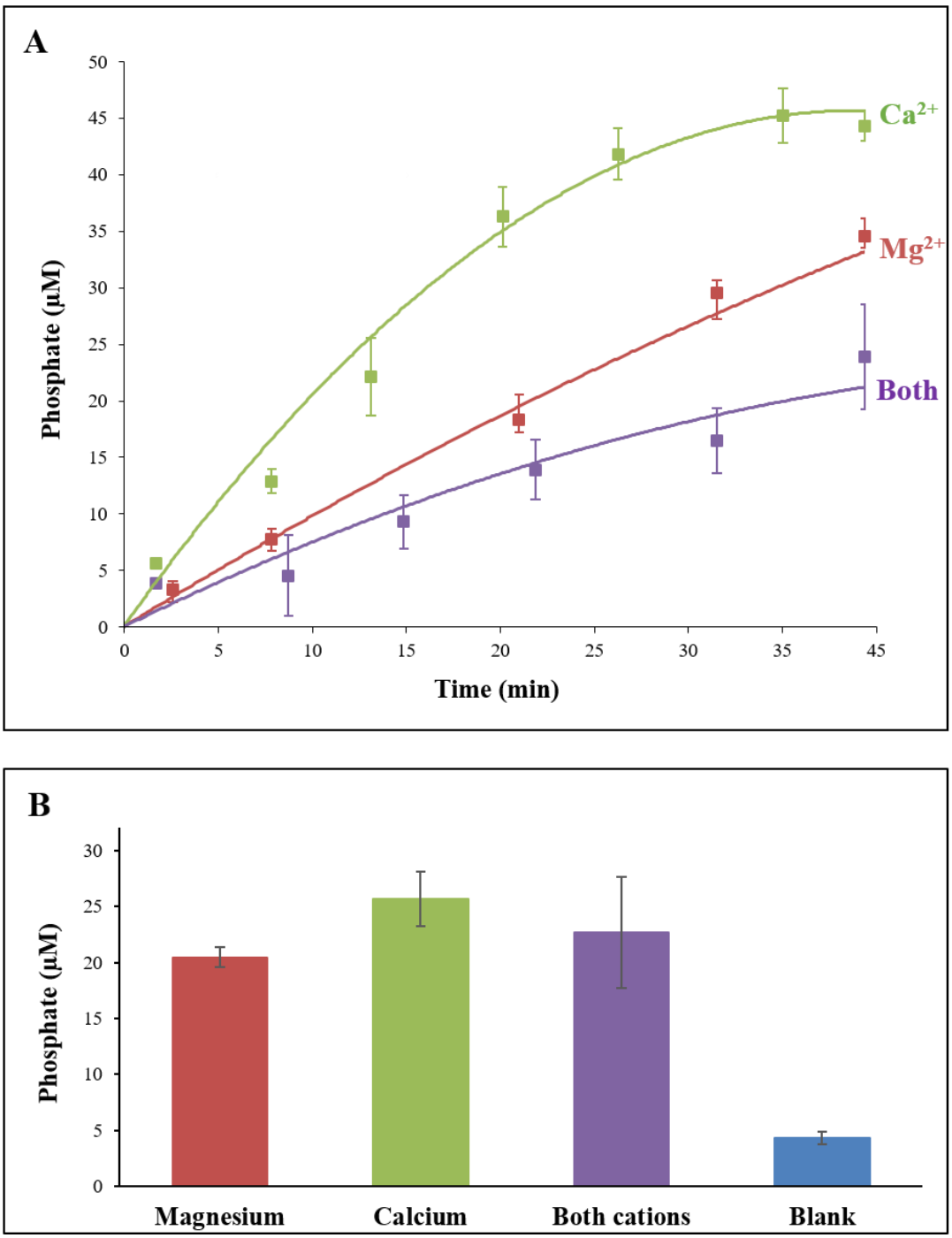

Figure 4.9. GTP hydrolytic activity of the hMiro2 xtal construct. (A) Kinetic assay using the malachite green assay kit (Cayman Chemicals, USA), with µM phosphate plotted against time in minutes. **(B)** Total phosphate generation after 45 minutes using the PiColorLock™Gold kit (Innova Biosciences, UK). Blank readings comprised assay buffer, both cations and GTP to assess for phosphate released by acid hydrolysis. Error bars represent standard error of the mean.

4.2.7 The hMiro1 and hMiro2 C-terminal GTPase domains display substrate promiscuity, showing hydrolytic activity against ATP and UTP

GTPases of the Ras superfamily typically exhibit substrate specificity towards GTP. However, owing to the unusual nature of the hMiro GTPases, each individual domain was assessed for the ability to hydrolyse ATP, CTP and UTP. The N-terminal GTPase domain of both hMiro1 and hMiro2 displayed specificity towards GTP as substrate Figure 4.9 for hMiro1, Figure 4.10 for hMiro2). These domains display largely classical Ras superfamily characteristics, so this was an expected result. However, as shown in Figure 4.11 for hMiro1 and 4.12 for hMiro2, the C-terminal GTPase domain for both Miros displayed the ability to hydrolyse ATP and UTP in addition to GTP. This may reflect the highly atypical nature of the C-terminal GTPase domains. CTP hydrolysis was not shown in any domain tested. In all assessments, $MgCl_2$ was utilised as cofactor.

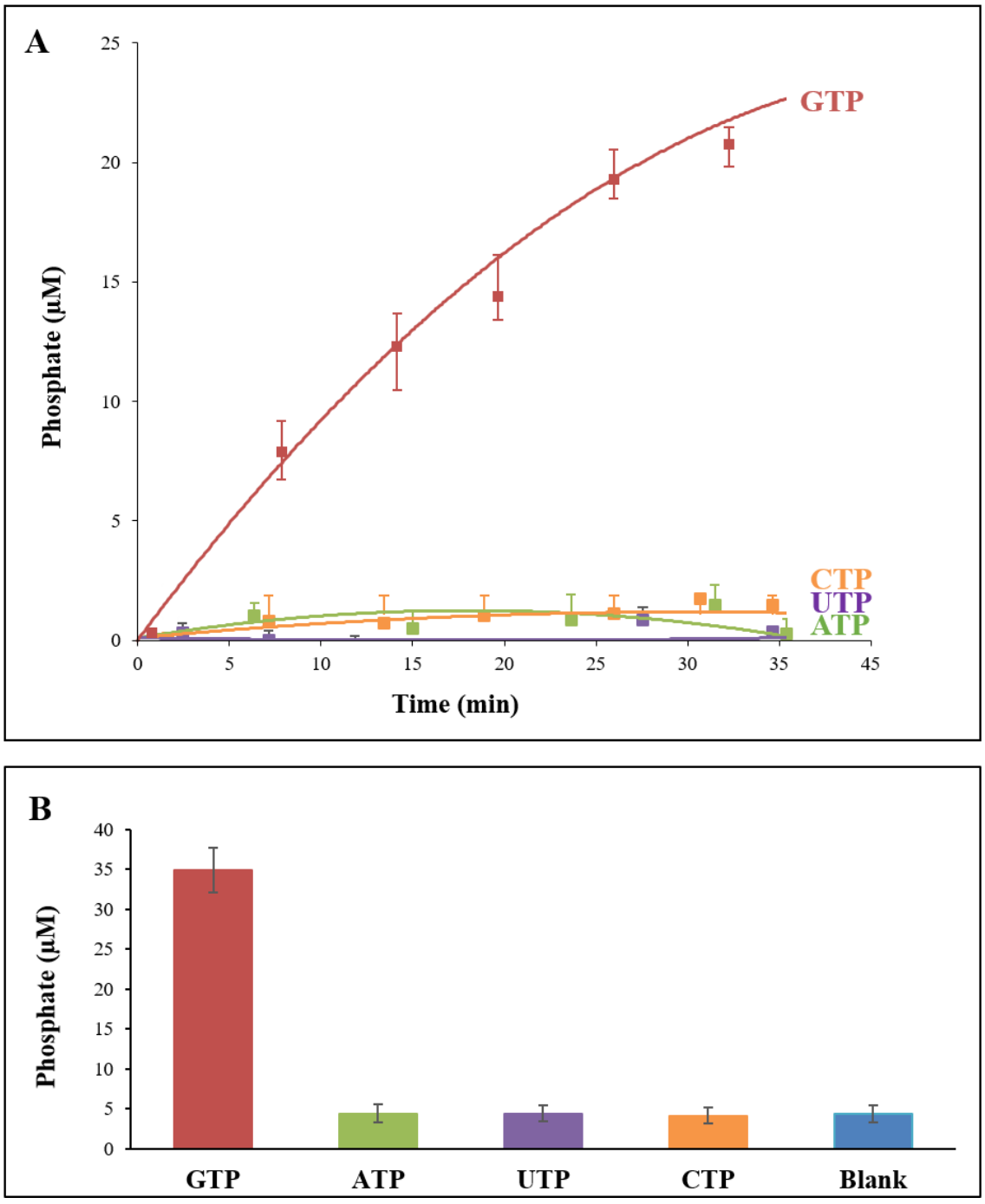

Figure 4.10. The hMiro1 N-terminal GTPase domain cannot hydrolyse ATP, UTP or CTP. **(A)** Kinetic assay using the malachite green assay kit (Cayman Chemicals, USA), with µM phosphate plotted against time in minutes. **(B)** Total phosphate generation after 45 minutes using the PiColorLock™Gold kit (Innova Biosciences, UK). Blank readings comprised assay buffer, both cations and GTP to assess for phosphate released by acid hydrolysis. Error bars represent standard error of the mean.

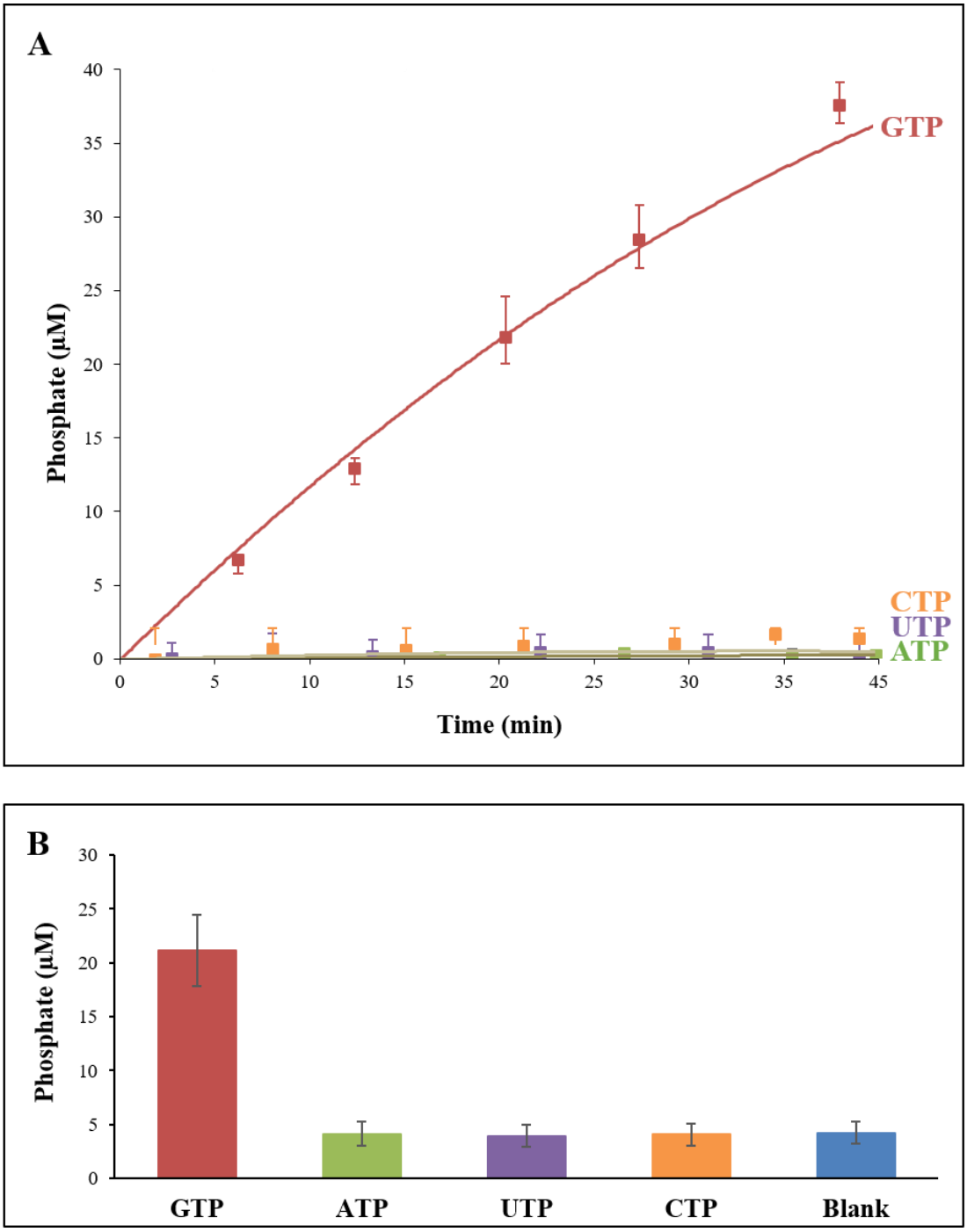

Figure 4.11. The hMiro2 N-terminal GTPase domain displays an absence of hydrolytic activity towards ATP, UTP and CTP. (A) Kinetic assay using the malachite green assay kit (Cayman Chemicals, USA), with µM phosphate plotted against time in minutes. **(B)** Total phosphate generation after 45 minutes using the PiColorLock™Gold kit (Innova Biosciences, UK). Blank readings comprised assay buffer, both cations and GTP to assess for phosphate released by acid hydrolysis. Error bars represent standard error of the mean.

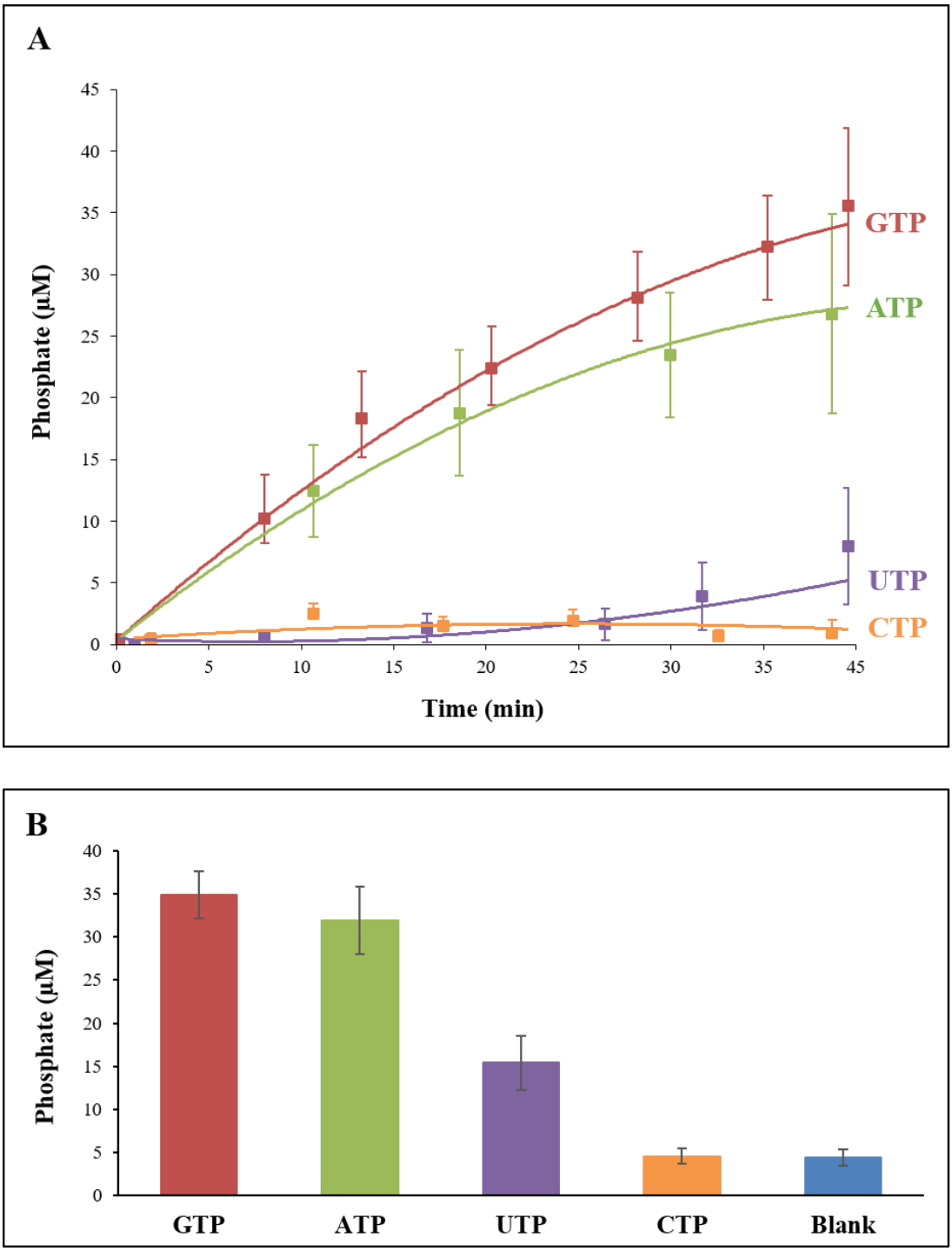

Figure 4.12. The hMiro1 C-terminal GTPase domain shows hydrolytic activity against ATP and UTP but not CTP. Samples were prepared in triplicate and assays undertaken at 25ºC according to the guidelines of the Cayman Chemicals Malachite Green assay kit. Readings are provided as blank-corrected readings. Blank readings comprised assay buffer, both cations and GTP to assess for phosphate released by acid hydrolysis.

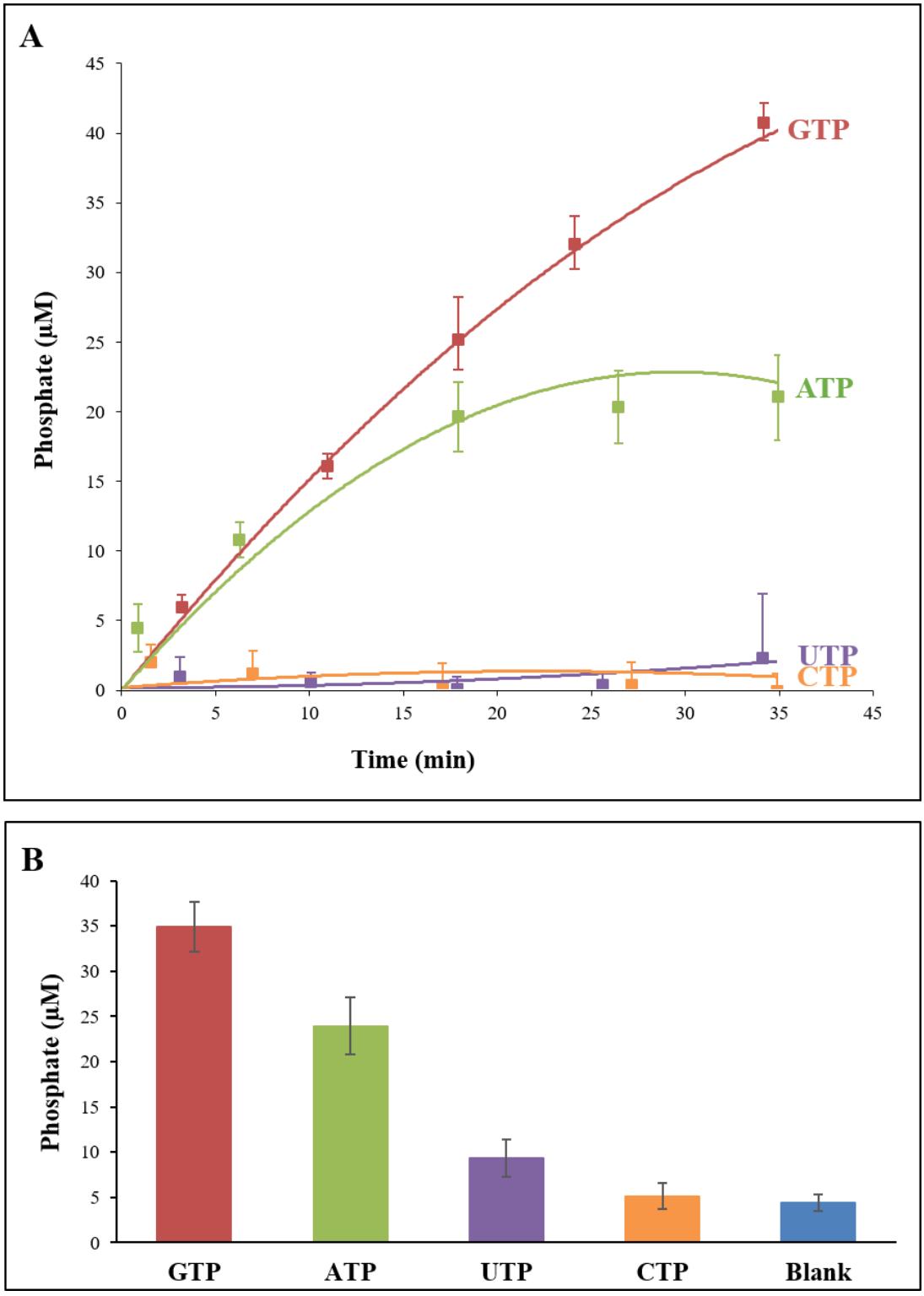

Figure 4.13. The hMiro2 C-terminal GTPase domain displays hydrolytic activity against ATP and UTP but not CTP. Samples were prepared in triplicate and assays undertaken at 25ºC according to the guidelines of the Cayman Chemicals Malachite Green assay kit. Readings are provided as blank-corrected readings. Blank readings comprised assay buffer, both cations and GTP to assess for phosphate released by acid hydrolysis.

4.2.8 hMiro1 and hMiro2 GTPase domains: assessment of enzymatic kinetic parameters

To assess the kinetic parameters for Miro1 and 2 GTPase domain hydrolytic activity towards GTP and ATP, reaction rates were calculated at varying substrate concentrations ranging from 0.5 mM – 2 mM substrate. All assays were performed in triplicate at 25ºC in previously described assay buffer supplemented with 2 mM $MgCl_2$ and either ATP or GTP at a specified concentration (0.5 mM, 1 mM, 1.5 mM or 2mM). Assay scatter plots from which kinetic parameters were derived are shown in Figure 4.13, while Lineweaver-Burke plots for each set of assays are displayed in Figure 4.14; these plots were used to calculate values for V_{max} and K_m displayed in Table 4.1, which displays a summary of the kinetic parameters obtained in this work, alongside K_{cat} rates of typical Ras superfamily enzymes as described in the literature. As shown in Table 4.1, the K_{cat} values calculated for the hMiro1 and hMiro2 GTPase domain are not dissimilar to the reaction rate constants (K_{cat} values) reported in the literature for typical Ras superfamily members, which ranged from 0.0031/min to 1.120/min (270-273). All of the K_{cat} values obtained for hMiro1 and hMiro2 fell within this range, although tended to be slightly higher than those reported in the literature for Ras superfamily enzymes (270-276). Kinetic values for dynamin and SEPT2 are also provided, which share similarities with Ras GTPase domain architecture, including the presence of G loops (277,278). All of the values shown in Table 4.1 describe intrinsic hydrolysis rates only. Unfortunately, most of the kinetic data available in the literature focuses on GAP-mediated hydrolysis, rather than the intrinsic hydrolysis, of small GTPases (270-273). Furthermore, where intrinsic hydrolysis rates were described, other kinetic values associated with intrinsic hydrolysis (such as V_{max} and K_M) were excluded (270-276). This, amongst other factors such as variances in experimental conditions (including, crucially, temperature), make it difficult to compare the values reported in the literature to those obtained here. However, in brief: the results obtained from kinetic studies indicate that both hMiro1 and hMiro2 NT and CT domains are able to hydrolyse GTP in the absence of GAP enzymes at rates similar to that observed for the basal GTP hydrolytic rates of classical Ras superfamily enzymes, including H-Ras, K-Ras, Cdc42, Ran, Rap1a and the Rac enzymes. Furthermore, the CT domain of hMiro1 and hMiro2 is capable of intrinsic hydrolysis of ATP at rates similar to that seen for GTP hydrolysis in canonical Ras superfamily enzymes. These results are examined in further detail in the discussion section, 4.5

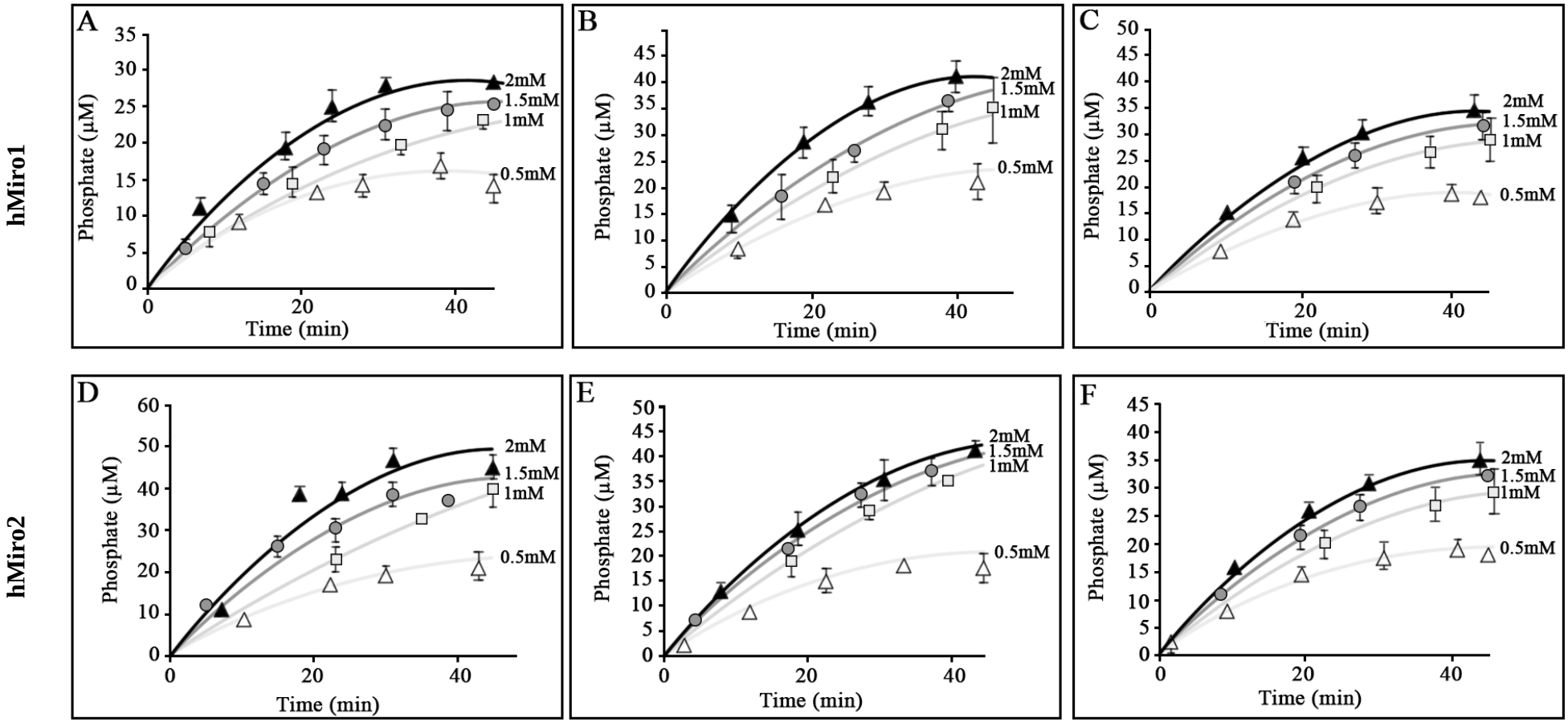

Figure 4.14. Hydrolytic activity of hMiro1 and 2 individual GTPase domains using varying substrate concentrations. (A) hMiro1 N-terminal GTPase domain using GTP as substrate. **(B)** and **(C)** hMiro1 C-terminal GTPase domain, using GTP and ATP as substrate, respectively. **(D)** hMiro2 N-terminal GTPase domain using GTP as substrate. **(E)** and **(F)** hMiro2 C-terminal GTPase domain, using GTP and ATP as substrate, respectively Samples were prepared in triplicate and assays undertaken at 25ºC according to the guidelines of the Cayman Chemical s Malachite Green assay kit. Readings are provided as blank-corrected readings. Blank readings comprised assay buffer, both cations and substrate to assess for phosphate released by acid hydrolysis.

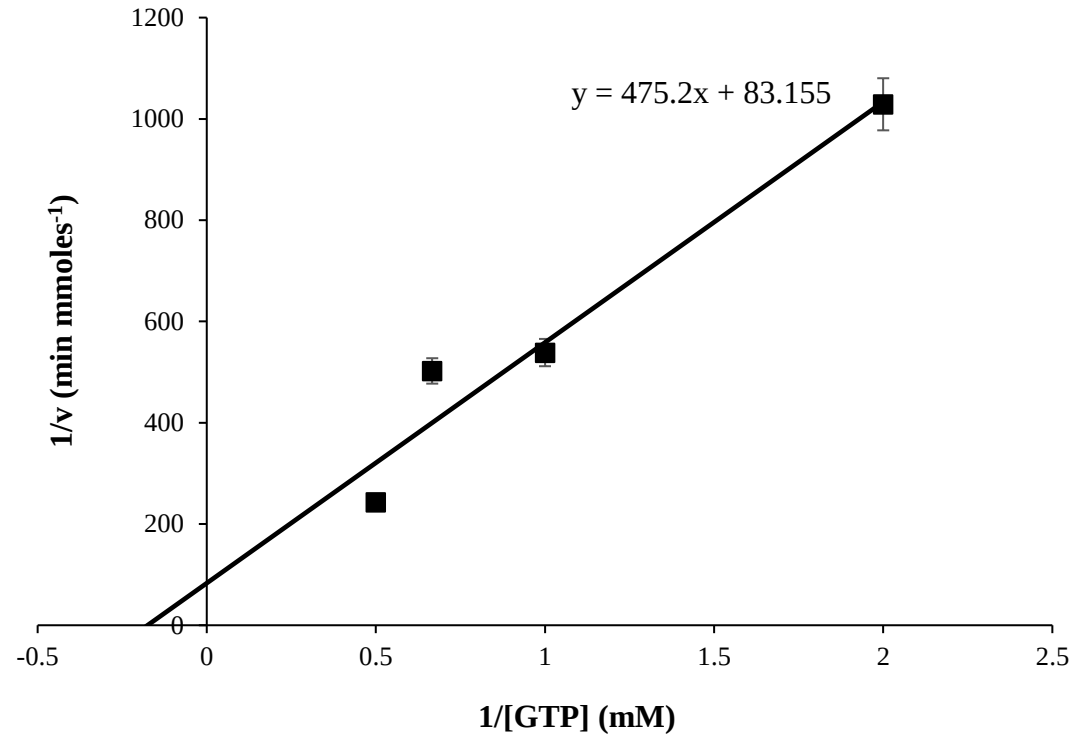

Figure 4.15. Lineweaver-Burke plot for hMiro1 N-terminal GTPase domain against GTP. The data were performed in triplicate, with error bars representing the standard deviation from the mean.

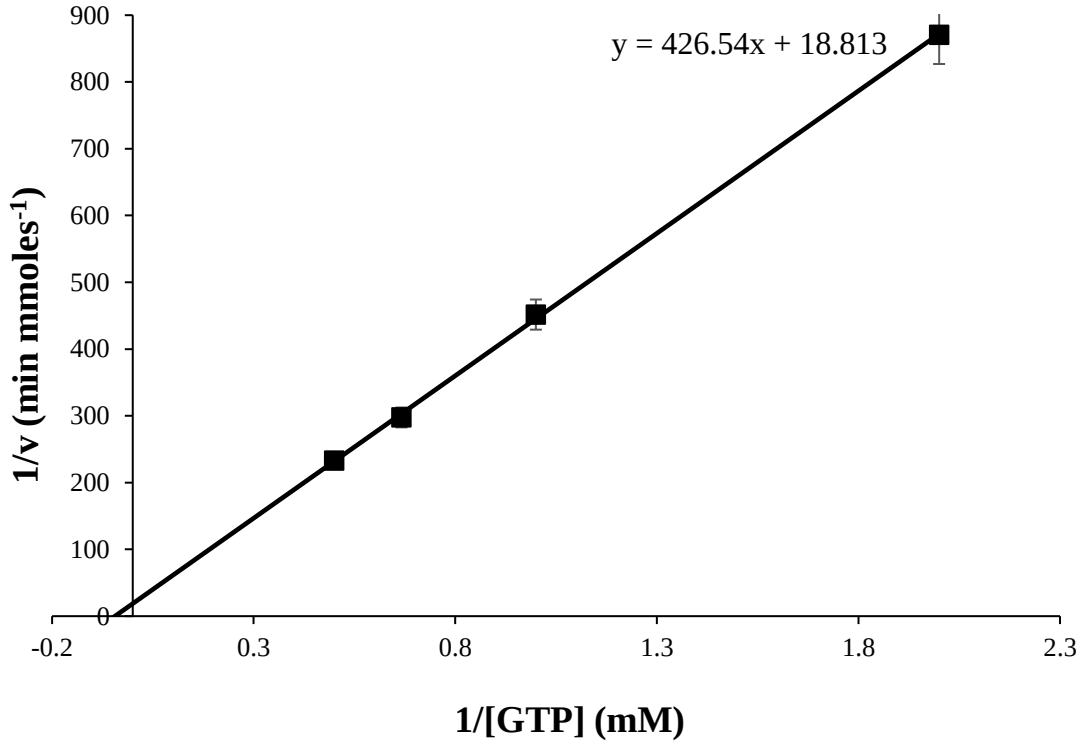

Figure 4.16. Lineweaver-Burke plot for hMiro2 N-terminal GTPase domain against GTP. The data were performed in triplicate, with error bars representing the standard deviation from the mean.

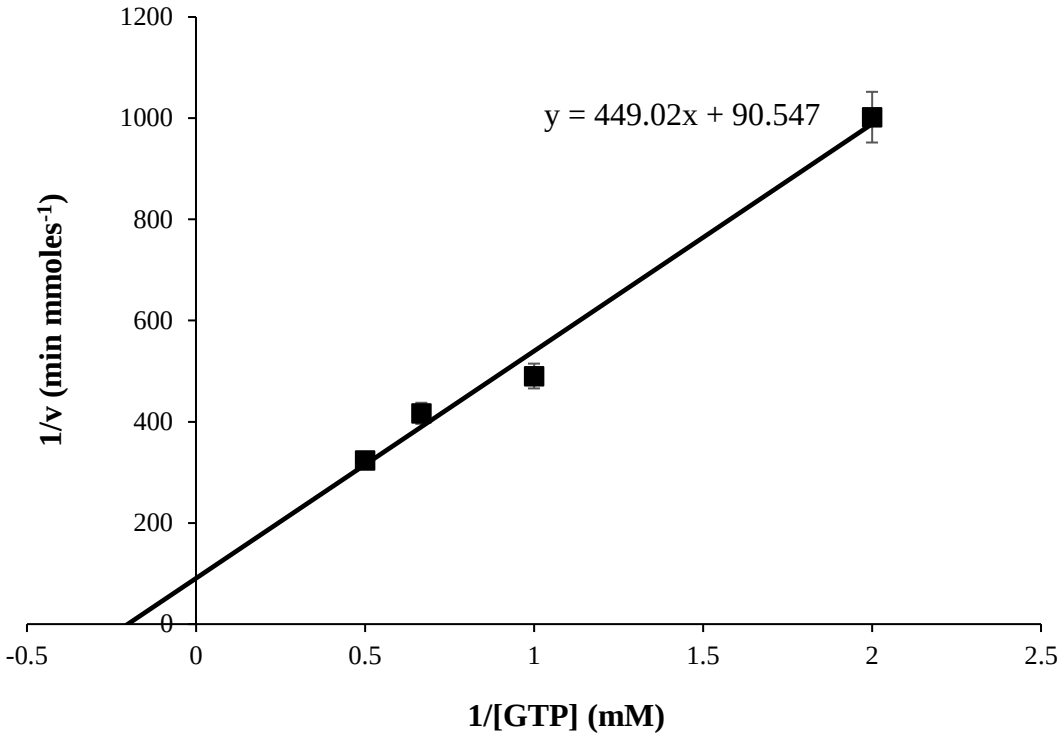

Figure 4.17. Lineweaver-Burke plot for hMiro1 C-terminal GTPase domain against GTP. The data were performed in triplicate, with error bars representing the standard deviation from the mean.

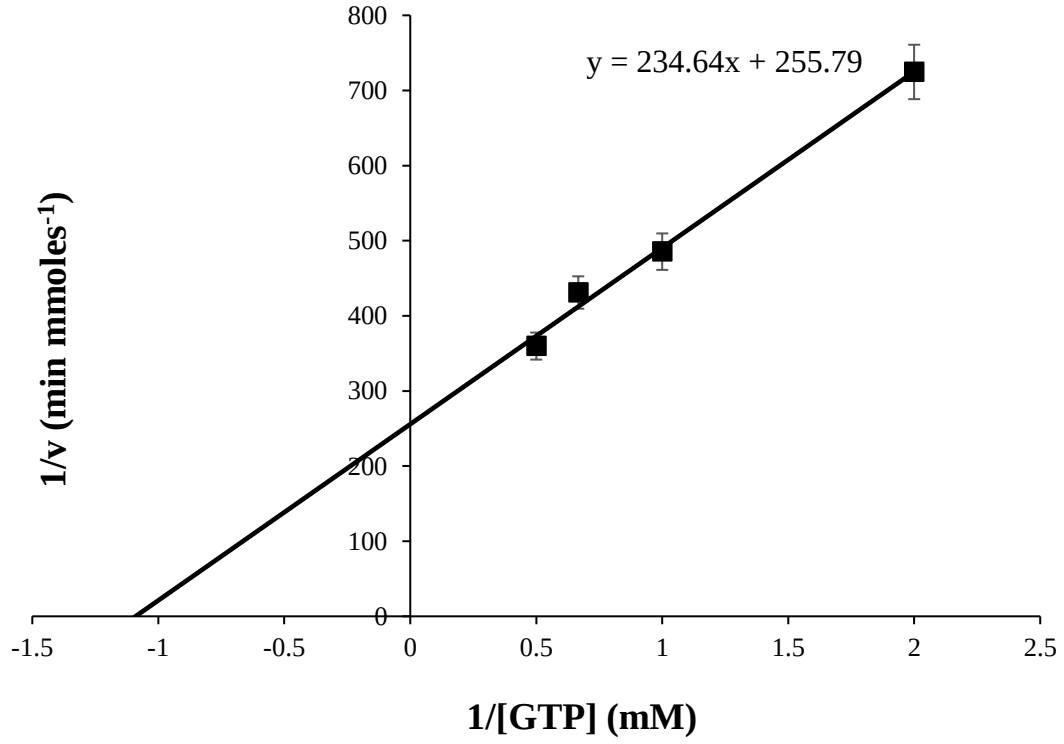

Figure 4.18. Lineweaver-Burke plot for hMiro2 C-terminal GTPase domain against GTP. The data were performed in triplicate, with error bars representing the standard deviation from the mean.

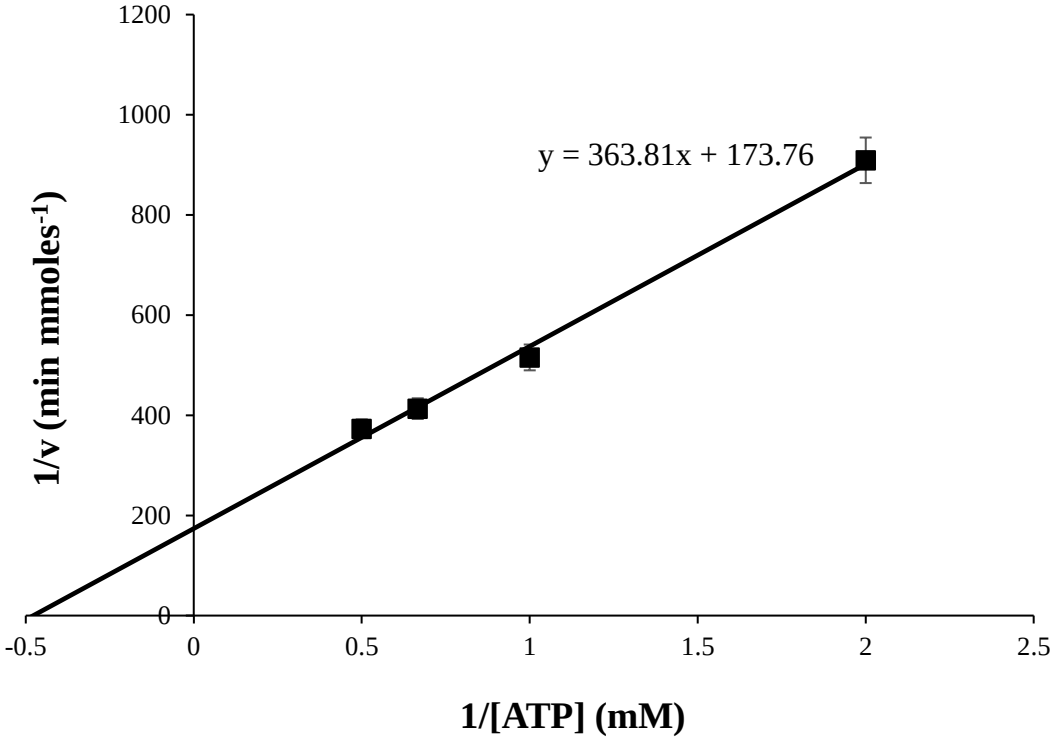

Figure 4.19. Lineweaver-Burke plot for hMiro1 C-terminal GTPase domain against ATP. The data were performed in triplicate, with error bars representing the standard deviation from the mean.

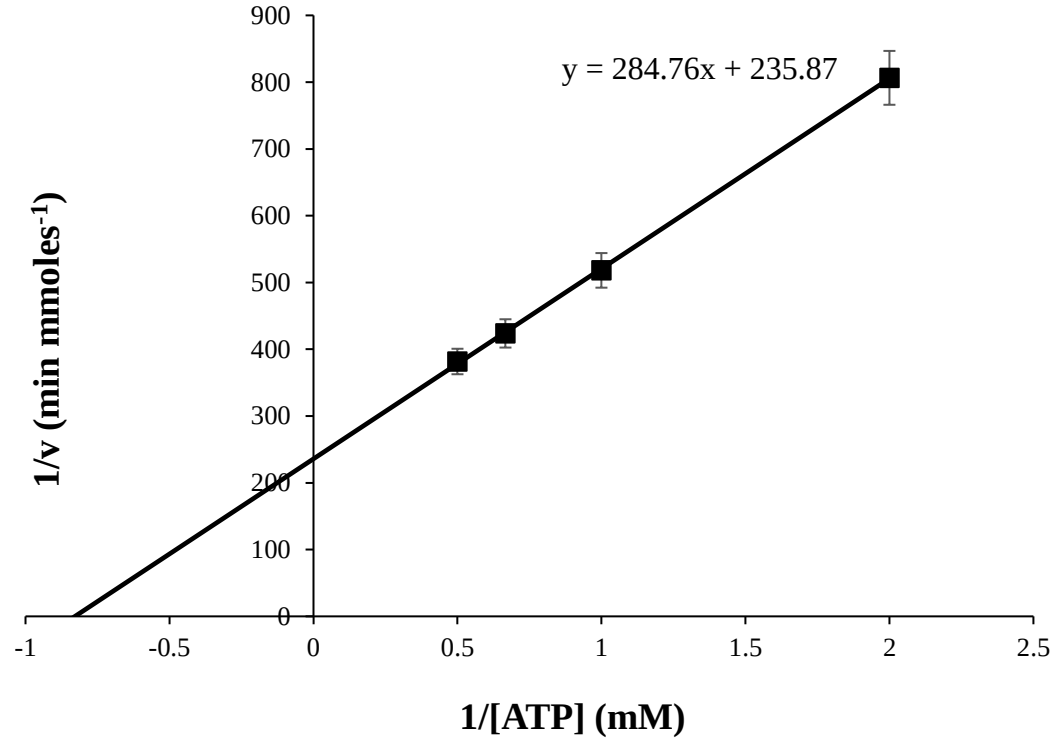

Figure 4.20. Lineweaver-Burke plot for hMiro2 C-terminal GTPase domain against ATP. The data were performed in triplicate, with error bars representing the standard deviation from the mean.

Table 4.1. Kinetic parameters for intrinsic hydrolysis of the hMiro constructs and typical Ras superfamily enzymes. Where 'NT' refers to the N-terminal GTPase domain and 'CT' refers to the C-terminal GTPase domain for each respective hMiro. Values for K_m and V_{max} were derived from the Lineweaver-Burk plots displayed in Figures 4.14-4.19. K_{cat} was calculated by dividing V_{max} by 50$_{\mu}$M, the total amount of enzyme used in each assay well.

	hMiro1			**hMiro2**			**H-Ras**	**K-Ras**	**Rac1**	**Rac2**	**Rac3**	**Cdc42**	**Rap1a**	**Ran**	**Dynamin**	**Sept2**
	GTPase domains			**GTPase domains**			**(272)**	**(271)**	**(270)**	**(270)**	**(270)**	**(273)**	**(272)**	**(272)**	**(278)**	**(277)**
Temperature (ºC)	25	25	25	25	25	25	37	20	25	25	25	30	37	37	22	23
$MgCl_2$ in buffer (mM)	2	2	2	2	2	2	5	10	2	2	2	5	5	5	2	5
Construct	NT	CT	CT	NT	CT	CT	WT	WT	WT	WT	WT	WT	WT	WT	WT	WT
Substrate	GTP	GTP	ATP	GTP	GTP	ATP	GTP	GTP	GTP	GTP	GTP	GTP	GTP	GTP	GTP	GTP
V_{max} (µM/min)	12.026	11.044	5.755	53.155	3.909	4.240	–	–	–	–	–	–	–	–	–	–
K_M (mM)	5.715	4.959	2.094	22.673	0.917	1.207	–	–	–	–	–	–	–	–	0.0034	0.00052
K_{cat} (min)	0.241	0.221	0.115	1.063	0.078	0.085	0.028	0.041*	0.11	0.16	0.18	1.120	0.0031	0.0032	0.19	0.0162*
K_{cat}/K_M (min/mM)	0.042	0.045	0.055	0.047	0.085	0.070	–	–	–	–	–	–	–	–	55.882	31.154

*Value originally provided with seconds as unit; adjusted here to represent minutes.

4.3 Function of the human Miro GTPases in mammalian cell lines: knock-down studies

4.3.1 Migration assays using PC3 cells

Migration assays were performed as described in 2.2.6.7, with knockdown conditions achieved using the reverse siRNA-mediated knockdown method detailed in 2.2.6.5. Each assay was performed for 24 hours, with conditions assessed in triplicate per assay. Overall, three separate assays were performed at different dates; this allowed for an investigation of hMiro knockdown at different PC3 cellular passages, and provided an enhanced confidence in the results obtained. As shown in Figure 4.20, knockdown of hMiro1 and hMiro2 produced numerical (albeit not significant) reductions in PC3 cell proliferation over the course of 24 hours. The effect was most prominent in hMiro1 knockdown conditions. A dual knockdown approach, in which both hMiro1 and hMiro2 were simultaneously knocked down, did not produce the lowest overall reduction in migration relative to control cells. Instead, hMiro1 knockdown alone produced the greatest reduction in PC3 cell proliferation. Although this result was surprising, it may be associated with the known difficulties of simultaneously knocking down two separate genes using the siRNA-mediated knockdown method utilised. Further data and information is provided in Appendix 10.

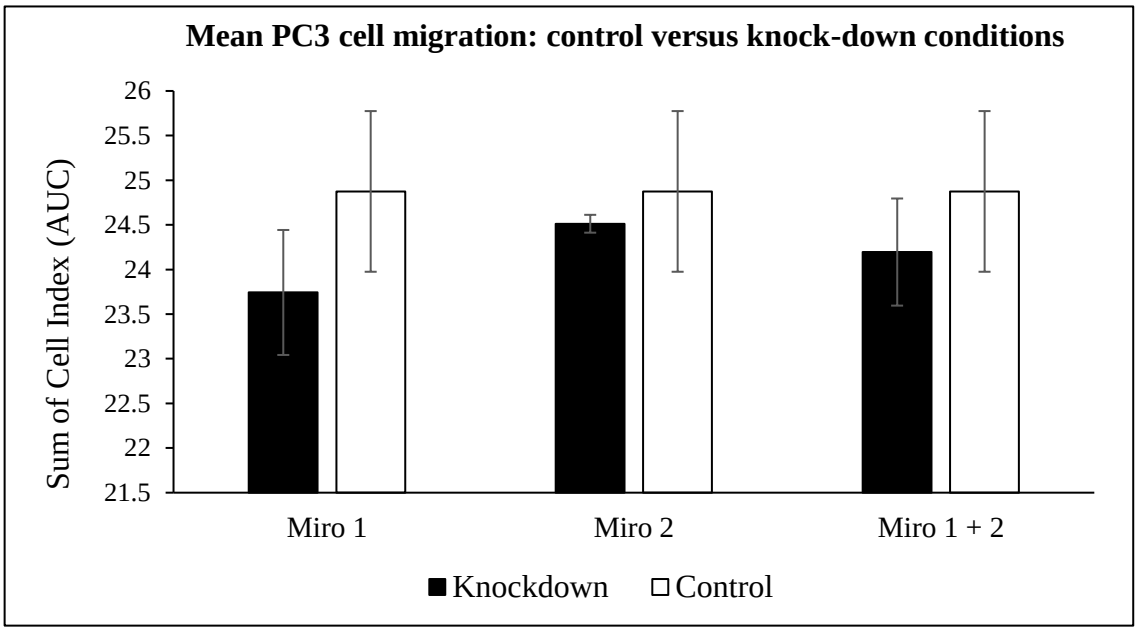

Figure 4.21. Knockdown of hMiro1, hMiro2 or both hMiros in PC3 cells reduces cell migration relative to controls. Knockdown conditions against control cell migration, where migration is classified as the sum of cell index over time using the area under the curve (AUC) approach. Here, the mean AUC of PC3 migration across 3 separate assays is provided.

4.3.2 Fluorescent microscopy

In order to assess any morphological changes arising from hMiro knockdown conditions, control and knockdown PC3 cells were prepared for fluorescent microscopy and viewed under a Leica DM5000 fluorescent microscope as previously described 2.2.6.8. In these microscopy studies, mitochondria were labelled with MitoTracker Deep Red FM, while nuclei were labelled with DAPI. Cells were also viewed under differential interference contrast (DIC), allowing for delineation of each cell without interference from fluorescent signals. Slides were prepared and viewed in triplicate for each condition. A summary of the primary findings from these microscopy studies is provided in the form of Table 4.2, below. Changes in mitochondrial morphology were not noticeable using the equipment available. Representative fluorescent microscopy images for control and knockdown cells are provided in the proceeding pages as follows: 20x objective magnification field view (Figure 4.21), 63x objective magnification (Figure 4.22) 100x objective magnification (Figure 4.23).

Table 4.2 Primary observations of fluorescent microscopy of control and knockdown PC3 cells.

Condition	Primary observation(s)
Control	MitoTracker signal distributed across cytoplasm; normal cell morphology.
hMiro1 knockdown	MitoTracker signal remains close to DAPI signal; cell morphology unchanged.
hMiro2 knockdown	MitoTracker signal remains close to DAPI signal; cell morphology unchanged.
Dual knockdown	MitoTracker signal remains close to DAPI nuclear stain signal; cell morphology frequently swollen.

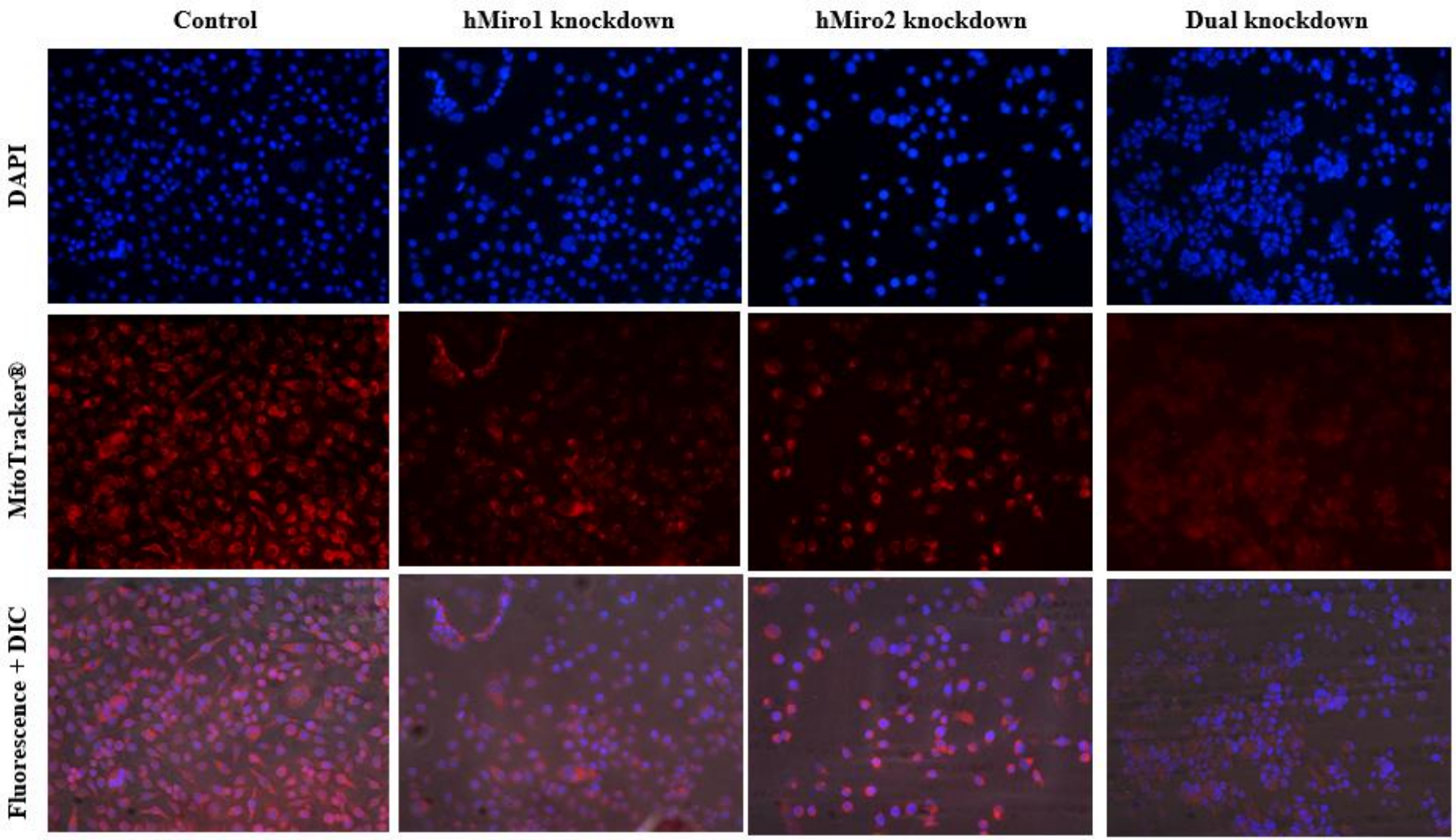

Figure 4.22. Fluorescent microscopy analysis of control PC3 cells versus hMiro1, hMiro2 or dual (hMiro1 and hMiro2) knockdown cells. 20x objective lens utilised.

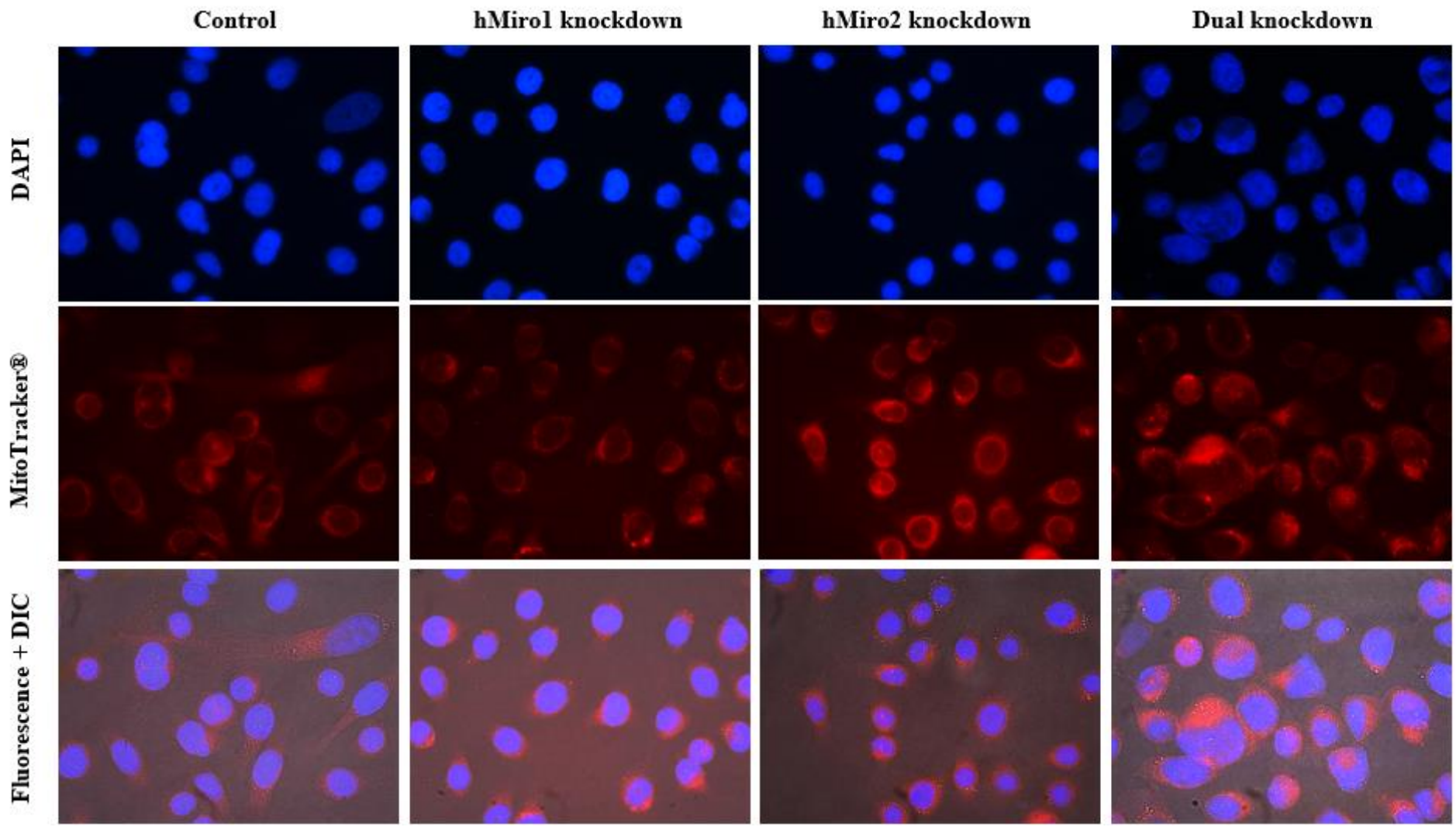

Figure 4.23. Fluorescent microscopy analysis of control PC3 cells versus hMiro1, hMiro2 or dual (hMiro1 and hMiro2) knockdown cells. 63x objective lens used.

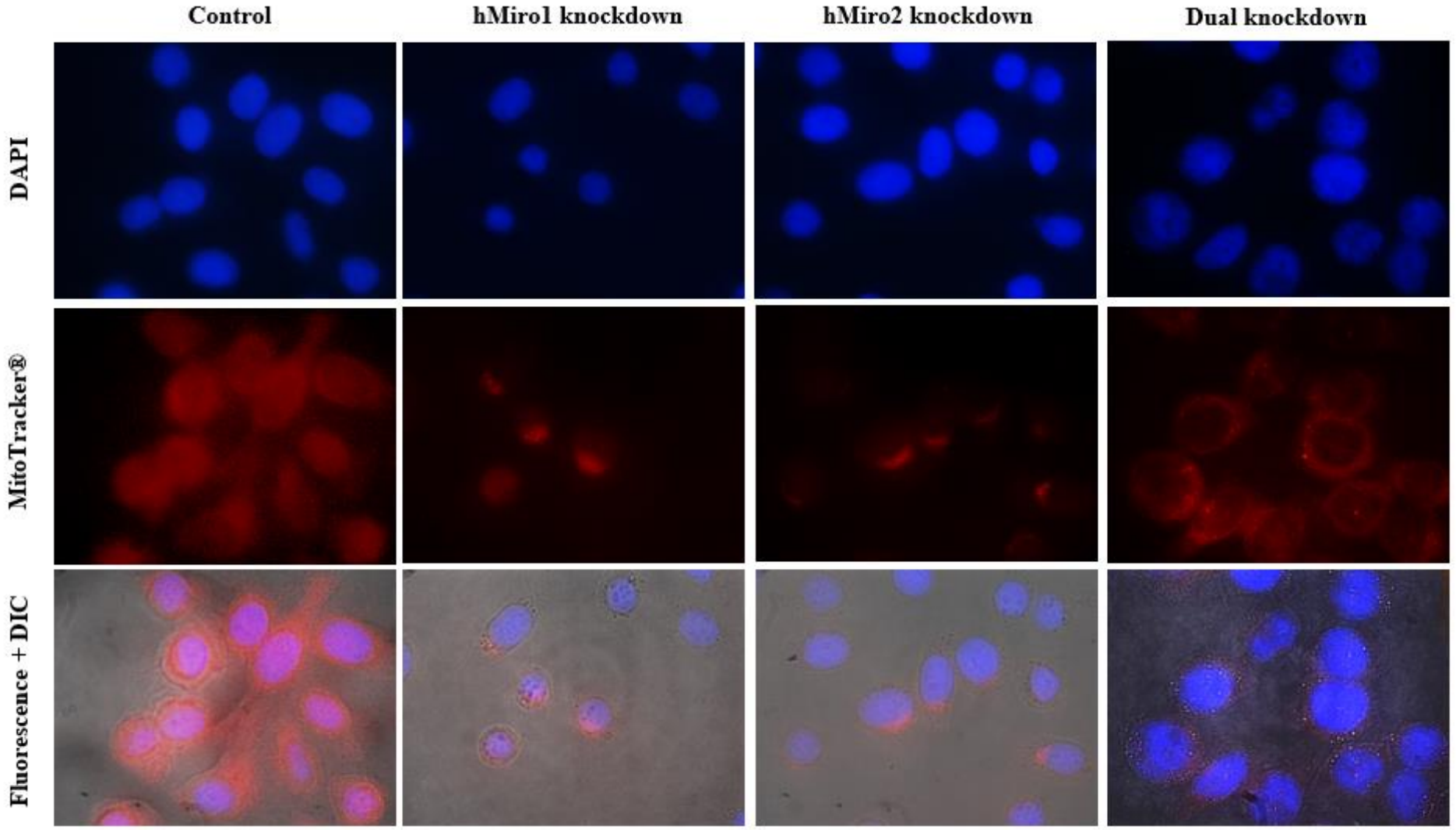

Figure 4.24. Fluorescent microscopy analysis of control PC3 cells versus hMiro1, hMiro2 or dual (hMiro1 and hMiro2) knockdown cells. 100x objective lens utilised.

4.4 Biophysical characterisation of the Miro GTPases

Dynamic light scattering (DLS) and circular dichroism (CD) thermal denaturation were performed as described in 2.2.5.4 and 2.2.5.5, respectively. As shown in Figure 4.24, both Miro1 and Miro2 Xtal constructs produced singular peak in DLS experiments (monomodal distribution). DLS, also known as Photon Correlation Spectroscopy or Quasi-Elastic Light Scattering, exploits the phenomenon of Brownian motion and represents an established technique for determination of the size and size distribution of molecules (279). The Brownian motion of particles in suspension results in the scattering of laser light at different intensities when the light hits the moving particles, with smaller-sized particles exhibiting faster Brownian motion (279,280). The average size, size distribution and polydispersity of particles in solution can be quantified by measuring the time scale of light intensity fluctuations (280). Mathematical analysis of these fluctuations enables the determination of the diffusion coefficient, and therefore the particle size, using the Stokes-Einstein relationship (280). The results shown in Figure 4.25 were used alongside Zetasizer software version 4 (Malvern, UK) to indicate the size of each hMiro$_{XTAL}$ construct. Figure 4.25 indicates pooled analyses of five separate DLS runs for each Miro$_{XTAL}$ construct, with (a) indicating a median particle size of 7.5 nm in diameter, corresponding to around 75Å. However, average particle size was calculated in Zetasizer as 5.56 ± 0.57 nm (approximately 55.6 Å), corresponding to around the expected size of hMiro1$_{XTAL}$ (E_{177}–R_{590}) with the hexahistidine tag attached, which was estimated to be ~5.2 nm (280,281). Figure 4.25 (b), however, indicates a median particle size of around 8 nm in diameter, corresponding to around 80Å. The average particle size calculated in Zetasizer was 5.72 ± 0.56 nm (approximately 58.2 Å), which was in the expected range for the calculated size of hMiro2$_{XTAL}$ (E_{177}–P_{586}) with the hexahistidine tag attached (~5.2 nm). As suggested by Zetasizer, analysis by average size, rather than median, was performed due to the large amount of data obtained and a low frequency of outlier readings. The monomodal distribution shown for hMiro1 and hMiro2 results is suggestive of a pure sample, while the average size calculated for each constructs suggests that these enzymes present monomerically (dimers would present with a higher diameter than the results indicate). Canonical monomeric Rho proteins, such as RhoA, would be expected to show a monomodal distribution with an average diameter of ~3.9–4 nm based on empirical results of several model proteins and enzymes (280,281).

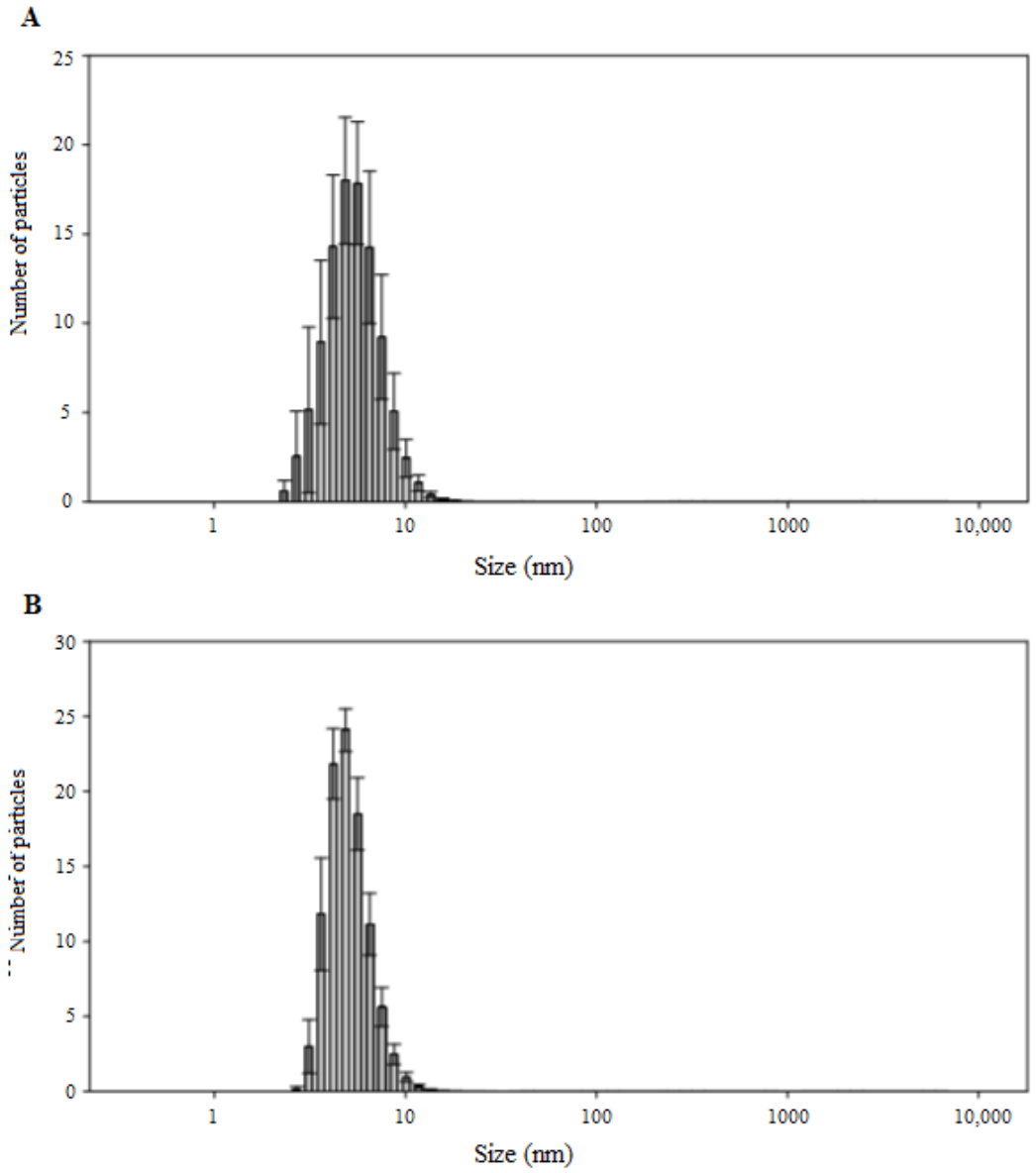

Figure 4.25. Both hMiro1 and hMiro2 exhibit monomeric behaviour *in vitro*. Dynamic light scattering (DLS) of IMAC and gel-purified hMiro1 and hMiro2 constructs, with results showing single peaks corresponding to the correct size in nanometers (nm) for each $hMiro_{XTAL}$ construct.

Thermal denaturation data are shown on the following page in Figures 4.26 (hMiro1) and 4.27 (hMiro2), respectively. The data shown displays the melting temperature (T_m) for the hMiro1 (Figure 4.26) and hMiro2 xtal (Figure 4.27) constructs. The thermal melt for each construct, measured at 220 nm, gave a melting temperature (T_m) of 54.4 ^oC for $hMiro1_{XTAL}$ and 57.4 ^oC for $hMiro2_{XTAL,}$ where T_m describes the temperature at which protein unfolding occurred. Thermal denaturation experiments were performed in order to gain insight as to the thermal stability of hMiro1 and hMiro2, and suggested that $hMiro1_{XTAL}$ and $hMiro2_{XTAL}$ possess similar thermal stabilities to each other and average thermal stabilities compared to many globular proteins (282) including H-Ras (283), as examined further in the discussion (section 4.5).

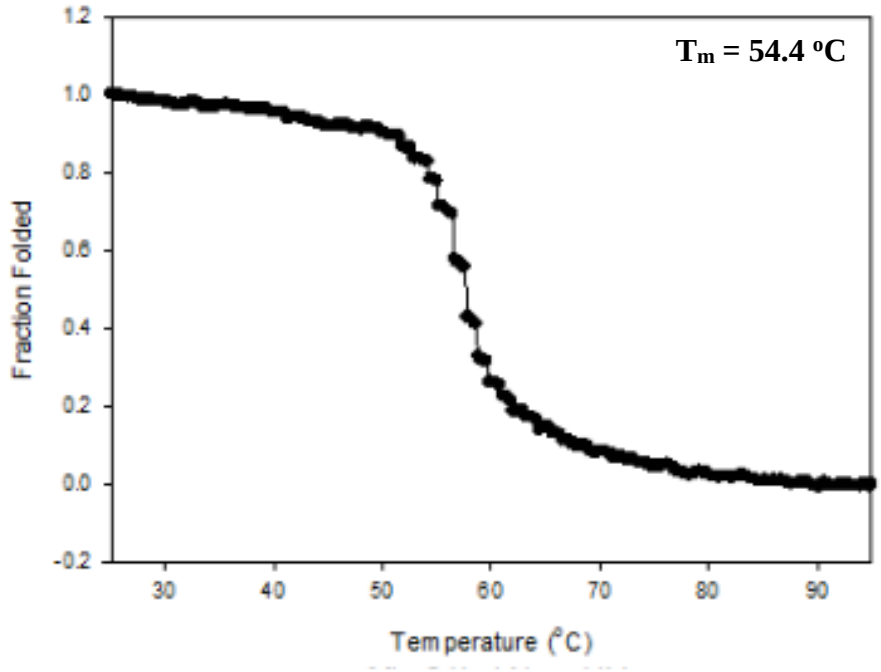

Figure 4.26. Thermal denaturation of hMiro1$_{XTAL}$. CD spectra at selected temperatures, showing thermal unfolding of the hMiro1$_{XTAL}$ construct.

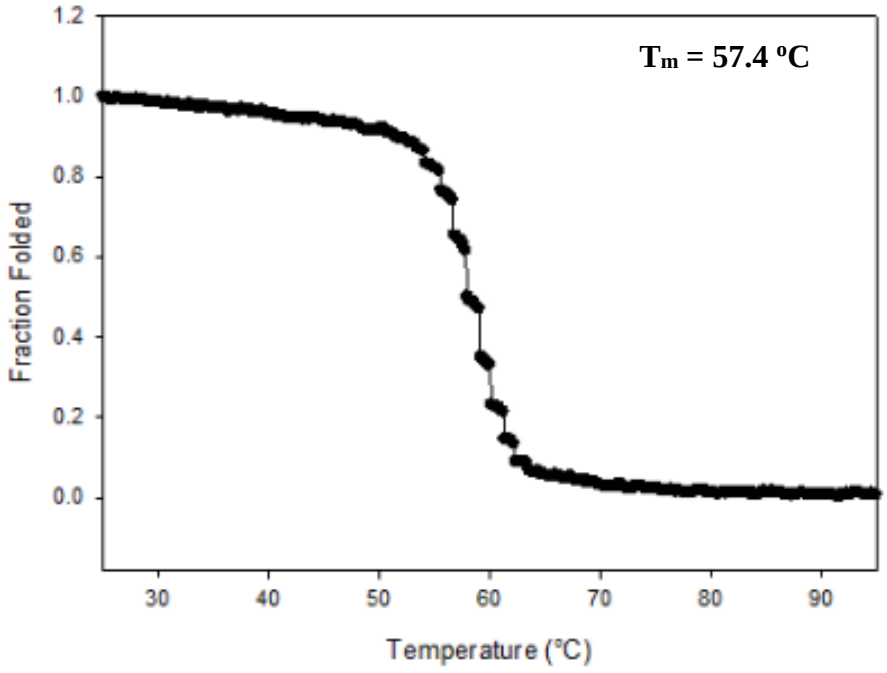

Figure 4.27. Thermal denaturation of hMiro2$_{XTAL}$. CD spectra at selected temperatures, showing thermal unfolding of the hMiro2$_{XTAL}$ construct

4.5 Discussion

4.5.1 Hydrolytic activity of hMiro1 and hMiro2 GTPase domains

GTPase hydrolytic activity was observed in all hMiro domains for the first time *in vitro*, using both the malachite green and PiColourLock™ Gold method. This was largely unsurprising for the N-terminal GTPase domains, considering the sequence similarities these domains share with Ras superfamily G domains and Rho GTPase domains in particular. In contrast to the hMiro N-terminal GTPase domains, the GTP hydrolytic activity of the C-terminal GTPase domains was wholly unexpected; these C-terminal GTPase domains had been previously disregard in the literature as artefact domains, and are only distantly related to other Ras superfamily GTPases, with the closest homologues being Rab42 for the hMiro1 C-terminal GTPase domain (40% identity) and Ras-like GTPase 11B for the hMiro2 C-terminal GTPase domain (27% identity) according to pBLAST searches. Both the isolated C-terminal GTPase domains and $hMiro_{XTAL}$ constructs exhibited hydrolytic activity towards GTP, suggesting that the EF hand domains present in the $hMiro_{XTAL}$ constructs are not functionally obstructive or inhibitory towards GTPase activity. The EF hand domains have previously been implicated in calcium-based pauses in mitochondrial transport (164). However, their lack of influence here suggests the EF hand domains do not achieve this effect through alteration of GTPase activity, at least in the constructs tested. In the absence of full length activity assays and other functional studies, it remains unknown whether intra domain interactions regulate the catalytic activity of individual GTPase domains or whether these domains are regulated by alternative means.

All constructs displayed hydrolytic activity in the presence of Mg^{2+}, Ca^{2+} or both Mg^{2+} and Ca^{2+}. No statistically significant differences in inorganic phosphate release were shown between these three cation conditions. However, hydrolytic activity was completely abrogated in the absence of divalent cations. Thus, similarly to typical Ras superfamily GTPases, the hMiro1 and 2 GTPase domains appear to require a divalent cation co-factor to enable hydrolytic activity. It is interesting, however, that these domains can use either Mg^{2+} or Ca^{2+} interchangeably. Mg^{2+} is generally regarded as an essential co-factor for classical members of the Ras Superfamily, enabling high affinity nucleotide binding (284). In the presence of Mg^{2+}, many Ras superfamily enzymes display extremely high binding affinities to guanine nucleotides (85-87). Indeed, chelation of Mg^{2+} by EDTA has been shown to dramatically decrease nucleotide binding capability in Rab3A

and Sec4 GTPases (88,89). Furthermore, certain GEFs have been shown to promote GDP dissociation partially through destabilisation of bound Mg^{2+} (90,91).

Although Ca^{2+} influences many classical Ras superfamily GTPases through a variety of mechanisms, such as through regulation of GAP and GEF enzymes or through the direct binding of calmodulin to the GTPase, canonical Ras superfamily enzymes have not been shown to bind Ca^{2+} as a co-factor in lieu of Mg^{2+}. As mentioned previously however, the function of Mg^{2+} may alter substantially across enzymes of the Ras superfamily even when structural similarities in the G domain are preserved, as has been noted for the Rho GTPases. It is possible, therefore, that some enzymes may be able to utilise Mg^{2+} or Ca^{2+} interchangeably as co-factors for GTP hydrolytic activity. Ca^{2+} itself typically binds to the carboxylate moieties of acidic residues (285) and requires six to eight co-ordinates (286). In fact, Ca^{2+} and Mg^{2+} preferentially bind to many of the same residues, namely: oxygen atoms of glutamic acid or aspartic acid, or main chain oxygen atoms. Both can also bind to the oxygen atoms of serine, threonine, asparagine or glutamine. Occasionally, binding between these cations and the nitrogen of histidine is also seen (286,287). Generally, however, Ca^{2+} binds with lower free energy gain (287-291) and displays a higher ionic radius than that of Mg^{2+} with the same co-ordination number (286,287). For example, the ionic radii of 6- and 8- co-ordinated Ca^{2+} are 1.00 and 1.12 Å, respectively, while relative values for Mg^{2+} are 0.72 and 0.89 Å (286). Relative to Mg^{2+}, Ca^{2+} also exhibits a greater propensity for bidentate carboxylate binding, albeit a lower affinity for water (292).

Interestingly, the aspartic acid (D) of the G_3 motif / Switch II (DxxG in classical GTPases) is present in the N-terminal GTPase domains, but not the C-terminal GTPase domains. This residue is typically involved in co-factor binding, but does not appear to greatly affect specificity or preference towards Mg^{2+} in the N-terminal GTPase domains relative to their C-terminal counterparts. In the class Ras protein H-Ras the G_3 motif is DTAG, while in the C-terminal GTPase domain of the hMiros the closest possible G_3-like motif is thought to be HDIS in hMiro1 and CEVG in hMiro2. In the hMiro1 and hMiro2 N-terminal GTPase domains, the G_3 motifs appear to be DYSE. While many of these residues may facilitate the binding of either Mg^{2+} or Ca^{2+}, the differences seen at the primary structure level between the hMiro GTPase domains and classical members of the Ras superfamily may confer this unusual ability to bind either divalent ion for the purposes of hydrolytic activity. It is also possible that, upon folding into the native 3D conformation, each hMiro GTPase domain produces a Mg^{2+} binding site resembling that

of the classical Ras enzymes but with the capacity to also bind Ca^{2+}, and that this may simply not be obvious when observing at the primary structure level. Indeed, recent crystallographic studies on Mg^{2+} and GDP-bound dMiro suggest that the following 3D ligand in the C-terminal GTPase domain associates with Mg^{2+}: JLVVSXFLKOJNIY-UHFFFAOYSA-N (where J indicates isoleucine or leucine and X indicates any amino acid). This is, in fact, identical to RhoA (PDB: 5C4M) and HRas (4RSG) Mg^{2+} binding ligands according to crystallographic studies. Interestingly, previous crystallographic studies on human HRas have demonstrated an ability for this enzyme to bind Ca^{2+} in the presence of DTT in a manner that shifts the GTPase towards the "on state" *via* the following ligand: BHPQYMZQTOCNFJ-UHFFFAOYSA-N (where Z indicates E or Q and B indicates D, N or J). Correspondingly, it seems entirely possible that the hMiro GTPases may bind either Mg^{2+} or Ca^{2+} as a co-factor during nucleotide hydrolysis. Intriguingly, dMiro crystal structures (PDB: 4C0K and 4C0L) indicate that the EF-hand domains are also able to bind both Ca^{2+} and Mg^{2+}. It is perhaps possible that this co-factor promiscuity is linked to putative calcium buffering functions for the hMiros. However, further experimental work is required to explore this.

Although both the hMiro1 and hMiro2 N-terminal GTPase domains displayed substrate specificity for GTP, the C-terminal GTPase domains of these enzymes were capable of hydrolysing UTP and ATP in addition to GTP. No constructs tested displayed hydrolytic activity against CTP. In classical small GTPases, substrate specificity towards non-phosphate regions of GTP is thought to occur, at least partly, through the G_4 motif ([N/T]KxD). In Ras, the lysine (K) and aspartic acid (D) residues of this motif are known to bind directly to the guanine ring, with substitution of the aspartic acid with asparagine resulting in increased substrate promiscuity in Ha-Ras p21 (293). These lysine and aspartic acid residues are present in all hMiro GTPase domains, although surrounding residues comprising the immediate tetrapeptide motif are quite different, as shown in Table 4.3, below. Again, of course, it is possible that the native 3D conformations of these enzymes serve to facilitate nucleotide binding promiscuity in a manner not explicitly obvious when observing the primary structure.

Table 4.3. G_4 motif residues exhibited by classical Ras superfamily enzymes in comparison to those shown by hMiro GTPase domains. Red indicates small and hydrophobic residues, blue indicates acidic residues, magenta indicates basic residues and green marks residues harbouring hydroxyl, sulphydryl or amine groups.

GTPase domain	G_4 motif ([N/T]KxD)
HRas G domain	NKCD
RhoA G domain	NKKD
hMiro1N-terminal GTPase domain	NKSD
hMiro2 N-terminal GTPase domain	NKSD
hMiro1 C-terminal GTPase domain	AKSD
hMiro2 C-terminal GTPase domain	SKAD

As for the kinetic values for basal GTPase activity attained, observed K_{cat} turnover values were similar to those previously reported for the intrinsic GTPase activities of canonical Ras superfamily enzymes (270-276) and for the GTPases dynamin and Sept2 (277,278), which contain G loop regions related to those exhibited by Ras superfamily members (277,278). K_{cat} values represent 'turnover' number, or the number of substrate molecules turned over per enzyme per unit time. In this case, K_{cat} can be considered to represent the number of Pi molecules released by the enzyme in question per minute due to GTP hydrolysis. As can be seen, the K_{cat} values obtained are low across the board, with a value of 1.063/min the highest value achieved in the hMiro experiments undertaken (corresponding to hMiro2 NT hydrolysing GTP) and Cdc42 exhibiting the highest K_{cat} amongst the canonical Ras superfamily enzymes listed in Table 4.1 with a K_{cat} of 1.120/min (273).

K_m and K_{cat}/K_m values were not reported in the literature sources for canonical Ras and Rho enzymes. K_m, also known as the 'Michaelis constant' is regarded as an inverse measure of affinity: for practical purposes, K_m represents the concentration of substrate which permits the enzyme to achieve half V_{max} (263). It therefore follows that a low K_m value corresponds to a high enzyme-substrate affinity (294). Interestingly, the hMiro1 CT domain showed more than twice the affinity for ATP than GTP (with K_m values of 4.959 for GTP and 2.094 for ATP, respectively). In contrast, the hMiro2 CT domain

displayed only a slightly higher affinity for GTP (K_m: 0.917) than ATP (K_m: 1.207). the K_m values obtained here were rather high compared to the K_m values of Dynamin (0.0034 mM) and Sept2 (0.00052 mM). For the hMiro domains tested, the hMiro1 NT and CT had similar Km values of 12.026 mM and 11.044 mM, respectively (mean Km: 11.535 mM). Meanwhile, hMiro2 NT had a Km value of 53.155 mM and hMiro2 CT a Km value of 0.917 mM. The Km values for ATP hydrolysis were 2.094 for hMiro1 CT and 1.207 for hMiro2 CT. In an analysis of kinetic data from thousands of enzymes in databases, Bar-Even and colleagues found a median Km of 0.1 mM across all enzymes tested, with around 60% of enzymes exhibiting Km values of 0.01–1mM (294). However, many enzymes showed Km values exceeding 10mM (294). The relatively high Km values shown here indicate that the hMiro1 and hMiro2 G domains possess a lower affinity for GTP than other GTPases and many enzymes for their substrate. As for the K_{cat}/Km values obtained, all hMiro domains assessed showed a K_{cat}/K_m value of <0.1, while dynamin and Sept2 exhibited values of 55.882 and 31.154, respectively. This suggests that the hMiro domains are not very efficient catalysts for GTP and ATP hydrolysis compared with dynamin and Sept7, seemingly as a result of the high K_m values (and thus low affinities for substrate) observed for the hMiro1 and hMiro2 constructs.

The high K_m values obtained for the hMiro constructs, relative to the GTPases dynamin and Sept2 (277,278) in addition to the K_m values discussed by Bar-Even and colleagues (294), may be associated with several factors. The nucleotide binding site may not be as accessible in the hMiro domains as in other GTPases, for example, or nucleotide binding may be adversely affected due to substitutions in amino acids usually strongly conserved for nucleotide binding. Indeed, an assessment of the G loop regions of the hMiro1 and hMiro2 NT and CT domains (see Table 4.4, following) indicates an absence of a normally strongly conserved threonine (T) at position 35 in canonical Ras superfamily enzymes. The hMiro NT domains and hMiro2 CT also lack the conserved glycine usually observed at residue 60. These residues typically engage in hydrogen bonding with the gamma phosphate of GTP as part of the ‘loaded spring’ mechanism described previously (37). Otherwise, the lysine (K) and serine/threonine [S/T] residues normally conserved at positions 17 and 18 and involved with beta and gamma phosphate oxygen interactions (55,69) are observed in all hMiro domains. Too, the valine (V) at position 14, involved in forcing the GTP into a strained position for hydrolysis (112), is conserved in all but hMiro1 NT. The nucleotide-binding lysine and

aspartic acid residues of the G_4 loop (96,97) are also conserved in hMiro1 and hMiro2 NT and CT domains. Thus, several residues involved in nucleotide binding (61,99) are conserved in the hMiro1 and hMiro2 domains, but others have been substituted. This may partly explain the high K_m values observed for the hMiro NT and CT domains. Indeed, analysis of a recently published crystal structure of a truncated version of hMiro1, containing the EF-hand domains and CT domain, indicates a lack of binding a non-hydrolysable analogue of GTP (295), which may influence affinity; gamma phosphate binding was observed for the same non-hydrolysable GTP analogue bound to Cdc42 (296). It is noteworthy to mention that some of the residues discussed above are also absent in dynamin and sept2. However, these enzymes are not representative of classical members of the Ras superfamily and that only indirect comparisons of the kinetic data attained should be conducted in this context, as discussed below.

Table 4.4 Differences in the G domain loop regions: classical versus atypical Ras superfamily enzymes

Protein	Identifier	G_1	G_2	G_3	G_4	G_5
----	Consensus sequence	GxxxxGK[S/T]	T	DxxG	[N/T]KxD	[S/C]A[L/T/K]
HRas	CAG38816.1	GAGGVGKS	T	DTAG	NKCD	SAK
RhoA	AAM21117.1	GDGACGKT	T	DTAG	NKKS	SAK
Cdc42	NP_426359.1	GDGAVGKT	T	DTAG	TQID	SAL
Rac1	CAB53579.5	GDGAVGKT	T	DTAG	TKLD	SAL
RhoH	AAM21122.1	GDSAVGKT	T	DTAG	TQTD	SAL
hMiro1 NT	AAI25105.1: 7-169	GEPRVGKT	P	DYSE	NKSD	SAK
hMiro1 CT	AAI25105.1: 415-592	GVKNCGKS	D	DISE	AKSD	NTA
hMiro2 NT	AAI25105.1: 3-169	GEAQVGKT	P	DYSE	NKSD	SAK
hMiro2 CT	AAI25105.1: 413-589	GARGVGKS	E	CEVG	SKAD	AGP
Dynamin	AAA88025.1	GGQSAGKS	G	DTPG	TKLD	VNR
Sept2	AAH33559.1	GESGLGKS	G	DILQ	AKAD	GSN

Several limitations should be borne in mind when considering the kinetic data obtained and comparing it to kinetic values derived from the literature. It should also be noted that the use of Lineweaver-Burke plots to obtain kinetic data is associated with a large degree of error, as taking the reciprocal of V_{max} can greatly increase small errors of measurement (297). Additionally, as aforementioned, comparing the kinetic data obtained during this study to data available in the literature is difficult for several reasons, namely due to differences across studies in: detection methods for Pi detection, experimental conditions (including temperature) and data interpretation. Reaction temperatures associated with literature-derived hydrolysis rates ranged from 20^{o}C (271) to 37^{o}C (272). This is significant, as increases in temperature are associated with higher reaction rates (298). Indeed, for many chemical reactions occurring at room temperature,

an increase in temperature by 10^{o}C is commonly thought to double the reaction rate (299,300). This generalisation is useful for acknowledging the effect of temperature on reaction rates, although it should be viewed cautiously and noted that for enzymatic reactions, temperatures above 40–50^{o}C will likely result in enzyme denaturation and a corresponding reduction in reaction rate (301). No reactions described in the literature were performed at >37^{o}C (physiological temperature), thus thermal denaturation should not have occurred. However, the range of temperatures reported is an important factor that should be considered when interpreting results against kinetic data obtained from the literature. Kinetic experiments for the hMiro NT and CT domains were undertaken at 25^{o}C, whereas only the values for the Rac enzymes shown in Table 4.1 appear to have been obtained from experiments also performed at 25^{o}C. Furthermore, various experimental techniques were utilised in kinetic experiments described in the literature, namely the use of: HPLC (272), colorimetric (271,278), fluorescent (270,271,273) and radioactivity (277) detection methods. The study involving dynamin basal GTP hydrolysis rates appeared to be the only study that made use of the malachite green method (278). Analysis of raw data obtained from hydrolytic activity assays was also varied across the studies, with some researchers employing the use of Lineweaver-Burke plots in the same manner performed herein (271,278) while others utilised automatic fitting software such as EnzFitter (Sigma-Aldritch, USA) (273). Of additional note, it should be considered that only sparse data is available on the intrinsic hydrolytic activities of the Ras GTPases, perhaps due to a focus on GAP-mediated hydrolysis in the literature (270-276). This is likely due to the fact that GAP enzymes are considered

critical regulatory enzymes for the Ras superfamily (2,302) and can vastly increase hydrolytic reaction rates (2,302,303); for example, the rate of GTP hydrolysis by the Rho enzyme Cdc42 is increased by more than 2,000 times the basal rate in the presence of the Cdc42GAP regulatory enzyme (303). Taken together, the differences listed indicate that direct comparisons across these studies should not be performed. Nonetheless, indirect comparisons of the measurements obtained, compared with kinetic values found in the literature, provide an insight into the capabilities of hMiro1 and hMiro2 intrinsic GTP hydrolysis.

4.5.2. Knockdown studies

The data obtained from knockdown studies is partly consistent with previous work, indicating that knockdown of the hMiros results in a reduction in cell migration and apparent perinuclear aggregation of mitochondria (29,96). However, the results were not statistically significant. Around 30–50% of dual knockdown cells displayed a swollen morphology, indicating hydropic degeneration: a marker of almost all forms of injury to cells and a feature typically exhibited by senescent cells (304). Although hydropic degeneration can occur through a variety of mechanisms (304,305), perhaps the most likely cause in this scenario is deficient mitochondrial transport resulting from hMiro1 and 2 ablation (29,96). A disruption in the ability of mitochondria to produce or deliver ATP to ATP-dependent ion-pumps at the plasma membrane, for example, can result in a build-up of intracellular sodium ions and a subsequent influx of water into the cell, producing bloating (306). It is unusual that the hMiro1 knockdown produced the greatest decrease in net migration during 24 hour migration assays, while this swollen morphology is only seen in dual knockdown cells. However, it is possible that only ~30-50% of the dual knockdown cells viewed had achieved knockdown of both hMiro1 and 2; several of the dual knockdown condition cells may only achieved knockdown of hMiro1 or 2. Additionally, knockdown may have failed altogether in some cells. Regardless of this, the results indicate a difference between control cells and knockdown cells.

4.5.3 Biophysical characterisation of hMiro1 and hMiro2

The biophysical properties assessed for hMiro1 and hMiro2 were very similar, with both constructs showing a similar size and thermal stability. The hMiro ‘xtal’ constructs were utilised in all biophysical characterisation studies, as these constructs represented the closest suitable constructs to full length hMiro1 and hMiro2.

4.5.3.2 Dynamic light scattering

Canonical members of the Ras superfamily are quintessentially monomeric. However, due to the atypical nature of the Miros, dynamic light scattering (DLS) was undertaken to clarify the oligomeric state of hMiro1 and hMiro2. Here, DLS experiments produced single peaks, with average sizes calculated as 5.56 ± 0.57 nm for hMiro1 $hMiro1_{XTAL}$ (E_{177}–R_{590}) and 5.72 ± 0.56 nm for $hMiro2_{XTAL}$ (E_{177}–P_{586}), which corresponded to the expected sizes of these enzymes and thus indicated that hMiro1 and hMiro2 exist monomerically. It has become increasingly apparent that fly and mammalian Miro proteins engage in a mitochondrial transport complex with several other proteins (191). This function of the Miros, in addition to the DLS results obtained herein, strongly suggest that the hMiros function as proteins that engage in prolonged interactions with other proteins rather than homo-oligomerising. In summary, these results indicate the presence of the human Miros in monomeric form. Considering that $hMiro1_{XTAL}$ and $hMiro2_{XTAL}$ are very similar dMiro, this may not simply be a construct effect and it is noteworthy that the human Miros may function as monomers under physiological conditions.

4.5.3.3 Thermal denaturation

The thermal melt for each construct, measured at 220 nm, gave a melting temperature (T_m) of 54.4 ^oC for $hMiro1_{XTAL}$ and 57.4 ^oC for $hMiro2_{XTAL}$, where T_m is defined as the temperature at which the protein unfolds. Relative to previous studies on the thermodynamics of various proteins, these T_m values are not unusually high or low, indicating that both hMiros possess average thermal stability. For example, a 1997 study on water-soluble globular proteins showed a mean T_m of 68.7^oC, with values ranging from 24.9–103.85^oC but most proteins displaying a T_m between 50–60 ^oC (282). Furthermore, the T_m of human H-Ras has previously been noted as 52.5^oC (283), while a set of Ras yeast paralogues showed T_m values ranging from 35–63 ^oC (307). T_m values exhibited by thermostable extremozymes have been documented to exceed 100^oC (308), with some showing T_m values as high as 176.9 ^oC (309). A correlation between protein stability and the arrangement of non-surface ionisable side-chains has been recently indicated, with thermophilic proteins typically possessing a smaller core network of residues with ionisable side-chains (307).

However, comparisons of thermodynamic properties between proteins should be considered carefully. The thermal stability and T_m of a given protein result from numerous complex factors associated with the protein itself and the environment in which is it present. For example, the $hMiro_{XTAL}$ constructs were suspended in the following buffer environment: 25 mM HEPES pH 7.4, 500 mM NaCl, 2 mM DTT and 2% glycerol. While these conditions appeared to be necessary for storing the hMiro constructs and preventing aggregation even at low temperatures (4 – 10^{o}C), all of these components have previously been found to affect the thermostability of proteins. For instance, although HEPES is frequently recommended as a buffer for CD, studies on the *Escherichia coli* protein RecA demonstrated that buffer choice in CD experiments can affect the melting temperature obtained by more than 50% (310). In this study, a phosphate buffer system produced a melting temperature of >105^{o}C regardless of pH (tested range: pH 6.5 - 8.5). When Tris, HEPES and MES were used in place of this phosphate buffer, Tm values were much lower. Furthermore, variation in recorded melting temperature at each pH was seen across all buffer systems utilised. For example, the melting temperature at pH 7.0 for Tris, MES, HEPES and phosphate buffering systems were respectively recorded as 65^{o}C, 88^{o}C, 78^{o}C and >105^{o}C. Interestingly, while these buffers affected thermostablity, they did not significantly affect the enzymatic function of RecA.

NaCl, DTT and glycerol have also been shown to influence protein thermostability. It has been long-established that NaCl has a significant impact on protein stability by altering interactions of the aqueous solvent with the protein by preferential hydration (the Hofmeister effect) (311). In some proteins, NaCl also influences thermal stability by screening electrostatic interactions between charged protein surface residues (312). For instance, if these surface charges are primarily repulsive of one another, the presence of NaCl will improve the stability of the folded protein by screening these electrostatic interactions. DTT is typically used to reduce protein disulphide bonds and prevent intramolecular and intermolecular disulphide bond formation between cysteine residues of proteins (313). In several studies, DTT has been shown to lower protein thermal stability when it is added to the protein buffer (314). This effect is not universal, however. In the biophysical experiments described in this chapter, DTT was utilised to discourage hMiro aggregation following expression and purification. Alternatively, glycerol was typically added to the hMiro buffers both as a cryoprotectant and stability-enhancing co-solvent, encouraging protection from freezing damage and discouraging aggregation, respectively. Glycerol is believed to encourage the native protein into a more compact

state, inhibiting unfolding and stabilising aggregation-prone intermediates through interactions with hydrophobic surface areas (315). As such, glycerol addition has been shown to improve T_m in various proteins (316).

In short, the factors that may influence the thermal stability and melting temperature of a protein are extensive and complex. This, alongside the limited CD experiments undertaken for these constructs, should be taken into account when considering the T_m values obtained. Overall, however, the CD data obtained indicates a relatively average thermostability for the hMiros.

4.5.4 Conclusions

Both the N- and C-terminal GTPase domains for hMiro1 and 2 are capable of hydrolysing GTP. While the N-terminal GTPase domains display substrate specificity towards GTP, the C-terminal GTPase domains display hydrolytic activity towards ATP and, to a much lesser extent, towards UTP. Knockdown of hMiro1, 2 or both hMiros (dual knockdown) in PC3 cells produces a decrease in cellular migration relative to control cells, with perinuclear aggregation of mitochondria exhibited by knockdown cells. Dual knockdown was also associated with a swollen cell morphology in ~30-50% of cells. Both hMiros appear to exist monomerically and present with average thermostability, showing T_m values ranging from 54.4^{o}C to 57.4^{o}C.

Chapter 5: Investigating Miro GTPase signalling pathways using proteomics and computer-based prediction software

5.1 Introduction

5.1.1 Objectives

Recent improvements in biological mass spectrometry and analysis software have allowed proteomics to emerge as a powerful tool for the characterisation of signalling pathways (317,318). The objective of the work undertaken in this chapter was to elucidate Miro GTPase signalling pathway components through the use of molecular biology, cell culture techniques and proteomics. An investigation of this kind has not been performed previously, and was hoped to enable the profiling and identification of pathways regulated by the hMiros.

5.1.2 Overview of proteomics applications

Intracellular biochemical reactions are principally regulated by highly specialised enzymes (319), which typically act within orchestrated signalling pathways with other proteins or intracellular components (320-326). Thus, proteins and their respective signalling pathways are prime mediators of cellular function and phenotype (327-330). Consequently, the identification, quantitation and characterisation of intracellular proteins is critical for understanding the molecular mechanisms associated with cellular physiology and phenotype. The term ‘proteome’ first arose in 1995, defined as 'the total protein complement of a genome' (331). This initial definition reflected what was known about protein expression at the time, acknowledging that not all proteins encoded by the genome are expressed at any one point and that protein expression is subject to a range of factors including physiological state (332), cell type (333) and developmental stage (334). Indeed, the abundance of a given protein is the result of four primary influences: protein synthesis, protein processing, protein secretion and protein degradation (335). Correspondingly, correlation between mRNA and protein levels is known to differ by 20-100 fold (336,337).

The term 'proteomics' itself relates to proteins expressed in a specified cell, tissue or organism. Proteomics approaches have been used to address a wide array of biological questions, including the investigation of changes to the proteome under pathological conditions relative to healthy control conditions (338-342), leading to the direct clinical

application of proteomic information (343,344). Indeed, proteomics is now established as a valuable tool in drug development (345,346) and biomarker discovery (347,348).

Although the emergence of robust, reliable mass spectrometers capable of analysing complex mixtures has brought vast improvements to the field of proteomics, proteomics-based experiments are still fraught with challenges at every stage: from sample preparation (349) and data acquisition (350-352) to database searching (353,354) and the interpretation of (often vast) datasets (355,356). Several different approaches and techniques are available for use at each phase of a proteomics experiment. However, a schematic diagram of a generalised overall approach for 'shotgun' proteomics (also referred to as 'discovery' proteomics) is provided below (Figure 5.1).

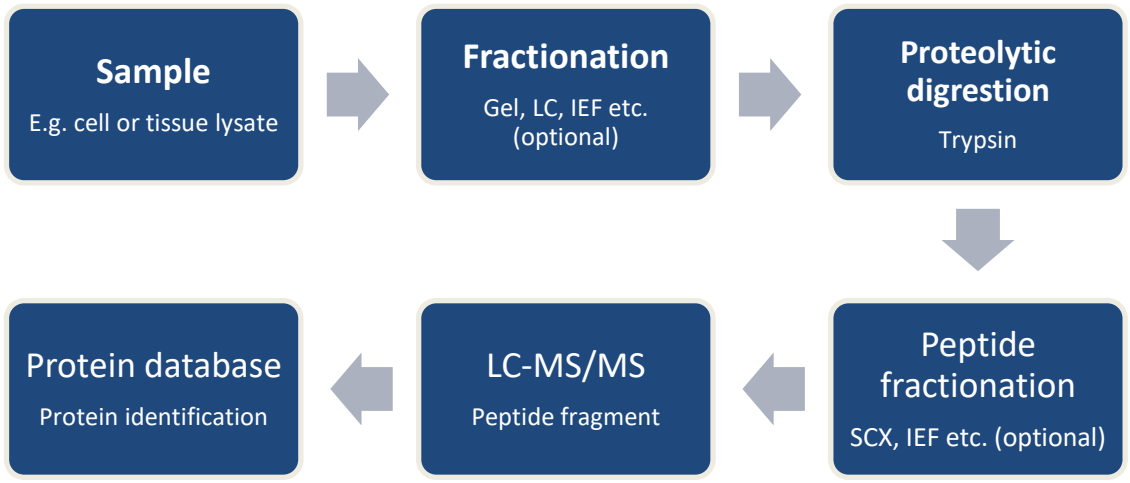

Figure 5.1. Schematic of a general 'shotgun' proteomics approach. Schematic of general 'shotgun' proteomics approach, adopted from a recent review (357). IEF denotes isoelectric focusing, while SCX denotes a strong cation exchange resin commonly used to fractionate proteins in some shotgun approaches. LC denotes liquid chromatography.

The 'shotgun' approach essentially involves the use of a LC-MS tandem mass spectrometry device to identify peptides that have been digested from a complex solution of proteins derived from a sample of interest. It is important to note that at least three biological replicates (preferably more) are necessary for the acquisition of reliable proteomics data, as variation between biological replicates for mammalian cell lines has been shown to vary by ~24-29% (358). Sample preparation and the LC-MS equipment used will also introduce technical variations. With this in mind, sample preparation (stage

1 of figure 5.1) should be followed in a meticulous fashion, as numerous variables may affect proteome composition (359); even small deviations from a precise sample preparation method may influence final results. Proteins such as human keratin, from the researcher(s) involved in the study, may also contaminate samples and manifest as hits downstream of the process during data analysis (360). As such, all stages of a proteomics experiment should be implemented in a precise and careful manner, preferably under a laminar flow hood to avoid sample contamination (360). Preparation may take anywhere from hours to weeks, depending on the nature of the study and the samples to be assessed.

Samples to be investigated, once prepared, are typically extracted and digested. An array of methods are available for the extraction of proteins, though the chosen approach is often dependent on the nature of the original sample (361-363). Digestion is typically accomplished by exploitation of trypsin alone (364), although some approaches incorporate the inclusion of additional proteases such as Lys-C, Lys-N, ArgC, AspN or GluC (365). Digestion is generally preformed at 37^{o}C for at least four hours. Proc *et al.*, suggested an optimal digestion time of 9 hours using trypsin alone (366), although it is considered conventional to digest overnight (367). Attempts to hasten the digestion process have involved the use of immobilised trypsin matrices (368) and high intensity focused ultrasound (369), the latter of which has been reported to digest protein samples in 60 seconds or less with comparable efficiency to a traditional overnight method. In some cases, successful digestion is followed by fractionation of peptides. Fractionation can be achieved through a variety of methods, such as peptide isoelectric focusing (pIEF) or strong cation exchange (SCX) chromatography, although some experiments will involve earlier fractionation of proteins prior to digestion (370). The primary aim of fractionation involves depleting unnecessary, highly abundant proteins to facilitate the discovery of specific protein groups within a sample (371). Depending on the aim of the experiment, however, fractionation may not be required. The resulting peptides are subsequently prepared for mass spectrometry and samples separated according to specific requirements suitable for the equipment and particular experiment at hand.

Analysis of raw data files is typically handled by highly specialised analysis software in conjunction with specialised database searching software such as MASCOT (372) or X!Tandem (373), which use algorithms to match experimental spectra with theoretical spectra based on enzymatic cleavage of proteins, and correspondingly suggest protein ‘hits’ (372,374). MASCOT makes use of a proprietary scoring algorithm developed from the molecular weight search (MOWSE) algorithm (375), comparing each experimental

spectra to a database of theoretic spectra originally derived from genomic information. Using this system, peptides that are predicted to arise from the same protein are grouped and the hit, or match, is assigned a confidence value corresponding to how well fitted the experimental spectra is to the theoretical spectra. A threshold value is implemented to assess whether the match has occurred by chance (372). X!Tandem operates in a similar manner, with the workflow separated into two distinct stages. First, a comparison of the experimental spectra to spectra in the database is performed. This is followed by the generation of a database containing only the identified protein 'hits'. The second stage then comprises the identification of modified peptides that match proteins in the generated databased. This two-staged method is employed to increase confidence scores, with scoring in X!Tandem based on probability scoring in a similar manner to MASCOT. A histogram is generated for each spectrum-to-sequence assignment and the protein with the highest score typically considered the correct identification. Probability scores are subsequently generated from the log transformed hyperscores to establish whether the match occurred by chance (376-378). Several methods for further validating protein hits, including resolution of conflicting hits, is generally available through specialised computer software. Ultimately, a list of protein hits is generated based on automated assessment of initial raw data and a degree of user input, enabling further downstream analysis according to experimental hypotheses or objectives.

The work presented in this chapter comprises efforts to utilise, for the first time, proteomics approaches in the identification of Miro signalling pathway components. including an establishment of protein expression alternations when the GTP hydrolytic capacity of the hMiro GTPase domains are altered, and a comparison of protein expression levels between these conditions in cultured mammalian cells.

5.2 Biological samples: hMiro overexpression and knockdown

5.2.1 hMiro overexpression studies

Pioneering studies on hMiro function involved the ectopic overexpression of wildtype and mutant hMiro proteins in mammalian cell lines, where mutations were designed to produce hMiro proteins bearing either constitutively active (V13) or dominant negative versions (N18) of the N-terminal GTPase domain (29,96). The mutants were produced based on known constitutively active and dominant negative mutations in Ras and Rho enzymes, where G12V or G13V produce constitutively GTP-bound enzymes through steric hinderance of GAP enzymes (58), and S18N mutants are associated with a loss of

Mg^{2+} and steric occlusion of the conserved nucleotide-binding phenylalanine (F) residue at position 28 (93). Furthermore, it is generally accepted that S18N mutants sequester GEF enzymes, depleting the intracellular pool and thus blocking activation usually mediated by these GEFs (379-381). It is generally accepted that S18N mutants remain constitutively bound to GDP (58). While these mutants were originally developed when it was unknown whether Miro GAP and GEFs existed, these mutants are known to exert biological effects (29) and have been used in the literature as constitutively active and dominant negative mutants, respectively (29,97,268,382,383). Indeed, overexpression of hMiro1 V13 mutants appeared to increase apoptotic rate relative to control cells and encouraged mitochondrial aggregation (29). Later studies involved the assessment of further mutants, including point mutations to the C-terminal GTPase domain and mutations disabling function of the EF hand domains (ΔEF) (268). The results, overall, implicated the status of the hMiro GTPase domains in mitochondrial morphology and aggregation, with hMiro1 mutations and mutations of the N-terminal GTPase domains producing the most striking phenotypes (162).

Here, in an attempt to elucidate the signalling pathways involved in hMiro GTPase domain and EF hand status, panels of plasmids encoding hMiro1 and 2 mutants were designed with the objective of ectopically expressing distinct hMiro mutants in mammalian cell lines. The expression of these mutants was hypothesised to trigger discreet intracellular signalling events, producing changes in the proteome that could be detected and assessed. pRK5-Myc plasmids encoding hMiro1 and hMiro2 WT, V13, N18 and ΔEF were kindly donated by the Pontus Aspenström Group (Karolinska Institutet, Sweden); these plasmids were utilised as template for site-directed mutagenesis to produce the panel of mutant-encoding plasmids shown in Table 5.1 (hMiro1 plasmids) and Table 5.2 (hMiro2 plasmids). All mutant-encoding plasmids were shipped for sequencing at an independent, commercial laboratory and showed the desired point mutations with no unwanted changes present (see Figure 5.2).

Table 5.1. Panel of hMiro1 plasmids intended for use in proteomics investigations. WT, V13, N18 and ΔEF encoding plasmids were provided by the Pontus Aspenström Group (Karolinska Institutet, Sweden). Note that for ΔEF mutants, functional abrogation of the EF hands was achieved by substitutions at position 208 and 328 with lysine (K).

Plasmid	Intended effect
hMiro1 WT	Full-length, wildtype hMiro1
hMiro1 S432N	Wildtype N-terminal GTPase domain and dominant negative C-terminal GTPase domain
hMiro1 G425V	Wildtype N-terminal GTPase domain and constitutively active C-terminal GTPase domain
hMiro1 N18	hMiro1 with dominant negative N-terminal GTPase domain and wildtype C-terminal GTPase domain
hMiro1 N18/S432N	hMiro1 with dominant negative N-terminal and C-terminal GTPase domains
hMiro1 N18/G425V	hMiro1 with dominant negative N-terminal GTPase domain and constitutively active C-terminal GTPase domain
hMiro1 V13	hMiro1 with constitutively active N-terminal GTPase domain and wildtpye C-terminal GTPase domain
hMiro1 V13/S432N	hMiro1 with constitutively active N-terminal GTPase domain and dominant negative C-terminal GTPase domain
hMiro1 V13/G425V	hMiro1 with constitutively active N-terminal and C-terminal GTPase domains
hMiro1 ΔEF	Full-length, wildtype hMiro1 with abolished EF hand calcium binding function

Table 5.2. Panel of hMiro2 plasmids designed for use in proteomics investigations. WT, V13, N18 and ΔEF encoding plasmids were provided by the Pontus Aspenström Group (Karolinska Institutet, Sweden). For ΔEF mutants, EF hand were rendered functionally obsolete by substitutions at position 208 and 328 with lysine (K).

Plasmid	Intended effect
hMiro2 WT	Full-length, wildtype hMiro1
hMiro2 S430N	Wildtype N-terminal GTPase domain and dominant negative C-terminal GTPase domain
hMiro2 G423V	Wildtype N-terminal GTPase domain and constitutively active C-terminal GTPase domain
hMiro2 N18	hMiro1 with dominant negative N-terminal GTPase domain and wildtype C-terminal GTPase domain
hMiro2 N18/S430N	hMiro1 with dominant negative N-terminal and C-terminal GTPase domains
hMiro2 N18/G423V	hMiro1 with dominant negative N-terminal GTPase domain and constitutively active C-terminal GTPase domain
hMiro2 V13	hMiro1 with constitutively active N-terminal GTPase domain and wildtpye C-terminal GTPase domain
hMiro2 V13/S430N	hMiro1 with constitutively active N-terminal GTPase domain and dominant negative C-terminal GTPase domain
hMiro2 V13/G423V	hMiro1 with constitutively active N-terminal and C-terminal GTPase domains
hMiro2 ΔEF	Full-length, wildtype hMiro1 with abolished EF hand calcium binding function

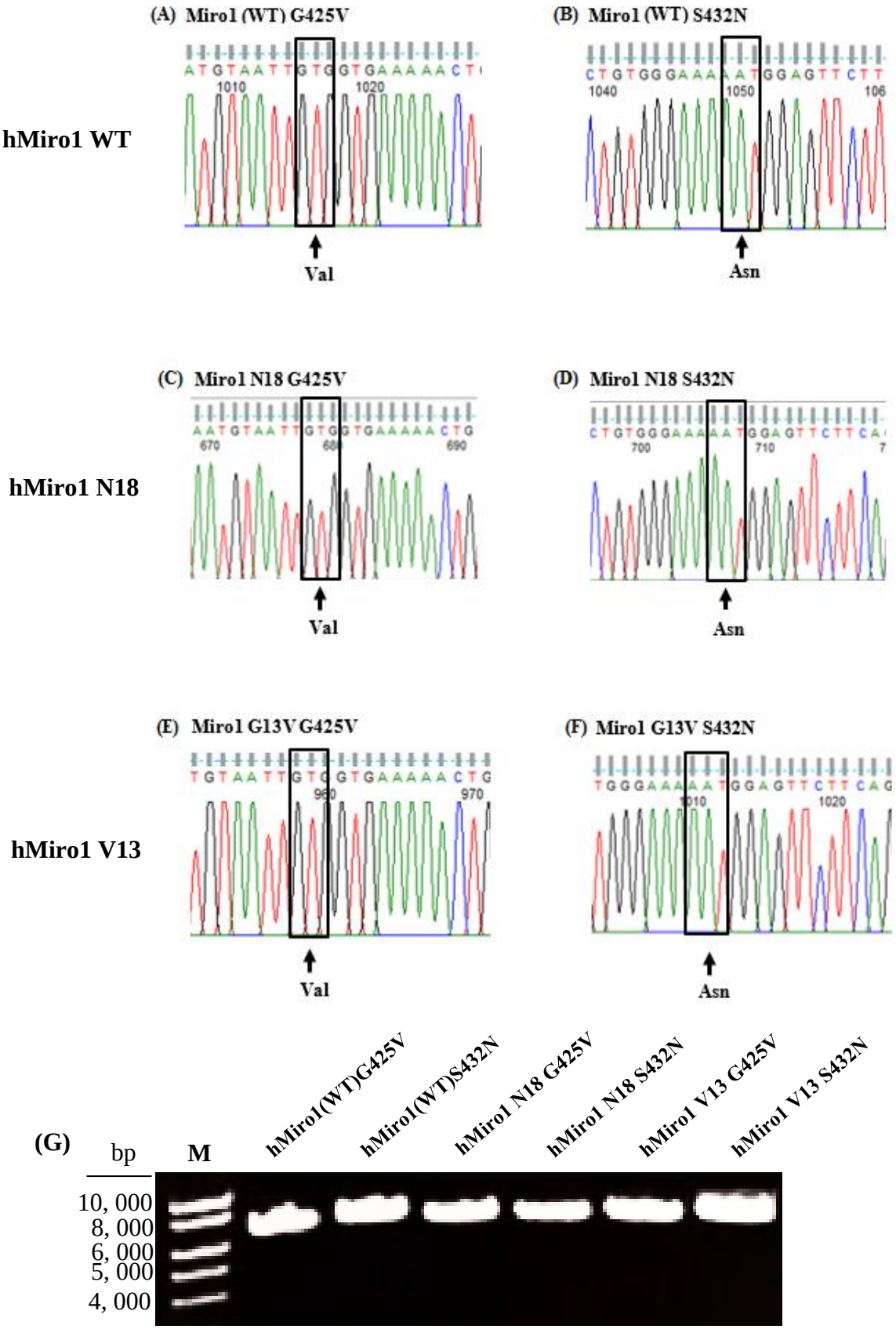

Figure 5.2. Sequence trace sections for hMiro1-encoding mutants, with relevant codons highlighted. Mutations were introduced to hMiro1 WT **(A-B)**, hMiro1N18 **(C-D)** and hMiro1V13 **(E-F)** plasmids previously donated and sequenced by the Pontus Aspenström Group, Sweeden. **(G)** Respective plasmids visualised on 1% agarose gel.

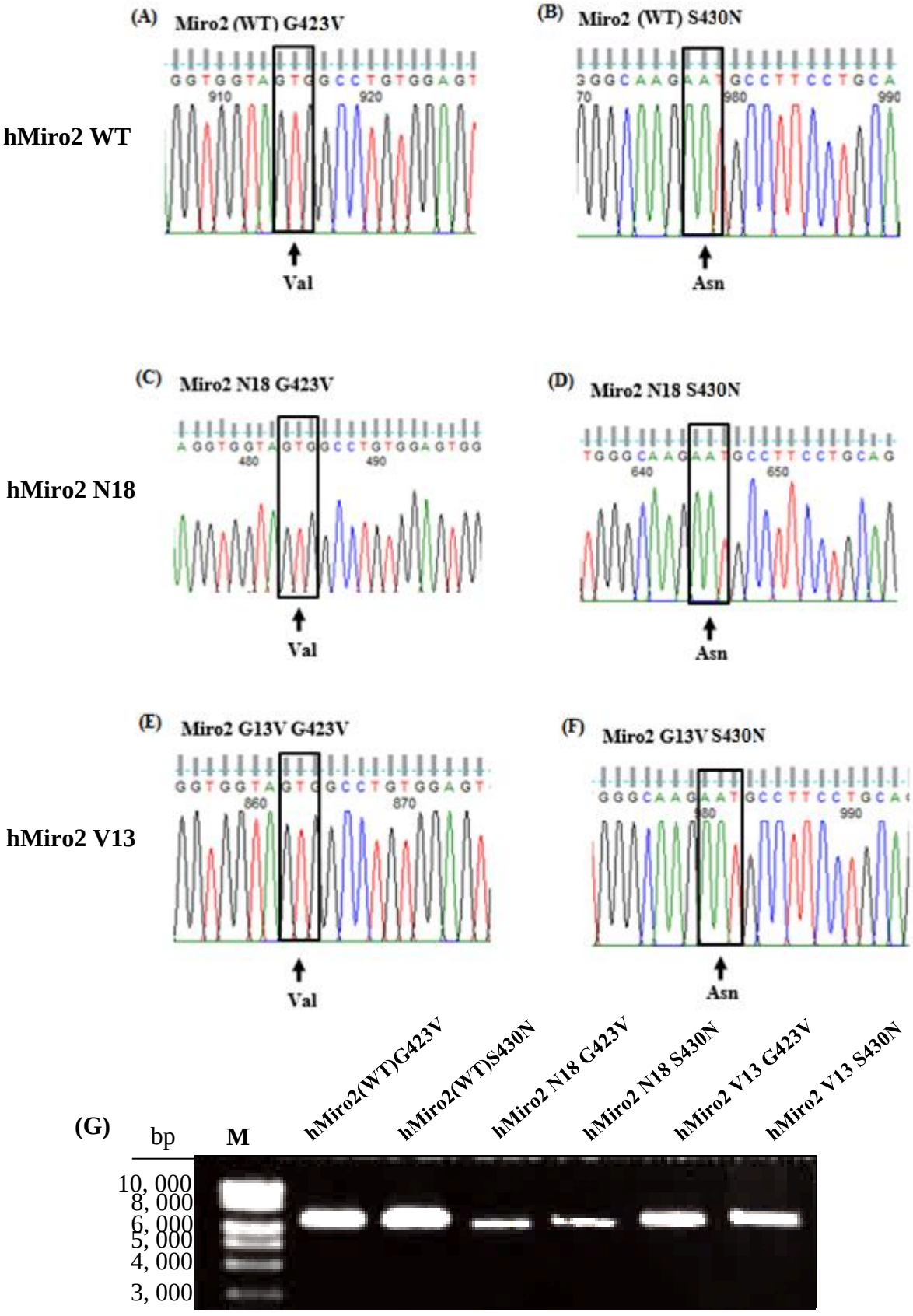

Figure 5.3. Sequence trace sections for hMiro2-encoding mutants, with relevant codons highlighted. Mutations were introduced to hMiro2 WT **(A-B)**, hMiro2N18 **(C-D)** and hMiro2V13 **(E-F)** plasmids previously donated and sequenced by the Pontus Aspenström Group, Sweeden. **(G)** SDM plasmids visualised on 1% agarose gel.

Plasmids confirmed to encode the desired hMiro mutant were transfected into COS7, HEK-293 or VSMC cells, respectively. Consistent with prior studies, the COS7 cells appeared the easiest cells to transfect for overexpression studies. Due to the strong phenotypes observed in the COS7 line in prior hMiro work using these plasmids, this cell line was selected. Wildtype and mutant hMiro was ectopically expressed as described in 2.2.6.4. Cells were incubated for 72 hours and subsequently processed for geLC-MS, as detailed in Chapter 2, sections 2.2.6.6 and 2.2.7.3. To confirm overexpression, 10 µg of each sample was retained and subjected to Western blotting (2.2.4.8); Figure 5.4 displays a typical Western blot exhibiting successful overexpression of target hMiros relative to control cells.

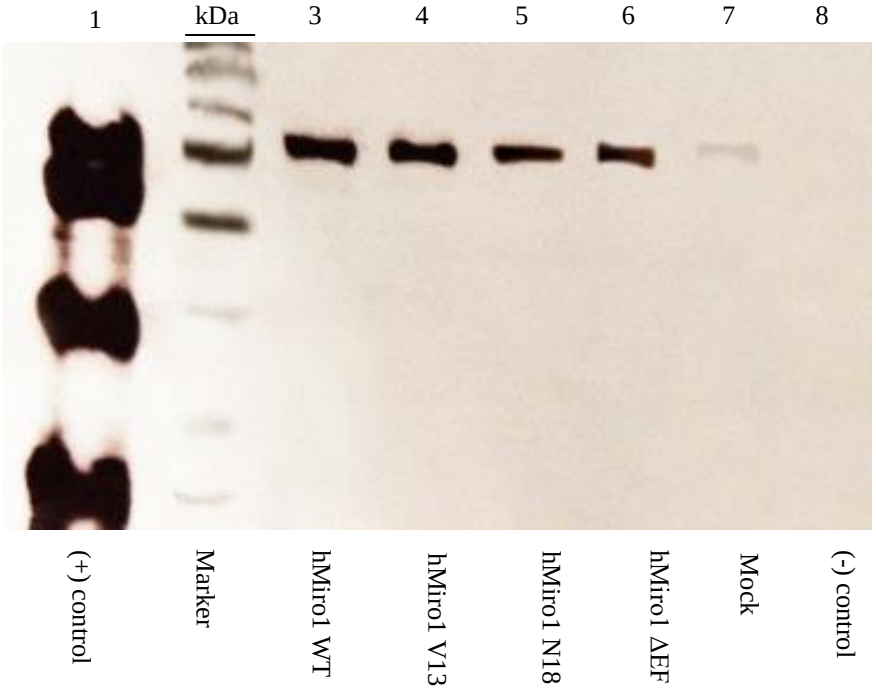

Figure 5.4. Immunoblot displaying successful overexpression of both wildtype and mutant hMiros.

20 µg of each validated sample was loaded onto a 12% SDS-PAGE gel and processed through the geLC-MS method discussed in section 2.2.7.3. LC-MS was undertaken (2.2.7.4) and samples analysed using Progenesis (2.2.7.5). Unfortunately, due to persistent technical issues with the available mass spectrometer throughout this study, a limited of samples were fully processed. The samples processed corresponded to the mutants V13, N18 and control samples for both hMiro1 and hMiro2.

5.2.2 Biological samples: hMiro knockdown samples

Knockdown samples were prepared as described in 2.2.6.5. Due to improved methodology tested by the NUOmics team, knockdown samples were not fractionated on the SDS-PAGE gel, and instead were intended to be loaded onto the LC-MS apparatus as one fraction with a longer gradient applied. Unfortunately, due to consistent technical issues with the Q-Exactive, the data retrieved from these samples was unsuitable for analysis. However, a full set of samples were prepared and will be processed for future confirmatory work.

5.3 Computer-based prediction of hMiro interaction partners

Experimental methods for detecting protein-protein interactions often yield false discoveries (384). Additionally, data derived from proteomics is typically complex and noisy. To enable further refinement of proteomics analysis, computer-based prediction of hMiro interaction partners was undertaken. Several approaches for the computer-based prediction of protein-protein interactions are available. However, the STRING online resource is highly regarded in the literature (385-387), providing a database of known and predicted protein-protein interactions through integration of several different methods including: collation of experimental data, automated literature (text) mining and the gathering of data from curated databases (388). Additionally, STRING infers functional relationships between proteins by assessing co-expression (whether other proteins are expressed and repressed in a similar manner to the query protein), co-occurrence (assessing genes that appear in the same phylogenetic lineage as the gene encoding the query protein), gene fusion (assessing whether the gene encoding the query protein is known to undergo fusion with other genes) and gene neighbourhoods (the extent to which there are genes frequently nearby the gene encoding the query protein; useful mostly for prokaryotic proteins) (388). After identifying putative interactors for the query protein, STRING is able to search curated databases such as the Kyoto Encyclopaedia of Genes and Genomes (KEGG) to examine whether any patterns of functional enrichment exist: essentially, whether the putative interactors are frequently associated with specific biological pathways or functions. With this considered, *in silico* predictions of hMiro1 and 2 interaction partners were first undertaken using the STRING database. STRING allows for the prediction of both direct interactions (1^{st} shell) and indirect interactions (2^{nd} shell), displayed as either coloured or clear globes, respectively.

Basic results from STRING are provided as Figure 5.5, with results for both hMiro1 and 2 shown. These results exhibit the 10 putative direct interactors (1st shell) with the highest confidence scores when all interaction sources are combined, with information on these interactors provided in tabular form alongside the visual output. For each output, top-scoring functional enrichment data related to biological processes and KEGG pathways are given in Table 5.3 for hMiro1 and 5.4 for hMiro2, respectively. STRING generated extensive lists of putative hMiro interactors and signalling networks (example table of hits displayed in Appendix 11, showing a small number of the hundreds of suggestions); these were used for cross-referencing proteomics results.

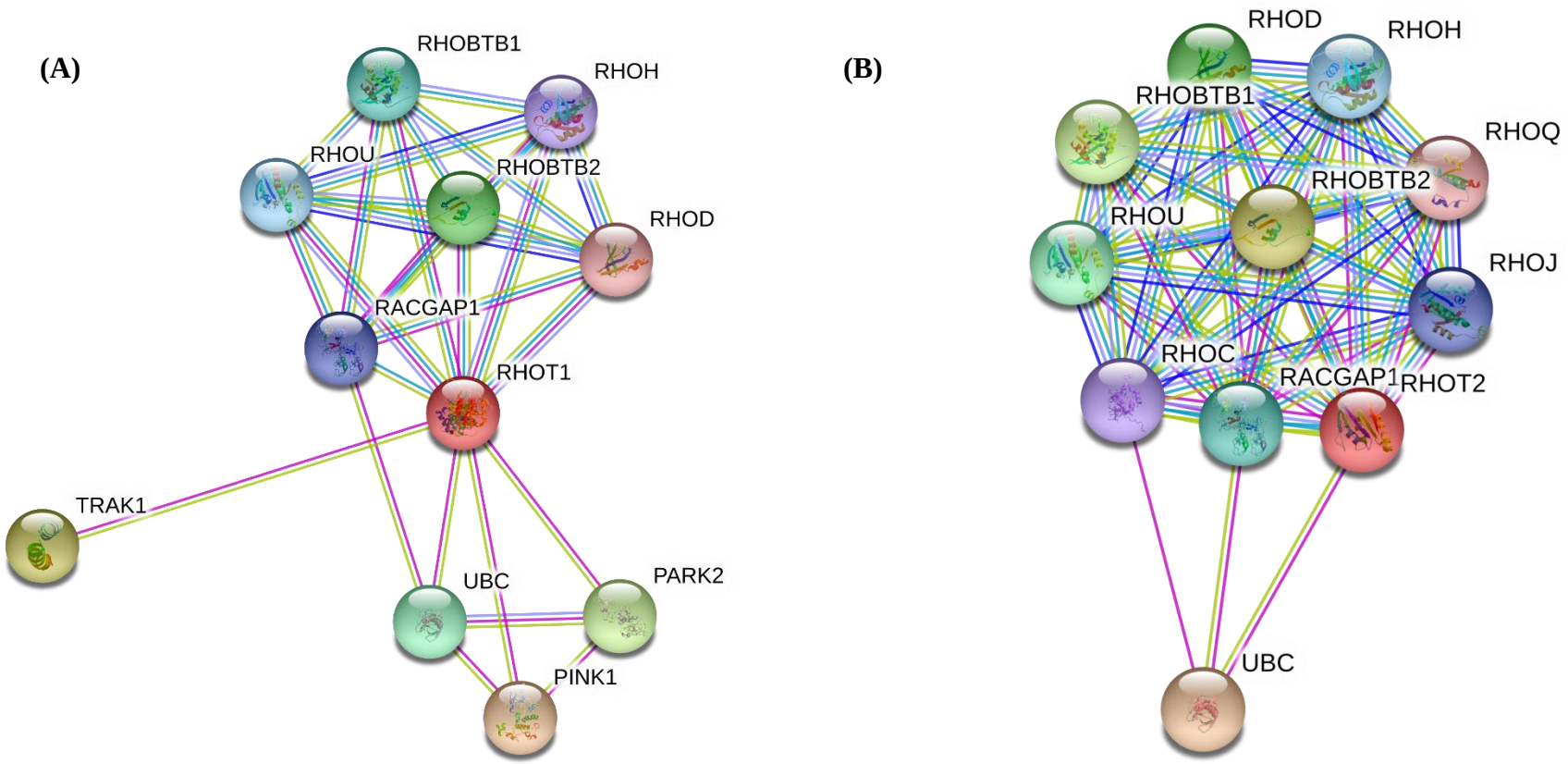

Figure 5.5. Basic results from the STRING online tool for (A) hMiro1 and (B) hMiro2. (A) Visual output of 10 putative direct interactors (1st shell) with the highest confidence scores when all interaction sources are combined. Note that RhoT1 and RhoT2 refer to hMiro1 and hMiro2, respectively.

Table 5.3. Pathways predicted to be associated with hMiro1. Based on automated functional enrichment analysis of the simple results shown in Figure 5.5 (A), with functional enrichment relating to biological processes and KEGG pathways are displayed in the table.

Pathway description	Observed gene count	False discovery rate
Regulation of small GTPase mediated signal transduction	7	4.62E-08
Regulation of intracellular signal transduction	9	4.42E-06
Regulation of signal transduction	10	8.13E-06
Intracellular signal transduction	8	0.000497
Small GTPase mediated signal transduction	6	0.000545
Negative regulation of oxidative stress-induced neuron intrinsic apoptotic signalling pathway	2	0.00402
Regulation of I-kappaB kinase/NF-kappaB signalling	4	0.00526
Regulation of protein targeting to mitochondrion	3	0.0163
Regulation of mitochondrial fission	2	0.0253
Single organism signalling	9	0.0311
Regulation of dopamine secretion	2	0.0325
Cellular response to toxic substance	2	0.0438
Ubiquitin-mediated proteolysis	3	0.0125

Table 5.4. Pathways predicted to be associated with hMiro2. Based on automated functional enrichment analysis of the simple results shown in Figure 5.5 (B), with functional enrichment relating to biological processes are shown.

Pathway description	Observed gene count	False discovery rate
regulation of small GTPase mediated signal transduction	10	1.50E-15
regulation of intracellular signal transduction	11	3.40E-10
small GTPase mediated signal transduction	8	2.82E-07
intracellular signal transduction	9	1.27E-05
actin cytoskeleton organization	5	0.00108
regulation of cell shape	3	0.0358
single organism signalling	9	0.0358
cell communication	9	0.0399

5.4 Proteomics analysis of prepared samples

Proteome analysis of COS7 cells bearing overexpressed hMiro mutants was undertaken and compared to control (mock transfection) conditions. Initial analysis of the data included a comparison of X!Tandem versus MASCOT, the two most widely used databases. For analytical purposes contaminant proteins (keratin, etc.) were omitted from analysis. The two programmes identified similar numbers of proteins, as shown in Table 5.5. Interestingly, the X!Tandem database consistently generated a greater number of hits. While direct comparisons of full protein lists generated by different database searching algorithms can be problematic (389), recent studies have shown improved confidence scores and increased peptide identifications when the results of multiple database programmes are combined (390).

The proteome was mapped for each condition in duplicate, with raw data processed using Progensis to identify any trends. First, principle component analysis (PCA) plots were generated to compare the automatically assigned alignment generated by Progenesis to a manually assigned alignment. This was necessary to validate the reference selected by Progenesis. No difference in trends nor any visible difference in distinct groupings were found between the PCA plots, suggesting that the Progenesis automatic assignment of alignment was suitable for use. Data was subsequently processed using Progenesis software and protein expression across each condition compared, enabling the identification of unique proteins expressed under each condition (Figure 5.6). To further refine results, comparisons were drawn between predicted interaction partners for each hMiro and the proteomics data. Each hMiro was assessed separately, with the unique proteins identified under control, V13 and N18 conditions compared to predicted putative interactors using STRING, known hMiro binding partners identified in the scientific literature by manual literature searching and known binding partners of proteins homologous to either the hMiro1 or 2 N-terminal GTPase, respectively. Homologous proteins were identified by the pBLAST server on NCBI and their known interactors identified using the STRING algorithms for curated database searching and literature mining. As shown in Figure 5.7 for hMiro1 and 5.8 for hMiro2, predicted interaction partners and unique hits for specific conditions were present, reinforcing the possibility of these hits as genuine binding partners. Tables 5.6 and 5.7 detail these unique hits. Unless otherwise stated, descriptions of the functional aspects of each hit are based on those assigned by RefSeq (391).

Table 5.5. Number of proteins identified for each condition (mean across duplicates), showing MASCOT versus X! Tandem.

Condition	MASCOT (n)	X! Tandem (n)
Control	676	694
hMiro1 V13	498	507
hMiro1 N18	623	645
hMiro2 V13	421	430
hMiro2 N18	846	856

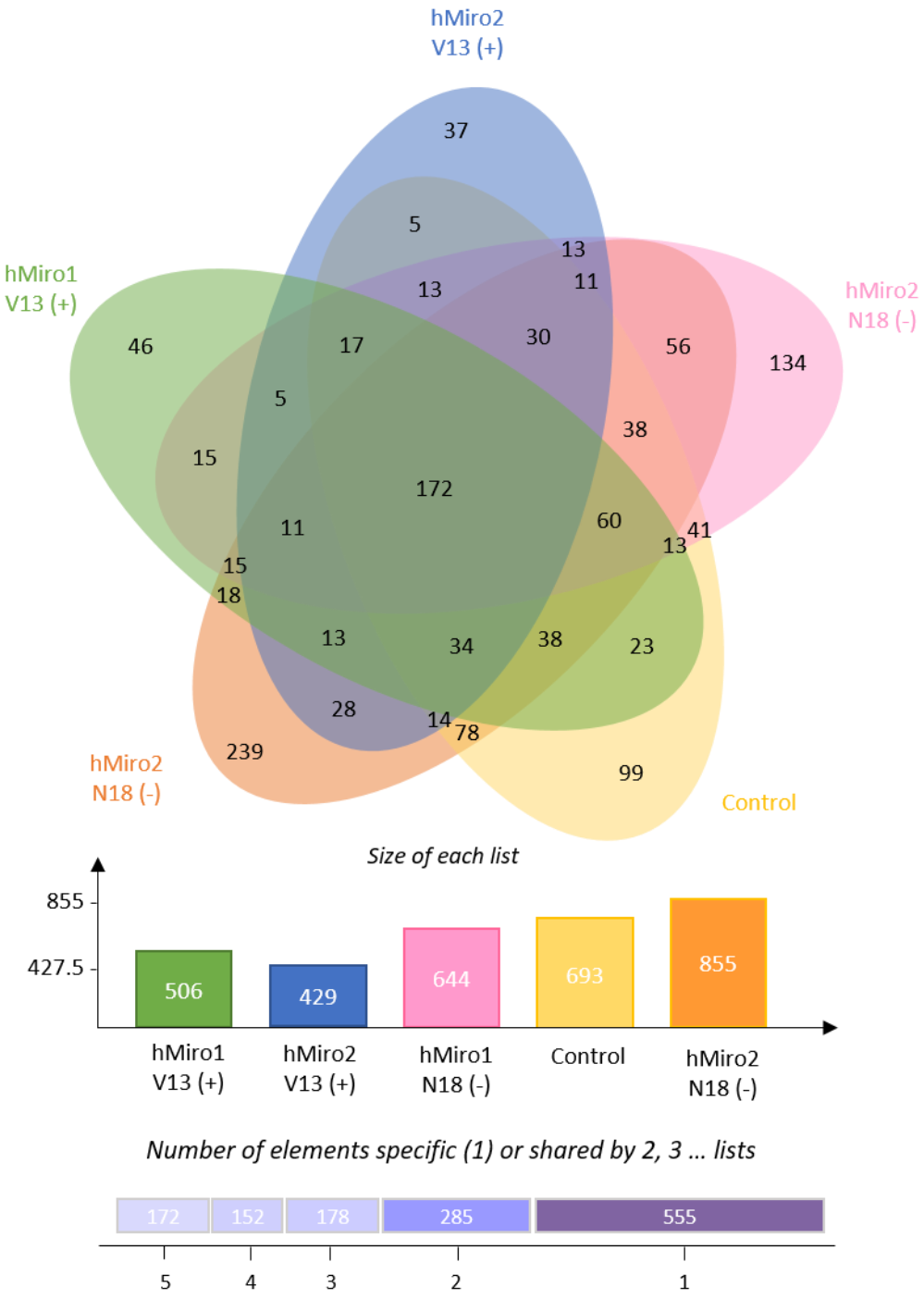

Figure 5.6. Number of proteins identified for each condition from the raw proteomics results, following hit filtering and conflict resolution in Progenesis.

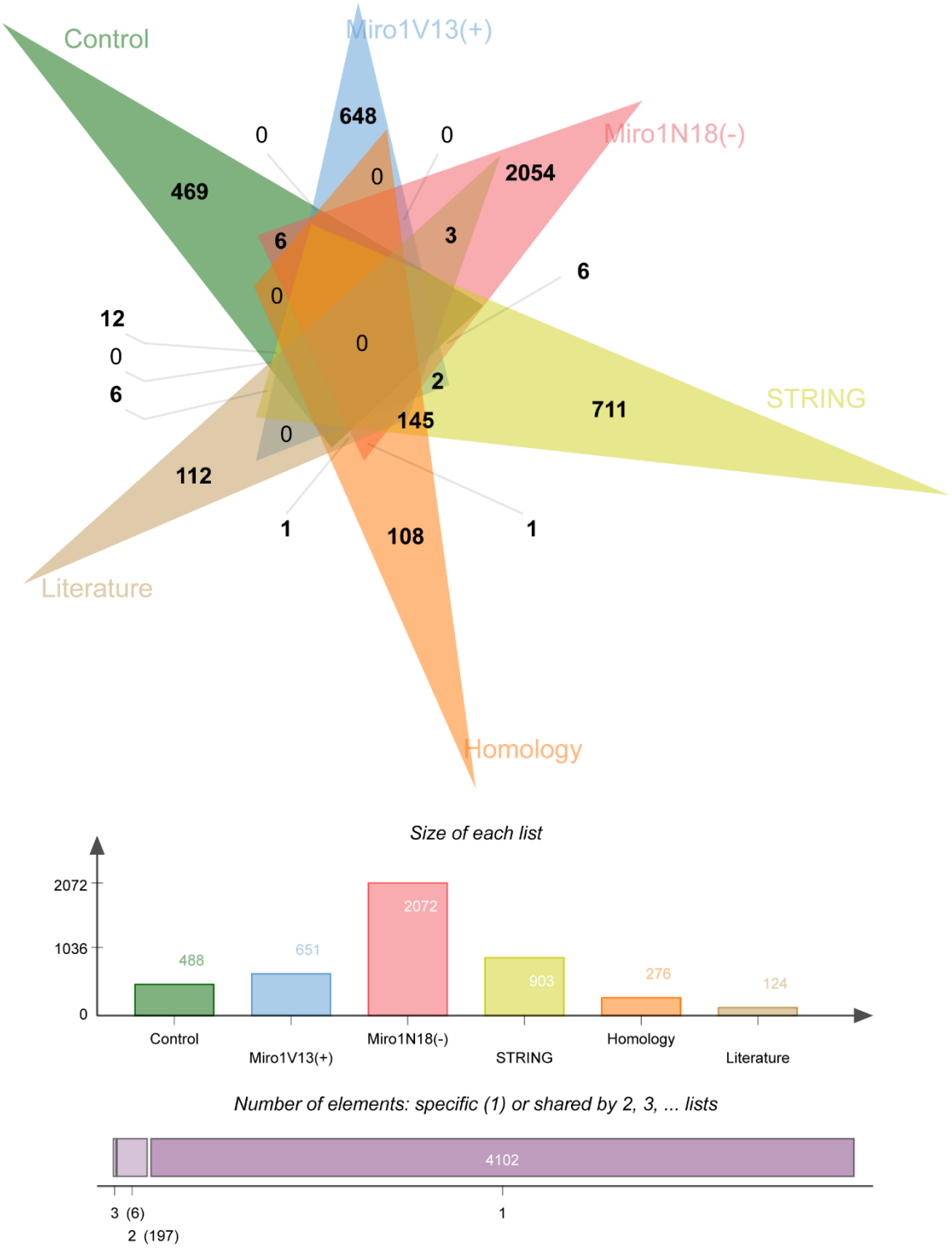

Figure 5.7. Number of hMiro1 proteins identified through proteomics endeavours, cross-checked against putative interactors identified by STRING, homology and literature searches.

Table 5.6. Identification of 13 proteins of interest associated with hMiro1 mutants. Proteins were identified through cross-referencing of experimental proteomics data with computer-based prediction methods. The condition in which each protein was uniquely present or enriched is shown, alongside a description of protein function. The STRING score provided reflects the combined STRING score when all STRING prediction and search methods are utilised, where ≥0.7 equates to high confidence and ≥0.9 equates to the highest STRING confidence.

Identifier	Protein function	STRING score
Miro1V13(+)/STRING		
GPAT, ATASE, PRAT	Regulatory allosteric enzyme; catalyses the first step of *de novo* purine nucleotide biosythetic pathway.	0.999
SUMO3, HSMT3, smt3A	Member of the small ubiquitin-related modifier (SUMO) family; becomes covalently conjugated to other proteins via post-translation sumolyation.	0.999
Miro1V13(+)/STRING/ Homology		
NEDD4-1, RPF1, KIAA0093	E3 ubiquitin protein ligase expressed in neuronal precursor cells; developmentally downregulated in the early central nervous system.	0.999
Miro1N18(-)/STRING		
EF2, EEF-2, SCA26, EF-2	Member of the GTP-binding translation elongation factor family; facilitates GTP-dependent ribosomal translocation during protein synthesis.	0.999
B-ALPHA-1, FLJ25113	Major microtubule component displaying enriched expression in morphologically differentiated neuronal cells.	0.986

Cortactin, EMS1	Promotes polymerisation and rearrangement of the actin cytoskeleton when stimulated by external stimuli.	0.985
RAB11A	Controls intracellular trafficking of the innate immune receptor TLR4. May facilitate protein trafficking. Associated with secretory pathways.	0.984
Nedd-8, NEDD-8	E3 ubiquitin protein ligase expressed in neuronal precursor cells; developmentally downregulated in the early central nervous system.	0.976
EPF5, E2EPF, E2-EPF	Ubiquitin conjugating enzyme E2 for targeting of proteins for proteasomal degradation.	0.973
Miro1N18(-)/Homology		
SMMHC, KIAA0866, AAT4, SMHC, FAA4	Myosin heavy chain 11; major contractile protein. Converts chemical energy into mechanical energy through ATP hydrolysis.	N/A
Miro1N18(-)/STRING/ Homology		
RhoC, ARHC, RHOH9	Stimulates reorganisation of the actin cytoskeleton and regulates cell shape, attachment, and motility.	0.973
PSMD4, pUB-R5, AF-1	Non-ATPase subunit of the 19S regulator lid of the 26S proteasome.	0.972
Miro1N18(-)/Literature		
Centromere protein F, PRO1779, CENPF	Protein that associates with the centromere-kinetochore complex; facilitates mitochondrial movement during cytokinesis.	N/A

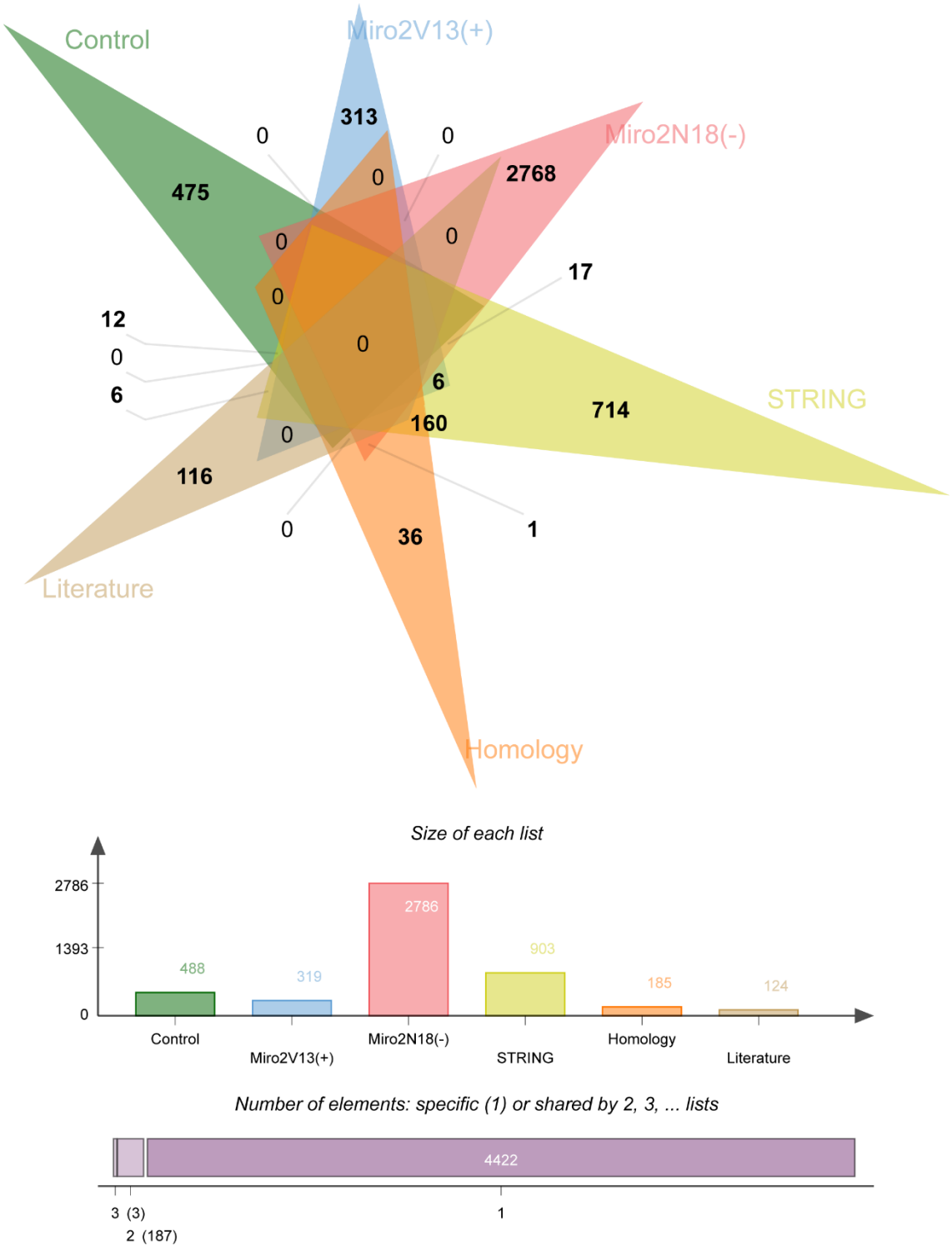

Figure 5.8. Number of hMiro2 proteins identified through proteomics endeavours, cross-checked against putative interactors identified by STRING, homology and literature searches.

Table 5.7. Identification of 24 proteins of interest related to hMiro2 signalling through cross-referencing of experimental proteomics data with computer-based prediction methods. The condition in which each protein was uniquely present or enriched is shown, alongside alternative identifiers for the protein and a description of the protein's known or putative function. The STRING score provided reflects the combined STRING score when all STRING prediction and search methods are utilised, with ≥0.7 representing 'high confidence' and ≥0.4 representing 'medium confidence'.

Identifier	**Protein function**	**STRING score**
Miro2V13(+)/STRING		0.999
PDHE1-B, PDHBD, PHE1B	E1 alpha 1 sub-unit of the pyruvate dehydrogenase (PDH) complex; catalyses overall conversion of pyruvate to acetyl-CoA and CO_2. Mutations in this gene are associated with pyruvate dehydrogenase E1-alpha deficiency and X-linked Leigh syndrome.	0.999
MC5DN4, COXPD22, ATP5A, ATPM, MOM2, OMR, hATP1, ATP5AL2, ORM, HEL-S-123m	ATP synthase, H+ transporting, mitochondrial F1 complex, alpha subunit 1; catalyses ATP synthesis during oxidative phosphorylation.	0.999
PSC5, HC5, PMSB1	Proteasome subunit beta 1. Component of the proteasome core; tightly linked to TBP (TATA-binding protein).	0.999
HDH-VIII, G3BP	G3BP stress granule assembly factor 1; facilitates DNA unwinding and acts as a signalling element of the Ras pathway, binding specifically to RasGAP.	0.999
S12, P40, MOV34, MOV34L, Rpn8	A non-ATPase subunit of the 19S proteasome regulator lid of the 26S proteasome complex.	0.999
EPS15R, eps15R	Epidermal growth factor receptor pathway substrate; constitutive component of clathrin-coated pits that is required for receptor-mediated endocytosis. Involved in cadherin binding associated with cell-cell adhesion.	0.999

Miro2N18(-)/STRING

S16	Ribosomal protein S16, a protein component of the 40S sub-unit.	0.999
ERO1LA, Ero1alpha, ERO1-L, ERO1-L-alpha, ERO1L, ERO1-alpha	Endoplasmic reticulum oxidoreductase 1 alpha; an oxidizing enzyme that exists in the endoplasmic reticulum and is induced under hypoxia.	0.962
EIEE31, DNM	Member of the dynamin subfamily of GTP-binding proteins, involved in tubulation and severing of membranes and associated with clathrin-mediated endocytosis and other vesicular trafficking processes.	0.942
HUWE1, KIAA1578, KIAA0312, MULE, LASU1, UREB1, URE-B1, Ib772, ARF-BP1, HECTH9, HSPC272	E3 ubiquitin ligase known to ubiquitinate the anti-apoptotic protein Mcl1 (myeloid cell leukemia sequence 1 (BCL2-related)). This protein also ubiquitinates the p53 tumor suppressor, core histones, and DNA polymerase beta.	0.9
VPS23, TSG10	Apparently inactive homolog of ubiquitin-conjugating enzymes. May act as a negative growth regulator. Appears important for genomic stability and cell cycle regulation.	0.867
PTPN1, PTP1B	A founding member of the protein tyrosine phosphatase (PTP) family. Catalyses the hydrolysis of the phosphate monoesters specifically on tyrosine residues.	0.818
hUba3, hUBA3, NAE2, UBE1C	Member of the E1 ubiquitin-activating enzyme family; associates with AppBp1, an amyloid beta precursor protein binding protein, to form a heterodimer, subsequently activating NEDD8, a ubiquitin-like protein, which regulates cell division, signalling and embryogenesis.	0.81
RAP1A, RAP1, SMGP21, C21KG, KREV-1, G-22K, KREV1	Counteracts the mitogenic function of RAS through its ability to interact with RAS GAPs and RAF in a competitive manner.	0.726
KIAA1794, FLJ10719	Fanconi anemia complementation group I, associated with Fanconi anaemia.	0.651
Active BCR-related, MDB	Contains a GTPase-activating protein domain; appears to play a role in vestibular morphogenesis.	0.472

UBCH7, E2-F1, L-UBC, UbcM4, UBCE7	Member of the E2 ubiquitin-conjugating enzyme family known to facilitate the ubiquitination of p53, c-Fos, and the NF-kB precursor p105 *in vitro*.	0.471
HEL-S-70p, PURH, AICAR, IMPCHASE, AICARFT	Acts as a 5-aminoimidazole-4-carboxamide ribonucleotide formyltransferase/IMP cyclohydrolase; enhances the rate of nucleotide re-synthesis, increasing adenosine generation from adenosine monophosphate during conditions of myocardial ischemia.	0.466
L23A, MDA20	Ribosomal protein L23a; may be one of the target proteins involved in mediating growth inhibition by interferon.	0.999
L10A, Csa-19, CSA19, NEDD6	Ribosomal protein downregulated in neural precursor cells during development.	0.999
Calnexin, CNX, IP90, P90	Calcium-binding, endoplasmic reticulum (ER)-associated protein; interacts transiently with newly synthesized N-linked glycoproteins, facilitating protein folding and assembly. Possible roles in facilitating protein folding and quality control.	0.999
PTER, HPHRP, RPR-1	Phosphotriesterase-related protein; may be involved in regulation of mitosis and transport of proteins to the cell surface.	0.774
CIP75, A1U, C1orf6, A1Up, UBIN	Ubiquilin 4; involved in regulation of protein degradation *via* the ubiquitin-proteasome system (UPS).	0.774
Miro2N18(-)/Homology		
CASP3, CPP32B, SCA-1, CPP32, Yama, apopain	Associated with apoptotitc signalling. Cleaves and activates caspases 6, 7 and 9. Is the principal caspase involved in the cleavage of amyloid-beta 4A precursor protein (a protein associated with neuronal death in Alzheimer's disease).	N/A

As shown in Figure 5.9, below, the majority of identified proteins exhibit functions that have been previously associated with the hMiro GTPases. A more detailed chart, displaying the function of proteins associated with either the V13 (constitutively active) or N18 (dominant negative) versions of hMiro1 and hMiro2 is provided on the following page as Figure 5.10.

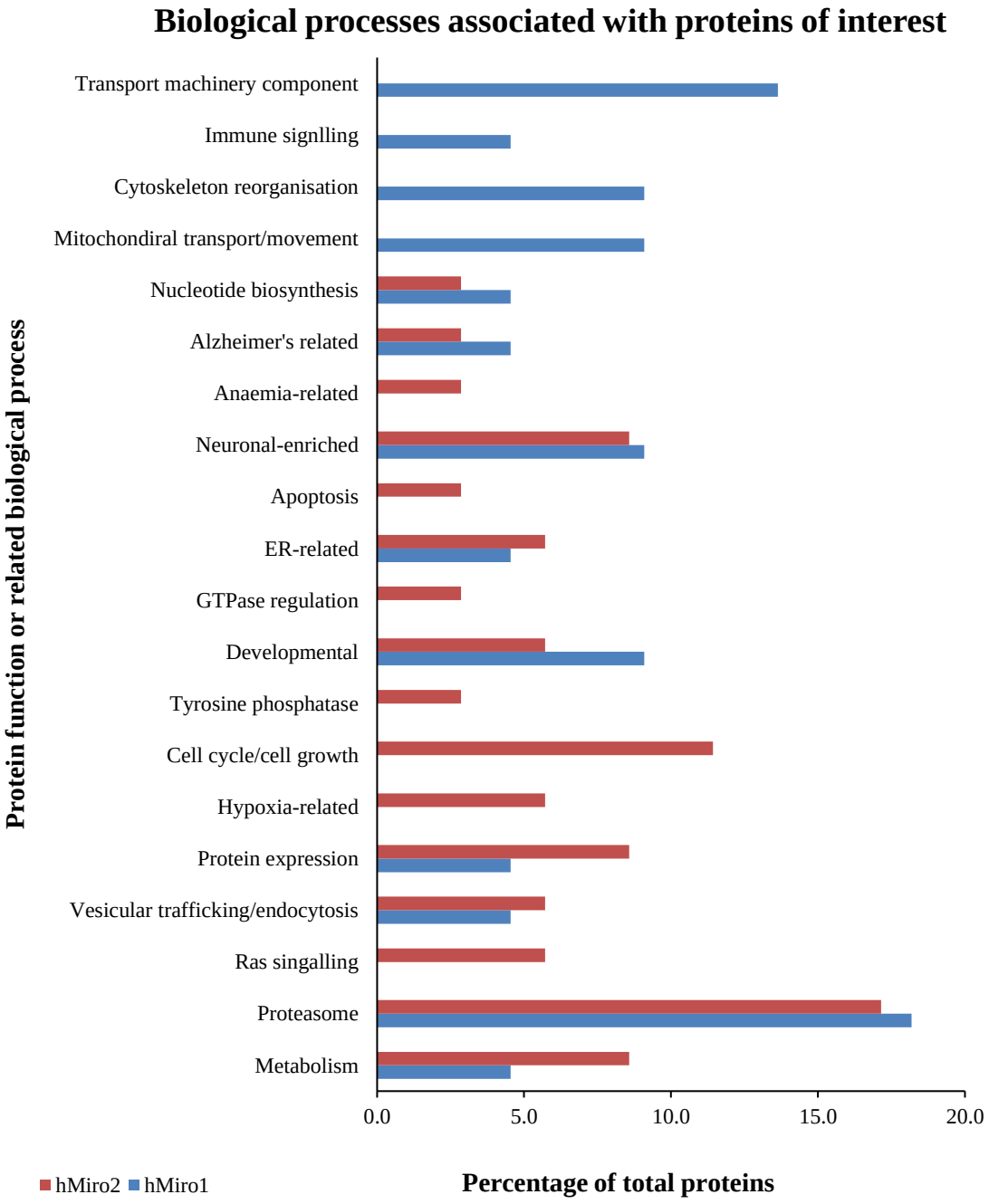

Figure 5.9. Major biological functions of the identified proteins of interest, shown as a percentage of the overall number of proteins for either hMiro1 or hMiro2.

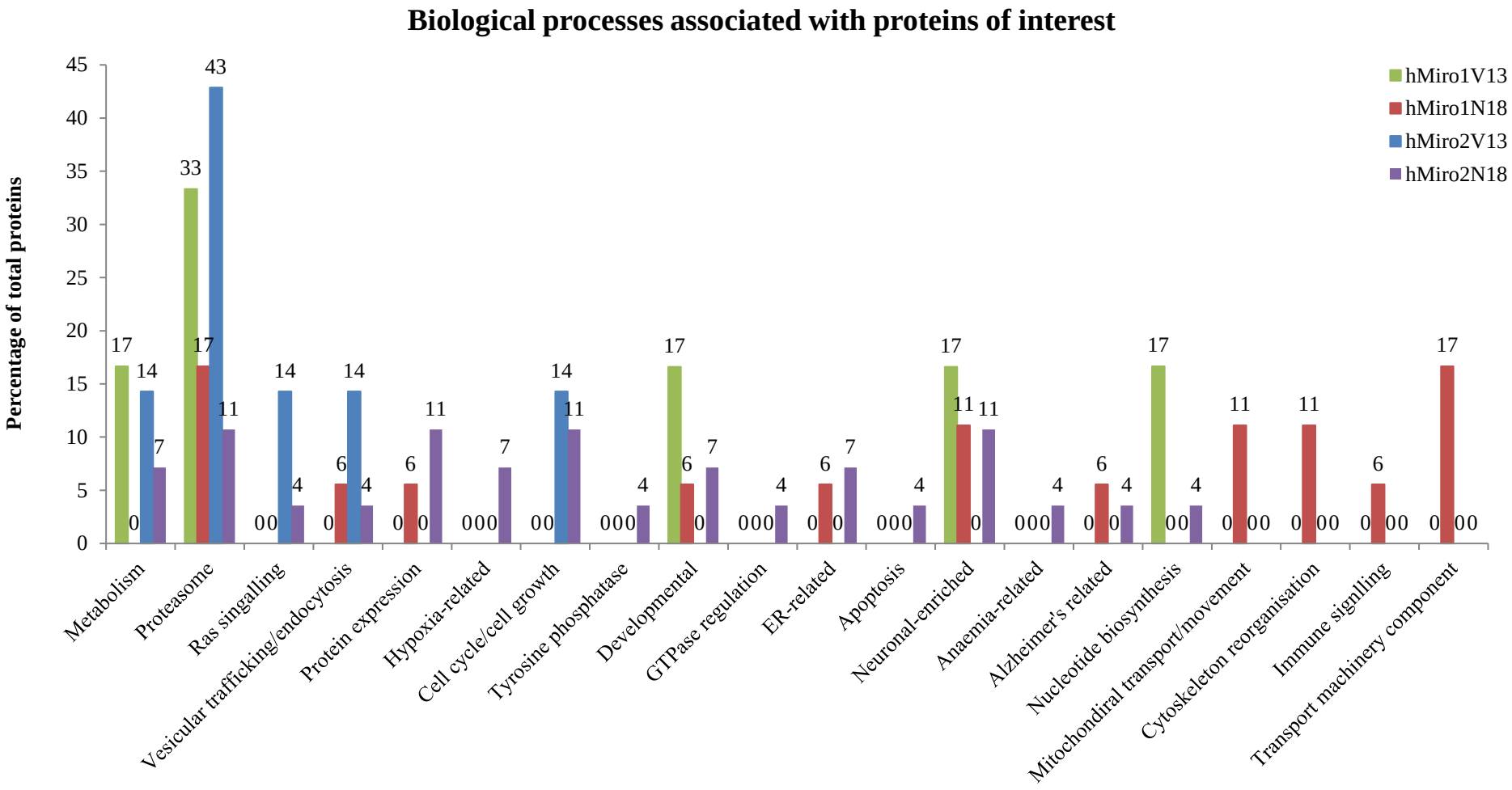

Figure 5.10 Summary of biological function(s) associated with the identified proteins of interest.

5.3 Discussion

5.3.1 Summary of results

Proteomics has become a powerful approach in recent years, providing greater detail on cellular function and interactions than genomics alone. Here, a number of promising putative interacting proteins for the hMiro GTPases were identified through cell biology and proteomics approaches. Interestingly, X!Tandem and MASCOT were found to identify a similar number of proteins. However, X!Tandem appeared to consistently identify slightly more proteins. Due to the challenges faced by technical issues throughout this study, the results obtained were cross-referenced against computer-based predictions of hMiro interactors to reduce noise and improve confidence in the results obtained. Proteomics data collected from over-expression of constitutively active and dominant negative N-terminal GTPase mutants for both hMiro1 and hMiro2 in COS-7 cells was compared, using cross-referencing of data from *in silico* prediction algorithms, manual literature searches and known interactors of the five closest homologues of hMiro1 and hMiro2, respectively. The majority of the proteins of interest showed a high confidence rating in STRING (≥0.7) alongside an enriched or unique expression pattern from the proteomics data, with 74% proteins exhibiting the highest STRING confidence values (≥0.9). Only 12% of proteins with a STRING score showed medium confidence (≥0.4). None of the proteins identified were classified as low confidence hits. Combined with experimental proteomics data, these matching computer-predicted interactors represent highly conceivable putative interacting proteins for the hMiro GTPases.

Overall, the results implicate several novel putative interaction partners for hMiro1 and hMiro2, with many interactors appearing to be influenced by the GTPase state of the hMiro1 or hMiro2 N-terminal GTPase domain. With the exception of the Fanconi anemia complementation group I protein and the nucleotide biosynthesis related proteins, all of the proteins of interest appear to be involved in biological processes that have been associated with hMiro1 or hMiro2 in the primary literature. Interestingly, only one of the proteins of interest (CenpF) has been definitively demonstrated in the literature as a binding partner of the hMiros, suggesting the possibility that other experimentally-validated interactors may not be influenced so readily by the status of the hMiro N-terminal GTPase domain.

5.3.2 Indicated differences between hMiro1 and hMiro2 signalling

Figure 5.9 suggests that hMiro1 plays major roles in signalling for mitochondrial transport and re-organisation of the actin cytoskeleton. Conversely, the results showed no obvious signs of this with hMiro2. Although hMiro2 has been previously shown to affect mitochondrial transport, prior studies indicate that hMiro2 influences mitochondrial transport and cell morphology to a much lesser extent than hMiro1; this trend is perhaps reflected in Figure 5.9 by the lack of candidate hMiro2 interactors associated with these functions. However, hMiro2 remains very poorly characterised in the literature, with its functions largely unknown. Correspondingly, the results shown here may represent a true indication of possible cellular functions that this enzyme participates in and regulates in humans. Closer analysis in Figure 5.10 suggests that the hMiro1 N-terminal GTPase domain is more likely to associate with proteins linked to mitochondrial transport and actin cytoskeleton re-organisation when this GTPase domain is GDP-bound: over-expression of the dominant negative hMiro1 mutant (N18) was associated with proteins of these functions, while over-expression of the constitutively active hMiro1 (V13) mutant was not. Furthermore, hMiro1 N18 experiments were associated with ER-related proteins, protein expression and endocytosis while hMiro V13 experiments were not. In fact, far fewer proteins of interest were identified for hMiro1 V13 conditions, amongst which: 33% were associated with proteasomal functions, 34% with neuronal or developmental functions, 17% with metabolism and 17% with nucleotide biosynthesis. A similar pattern is seen with hMiro2 V13, with 43% of the associated proteins linked to proteasomal degradation. This may indicate that the N-terminal GTPase domain in both hMiro1 and hMiro2 is targeted for degradation, or up-regulates proteasomal degradation, when GTP-bound, and that this mechanism may be associated with intracellular metabolism including ATP generation and nucleotide biosynthesis. Meanwhile, dominant negative (GDP-bound) hMiro appears to associated with a broader range of biological processes. Notably, however, unlike with hMiro1, proteins associated with endocytosis and cell cycle growth were present in hMiro2 V13 conditions. Overall, it appears that over-expression of dominant negative versions of the hMiro1 and hMiro2 N-terminal GTPase domain is associated with a wide range of biological processes, while over-expression of the constitutively active version is associated with a much smaller range of processes. This implies that the GTP-status of the hMiro1 and hMiro2 N-terminal GTPase domains are important for triggering intracellular signalling changes, and that discreet

changes in the status of this domain may serve to trigger events such as ubiquitination and proteasomal degradation.

5.3.3 Identified proteins of particular note

Of the proteins of interest identified, three were particularly noteworthy: RhoC, rUB-R5 and NEDD4. These proteins were identified as potential interactors across three separate search mechanisms, including experimental analysis, homology studies and the extensive database searches performed by STRING. NEDD4 was linked to hMiro1-V13 overexpression, while RhoC and PSMD4 were associated with hMiro1-N18 over-expression. All 3 of these proteins possessed functions that showed an enriched presence in the other proteins of interest, namely: reorganisation of the cytoskeleton (RhoC, NEDD4), neuronal cell involvement (NEDD4) and links to ubiquitin-mediated proteasomal degradation (NEDD4, PSMD4). However, it should be noted that further evidence is required to validate these proteins as true interactors of the hMiros; the following sections should be read in consideration of this.

5.3.3.1 Neuronal precursor developmentally downregulated (NEDD) proteins

Beyond NEDD4, several other neurone-related proteins identified were NEDD proteins (NEDD6, NEDD8) or proteins found to act within NEDD-related pathways (hUba3, Ras, AppB1). This implies a role for hMiros in neuronal signalling associated with proteins that are commonly downregulated in neuronal precursor cells. Intriguingly, NEDD4 was the only neurone-related protein to be associated with a V13 mutant; all of the other neuronally enriched proteins identified were associated with N18 hMiro mutants, suggesting that the status of the N-terminal GTPase domain is important in mediating neuronally-enriched signalling pathways. Indeed, while the NEDD proteins were originally identified as ‘neural precursor cell expressed, developmentally downregulated’ proteins, these proteins are frequently functionally diverse and do not necessarily occur within the same signalling pathways. Thus, while a GTP-bound version of the N-terminal GTPase domain may influence one pathway, a change of status to the GDP-bound version may influence another.

NEDD4 itself is classified as an E3 ubiquitin ligase localised to the cytoplasm, and has been demonstrated to mediate a range of important cellular processes including neuronal development, cellular growth and intracellular homeostasis (392). NEDD4 functions through ubiquitination ligase activity and other mechanisms which are not fully

understood. However, it has been established that NEDD4 can be activated by a variety of signalling molecules, and that auto-inhibition can occur in the absence of calcium (393). Intriguingly, all of the NEDD-related proteins are developmentally downregulated in neuronal cells and many appear to play roles in normal development of the nervous system (391). Similar functions have been noted for mammalian and fly Miro, with homozygous Miro1$^{-/-}$ ablation in mice resulting in dysfunctional neuronal developmental, most critically resulting in incomplete lung innervation (235). It is possible that the mammalian Miros may act within pathways that regulate NEDD4 activity, and that disruption of Miros during development prevents adequate downregulation of NEDD4 and other NEDD proteins. Conversely, a functional link between these proteins during development may not exist, and the hMiros could represent a ubiquitination target for NEDD4. Further experimental work is required to explore these possibilities. Curiously, NEDD4 has also been implicated in schizophrenia (394), a serious psychiatric condition commonly presenting with delusions, hallucinations and profound disturbances in cognition and emotion (395). This is in congruence with the hMiro1, which has been previously linked to schizophrenia through interaction with the DISC1 multifunctional scaffolding protein (231). Even more interestingly, DISC1 has been linked to stress-induced psychosis in schizophrenic individuals (396), a clinical feature that is presented more frequent in patients harbouring specific NEDD4 genotypes (394). It is therefore possible that these proteins act within the same, or related, signalling pathways.

NEDD4 may also fit into the presently elusive link between Miro proteins and cellular metabolism. Prior implications in the Miro GTPases with cellular metabolism have been limited to studies in yeast (160), so the presence of several proteins related to cellular metabolism is rather intriguing, suggesting that these roles for cellular metabolism may be conserved in higher organisms. Several of the proteins of interest identified were involved in cellular metabolism, and oxidative stress has been shown to activate NEDD4 in a pathway leading to the activation of transcription factors (397). One possibility is that signalling for excessive production of free radicals arising from oxidative metabolism occurs through Miro proteins to proteins such as NEDD4. However, this remains to be explored.

NEDD6 is perhaps less exciting. A ribosomal protein displaying developmental downregulation in neuronal precursor cells (398), NEDD6 presently appears to be involved in protein expression alone. NEDD8, however, represents an apparently multifunctional ubiquitin-like protein (ULP) sharing ~60% amino acid identity with

ubiquitin (399). appears to possess tumour suppressive roles (400) and has been reported in the literature as a regulator of caspase-1 (401). Additionally, NEDD8 has been shown to play crucial roles in endometrial function (402).

5.3.3.2 RhoC

The suggested link between RhoC and hMiro1-N18 is also interesting, fitting into the theme that dominant negative versions of the hMiro N-terminal GTPase domain are involved in a wider range of pathways than the constitutively active versions. Rho proteins are typically associated with cytoskeletal reorganisation, although the fine-tuning of RhoC activity appears to particularly influence cell motility (403). A link between RhoC signalling and the Miro GTPases therefore seems logical, in light of the cell migration results obtained in Chapter 4 and previous studies implicating the Miros in cell motility and migration. Due to the primary localisation of RhoC at the plasma membrane (7), it is unlikely that the Miros directly interact with RhoC. However, these results indicate that hMiro1 acts downstream of the RhoC pathway in a manner that may be related to the GTPase state of the N-terminal GTPase domain.

5.3.3.3 PSMD4 and proteasomal degradation signalling components

The notable presence of PSMD4 was initially somewhat puzzling, resisting the trend of hMiro V13 mutants being more likely to be associated with components of the proteasome complex. PSDM4 is an essential constituent of the 19S proteasomal regulatory complex (391,404), responsible for proteasome substrate recognition and known to play important roles in sperm-zona pellucida penetration during fertilisation (405). However, while this protein is related to the UBS, it is predominantly involved in ensuring that only correctly labelled (ubiquitinated) proteins are processed for degradation (391). No components of the UBS directly linked to actual degradation were associated with hMiro N18 mutants in this study, although several proteins related to ubiquitination or the sorting of ubiquitinated proteins were. Conversely, V13 mutants were associated with both ubiquitination proteins and, in the case of hMiro2-V13, components of the proteasome protein core directly involved in proteasomal degradation. Potentially, this could indicate that Miro proteins that are active in the N-terminal GTPase domain are more likely to be ubiquitinated and subsequently degraded by the UBS, while that Miro proteins that are inactive in this domain may still be ubiquitinated but are more likely to be thoroughly checked prior to degradation. This is conjecture, however. The targeting of proteins for proteasomal degradation is complex and influenced by several

signalling pathways. Thus, further investigation of the relationship between the Miro N-terminal GTPase state and propensity towards UBS-mediated degradation is required.

5.3.3.4 Proteins involved in endoplasmic reticulum signalling

Beyond RhoC, rUB-R5 and NEDD, the two hMiro2-N18 associated proteins linked to the endoplasmic reticulum (ERO1LA and calnexin), were particularly interesting. ERO1LA, also known as endoplasmic reticulum oxidoreductase 1, pairs oxidation of thiols to the reduction of molecular oxygen to produce hydrogen peroxide (H_2O_2) and has been implicated in cancer progression and immune signalling (406-408). ERO1LA has also been implicated in the regulation of Ca^{2+} fluxes at the interface between the endoplasmic reticulum and mitochondria (409). Conversely, calnexin is a calcium-binding protein localised to contact points between mitochondria and the endoplasmic reticulum, displaying roles either as a quality control chaperon (when non-palmitoylated) or a calcium signalling protein (when palmitoylated) (410). Interestingly, Miro proteins have been implicated in intracellular calcium buffering and have been shown to localise to ER-mitochondrial contact points. Additionally, the yeast Miro Gem1p interacts with the ER-mitochondria encounter structure (ERMES). While a direct association between Miro and ERMES in humans has not yet been established, the presence of Calnexin and another ER-related protein, ERO1A, in this study is noteworthy, suggesting that the hMiros indeed interact with ERMES-like proteins at ER-mitochondria contact points (189,216). Other notable groups of proteins identified in this study included proteins related to protein expression, which were enriched across various data sources and may indicate that regulation of the hMiro signalling pathways occurs, at least partly, at the level of expression. Whether the Miro proteins themselves are significantly regulated at the level of expression is unknown, though this phenomenon has been demonstrated for other atypical GTPases, such as the Rnd proteins and RhoH (30).

5.3.3.5 Proteins associated with neurodegeneration

Finally, the presence of several Alzheimer's and cancer related proteins identified in this study are noteworthy. The Miro GTPases have been implicated in both neurodegenerative diseases and neoplastic disorders when dysregulated. According to the results obtained here, the development of these disorders may occur in some situations through the GTPase status of the hMiro N-terminal GTPase domain. It is uncertain why an enrichment in Alzheimer's related proteins was demonstrated, but not other proteins associated with neurological disorders. While Miro inhibition has been linked to Alzheimer's through

activation of the PAR-1/MARK family kinases and subsequent promotion of pathological tau phosphorylation (23), links to other neurological disorders such as Parkinson's and ALS are repeatedly noted in the literature. The enhanced presence of Alzheimer's-related proteins here, however, may partly reflect that Alzheimer's is the most common form of dementia (411) and correspondingly heavily researched. Thus, proteins implicated to Alzheimer's are more likely to be labelled as such in the literature. Regardless, the presence of proteins implicated in neoplasia and Alzheimer's disease is in congruence with previous reports of Miro function and the development of these pathologies. Too, it is quite possible that some proteins considered 'Alzheimer's-related' actually engage in other neuropathological states when dysregulated (412).

5.4 Conclusions

The results obtained in this study suggest several novel putative components of Miro-related signalling pathways. These findings were generally in congruence with prior experimental reports, or otherwise reinforced hypothesised functional roles for the hMiros. There is strong evidence in this study for neuronally enriched functions for the hMiros, particularly with regards to Miro signalling within NEDD-related pathways. This may also indicate critical involvement for the hMiros in the developing nervous system, a functional role that has only been partially explored in mice and Drosophila. Distinct interactors or signalling pathways may be associated with the state of the N-terminal GTPase state in the hMiros, with an active N-terminal GTPase state seemingly more likely to result in increased UBS-mediated degradation. However, although this study indicated several interesting trends, themes and putative interactors, further experimental evidence is desirable to validate these results and fully explore the functional consequences of changes to these putative interactors on Miro function *in vivo*.

Chapter 6: characterisation of the atypical GTPase human RhoH

6.1 Introduction

6.1.1 Objectives

The main objective of the work undertaken in this chapter was to characterise the highly atypical GTPase human RhoH, using techniques established in earlier work for use in characterising the human Miro GTPases. An enhanced knowledge and practical ability of these techniques guided the development of this chapter.

6.1.2 RhoH at a glance

RhoH, also known as translocation three four (TTF), is a highly atypical member of the Rho GTPase family that was first identified as a fusion partner with the *LAZ3*/*BCL-6* gene, a gene commonly disrupted in B-diffuse large cell non-Hodgkin's lymphoma (413). This indicated a medical relevance for RhoH, further reinforced by the observation that disruptions in the *RhoH* gene are associated with specific types of lymphomas and multiple myeloma (414-416). RhoH predominantly exhibits haematopoietic expression, including bone marrow progenitor cells in addition of differentiated lymphoid and myeloid cells (142,413,417), but has also been detected in various tissue samples from normal individuals including breast, pancreas and liver tissue (418,419). Amongst haematopoietic cells, RhoH displays varied expression even within cell type sub-populations (417). For example, higher levels of RhoH are seen in type I helper T cells relative to the type II sub-population (420). Additionally, high levels of RhoH are shown in lymphoid-originating cells relative to primitive progenitor cells and myeloid lineages (417,420,421).

RhoH is highly atypical structurally and functionally, performing unexpected roles for a Rho family enzyme. Perhaps most remarkably, RhoH is unable to hydrolyse GTP (420). The protein remains in the active GTP-bound state as a result of mutations in glycine-12 and glutamine-61 (420), residues normally involved in nucleotide binding in classical Rho GTPases. Furthermore, in contrast to the typical scheme of regulation for Ras superfamily GTPases, RhoH appears to be primarily regulated at the level of transcription: T-cell signalling has been shown to transcriptionally alter RhoH expression (420), while PMA-treated Jurkat cells consistently showed down-regulation of RhoH mRNA (420). Regulation also appears to occur through lysosomal degradation (422),

phosphorylation (423), and through the action of other GTPases. Functionally, RhoH is currently believed to act as an antagonist for many classical members of the Rho family (420). Notably, implications of aberrant RhoH in a variety of blood cancers (31,33,413-416,424-426), including chronic lymphocytic leukaemia (CLL) (32,33,427), have presented this unusual GTPase as a protein of great clinical relevance.

6.1.3 RhoH domain architecture

RhoH has not yet been successfully crystallised, therefore a definitive structure is not available. However, the amino acid composition of wildtype RhoH in *Homo sapiens* and several other species is known, making it possible to assess this sequence in comparison to other small GTPases of interest, including the classical Rho GTPases. A schematic diagram of putative RhoH molecular structure is provided in the form of Figure 6.1, below. This original figure was produced *via* study of the amino acid composition of human RhoH and information provided in the scientific literature. A comprehensive assessment of the 191 amino acid human RhoH sequence in comparison to the classical Rho GTPases RhoA, Rac1 and Cdc42 (the closest classical homologue to RhoH) is additionally provided in the form of Figure 6.2, allowing for the illustrative comparison of RhoH primary structure against that of canonical GTPases of the Rho family.

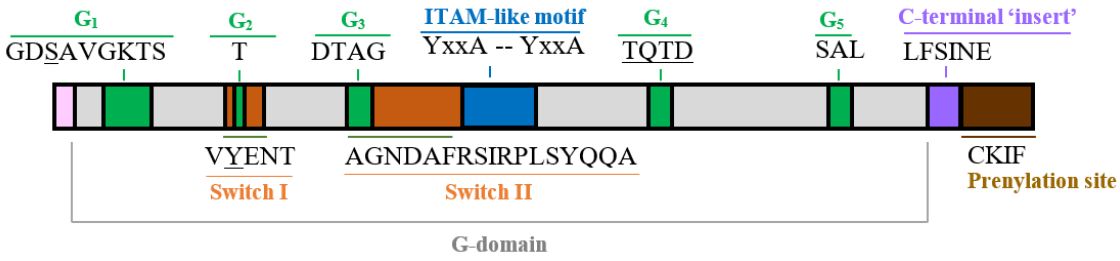

Figure 6.1 Schematic diagram of putative RhoH domain architecture. Original diagram produced by assessment of the literature pertaining to RhoH and a comparison of the secondary structure of human RhoH against other human GTPases of the Rho family. Note that underlined residues indicate areas that appear strikingly different when compared to comparative residues in canonical Rho GTPases. For example, the serine (S) underlined in the G_1 box is highly atypical for Rho GTPases, inferring an inability for RhoH to hydrolyse GTP

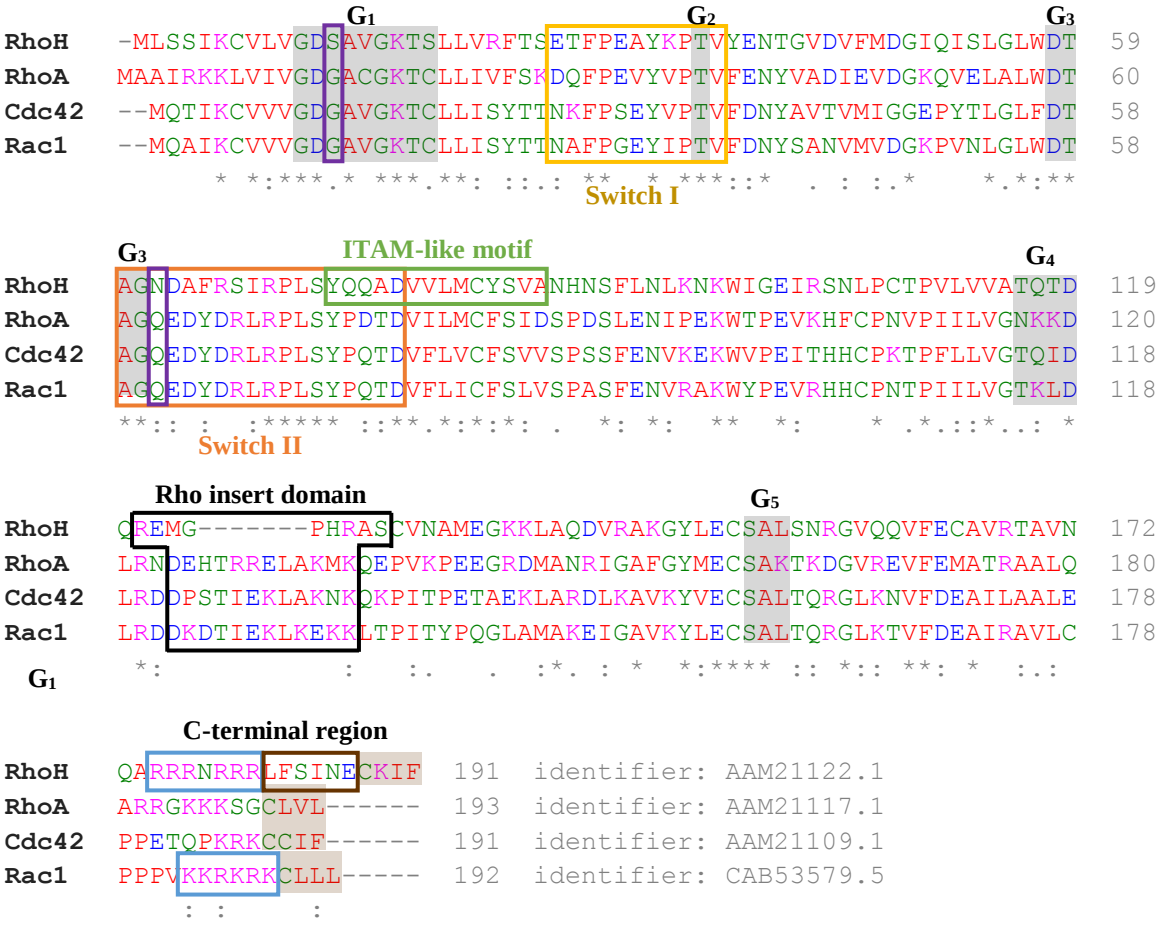

Figure 6.2 Comparison of RhoH secondary structure against the canonical Rho GTPases Rac1, RhoA and Cdc42. Annotated CLUSTAL OMEGA alignment of the amino acid composition of the human homologues of RhoH, RhoA, Cdc42 and Rac1. Asterisks (*) specify positions in which single, fully conserved residues are present, while colons (:) denote the conservation of residues with strongly similar properties. Periods (.) specify conservation of residues with weakly similar properties. Colour coding is used to represent the properties of each residue, where red denotes small and hydrophobic residues, blue denotes acidic residues, magenta denotes basic residues, green denotes residues bearing hydroxyl, sulphydryl or amine groups and grey represents unusual amino acid residues. G loops are shaded in grey and marked, while the prenylation (CAAX motif) of each protein is shaded grey-brown. Other domains are shown in transparent boxed outlined in black (Rho insert domain), yellow (switch I region), orange (switch II region), green (ITAM-like motif), blue (polybasic C-terminal region) or brown (LFSINE motif). Identifiers for each protein are provided at the end of each sequence.

As shown in Figure 6.2, several residues in the RhoH primary structure differ largely from those seen in classical Rho proteins. For ease of discussion, the main differences

between RhoH primary structure and that of classical Rho GTPases are shown in Table 6.1, below. These differences are subsequently discussed in turn, below.

Table 6.1. Main differences between RhoH and its closest classical Rho GTPase homologue, Cdc42. Consensus residues for notable regions in typical Ras and Rho GTPases are shown, alongside corresponding residues in RhoH and its closest homologue, Cdc42.

Feature	Consensus residues	Residues in RhoH	Residues in Cdc42 (closest RhoH homologue)
G_1	$G_{10}xxxxGK[S/T]_{17}$	$G_{11}DSAVGKT_{18}$	$G_{10}DGAVGKT_{17}$
G_2	T_{35}	T_{36}	T_{35}
G_3 and Q_{61}	$D_{57}xxGQ_{61}$	$D_{58}TAGN_{62}$	$D_{57}TAGQ_{61}$
ITAM-motif	$Yxx I/Lx_{6-12}YxxI/L$	$Y_{73}QQADVVLMCY_{83}$	----------
G_4	$[N/T]_{116}KxD_{119}$	$T_{116}QTD_{119}$	$T_{115}QID_{118}$
Rho insert	-------	$R_{121}EMGPHRAS_{129}$	$D_{122}PSTIEKLAKNK_{133}$
G_5	$[S/C]_{145}A[L/T/K]_{147}$	$S_{152}AL_{154}$	$S_{158}AL_{160}$
Polybasic region	-------	$R_{175}RRNRRR_{181}$	$K_{183}KRKRK_{188}$*
C-terminal region	------	$L_{182}FSINE_{187}$	------
CaaX box	$C_{188}aaX_{191}$	$C_{188}KIF_{191}$	$C_{188}CIF_{191}$

* signifies residues in Rac1, as Cdc42 does not possess a polybasic C-terminal domain.

Differences in normally well-conserved residues are thought to produce the constitutively active nature of RhoH. For example, the presence of a serine (S) at position 12 in place of a usually strongly conserved glycine (G) is thought to render RhoH GTPase-deficient through steric interference of GAP enzymes (58,428). Glycine-12 is an essential residue of the phosphate binding loop in canonical Rho and Ras proteins (2,58,428), and as shown in Figure 6.3, the additional steric bulk associated with side chains other than glycine's single hydrogen appears to obstruct the space normally required for the efficient activity of GAP regulatory enzymes (59,429).

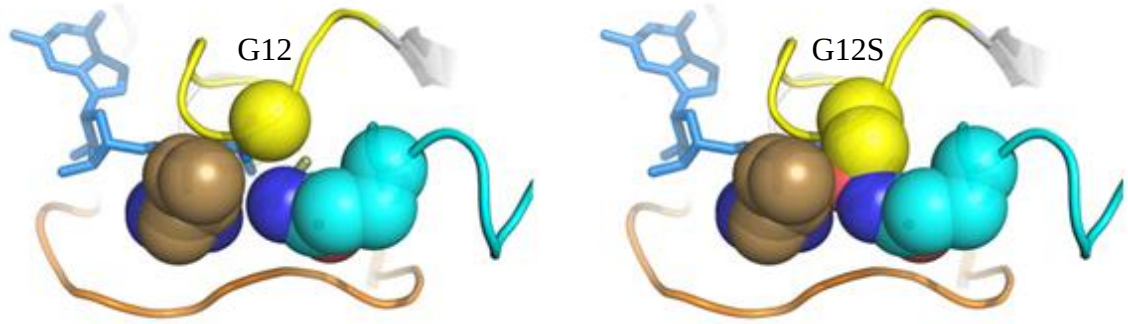

Figure 6.3. Substitution of Glycine-12 in Rho and Ras superfamily enzymes results in steric hindrance of GAP. Schematic illustration showing steric occlusion of the GAP arginine finger (brown) from the Ras/Rho nucleotide binding site when Glycine-12 is substituted for serine. Figure adopted from Mishra *et al.* (430).

Beyond Glycine-12, another canonically essential residue for GTP hydrolysis is the highly conserved glutamine (Q) typically found at position 61, which is absent in RhoH and instead replaced by asparagine (N) (Figure 6.2; Table 6.1). Glutamine-61 is thought predominantly to stabilise GAP interactions with Ras superfamily, at least partially through organisation with the GAP R789 arginine finger (58). As shown in Figure 6.4, the arginine finger provided by GAP interacts with the α- and γ-phosphates GTP, while the side chain carbonyl group of Glutamine-61 interacts with the catalytic H_2O molecule (58,302). The stabilisation provided by the arginine finger enables the Glutamine-61 residue to extract a hydrogen atom from the H_2O, resulting in a negative hydroxyl ion (OH^-) capable of attacking the GTP γ-phosphate and thus resulting in GAP-mediated GTP hydrolysis (58,302). Glutamine-61 mutations in Ras have also been shown to alter the switch II region, producing a network of hydrophobic interactions that serve to bury the

guanine nucleotide and an essential pre-catalytic water molecule, with this water molecule and a Tyrosine-32 normally binding γ-phosphate in wildtype proteins for participation in basal GTP hydrolysis (431). These critical substitutions of residues 12 and 61, normally highly engaged in the canonical GAP-mediated GTP-hydrolytic mechanism, are believed to play a central role in the apparent inability of RhoH to hydrolyse GTP, rendering the enzyme constitutively active (123).

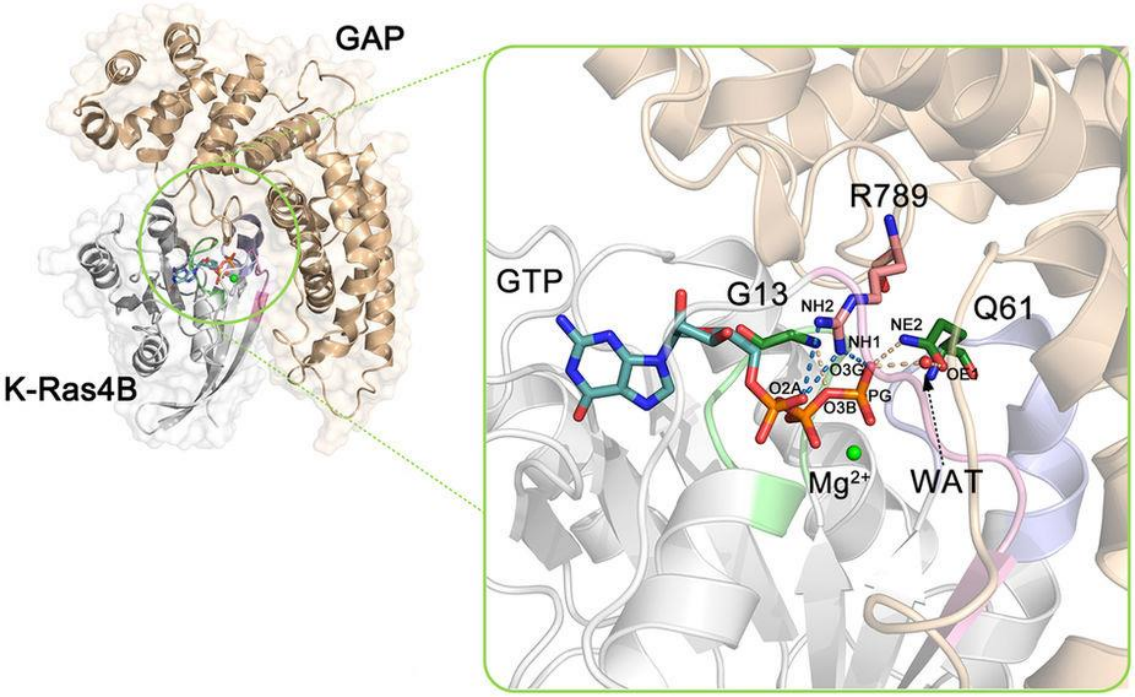

Figure 6.4. The role of Ras/Rho Glutamine-61 and the GAP arginine finger in GAP-mediated GTP hydrolysis. Illustration adopted from Lu *et al*. (58), showing interaction of the GAP arginine finger with the α- and γ-phosphates GTP, enabling Glutamine-61 to prepare the catalytic H_2O molecule (WAT) for the nucleophilic attack of the GTP γ-phosphate.

Although RhoH displays critical substitutions of the normally highly conserved Glycine-12 and Glutamine-61, the other G loop regions appear to be relatively conserved, with the highly conserved G_2 loop Threonine-35 intact (at position 36 in RhoH) and the G_3 (residues 58–61), G_4 (residues 116–119) and G_5 (residues 152–154) loops adhering to consensus sequences for typical Ras and Rho GTPases (see Table 6.1). In congruence with classical Rho GTPases, RhoH also contains a C-terminal 'CaaX' box beginning at position 188; the CaaX box comprises a conserved domain in Ras and Rho GTPases, necessary for intracellular localisation to the plasma membrane (2,63). In RhoH, this

'CaaX' motif is represented by the CKIF tetrapeptide at the C-terminus (residues 188–191), with RhoH localisation to the plasma membrane disrupted upon CKIF deletion (432). In addition to this CKIF localisation motif, RhoH exhibits a polybasic RRRNRRR (residues 175–181) domain followed by a novel C-terminal insert domain, LFSINE (residues 182–187); both of these domains have been specified in Figure 6.2 and Table 6.1. In the classical Rho protein Rac1, a similar polybasic domain to RRRNRRR is present (residues 183–188, see Figure 6.2) and appears to be involved in targeting Rac1 to specific membrane domains such as lipid rafts (433). Indeed, RRRNRRR ablation in RhoH significantly disrupts localisation to the plasma membrane (432). This effect was also seen with deletion of the LFSINE domain, with LFSINE removal shown to produce significant accumulation of RhoH in the cytoplasm (434). Interestingly, the LFSINE domain appeared to be necessary for the lysosomal uptake and degradation of RhoH by chaperone-mediated autophagy (CMA), with LFSINE-deficient RhoH exhibiting resistance to CMA (435). No impairment or enhancement of RhoH function was seen when the LFSINE domain was ablated, however, indicating that this domain is involved in RhoH stability and regulation but does not directly affect normal RhoH function (435).

RhoH also contains a small Rho insert domain (residues 121–129; Figure 6.2). The Rho insert domain is a surface-exposed alpha helical domain specific to the Rho GTPase family and typically composed of 13 amino acid residues between the fifth β-strand and fourth α-helix (7). In some Rho GTPases, this Rho insert domain has been demonstrated to be involved in Rho protein functionality and the binding of Rho-specific effector proteins (436-438). In RhoH, however, this Rho 'insert domain' is relatively small and does not contain the expected residues for such a domain (7,436). At present, relatively little is known of this domain, though it generally remains considered a 'Rho insert' domain (7).

Another unique aspect of the RhoH primary structure is the presence of a motif resembling the immunoreceptor tyrosine based activation motif (ITAM). ITAM motifs ($YxxI/Lx_{6\text{-}12}YxxI/L$) were initially observed on cytoplasmic subunits associated with the T and B cell antigen receptors in addition to the FcεRI receptor (439,440). Signalling through receptors containing ITAMs *via* tyrosine phopshorylation is involved in the activation of several cellular processes, including degranulation, phagocytosis and antibody-dependent cell-mediated cytotoxicity (441). It was previously believed that signalling through ITAM predominantly involved activation events, so-called

immunoreceptor tyrosine based inhibition motifs (ITIMs) mediated inhibitory events (442); ITIMs harbour the following consensus sequence: S/I/V/LxYxxI/V/L (443). However, it is now apparent that the situation is more complex. In some contexts, ITAMs can modulate inhibitory signals while ITIMs can mediate activation signals (444). Furthermore, several ITAM-encoding proteins appear to contain potential 'closet' ITIM-associated areas within the ITAM motif (444). The consensus sequence for an ITAM (YxxI/Lx_{6-12}YxxI/L) differs from that seen in RhoH (YxxA/$_{x6}$/YxxA). Furthermore, the RhoH ITAM-like motif appears to comprise a non-exposed beta sheet, with the initial tyrosine residue (Y) locked within a hydrophobic core; unless RhoH is able to undergo a conformational change enabling exposure of this region, it is difficult to envision many meaningful interactions of this ITAM-like motif with effectors. Despite these differences, however, previous studies have indicated that the RhoH ITAM-like motif is able to bind effectors upon phosphorylation of its tyrosine residues, much like canonical ITAM motifs (445,446). Furthermore, when phosphorylated at the ITAM-like region, RhoH appears to bind some traditional ITAM effectors such as Zap-70 (447-450).

6.1.4 RhoH function

6.1.4.1 RhoH as an antagonist of classical Rho family GTPases

RhoH is functionally diverse to classical Rho GTPases, and is presently thought to act as an antagonist of traditional Rho proteins (421,445). Rho proteins are typically involved in the regulating actin cytoskeleton reorganisation (451). In non-haematopoietic cells, RhoH did not appear to significantly influence re-organisation of the actin cytoskeleton or meaningfully impact cell morphology (420). Furthermore, while Rho-related proteins typically act as potent activators of several transcriptional pathways (452-454), RhoH has been shown to inhibit p38-MAPK and NF-κB activation (420). Indeed, RhoH specifically inhibits the Cdc42, Rac1 or RhoA-induced activation of NF-κB (420), and RhoH over-expression appears to decrease Rac1 activation (432). The consequences of these effects are seen in RhoH over-expression and ablation studies in haematopoietic stem cells (HSCs) (417). Increased RhoH expression levels in HSCs resulted in impaired activation of Rac GTPases, reduced cellular proliferation and chemotaxis, increased apoptosis and defective actin polymerisation (417). Defective haematopoietic reconstitution in transplant assays is also demonstrated in the context of RhoH overexpression (417). In contrast, suppression of RhoH encourages proliferation, survival and stroma cell-derived

factor 1 (SDF-1)-induced migration in HSCs (417) in part through activity of traditional Rho proteins. Thus, RhoH acts as an antagonist of several classical Rho proteins.

6.1.4.2 RhoH in T-cell biology

RhoH plays important roles in T-cell development through regulation of T-cell receptor (TCR) signalling (446,455-457). This important regulatory activity is thought predominantly to occur through RhoH's interactions with zeta-chain-associated protein kinase 70 (Zap70) (446), a Syk-family protein tyrosine kinase (PTK) normally present in the cytoplasm but required at the plasma membrane for its TCR signalling-related functions (458). Immunoprecipitation experiments and *in vitro* binding demonstrated that the tandem SH2 domains in Zap70 bind to the ITAM-like motifs in RhoH when the tyrosine residues of these motifs are phosphorylated, and that RhoH is required for Zap70 recruitment to the cytoplasm and immunological synapse (446,455). As shown schematically in Figure 6.5, Zap70 delivers critical roles in T cell biology, while RhoH dysfunction or ablation produces similar effects.

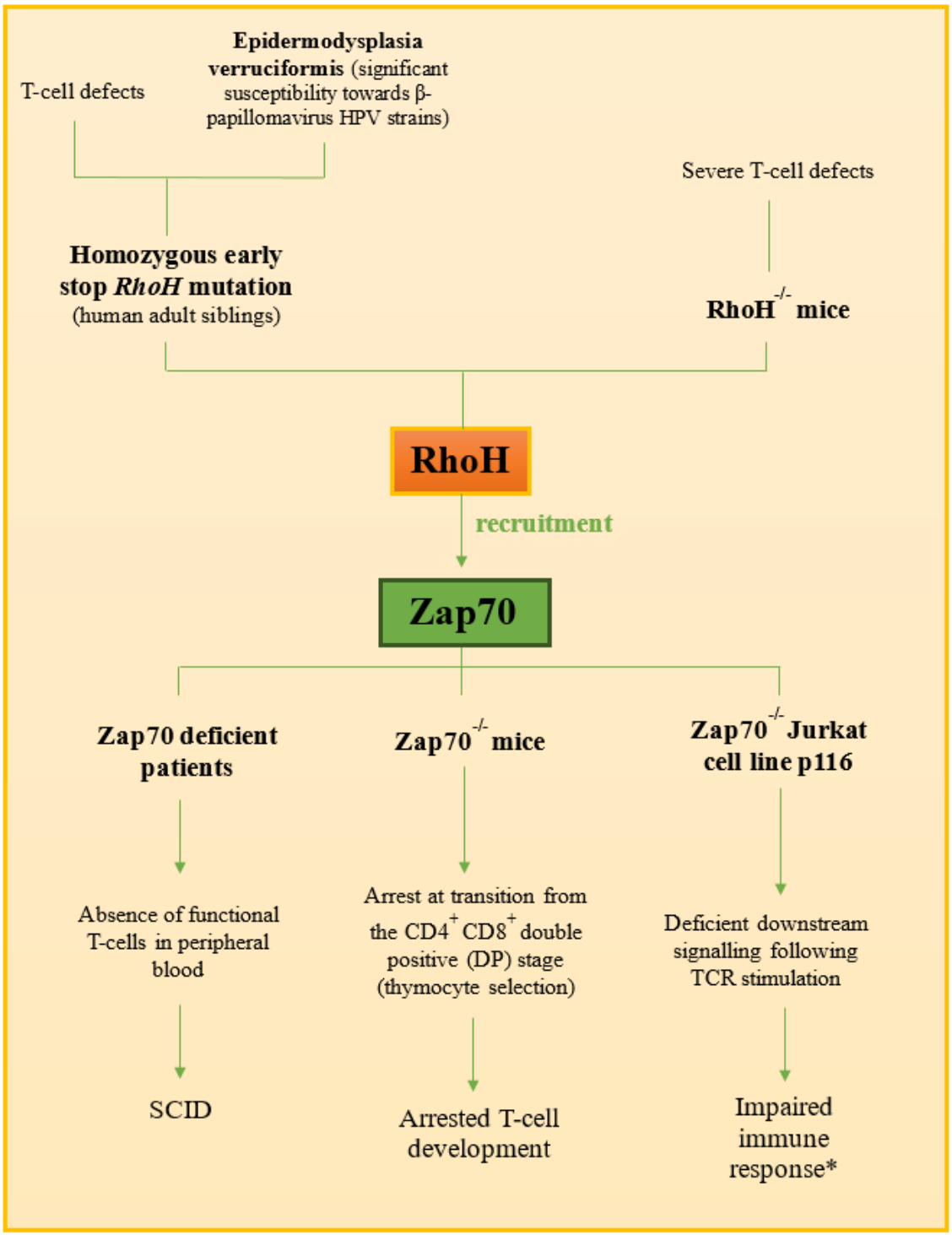

Figure 6.5 RhoH acts upstream of Zap70 to mediate T cell function. References as follows: Homozygous RhoH mutation (459), $RhoH^{-/-}$ mice (459), Zap70 deficient patients (53)(460-462), $Zap70^{-/-}$ mice (463,464), $Zap70^{-/-}$ Jurkat cell line p116 (465). *Note that impaired immune response is inferred from cell line study, here. (43)(54)(61)(54)

Indeed, one can infer that RhoH mediates important roles in T cell biology through recruitment of Zap70. Perhaps most significantly, RhoH appears to regulate the selection and maturation of lymphocytes (455), and has previously been implicated as a central signalling molecule in maintaining lymphocytes in their resting state (466). As shown in Figure 6.5, interruption of RhoH signalling is capable of producing severe T-cell defects and, consequently, impaired immunity (459-465).

Following activation of the T-cell receptor (TCR), RhoH recruitment of Zap70 is believed to enable Zap70-mediated phosphorylation of the linker of activated T-cells (LAT). LAT, in turn, activates the "LAT signalosome" (455), facilitating signalling through the TCR *via* recruitment of multiple adaptor proteins and activation downstream signalling events (467). RhoH abrogation appears to significantly impair phosphorylation of LAT and the LAT-associated proteins Vav1 and PLCγ1 (455). Furthermore, activation of Erk and calcium influx, downstream of PLCγ1, appear dramatically diminished in RhoH-depleted thymocytes (455,468). This indicates that RhoH specifically interferes with the LAT-associated branch of Zap70 signalling. Another enzyme of note, however, is the Src-family tyrosine kinase Lck. Lck significantly enhances the interaction between RhoH and Zap70 SH2 domains (423). Additionally, a schematic illustration of RhoH-related signalling in T-cells is provided as Figure 6.6.

Table 6.2. Downstream targets of Zap70 tyrosine phosphorylation that are compromised in the absence of RhoH.

Abbreviation	Full identifier	Function (when activated by phosphorylation)
LAT	Linker of activated T-cells	Recruits multiple adaptor and signalling proteins to form a signalling complex near the T-cell receptor engagement site (467)
PLCγ1	Phospholipase C γ1	Catalyses hydrolysis of phosphatidylinositol 4,5-bisphosphate (PIP2) to inositol 1, 4, 5-trisphosphate (IP3) and diacylglycerol (DAG). Increase of IP3 results in elevated intracellular free Ca^{2+} (469)
Vav1	Vav1	Haematopoiesis and activation of T and B cells (470)

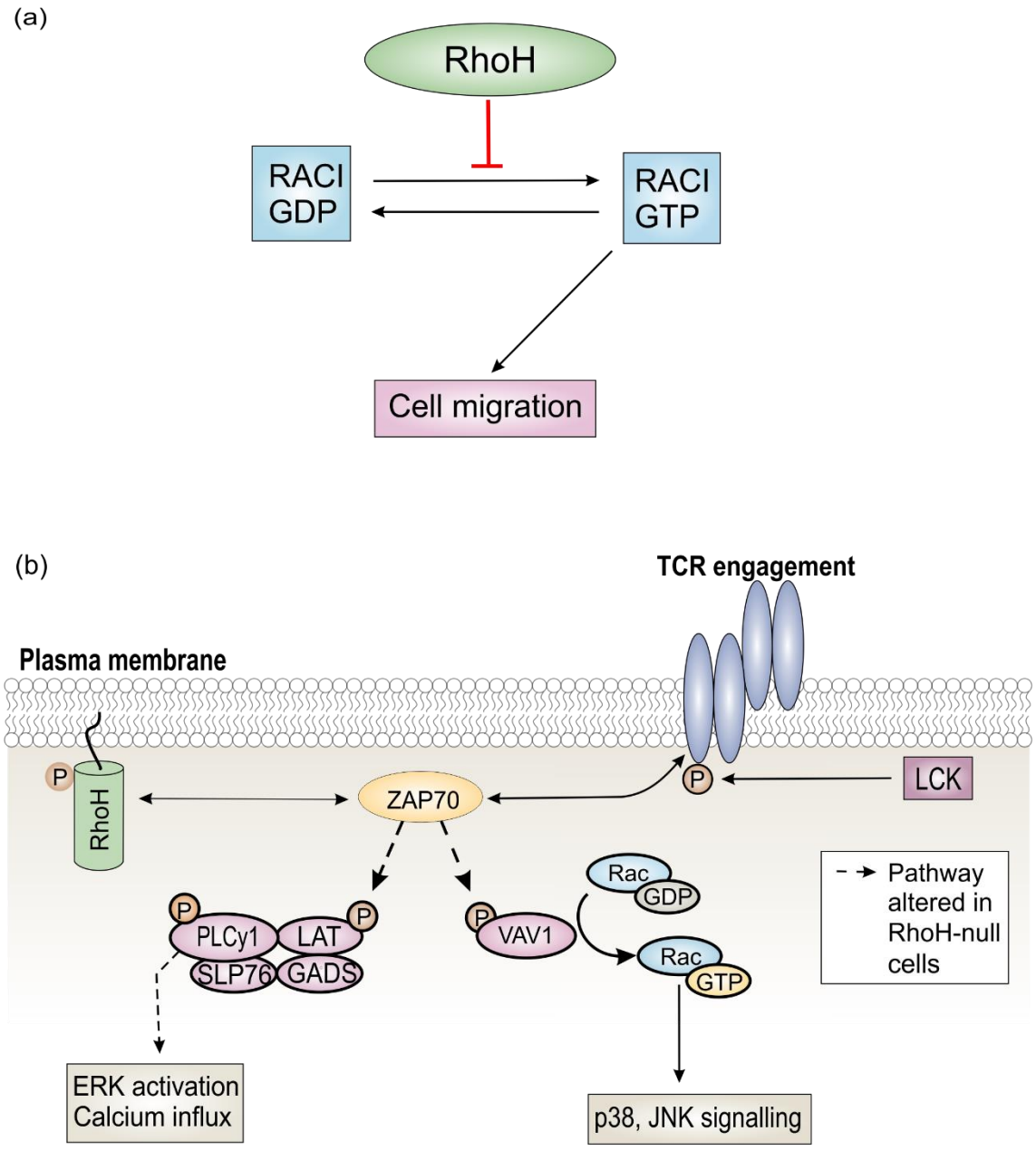

Figure 6.6. Summary of known RhoH interactions in T-cell biology. (a) RhoH inhibits Rac1 and other classical Rho family GTPases. **(b)** T-cell receptor (TCR) engagement activates Lck. Lck-mediated phosphorylation of cluster of differentiation-3zeta (CD3zeta) subsequently serves as a docking site Zap70. The resulting downstream signalling from activated ZaP70 includes phosphorylation of the adaptor protein LAT (linker for activation of T cells) and phospholipase Cgamma1 (PLCgamma1) and can produce a variety of responses, cell proliferation, calcium influx and changes in gene expression. RhoH interacts with Zap70, and this interaction is enhanced in the presence of Lck. RhoH is required for recruitment of Zap70 to the TCR and subsequent downstream signalling of Zap70 following TCR engagement. Other proteins shown: GADS, GRB2-related adaptor downstream of Shc; JNK, Jun N-terminal kinase; SLP76, SH2 domain-containing leukocyte protein of 76 kDa. Figure obtained from literature (423).

Beyond the proteins described in Table 6.2, a non-biased large scale proteomic analysis of tyrosine phosphorylation events induced by T-cell and B-cell receptor activation showed that RhoH interacts with protein tyrosine kinases Syk and Zap70 in addition to phospholipase Cγ2 (PLCγ2) (471). While Zap70 has been extensively linked to T cell signalling (458), Syk and PLCγ2 are implicated with B cell receptor signalling (472).

6.1.4.3 RhoH in malignant B-cell lineages: implications in chronic lymphocytic leukaemia (CLL)

The functional importance of RhoH in T-cell biology is now well established. However, RhoH also appears to play functional roles in B-cells and has been implicated in malignant B-cell lineages such as chronic lymphocytic leukaemia (CLL). CLL is the most prevalent form of leukaemia (473,474) and is characterised by the progressive accumulation of monoclonal CD5+ B cells in the blood (473). RhoH expression is significantly increased in primary human CLL cells relative to normal B-cells, with this increased RhoH expression positively correlated with Zap70 expression (32). Indeed, a regulatory role for Zap70 in B-cell receptor (BCR) signalling in CLL has been demonstrated (427), and Zap70 identified as a negative prognostic factor in CLL (475,476). Correspondingly, a genetic mouse model for CLL with RhoH depletion produced a delayed accumulation of leukemic cells in peripheral blood and reduced leukemic burden in lymphoid tissues (32,33). RhoH therefore appears to influence the progression and development of CLL (32). Further to this, RhoH ablation prevents homing, migration and contact of CLL cells to supportive cells of the microenvironment that arbitrate the survival and proliferation of leukemic cells, and produces aberrant localisation and diminished activity of Rac and RhoA (33). These canonical Rho GTPases are considered critical for the co-ordinated cell migration of numerous hematopoietic cells (423,477,478), which may clarify the impaired migration of $RhoH^{-/-}$ CLL cells (33).

6.1.4.4 RhoH involvement in other myeloproliferative disorders

The myeloproliferative disorders comprise a group of haematologic neoplasms thought to arise from a transformation in a haematopoietic stem cell (479). When dysfunctional, RhoH has been linked extensively to a variety of myeloproliferative disorders. Multiple studies have implicated the gene encoding RhoH as a frequent target of genetic alteration, with such alterations found in a variety of human cancers (445). Two mechanisms appear to account for these genetic alterations: translocation of the RhoH gene (413) and aberrant somatic hypermutation (415). However, the underexpression of RhoH has also been

implicated in the development in some forms of leukaemia (31,425). Table 6.3 (following page) provides an overview of the mechanisms by which RhoH dysfunction has been implicated in lymphomas and leukaemias.

Table 6.3. Involvement of aberrant RhoH in lymphomas and leukaemias.

Form of RhoH dysfunction		
Somatic hypermutation	**Chromosomal translocation**	**RhoH under-expression**
Nodular lymphocyte predominant Hodgkin's lymphoma	Nodal marginal zone B-cell lymphoma	Hairy cell leukaemia
Classical Hodgkin's lymphoma	Follicular lymphoma	Acute myeloid leukaemia
Diffuse large B-cell lymphoma	Plasma cell myeloma	
Extranodal marginal zone B-cell lymphoma (MALT)	Splenic marginal zone B-cell lymphoma	
Follicular lymphomas		
Nodal marginal zone B-cell lymphoma		
Chronic lymphocytic leukaemia		
Splenic marginal zone B-cell lymphoma		
Monomorphic lymphoma		
HCV and AIDs-associated non-Hodgkin's lymphoma		

6.1.5 DRAK2 as a putative interactor of RhoH

To date, the molecular interactors of RhoH remain relatively obscure, despite observed roles in T-cell biology and, moreover, implications in several forms of leukaemia and lymphoma. However, the death-associated protein kinase DRAK2 shows several functional overlaps with RhoH; indeed, increasing evidence suggests that these enzymes may interact. This section is therefore dedicated to a discussion of the known structural and functional aspects of DRAK2 in relation to RhoH.

6.1.5.1 DRAK2 domain architecture

DRAK2 is a member of the death-associated protein kinase (DAPK) family of serine/threonine kinases, comprised of the following members: DAPK1, DAPK2 (DRP-1), DAPK3 (ZIPK), DRAK1 and DRAK2 (Figure 6.7). As shown in Figure 6.7, these proteins vary in size and subcellular localisation, with DAPK2 and DAPK3 sharing the highest homology (approximately 80% in the N terminus kinase domain) (480,481). DRAK1 and 2, however, share approximately 50% homology with DAPK1, the founding member of this family. DAPK1 and DAPK2 contain calmodulin (CaM) regulatory domains which bind calmodulin to modulate the DAPK's catalytic activity. While differences in size and localisation exist in the DAPK family, each family member appears to be involved in apoptotic stimulation (480). Indeed, DRAK2 has been shown to induce apoptosis when over-expressed (482), and its nuclear localisation and phosphorylation are implicated in UV-induced cell death (483). Curiously, however, $DRAK2^{-/-}$ mice exhibit enhanced rather than attenuated apoptosis (484). Furthermore, this remarkable enzyme is implicated in T-cell biology and CLL development, displaying several functional overlaps with RhoH.

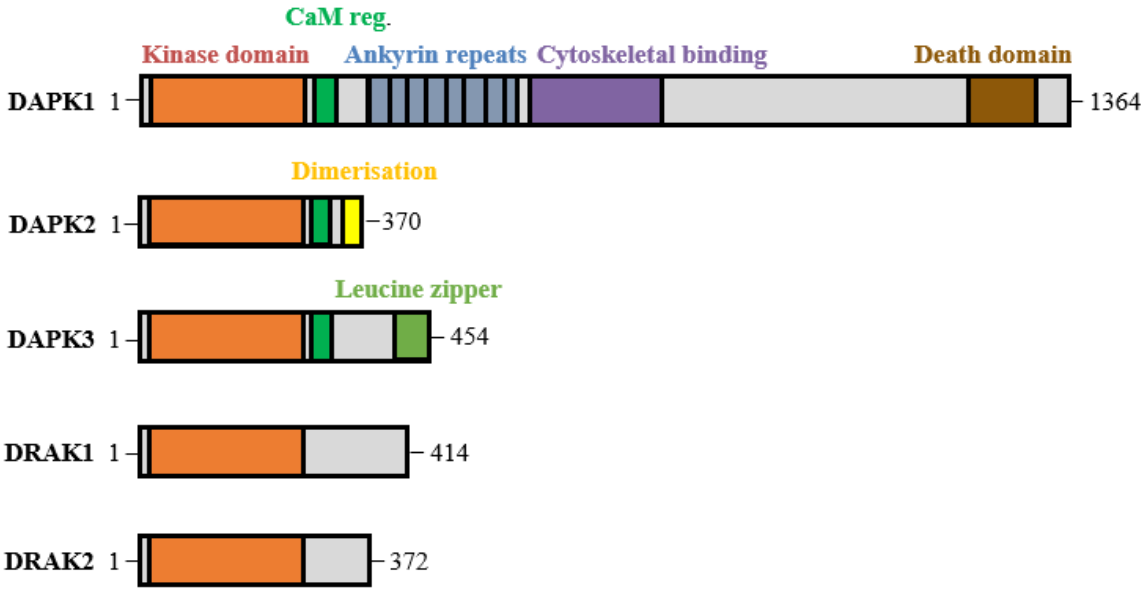

Figure 6.7. Molecular structure of the DAPK family of serine/threonine kinases. Schematic illustrations of the DAPK family, with the sub-cellular localisation of each corresponding kinase given to the right of its diagram.

6.1.5.2 DRAK2 in T-cell biology

DRAK2 is broadly expressed at low levels, but shows enriched expression in haematopoietic cells (485,486) and displays several functional roles in T-cell biology, including thymocyte selection (487,488) and apparent modulation of TCR stimulation sensitivity (489). Indeed, DRAK2 abrogation in T cells appears to enhance sensitivity to TCR-mediated stimulation (489), producing a decreased requirement for co-stimulation. This suggests that DRAK2 functions as a negative regulator for TCR signalling, raising the threshold for stimulation (490). Related to this, DRAK2 has been implicated in Ca^{2+} mobilisation. In T-cells, 75% of all activation-regulated genes require a Ca^{2+} influx (491). Consequently, a reduction in Ca^{2+} mobilisation dramatically attenuates (and can prevent) T-cell activation and proliferation (491-493). Germline ablation of DRAK2 has been shown to produce hyperactive Ca^{2+} mobilisation, even under sub-optimal TCR stimulation (485,494). It has therefore been hypothesised that DRAK2 serves both as a rheostat (sensor/regulator) for Ca^{2+} signalling (487,488) and as a negative regulator of TCR signalling (490). In fact, DRAK2 itself is activated by Ca^{2+} mobilisation (487,488). Additionally, ectopic expression of DRAK2 in double positive thymocytes raises the threshold for both negative and positive selection (487,488).

6.1.5.3 DRAK2 in autoimmunity

Depletion of the *Drak2* gene in animal models produces reduced autoimmune susceptibility, with diminished clinical severity shown in animal autoimmune models for multiple sclerosis (experimental autoimmune encephalomyelitis) and type I diabetes-prone-non-obese diabetic (NOD) mice (494-497). This lowered susceptibility towards autoimmunity is thought to occur, at least partially, through reduced survival of activated effector T-cells, potentially as a result of impaired Ca^{2+} homeostasis (495-497). However, the exact signalling components associated with diminished autoreactive cell survival in DRAK2 abrogation remain unknown. Curiously, despite an increased sensitivity to death in $DRAK2^{-/-}$ T-cells, pathogen clearance and tumour surveillance are maintained in $DRAK2^{-/-}$ mice (494,496,498,499). As DRAK2 does not appear to play essential tumour suppressive roles (500), this kinase represents a promising therapeutic target for treating organ-specific autoimmunity without producing widespread immunosuppression.

6.1.5.4 DRAK2 in transplantation

DRAK2 has been shown to significantly promote allogeneic graft acceptance in two separate transplant models without producing general immunosuppression (499). This is remarkably medically relevant. Allorecognition of transplated biological material from a foreign donor typically results in T-cell activation and destruction of the allograft (501). To prevent allograft rejection, transplant patients currently must endure lifelong administration of powerful immunosuppressants such as cyclosporine A or FK506, which often produce problematic side effects and are associated with greatly diminished quality of life (502). Formation of allogeneic memory was diminished in $DRAK2^{-/-}$ T-cells, with transferred $DRAK2^{-/-}$ memory T-cells failing to produce allograft rejection in the Balb/C->C57BL/BJ murine model (499). Long-term allogeneic skin graft was accepted through administration of Cytotoxic T-Lymphocyte Antigen 4 fusion protein (CTLA4-Ig), which synergised with DRAK2 depletion. Meanwhile, earlier *in vitro* studies showed that $DRAK2^{-/-}$ CD8+ T-cells exhibited a significantly reduced response to allogenic stimulation versus wildtype T-cells when evaluated by CFSE dilution (499). These studies suggest crucial roles for DRAK2 in primary and memory T-cell responsiveness to allografts, and demonstrate the potential of DRAK2 as a target in the prevention of allogeneic graft rejection.

6.1.6 RhoH and DRAK2: convergence of functional roles and potential clinical relevance

RhoH and DRAK2 are functionally active within the same contexts and often exhibit convergent roles. Interestingly, RhoH and DRAK2 appear to play opposing roles in Ca^{2+} mobilisation, with RhoH abrogation associated with decreased Ca^{2+} mobilisation (455,468) and DRAK2 abrogation implicated in hyperactive Ca^{2+} mobilisation (485,494). Significantly, RhoH appears to act as a positive regulator of TCR signalling (417,446,455), while DRAK2 exhibits the opposite function and is regarded as a negative regulator of TCR signalling (490). Both DRAK2 and RhoH show haematopoetically enriched expression patterns and are involved in signalling for T cell development including thymocyte selection. While DRAK2 and RhoH appear to share similar functional roles and are likely involved mutual signalling pathways, however, no direct link between these two proteins has been demonstrated. Akin to RhoH, however, DRAK2 may play roles in the development of CLL. The founding member of the DAPK family, DAPK1, has been previously identified as a heritable pre-disposing factor in CLL (503). Moreover, DRAK2 has been previously implicated as a negative regulator of transforming growth factor β Receptor I (TGF-βRI), controlling TGF-β/Smads signalling in solid tumours (504). A positive correlation between TGF-βRI and DRAK2 mRNA levels has recently been identified. Perhaps most strikingly, however, is the recent association between DRAK2 expression and CLL patient survival, with patients expressing low DRAK2 levels associated with significantly shorter survival (505). While this same study found no correlation between RhoH mRNA levels and overall survival in CLL patients, RhoH mRNA levels were also found to be positively correlated with levels of DRAK2 mRNA. Thus, a functional link between RhoH and DRAK2 may exist that is of clinical relevance in CLL. Given these exciting new revelations in the scientific literature and the availability of materials at Northumbria University, a series of experiments were utilised to further characterise the unusual GTPase RhoH and to assess putative interactions between RhoH and DRAK2 *in vitro*.

6.2 Results

6.2.1 Cloning of full length and truncated versions of human RhoH

A pCMS-EGFP mammalian expression vector encoding EGFP-tagged full-length human RhoH was kindly donated by the Structural Genomics Consortium at the University of Oxford, UK. This vector was utilised as a template for the PCR-based cloning of the nucleotide sequence encoding full-length human RhoH, in addition to truncated versions thereof (Figure 6.8). The pET15b-TEV vector enables the bacterial expression of recombinant proteins containing a TEV-cleavable N-terminal hexahistidine tag (His-tag). For each cloning procedure, PCR products were generated via the programme described in 2.2.2.3 and using the desired primers: either those shown in 2.1.3.9 (for cloning RhoH full length), 2.1.3.10 (for cloning RhoH truncation 1, S_4–A_{174}) or 2.1.3.11 (for cloning RhoH truncation 2, V_{10}–S_{184}). Boundaries for each truncation were chosen based on the notion of removing the C-terminal CaaX box in RhoH and in facilitating bacterial expression with sequences that were believed to be more soluble and more easily expressed by *E.coli*.

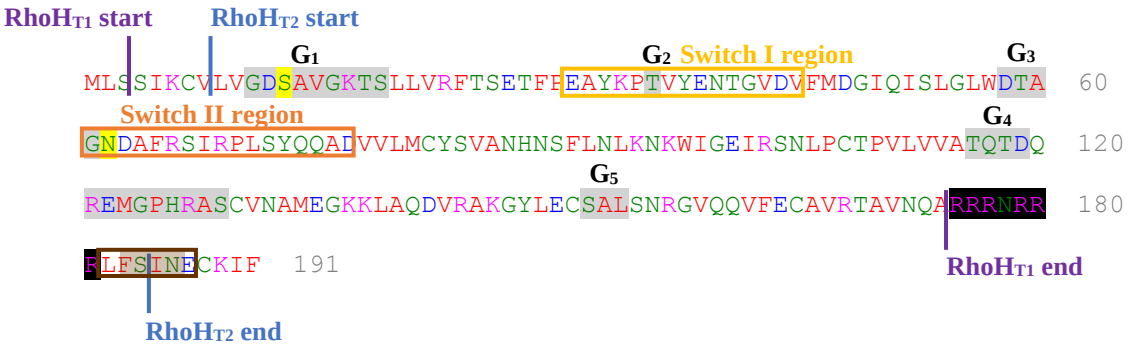

Figure 6.8. RhoH amino acid sequence, showing cut-off points for the RhoH$_{T1}$ and RhoH$_{T2}$ truncates.

In each case, the presence of the *NdeI* restriction site on the forward primer and the *XhoI* restriction site on the reverse primer, enabling later ligation of these products into *NdeI/XhoI* restriction digested pET15b-TEV. PCR product samples were subjected to agarose gel electrophoresis (2.2.3.7) and assessed under UV light following ethidium bromide staining (2.2.3.8). As in Figure 6.9, the presence of bands of the correct size relative to the Hyperladder I side standard (Bioline) indicated successful PCR-based amplification of target sequences. Succesful PCR products were subjected to a standard PCR clean-up procedure followed by a 4 hour *NdeI/XhoI* double digest as previously indicated (2.2.3.6). Digested PCR products were then purified by agarose gel purification (2.2.3.9), ligated into *NdeI/XhoI* digested pET15b-TEV and the products of ligation used to transform chemically competent TOP10 cells (2.2.2.2). At least 2 colonies from each plate of transformed TOP10 *E.coli* were then screened for the presence of pET15b-TEV harbouring the desired RhoH encoding insert; the screening method utilised was NdeI/XhoI restriction digestion of a sample of plasmid DNA (pDNA) extracted from each colony (2.2.3.2; 2.2.3.6) in order to liberate the insert, followed by agarose gel electrophoresis (2.2.3.7), subsequent ethidium bromide staining and UV visualisation (2.2.3.8). As exhibited in Figure 6.10, the presence of bands corresponding to the correct size for each desired insert indicated a pET15b-TEV plasmid containing the target insert. For each RhoH construct of interest, two samples of pDNA appearing to harbour the correct insert were shipped for sequencing using the standard T7 promoter primer, with the desired sequence indicated in each instance and no unwanted mutations observed. Only pDNA confirmed by sequencing was taken forward for subsequent use in expression trials and further work.

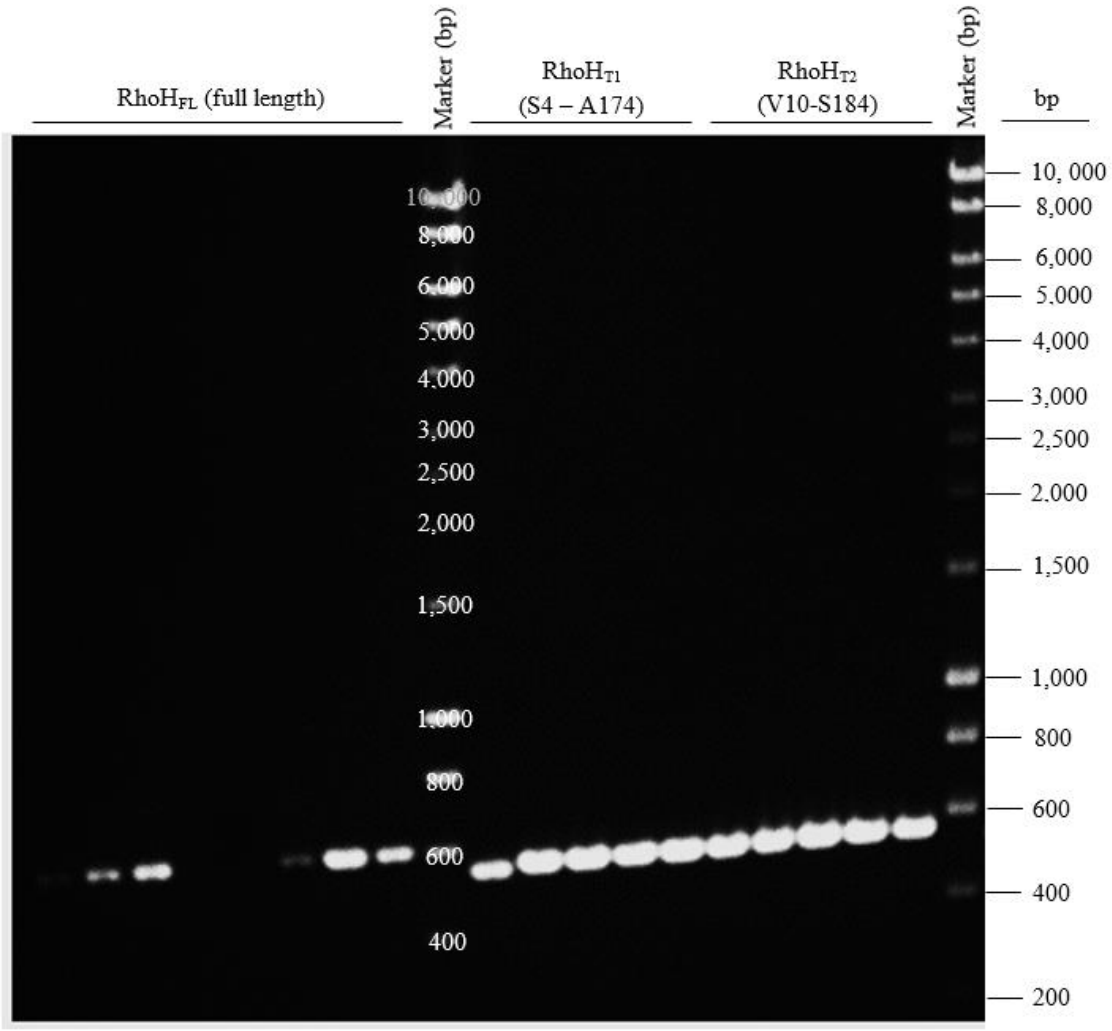

Figure 6.9 PCR products yielded from the PCR-based amplification of RhoH full length, RhoH truncation 1 (S4-SA174) and RhoH truncation 2 (V10-S184). 1% agarose gel showing electrophoresised PCR products following the PCR-based amplification of RhoH-encoding sequences of interest.

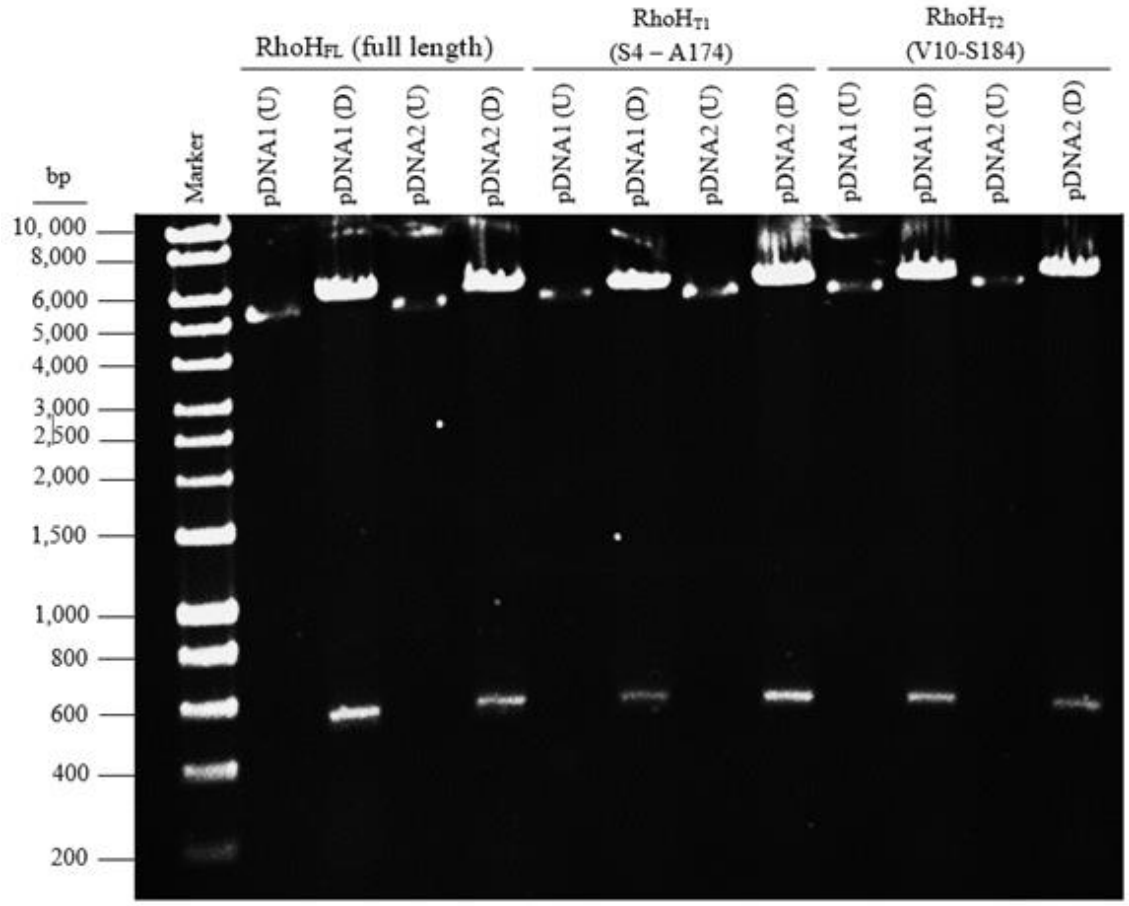

Figure 6.10 Analytical restriction digest for confirmation of the presence of RhoH-encoding sequences into pET15b-TEV. 1% agarose gel showing the presence of RhoH encoding sequences in separate pDNA samples isolated from TOP10 *E.coli* transformants. Marker shown in lane 1 (Hyperladder I, BioLine).

6.2.2 Expression trials

BL21 (DE3), C41 (DE3), C43 (DE3) and Tuner (DE3) $CaCl_2$ competent *E.coli* cells were transformed with the pDNA for each successful human RhoH clone of interest, namely: RhoH full length ($RhoH_{FL}$), truncation 1 ($RhoH_{T1}$) or truncation 2 ($RhoH_{T2}$). 50mL of the recombinant *E.coli* strains were grown in separate flasks to mid-log phase and varying concentrations of IPTG administered in order to assess a number of expression conditions (either 0.1mM, 0.5mM or 1mM). Following administration of IPTG, the recombinant *E.coli* cells were allowed to express the RhoH construct of interest either at 37^{o}C (4 hours), 25^{o}C (10 hours) or 18^{o}C (16 hours). This provided a range of expression conditions to assess suitable expression strains, IPTG concentrations and expression temperatures for each RhoH construct of interest (summary of results provided in the form of Table 6.4; SDS-gel showing best expression trial results provided as Figure 6.11).

The best conditions indicated by expression trials were subsequently taken forward for target protein identification confirmation and expression up-scale and purification, enabling the completion of further downstream experiments. For all expression trials, cells were harvested and subsequently sonicated until fully broken open as previously indicated (section 2.2.2.6). Cell debris was removed by centrifugation and each construct was purified initially by immobilised metal affinity chromatography (IMAC). During expression trials, manual IMAC was performed (2.2.4.4) wherein only 2 elution buffers were used to elute bound proteins: buffers containing either 50mM imidazole or 300mM imidazole. This enabled an initial, quick assessment of the expression conditions tested without the need for timely purification procedures.

IPTG concentration (mM)		RhoH full length expression			$RhoH_{T1}$ (S4 – A174) expression			$RhoH_{T2}$ (V10 – S184) expression		
		Temperature (°C)			Temperature (°C)			Temperature (°C)		
		37	25	18	37	25	18	37	25	18
BL21	0.1	+	++	++	+++	+++	+++	-	-	-
	0.5	+	+	++	+++	+++	+++	-	-	-
	1.0	+	+	++	++	+++	+++	-	-	-/+
C41	0.1	+	++	+++	+++	+++	+++	-	+	+
	0.5	+	++	+++	+++	+++	+++	-	+	+
	1.0	+	++	+++	++	+++	+++	-	-	-
										-
C43	0.1	++	++	+++	+++	+++	+++	-	+	+
	0.5	+	++	+++	+++	+++	+++	-	+	+
	1.0	+	++	+++	+++	+++	+++	-	-	-
Tuner	0.1	+	++	++	+++	+++	+++	-	-	-
	0.5	+	+	++	+++	+++	+++	-	-	-
	1.0	+	+	++	++	+++	+++	-	-	-

Table 6.4. Expression optimisation of recombinant human RhoH constructs. Expression of the three recombinant RhoH constructs (full length, RhoH S3-A174 and RhoH V10-S184) using LB broth, a variety of *E.coli* expression DE3 strains (BL21, C41, C43 and Tuner cells), total IPTG concentrations (0.1mM, 0.5mM or 1mM) and a temperatures (18°C for 16 hours, 25°C for 10 hours or 37°C for 4 hours) were trialled. - denotes no visible expression, + denotes some visible expression, ++ denotes notable expression and +++ denotes excellent recombinant target protein expression.

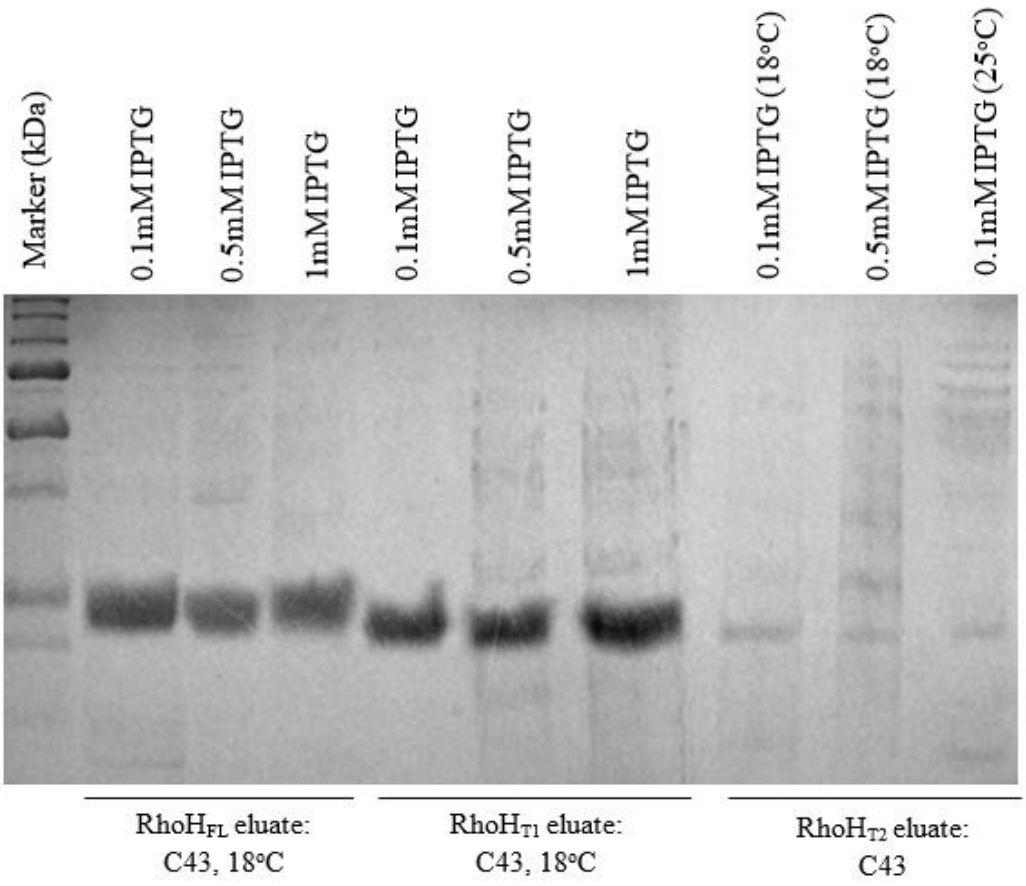

Figure 6.11 Expression trials show promising expression for RhoH$_{FL}$ and RhoH$_{T1}$. 12% SDS-PAGE gel showing the most promising results from the expression trials. Note that expression of RhoH$_{T2}$ appears minimal.

6.2.3 Confirmation of target protein expression

In order to confirm that the proteins observed during expression trials corresponded to the desired target proteins, the following methods were utilised: Western blotting (using anti-human RhoH as the primary antibody) and LC-MS on trypsinised excised SDS-PAGE gel segments (section 2.2.7.2). Western blotting was performed as previously described (2.2.4.8) *via* application of the ab138123 anti-RhoH polyclonal from AbCam as the primary antibody, using the dilutions shown in 2.1.1.4. As shown in Figure 6.12, the Western blotting procedure produced chemiluminescent signals at the expected molecular weight for $RhoH_{FL}$ and $RhoH_{T1}$ and $RhoH_{T2}$, suggesting that the correct target proteins had been expressed. However, in order to further improve confidence in the identity of the proteins expressed during expression trials, the best condition for each construct was repeated and target recombinant proteins purified using manual IMAC involving the normal range of elution buffers (2.2.4.4). A purified sample of each construct was then run on a 12% SDS-PAGE gel and subjected to gel excision and trypsinisation followed by LC-MS (2.2.7.4), with raw data analysed by running the .MGF files obtained from Progenesis analysis software through the X! P3 MS/MS ion search server (2.2.7.5). As shown in Figures 6.13–6.14, the results from X! P3 indicated that the correct target recombinant protein had been over-expressed for $RhoH_{FL}$ and $RhoH_{T1}$, with the top score for each protein corresponding to human RhoH, thus indicating that peptide sequences run *via* LC-MS matched the amino acid sequence of human RhoH as described in the National Centre for Biotechnology Information (NCBI) database (sequence coverage: 40% for $RhoH_{FL}$, 37% for $RhoH_{T1}$). Taken together, the results from Western blotting and LC-MS (in addition to pDNA sequencing information and the perceived molecular weight of the over-expressed proteins) strongly indicated that the proteins over-expressed during expression trials represented the desired target RhoH constructs.

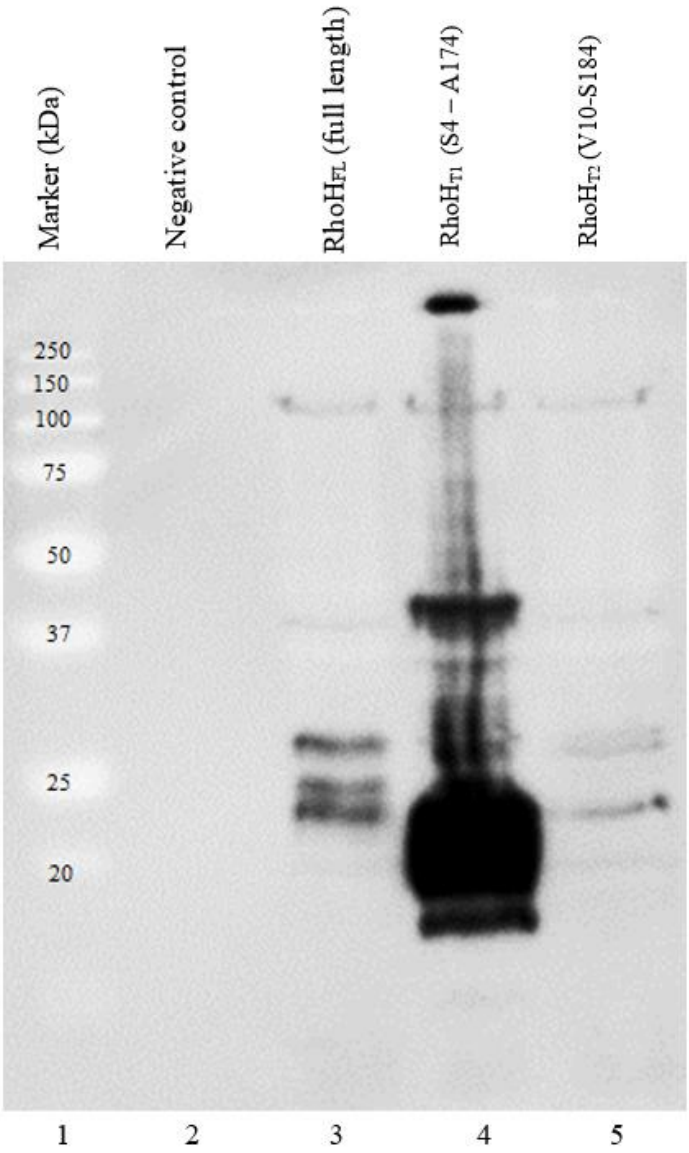

Figure 6.12 Anti-RhoH Western blot of RhoH samples obtained from expression trials. Western blot of IMAC-purified RhoH$_{FL}$ (lane 3), RhoH$_{T1}$ (lane 4) and RhoH$_{T2}$ (lane 5) samples. Each sample chosen represented what was considered the best expression condition for the given construct, as shown in Table 6.4.

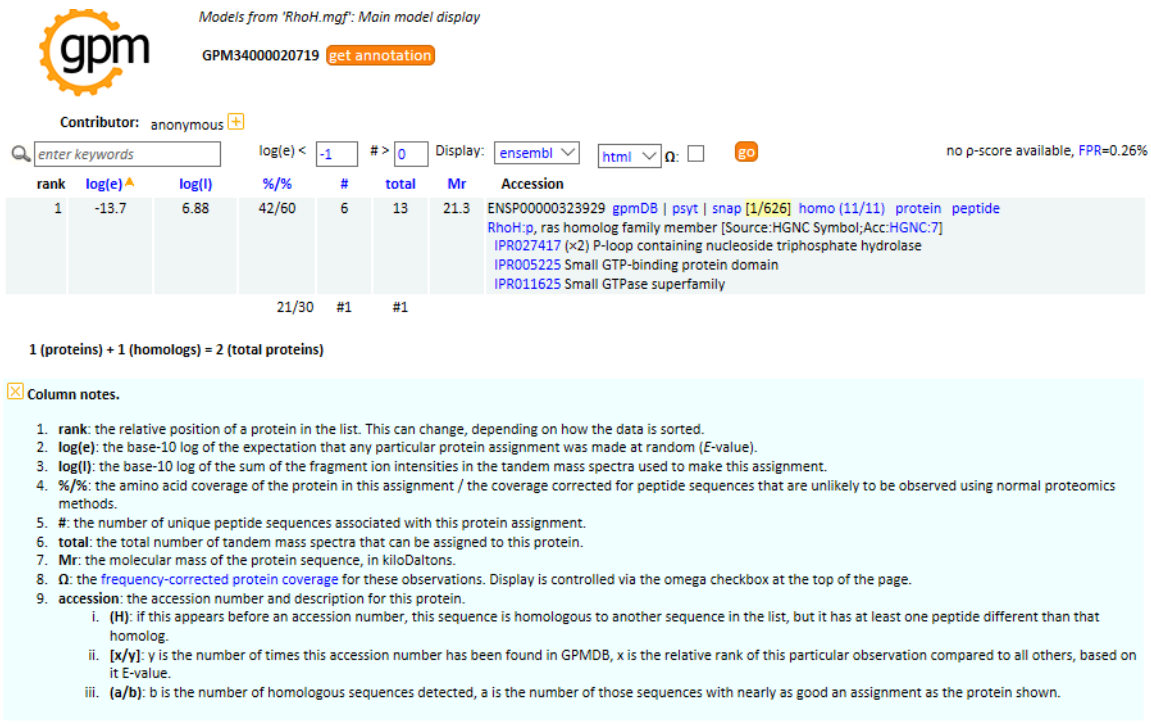

Models from 'RhoH.mgf': Main model display

GPM34000020719 get annotation

Contributor: anonymous

enter keywords | log(e) < -1 | # > 0 | Display: ensembl | html | Ω: | go | no p-score available, FPR=0.26%

rank	log(e)	log(I)	%/%	#	total	Mr	Accession
1	-13.7	6.88	42/60	6	13	21.3	ENSP00000323929 gpmDB | psyt | snap [1/626] homo (11/11) protein peptide RhoH:p, ras homolog family member [Source:HGNC Symbol;Acc:HGNC:7] IPR027417 (×2) P-loop containing nucleoside triphosphate hydrolase IPR005225 Small GTP-binding protein domain IPR011625 Small GTPase superfamily
			21/30	#1	#1		

1 (proteins) + 1 (homologs) = 2 (total proteins)

Column notes.

1. **rank**: the relative position of a protein in the list. This can change, depending on how the data is sorted.
2. **log(e)**: the base-10 log of the expectation that any particular protein assignment was made at random (*E*-value).
3. **log(I)**: the base-10 log of the sum of the fragment ion intensities in the tandem mass spectra used to make this assignment.
4. **%/%**: the amino acid coverage of the protein in this assignment / the coverage corrected for peptide sequences that are unlikely to be observed using normal proteomics methods.
5. **#**: the number of unique peptide sequences associated with this protein assignment.
6. **total**: the total number of tandem mass spectra that can be assigned to this protein.
7. **Mr**: the molecular mass of the protein sequence, in kiloDaltons.
8. **Ω**: the frequency-corrected protein coverage for these observations. Display is controlled via the omega checkbox at the top of the page.
9. **accession**: the accession number and description for this protein.
   i. **(H)**: if this appears before an accession number, this sequence is homologous to another sequence in the list, but it has at least one peptide different than that homolog.
   ii. **[x/y]**: y is the number of times this accession number has been found in GPMDB, x is the relative rank of this particular observation compared to all others, based on it E-value.
   iii. **(a/b)**: b is the number of homologous sequences detected, a is the number of those sequences with nearly as good an assignment as the protein shown.

Figure 6.13 LC-MS results indicating the presence of RhoH in the excised RhoH$_{FL}$ SDS-PAGE band. X! P3 MS/MS ion search results using the Global Proteome Machine (GPM), preferentially matching RhoH to the peptides run through the LC-MS system (with 42% amino acid coverage for RhoH and 60% when corrected for peptide sequences that are unlikely to be observed using normal proteomics methods).

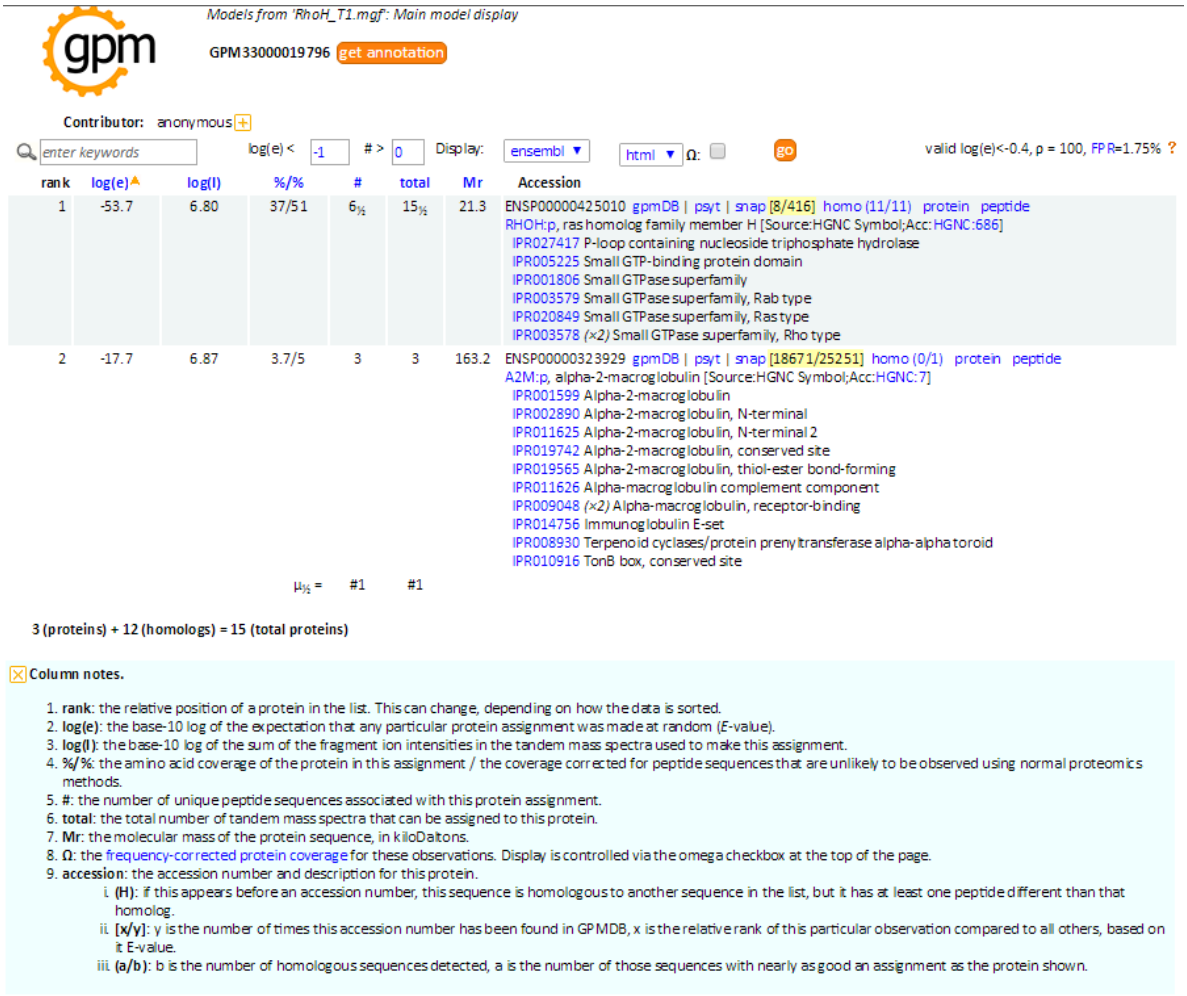

Figure 6.14 LC-MS results indicating the presence of RhoH in the excised RhoH$_{T1}$ SDS-PAGE band. X! P3 MS/MS ion search results using the Global Proteome Machine (GPM), preferentially matching RhoH to the peptides run through the LC-MS system (with 37% amino acid coverage for RhoH and 51% when corrected for peptide sequences that are unlikely to be observed using normal proteomics methods).

6.2.4 Expression up-scale and purification

The most favourable conditions from the expression trials (6.2.2) were up-scaled. Cells were harvested, lysed and cell-free supernatant attained as previously discussed (2.2.26). The recombinant target proteins were subsequently purified by IMAC using a Nickel NTA column attached to an ÄKTA Prime fast protein liquid chromatography (FPLC) system (2.2.4.4). Figures 6.15–6.16 show the successful purification of full length recombinant human RhoH ($RhoH_{FL}$), while Figures 6.17–6.18 show the successful purification of the $RhoH_{T1}$ construct (human RhoH $S_4 – A_{174}$). As Large scale expression and IMAC purification of $RhoH_{T2}$ (human RhoH $V_{10} – S_{184}$) appeared unsuccessful, with an absence of soluble over-expressed protein obtained. Indeed, an assessment of the insoluble fractions for each expression and purification indicated that the $RhoH_{T2}$ construct was highly insoluble. This notion of insolubility was further supported by Western blotting (Figure 6.19), with a strong chemiluminescent signal found in the $RhoH_{T2}$ insoluble fraction sample. Although a certain degree of insolubility can be expected when over-expressing proteins, over-expression of soluble $RhoH_{T1}$ was high relative to $RhoH_{T2}$ and thus $RhoH_{T1}$ was pursued while further attempts to over-express and purify $RhoH_{T2}$ were discontinued; this enabled a streamlined workflow with $RhoH_{T1}$ and $RhoH_{FL}$ in parallel.

Following IMAC purification, suitably pure fractions of $RhoH_{FL}$ and $RhoH_{T1}$ were concentrated to a single 2mL fraction and each 2mL fraction loaded separately onto a 2mL superloop for size exclusion chromatography using a HiPrep™ 16/60 Sephacryl™ S-200 gel filtration column connected to the ÄKTA Prime FPLC system (2.2.4.5). Figures 6.15 ($RhoH_{FL}$) and 6.17 ($RhoH_{T1}$) show that this method produced successful purification of these constructs. Pure $RhoH_{FL}$ and $RhoH_{T1}$ fractions from gel filtration were concentrated to the desired concentration for each downstream process. However, it was first necessary to again confirm that these purified proteins represented the desired target proteins. Western blotting was therefore undertaken on gel purified samples via the typical procedure (2.2.4.8; dilutions shown in 2.1.1.4) using the aforementioned ab138123 anti-RhoH polyclonal as the primary antibody. As shown in Figure 6.19, the presence of bands of the correct molecular weight for each RhoH construct suggested that the fractions of pure proteins obtained were indeed fractions of $RhoH_{FL}$ and $RhoH_{T1}$.

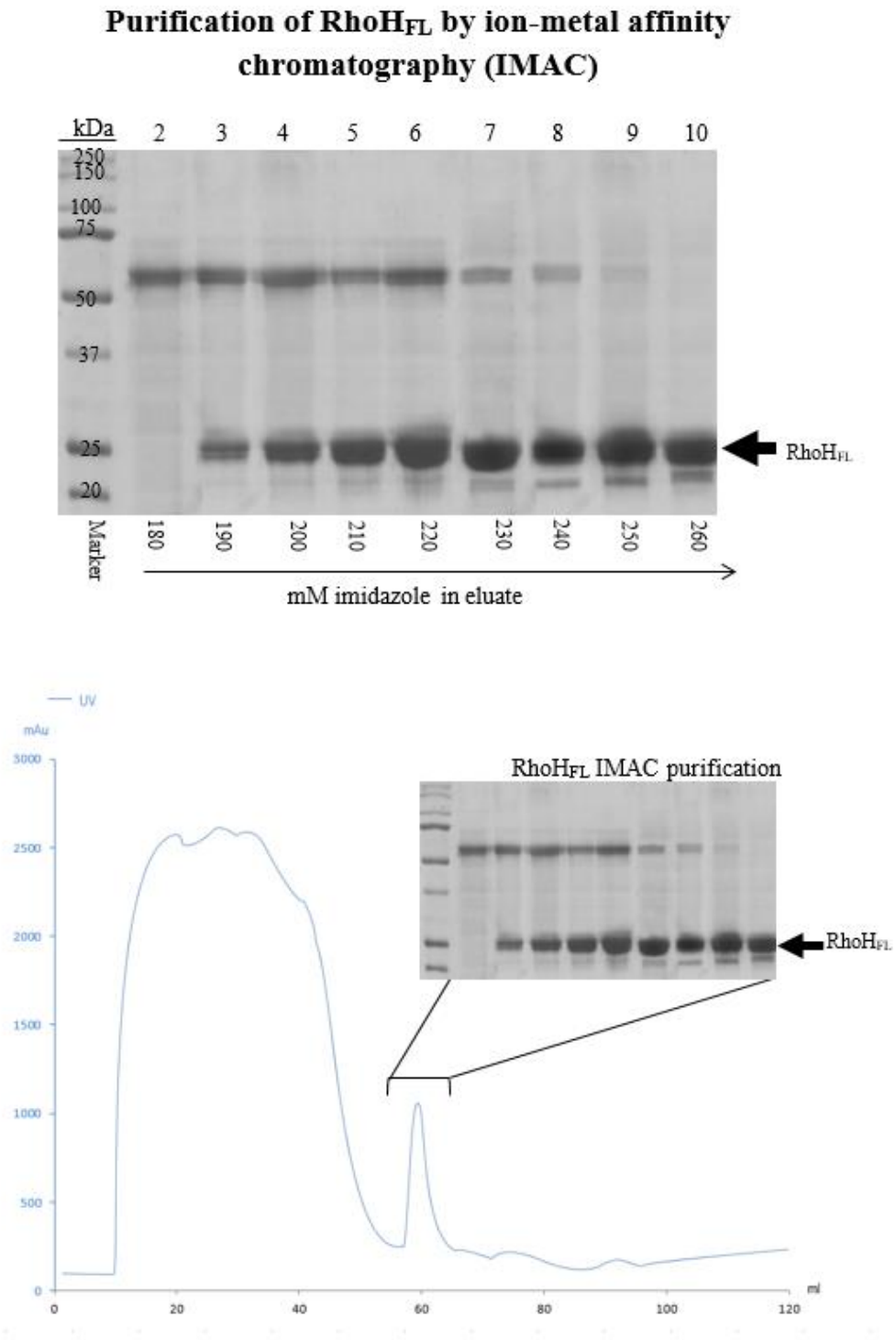

Figure 6.15 IMAC purified fractions of $RhoH_{FL}$ obtained from lysed recombinant C43 (DE3) *E.coli* extract. (a) 12% SDS-PAGE gel showing successfully purified fractions of $RhoH_{FL}$ obtained from IMAC. (b) Representative chromatogram from IMAC purification, with the area of the chromatogram corresponding to the purified $RhoH_{FL}$ fractions denoted.

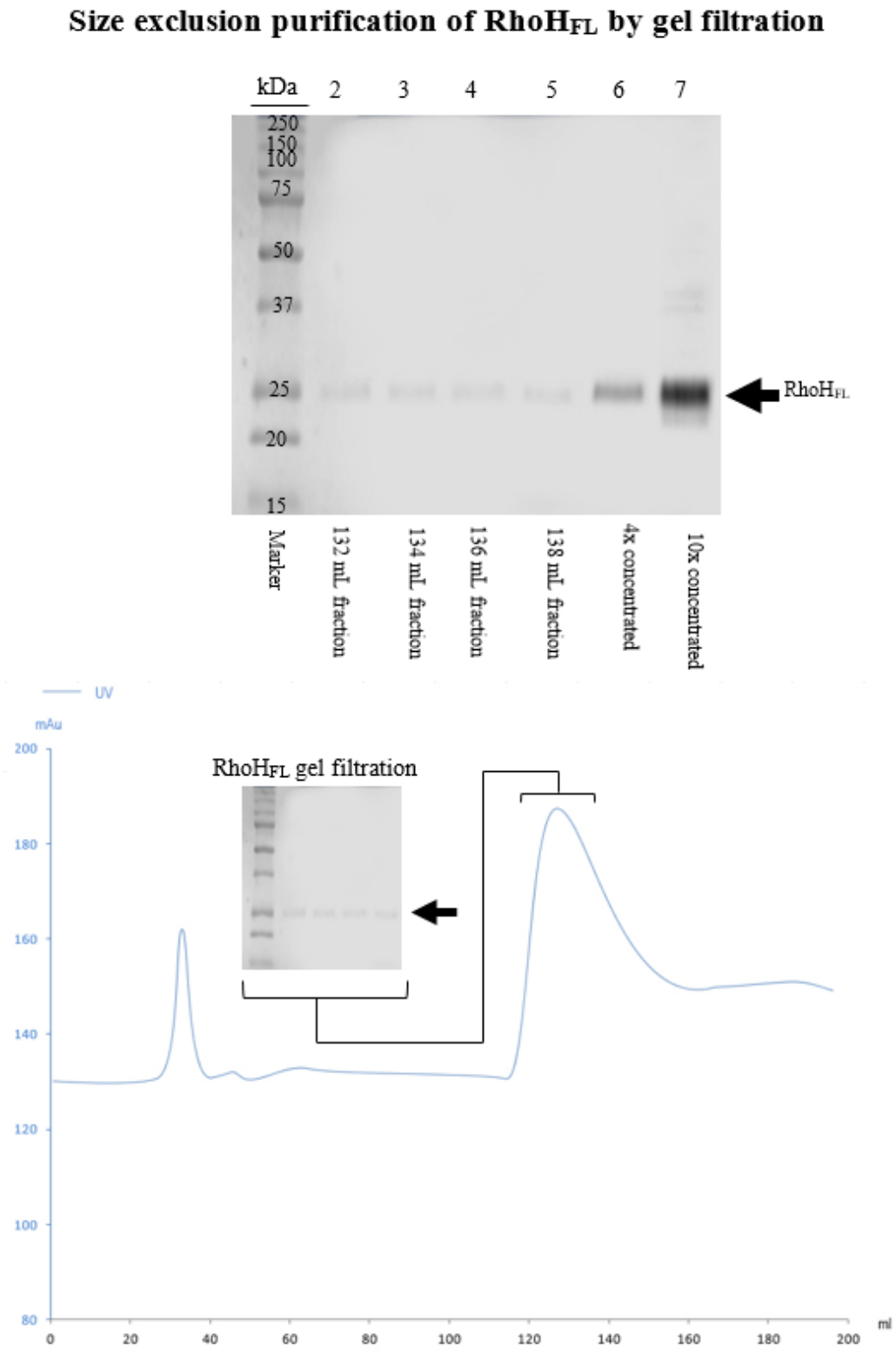

Figure 6.16 Successful size exclusion purification of RhoH$_{FL}$ from lysed recombinant C43 (DE3) *E.coli* extract. (a) Successful size exclusion purification of RhoH$_{FL}$ shown on an 12% SDS-PAGE gel (b) Representative chromatogram trace from gel filtration purification, with the area of the chromatogram corresponding to the purified RhoH$_{FL}$ fractions shown.

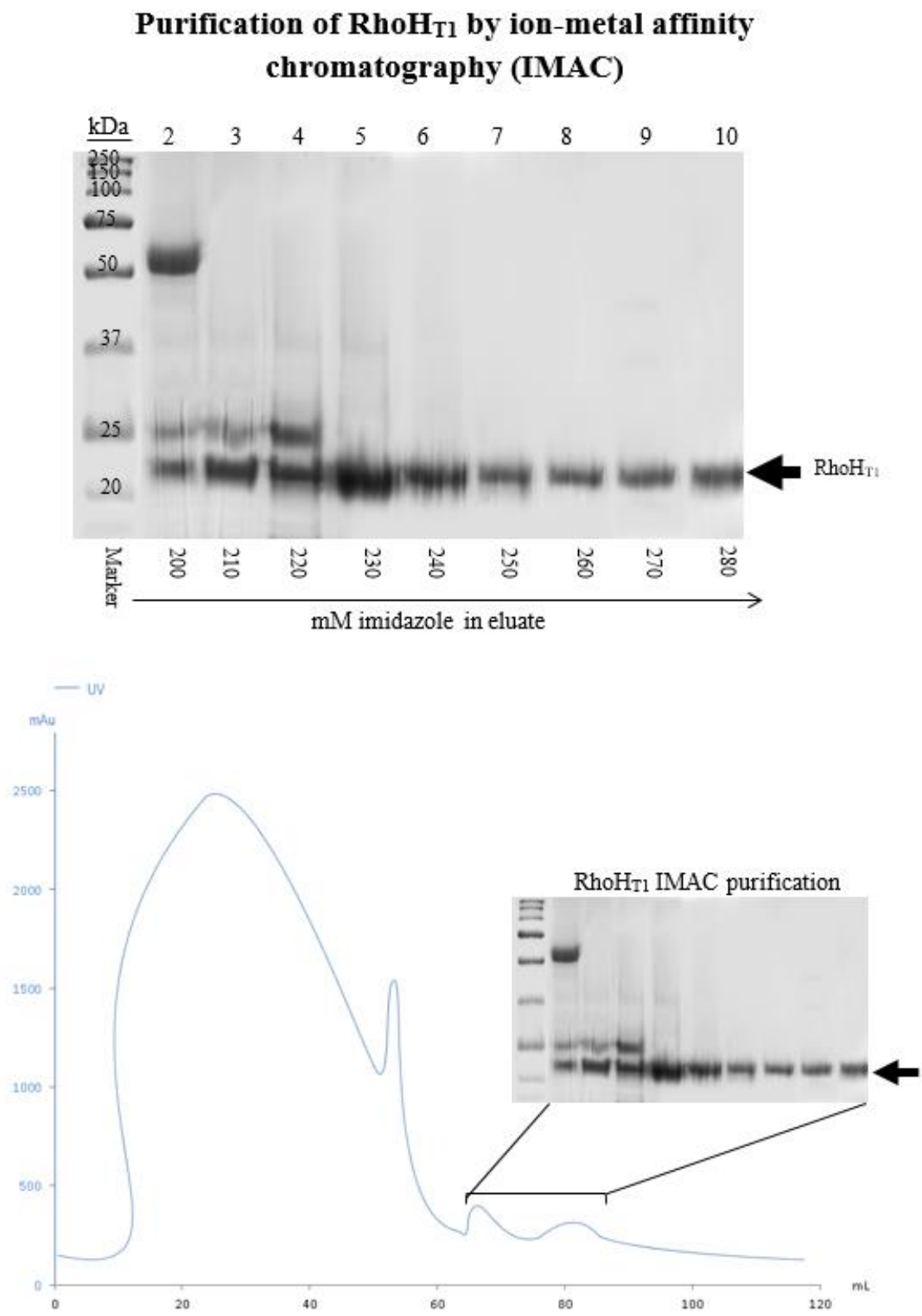

Figure 6.17 Succesful IMAC purification of RhoH$_{T1}$ from lysed recombinant C43 (DE3) *E.coli* extract. (a) 12% SDS-PAGE gel showing successfully purified fractions of RhoH$_{T1}$ obtained f rom IMAC. (b) Representative chromatogram trace from IMAC purification, with the area of the chromatogram corresponding to the purified RhoH$_{T1}$ fractions shown.

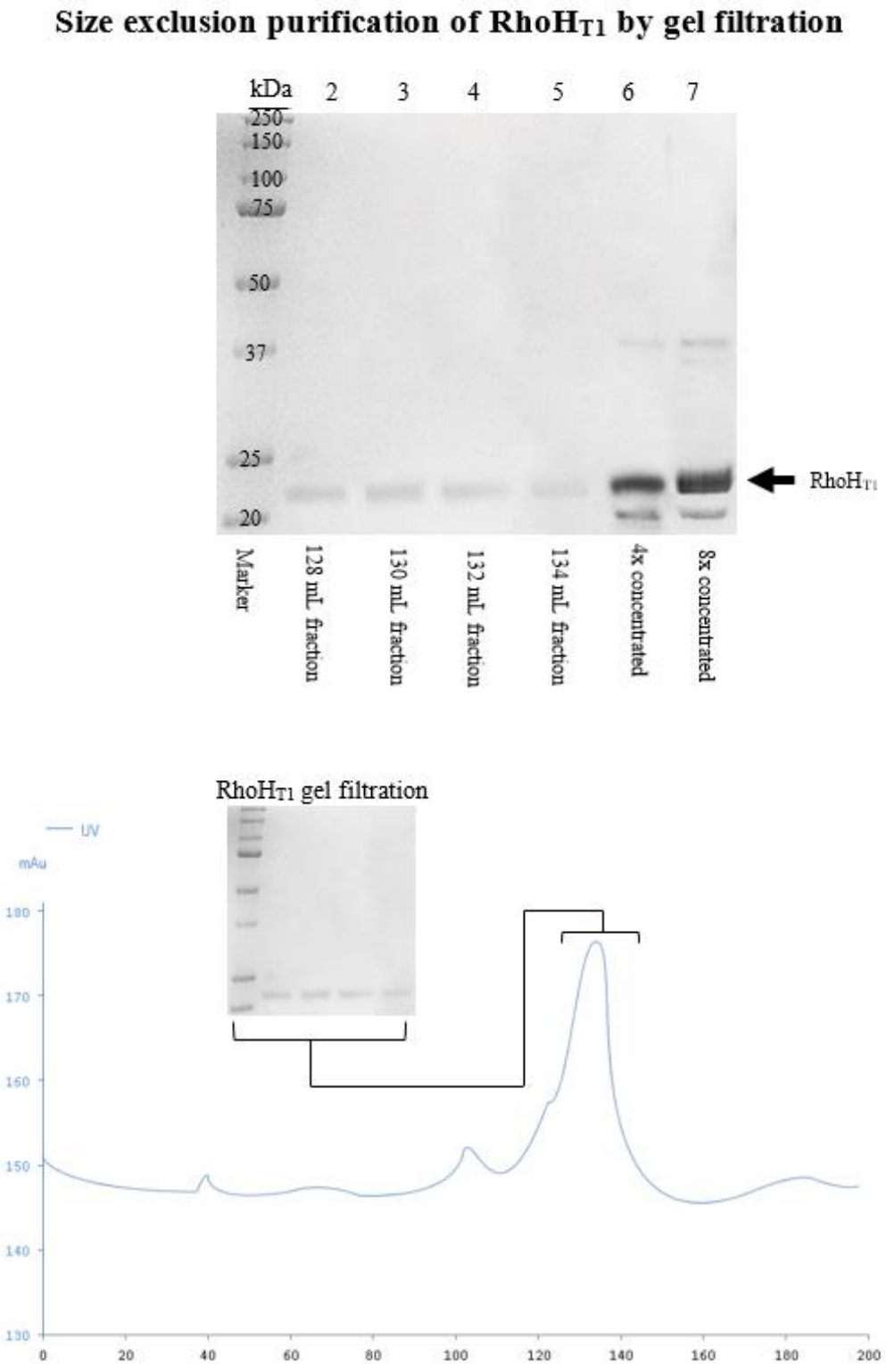

Figure 6.18 Gel filtration leading to successful size exclusion purification of RhoH$_{T1}$ from lysed recombinant C43 (DE3) *E.coli* extract. (a) Successful size exclusion purification of RhoH$_{T1}$ exhibited on a 12% SDS-PAGE gel (b) Representative chromatogram from the RhoH$_{T1}$ gel filtration purification; area of the chromatogram corresponding to the purified RhoH$_{T1}$ fractions emphasised.

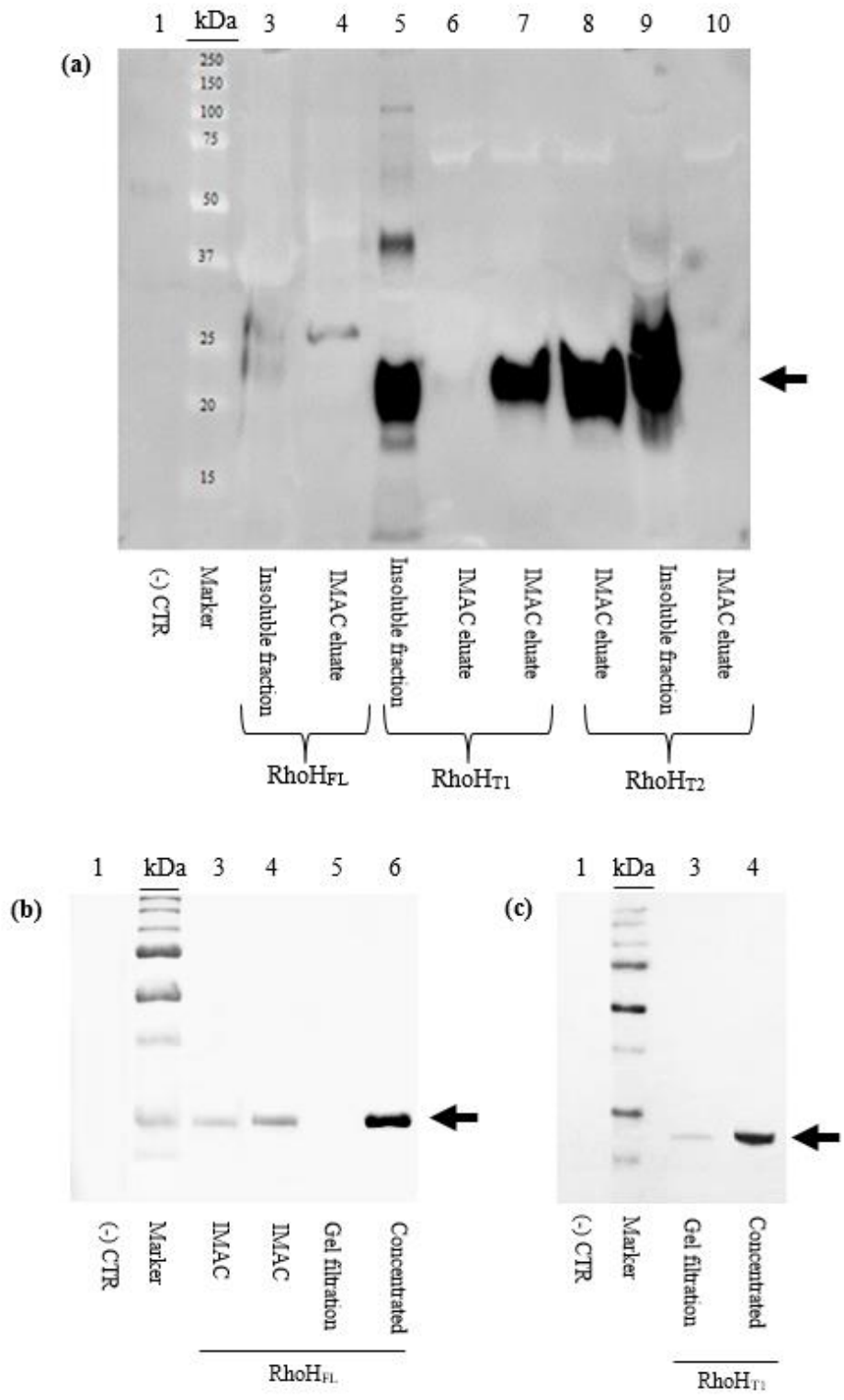

Figure 6.19 Anti-RhoH immunoblots showing presence of RhoH in purified $RhoH_{FL}$ and $RhoH_{T1}$ samples. (a) Immunoblot showing presence of RhoH constructs in either insoluble or soluble fractions, as illustrated. **(b)** Immunoblot showing presence of $RhoH_{FL}$ in IMAC and gel filtrated samples, including the concentrated sample taken forward for downstream use. **(c)** Immunoblot showing presence of $RhoH_{T1}$ in gel purified sample, including the concentrated sample taken forward for downstream utilisation.

6.2.5 *In vitro* characterisation

As discussed in the introduction of this chapter, previous studies in animal models and cell lines have provided initial insights to the cellular functions of RhoH. Despite this, several aspects of this remarkable GTPase remain uncharacterised. Consequently, several attempts to further characterise this enzyme were undertaken in this project. First, dynamic light scattering (DLS) was utilised in combination with gel filtration chromatography to assess the oligomeric state of this highly atypical GTPase. Secondly, numerous attempts to structurally characterise RhoH through x-ray crystallography were undertaken. Further to this, *in silico* modelling of RhoH was performed in the hope of elucidating the possible tertiary structure of this highly atypical and medically important GTPase. Finally, following promising implications in the literature, several *in vitro* assays were performed using $RhoH_{FL}$ and Rho_{T1} in the presence of the putative RhoH-regulating kinase DRAK2. The results show that RhoH highly difficult to crystallise, but is most closely related to the Rho GTPases Cdc42, RhoE and RhoD. *In silico* modelling of Rho Hans assessment of primary structure suggests a GTPase containing some overt classical Rho characteristics while also exhibiting unique and remarkably atypical features. No clear evidence was obtained for the presence of RhoH multimers and RhoH appears to present monomerically *in vitro*. However, this remains to be confirmed.

6.2.5.1 RhoH appears to present monomerically

Canonically, GTPases of the Ras superfamily are monomeric in nature. However, the atypical presentation of RhoH prompted an investigation as to whether this monomeric nature is also displayed by RhoH. While bioinformatics analysis of the primary structure of $RhoH_{FL}$ and $RhoH_{T1}$ did not imply a strong propensity towards oligomeric states, *in silico* attempts at identifying protein oligomeric state are not routinely used as definitive investigative tools. Instead, experimental assessments in the wet lab are considered standard and highly necessary. *In vitro* results obtained throughout this study indicated that RhoH indeed presents monomerically. While IMAC-purified RhoH typically displayed a band at the expected molecular weight in addition to a band of double this expected molecular weight, early analysis by mass spectrometry indicated that the peptide comprising this larger protein did not identify with RhoH. Further to this, size exclusion chromatography of RhoH *via* gel filtration chromatography did not produce multiple RhoH-identifying peaks. The use of dynamic light scattering (DLS) on RhoH (Appendix 13) produced poor results due to the apparent inherent propensity for $RhoH_{FL}$ and $RhoH_{T1}$

to aggregate. Despite centrifugation of samples prior to DLS, results suggested the presence of a particle of small diameter in addition to two much larger particles likely to represent aggregates. Overall, difficulties in handling RhoH led to challenging downstream processing. The results obtained indicated that RhoH is monomeric *in vitro*. Future use of analytical ultracentrifugation may allow for further clarification of RhoH oligomeric state. However, difficulties in obtaining high protein yield and handing this GTPase *in vitro*, in addition to the lack of promising leads from DLS and gel filtration, dissuaded the use of analytical ultracentrifugation; instead, pure samples of this difficult protein were prioritised for other downstream experiments.

6.2.5.2 Human RhoH crystallisation attempts

Numerous attempts to crystallise $RhoH_{FL}$ and $RhoH_{T1}$ were undertaken using the manual drop method described previously (2.2.4.9). Attempts to maintain pure $RhoH_{FL}$ and $RhoH_{T1}$ at concentrations >2 mg/mL resulted in rapid aggregation of these proteins within 24 hours; correspondingly, all crystallisation attempts $RhoH_{FL}$ and $RhoH_{T1}$ were concentrated to no more than 2 mg/mL. As both polypeptides were most stable in high salt buffers (~500 mM), crystallisation was attempted in the following buffer: 50 mM HEPES (pH 7.4), 5 mM DTT, 2% glycerol and either 500 mM or 300 mM NaCl. The proteins were concentrated using 15 mL centrifugal concentrators, as previously described (2.2.4.6). The following crystallisation screens were utilised (developed by Hampton Research Corp., United States): Hampton I, Hampton II and the PEG/Ion screen. No positive results were obtained, though a range of drops were observed: most drops showed some aggregations, while some drops were clear. No promising crystals were observed. Although other Rho GTPases have been previously crystallised, other research groups have noted difficulties in crystallising the atypical Rho GTPases. As such, *in silico* modelling approach was adopted as discussed in the following section.

6.2.5.3 *In silico* modelling indicates some canonical Rho characteristics for RhoH in addition to atypical components

In recent years, *in silico* modelling of protein tertiary structure has become increasingly sophisticated. It is now possible to generate 3D models using a variety of approaches online, with results generated at unprecedented speeds. Table 6.5, summarises the modelling results obtained from three separate online modelling servers, with the rationale behind the use of each server is provided in brief. Further information derived from these modelling servers can be found in Appendix 14. Use of the LOcal Meta

Threading-Server (LOMETS) generates models from separate local threading programs and automatically displays the top models from each program on the display page. The top LOMETS results for $RhoH_{FL}$ and $RhoH_{T1}$ were rendered in PyMol (Schrödinger Inc., United States) for further analysis, as shown in Figure 6.20 and 6.21, respectively. The models obtained for $RhoH_{FL}$ (Figure 6.20) and $RhoH_{T1}$ (Figure 6.21) suggest that RhoH is similar to many classical Ras and Rho enzymes with regards to overall structure, containing the classical five alpha helices and six beta sheets in the correct order, in addition to G loops and switch regions that resembles those observed for other members of the Rho family (53,296). Further to this, a Rho insert domain is noticeable in both models, appearing as a loop and short alpha helical section between the fifth beta strand and fourth alpha helix, as is seen in other Rho enzymes (34). Interestingly, according to the models, the ITAM-like motif described in the literature (447-450) appears to more accessible than initially suggested by a survey of RhoH's primary amino acid sequence, which indicated that this domain would likely be buried in a hydrophobic core. In terms of a comparison of the $RhoH_{T1}$ model versus the $RhoH_{FL}$ model, an extended C-terminal region is seen for $RhoH_{FL}$, comprising the polybasic, LFSINE and 'CaaX' box areas. As this area was largely truncated in $RhoH_{T1}$, this region is not visible in the $RhoH_{T1}$ model. Other than this noticeable difference, the two models are very compatible, as expected. To gain further insight as to any major differences between the *in silico* models for $RhoH_{FL}$ and $RhoH_{T1}$ compared to classical Rho enzymes, both models were superimposed against Cdc42, the closest classical homologue to RhoH. Superimposition was achieved using the automatic fitting feature in PyMol, which also automatically generates a root mean square deviation (RMSD) indicating is the measure of the average distance between backbone atoms of the superimposed proteins. The results for $RhoH_{T1}$ (Figure 6.22) and $RhoH_{FL}$ (Figure 6.23) are again, rather similar, showing similar differences to Cdc42 including differences in the following areas: the P-loop and switch I region (see 6.22b), Rho insert region (6.22c) and the β1, β2, β3 and β6 sheet regions (as shown in Figures 6.22 and 6.23). Although Cdc42 did display with an extended C-terminal region, the C-terminal region in $RhoH_{FL}$ was even further extended (see 6.23c). The RMSD values obtained were 0.514Å and 0.655Å for $RhoH_{T1}$ and $RhoH_{FL}$, respectively, suggesting that $RhoH_{T1}$ fits slightly to Cdc42, although this was likely due to the $RhoH_{FL}$ C-terminal region. Overall, the results suggest that RhoH broadly resembles another Rho classical Rho enzyme, Cdc42, but presents with variances in specific regions (discussed further in 6.3).

Table 6.5 Top-scoring models for the prediction of RhoHFL and RhoHT1 3D structure.

Modelling server	Rationale for use of server	RhoH $_{FL}$ top model	RhoH$_{T1}$ top model
LOMETS (LOcal MEta-Threading-Server)	Free, fast online web service for the prediction of protein structure. Generates 3D models *via* collection of high-scoring target-to-template alignments from 9 separate local threading programs (Hsearch, MUSTER, pGenTHREADER, FFAS-3D, PPAS, PROSPECT2, PRC, SP3 and SPARKS-X).	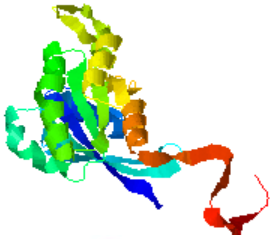	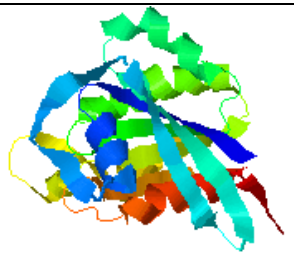
HHPred	100x faster than many leading servers and assessed as one of best servers for template-based protein structure prediction in the 2010 Critical Assessment of protein Structure Prediction (CASP).	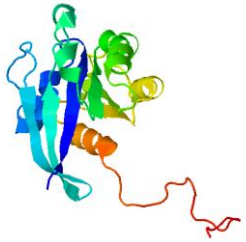	
Raptor X	Excels at aligning hard targets according to the 2010 CASP9 experiments. RaptorX generates the significantly better alignments for the hardest 50 CASP9 template-based modelling targets than other servers including those using consensus and refinement methods.	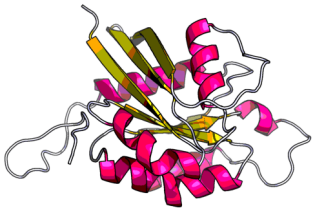	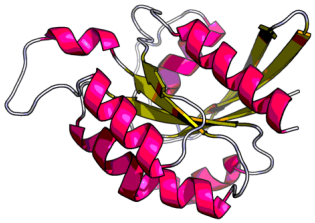

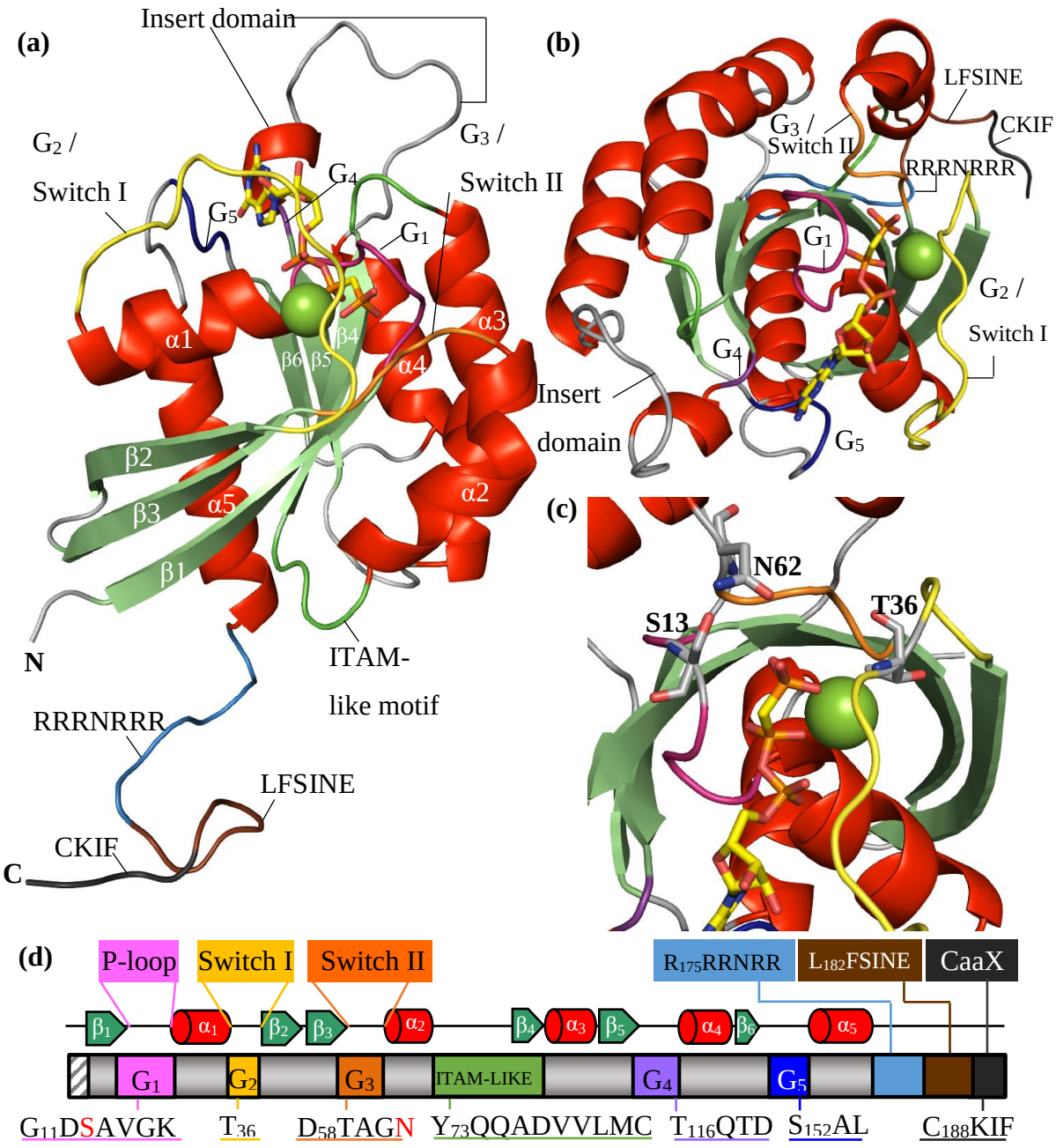

Figure 6.20. *In silico* model of RhoH$_{FL}$ 3D structure. Top LOMETS result for RhoH$_{FL}$, showing **(a)** anterior and **(b)** alternative views in addition to **(c)** a close-up of the nucleotide binding site (with relevant residues shown) and **(d)** a schematic diagram of RhoH domain architecture, with significant amino acid residues shown in red. The colour scheme utilised in **(d)** is also applicable to **(a–c)**. Mg^{2+} (shown as a green sphere) and GCP, a non-hydrolysable analogue of GTP, are shown in **(a–c)** and are positioned as a direct result of superimposition of Cdc42 with the RhoFL model (Cdc42 hidden, but GCP and Mg^{2+} visible). RhoH$_{FL}$ Model rendered in PyMol (Schrödinger Inc., United States).

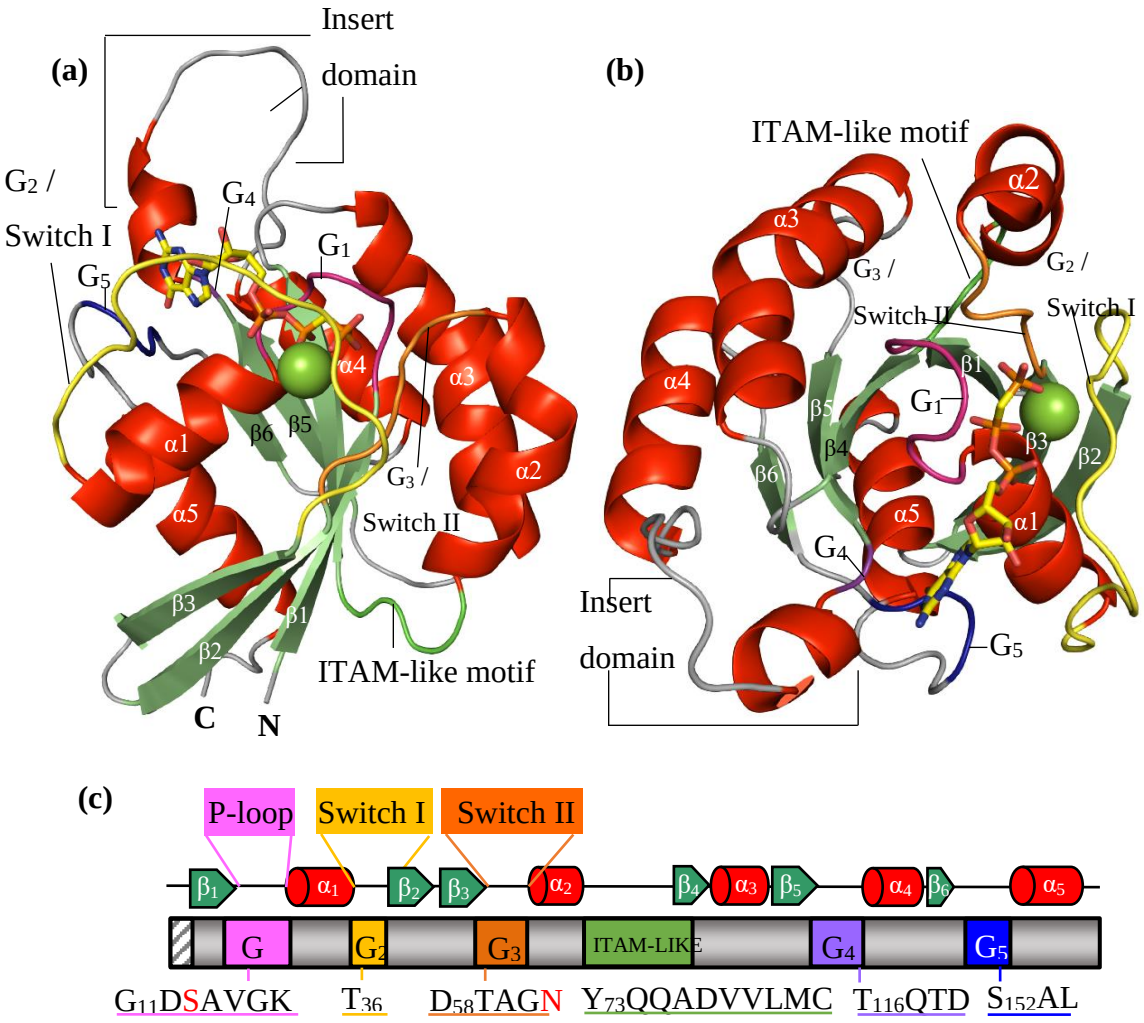

Figure 6.21. *In silico* model of RhoH$_{T1}$ 3D structure. Top LOMETS result for RhoH$_{FL}$, showing rendered 3D models of RhoH$_{T1}$ **(a)** anterior and **(b)** alternative views. Additionally, **(c)** shows a schematic diagram of the RhoH$_{T1}$ construct domain architecture, with significant amino acid residues shown in red. The colour scheme utilised in **(c)** is also applicable to **(a)** and **(b)**. Mg^{2+} (shown as a green sphere) and GCP, a non-hydrolysable analogue of GTP, are shown in **(a)** and **(b)**, and are positioned as a direct result of superimposition of Cdc42 with the RhoFL model (Cdc42 hidden, but GCP and Mg^{2+} visible). RhoH$_{T1}$ model rendered in PyMol (Schrödinger Inc., United States).

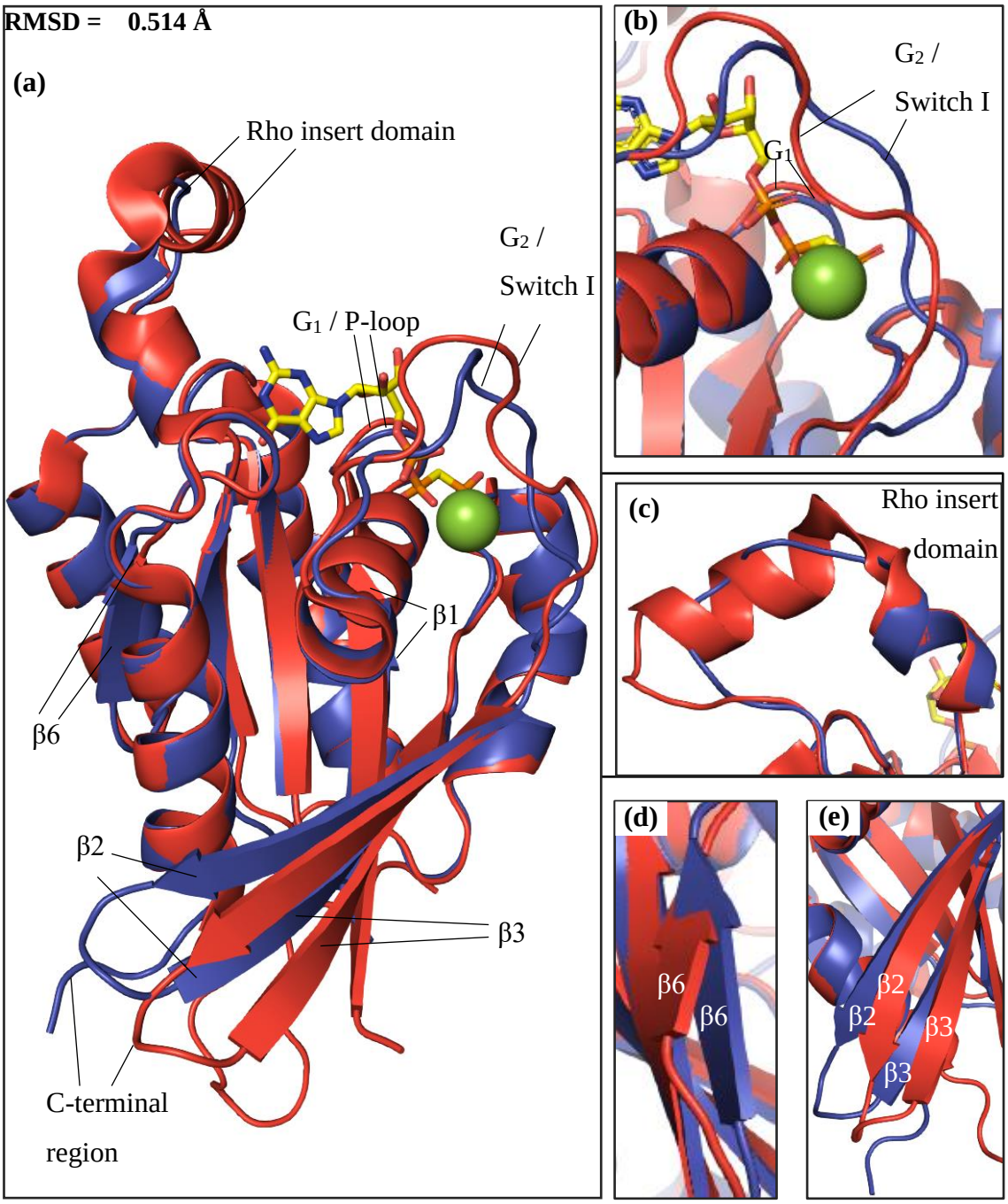

Figure 6.22. Visualisation of a 3D model of $RhoH_{T1}$ (blue) superimposed with the known 3D crystallographic structure of Cdc42 (red). Cdc42 (PDB: 2QRZ) aligned and superimposed against the top LOMETs model of $RhoH_{T1}$, with a **(a)** full structure shown alongside close-up visualisation of: **(b)** the P-loop (G_1) and switch I region, **(c)** the Rho insert domain, **(d)** the β6 sheet and **(e)** the β2 and β3 sheets. The Cdc42 structure was bound Mg^{2+} and GCP, a non-hydrolysable GTP analogue. Models were rendered and superimposed in PyMol (Schrödinger Inc., United States). The overall root mean square deviation (RMSD) for this superimposition was automatically generated by PyMol and is provided above **(a)**.

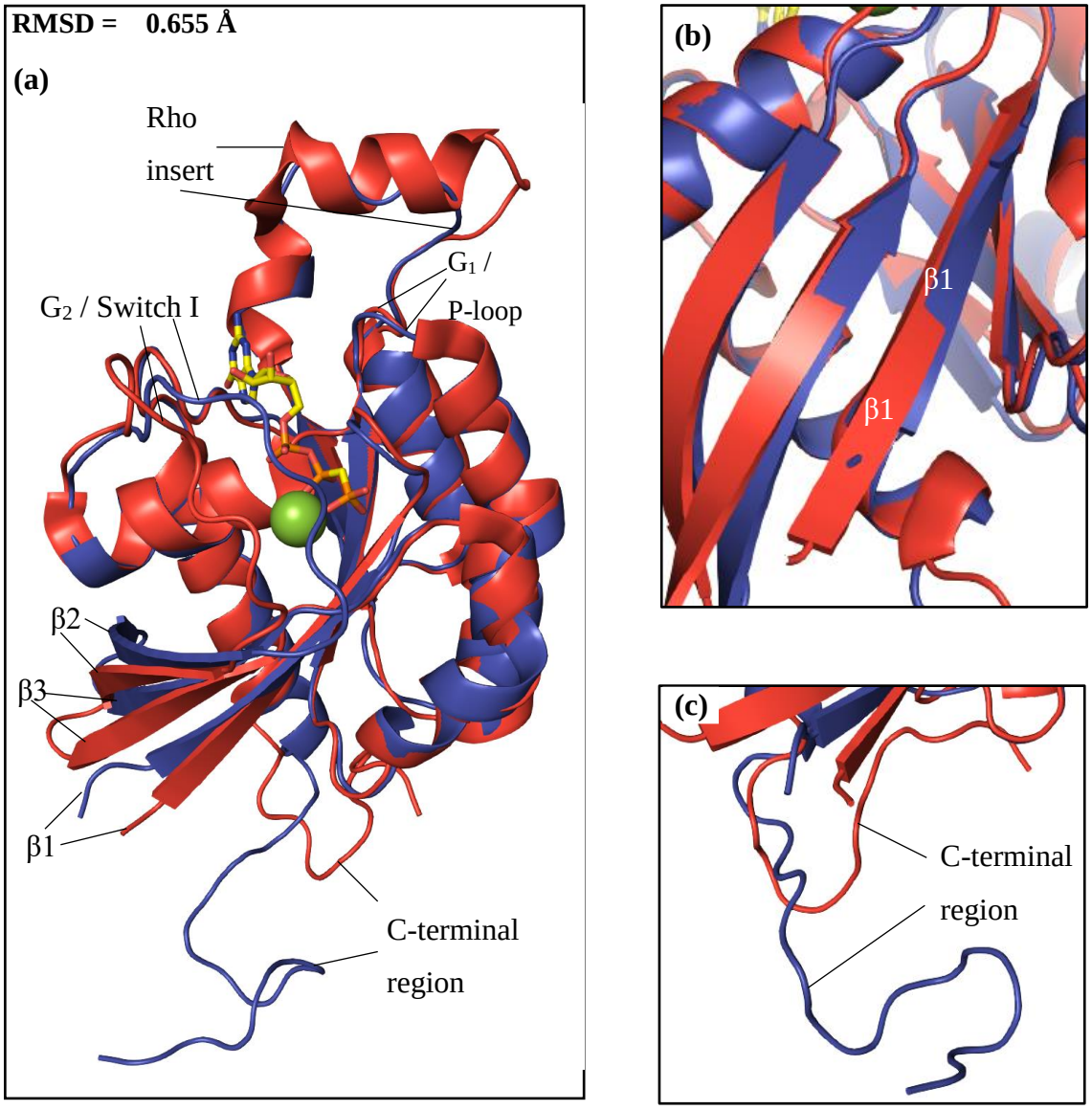

Figure 6.23. Superimposition of a 3D model of $RhoH_{FL}$ (blue) against the known 3D crystallographic structure of Cdc42 (red). Top LOMETs model of $RhoH_{FL}$, aligned and superimposed against the 3D structure of classical Rho GTPase Cdc42 (PDB: 2QRZ), with an **(a)** anterior visualisation shown, in addition to a close-up of **(b)** the β1 sheet region and **(c)** the C-terminal regions of each protein. The Cdc42 structure shown was bound Mg^{2+} and the non-hydrolysable GTP analogue GCP. Models were rendered and superimposed in PyMol (Schrödinger Inc., United States). The overall root mean square deviation (RMSD) is provided below **(a)**, following automatic generatation in the PyMol molecular visualisation system.

6.2.6 Phosphorylation assays

In parallel with the large scale expression and purification of $RhoH_{FL}$ (full length) and $RhoH_{T1}$ (S_4–A_{174}), two constructs of the death-related kinase DRAK2 were expressed and purified: $DRAK2_{FL}$ (full length) and $DRAK2_{XTAL}$ (M_1–K_{327}).This was possible through the kind donation of pNIC28-Bsa4 vectors bearing the nucleotides encoding either $DRAK2_{FL}$ or $DRAK2_{XTAL}$, respectively, courtesy of the Oxford University Structural Genomics Consortium. The scheme of expression and purification of these constructs was guided by prior expression trials, resulting in a recombinant protein yield of ~2mg/mL from 1–2 L C43 culture and single bands on SDS-PAGE gels (IMAC and gel filtration purification utilised; see Figure 6.24–6.27).

As discussed in 6.1, DRAK2 is a strong putative RhoH interaction partner and it is believed that this kinase may phosphorylate RhoH. As such, a series of phosphorylation assays were implemented as discussed in 2.2.7.1., with samples taken at time zero (0 min), 10 minutes and 45 minutes after initiation of the reaction. As discussed in detail previously (2.2.5.3), the reaction mixture consisted of a set concentration of kinase (10µM or 20µM) in combination with either 5 times or 10 times the amount of RhoH construct; the reaction occurred in gel filtration buffer (2.1.5.3.3) supplemented with 2mM $MgCl_2$ and 1mM ATP. Samples were collected in 1.5mL eppendorphs and frozen immediately at -80^{o}C upon collection. When required, samples were then thawed and an appropriate amount of SDS-PAGE buffer (2.1.5.1.5**)** added. The samples were subjected to SDS-PAGE electrophoresis (2.2.4.1) and Western blotting was performed (2.2.4.8) using the ab17464 Anti-phosphoSer/phosphoThr polyclonal (AbCam, United Kingdom) in the dilutions shown in Table 2.4 (2.1.1.4). To ensure loading consistency for Western blotting, select blots were stripped and re-probed with either an anti-RhoH or anti-DRAK2 primary antibody in the dilutions shown in Table 2.4 (2.1.1.4). Additionally, all SDS-PAGE gels used in Western blotting were also dyed in Coomassie blue (2.2.4.2) post-transfer as a means to further assess the loading efficiency of samples. Overall, the Western blotting results (Figures 6.28–6.35) from these assays indicate that both $DRAK2_{FL}$ and $DRAK2_{XTAL}$ are capable of phosphorylating RhoH, with both $RhoH_{FL}$ and $RhoH_{T1}$ forming suitable targets. This effect was seen across all variations of the phosphorylation assay tested. Interestingly, however, $DRAK2_{FL}$ appeared to become auto-phosphorylated throughout these assays, while $DRAK_{2XTAL}$ did not.

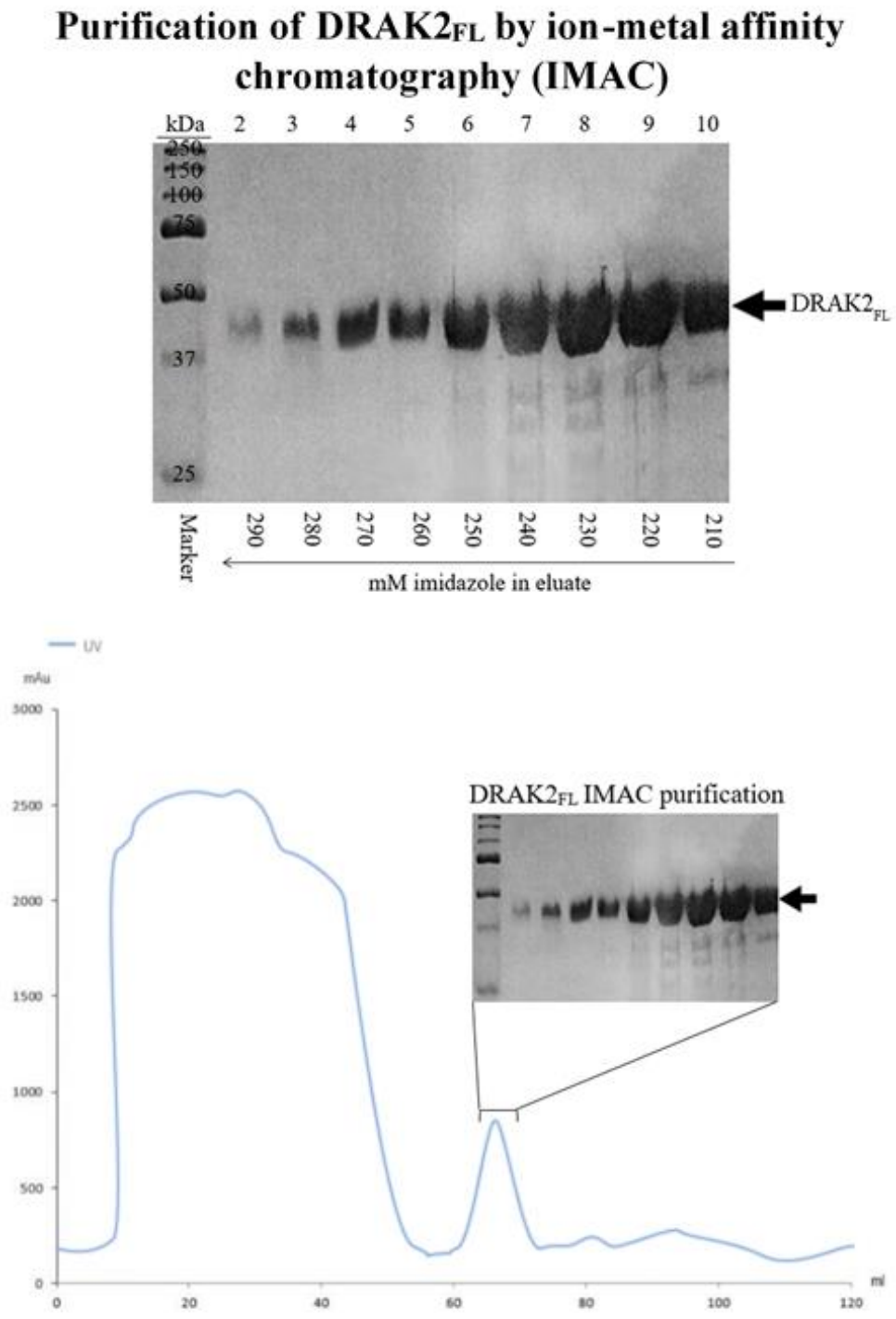

Figure 6.24 Successful IMAC purification of DRAK2FL from lysed recombinant C43 (DE3) *E.coli* extract. (a) 12% SDS-PAGE gel showing IMAC-purified fractions of DRAK2FL. (b) Representative chromatogram trace from IMAC purification, with the area of the chromatogram corresponding to the purified DRAK2FL fractions shown.

Size exclusion purification of DRAK2$_{FL}$ by gel filtration

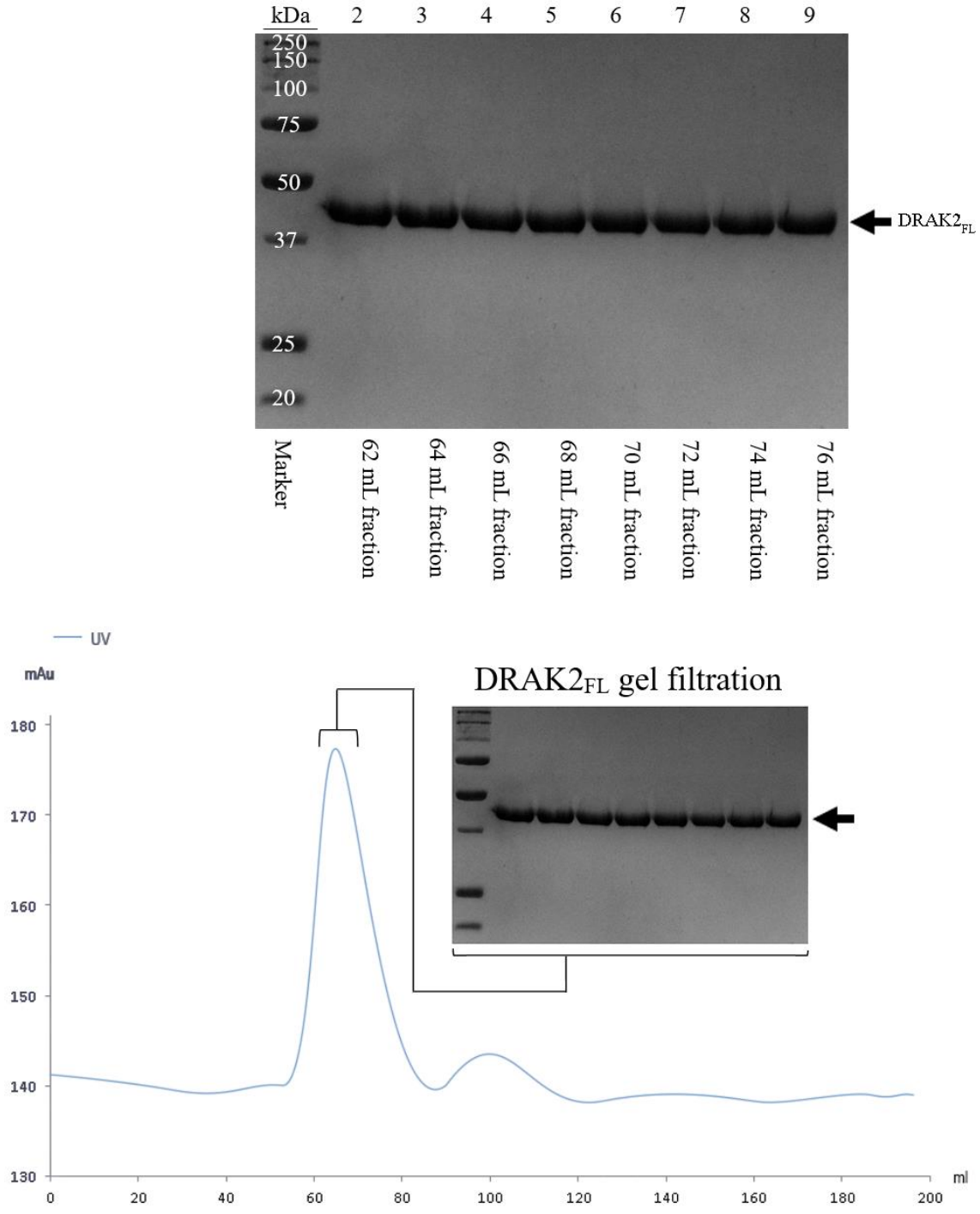

Figure 6.25 Successful size exclusion purification of DRAK2$_{FL}$ from lysed recombinant C43 (DE3) *E.coli* extract. (a) 12% SDS-PAGE gel showing successful size exclusion purification of DRAK2$_{FL}$ **(b)** Representative chromatogram from the DRAK2$_{FL}$ size exclusion (gel filtration) purification; area of the chromatogram corresponding to the purified DRAK2$_{FL}$ fractions clearly displayed.

Purification of DRAK2$_{XTAL}$ by ion-metal affinity chromatography (IMAC)

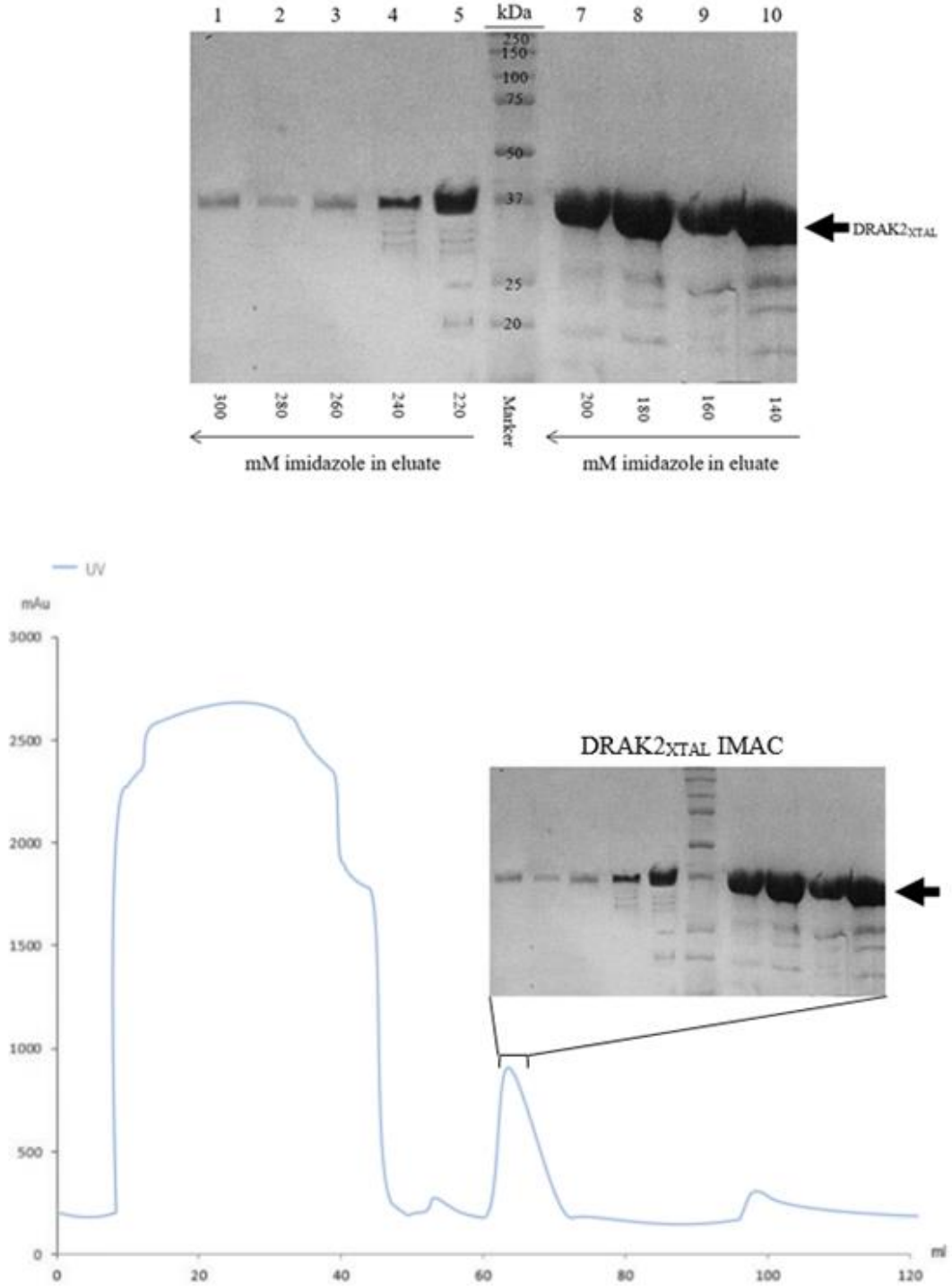

Figure 6.26 IMAC purification of DRAK2$_{XTAL}$ from lysed recombinant C43 (DE3) *E.coli* extract. (a) 12% SDS-PAGE gel showing successfully IMAC-purified fractions of DRAK2$_{XTAL}$. **(b)** Representative chromatogram trace from IMAC purification, with the area of the chromatogram corresponding to the purified DRAK2$_{XTAL}$ fractions displayed.

Size exclusion purification of DRAK2$_{XTAL}$ by gel filtration

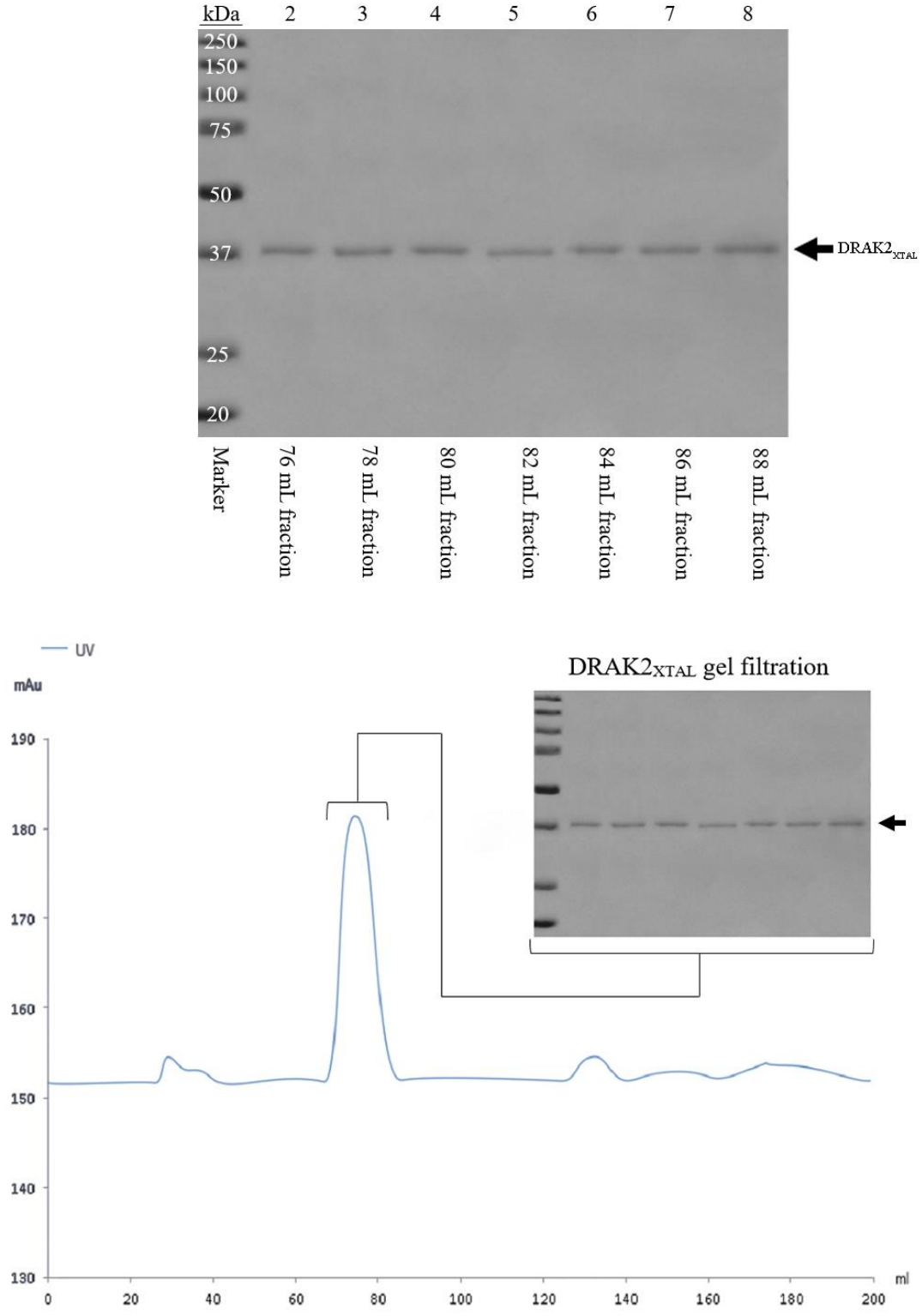

Figure 6.27 Successful size exclusion purification of DRAK2$_{XTAL}$ from lysed recombinant C43 (DE3) *E.coli* extract. (a) 12% SDS-PAGE gel showing successful size exclusion purification of DRAK2$_{XTAL}$ **(b)** Representative chromatogram from the DRAK2$_{XTAL}$ size exclusion (gel filtration) purification; area of the chromatogram corresponding to the purified DRAK2$_{XTAL}$ fractions clearly displayed

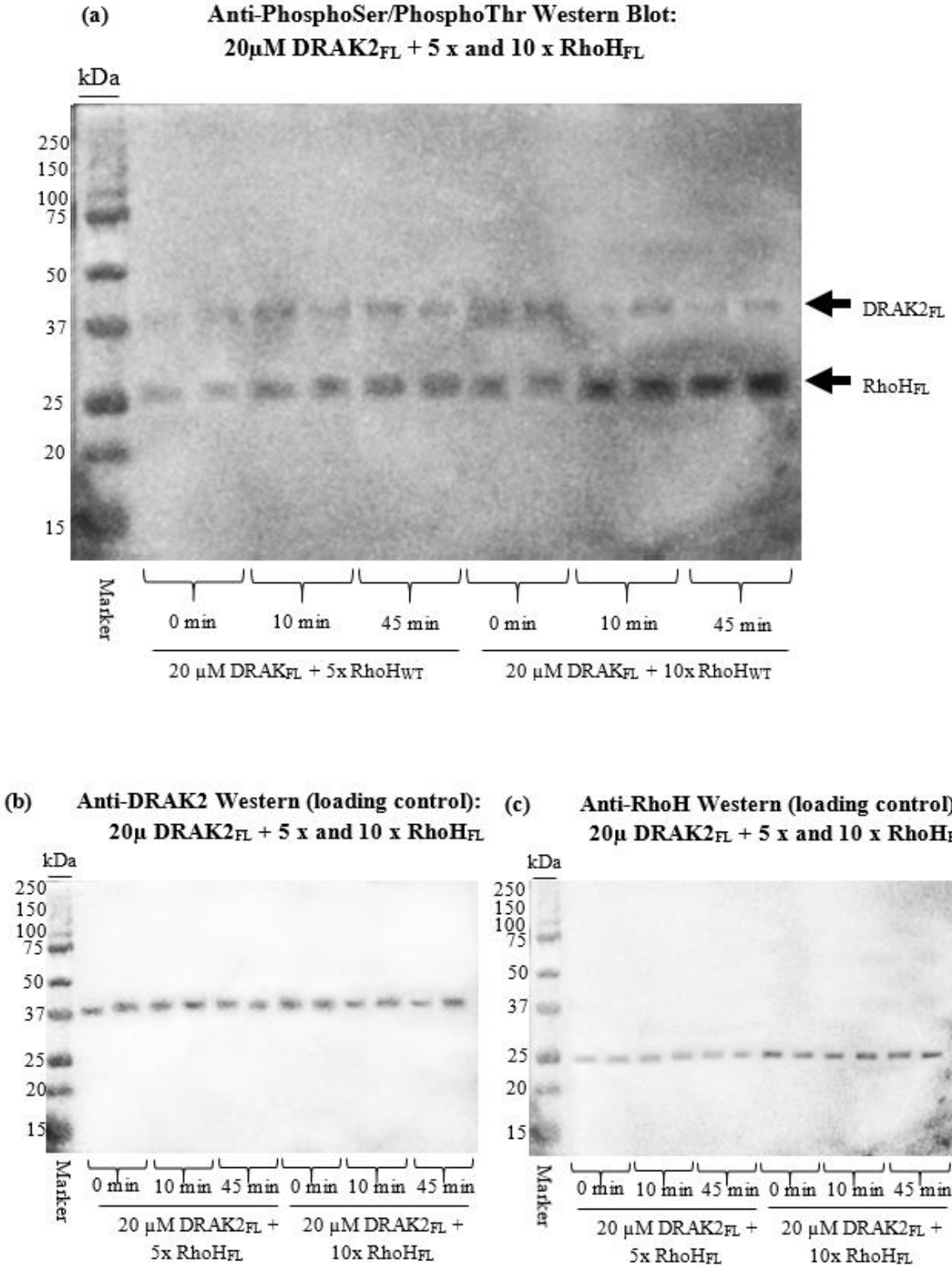

Figure 6.28 20µM $DRAK2_{FL}$ phosphorylates $RhoH_{FL}$ and appears capable of autophosphorylation. (a) Anti-PhosphoSer/PhosphoThr Western blot, showing phosphorylation of $RhoH_{FL}$by 20µM $DRAK2_{FL}$ in the presence of either 5 times (50µM) or ten times (100µM) $RhoH_{FL}$. Stripping and reprobing this blot with **(b)** anti-DRAK2 and subsequently **(c)** anti-RhoH indicated that loading of the DRAK2 and RhoH was controlled.

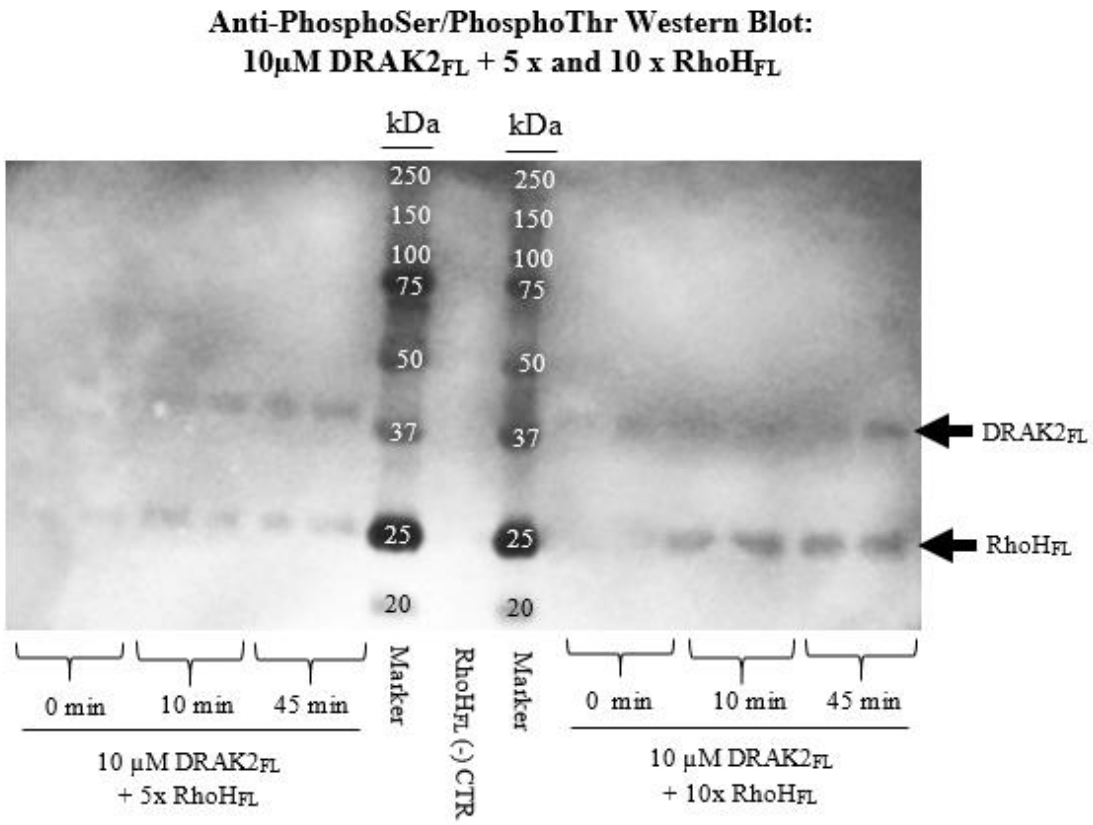

Figure 6.29 10µM $DRAK2_{FL}$ phosphorylates $RhoH_{FL}$ and appears to undergo autophosphorylation. Anti-PhosphoSer/PhosphoThr Western blot, showing phosphorylation of $RhoH_{FL}$by $DRAK2_{FL}$ in the presence of either 5 times (50µM) or ten times (100µM) $RhoH_{FL}$.

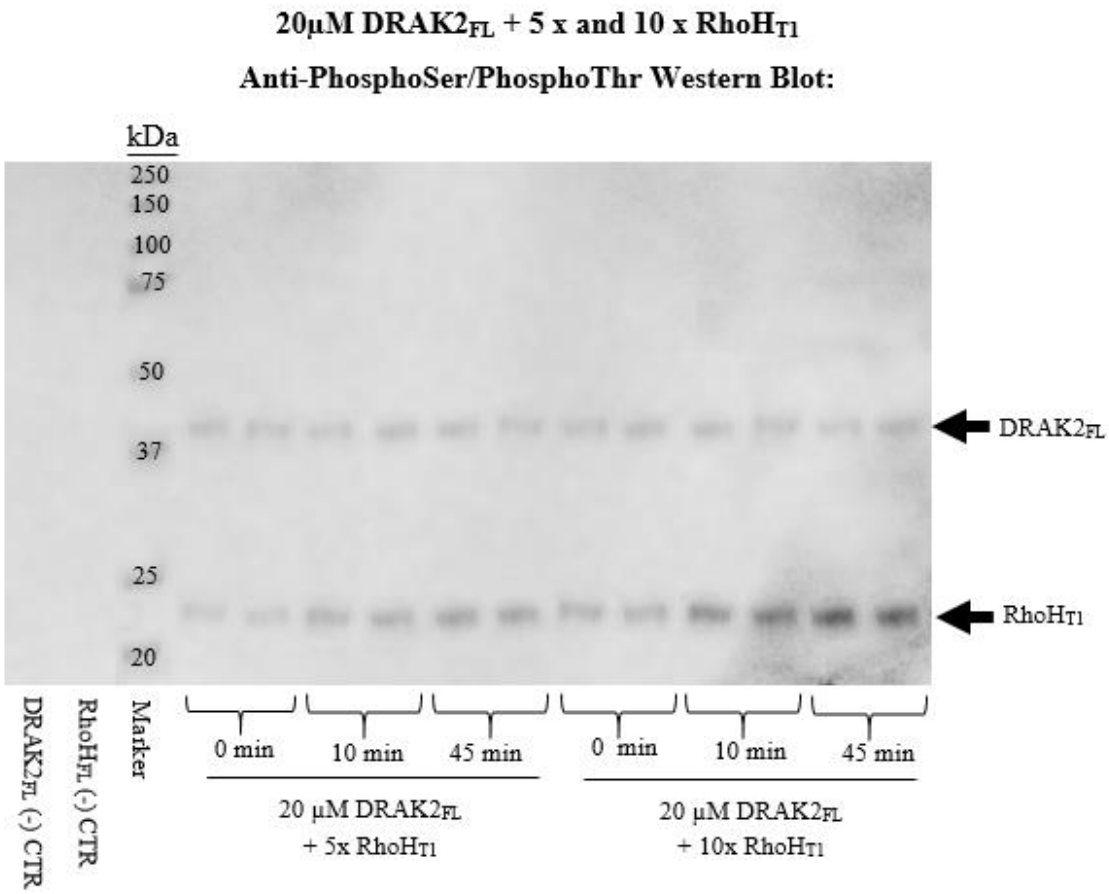

Figure 6.30 20µM $DRAK2_{FL}$ phosphorylates $RhoH_{T1}$ and appears to undergo autophosphorylation. Anti-PhosphoSer/PhosphoThr Western blot from phosphorylation assays, indicating phosphorylation of $RhoH_{T1}$ by 20µM $DRAK2_{FL}$ in the presence of either 5 times (50µM) or ten times (100µM) $RhoH_{T1}$.

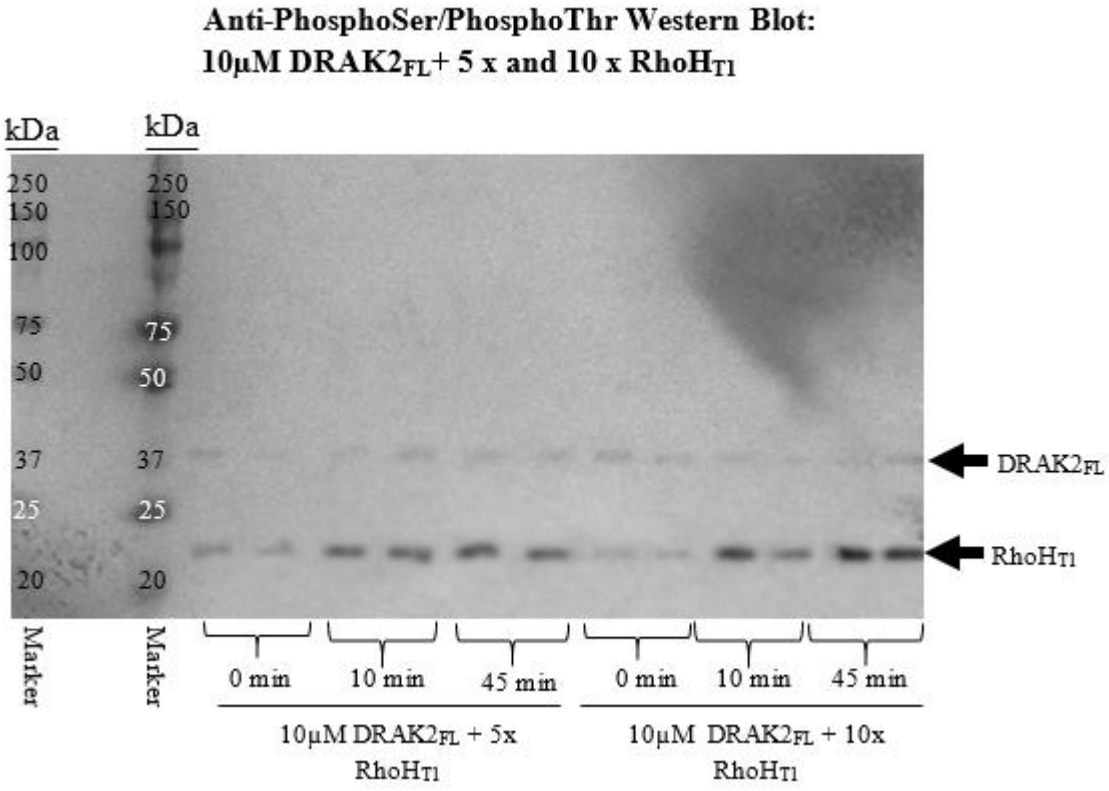

Figure 6.31 10µM DRAK2$_{FL}$ appears to autophosphorylate in the presence of magnesium and ATP, and is able to phosphorylate DRAK2$_{FL}$. Anti-PhosphoSer/PhosphoThr Western blot, denoting phosphorylation of RhoH$_{T1}$ by 10µM DRAK2$_{FL}$ in the presence of either 5 times (50µM) or ten times (100µM) RhoH$_{T1}$.

Anti-PhosphoSer/PhosphoThr Western Blot:

10µM DRAK2$_{XTAL}$ + 5 x and 10 x RhoH$_{T1}$

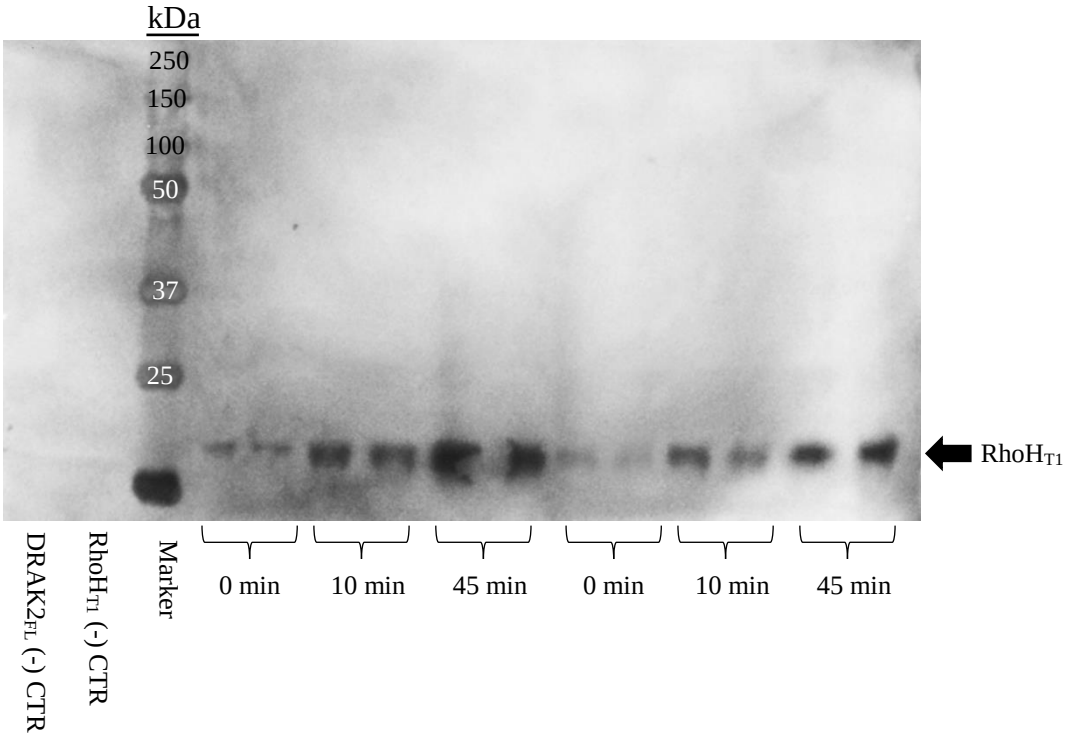

Figure 6.32 Phosphorylation of RhoH$_{FL}$ by 20µM DRAK2$_{XTAL}$ in the presence of magnesium and ATP. Anti-PhosphoSer/PhosphoThr immunoblot, showing phosphorylation of RhoH$_{FL}$ by 20µM DRAK2$_{XTAL}$.

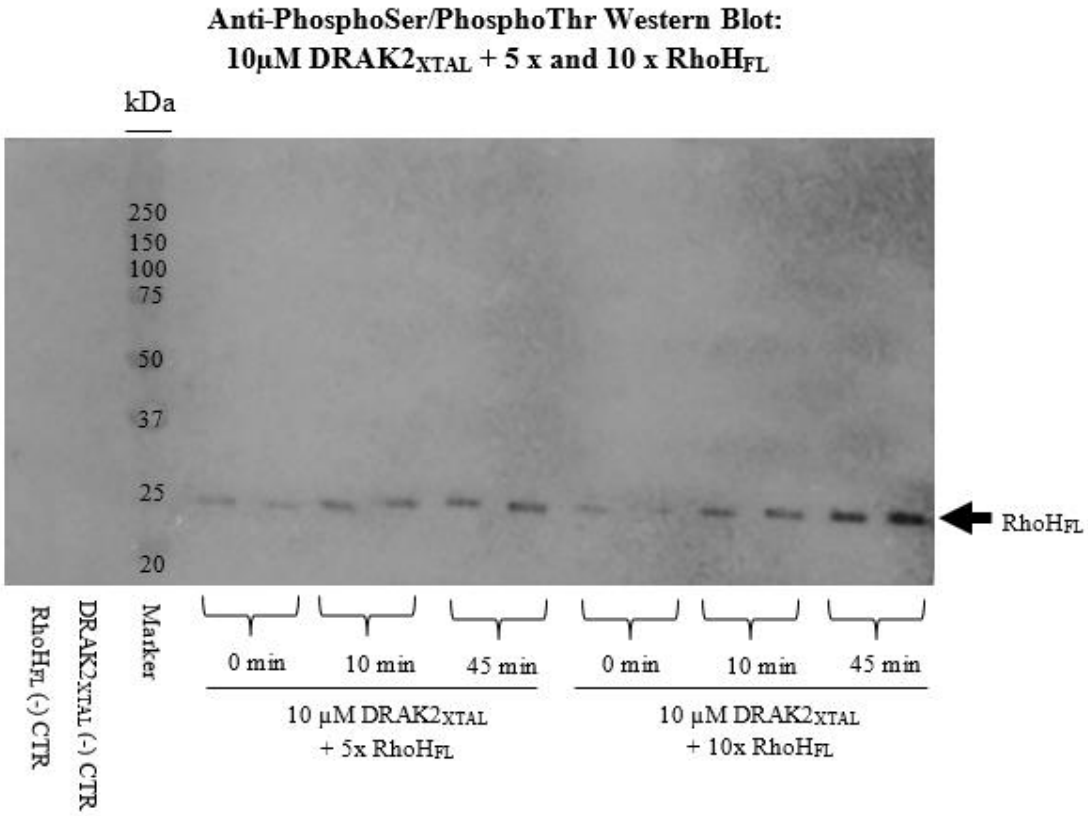

Figure 6.33 $RhoH_{FL}$ is phosphorylated by 10µM $DRAK2_{XTAL}$ in the presence of magnesium and ATP. Anti-PhosphoSer/PhosphoThr Western, indicating phosphorylation of $RhoH_{FL}$ by 10µM $DRAK2_{XTAL}$.

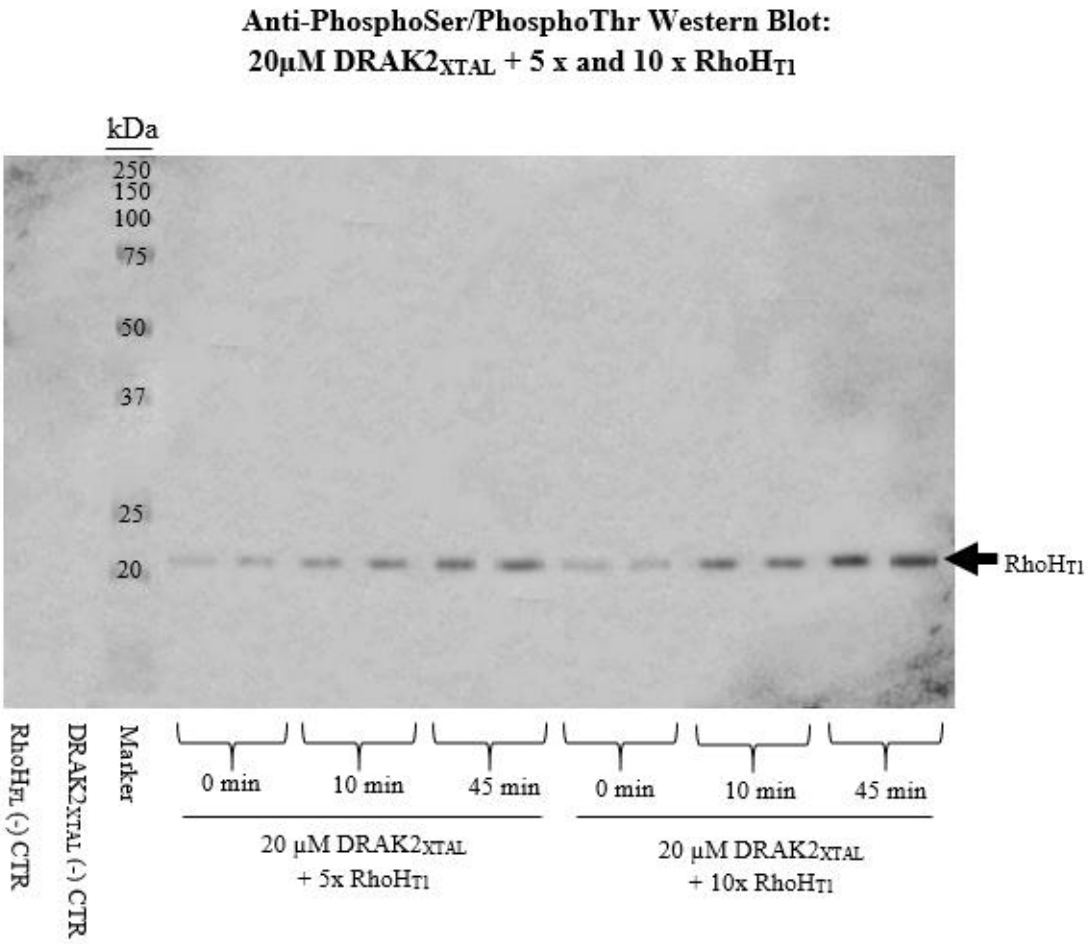

Figure 6.34 Phosphorylation of $RhoH_{T1}$ by 20µM $DRAK2_{XTAL}$ in the presence of magnesium and ATP. (a) Anti-PhosphoSer/PhosphoThr immunoblot, exhibiting phosphorylation of $RhoH_{T1}$ by 20µM $DRAK2_{XTAL}$.

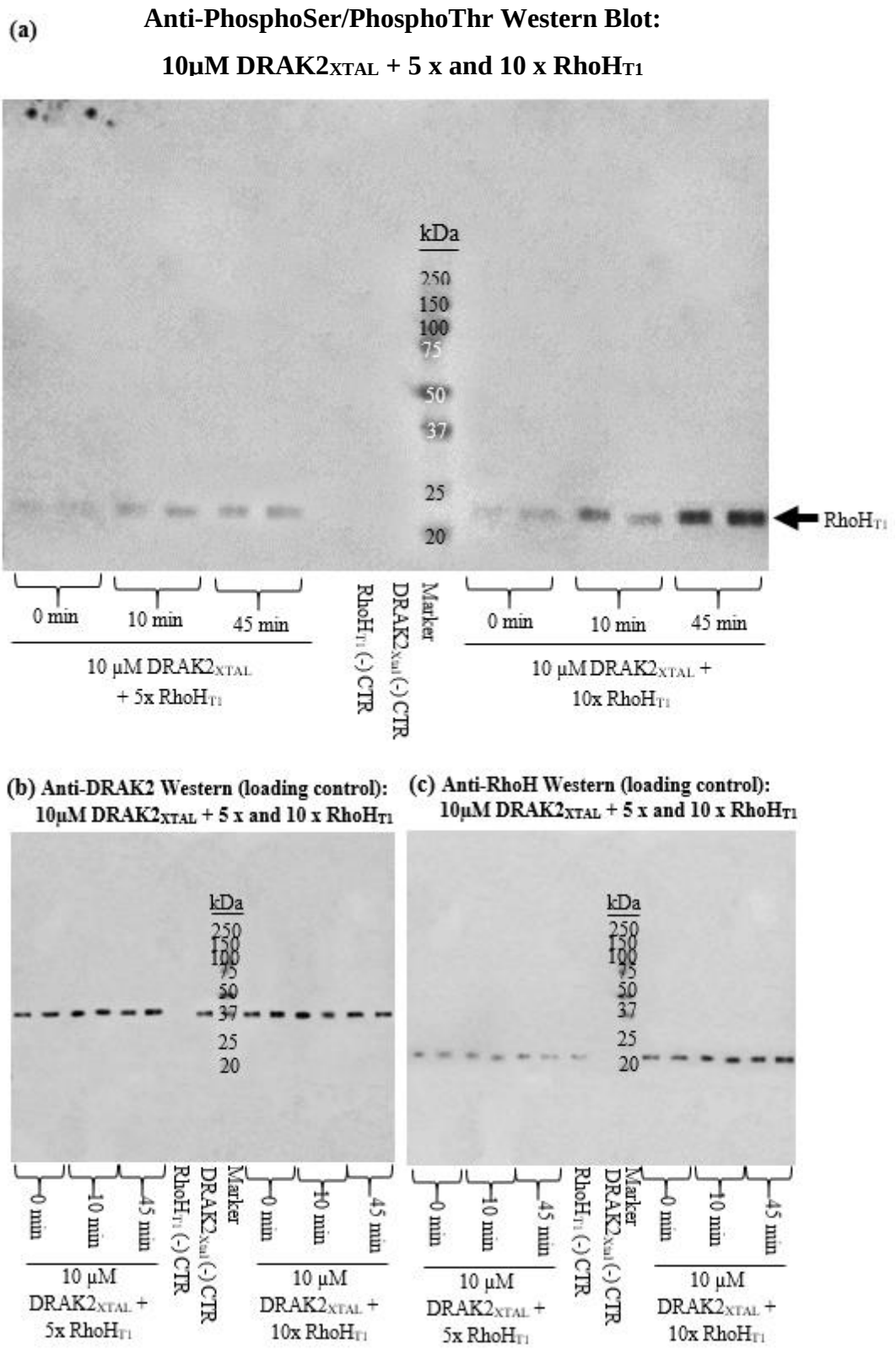

Figure 6.35 10µM DRAK2$_{XTAL}$ phosphorylates RhoH$_{T1}$ in the presence of magnesium and ATP. (a) Anti-PhosphoSer/PhosphoThr Western blot indicating phosphorylation of RhoH$_{T1}$ by 20µM DRAK2$_{XTAL}$ in the presence of either 5 times (50µM) or ten times (100µM) RhoH$_{FL}$. Stripping and reprobing this blot with **(b)** anti-DRAK2 and **(c)** anti-RhoH utilised as loading controls.

Unless otherwise indicated, the term ‘phosphorylation’ will subsequently be used to indicate serine/threonine phosphorylation only. In Figures 6.28 and 6.29, two distinct bands are consistently observed at positions suggesting that both $RhoH_{FL}$ and $DRAK2_{FL}$ are phosphorylated throughout the assays; this effect is also observed in Figures 6.30 and 6.31, indicating that both $DRAK2_{FL}$ and $RhoH_{T1}$ were phosphorylated throughout the experiments. In Figures 6.32 and 6.33, $RhoH_{FL}$ appears to have undergone phosphorylation; correspondingly, Figures 6.34 and 6.35 indicate that $RhoH_{T1}$ is phosphorylated under these experimental conditions. A pattern therefore emerges: while $DRAK2_{FL}$ appeared to be consistently phosphorylated in these studies, $DRAK2_{XTAL}$ did not. One potential explanation could be that $DRAK2_{FL}$ experiences autophosphorylation in residues not present in the $DRAK2_{XTAL}$ truncate. Serine-12 in DRAK2 has been previously identified as an important residue for regulatory autophopshorylation, although serine and threonine residues at positions 328, 333, 348, 351 and 362 have also been implicated as targets for DRAK2 autophosphorylation (487). As $DRAK2_{XTAL}$ is truncated at residue 327, it may simply be that $DRAK2_{FL}$ is experiencing autophosphorylation at these other reported serine and/or threonine residues. Alternatively, $DRAK2_{XTAL}$ may be partaking in serine-12 autophosphorylaton at a level not detectable with the conditions tested and methodology applied. Whatever the case, the results obtained may indicate that serine and/or threonine residues after position 327, the cut-off boundary for $DRAK2_{XTAL}$, engage in autophosphorylation *in vitro* under these experimental conditions in a detectable manner. One weakness with the phosphorylation assay data are the presence of bands at time zero. Since the proteins used in these assays were all gel purified (producing single bands on SDS-PAGE gels), it is unlikely that the bands present at time zero indicate phosphorylation of an off-target protein. One explanation may be that some serine and/or threonine residues experienced phosphorylation by endogenous *E.coli* kinases prior to purification; indeed, phosphorylation of proteins by kinases has been known to survive the gel filtration process (506). Generally, however, an increasing signal was observed over time in the anti-PhosphoSer/PhosphoThr blots; this indicates that phosphorylation of $RhoH_{FL}$, $RhoH_{T1}$ and $DRAK2_{FL}$ was indeed progressively occurring.

6.3 Conclusions and discussion

6.3.1 RhoH characteristics *in vitro*

The data exhibited in this chapter show that both full length human RhoH ($RhoH_{FL}$) and the corresponding human RhoH truncate S_4–A_{174} ($RhoH_{T1}$) express well in *E.coli* expression strains BL21 (DE3), C41 (DE3) and C43 (DE3). However, these enzymes are difficult to process downstream and display the propensity to aggregate even in the presence of optimised buffers. The use of protease inhibitors and swift purification prevented normal degradation of RhoH in this context. Although not directly comparable, it is interesting to note that the half-life of full length RhoH in Jurkat human T lymphocytes has previously been described as less than 3 hours, with truncations of RhoH lacking the CaaX box or polybasic domain displaying an even shorter half-life in these cells (435). Interestingly, $RhoH_{T1}$ tended to exhibit a longer half-life than its full length counterpart *in vitro*. Indeed, submission of the $RhoH_{FL}$ and $RhoH_{T1}$ amino acid sequences into the XtalPred-RF online server yielded instability index (II) scores of 41.26 and 27.59, respectively (507). This indicated that $RhoH_{FL}$ is unlikely to show stability *in vitro* while $RhoH_{T1}$ may show a degree of stability. It is possible that while a truncated version of RhoH is inherently more stable than $RhoH_{FL}$, displacement of RhoH from its site of action at the plasma membrane (due to a $RhoH_{T1}$-like C-terminal truncation) produces an enhanced vulnerability to targeted degradation in living cells. However, this remains to be confirmed experimentally. It should also be noted that it was difficult to definitively assess the half-life of human $RhoH_{FL}$ and $RhoH_{T1}$ *in vitro* due to aggregation issues and the use of protease inhibitors. Regardless of this, the available time for downstream use of both $RhoH_{FL}$ and $RhoH_{T1}$ before excessive aggregation and degradation was low. Typically, a window of ~36 hours was available following IMAC purification in order to acquire meaningful data. This brought great difficulties with regards to crystallisation, with a distinct absence of meaningful crystals in all tested conditions. Regardless of this short timeframe for action, crystallisation prediction scores for both $RhoH_{FL}$ and $RhoH_{T1}$ primary sequences inputted into the XtalPred-RF online server indicated that these proteins would be difficult to crystallise with or without the presence of a hexahistidine tag. The one anomaly for this was $RhoH_{T1}$ under the expert pool (EP) method of prediction, which implied a high likelihood of $RhoH_{T1}$ crystallisation. Intriguingly, the random forest (RF) crystallisation prediction score for $RhoH_{T1}$ suggested somewhat the

opposite of the EP method, indicating that $RhoH_{T1}$ did not show a particularly promising likelihood for crystallisation.

In silico modelling attempts produced 3D structures broadly similar to typical Ras superfamily G domains. Akin to classical small GTPases, five alpha helices and six beta sheets were observed. Additionally, two regions resembling the classical switch I and II regions were shown. Superimposition of $RhoH_{T1}$ and $RhoH_{FL}$ against the canonical Rho GTPase Cdc42 (296) showed that both proteins fit well against Cdc42 general structure, with RMSD values of 0.514Å and 0.655Å. The most noticeable differences between the RhoH models and Cdc42 were observed in the P loop and switch I regions, producing a tighter nucleotide binding site in the RhoH models; this may contribute to the constitutively GTP-bound state of RhoH (420), alongside the G13S and Q62N substitutions in RhoH (shown in Figure 6.20) believed to maintain RhoH in a constitutively active state (58,420,428) relative to typical Ras and Rho enzymes due to steric interference of the catalytic arginine finger of GAP regulatory enzymes (2,58,428).

Interestingly, while RhoH appeared monomeric *in vitro*, this still remains to be fully explored. Indeed, many proteins harbouring ITAM motifs act as dimers intracellularly. Thus, it is possible that RhoH may be capable of dimerisation within the cell. Ultimately, analytical ultracentrifugation would provide a definitive answer to RhoH's ability to dimerise *in vitro*. However, the results obtained indicate that RhoH shows a monomeric appearance *in vitro*.

6.3.4 DRAK2 as a regulator of RhoH

RhoH does not follow the tight canonical scheme of regulation exhibited by the majority of Ras superfamily GTPases, instead displaying constitutive activity due to point mutations at glycine-12 and glutamine-61. However, several other means of regulating this enzyme appear to exist, including phosphorylation. While phosphorylation of the tyrosine residues of the RhoH ITAM-like motifs appears to be important for Zap70 recruitment, many canonical Rho GTPases are phosphorylated by serine/threonine kinases (420,508-510) and it is likely that RhoH also undergoes regulation through phosphorylation at serine or threonine residues. In T lymphocytes, RhoH and DRAK2 appear to exhibit several shared functional roles and downstream effectors, suggesting that they act within the same or similar signalling pathways (6.1.6). Additionally, these proteins have both been independently implicated in the development of chronic

lymphocytic leukaemia (CLL). This information, together with recent reports that RhoH mRNA levels positively correlate with levels of DRAK2 mRNA (505), prompted the *in vitro* phosphorylation assays undertaken in this project which demonstrate that both DRAK2 and the $DRAK2_{XTAL}$ (1-327) truncate are capable of phosphorylating $RhoH_{FL}$ and $RhoH_{T1}$. Although this interaction remains to be experimentally confirmed *in vivo*, these results indicate that RhoH may be regulated by DRAK2, inviting new avenues of research for exploring RhoH kinase interaction partners. Indeed, this information may prove useful in developing future novel therapeutics against some forms of CLL. Curiously, $DRAK2_{FL}$ consistently exhibited autophosphorylation in these studies, while $DRAK2_{XTAL}$ did not. This suggests that crucial serine or threonine residues necessary for DRAK2 autophosphorylation are not present in the $DRAK2_{XTAL}$ construct. Serine 12 in DRAK2 has been previously identified as an important residue for regulatory autophopshorylation, although serine and threonine residues at positions 328, 333, 348, 351 and 362 have also been implicated as targets for DRAK2 autophosphorylation (487). As $DRAK2_{XTAL}$ is truncated at residue 327, it may simply be that $DRAK2_{FL}$ is experiencing autophosphorylation at these other reported serine residues. Alternatively, $DRAK2_{XTAL}$ may be partaking in serine-12 autophosphorylaton at a level not detectable with the conditions tested and methodology applied. Whatever the case, the results obtained suggest that serine residues after position 327, the cut-off boundary for $DRAK2_{XTAL}$, engage in autophosphorylation *in vitro* under these experimental conditions in a detectable manner.

7: Concluding remarks

7.1 Summary

Despite implications in serious pathologies such as neoplastic disorders or neurodegenerative disease, many atypical GTPases of the Ras superfamily remain largely uncharacterised at the functional, structural or biochemical level. Here, a range of experimental approaches were utilised to elucidate the molecular function and interactors of three highly atypical human Rho GTPases: hMiro1, hMiro2 and RhoH. The results demonstrate, for the first time, the hydrolytic activities of the hMiro1 and hMiro2 individual GTPase domains, and show that the hMiro C-terminal GTPase domains are capable of substrate promiscuity, displaying hydrolytic activity against ATP and UTP in addition to GTP. Novel kinetic parameters are provided pertaining to the basal hydrolytic activity of these domains, with the domains broadly exhibiting similar GTP hydrolytic efficiencies to those of unstimulated classical Rho GTPases. RNAi ablation of the hMiros led to a reduction in the migration of live PC3 cancer cells and produced distinctive phenotypes of perinuclear mitochondrial aggregation (hMiro1 and hMiro2 RNAi) and bloating (dual RNAi of both hMiros), while biophysical characterisation of the $hMiro_{XTAL}$ constructs suggested that the hMiros exist monomerically and possess average thermal stability. Cell studies and proteomics analysis of over-expressed hMiro mutants indicated important roles for the state of the hMiro GTPase domains in tuning cell signalling, with active and inactive GTPase domains associating with diverse interactors and signalling components. Through these studies, several novel hMiro interactors were indicated. Computer-based prediction of hMiro signalling partners enhanced the proteomics data obtained and brought greater legitimacy to the data set, with several unique binding partners indicated for each condition. Finally, *in vitro* binding between DRAK2 serine threonine kinase and RhoH, another Rho family atypical GTPase was shown for the first time. The implications for DRAK2 and RhoH binding *in vivo* are significant, with a clinical relevance indicated for chronic lymphocytic leukaemia (CLL).

7.2 Perspectives and future directions

Although the results obtained throughout this work have provided novel insights to the molecular functions and interactors associated with the human Miros and RhoH, new functions for the atypical GTPases continue to emerge in the literature. These functions

often provide more questions than answers: numerous cellular processes regulated by the Ras superfamily, and particularly atypical GTPases of this superfamily, remain to be completely elucidated.

Here, a glimpse of hMiro molecular interactors was achieved through proteomic studies, though a more complete insight would be possible with utilisation of hMiro knockdown samples and the full panel of mutants engineered. Expanding these omics studies even further could enable the elucidation of hMiro-centred signalling interactions in serious pathologies. If possible, an assessment of the influence of hMiro1 and hMiro2 GTPase domain state on whole cell metabolomics would be highly interesting: particularly given the poorly understood links between the Miro GTPases and metabolism. Further to this, an assessment of the influence of hMiro1 and hMiro2 on the proteomics of neuronal cells would be intriguing, particularly if the proteome was mapped throughout neuronal development and during ageing in the context of Miro abrogation, as the former has been implicated in neonatal death and the latter has been consistently associated with the development of neurodegenerative symptoms in animal models. Of course, validating the signalling pathways and the underlying molecular mechanism mediated by hMiro and RhoH would be of great value to investigate new avenues for therapeutics to treat B cell leukaemias and neurodegeneration amongst others.

The characterisation performed here for RhoH suggests that this enzyme may be regulated by serine/threonine kinases. However, no search for RhoH serine/threonine kinase interactors currently exists. Exploiting this uncharted avenue with the likes of kinase arrays, mutational analyses and mass spectrometry would likely identify further novel kinases associated with RhoH and their sites of phosphorylation on this unusual GTPase. Furthermore, to assess whether the novel *in vitro* interactions discovered between RhoH and DRAK2 occur *in vivo* and in a clinically relevant manner, it would be interesting to expand the work performed in chapter 6 to encompass the processing of neoplastic samples derived from CLL patients. Comparing these samples to normal controls from healthy individuals would establish whether a clinical significance exists for the association between RhoH and DRAK2.

Finally, approaches to further characterise other atypical GTPases of the Ras superfamily would be highly informative. Many of these unusual enzymes engage in the development of serious pathological states. Despite this, these GTPases and their interactors generally

remain poorly understood. Further efforts to characterise these remarkable enzymes and their binding partners would likely yield great benefit in understanding many cellular processes, including pathological processes implicated in diseases such as various malignancies and neurodegenerative disorders.

8: References

1. Goitre, L., Trapani, E., Trabalzini, L., and Retta, S. F. (2014) The Ras superfamily of small GTPases: the unlocked secrets. *Methods in molecular biology* **1120**, 1-18
2. Wennerberg, K., Rossman, K. L., and Der, C. J. (2005) The Ras superfamily at a glance. *J Cell Sci* **118**, 843-846
3. Aspenstrom, P. (2004) Integration of signalling pathways regulated by small GTPases and calcium. *Biochimica et biophysica acta* **1742**, 51-58
4. Gomez, J., Martinez, A. C., Gonzalez, A., and Rebollo, A. (1998) Dual role of Ras and Rho proteins: at the cutting edge of life and death. *Immunology and cell biology* **76**, 125-134
5. Valencia, A., Chardin, P., Wittinghofer, A., and Sander, C. (1991) The ras protein family: evolutionary tree and role of conserved amino acids. *Biochemistry* **30**, 4637-4648
6. Rojas, A. M., Fuentes, G., Rausell, A., and Valencia, A. (2012) The Ras protein superfamily: evolutionary tree and role of conserved amino acids. *J Cell Biol* **196**, 189-201
7. Wennerberg, K., and Der, C. J. (2004) Rho-family GTPases: it's not only Rac and Rho (and I like it). *J Cell Sci* **117**, 1301-1312
8. Hutagalung, A. H., and Novick, P. J. (2011) Role of Rab GTPases in membrane traffic and cell physiology. *Physiol Rev* **91**, 119-149
9. Biou, V., and Cherfils, J. (2004) Structural principles for the multispecificity of small GTP-binding proteins. *Biochemistry* **43**, 6833-6840
10. Fernandez-Medarde, A., and Santos, E. (2011) Ras in cancer and developmental diseases. *Genes Cancer* **2**, 344-358
11. Orgaz, J. L., Herraiz, C., and Sanz-Moreno, V. (2014) Rho GTPases modulate malignant transformation of tumor cells. *Small GTPases* **5**, e29019
12. Mitra, S., Cheng, K. W., and Mills, G. B. (2011) Rab GTPases implicated in inherited and acquired disorders. *Semin Cell Dev Biol* **22**, 57-68
13. Stein, M. P., Muller, M. P., and Wandinger-Ness, A. (2012) Bacterial pathogens commandeer Rab GTPases to establish intracellular niches. *Traffic* **13**, 1565-1588
14. Caceres-Gorriti, K. Y., Carmona, E., Barres, V., Rahimi, K., Letourneau, I. J., Tonin, P. N., Provencher, D., and Mes-Masson, A. M. (2014) RAN nucleo-cytoplasmic transport and mitotic spindle assembly partners XPO7 and TPX2 are new prognostic biomarkers in serous epithelial ovarian cancer. *PLoS One* **9**, e91000
15. Li, Y., Ling, K., and Hu, J. (2012) The emerging role of Arf/Arl small GTPases in cilia and ciliopathies. *J Cell Biochem* **113**, 2201-2207
16. Morgan, C., Lewis, P. D., Hopkins, L., Burnell, S., Kynaston, H., and Doak, S. H. (2015) Increased expression of ARF GTPases in prostate cancer tissue. *Springerplus* **4**, 342
17. Tang, B. L. (2015) MIRO GTPases in Mitochondrial Transport, Homeostasis and Pathology. *Cells* **5**
18. Baines, A. T., Xu, D., and Der, C. J. (2011) Inhibition of Ras for cancer treatment: the search continues. *Future Med Chem* **3**, 1787-1808
19. Aoki, Y., Niihori, T., Kawame, H., Kurosawa, K., Ohashi, H., Tanaka, Y., Filocamo, M., Kato, K., Suzuki, Y., Kure, S., and Matsubara, Y. (2005)

Germline mutations in HRAS proto-oncogene cause Costello syndrome. *Nat Genet* **37**, 1038-1040
20. Rauen, K. A. (1993) Cardiofaciocutaneous Syndrome. in *GeneReviews(R)* (Pagon, R. A., Adam, M. P., Ardinger, H. H., Wallace, S. E., Amemiya, A., Bean, L. J. H., Bird, T. D., Fong, C. T., Mefford, H. C., Smith, R. J. H., and Stephens, K. eds.), Seattle (WA). pp
21. Ekvall, S., Wilbe, M., Dahlgren, J., Legius, E., van Haeringen, A., Westphal, O., Anneren, G., and Bondeson, M. L. (2015) Mutation in NRAS in familial Noonan syndrome--case report and review of the literature. *BMC Med Genet* **16**, 95
22. Niemeyer, C. M. (2014) RAS diseases in children. *Haematologica* **99**, 1653-1662
23. Iijima-Ando, K., Sekiya, M., Maruko-Otake, A., Ohtake, Y., Suzuki, E., Lu, B., and Iijima, K. M. (2012) Loss of axonal mitochondria promotes tau-mediated neurodegeneration and Alzheimer's disease-related tau phosphorylation via PAR-1. *PLoS Genet* **8**, e1002918
24. Mastroeni, D., Chouliaras, L., Grover, A., Liang, W. S., Hauns, K., Rogers, J., and Coleman, P. D. (2013) Reduced RAN expression and disrupted transport between cytoplasm and nucleus; a key event in Alzheimer's disease pathophysiology. *PLoS One* **8**, e53349
25. Jiang, S., Shen, D., Jia, W. J., Han, X., Shen, N., Tao, W., Gao, X., Xue, B., and Li, C. J. (2016) GGPPS-mediated Rab27A geranylgeranylation regulates beta cell dysfunction during type 2 diabetes development by affecting insulin granule docked pool formation. *J Pathol* **238**, 109-119
26. Kowluru, A. (2010) Small G proteins in islet beta-cell function. *Endocr Rev* **31**, 52-78
27. Cai, A., Zhou, Y., and Li, L. (2015) Rho-GTPase and Atherosclerosis: Pleiotropic Effects of Statins. *J Am Heart Assoc* **4**
28. Shimokawa, H., Sunamura, S., and Satoh, K. (2016) RhoA/Rho-Kinase in the Cardiovascular System. *Circ Res* **118**, 352-366
29. Fransson, A., Ruusala, A., and Aspenstrom, P. (2003) Atypical Rho GTPases have roles in mitochondrial homeostasis and apoptosis. *The Journal of biological chemistry* **278**, 6495-6502
30. Aspenstrom, P., Ruusala, A., and Pacholsky, D. (2007) Taking Rho GTPases to the next level: the cellular functions of atypical Rho GTPases. *Exp Cell Res* **313**, 3673-3679
31. Iwasaki, T., Katsumi, A., Kiyoi, H., Tanizaki, R., Ishikawa, Y., Ozeki, K., Kobayashi, M., Abe, A., Matsushita, T., Watanabe, T., Amano, M., Kojima, T., Kaibuchi, K., and Naoe, T. (2008) Prognostic implication and biological roles of RhoH in acute myeloid leukaemia. *Eur J Haematol* **81**, 454-460
32. Sanchez-Aguilera, A., Rattmann, I., Drew, D. Z., Muller, L. U., Summey, V., Lucas, D. M., Byrd, J. C., Croce, C. M., Gu, Y., Cancelas, J. A., Johnston, P., Moritz, T., and Williams, D. A. (2010) Involvement of RhoH GTPase in the development of B-cell chronic lymphocytic leukemia. *Leukemia* **24**, 97-104
33. Troeger, A., Johnson, A. J., Wood, J., Blum, W. G., Andritsos, L. A., Byrd, J. C., and Williams, D. A. (2012) RhoH is critical for cell-microenvironment interactions in chronic lymphocytic leukemia in mice and humans. *Blood* **119**, 4708-4718
34. Zhang, F., Wang, W., Siedlak, S. L., Liu, Y., Liu, J., Jiang, K., Perry, G., Zhu, X., and Wang, X. (2015) Miro1 deficiency in amyotrophic lateral sclerosis. *Front Aging Neurosci* **7**, 100

35. Kazlauskaite, A., Kelly, V., Johnson, C., Baillie, C., Hastie, C. J., Peggie, M., Macartney, T., Woodroof, H. I., Alessi, D. R., Pedrioli, P. G., and Muqit, M. M. (2014) Phosphorylation of Parkin at Serine65 is essential for activation: elaboration of a Miro1 substrate-based assay of Parkin E3 ligase activity. *Open Biol* **4**, 130213
36. Birsa, N., Norkett, R., Wauer, T., Mevissen, T. E., Wu, H. C., Foltynie, T., Bhatia, K., Hirst, W. D., Komander, D., Plun-Favreau, H., and Kittler, J. T. (2014) Lysine 27 ubiquitination of the mitochondrial transport protein Miro is dependent on serine 65 of the Parkin ubiquitin ligase. *The Journal of biological chemistry* **289**, 14569-14582
37. Vetter, I. R., and Wittinghofer, A. (2001) The guanine nucleotide-binding switch in three dimensions. *Science* **294**, 1299-1304
38. Erijman, A., and Shifman, J. M. (2016) RAS/Effector Interactions from Structural and Biophysical Perspective. *Mini Rev Med Chem* **16**, 370-375
39. Bishop, A. L., and Hall, A. (2000) Rho GTPases and their effector proteins. *Biochem J* **348 Pt 2**, 241-255
40. Cherfils, J., and Chardin, P. (1999) GEFs: structural basis for their activation of small GTP-binding proteins. *Trends Biochem Sci* **24**, 306-311
41. Cherfils, J., and Zeghouf, M. (2013) Regulation of small GTPases by GEFs, GAPs, and GDIs. *Physiol Rev* **93**, 269-309
42. Mishra, A. K., and Lambright, D. G. (2016) Invited review: Small GTPases and their GAPs. *Biopolymers* **105**, 431-448
43. Olofsson, B. (1999) Rho guanine dissociation inhibitors: pivotal molecules in cellular signalling. *Cell Signal* **11**, 545-554
44. Seabra, M. C., and Wasmeier, C. (2004) Controlling the location and activation of Rab GTPases. *Curr Opin Cell Biol* **16**, 451-457
45. Fukumoto, Y., Kaibuchi, K., Hori, Y., Fujioka, H., Araki, S., Ueda, T., Kikuchi, A., and Takai, Y. (1990) Molecular cloning and characterization of a novel type of regulatory protein (GDI) for the rho proteins, ras p21-like small GTP-binding proteins. *Oncogene* **5**, 1321-1328
46. Milburn, M. V., Tong, L., deVos, A. M., Brunger, A., Yamaizumi, Z., Nishimura, S., and Kim, S. H. (1990) Molecular switch for signal transduction: structural differences between active and inactive forms of protooncogenic ras proteins. *Science* **247**, 939-945
47. Hancock, J. F., Magee, A. I., Childs, J. E., and Marshall, C. J. (1989) All ras proteins are polyisoprenylated but only some are palmitoylated. *Cell* **57**, 1167-1177
48. Moores, S. L., Schaber, M. D., Mosser, S. D., Rands, E., O'Hara, M. B., Garsky, V. M., Marshall, M. S., Pompliano, D. L., and Gibbs, J. B. (1991) Sequence dependence of protein isoprenylation. *The Journal of biological chemistry* **266**, 14603-14610
49. Wittinghofer, F., Krengel, U., John, J., Kabsch, W., and Pai, E. F. (1991) Three-dimensional structure of p21 in the active conformation and analysis of an oncogenic mutant. *Environ Health Perspect* **93**, 11-15
50. Pasqualato, S., Renault, L., and Cherfils, J. (2002) Arf, Arl, Arp and Sar proteins: a family of GTP-binding proteins with a structural device for 'front-back' communication. *EMBO Rep* **3**, 1035-1041
51. Abramovitz, A., Gutman, M., and Nachliel, E. (2012) Structural coupling between the Rho-insert domain of Cdc42 and the geranylgeranyl binding site of RhoGDI. *Biochemistry* **51**, 715-723

52. Zong, H., Kaibuchi, K., and Quilliam, L. A. (2001) The insert region of RhoA is essential for Rho kinase activation and cellular transformation. *Mol Cell Biol* **21**, 5287-5298
53. Ihara, K., Muraguchi, S., Kato, M., Shimizu, T., Shirakawa, M., Kuroda, S., Kaibuchi, K., and Hakoshima, T. (1998) Crystal structure of human RhoA in a dominantly active form complexed with a GTP analogue. *The Journal of biological chemistry* **273**, 9656-9666
54. Bourne, H. R., Sanders, D. A., and McCormick, F. (1991) The GTPase superfamily: conserved structure and molecular mechanism. *Nature* **349**, 117-127
55. Vetter, I. R. (2014) The Structure of the G Domain of the Ras Superfamily. in *Ras Superfamily Small G Proteins: Biology and Mechanisms 1* (Wittinghofer, A. ed.), 1 Ed., Springer Vienna, Vienna. pp 25-50
56. Pathak, E., Atri, N., and Mishra, R. (2013) Role of highly central residues of P-loop and it's flanking region in preserving the archetypal conformation of Walker A motif of diverse P-loop NTPases. *Bioinformation* **9**, 23-28
57. Runquist, J. A., Rios, S. E., Vinarov, D. A., and Miziorko, H. M. (2001) Functional evaluation of serine/threonine residues in the P-Loop of Rhodobacter sphaeroides phosphoribulokinase. *Biochemistry* **40**, 14530-14537
58. Lu, S., Jang, H., Nussinov, R., and Zhang, J. (2016) The Structural Basis of Oncogenic Mutations G12, G13 and Q61 in Small GTPase K-Ras4B. *Sci Rep* **6**, 21949
59. Schubbert, S., Shannon, K., and Bollag, G. (2007) Hyperactive Ras in developmental disorders and cancer. *Nature reviews. Cancer* **7**, 295-308
60. Soundararajan, M., and Eswaran, J. (2012) Atypical GTPases as drug targets. *Anti-cancer agents in medicinal chemistry* **12**, 19-28
61. Paduch, M., Jelen, F., and Otlewski, J. (2001) Structure of small G proteins and their regulators. *Acta biochimica Polonica* **48**, 829-850
62. Zhang, B., Zhang, Y., Wang, Z., and Zheng, Y. (2000) The role of Mg2+ cofactor in the guanine nucleotide exchange and GTP hydrolysis reactions of Rho family GTP-binding proteins. *The Journal of biological chemistry* **275**, 25299-25307
63. Colicelli, J. (2004) Human RAS superfamily proteins and related GTPases. *Science's STKE : signal transduction knowledge environment* **2004**, RE13
64. Joneson, T., White, M. A., Wigler, M. H., and Bar-Sagi, D. (1996) Stimulation of membrane ruffling and MAP kinase activation by distinct effectors of RAS. *Science* **271**, 810-812
65. Rodriguez-Viciana, P., Warne, P. H., Khwaja, A., Marte, B. M., Pappin, D., Das, P., Waterfield, M. D., Ridley, A., and Downward, J. (1997) Role of phosphoinositide 3-OH kinase in cell transformation and control of the actin cytoskeleton by Ras. *Cell* **89**, 457-467
66. White, M. A., Nicolette, C., Minden, A., Polverino, A., Van Aelst, L., Karin, M., and Wigler, M. H. (1995) Multiple Ras functions can contribute to mammalian cell transformation. *Cell* **80**, 533-541
67. Mazhab-Jafari, M. T., Marshall, C. B., Ho, J., Ishiyama, N., Stambolic, V., and Ikura, M. (2014) Structure-guided mutation of the conserved G3-box glycine in Rheb generates a constitutively activated regulator of mammalian target of rapamycin (mTOR). *The Journal of biological chemistry* **289**, 12195-12201
68. Dever, T. E., Glynias, M. J., and Merrick, W. C. (1987) GTP-binding domain: three consensus sequence elements with distinct spacing. *Proceedings of the National Academy of Sciences of the United States of America* **84**, 1814-1818

69. Pai, E. F., Kabsch, W., Krengel, U., Holmes, K. C., John, J., and Wittinghofer, A. (1989) Structure of the guanine-nucleotide-binding domain of the Ha-ras oncogene product p21 in the triphosphate conformation. *Nature* **341**, 209-214
70. Coleman, D. E., Berghuis, A. M., Lee, E., Linder, M. E., Gilman, A. G., and Sprang, S. R. (1994) Structures of active conformations of Gi alpha 1 and the mechanism of GTP hydrolysis. *Science* **265**, 1405-1412
71. Lambright, D. G., Noel, J. P., Hamm, H. E., and Sigler, P. B. (1994) Structural determinants for activation of the alpha-subunit of a heterotrimeric G protein. *Nature* **369**, 621-628
72. Noel, J. P., Hamm, H. E., and Sigler, P. B. (1993) The 2.2 A crystal structure of transducin-alpha complexed with GTP gamma S. *Nature* **366**, 654-663
73. Guilfoyle, A. P., Deshpande, C. N., Schenk, G., Maher, M. J., and Jormakka, M. (2014) Exploring the correlation between the sequence composition of the nucleotide binding G5 loop of the FeoB GTPase domain (NFeoB) and intrinsic rate of GDP release. *Bioscience Rep* **34**, 789-796
74. Weng, G., Chen, C. X., Balogh-Nair, V., Callender, R., and Manor, D. (1994) Hydrogen bond interactions of G proteins with the guanine ring moiety of guanine nucleotides. *Protein science : a publication of the Protein Society* **3**, 22-29
75. Feig, L. A., and Cooper, G. M. (1988) Relationship among guanine nucleotide exchange, GTP hydrolysis, and transforming potential of mutated ras proteins. *Mol Cell Biol* **8**, 2472-2478
76. Edkins, S., O'Meara, S., Parker, A., Stevens, C., Reis, M., Jones, S., Greenman, C., Davies, H., Dalgliesh, G., Forbes, S., Hunter, C., Smith, R., Stephens, P., Goldstraw, P., Nicholson, A., Chan, T. L., Velculescu, V. E., Yuen, S. T., Leung, S. Y., Stratton, M. R., and Futreal, P. A. (2006) Recurrent KRAS codon 146 mutations in human colorectal cancer. *Cancer biology & therapy* **5**, 928-932
77. Janakiraman, M., Vakiani, E., Zeng, Z., Pratilas, C. A., Taylor, B. S., Chitale, D., Halilovic, E., Wilson, M., Huberman, K., Ricarte Filho, J. C., Persaud, Y., Levine, D. A., Fagin, J. A., Jhanwar, S. C., Mariadason, J. M., Lash, A., Ladanyi, M., Saltz, L. B., Heguy, A., Paty, P. B., and Solit, D. B. (2010) Genomic and biological characterization of exon 4 KRAS mutations in human cancer. *Cancer research* **70**, 5901-5911
78. Tyner, J. W., Erickson, H., Deininger, M. W., Willis, S. G., Eide, C. A., Levine, R. L., Heinrich, M. C., Gattermann, N., Gilliland, D. G., Druker, B. J., and Loriaux, M. M. (2009) High-throughput sequencing screen reveals novel, transforming RAS mutations in myeloid leukemia patients. *Blood* **113**, 1749-1755
79. Zampino, G., Pantaleoni, F., Carta, C., Cobellis, G., Vasta, I., Neri, C., Pogna, E. A., De Feo, E., Delogu, A., Sarkozy, A., Atzeri, F., Selicorni, A., Rauen, K. A., Cytrynbaum, C. S., Weksberg, R., Dallapiccola, B., Ballabio, A., Gelb, B. D., Neri, G., and Tartaglia, M. (2007) Diversity, parental germline origin, and phenotypic spectrum of de novo HRAS missense changes in Costello syndrome. *Human mutation* **28**, 265-272
80. Araki, M., Shima, F., Yoshikawa, Y., Muraoka, S., Ijiri, Y., Nagahara, Y., Shirono, T., Kataoka, T., and Tamura, A. (2011) Solution structure of the state 1 conformer of GTP-bound H-Ras protein and distinct dynamic properties between the state 1 and state 2 conformers. *The Journal of biological chemistry* **286**, 39644-39653
81. Shima, F., Ijiri, Y., Muraoka, S., Liao, J., Ye, M., Araki, M., Matsumoto, K., Yamamoto, N., Sugimoto, T., Yoshikawa, Y., Kumasaka, T., Yamamoto, M.,

Tamura, A., and Kataoka, T. (2010) Structural basis for conformational dynamics of GTP-bound Ras protein. *The Journal of biological chemistry* **285**, 22696-22705
82. Vetter, I. R., and Wittinghofer, A. (1999) Nucleoside triphosphate-binding proteins: different scaffolds to achieve phosphoryl transfer. *Q Rev Biophys* **32**, 1-56
83. Kanfer, G., Courtheoux, T., Peterka, M., Meier, S., Soste, M., Melnik, A., Reis, K., Aspenstrom, P., Peter, M., Picotti, P., and Kornmann, B. (2015) Mitotic redistribution of the mitochondrial network by Miro and Cenp-F. *Nat Commun* **6**, 8015
84. Ostrem, J. M., and Shokat, K. M. (2016) Direct small-molecule inhibitors of KRAS: from structural insights to mechanism-based design. *Nat Rev Drug Discov* **15**, 771-785
85. Feuerstein, J., Goody, R. S., and Wittinghofer, A. (1987) Preparation and characterization of nucleotide-free and metal ion-free p21 "apoprotein". *The Journal of biological chemistry* **262**, 8455-8458
86. John, J., Rensland, H., Schlichting, I., Vetter, I., Borasio, G. D., Goody, R. S., and Wittinghofer, A. (1993) Kinetic and structural analysis of the Mg(2+)-binding site of the guanine nucleotide-binding protein p21H-ras. *The Journal of biological chemistry* **268**, 923-929
87. John, J., Sohmen, R., Feuerstein, J., Linke, R., Wittinghofer, A., and Goody, R. S. (1990) Kinetics of interaction of nucleotides with nucleotide-free H-ras p21. *Biochemistry* **29**, 6058-6065
88. Kabcenell, A. K., Goud, B., Northup, J. K., and Novick, P. J. (1990) Binding and hydrolysis of guanine nucleotides by Sec4p, a yeast protein involved in the regulation of vesicular traffic. *The Journal of biological chemistry* **265**, 9366-9372
89. Burstein, E. S., and Macara, I. G. (1992) Interactions of the ras-like protein p25rab3A with Mg2+ and guanine nucleotides. *Biochem J* **282 (Pt 2)**, 387-392
90. Beraud-Dufour, S., Robineau, S., Chardin, P., Paris, S., Chabre, M., Cherfils, J., and Antonny, B. (1998) A glutamic finger in the guanine nucleotide exchange factor ARNO displaces Mg2+ and the beta-phosphate to destabilize GDP on ARF1. *The EMBO journal* **17**, 3651-3659
91. Boriack-Sjodin, P. A., Margarit, S. M., Bar-Sagi, D., and Kuriyan, J. (1998) The structural basis of the activation of Ras by Sos. *Nature* **394**, 337-343
92. Goldberg, J. (1999) Structural and functional analysis of the ARF1-ARFGAP complex reveals a role for coatomer in GTP hydrolysis. *Cell* **96**, 893-902
93. Nassar, N., Singh, K., and Garcia-Diaz, M. (2010) Structure of the dominant negative S17N mutant of Ras. *Biochemistry* **49**, 1970-1974
94. Suzuki, M., Danilchanka, O., and Mekalanos, J. J. (2014) Vibrio cholerae T3SS Effector VopE Modulates Mitochondrial Dynamics and Innate Immune Signaling by Targeting Miro GTPases. *Cell Host Microbe* **16**, 581-591
95. Waterman-Storer, C. M., and Salmon, E. D. (1998) Endoplasmic reticulum membrane tubules are distributed by microtubules in living cells using three distinct mechanisms. *Current biology : CB* **8**, 798-806
96. Desai, S. P., Bhatia, S. N., Toner, M., and Irimia, D. (2013) Mitochondrial localization and the persistent migration of epithelial cancer cells. *Biophys J* **104**, 2077-2088
97. Saotome, M., Safiulina, D., Szabadkai, G., Das, S., Fransson, A., Aspenstrom, P., Rizzuto, R., and Hajnoczky, G. (2008) Bidirectional Ca2+-dependent control

of mitochondrial dynamics by the Miro GTPase. *Proceedings of the National Academy of Sciences of the United States of America* **105**, 20728-20733
98. LaMonte, B. H., Wallace, K. E., Holloway, B. A., Shelly, S. S., Ascano, J., Tokito, M., Van Winkle, T., Howland, D. S., and Holzbaur, E. L. (2002) Disruption of dynein/dynactin inhibits axonal transport in motor neurons causing late-onset progressive degeneration. *Neuron* **34**, 715-727
99. Carvalho, A. T., Szeler, K., Vavitsas, K., Aqvist, J., and Kamerlin, S. C. (2015) Modeling the mechanisms of biological GTP hydrolysis. *Arch Biochem Biophys* **582**, 80-90
100. Krengel, U., Schlichting, I., Scherer, A., Schumann, R., Frech, M., John, J., Kabsch, W., Pai, E. F., and Wittinghofer, A. (1990) Three-dimensional structures of H-ras p21 mutants: molecular basis for their inability to function as signal switch molecules. *Cell* **62**, 539-548
101. Pai, E. F., Krengel, U., Petsko, G. A., Goody, R. S., Kabsch, W., and Wittinghofer, A. (1990) Refined crystal structure of the triphosphate conformation of H-ras p21 at 1.35 A resolution: implications for the mechanism of GTP hydrolysis. *The EMBO journal* **9**, 2351-2359
102. Sondek, J., Lambright, D. G., Noel, J. P., Hamm, H. E., and Sigler, P. B. (1994) GTPase mechanism of Gproteins from the 1.7-A crystal structure of transducin alpha-GDP-AIF-4. *Nature* **372**, 276-279
103. Graham, D. L., Lowe, P. N., Grime, G. W., Marsh, M., Rittinger, K., Smerdon, S. J., Gamblin, S. J., and Eccleston, J. F. (2002) MgF(3)(-) as a transition state analog of phosphoryl transfer. *Chem Biol* **9**, 375-381
104. Scheffzek, K., Ahmadian, M. R., Kabsch, W., Wiesmuller, L., Lautwein, A., Schmitz, F., and Wittinghofer, A. (1997) The Ras-RasGAP complex: structural basis for GTPase activation and its loss in oncogenic Ras mutants. *Science* **277**, 333-338
105. Buhrman, G., Holzapfel, G., Fetics, S., and Mattos, C. (2010) Allosteric modulation of Ras positions Q61 for a direct role in catalysis. *Proceedings of the National Academy of Sciences of the United States of America* **107**, 4931-4936
106. Kosloff, M., and Selinger, Z. (2001) Substrate assisted catalysis -- application to G proteins. *Trends Biochem Sci* **26**, 161-166
107. Scheidig, A. J., Franken, S. M., Corrie, J. E., Reid, G. P., Wittinghofer, A., Pai, E. F., and Goody, R. S. (1995) X-ray crystal structure analysis of the catalytic domain of the oncogene product p21H-ras complexed with caged GTP and mant dGppNHp. *J Mol Biol* **253**, 132-150
108. Frech, M., Darden, T. A., Pedersen, L. G., Foley, C. K., Charifson, P. S., Anderson, M. W., and Wittinghofer, A. (1994) Role of glutamine-61 in the hydrolysis of GTP by p21H-ras: an experimental and theoretical study. *Biochemistry* **33**, 3237-3244
109. Berghuis, A. M., Lee, E., Raw, A. S., Gilman, A. G., and Sprang, S. R. (1996) Structure of the GDP-Pi complex of Gly203-->Ala gialpha1: a mimic of the ternary product complex of galpha-catalyzed GTP hydrolysis. *Structure* **4**, 1277-1290
110. Tesmer, J. J., Berman, D. M., Gilman, A. G., and Sprang, S. R. (1997) Structure of RGS4 bound to AlF4--activated G(i alpha1): stabilization of the transition state for GTP hydrolysis. *Cell* **89**, 251-261
111. Resat, H., Straatsma, T. P., Dixon, D. A., and Miller, J. H. (2001) The arginine finger of RasGAP helps Gln-61 align the nucleophilic water in GAP-stimulated hydrolysis of GTP. *Proceedings of the National Academy of Sciences of the United States of America* **98**, 6033-6038

112. Cheng, H., Sukal, S., Callender, R., and Leyh, T. S. (2001) gamma-phosphate protonation and pH-dependent unfolding of the Ras.GTP.Mg2+ complex: a vibrational spectroscopy study. *The Journal of biological chemistry* **276**, 9931-9935
113. Allin, C., and Gerwert, K. (2001) Ras catalyzes GTP hydrolysis by shifting negative charges from gamma- to beta-phosphate as revealed by time-resolved FTIR difference spectroscopy. *Biochemistry* **40**, 3037-3046
114. Derewenda, U., Oleksy, A., Stevenson, A. S., Korczynska, J., Dauter, Z., Somlyo, A. P., Otlewski, J., Somlyo, A. V., and Derewenda, Z. S. (2004) The crystal structure of RhoA in complex with the DH/PH fragment of PDZRhoGEF, an activator of the Ca(2+) sensitization pathway in smooth muscle. *Structure* **12**, 1955-1965
115. Garrard, S. M., Capaldo, C. T., Gao, L., Rosen, M. K., Macara, I. G., and Tomchick, D. R. (2003) Structure of Cdc42 in a complex with the GTPase-binding domain of the cell polarity protein, Par6. *The EMBO journal* **22**, 1125-1133
116. Hirshberg, M., Stockley, R. W., Dodson, G., and Webb, M. R. (1997) The crystal structure of human rac1, a member of the rho-family complexed with a GTP analogue. *Nature structural biology* **4**, 147-152
117. Adams, P. D., and Oswald, R. E. (2007) NMR assignment of Cdc42(T35A), an active Switch I mutant of Cdc42. *Biomolecular NMR assignments* **1**, 225-227
118. Marshall, C. B., Meiri, D., Smith, M. J., Mazhab-Jafari, M. T., Gasmi-Seabrook, G. M., Rottapel, R., Stambolic, V., and Ikura, M. (2012) Probing the GTPase cycle with real-time NMR: GAP and GEF activities in cell extracts. *Methods* **57**, 473-485
119. Maurer, T., and Wang, W. (2013) NMR study to identify a ligand-binding pocket in Ras. *The Enzymes* **33 Pt A**, 15-39
120. Smith, M. J., Neel, B. G., and Ikura, M. (2013) NMR-based functional profiling of RASopathies and oncogenic RAS mutations. *Proceedings of the National Academy of Sciences of the United States of America* **110**, 4574-4579
121. Correll, R. N., Pang, C., Niedowicz, D. M., Finlin, B. S., and Andres, D. A. (2008) The RGK family of GTP-binding proteins: regulators of voltage-dependent calcium channels and cytoskeleton remodeling. *Cell Signal* **20**, 292-300
122. Soundararajan, M., Yang, X., Elkins, J. M., Sobott, F., and Doyle, D. A. (2007) The centaurin gamma-1 GTPase-like domain functions as an NTPase. *Biochem J* **401**, 679-688
123. Li, X., Bu, X., Lu, B., Avraham, H., Flavell, R. A., and Lim, B. (2002) The hematopoiesis-specific GTP-binding protein RhoH is GTPase deficient and modulates activities of other Rho GTPases by an inhibitory function. *Mol Cell Biol* **22**, 1158-1171
124. Chardin, P. (2006) Function and regulation of Rnd proteins. *Nature reviews. Molecular cell biology* **7**, 54-62
125. Rivero, F., Dislich, H., Glockner, G., and Noegel, A. A. (2001) The Dictyostelium discoideum family of Rho-related proteins. *Nucleic Acids Res* **29**, 1068-1079
126. Manjarrez, J. R., Sun, L., Prince, T., and Matts, R. L. (2014) Hsp90-dependent assembly of the DBC2/RhoBTB2-Cullin3 E3-ligase complex. *PLoS One* **9**, e90054

127. Espinosa, E. J., Calero, M., Sridevi, K., and Pfeffer, S. R. (2009) RhoBTB3: a Rho GTPase-family ATPase required for endosome to Golgi transport. *Cell* **137**, 938-948
128. Ji, W., and Rivero, F. (2016) Atypical Rho GTPases of the RhoBTB Subfamily: Roles in Vesicle Trafficking and Tumorigenesis. *Cells* **5**
129. Liu, S., Sawada, T., Lee, S., Yu, W., Silverio, G., Alapatt, P., Millan, I., Shen, A., Saxton, W., Kanao, T., Takahashi, R., Hattori, N., Imai, Y., and Lu, B. (2012) Parkinson's disease-associated kinase PINK1 regulates Miro protein level and axonal transport of mitochondria. *PLoS Genet* **8**, e1002537
130. Aspenstrom, P., Fransson, A., and Saras, J. (2004) Rho GTPases have diverse effects on the organization of the actin filament system. *Biochemical Journal* **377**, 327-337
131. Klosowiak, J. L., Focia, P. J., Chakravarthy, S., Landahl, E. C., Freymann, D. M., and Rice, S. E. (2013) Structural coupling of the EF hand and C-terminal GTPase domains in the mitochondrial protein Miro. *EMBO Rep* **14**, 968-974
132. Guo, X., Macleod, G. T., Wellington, A., Hu, F., Panchumarthi, S., Schoenfield, M., Marin, L., Charlton, M. P., Atwood, H. L., and Zinsmaier, K. E. (2005) The GTPase dMiro is required for axonal transport of mitochondria to Drosophila synapses. *Neuron* **47**, 379-393
133. Jadhav, B., Wild, K., Pool, M. R., and Sinning, I. (2015) Structure and Switch Cycle of SRbeta as Ancestral Eukaryotic GTPase Associated with Secretory Membranes. *Structure* **23**, 1838-1847
134. Tajima, S., Lauffer, L., Rath, V. L., and Walter, P. (1986) The signal recognition particle receptor is a complex that contains two distinct polypeptide chains. *J Cell Biol* **103**, 1167-1178
135. Bange, G., and Sinning, I. (2013) SIMIBI twins in protein targeting and localization. *Nat Struct Mol Biol* **20**, 776-780
136. Ogg, S. C., Barz, W. P., and Walter, P. (1998) A functional GTPase domain, but not its transmembrane domain, is required for function of the SRP receptor beta-subunit. *J Cell Biol* **142**, 341-354
137. Jekely, G. (2003) Small GTPases and the evolution of the eukaryotic cell. *Bioessays* **25**, 1129-1138
138. Schwartz, T. U., Schmidt, D., Brohawn, S. G., and Blobel, G. (2006) Homodimerization of the G protein SRbeta in the nucleotide-free state involves proline cis/trans isomerization in the switch II region. *Proceedings of the National Academy of Sciences of the United States of America* **103**, 6823-6828
139. Helmers, J., Schmidt, D., Glavy, J. S., Blobel, G., and Schwartz, T. (2003) The beta-subunit of the protein-conducting channel of the endoplasmic reticulum functions as the guanine nucleotide exchange factor for the beta-subunit of the signal recognition particle receptor. *The Journal of biological chemistry* **278**, 23686-23690
140. Schwartz, T., and Blobel, G. (2003) Structural basis for the function of the beta subunit of the eukaryotic signal recognition particle receptor. *Cell* **112**, 793-803
141. Berthold, J., Schenkova, K., and Rivero, F. (2008) Rho GTPases of the RhoBTB subfamily and tumorigenesis. *Acta Pharmacol Sin* **29**, 285-295
142. Boureux, A., Vignal, E., Faure, S., and Fort, P. (2007) Evolution of the Rho family of ras-like GTPases in eukaryotes. *Mol Biol Evol* **24**, 203-216
143. Aspenstrom, P., Fransson, A., and Saras, J. (2004) Rho GTPases have diverse effects on the organization of the actin filament system. *Biochem J* **377**, 327-337

144. Chang, F. K., Sato, N., Kobayashi-Simorowski, N., Yoshihara, T., Meth, J. L., and Hamaguchi, M. (2006) DBC2 is essential for transporting vesicular stomatitis virus glycoprotein. *J Mol Biol* **364**, 302-308
145. Freeman, S. N., Ma, Y., and Cress, W. D. (2008) RhoBTB2 (DBC2) is a mitotic E2F1 target gene with a novel role in apoptosis. *The Journal of biological chemistry* **283**, 2353-2362
146. McKinnon, C. M., Lygoe, K. A., Skelton, L., Mitter, R., and Mellor, H. (2008) The atypical Rho GTPase RhoBTB2 is required for expression of the chemokine CXCL14 in normal and cancerous epithelial cells. *Oncogene* **27**, 6856-6865
147. Yoshihara, T., Collado, D., and Hamaguchi, M. (2007) Cyclin D1 down-regulation is essential for DBC2's tumor suppressor function. *Biochem Biophys Res Commun* **358**, 1076-1079
148. Berthold, J., Schenkova, K., Ramos, S., Miura, Y., Furukawa, M., Aspenstrom, P., and Rivero, F. (2008) Characterization of RhoBTB-dependent Cul3 ubiquitin ligase complexes--evidence for an autoregulatory mechanism. *Exp Cell Res* **314**, 3453-3465
149. Aravind, L., and Koonin, E. V. (1999) Fold prediction and evolutionary analysis of the POZ domain: structural and evolutionary relationship with the potassium channel tetramerization domain. *J Mol Biol* **285**, 1353-1361
150. Stogios, P. J., Downs, G. S., Jauhal, J. J., Nandra, S. K., and Prive, G. G. (2005) Sequence and structural analysis of BTB domain proteins. *Genome Biol* **6**, R82
151. Ramos, S., Khademi, F., Somesh, B. P., and Rivero, F. (2002) Genomic organization and expression profile of the small GTPases of the RhoBTB family in human and mouse. *Gene* **298**, 147-157
152. Lu, A., and Pfeffer, S. R. (2013) Golgi-associated RhoBTB3 targets cyclin E for ubiquitylation and promotes cell cycle progression. *J Cell Biol* **203**, 233-250
153. Hamaguchi, M., Meth, J. L., von Klitzing, C., Wei, W., Esposito, D., Rodgers, L., Walsh, T., Welcsh, P., King, M. C., and Wigler, M. H. (2002) DBC2, a candidate for a tumor suppressor gene involved in breast cancer. *Proceedings of the National Academy of Sciences of the United States of America* **99**, 13647-13652
154. Beder, L. B., Gunduz, M., Ouchida, M., Gunduz, E., Sakai, A., Fukushima, K., Nagatsuka, H., Ito, S., Honjo, N., Nishizaki, K., and Shimizu, K. (2006) Identification of a candidate tumor suppressor gene RHOBTB1 located at a novel allelic loss region 10q21 in head and neck cancer. *J Cancer Res Clin Oncol* **132**, 19-27
155. Knowles, M. A., Aveyard, J. S., Taylor, C. F., Harnden, P., and Bass, S. (2005) Mutation analysis of the 8p candidate tumour suppressor genes DBC2 (RHOBTB2) and LZTS1 in bladder cancer. *Cancer Lett* **225**, 121-130
156. Collado, D., Yoshihara, T., and Hamaguchi, M. (2007) DBC2 resistance is achieved by enhancing 26S proteasome-mediated protein degradation. *Biochem Biophys Res Commun* **360**, 600-603
157. Lee, C. Y., Clough, E. A., Yellon, P., Teslovich, T. M., Stephan, D. A., and Baehrecke, E. H. (2003) Genome-wide analyses of steroid- and radiation-triggered programmed cell death in Drosophila. *Current biology : CB* **13**, 350-357
158. Frederick, R. L., McCaffery, J. M., Cunningham, K. W., Okamoto, K., and Shaw, J. M. (2004) Yeast Miro GTPase, Gem1p, regulates mitochondrial morphology via a novel pathway. *J Cell Biol* **167**, 87-98
159. Reis, K., Fransson, A., and Aspenstrom, P. (2009) The Miro GTPases: at the heart of the mitochondrial transport machinery. *FEBS letters* **583**, 1391-1398

160. Vlahou, G., Elias, M., von Kleist-Retzow, J. C., Wiesner, R. J., and Rivero, F. (2011) The Ras related GTPase Miro is not required for mitochondrial transport in Dictyostelium discoideum. *European journal of cell biology* **90**, 342-355
161. Yamaoka, S., and Leaver, C. J. (2008) EMB2473/MIRO1, an Arabidopsis Miro GTPase, is required for embryogenesis and influences mitochondrial morphology in pollen. *The Plant cell* **20**, 589-601
162. Fransson, S., Ruusala, A., and Aspenstrom, P. (2006) The atypical Rho GTPases Miro-1 and Miro-2 have essential roles in mitochondrial trafficking. *Biochem Biophys Res Commun* **344**, 500-510
163. MacAskill, A. F., Brickley, K., Stephenson, F. A., and Kittler, J. T. (2009) GTPase dependent recruitment of Grif-1 by Miro1 regulates mitochondrial trafficking in hippocampal neurons. *Molecular and cellular neurosciences* **40**, 301-312
164. Macaskill, A. F., Rinholm, J. E., Twelvetrees, A. E., Arancibia-Carcamo, I. L., Muir, J., Fransson, A., Aspenstrom, P., Attwell, D., and Kittler, J. T. (2009) Miro1 is a calcium sensor for glutamate receptor-dependent localization of mitochondria at synapses. *Neuron* **61**, 541-555
165. Russo, G. J., Louie, K., Wellington, A., Macleod, G. T., Hu, F., Panchumarthi, S., and Zinsmaier, K. E. (2009) Drosophila Miro is required for both anterograde and retrograde axonal mitochondrial transport. *The Journal of neuroscience : the official journal of the Society for Neuroscience* **29**, 5443-5455
166. Wang, X., and Schwarz, T. L. (2009) The mechanism of Ca2+ -dependent regulation of kinesin-mediated mitochondrial motility. *Cell* **136**, 163-174
167. Itoh, K., Nakamura, K., Iijima, M., and Sesaki, H. (2013) Mitochondrial dynamics in neurodegeneration. *Trends in cell biology* **23**, 64-71
168. Mattson, M. P., Gleichmann, M., and Cheng, A. (2008) Mitochondria in neuroplasticity and neurological disorders. *Neuron* **60**, 748-766
169. McInnes, J. (2013) Insights on altered mitochondrial function and dynamics in the pathogenesis of neurodegeneration. *Translational neurodegeneration* **2**, 12
170. Xie, A., Gao, J., Xu, L., and Meng, D. (2014) Shared mechanisms of neurodegeneration in Alzheimer's disease and Parkinson's disease. *BioMed research international* **2014**, 648740
171. Beal, M. F. (2007) Mitochondria and neurodegeneration. *Novartis Foundation symposium* **287**, 183-192; discussion 192-186
172. Mazhab-Jafari, M. T., Marshall, C. B., Ishiyama, N., Ho, J., Di Palma, V., Stambolic, V., and Ikura, M. (2012) An autoinhibited noncanonical mechanism of GTP hydrolysis by Rheb maintains mTORC1 homeostasis. *Structure* **20**, 1528-1539
173. Yamaoka, S., and Hara-Nishimura, I. (2014) The mitochondrial Ras-related GTPase Miro: views from inside and outside the metazoan kingdom. *Frontiers in plant science* **5**, 350
174. Freeman, J. L., Abo, A., and Lambeth, J. D. (1996) Rac "insert region" is a novel effector region that is implicated in the activation of NADPH oxidase, but not PAK65. *The Journal of biological chemistry* **271**, 19794-19801
175. Walker, S. J., and Brown, H. A. (2002) Specificity of Rho insert-mediated activation of phospholipase D1. *The Journal of biological chemistry* **277**, 26260-26267
176. Houdusse, A., and Cohen, C. (1996) Structure of the regulatory domain of scallop myosin at 2 A resolution: implications for regulation. *Structure* **4**, 21-32
177. Vinogradova, M. V., Stone, D. B., Malanina, G. G., Karatzaferi, C., Cooke, R., Mendelson, R. A., and Fletterick, R. J. (2005) Ca(2+)-regulated structural

changes in troponin. *Proceedings of the National Academy of Sciences of the United States of America* **102**, 5038-5043
178. Ames, J. B., Levay, K., Wingard, J. N., Lusin, J. D., and Slepak, V. Z. (2006) Structural basis for calcium-induced inhibition of rhodopsin kinase by recoverin. *The Journal of biological chemistry* **281**, 37237-37245
179. Tanaka, T., Ames, J. B., Harvey, T. S., Stryer, L., and Ikura, M. (1995) Sequestration of the membrane-targeting myristoyl group of recoverin in the calcium-free state. *Nature* **376**, 444-447
180. Neudecker, P., Nerkamp, J., Eisenmann, A., Nourse, A., Lauber, T., Schweimer, K., Lehmann, K., Schwarzinger, S., Ferreira, F., and Rosch, P. (2004) Solution structure, dynamics, and hydrodynamics of the calcium-bound cross-reactive birch pollen allergen Bet v 4 reveal a canonical monomeric two EF-hand assembly with a regulatory function. *J Mol Biol* **336**, 1141-1157
181. Stephen, R., Palczewski, K., and Sousa, M. C. (2006) The crystal structure of GCAP3 suggests molecular mechanism of GCAP-linked cone dystrophies. *J Mol Biol* **359**, 266-275
182. Morlino, G., Barreiro, O., Baixauli, F., Robles-Valero, J., Gonzalez-Granado, J. M., Villa-Bellosta, R., Cuenca, J., Sanchez-Sorzano, C. O., Veiga, E., Martin-Cofreces, N. B., and Sanchez-Madrid, F. (2014) Miro-1 links mitochondria and microtubule Dynein motors to control lymphocyte migration and polarity. *Mol Cell Biol* **34**, 1412-1426
183. Norkett, R., Modi, S., Birsa, N., Atkin, T. A., Ivankovic, D., Pathania, M., Trossbach, S. V., Korth, C., Hirst, W. D., and Kittler, J. T. (2016) DISC1-dependent Regulation of Mitochondrial Dynamics Controls the Morphogenesis of Complex Neuronal Dendrites. *The Journal of biological chemistry* **291**, 613-629
184. Lopez-Domenech, G., Serrat, R., Mirra, S., D'Aniello, S., Somorjai, I., Abad, A., Vitureira, N., Garcia-Arumi, E., Alonso, M. T., Rodriguez-Prados, M., Burgaya, F., Andreu, A. L., Garcia-Sancho, J., Trullas, R., Garcia-Fernandez, J., and Soriano, E. (2012) The Eutherian Armcx genes regulate mitochondrial trafficking in neurons and interact with Miro and Trak2. *Nat Commun* **3**, 814
185. Li, Y., Lim, S., Hoffman, D., Aspenstrom, P., Federoff, H. J., and Rempe, D. A. (2009) HUMMR, a hypoxia- and HIF-1alpha-inducible protein, alters mitochondrial distribution and transport. *J Cell Biol* **185**, 1065-1081
186. Wang, X., Winter, D., Ashrafi, G., Schlehe, J., Wong, Y. L., Selkoe, D., Rice, S., Steen, J., LaVoie, M. J., and Schwarz, T. L. (2011) PINK1 and Parkin target Miro for phosphorylation and degradation to arrest mitochondrial motility. *Cell* **147**, 893-906
187. Misko, A., Jiang, S., Wegorzewska, I., Milbrandt, J., and Baloh, R. H. (2010) Mitofusin 2 is necessary for transport of axonal mitochondria and interacts with the Miro/Milton complex. *The Journal of neuroscience : the official journal of the Society for Neuroscience* **30**, 4232-4240
188. Glater, E. E., Megeath, L. J., Stowers, R. S., and Schwarz, T. L. (2006) Axonal transport of mitochondria requires milton to recruit kinesin heavy chain and is light chain independent. *Journal of Cell Biology* **173**, 545-557
189. Kornmann, B., Osman, C., and Walter, P. (2011) The conserved GTPase Gem1 regulates endoplasmic reticulum-mitochondria connections. *Proceedings of the National Academy of Sciences of the United States of America* **108**, 14151-14156

190. Vlahou, G., and Rivero, F. (2006) Rho GTPase signaling in Dictyostelium discoideum: insights from the genome. *European journal of cell biology* **85**, 947-959
191. Schwarz, T. L. (2013) Mitochondrial trafficking in neurons. *Cold Spring Harbor perspectives in biology* **5**
192. Sheng, Z. H. (2014) Mitochondrial trafficking and anchoring in neurons: New insight and implications. *J Cell Biol* **204**, 1087-1098
193. Lovas, J. R., and Wang, X. (2013) The meaning of mitochondrial movement to a neuron's life. *Biochimica et biophysica acta* **1833**, 184-194
194. Saxton, W. M., and Hollenbeck, P. J. (2012) The axonal transport of mitochondria. *J Cell Sci* **125**, 2095-2104
195. van Spronsen, M., Mikhaylova, M., Lipka, J., Schlager, M. A., van den Heuvel, D. J., Kuijpers, M., Wulf, P. S., Keijzer, N., Demmers, J., Kapitein, L. C., Jaarsma, D., Gerritsen, H. C., Akhmanova, A., and Hoogenraad, C. C. (2013) TRAK/Milton motor-adaptor proteins steer mitochondrial trafficking to axons and dendrites. *Neuron* **77**, 485-502
196. Babic, M., Russo, G. J., Wellington, A. J., Sangston, R. M., Gonzalez, M., and Zinsmaier, K. E. (2015) Miro's N-Terminal GTPase Domain Is Required for Transport of Mitochondria into Axons and Dendrites. *Journal of Neuroscience* **35**, 5754-5771
197. Pozo, K. B. K., and Stephenson, F. A. (2011) N-acetylglucosamine transferase is an integral component of a kinesin-directed mitochondrial trafficking complex. *Bba-Mol Cell Res* **1813**, 269-281
198. Trinidad, J. C., Barkan, D. T., Gulledge, B. F., Thalhammer, A., Sali, A., Schoepfer, R., and Burlingame, A. L. (2012) Global Identification and Characterization of Both O-GlcNAcylation and Phosphorylation at the Murine Synapse. *Mol Cell Proteomics* **11**, 215-229
199. Pekkurnaz, G., Trinidad, J. C., Wang, X., Kong, D., and Schwarz, T. L. (2014) Glucose regulates mitochondrial motility via Milton modification by O-GlcNAc transferase. *Cell* **158**, 54-68
200. Jeyaraju, D. V., Cisbani, G., and Pellegrini, L. (2009) Calcium regulation of mitochondria motility and morphology. *Biochimica et biophysica acta* **1787**, 1363-1373
201. Chang, K. T., Niescier, R. F., and Min, K. T. (2011) Mitochondrial matrix Ca2+ as an intrinsic signal regulating mitochondrial motility in axons. *Proceedings of the National Academy of Sciences of the United States of America* **108**, 15456-15461
202. Niescier, R. F., Chang, K. T., and Min, K. T. (2013) Miro, MCU, and calcium: bridging our understanding of mitochondrial movement in axons. *Front Cell Neurosci* **7**
203. Chen, Y., and Sheng, Z. H. (2013) Kinesin-1-syntaphilin coupling mediates activity-dependent regulation of axonal mitochondrial transport. *J Cell Biol* **202**, 351-364
204. Birsa, N., Norkett, R., Wauer, T., Mevissen, T. E. T., Wu, H. C., Foltynie, T., Bhatia, K., Hirst, W. D., Komander, D., Plun-Favreau, H., and Kittler, J. T. (2014) Lysine 27 Ubiquitination of the Mitochondrial Transport Protein Miro Is Dependent on Serine 65 of the Parkin Ubiquitin Ligase. *Journal of Biological Chemistry* **289**, 14569-14582
205. Jouaville, L. S., Pinton, P., Bastianutto, C., Rutter, G. A., and Rizzuto, R. (1999) Regulation of mitochondrial ATP synthesis by calcium: evidence for a long-

term metabolic priming. *Proceedings of the National Academy of Sciences of the United States of America* **96**, 13807-13812
206. McCormack, J. G., and Denton, R. M. (1990) Intracellular calcium ions and intramitochondrial Ca2+ in the regulation of energy metabolism in mammalian tissues. *The Proceedings of the Nutrition Society* **49**, 57-75
207. Bolea, I., Gan, W. B., Manfedi, G., and Magrane, J. (2014) Imaging of mitochondrial dynamics in motor and sensory axons of living mice. *Methods Enzymol* **547**, 97-110
208. Pham, A. H., and Chan, D. C. (2014) Analyzing mitochondrial dynamics in mouse organotypic slice cultures. *Methods Enzymol* **547**, 111-129
209. Bassel, G. W., Fung, P., Chow, T. F. F., Foong, J. A., Provart, N. J., and Cutler, S. R. (2008) Elucidating the germination transcriptional program using small molecules. *Plant Physiol* **147**, 143-155
210. Day, R. C., Herridge, R. P., Ambrose, B. A., and Macknight, R. C. (2008) Transcriptome analysis of proliferating Arabidopsis endosperm reveals biological implications for the control of syncytial division, cytokinin signaling, and gene expression regulation. *Plant Physiol* **148**, 1964-1984
211. Sormo, C. G., Brembu, T., Winge, P., and Bones, A. M. (2011) Arabidopsis thaliana MIRO1 and MIRO2 GTPases Are Unequally Redundant in Pollen Tube Growth and Fusion of Polar Nuclei during Female Gametogenesis. *Plos One* **6**
212. Yamaoka, S., Nakajima, M., Fujimoto, M., and Tsutsumi, N. (2011) MIRO1 influences the morphology and intracellular distribution of mitochondria during embryonic cell division in Arabidopsis. *Plant Cell Rep* **30**, 239-244
213. Frederick, R. L., Okamoto, K., and Shaw, J. M. (2008) Multiple pathways influence mitochondrial inheritance in budding yeast. *Genetics* **178**, 825-837
214. Ding, L., Lei, Y., Han, Y., Li, Y., Ji, X., and Liu, L. (2016) Vimar Is a Novel Regulator of Mitochondrial Fission through Miro. *PLoS Genet* **12**, e1006359
215. Liu, X., and Hajnoczky, G. (2009) Ca2+-dependent regulation of mitochondrial dynamics by the Miro-Milton complex. *Int J Biochem Cell Biol* **41**, 1972-1976
216. Michel, A. H., and Kornmann, B. (2012) The ERMES complex and ER-mitochondria connections. *Biochem Soc Trans* **40**, 445-450
217. Murley, A., Lackner, L. L., Osman, C., West, M., Voeltz, G. K., Walter, P., and Nunnari, J. (2013) ER-associated mitochondrial division links the distribution of mitochondria and mitochondrial DNA in yeast. *Elife* **2**, e00422
218. Prinz, W. A. (2014) Bridging the gap: membrane contact sites in signaling, metabolism, and organelle dynamics. *J Cell Biol* **205**, 759-769
219. Traaseth, N., Elfering, S., Solien, J., Haynes, V., and Giulivi, C. (2004) Role of calcium signaling in the activation of mitochondrial nitric oxide synthase and citric acid cycle. *Biochimica et biophysica acta* **1658**, 64-71
220. Rowland, A. A., and Voeltz, G. K. (2012) Endoplasmic reticulum-mitochondria contacts: function of the junction. *Nature reviews. Molecular cell biology* **13**, 607-625
221. de Brito, O. M., and Scorrano, L. (2008) Mitofusin 2 tethers endoplasmic reticulum to mitochondria. *Nature* **456**, 605-610
222. Duchen, M. R. (2000) Mitochondria and Ca(2+) in cell physiology and pathophysiology. *Cell Calcium* **28**, 339-348
223. Garcia-Bermudez, J., and Cuezva, J. M. (2016) The ATPase Inhibitory Factor 1 (IF1): A master regulator of energy metabolism and of cell survival. *Biochimica et biophysica acta* **1857**, 1167-1182
224. Giampazolias, E., and Tait, S. W. (2016) Mitochondria and the hallmarks of cancer. *FEBS J* **283**, 803-814

225. Cardenas, C., Muller, M., McNeal, A., Lovy, A., Jana, F., Bustos, G., Urra, F., Smith, N., Molgo, J., Diehl, J. A., Ridky, T. W., and Foskett, J. K. (2016) Selective Vulnerability of Cancer Cells by Inhibition of Ca2+ Transfer from Endoplasmic Reticulum to Mitochondria (vol 14, pg 2313, 2016). *Cell Rep* **15**, 219-220
226. Mehlen, P., and Puisieux, A. (2006) Metastasis: a question of life or death. *Nature reviews. Cancer* **6**, 449-458
227. Ahmad, T., Mukherjee, S., Pattnaik, B., Kumar, M., Singh, S., Kumar, M., Rehman, R., Tiwari, B. K., Jha, K. A., Barhanpurkar, A. P., Wani, M. R., Roy, S. S., Mabalirajan, U., Ghosh, B., and Agrawal, A. (2014) Miro1 regulates intercellular mitochondrial transport & enhances mesenchymal stem cell rescue efficacy. *The EMBO journal* **33**, 994-1010
228. Young, J. Z. (1944) The structure, degeneration and repair of nerve fibres. *Proc R Inst G B* **33**, 344-355
229. Tzvetanova, I. D., and Nave, K. A. (2014) Axons hooked to Schwann cell metabolism. *Nat Neurosci* **17**, 1293-1295
230. Morotz, G. M., De Vos, K. J., Vagnoni, A., Ackerley, S., Shaw, C. E., and Miller, C. C. (2012) Amyotrophic lateral sclerosis-associated mutant VAPBP56S perturbs calcium homeostasis to disrupt axonal transport of mitochondria. *Hum Mol Genet* **21**, 1979-1988
231. Ogawa, F., Malavasi, E. L., Crummie, D. K., Eykelenboom, J. E., Soares, D. C., Mackie, S., Porteous, D. J., and Millar, J. K. (2014) DISC1 complexes with TRAK1 and Miro1 to modulate anterograde axonal mitochondrial trafficking. *Hum Mol Genet* **23**, 906-919
232. Bowman, A. B., Kamal, A., Ritchings, B. W., Philp, A. V., McGrail, M., Gindhart, J. G., and Goldstein, L. S. B. (2000) Kinesin-dependent axonal transport is mediated by the Sunday driver (SYD) protein. *Cell* **103**, 583-594
233. Gunawardena, S., and Goldstein, L. S. (2001) Disruption of axonal transport and neuronal viability by amyloid precursor protein mutations in Drosophila. *Neuron* **32**, 389-401
234. Hurd, D. D., and Saxton, W. M. (1996) Kinesin mutations cause motor neuron disease phenotypes by disrupting fast axonal transport in Drosophila. *Genetics* **144**, 1075-1085
235. Nguyen, T. T., Oh, S. S., Weaver, D., Lewandowska, A., Maxfield, D., Schuler, M. H., Smith, N. K., Macfarlane, J., Saunders, G., Palmer, C. A., Debattisti, V., Koshiba, T., Pulst, S., Feldman, E. L., Hajnoczky, G., and Shaw, J. M. (2014) Loss of Miro1-directed mitochondrial movement results in a novel murine model for neuron disease. *Proceedings of the National Academy of Sciences of the United States of America* **111**, E3631-3640
236. Youle, R. J., and Narendra, D. P. (2011) Mechanisms of mitophagy. *Nature reviews. Molecular cell biology* **12**, 9-14
237. Medina, M., and Avila, J. (2015) Further understanding of tau phosphorylation: implications for therapy. *Expert Rev Neurother* **15**, 115-122
238. Simic, G., Babic Leko, M., Wray, S., Harrington, C., Delalle, I., Jovanov-Milosevic, N., Bazadona, D., Buee, L., de Silva, R., Di Giovanni, G., Wischik, C., and Hof, P. R. (2016) Tau Protein Hyperphosphorylation and Aggregation in Alzheimer's Disease and Other Tauopathies, and Possible Neuroprotective Strategies. *Biomolecules* **6**, 6
239. Rossi, G., and Tagliavini, F. (2015) Frontotemporal lobar degeneration:: old knowledge and new insight into the pathogenetic mechanisms of tau mutations. *Frontiers in Aging Neuroscience* **7**

240. Long, L., Cai, X. D., Wei, X. B., Liao, J. C., Xu, Y. Q., Gao, H. M., Chen, X. H., and Wang, Q. (2015) Progressive supranuclear palsy: what do we know about it? *Curr Med Chem* **22**, 1182-1193
241. Chin, J. Y., Knowles, R. B., Schneider, A., Drewes, G., Mandelkow, E. M., and Hyman, B. T. (2000) Microtubule-affinity regulating kinase (MARK) is tightly associated with neurofibrillary tangles in Alzheimer brain: A fluorescence resonance energy transfer study. *J Neuropath Exp Neur* **59**, 966-971
242. Wang, J. W., Imai, Y., and Lu, B. (2007) Activation of PAR-1 kinase and stimulation of tau phosphorylation by diverse signals require the tumor suppressor protein LKB1. *The Journal of neuroscience : the official journal of the Society for Neuroscience* **27**, 574-581
243. Zempel, H., Thies, E., Mandelkow, E., and Mandelkow, E. M. (2010) Abeta oligomers cause localized Ca(2+) elevation, missorting of endogenous Tau into dendrites, Tau phosphorylation, and destruction of microtubules and spines. *The Journal of neuroscience : the official journal of the Society for Neuroscience* **30**, 11938-11950
244. Shibata, T., Yamagata, H., Uchida, S., Otsuki, K., Hobara, T., Higuchi, F., Abe, N., and Watanabe, Y. (2013) The alteration of hypoxia inducible factor-1 (HIF-1) and its target genes in mood disorder patients. *Prog Neuropsychopharmacol Biol Psychiatry* **43**, 222-229
245. Kerner, N. A., and Roose, S. P. (2016) Obstructive Sleep Apnea is Linked to Depression and Cognitive Impairment: Evidence and Potential Mechanisms. *Am J Geriat Psychiat* **24**, 496-508
246. Mozes, V., Bence, M., Sasvari-Szekely, M., and Keszler, G. (2010) [Dopamine D4 receptor hypoxia sensitivity and child psychiatric disorders]. *Neuropsychopharmacol Hung* **12**, 289-293
247. Saito, S., and Ihara, M. (2016) Interaction between cerebrovascular disease and Alzheimer pathology. *Curr Opin Psychiatr* **29**, 168-173
248. Raz, L., Knoefel, J., and Bhaskar, K. (2016) The neuropathology and cerebrovascular mechanisms of dementia. *J Cereb Blood Flow Metab* **36**, 172-186
249. Crowley, P. B., Kyne, C., and Monteith, W. B. (2012) Simple and inexpensive incorporation of 19F-tryptophan for protein NMR spectroscopy. *Chemical communications* **48**, 10681-10683
250. Li, Z., Nimtz, M., and Rinas, U. (2014) The metabolic potential of Escherichia coli BL21 in defined and rich medium. *Microbial cell factories* **13**, 45
251. Miroux, B., and Walker, J. E. (1996) Over-production of proteins in Escherichia coli: mutant hosts that allow synthesis of some membrane proteins and globular proteins at high levels. *J Mol Biol* **260**, 289-298
252. Wagner, S., Klepsch, M. M., Schlegel, S., Appel, A., Draheim, R., Tarry, M., Hogbom, M., van Wijk, K. J., Slotboom, D. J., Persson, J. O., and de Gier, J. W. (2008) Tuning Escherichia coli for membrane protein overexpression. *Proceedings of the National Academy of Sciences of the United States of America* **105**, 14371-14376
253. Doron, N. (2015) Bacterial Strains for Protein Expression. The Wolfson Centre for Applied Structural Biology, The Hebrew University of Jerusalem, Jerusalem
254. Studier, F. W., and Moffatt, B. A. (1986) Use of bacteriophage T7 RNA polymerase to direct selective high-level expression of cloned genes. *J Mol Biol* **189**, 113-130

255. Wurm, D. J., Veiter, L., Ulonska, S., Eggenreich, B., Herwig, C., and Spadiut, O. (2016) The E. coli pET expression system revisited-mechanistic correlation between glucose and lactose uptake. *Appl Microbiol Biotechnol* **100**, 8721-8729
256. Cohen, S. N., Chang, A. C., and Hsu, L. (1972) Nonchromosomal antibiotic resistance in bacteria: genetic transformation of Escherichia coli by R-factor DNA. *Proceedings of the National Academy of Sciences of the United States of America* **69**, 2110-2114
257. Froger, A., and Hall, J. E. (2007) Transformation of plasmid DNA into E. coli using the heat shock method. *Journal of visualized experiments : JoVE*, 253
258. Lapid, C. G., Y. (2003) PrimerX: automated design of mutagenic primers for site-directed mutagenesis. University of the Philippines, National Institute of Molecular Biology and Biotechnology (NIMBB), University of the Philippines
259. Kholmukhamedov, A., Schwartz, J. M., and Lemasters, J. J. (2013) Isolated mitochondria infusion mitigates ischemia-reperfusion injury of the liver in rats: mitotracker probes and mitochondrial membrane potential. *Shock* **39**, 543
260. Hellman, U., Wernstedt, C., Gonez, J., and Heldin, C. H. (1995) Improvement of an in-Gel Digestion Procedure for the Micropreparation of Internal Protein-Fragments for Amino-Acid Sequencing. *Anal Biochem* **224**, 451-455
261. Perkins, D. N., Pappin, D. J. C., Creasy, D. M., and Cottrell, J. S. (1999) Probability-based protein identification by searching sequence databases using mass spectrometry data. *Electrophoresis* **20**, 3551-3567
262. Hollister, B. M., Oonk, K. A., Weiser, D. C., and Walsh, S. (2016) Characterization of the three zebrafish orthologs of the mitochondrial GTPase Miro/Rhot. *Comp Biochem Physiol B Biochem Mol Biol* **191**, 126-134
263. Purich, D. L. (2010) *Enzyme Kinetics: Catalysis & Control*, First Edition ed., Elsevier, London, UK
264. Clough, R. R., Sidhu, R. S., and Bhullar, R. P. (2002) Calmodulin binds RalA and RalB and is required for the thrombin-induced activation of Ral in human platelets. *Journal of Biological Chemistry* **277**, 28972-28980
265. Hoshino, M., and Nakamura, S. (2003) Small GTPase Rin induces neurite outgrowth through Rac/Cdc42 and calmodulin in PC12 cells. *Journal of Cell Biology* **163**, 1067-1076
266. Moyers, J. S., Bilan, P. J., Zhu, J. H., and Kahn, C. R. (1997) Rad and Rad-related GTPases interact with calmodulin and calmodulin-dependent protein kinase II. *Journal of Biological Chemistry* **272**, 11832-11839
267. Aspenstrom, P. (2004) Integration of signalling pathways regulated by small GTPases and calcium. *Bba-Mol Cell Res* **1742**, 51-58
268. Fransson, A., Ruusala, A., and Aspenstom, P. (2006) The atypical Rho GTPases Miro-1 and Miro-2 have essential roles in mitochondrial trafficking. *Biochem Bioph Res Co* **344**, 500-510
269. Reis, K., Fransson, A., and Aspenstrom, P. (2009) The Miro GTPases: At the heart of the mitochondrial transport machinery. *Febs Lett* **583**, 1391-1398
270. Haeusler, L. C., Hemsath, L., Fiegen, D., Blumenstein, L., Herbrand, U., Stege, P., Dvorsky, R., and Ahmadian, M. R. (2006) Purification and biochemical properties of Rac1, 2, 3 and the splice variant Rac1b. *Methods Enzymol* **406**, 1-11
271. Hunter, J. C., Manandhar, A., Carrasco, M. A., Gurbani, D., Gondi, S., and Westover, K. D. (2015) Biochemical and Structural Analysis of Common Cancer-Associated KRAS Mutations. *Molecular cancer research : MCR* **13**, 1325-1335

272. Schweins, T., Scheffzek, K., Assheuer, R., and Wittinghofer, A. (1997) The role of the metal ion in the p21ras catalysed GTP-hydrolysis: Mn2+ versus Mg2+. *J Mol Biol* **266**, 847-856
273. Zhang, B., Chernoff, J., and Zheng, Y. (1998) Interaction of Rac1 with GTPase-activating proteins and putative effectors. A comparison with Cdc42 and RhoA. *The Journal of biological chemistry* **273**, 8776-8782
274. Menard, L., Tomhave, E., Casey, P. J., Uhing, R. J., Snyderman, R., and Didsbury, J. R. (1992) Rac1, a low-molecular-mass GTP-binding-protein with high intrinsic GTPase activity and distinct biochemical properties. *European journal of biochemistry* **206**, 537-546
275. Neal, S. E., Eccleston, J. F., Hall, A., and Webb, M. R. (1988) Kinetic analysis of the hydrolysis of GTP by p21N-ras. The basal GTPase mechanism. *The Journal of biological chemistry* **263**, 19718-19722
276. Wilson, D. B., and Wilson, M. P. (1992) Identification and subcellular localization of human rab5b, a new member of the ras-related superfamily of GTPases. *The Journal of clinical investigation* **89**, 996-1005
277. Huang, Y. W., Surka, M. C., Reynaud, D., Pace-Asciak, C., and Trimble, W. S. (2006) GTP binding and hydrolysis kinetics of human septin 2. *FEBS J* **273**, 3248-3260
278. Song, B. D., Leonard, M., and Schmid, S. L. (2004) Dynamin GTPase domain mutants that differentially affect GTP binding, GTP hydrolysis, and clathrin-mediated endocytosis. *The Journal of biological chemistry* **279**, 40431-40436
279. Lorber, B., Fischer, F., Bailly, M., Roy, H., and Kern, D. (2012) Protein analysis by dynamic light scattering: methods and techniques for students. *Biochem Mol Biol Educ* **40**, 372-382
280. Stetefeld, J., McKenna, S. A., and Patel, T. R. (2016) Dynamic light scattering: a practical guide and applications in biomedical sciences. *Biophys Rev* **8**, 409-427
281. Erickson, H. P. (2009) Size and shape of protein molecules at the nanometer level determined by sedimentation, gel filtration, and electron microscopy. *Biol Proced Online* **11**, 32-51
282. Rees, D. C., and Robertson, A. D. (2001) Some thermodynamic implications for the thermostability of proteins. *Protein science : a publication of the Protein Society* **10**, 1187-1194
283. Robertson, A. D., and Murphy, K. P. (1997) Protein Structure and the Energetics of Protein Stability. *Chemical reviews* **97**, 1251-1268
284. Pan, J. Y., Sanford, J. C., and Wessling-Resnick, M. (1996) Influence of Mg2+ on the structure and function of Rab5. *The Journal of biological chemistry* **271**, 1322-1328
285. Pidcock, E., and Moore, G. R. (2001) Structural characteristics of protein binding sites for calcium and lanthanide ions. *Journal of biological inorganic chemistry : JBIC : a publication of the Society of Biological Inorganic Chemistry* **6**, 479-489
286. Dudev, T., and Lim, C. (2003) Principles governing Mg, Ca, and Zn binding and selectivity in proteins. *Chemical reviews* **103**, 773-787
287. Dudev, T., and Lim, C. (2000) Metal binding in proteins: The effect of the dielectric medium. *J Phys Chem B* **104**, 3692-3694
288. Bock, C. W., Katz, A. K., Markham, G. D., and Glusker, J. P. (1999) Manganese as a replacement for magnesium and zinc: Functional comparison of the divalent ions. *J Am Chem Soc* **121**, 7360-7372

289. Garmer, D. R., and Gresh, N. (1994) A Comprehensive Energy Component Analysis of the Interaction of Hard and Soft Dications with Biological Ligands. *J Am Chem Soc* **116**, 3556-3567
290. Gresh, N., and Garmer, D. R. (1996) Comparative binding energetics of Mg2+, Ca2+, Zn2+, and Cd2+ to biologically relevant ligands: Combined ab initio SCF supermolecule and molecular mechanics investigation. *J Comput Chem* **17**, 1481-1495
291. Jernigan, R., Raghunathan, G., and Bahar, I. (1994) Characterization of Interactions and Metal-Ion Binding-Sites in Proteins. *Curr Opin Struc Biol* **4**, 256-263
292. Katz, A. K., Glusker, J. P., Beebe, S. A., and Bock, C. W. (1996) Calcium ion coordination: A comparison with that of beryllium, magnesium, and zinc. *J Am Chem Soc* **118**, 5752-5763
293. Zhong, J. M., Chen-Hwang, M. C., and Hwang, Y. W. (1995) Switching nucleotide specificity of Ha-Ras p21 by a single amino acid substitution at aspartate 119. *The Journal of biological chemistry* **270**, 10002-10007
294. Bar-Even, A., Noor, E., Savir, Y., Liebermeister, W., Davidi, D., Tawfik, D. S., and Milo, R. (2011) The moderately efficient enzyme: evolutionary and physicochemical trends shaping enzyme parameters. *Biochemistry* **50**, 4402-4410
295. Klosowiak, J. L., Park, S., Smith, K. P., French, M. E., Focia, P. J., Freymann, D. M., and Rice, S. E. (2016) Structural insights into Parkin substrate lysine targeting from minimal Miro substrates. *Sci Rep* **6**, 33019
296. Phillips, M. J., Calero, G., Chan, B., Ramachandran, S., and Cerione, R. A. (2008) Effector proteins exert an important influence on the signaling-active state of the small GTPase Cdc42. *The Journal of biological chemistry* **283**, 14153-14164
297. Dowd, J. E., and Riggs, D. S. (1965) A Comparison of Estimates of Michaelis-Menten Kinetic Constants from Various Linear Transformations. *The Journal of biological chemistry* **240**, 863-869
298. Peterson, M. E., Daniel, R. M., Danson, M. J., and Eisenthal, R. (2007) The dependence of enzyme activity on temperature: determination and validation of parameters. *Biochem J* **402**, 331-337
299. Myers, R. L. (2003) *The basics of chemistry*, Greenwood Press, Westport, Conn. ; London
300. Pauling, L. (1988) *General chemistry*, Altered and corr. republication. ed., Dover
301. Garrett, R., and Grisham, C. M. (2010) *Biochemistry*, 4th ed., International ed. ed., Brooks/Cole ; Cengage Learning, Australia ; United Kingdom
302. Bos, J. L., Rehmann, H., and Wittinghofer, A. (2007) GEFs and GAPs: critical elements in the control of small G proteins. *Cell* **129**, 865-877
303. Zhang, B., Wang, Z. X., and Zheng, Y. (1997) Characterization of the interactions between the small GTPase Cdc42 and its GTPase-activating proteins and putative effectors. Comparison of kinetic properties of Cdc42 binding to the Cdc42-interactive domains. *The Journal of biological chemistry* **272**, 21999-22007
304. Kumar, V., Abbas, A. K., Aster, J. C., and Perkins, J. A. (2018) *Robbins basic pathology*, Tenth edition. ed., Elsevier, Philadelphia, Pennsylvania
305. Kovacs, G. G., and Budka, H. (2008) Prion diseases: from protein to cell pathology. *Am J Pathol* **172**, 555-565

306. Suhail, M. (2010) Na, K-ATPase: Ubiquitous Multifunctional Transmembrane Protein and its Relevance to Various Pathophysiological Conditions. *J Clin Med Res* **2**, 1-17
307. Isom, D. G., Sridharan, V., and Dohlman, H. G. (2016) Regulation of Ras Paralog Thermostability by Networks of Buried Ionizable Groups. *Biochemistry* **55**, 534-542
308. Pfeil, W., Gesierich, U., Kleemann, G. R., and Sterner, R. (1997) Ferredoxin from the hyperthermophile Thermotoga maritima is stable beyond the boiling point of water. *J Mol Biol* **272**, 591-596
309. Hiller, R., Zhou, Z. H., Adams, M. W., and Englander, S. W. (1997) Stability and dynamics in a hyperthermophilic protein with melting temperature close to 200 degrees C. *Proceedings of the National Academy of Sciences of the United States of America* **94**, 11329-11332
310. Metrick, M. A., Temple, J. E., and MacDonald, G. (2013) The effects of buffers and pH on the thermal stability, unfolding and substrate binding of RecA. *Biophysical chemistry* **184**, 29-36
311. Baldwin, R. L. (1996) How Hofmeister ion interactions affect protein stability. *Biophysical Journal* **71**, 2056-2063
312. Perez-Jimenez, R., Godoy-Ruiz, R., Ibarra-Molero, B., and Sanchez-Ruiz, J. M. (2004) The efficiency of different salts to screen charge interactions in proteins: a Hofmeister effect? *Biophys J* **86**, 2414-2429
313. Cleland, W. W. (1964) Dithiothreitol, a New Protective Reagent for Sh Groups. *Biochemistry* **3**, 480-482
314. Takahashi, N., and Hirose, M. (1992) Reversible Denaturation of Disulfide-Reduced Ovalbumin and Its Reoxidation Generating the Native Cystine Cross-Link. *Journal of Biological Chemistry* **267**, 11565-11572
315. Vagenende, V., Yap, M. G., and Trout, B. L. (2009) Mechanisms of protein stabilization and prevention of protein aggregation by glycerol. *Biochemistry* **48**, 11084-11096
316. Back, J. F., Oakenfull, D., and Smith, M. B. (1979) Increased thermal stability of proteins in the presence of sugars and polyols. *Biochemistry* **18**, 5191-5196
317. Harsha, H. C., Pinto, S. M., and Pandey, A. (2013) Proteomic strategies to characterize signaling pathways. *Methods in molecular biology* **1007**, 359-377
318. Kolch, W., and Pitt, A. (2010) Functional proteomics to dissect tyrosine kinase signalling pathways in cancer. *Nature Reviews Cancer* **10**, 618-629
319. Alberts, B. (2015) *Molecular biology of the cell*, Sixth edition. ed., Garland Science, Taylor and Francis Group, New York, NY
320. Bu, Z., and Callaway, D. J. (2011) Proteins move! Protein dynamics and long-range allostery in cell signaling. *Adv Protein Chem Struct Biol* **83**, 163-221
321. Alberts, B. (2002) *Molecular biology of the cell*, 4th ed / Bruce Alberts ... [et al.] ed., Garland Science, New York
322. Cooper, G. M., and Hausman, R. E. (2013) *The cell : a molecular approach*, 6th ed. ed., Sinauer Associates, Sunderland, MA
323. Donzelli, S., Cioce, M., Muti, P., Strano, S., Yarden, Y., and Blandino, G. (2016) MicroRNAs: Non-coding fine tuners of receptor tyrosine kinase signalling in cancer. *Semin Cell Dev Biol* **50**, 133-142
324. Ryan, R. P., and Dow, J. M. (2011) Communication with a growing family: diffusible signal factor (DSF) signaling in bacteria. *Trends Microbiol* **19**, 145-152
325. Varshney, P., Yadav, V., and Saini, N. (2016) Lipid rafts in immune signalling: current progress and future perspective. *Immunology* **149**, 13-24

326. Wu, X. Q., Dai, Y., Yang, Y., Huang, C., Meng, X. M., Wu, B. M., and Li, J. (2016) Emerging role of microRNAs in regulating macrophage activation and polarization in immune response and inflammation. *Immunology* **148**, 237-248
327. Jabbour, H. N., and Sales, K. J. (2004) Prostaglandin receptor signalling and function in human endometrial pathology. *Trends Endocrinol Metab* **15**, 398-404
328. Jules, J., Maiguel, D., and Hudson, B. I. (2013) Alternative splicing of the RAGE cytoplasmic domain regulates cell signaling and function. *PLoS One* **8**, e78267
329. Volinsky, N., McCarthy, C. J., von Kriegsheim, A., Saban, N., Okada-Hatakeyama, M., Kolch, W., and Kholodenko, B. N. (2015) Signalling mechanisms regulating phenotypic changes in breast cancer cells. *Biosci Rep* **35**
330. Wiley, C. D., Velarde, M. C., Lecot, P., Liu, S., Sarnoski, E. A., Freund, A., Shirakawa, K., Lim, H. W., Davis, S. S., Ramanathan, A., Gerencser, A. A., Verdin, E., and Campisi, J. (2016) Mitochondrial Dysfunction Induces Senescence with a Distinct Secretory Phenotype. *Cell Metab* **23**, 303-314
331. Fleischmann, R. D., Adams, M. D., White, O., Clayton, R. A., Kirkness, E. F., Kerlavage, A. R., Bult, C. J., Tomb, J. F., Dougherty, B. A., Merrick, J. M., and et al. (1995) Whole-genome random sequencing and assembly of Haemophilus influenzae Rd. *Science* **269**, 496-512
332. Riis, S., Stensballe, A., Emmersen, J., Pennisi, C. P., Birkelund, S., Zachar, V., and Fink, T. (2016) Mass spectrometry analysis of adipose-derived stem cells reveals a significant effect of hypoxia on pathways regulating extracellular matrix. *Stem Cell Res Ther* **7**, 52
333. Lian, Z., Kluger, Y., Greenbaum, D. S., Tuck, D., Gerstein, M., Berliner, N., Weissman, S. M., and Newburger, P. E. (2002) Genomic and proteomic analysis of the myeloid differentiation program: global analysis of gene expression during induced differentiation in the MPRO cell line. *Blood* **100**, 3209-3220
334. Fountoulakis, M., Juranville, J. F., Dierssen, M., and Lubec, G. (2002) Proteomic analysis of the fetal brain. *Proteomics* **2**, 1547-1576
335. Tuller, T., Kupiec, M., and Ruppin, E. (2007) Determinants of protein abundance and translation efficiency in S. cerevisiae. *PLoS Comput Biol* **3**, e248
336. Gygi, S. P., Rochon, Y., Franza, B. R., and Aebersold, R. (1999) Correlation between protein and mRNA abundance in yeast. *Mol Cell Biol* **19**, 1720-1730
337. Greenbaum, D., Colangelo, C., Williams, K., and Gerstein, M. (2003) Comparing protein abundance and mRNA expression levels on a genomic scale. *Genome Biol* **4**, 117
338. Deng, B., Ye, N., Luo, G., Chen, X., and Wang, Y. (2005) Proteomics analysis of stage-specific proteins expressed in human squamous cell lung carcinoma tissues. *Cancer Biomark* **1**, 279-286
339. Jungblut, P. R., Zimny-Arndt, U., Zeindl-Eberhart, E., Stulik, J., Koupilova, K., Pleissner, K. P., Otto, A., Muller, E. C., Sokolowska-Kohler, W., Grabher, G., and Stoffler, G. (1999) Proteomics in human disease: cancer, heart and infectious diseases. *Electrophoresis* **20**, 2100-2110
340. Lindoso, R. S., Sandim, V., Collino, F., Carvalho, A. B., Dias, J., da Costa, M. R., Zingali, R. B., and Vieyra, A. (2016) Proteomics of cell-cell interactions in health and disease. *Proteomics* **16**, 328-344
341. Saia-Cereda, V. M., Cassoli, J. S., Martins-de-Souza, D., and Nascimento, J. M. (2016) Psychiatric disorders biochemical pathways unraveled by human brain proteomics. *Eur Arch Psychiatry Clin Neurosci*

342. Swami, M. (2010) Proteomics: A discovery strategy for novel cancer biomarkers. *Nature reviews. Cancer* **10**, 597
343. Alessandro, R., Fontana, S., Kohn, E., and De Leo, G. (2005) Proteomic strategies and their application in cancer research. *Tumori* **91**, 447-455
344. Tyanova, S., Albrechtsen, R., Kronqvist, P., Cox, J., Mann, M., and Geiger, T. (2016) Proteomic maps of breast cancer subtypes. *Nat Commun* **7**, 10259
345. Chapal, N., Molina, L., Molina, F., Laplanche, M., Pau, B., and Petit, P. (2004) Pharmacoproteomic approach to the study of drug mode of action, toxicity, and resistance: applications in diabetes and cancer. *Fundam Clin Pharmacol* **18**, 413-422
346. Hess, S. (2013) The emerging field of chemo- and pharmacoproteomics. *Proteomics Clin Appl* **7**, 171-180
347. Chatterjee, S. K., and Zetter, B. R. (2005) Cancer biomarkers: knowing the present and predicting the future. *Future Oncol* **1**, 37-50
348. Zhang, J., Goodlett, D. R., and Montine, T. J. (2005) Proteomic biomarker discovery in cerebrospinal fluid for neurodegenerative diseases. *J Alzheimers Dis* **8**, 377-386
349. Feist, P., and Hummon, A. B. (2015) Proteomic challenges: sample preparation techniques for microgram-quantity protein analysis from biological samples. *Int J Mol Sci* **16**, 3537-3563
350. Mancuso, F., Bunkenborg, J., Wierer, M., and Molina, H. (2012) Data extraction from proteomics raw data: an evaluation of nine tandem MS tools using a large Orbitrap data set. *J Proteomics* **75**, 5293-5303
351. Savitski, M. M., Fischer, F., Mathieson, T., Sweetman, G., Lang, M., and Bantscheff, M. (2010) Targeted data acquisition for improved reproducibility and robustness of proteomic mass spectrometry assays. *J Am Soc Mass Spectrom* **21**, 1668-1679
352. Yates, J. R., Ruse, C. I., and Nakorchevsky, A. (2009) Proteomics by mass spectrometry: approaches, advances, and applications. *Annu Rev Biomed Eng* **11**, 49-79
353. Fraser, A. (1977) Looking through the microscope. *Aust Fam Physician* **6**, 1104-1112
354. Paulo, J. A. (2013) Practical and Efficient Searching in Proteomics: A Cross Engine Comparison. *Webmedcentral* **4**
355. Carnielli, C. M., Winck, F. V., and Paes Leme, A. F. (2015) Functional annotation and biological interpretation of proteomics data. *Biochimica et biophysica acta* **1854**, 46-54
356. Nesvizhskii, A. I., and Aebersold, R. (2005) Interpretation of shotgun proteomic data: the protein inference problem. *Mol Cell Proteomics* **4**, 1419-1440
357. Zhang, Y., Fonslow, B. R., Shan, B., Baek, M. C., and Yates, J. R., 3rd. (2013) Protein analysis by shotgun/bottom-up proteomics. *Chemical reviews* **113**, 2343-2394
358. Molloy, M. P., Brzezinski, E. E., Hang, J. Q., McDowell, M. T., and VanBogelen, R. A. (2003) Overcoming technical variation and biological variation in quantitative proteomics. *Proteomics* **3**, 1912-1919
359. Piehowski, P. D., Petyuk, V. A., Orton, D. J., Xie, F., Moore, R. J., Ramirez-Restrepo, M., Engel, A., Lieberman, A. P., Albin, R. L., Camp, D. G., Smith, R. D., and Myers, A. J. (2013) Sources of technical variability in quantitative LC-MS proteomics: human brain tissue sample analysis. *J Proteome Res* **12**, 2128-2137

360. Hodge, K., Have, S. T., Hutton, L., and Lamond, A. I. (2013) Cleaning up the masses: exclusion lists to reduce contamination with HPLC-MS/MS. *J Proteomics* **88**, 92-103
361. Cilia, M., Fish, T., Yang, X., McLaughlin, M., Thannhauser, T. W., and Gray, S. (2009) A comparison of protein extraction methods suitable for gel-based proteomic studies of aphid proteins. *J Biomol Tech* **20**, 201-215
362. Lakshman, D. K., Natarajan, S. S., Lakshman, S., Garrett, W. M., and Dhar, A. K. (2008) Optimized protein extraction methods for proteomic analysis of Rhizoctonia solani. *Mycologia* **100**, 867-875
363. Shevchenko, G., Musunuri, S., Wetterhall, M., and Bergquist, J. (2012) Comparison of extraction methods for the comprehensive analysis of mouse brain proteome using shotgun-based mass spectrometry. *J Proteome Res* **11**, 2441-2451
364. Vandermarliere, E., Mueller, M., and Martens, L. (2013) Getting intimate with trypsin, the leading protease in proteomics. *Mass Spectrom Rev* **32**, 453-465
365. Swaney, D. L., Wenger, C. D., and Coon, J. J. (2010) Value of using multiple proteases for large-scale mass spectrometry-based proteomics. *J Proteome Res* **9**, 1323-1329
366. Proc, J. L., Kuzyk, M. A., Hardie, D. B., Yang, J., Smith, D. S., Jackson, A. M., Parker, C. E., and Borchers, C. H. (2010) A quantitative study of the effects of chaotropic agents, surfactants, and solvents on the digestion efficiency of human plasma proteins by trypsin. *J Proteome Res* **9**, 5422-5437
367. Egeland, S. V., Reubsaet, L., and Halvorsen, T. G. (2016) The pros and cons of increased trypsin-to-protein ratio in targeted protein analysis. *J Pharm Biomed Anal* **123**, 155-161
368. Fan, C., Shi, Z., Pan, Y., Song, Z., Zhang, W., Zhao, X., Tian, F., Peng, B., Qin, W., Cai, Y., and Qian, X. (2014) Dual matrix-based immobilized trypsin for complementary proteolytic digestion and fast proteomics analysis with higher protein sequence coverage. *Anal Chem* **86**, 1452-1458
369. Lopez-Ferrer, D., Capelo, J. L., and Vazquez, J. (2005) Ultra fast trypsin digestion of proteins by high intensity focused ultrasound. *J Proteome Res* **4**, 1569-1574
370. Manadas, B., Mendes, V. M., English, J., and Dunn, M. J. (2010) Peptide fractionation in proteomics approaches. *Expert Rev Proteomics* **7**, 655-663
371. Chandramouli, K., and Qian, P. Y. (2009) Proteomics: challenges, techniques and possibilities to overcome biological sample complexity. *Hum Genomics Proteomics* **2009**
372. Perkins, D. N., Pappin, D. J., Creasy, D. M., and Cottrell, J. S. (1999) Probability-based protein identification by searching sequence databases using mass spectrometry data. *Electrophoresis* **20**, 3551-3567
373. Kapp, E. A., Schutz, F., Connolly, L. M., Chakel, J. A., Meza, J. E., Miller, C. A., Fenyo, D., Eng, J. K., Adkins, J. N., Omenn, G. S., and Simpson, R. J. (2005) An evaluation, comparison, and accurate benchmarking of several publicly available MS/MS search algorithms: sensitivity and specificity analysis. *Proteomics* **5**, 3475-3490
374. Elias, J. E., Haas, W., Faherty, B. K., and Gygi, S. P. (2005) Comparative evaluation of mass spectrometry platforms used in large-scale proteomics investigations. *Nat Methods* **2**, 667-675
375. Pappin, D. J., Hojrup, P., and Bleasby, A. J. (1993) Rapid identification of proteins by peptide-mass fingerprinting. *Current biology : CB* **3**, 327-332

376. Bjornson, R. D., Carriero, N. J., Colangelo, C., Shifman, M., Cheung, K. H., Miller, P. L., and Williams, K. (2008) X!!Tandem, an improved method for running X!tandem in parallel on collections of commodity computers. *J Proteome Res* **7**, 293-299
377. Craig, R., and Beavis, R. C. (2003) A method for reducing the time required to match protein sequences with tandem mass spectra. *Rapid Commun Mass Spectrom* **17**, 2310-2316
378. Craig, R., and Beavis, R. C. (2004) TANDEM: matching proteins with tandem mass spectra. *Bioinformatics* **20**, 1466-1467
379. Farnsworth, C. L., and Feig, L. A. (1991) Dominant inhibitory mutations in the Mg(2+)-binding site of RasH prevent its activation by GTP. *Mol Cell Biol* **11**, 4822-4829
380. Powers, S., O'Neill, K., and Wigler, M. (1989) Dominant yeast and mammalian RAS mutants that interfere with the CDC25-dependent activation of wild-type RAS in Saccharomyces cerevisiae. *Mol Cell Biol* **9**, 390-395
381. Stacey, D. W., Feig, L. A., and Gibbs, J. B. (1991) Dominant inhibitory Ras mutants selectively inhibit the activity of either cellular or oncogenic Ras. *Mol Cell Biol* **11**, 4053-4064
382. Suzuki, M., Danilchanka, O., and Mekalanos, J. J. (2014) Vibrio cholerae T3SS effector VopE modulates mitochondrial dynamics and innate immune signaling by targeting Miro GTPases. *Cell Host Microbe* **16**, 581-591
383. Babic, M., Russo, G. J., Wellington, A. J., Sangston, R. M., Gonzalez, M., and Zinsmaier, K. E. (2015) Miro's N-terminal GTPase domain is required for transport of mitochondria into axons and dendrites. *The Journal of neuroscience : the official journal of the Society for Neuroscience* **35**, 5754-5771
384. Braun, P., Tasan, M., Dreze, M., Barrios-Rodiles, M., Lemmens, I., Yu, H., Sahalie, J. M., Murray, R. R., Roncari, L., de Smet, A. S., Venkatesan, K., Rual, J. F., Vandenhaute, J., Cusick, M. E., Pawson, T., Hill, D. E., Tavernier, J., Wrana, J. L., Roth, F. P., and Vidal, M. (2009) An experimentally derived confidence score for binary protein-protein interactions. *Nat Methods* **6**, 91-97
385. Hsia, C. W., Ho, M. Y., Shui, H. A., Tsai, C. B., and Tseng, M. J. (2015) Analysis of dermal papilla cell interactome using STRING database to profile the ex vivo hair growth inhibition effect of a vinca alkaloid drug, colchicine. *Int J Mol Sci* **16**, 3579-3598
386. Szklarczyk, D., Franceschini, A., Kuhn, M., Simonovic, M., Roth, A., Minguez, P., Doerks, T., Stark, M., Muller, J., Bork, P., Jensen, L. J., and von Mering, C. (2011) The STRING database in 2011: functional interaction networks of proteins, globally integrated and scored. *Nucleic Acids Res* **39**, D561-568
387. Taboada, B., Verde, C., and Merino, E. (2010) High accuracy operon prediction method based on STRING database scores. *Nucleic Acids Res* **38**, e130
388. Szklarczyk, D., Franceschini, A., Wyder, S., Forslund, K., Heller, D., Huerta-Cepas, J., Simonovic, M., Roth, A., Santos, A., Tsafou, K. P., Kuhn, M., Bork, P., Jensen, L. J., and von Mering, C. (2015) STRING v10: protein-protein interaction networks, integrated over the tree of life. *Nucleic Acids Res* **43**, D447-452
389. Keller, A., Eng, J., Zhang, N., Li, X. J., and Aebersold, R. (2005) A uniform proteomics MS/MS analysis platform utilizing open XML file formats. *Molecular systems biology* **1**, 2005 0017

390. Searle, B. C., Turner, M., and Nesvizhskii, A. I. (2008) Improving sensitivity by probabilistically combining results from multiple MS/MS search methodologies. *J Proteome Res* **7**, 245-253
391. Cooper, P. S., Lipshultz, D., Matten, W. T., McGinnis, S. D., Pechous, S., Romiti, M. L., Tao, T., Valjavec-Gratian, M., and Sayers, E. W. (2010) Education resources of the National Center for Biotechnology Information. *Brief Bioinform* **11**, 563-569
392. Boase, N. A., and Kumar, S. (2015) NEDD4: The founding member of a family of ubiquitin-protein ligases. *Gene* **557**, 113-122
393. Wang, J., Peng, Q., Lin, Q., Childress, C., Carey, D., and Yang, W. (2010) Calcium activates Nedd4 E3 ubiquitin ligases by releasing the C2 domain-mediated auto-inhibition. *The Journal of biological chemistry* **285**, 12279-12288
394. Bi, X., Cui, K., Han, C., Sun, M., Wang, L., Yang, L., Qiao, D., Han, W., and Liu, L. (2015) [Association of NEDD4 gene polymorphisms with schizophrenia and its clinical characteristics in Chinese Han population]. *Zhonghua Yi Xue Yi Chuan Xue Za Zhi* **32**, 385-390
395. Freedman, R. (2003) Schizophrenia. *N Engl J Med* **349**, 1738-1749
396. Gamo, N. J., Duque, A., Paspalas, C. D., Kata, A., Fine, R., Boven, L., Bryan, C., Lo, T., Anighoro, K., Bermudez, L., Peng, K., Annor, A., Raja, A., Mansson, E., Taylor, S. R., Patel, K., Simen, A. A., and Arnsten, A. F. (2013) Role of disrupted in schizophrenia 1 (DISC1) in stress-induced prefrontal cognitive dysfunction. *Transl Psychiatry* **3**, e328
397. Kwak, Y. D., Wang, B., Li, J. J., Wang, R., Deng, Q., Diao, S., Chen, Y., Xu, R., Masliah, E., Xu, H., Sung, J. J., and Liao, F. F. (2012) Upregulation of the E3 ligase NEDD4-1 by oxidative stress degrades IGF-1 receptor protein in neurodegeneration. *The Journal of neuroscience : the official journal of the Society for Neuroscience* **32**, 10971-10981
398. Olvera, J., and Wool, I. G. (1996) The primary structure of rat ribosomal protein L10a. *Biochem Biophys Res Commun* **220**, 954-957
399. Abidi, N., and Xirodimas, D. P. (2015) Regulation of cancer-related pathways by protein NEDDylation and strategies for the use of NEDD8 inhibitors in the clinic. *Endocr Relat Cancer* **22**, T55-70
400. Li, T., Guan, J., Huang, Z., Hu, X., and Zheng, X. (2014) RNF168-mediated H2A neddylation antagonizes ubiquitylation of H2A and regulates DNA damage repair. *J Cell Sci* **127**, 2238-2248
401. Segovia, J. A., Tsai, S. Y., Chang, T. H., Shil, N. K., Weintraub, S. T., Short, J. D., and Bose, S. (2015) Nedd8 regulates inflammasome-dependent caspase-1 activation. *Mol Cell Biol* **35**, 582-597
402. Liao, Y., Jiang, Y., He, H., Ni, H., Tu, Z., Zhang, S., Wang, B., Lou, J., Quan, S., and Wang, H. (2015) NEDD8-mediated neddylation is required for human endometrial stromal proliferation and decidualization. *Hum Reprod* **30**, 1665-1676
403. Bravo-Cordero, J. J., Sharma, V. P., Roh-Johnson, M., Chen, X., Eddy, R., Condeelis, J., and Hodgson, L. (2013) Spatial regulation of RhoC activity defines protrusion formation in migrating cells. *J Cell Sci* **126**, 3356-3369
404. Wang, Y. F., Li, Y., Liu, B., Yu, M., Fan, B., Zhu, M. J., Xiong, T. A., and Li, K. (2005) Partial molecular characterization, polymorphism and chromosomal localization of the porcine PSMD4 gene. *J Anim Breed Genet* **122**, 247-250
405. Yi, Y. J., Manandhar, G., Sutovsky, M., Zimmerman, S. W., Jonakova, V., van Leeuwen, F. W., Oko, R., Park, C. S., and Sutovsky, P. (2010) Interference with the 19S proteasomal regulatory complex subunit PSMD4 on the sperm surface

inhibits sperm-zona pellucida penetration during porcine fertilization. *Cell Tissue Res* **341**, 325-340
406. Araki, K., and Nagata, K. (2011) Functional in vitro analysis of the ERO1 protein and protein-disulfide isomerase pathway. *The Journal of biological chemistry* **286**, 32705-32712
407. Kutomi, G., Tamura, Y., Tanaka, T., Kajiwara, T., Kukita, K., Ohmura, T., Shima, H., Takamaru, T., Satomi, F., Suzuki, Y., Torigoe, T., Sato, N., and Hirata, K. (2013) Human endoplasmic reticulum oxidoreductin 1-alpha is a novel predictor for poor prognosis of breast cancer. *Cancer Sci* **104**, 1091-1096
408. Tanaka, T., Kajiwara, T., Torigoe, T., Okamoto, Y., Sato, N., and Tamura, Y. (2015) Cancer-associated oxidoreductase ERO1-alpha drives the production of tumor-promoting myeloid-derived suppressor cells via oxidative protein folding. *J Immunol* **194**, 2004-2010
409. Anelli, T., Bergamelli, L., Margittai, E., Rimessi, A., Fagioli, C., Malgaroli, A., Pinton, P., Ripamonti, M., Rizzuto, R., and Sitia, R. (2012) Ero1alpha regulates Ca(2+) fluxes at the endoplasmic reticulum-mitochondria interface (MAM). *Antioxid Redox Signal* **16**, 1077-1087
410. McCaffrey, K., and Braakman, I. (2016) Protein quality control at the endoplasmic reticulum. *Essays Biochem* **60**, 227-235
411. Querfurth, H. W., and LaFerla, F. M. (2010) Alzheimer's disease. *N Engl J Med* **362**, 329-344
412. Zhang, L., Sheng, R., and Qin, Z. (2009) The lysosome and neurodegenerative diseases. *Acta Biochim Biophys Sin (Shanghai)* **41**, 437-445
413. Dallery, E., Galiegue-Zouitina, S., Collyn-d'Hooghe, M., Quief, S., Denis, C., Hildebrand, M. P., Lantoine, D., Deweindt, C., Tilly, H., Bastard, C., and et al. (1995) TTF, a gene encoding a novel small G protein, fuses to the lymphoma-associated LAZ3 gene by t(3;4) chromosomal translocation. *Oncogene* **10**, 2171-2178
414. Gaidano, G., Pasqualucci, L., Capello, D., Berra, E., Deambrogi, C., Rossi, D., Maria Larocca, L., Gloghini, A., Carbone, A., and Dalla-Favera, R. (2003) Aberrant somatic hypermutation in multiple subtypes of AIDS-associated non-Hodgkin lymphoma. *Blood* **102**, 1833-1841
415. Pasqualucci, L., Neumeister, P., Goossens, T., Nanjangud, G., Chaganti, R. S., Kuppers, R., and Dalla-Favera, R. (2001) Hypermutation of multiple proto-oncogenes in B-cell diffuse large-cell lymphomas. *Nature* **412**, 341-346
416. Preudhomme, C., Roumier, C., Hildebrand, M. P., Dallery-Prudhomme, E., Lantoine, D., Lai, J. L., Daudignon, A., Adenis, C., Bauters, F., Fenaux, P., Kerckaert, J. P., and Galiegue-Zouitina, S. (2000) Nonrandom 4p13 rearrangements of the RhoH/TTF gene, encoding a GTP-binding protein, in non-Hodgkin's lymphoma and multiple myeloma. *Oncogene* **19**, 2023-2032
417. Gu, Y., Jasti, A. C., Jansen, M., and Siefring, J. E. (2005) RhoH, a hematopoietic-specific Rho GTPase, regulates proliferation, survival, migration, and engraftment of hematopoietic progenitor cells. *Blood* **105**, 1467-1475
418. Uhlén, M. (2016) Cancer Atlas: RhoH. in *The Human Protein Atlas*, Science for Life Laboratory, KTH-Royal Institute of Technology, Stockholm, Sweden
419. Uhlen, M., Fagerberg, L., Hallstrom, B. M., Lindskog, C., Oksvold, P., Mardinoglu, A., Sivertsson, A., Kampf, C., Sjostedt, E., Asplund, A., Olsson, I., Edlund, K., Lundberg, E., Navani, S., Szigyarto, C. A., Odeberg, J., Djureinovic, D., Takanen, J. O., Hober, S., Alm, T., Edqvist, P. H., Berling, H., Tegel, H., Mulder, J., Rockberg, J., Nilsson, P., Schwenk, J. M., Hamsten, M., von Feilitzen, K., Forsberg, M., Persson, L., Johansson, F., Zwahlen, M., von Heijne,

G., Nielsen, J., and Ponten, F. (2015) Proteomics. Tissue-based map of the human proteome. *Science* **347**, 1260419
420. Forget, M. A., Desrosiers, R. R., Gingras, D., and Beliveau, R. (2002) Phosphorylation states of Cdc42 and RhoA regulate their interactions with Rho GDP dissociation inhibitor and their extraction from biological membranes. *Biochemical Journal* **361**, 243-254
421. Gu, Y., Zheng, Y., and Williams, D. A. (2005) RhoH GTPase: a key regulator of hematopoietic cell proliferation and apoptosis? *Cell Cycle* **4**, 201-202
422. Schmidt-Mende, J., Geering, B., Yousefi, S., and Simon, H. U. (2010) Lysosomal degradation of RhoH protein upon antigen receptor activation in T but not B cells. *Eur J Immunol* **40**, 525-529
423. Heasman, S. J., and Ridley, A. J. (2008) Mammalian Rho GTPases: new insights into their functions from in vivo studies. *Nature reviews. Molecular cell biology* **9**, 690-701
424. Bernicot, I., Morel, F., Le Bris, M. J., Bail, J. P., Douet-Guilbert, N., and De Braekeleer, M. (2006) Rearrangement of the RHOH gene in a case of splenic lymphoma with villous lymphocytes. *Cancer genetics and cytogenetics* **170**, 78-79
425. Galiegue-Zouitina, S., Delestre, L., Dupont, C., Troussard, X., and Shelley, C. S. (2008) Underexpression of RhoH in Hairy Cell Leukemia. *Cancer research* **68**, 4531-4540
426. Hiraga, J., Katsumi, A., Iwasaki, T., Abe, A., Kiyoi, H., Matsushita, T., Kinoshita, T., and Naoe, T. (2007) Prognostic analysis of aberrant somatic hypermutation of RhoH gene in diffuse large B cell lymphoma. *Leukemia* **21**, 1846-1847
427. Chen, L., Huynh, L., Apgar, J., Tang, L., Rassenti, L., Weiss, A., and Kipps, T. J. (2008) ZAP-70 enhances IgM signaling independent of its kinase activity in chronic lymphocytic leukemia. *Blood* **111**, 2685-2692
428. Wang, Y., Kaiser, C. E., Frett, B., and Li, H. Y. (2013) Targeting mutant KRAS for anticancer therapeutics: a review of novel small molecule modulators. *J Med Chem* **56**, 5219-5230
429. Ostrem, J. M., Peters, U., Sos, M. L., Wells, J. A., and Shokat, K. M. (2013) K-Ras(G12C) inhibitors allosterically control GTP affinity and effector interactions. *Nature* **503**, 548-551
430. Mishra, A. K., Del Campo, C. M., Collins, R. E., Roy, C. R., and Lambright, D. G. (2013) The Legionella pneumophila GTPase activating protein LepB accelerates Rab1 deactivation by a non-canonical hydrolytic mechanism. *The Journal of biological chemistry* **288**, 24000-24011
431. Buhrman, G., Wink, G., and Mattos, C. (2007) Transformation efficiency of RasQ61 mutants linked to structural features of the switch regions in the presence of Raf. *Structure* **15**, 1618-1629
432. Chae, H. D., Lee, K. E., Williams, D. A., and Gu, Y. (2008) Cross-talk between RhoH and Rac1 in regulation of actin cytoskeleton and chemotaxis of hematopoietic progenitor cells. *Blood* **111**, 2597-2605
433. van Hennik, P. B., ten Klooster, J. P., Halstead, J. R., Voermans, C., Anthony, E. C., Divecha, N., and Hordijk, P. L. (2003) The C-terminal domain of Rac1 contains two motifs that control targeting and signaling specificity. *The Journal of biological chemistry* **278**, 39166-39175
434. Troeger, A., Chae, H. D., Wood, J., and Williams, D. A. (2011) Functional Characterization of the RhoH c-Terminus and Insert Domain As Potential Drug Targets. *Blood* **118**, 777-777

435. Troeger, A., Chae, H. D., Senturk, M., Wood, J., and Williams, D. A. (2013) A unique carboxyl-terminal insert domain in the hematopoietic-specific, GTPase-deficient Rho GTPase RhoH regulates post-translational processing. *The Journal of biological chemistry* **288**, 36451-36462
436. Zong, H., Kaibuchi, K., and Quilliam, L. A. (2001) The insert region of RhoA is essential for Rho kinase activation and cellular transformation. *Molecular and cellular biology* **21**, 5287-5298
437. Diekmann, D., Nobes, C. D., Burbelo, P. D., Abo, A., and Hall, A. (1995) Rac Gtpase Interacts with Gaps and Target Proteins through Multiple Effector Sites. *Embo Journal* **14**, 5297-5305
438. Freeman, J. L., Abo, A., and Lambeth, J. D. (1996) Rac "insert region" is a novel effector region that is implicated in the activation of NADPH oxidase, but not PAK65. *Journal of Biological Chemistry* **271**, 19794-19801
439. Reth, M. (1989) Antigen receptor tail clue. *Nature* **338**, 383-384
440. Cambier, J. C. (1995) Antigen and Fc receptor signaling. The awesome power of the immunoreceptor tyrosine-based activation motif (ITAM). *J Immunol* **155**, 3281-3285
441. Getahun, A., and Cambier, J. C. (2015) Of ITIMs, ITAMs, and ITAMis: revisiting immunoglobulin Fc receptor signaling. *Immunological reviews* **268**, 66-73
442. Billadeau, D. D., and Leibson, P. J. (2002) ITAMs versus ITIMs: striking a balance during cell regulation. *The Journal of clinical investigation* **109**, 161-168
443. Ravetch, J. V., and Lanier, L. L. (2000) Immune inhibitory receptors. *Science* **290**, 84-89
444. Barrow, A. D., and Trowsdale, J. (2006) You say ITAM and I say ITIM, let's call the whole thing off: the ambiguity of immunoreceptor signalling. *Eur J Immunol* **36**, 1646-1653
445. Fueller, F., and Kubatzky, K. F. (2008) The small GTPase RhoH is an atypical regulator of haematopoietic cells. *Cell Commun Signal* **6**, 6
446. Gu, Y., Chae, H. D., Siefring, J. E., Jasti, A. C., Hildeman, D. A., and Williams, D. A. (2006) RhoH GTPase recruits and activates Zap70 required for T cell receptor signaling and thymocyte development. *Nat Immunol* **7**, 1182-1190
447. Sloan-Lancaster, J., Presley, J., Ellenberg, J., Yamazaki, T., Lippincott-Schwartz, J., and Samelson, L. E. (1998) ZAP-70 association with T cell receptor zeta (TCRzeta): fluorescence imaging of dynamic changes upon cellular stimulation. *J Cell Biol* **143**, 613-624
448. Love, P. E., and Hayes, S. M. (2010) ITAM-mediated signaling by the T-cell antigen receptor. *Cold Spring Harbor perspectives in biology* **2**, a002485
449. Wang, H., Zeng, X., Fan, Z., and Lim, B. (2011) RhoH modulates pre-TCR and TCR signalling by regulating LCK. *Cell Signal* **23**, 249-258
450. Chae, H. D., Siefring, J. E., Hildeman, D. A., Gu, Y., and Williams, D. A. (2010) RhoH regulates subcellular localization of ZAP-70 and Lck in T cell receptor signaling. *PLoS One* **5**, e13970
451. Ridley, A. J. (2015) Rho GTPase signalling in cell migration. *Curr Opin Cell Biol* **36**, 103-112
452. Hill, C. S., Wynne, J., and Treisman, R. (1995) The Rho family GTPases RhoA, Rac1, and CDC42Hs regulate transcriptional activation by SRF. *Cell* **81**, 1159-1170

453. Pelletier, S., Duhamel, F., Coulombe, P., Popoff, M. R., and Meloche, S. (2003) Rho family GTPases are required for activation of Jak/STAT signaling by G protein-coupled receptors. *Mol Cell Biol* **23**, 1316-1333
454. Su, L. F., Knoblauch, R., and Garabedian, M. J. (2001) Rho GTPases as modulators of the estrogen receptor transcriptional response. *The Journal of biological chemistry* **276**, 3231-3237
455. Dorn, T., Kuhn, U., Bungartz, G., Stiller, S., Bauer, M., Ellwart, J., Peters, T., Scharffetter-Kochanek, K., Semmrich, M., Laschinger, M., Holzmann, B., Klinkert, W. E., Straten, P. T., Kollgaard, T., Sixt, M., and Brakebusch, C. (2007) RhoH is important for positive thymocyte selection and T-cell receptor signaling. *Blood* **109**, 2346-2355
456. Baker, C. M., Comrie, W. A., Hyun, Y. M., Chung, H. L., Fedorchuk, C. A., Lim, K., Brakebusch, C., McGrath, J. L., Waugh, R. E., Meier-Schellersheim, M., and Kim, M. (2012) Opposing roles for RhoH GTPase during T-cell migration and activation. *Proceedings of the National Academy of Sciences of the United States of America* **109**, 10474-10479
457. Tamehiro, N., Oda, H., Shirai, M., and Suzuki, H. (2015) Overexpression of RhoH Permits to Bypass the Pre-TCR Checkpoint. *PLoS One* **10**, e0131047
458. Wang, H., Kadlecek, T. A., Au-Yeung, B. B., Goodfellow, H. E., Hsu, L. Y., Freedman, T. S., and Weiss, A. (2010) ZAP-70: an essential kinase in T-cell signaling. *Cold Spring Harbor perspectives in biology* **2**, a002279
459. Crequer, A., Troeger, A., Patin, E., Ma, C. S., Picard, C., Pedergnana, V., Fieschi, C., Lim, A., Abhyankar, A., Gineau, L., Mueller-Fleckenstein, I., Schmidt, M., Taieb, A., Krueger, J., Abel, L., Tangye, S. G., Orth, G., Williams, D. A., Casanova, J. L., and Jouanguy, E. (2012) Human RHOH deficiency causes T cell defects and susceptibility to EV-HPV infections. *The Journal of clinical investigation* **122**, 3239-3247
460. Arpaia, E., Shahar, M., Dadi, H., Cohen, A., and Roifman, C. M. (1994) Defective T cell receptor signaling and CD8+ thymic selection in humans lacking zap-70 kinase. *Cell* **76**, 947-958
461. Chan, A. C., Kadlecek, T. A., Elder, M. E., Filipovich, A. H., Kuo, W. L., Iwashima, M., Parslow, T. G., and Weiss, A. (1994) ZAP-70 deficiency in an autosomal recessive form of severe combined immunodeficiency. *Science* **264**, 1599-1601
462. Elder, M. E., Lin, D., Clever, J., Chan, A. C., Hope, T. J., Weiss, A., and Parslow, T. G. (1994) Human severe combined immunodeficiency due to a defect in ZAP-70, a T cell tyrosine kinase. *Science* **264**, 1596-1599
463. Negishi, I., Motoyama, N., Nakayama, K., Nakayama, K., Senju, S., Hatakeyama, S., Zhang, Q., Chan, A. C., and Loh, D. Y. (1995) Essential role for ZAP-70 in both positive and negative selection of thymocytes. *Nature* **376**, 435-438
464. Kadlecek, T. A., van Oers, N. S., Lefrancois, L., Olson, S., Finlay, D., Chu, D. H., Connolly, K., Killeen, N., and Weiss, A. (1998) Differential requirements for ZAP-70 in TCR signaling and T cell development. *J Immunol* **161**, 4688-4694
465. Williams, B. L., Schreiber, K. L., Zhang, W., Wange, R. L., Samelson, L. E., Leibson, P. J., and Abraham, R. T. (1998) Genetic evidence for differential coupling of Syk family kinases to the T-cell receptor: reconstitution studies in a ZAP-70-deficient Jurkat T-cell line. *Mol Cell Biol* **18**, 1388-1399
466. Cherry, L. K., Li, X., Schwab, P., Lim, B., and Klickstein, L. B. (2004) RhoH is required to maintain the integrin LFA-1 in a nonadhesive state on lymphocytes. *Nat Immunol* **5**, 961-967

467. Malissen, B., Aguado, E., and Malissen, M. (2005) Role of the LAT adaptor in T-cell development and Th2 differentiation. *Adv Immunol* **87**, 1-25
468. Saoudi, A., Kassem, S., Dejean, A., and Gaud, G. (2014) Rho-GTPases as key regulators of T lymphocyte biology. *Small GTPases* **5**
469. Babich, A., and Burkhardt, J. K. (2013) Coordinate control of cytoskeletal remodeling and calcium mobilization during T-cell activation. *Immunological reviews* **256**, 80-94
470. Katzav, S. (2009) Vav1: a hematopoietic signal transduction molecule involved in human malignancies. *Int J Biochem Cell Biol* **41**, 1245-1248
471. Matsumoto, M., Oyamada, K., Takahashi, H., Sato, T., Hatakeyama, S., and Nakayama, K. I. (2009) Large-scale proteomic analysis of tyrosine-phosphorylation induced by T-cell receptor or B-cell receptor activation reveals new signaling pathways. *Proteomics* **9**, 3549-3563
472. Seda, V., and Mraz, M. (2015) B-cell receptor signalling and its crosstalk with other pathways in normal and malignant cells. *Eur J Haematol* **94**, 193-205
473. Nabhan, C., and Rosen, S. T. (2014) Chronic lymphocytic leukemia: a clinical review. *JAMA* **312**, 2265-2276
474. Byrd, J. C. (2015) Introduction to a series of reviews on chronic lymphocytic leukemia. *Blood* **126**, 427
475. Crespo, M., Bosch, F., Villamor, N., Bellosillo, B., Colomer, D., Rozman, M., Marce, S., Lopez-Guillermo, A., Campo, E., and Montserrat, E. (2003) ZAP-70 expression as a surrogate for immunoglobulin-variable-region mutations in chronic lymphocytic leukemia. *N Engl J Med* **348**, 1764-1775
476. Rassenti, L. Z., Huynh, L., Toy, T. L., Chen, L., Keating, M. J., Gribben, J. G., Neuberg, D. S., Flinn, I. W., Rai, K. R., Byrd, J. C., Kay, N. E., Greaves, A., Weiss, A., and Kipps, T. J. (2004) ZAP-70 compared with immunoglobulin heavy-chain gene mutation status as a predictor of disease progression in chronic lymphocytic leukemia. *N Engl J Med* **351**, 893-901
477. Cancelas, J. A., Jansen, M., and Williams, D. A. (2006) The role of chemokine activation of Rac GTPases in hematopoietic stem cell marrow homing, retention, and peripheral mobilization. *Exp Hematol* **34**, 976-985
478. del Pozo, M. A., Vicente-Manzanares, M., Tejedor, R., Serrador, J. M., and Sanchez-Madrid, F. (1999) Rho GTPases control migration and polarization of adhesion molecules and cytoskeletal ERM components in T lymphocytes. *Eur J Immunol* **29**, 3609-3620
479. Campbell, P. J., and Green, A. R. (2006) The myeloproliferative disorders. *N Engl J Med* **355**, 2452-2466
480. Gozuacik, D., and Kimchi, A. (2006) DAPk protein family and cancer. *Autophagy* **2**, 74-79
481. Shiloh, R., Bialik, S., and Kimchi, A. (2014) The DAPK family: a structure-function analysis. *Apoptosis* **19**, 286-297
482. Sanjo, H., Kawai, T., and Akira, S. (1998) DRAKs, novel serine/threonine kinases related to death-associated protein kinase that trigger apoptosis. *Journal of Biological Chemistry* **273**, 29066-29071
483. Kuwahara, H., Nishizaki, M., and Kanazawa, H. (2008) Nuclear localization signal and phosphorylation of Serine350 specify intracellular localization of DRAK2. *J Biochem* **143**, 349-358
484. Ramos, S. J., Hernandez, J. B., Gatzka, M., and Walsh, C. M. (2008) Enhanced T Cell Apoptosis within Drak2-Deficient Mice Promotes Resistance to Autoimmunity. *Journal of Immunology* **181**, 7606-7616

485. Friedrich, M. L., Wen, B. G., Bain, G., Kee, B. L., Katayama, C., Murre, C., Hedrick, S. M., and Walsh, C. M. (2005) DRAK2, a lymphoid-enriched DAP kinase, regulates the TCR activation threshold during thymocyte selection. *Int Immunol* **17**, 1379-1390
486. Mao, J. N., Qiao, X. Y., Luo, H. Y., and Wu, J. P. (2006) Transgenic Drak2 overexpression in mice leads to increased T cell apoptosis and compromised memory T cell development. *Journal of Biological Chemistry* **281**, 12587-12595
487. Friedrich, M. L., Cui, M., Hernandez, J. B., Weist, B. M., Andersen, H. M., Zhang, X., Huang, L., and Walsh, C. M. (2007) Modulation of DRAK2 autophosphorylation by antigen receptor signaling in primary lymphocytes. *The Journal of biological chemistry* **282**, 4573-4584
488. Gatzka, M., Newton, R. H., and Walsh, C. M. (2009) Altered thymic selection and increased autoimmunity caused by ectopic expression of DRAK2 during T cell development. *J Immunol* **183**, 285-297
489. Friedrich, M. L., Wen, B. G., Bain, G., Kee, B. L., Katayama, C., Murre, C., Hedrick, S. M., and Walsh, C. M. (2005) DRAK2, a lymphoid-enriched DAP kinase, regulates the TCR activation threshold during thymocyte selection. *Int Immunol* **17**, 1379-1390
490. Honey, K. (2005) T-cell signalling - DRAK2 puts the brakes on T-cell responses. *Nat Rev Immunol* **5**, 98-99
491. Feske, S., Giltnane, J., Dolmetsch, R., Staudt, L. M., and Rao, A. (2001) Gene regulation mediated by calcium signals in T lymphocytes. *Nat Immunol* **2**, 316-324
492. Fanger, C. M., Hoth, M., Crabtree, G. R., and Lewis, R. S. (1995) Characterization of T cell mutants with defects in capacitative calcium entry: genetic evidence for the physiological roles of CRAC channels. *J Cell Biol* **131**, 655-667
493. Le Deist, F., Hivroz, C., Partiseti, M., Thomas, C., Buc, H. A., Oleastro, M., Belohradsky, B., Choquet, D., and Fischer, A. (1995) A primary T-cell immunodeficiency associated with defective transmembrane calcium influx. *Blood* **85**, 1053-1062
494. McGargill, M. A., Wen, B. G., Walsh, C. M., and Hedrick, S. M. (2004) A deficiency in Drak2 results in a T cell hypersensitivity and an unexpected resistance to autoimmunity. *Immunity* **21**, 781-791
495. McGargill, M. A., Choy, C., Wen, B. G., and Hedrick, S. M. (2008) Drak2 regulates the survival of activated T cells and is required for organ-specific autoimmune disease. *J Immunol* **181**, 7593-7605
496. Ramos, S. J., Hardison, J. L., Stiles, L. N., Lane, T. E., and Walsh, C. M. (2007) Anti-viral effector T cell responses and trafficking are not dependent upon DRAK2 signaling following viral infection of the central nervous system. *Autoimmunity* **40**, 54-65
497. Ramos, S. J., Hernandez, J. B., Gatzka, M., and Walsh, C. M. (2008) Enhanced T cell apoptosis within Drak2-deficient mice promotes resistance to autoimmunity. *Journal of immunology* **181**, 7606-7616
498. Wang, S., Welte, T., McGargill, M., Town, T., Thompson, J., Anderson, J. F., Flavell, R. A., Fikrig, E., Hedrick, S. M., and Wang, T. (2008) Drak2 contributes to West Nile virus entry into the brain and lethal encephalitis. *J Immunol* **181**, 2084-2091
499. Weist, B. M., Hernandez, J. B., and Walsh, C. M. (2012) Loss of DRAK2 signaling enhances allogeneic transplant survival by limiting effector and memory T cell responses. *Am J Transplant* **12**, 2220-2227

500. Edwards, B. A., Harris, T. L., Floersh, H., Lukens, J. R., Zaki, M. H., Vogel, P., Kanneganti, T. D., Bui, J. D., and McGargill, M. A. (2015) Drak2 is not required for tumor surveillance and suppression. *Int Immunol* **27**, 161-166
501. Felix, N. J., and Allen, P. M. (2007) Specificity of T-cell alloreactivity. *Nat Rev Immunol* **7**, 942-953
502. Lechler, R. I., Sykes, M., Thomson, A. W., and Turka, L. A. (2005) Organ transplantation--how much of the promise has been realized? *Nature medicine* **11**, 605-613
503. Wei, Q. X., Claus, R., Hielscher, T., Mertens, D., Raval, A., Oakes, C. C., Tanner, S. M., de la Chapelle, A., Byrd, J. C., Stilgenbauer, S., and Plass, C. (2013) Germline allele-specific expression of DAPK1 in chronic lymphocytic leukemia. *PLoS One* **8**, e55261
504. Yang, K. M., Kim, W., Bae, E., Gim, J., Weist, B. M., Jung, Y., Hyun, J. S., Hernandez, J. B., Leem, S. H., Park, T., Jeong, J., Walsh, C. M., and Kim, S. J. (2012) DRAK2 participates in a negative feedback loop to control TGF-beta/Smads signaling by binding to type I TGF-beta receptor. *Cell Rep* **2**, 1286-1299
505. Ciardullo, C., Zhou, P., Willmore, E., Harrison, C. J., Hall, A., Eswaran, J. & Soundararajan, M. (2016) Impact of the apoptotic regulator DRAK2 in chronic lymphocytic leukemia. in *36th World Congress of the International Society of Hematology*, Glasgow, UK
506. Satishchandran, C., Hickman, Y. N., and Markham, G. D. (1992) Characterization of the phosphorylated enzyme intermediate formed in the adenosine 5'-phosphosulfate kinase reaction. *Biochemistry* **31**, 11684-11688
507. Guruprasad, K., Reddy, B. V., and Pandit, M. W. (1990) Correlation between stability of a protein and its dipeptide composition: a novel approach for predicting in vivo stability of a protein from its primary sequence. *Protein engineering* **4**, 155-161
508. Schoentaube, J., Olling, A., Tatge, H., Just, I., and Gerhard, R. (2009) Serine-71 phosphorylation of Rac1/Cdc42 diminishes the pathogenic effect of Clostridium difficile toxin A. *Cell Microbiol* **11**, 1816-1826
509. Ellerbroek, S. M., Wennerberg, K., and Burridge, K. (2003) Serine phosphorylation negatively regulates RhoA in vivo. *Journal of Biological Chemistry* **278**, 19023-19031
510. Jones, S. E., and Palmer, T. M. (2012) Protein kinase A-mediated phosphorylation of RhoA on serine 188 triggers the rapid induction of a neuroendocrine-like phenotype in prostate cancer epithelial cells. *Cellular Signalling* **24**, 1504-1514

Appendices

Appendix 1: General laboratory equipment use

Sterilisation

Autoclave sterilisation was achieved at 121°C for 30 min using a bench-top Prestige Medical 2100 Classic autoclave or 121°C for 40 min in a Rodwell Gemini front-loading autoclave.

Filter sterilisation was performed through a 0.2 µm Minisart® filter unit (Sartorius) attached to a sterile syringe of appropriate volume (Plastipak®, Becton Dickinson)

Incubators

For bacterial growth in liquid cultures, an Innova 44 orbital shaker Brunswick Scientific (BRS) was utilised. Growth of bacteria on solid media was performed in a static GallenKamp incubator.

pH meter

A Jenway Ion Meter 3340 (calibrated with buffers at pH 4.0, 7.0 and 9.2) was utilised for all alterations of solution pH.

Micro-centrifugation

Centrifugation of volumes up to 2 mL was achieved using a small Sigma (SIG) 1-15 benchtop micro-centrifuge. A MSE Microcentaur bench-top centrifuge was utilised to centrifuge PCR tubes.

Agarose gel electrophoresis

Electrophoresis of DNA was undertaken using an electrophoresis system (BR) powered by a power PAC 300 apparatus (BR).

Sodium dodecyl sulphate-polyacrylamide gel electrophoresis (SDS-PAGE) gel kit

A Mini-PROTEAN™ 3 Cell kit powered (BR) by a power PAC 300 apparatus (BR) was utilised for SDS-PAGE purposes.

Sonication

A MSE Soniprep 150 ultra-sonication machine (Sanyo) was utilised for sonication.

Spectrophotometer

Spectrophotometric measurements were made using a UV-visible HeƷios α Spectronic Unicam spectrophotometer (TS).

PCR

All PCR reactions were performed using a Mastercycler® gradient thermocycler (Eppendorf).

Vortexing

A Fisher Scientific (FIS) whirlmixer was used to vortex samples.

Waterbath

Grant (SUB series) incubator water baths were used to incubate samples at digitally controlled temperatures.

Pippetting

Gilson P2-P5000 pipettes were used to accurately pipette samples and reagents from 0.01-5000 µL

Weighing Reagents

A Mettler AT250 analytical balance used to measure µg quantities of chemicals and reagents.

Appendix 2: Gel filtration calibration curve

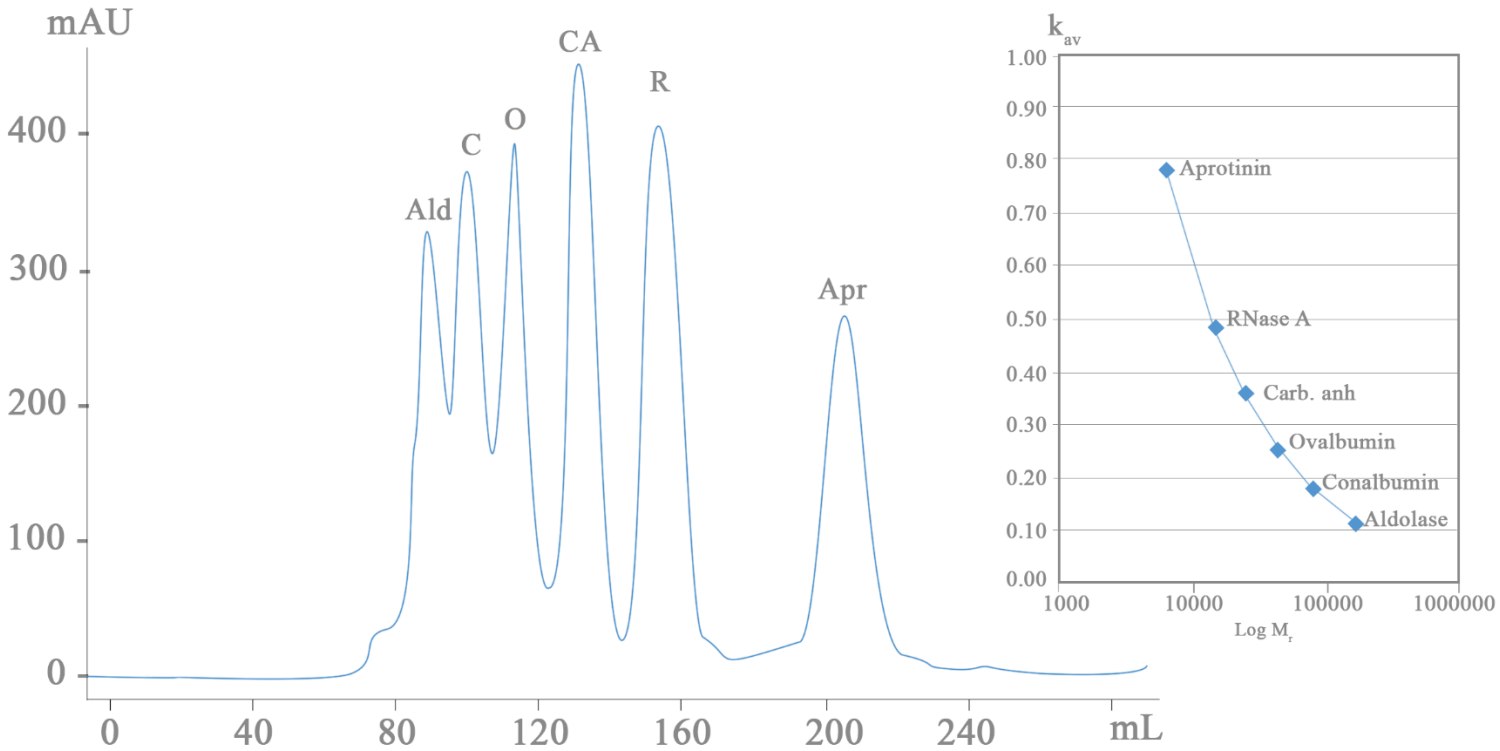

Figure A2.1 Typical gel filtration calibration curve. Obtained from the sephacryl™ S-200 HR HiPrep™ 16/60 column used, attached to an automated FPLC system using the following the protocol outlined in the methods section.

Appendix 3: PCR protocols

Optimised PCR programmes for each sequence cloned are shown in the following tables. Most programmes were based on recommendations suggested by Novagen for PCR using KOD polymerase. Optimised reactions typically comprised: 10 ng template, 0.3 µM of each primer and 25 µL KOD Hot Start Mastermix (Novagen, United Kingdom) brought to a final volume of 50 µL with PCR grade water. In each case, 2% DMSO was utilised for optimisation of sequence amplification.

Table A3.1 PCR programmes utilised for the amplification of hMiro1 and hMiro2 full-length wildtype encoding sequences.

$hMiro1_{FL}$		**$hMiro2_{FL}$**	
Step	**Command**	**Step**	**Command**
1	94ºC for 2 minutes	**1**	94ºC for 2 minutes
2	94ºC for 15 seconds	**2**	94ºC for 15 seconds
3	62ºC for 30 seconds	**3**	60ºC for 30 seconds
4	72ºC for 40 seconds	**4**	72ºC for 40 seconds
5	Repeat steps 2-4 for 30 cycles	**5**	Repeat steps 2-4 for 30 cycles
6	4ºC hold	**6**	4ºC hold

Table A3.2 PCR programmes utilised for the amplification of hMiro1 and hMiro2 N-terminal (NT) GTPase encoding sequences.

$hMiro1_{NT}$ (K3 – P169)		**$hMiro2_{NT}$ (R3 – P169)**	
Step	**Command**	**Step**	**Command**
1	94ºC for 2 minutes	**1**	94ºC for 2 minutes
2	94ºC for 15 seconds	**2**	94ºC for 15 seconds
3	62ºC for 30 seconds	**3**	62ºC for 30 seconds
4	72ºC for 40 seconds	**4**	72ºC for 40 seconds
5	Repeat steps 2-4 for 30 cycles	**5**	Repeat steps 2-4 for 30 cycles
6	4ºC hold	**6**	4ºC hold

Table A3.3 PCR programmes utilised for the amplification of hMiro1 and hMiro2 C-terminal GTPase (CT) encoding sequences.

$hMiro1_{CT}$ (Q415-P580)		**$hMiro2_{CT}$ (Q413-F589)**	
Step	**Command**	**Step**	**Command**
1	94ºC for 2 minutes	**1**	94ºC for 2 minutes
2	94ºC for 15 seconds	**2**	94ºC for 15 seconds
3	58ºC for 30 seconds	**3**	62ºC for 30 seconds
4	72ºC for 40 seconds	**4**	72ºC for 40 seconds
5	Repeat steps 2-4 for 30 cycles	**5**	Repeat steps 2-4 for 30 cycles
6	4ºC hold	**6**	4ºC hold

Table A3.4 PCR programmes utilised for the amplification of $hMiro1_{XTAL}$ and $hMiro2_{XTAL}$ encoding sequences.

$RhoH_{FL}$		**$RhoH_{T1}$**	
Step	**Command**	**Step**	**Command**
1	94ºC for 2 minutes	**1**	94ºC for 2 minutes
2	94ºC for 15 seconds	**2**	94ºC for 15 seconds
3	49ºC for 30 seconds	**3**	53ºC for 30 seconds
4	72ºC for 40 seconds	**4**	72ºC for 40 seconds
5	Repeat steps 2-4 for 30 cycles	**5**	Repeat steps 2-4 for 30 cycles
6	4ºC hold	**6**	4ºC hold

Table A3.5 PCR programmes utilised for the amplification of $RhoH_{FL}$, $RhoH_{T1}$ and $RhoH_{T2}$ encoding sequences.

$RhoH_{FL}$		$RhoH_{T1}$ and $RhoH_{T2}$	
Step	**Command**	**Step**	**Command**
1	94ºC for 2 minutes	**1**	94ºC for 2 minutes
2	94ºC for 15 seconds	**2**	94ºC for 15 seconds
3	58ºC for 30 seconds	**3**	54ºC for 30 seconds
4	72ºC for 40 seconds	**4**	72ºC for 40 seconds
5	Repeat steps 2-4 for 30 cycles	**5**	Repeat steps 2-4 for 30 cycles
6	4ºC hold	**6**	4ºC hold

Appendix 4: Mutant primers for site-directed mutagenesis (SDM)

Primers used for site-directed mutagenesis (SDM) are provided below. These primers were utilised with a number of hMiro templates to produce the desired panel of mutants displayed in Chapter 5.

Oligonucleotide primer for G425V hMiro1 mutagenesis

Forward: 5'-GTTCAGATGTAATGTAATTGTGGTGAAAAACTGTGGGAAAAG-3'

Reverse: 5'-CTTTTCCCACAGTTTTTCACCACAATTACATTACATCTGAAC-3'

Oligonucleotide primer for S432N hMiro1 mutagenesis

Forward: 5'- GAAAAACTGTGGGAAAAATGGAGTTCTTCAGGCTC-3'

Reverse: 5'-GAGCCTGAAGAACTCCATTTTTCCCACAGTTTTTC-3'

Oligonucleotide primer for G423V hMiro2 mutagenesis

Forward: 5'-GTTCAGATGTAATGTAATTGTGGTGAAAAACTGTGGGAAAAG-3'

Reverse: 5'-CTTTTCCCACAGTTTTTCACCACAATTACATTACATCTGAAC-3'

Oligonucleotide primer for S430N hMiro2 mutagenesis

Forward: 5'- GAAAAACTGTGGGAAAAATGGAGTTCTTCAGGCTC-3'

Reverse: 5'-GAGCCTGAAGAACTCCATTTTTCCCACAGTTTTTC-3'

Appendix 5: Cell line data

Table A5.1. Cell line data.

Cell	Description	Tissue	Karyotype	Gender	Species
COS7	Kidney cell line	Kidney	---	M	*Cercopithecus aethiops*
MCF-7	Mammary gland adenocarcinoma	Breast	Cancer	F	*Homo sapiens*
hVSMC	Human vascular smooth muscle cells	Vascular (aortic)	Normal	M	*Homo sapiens*
PC3	Prostate cancer cell derived from grade IV patient	Prostate	Cancer	M	*Homo sapiens*

HEK-293	Embryonic kidney (contains adenovirus 5 DNA)	Kidney	---	U	*Homo sapiens*

Appendix 6: Additional growth components for VSMCs

Vascular smooth muscle cells (VSMCs) were maintained in vascular cell basal media (Lonza, United Kingdom) supplemented with the components shown in Table A7.1 to produce complete media for these cells. This complete media was to be kept at 4^{o}C in the dark and was stable for 30 days under these conditions.

Table A6.1. Additional growth components for VSMC culture.

Component	Volume	Final Concentration
rh FGF-basic	0.5 mL	5 ng/mL
rh Insulin	0.5 mL	5 µg/mL
Ascorbic acid	0.5 mL	50 µg/mL
L-glutamine	25.0 mL	10 mM
rh EGF	0.5 mL	5 ng/mL
Fetal Bovine Serum	25.0 mL	5%

Appendix 7: X!Tandem search parameters

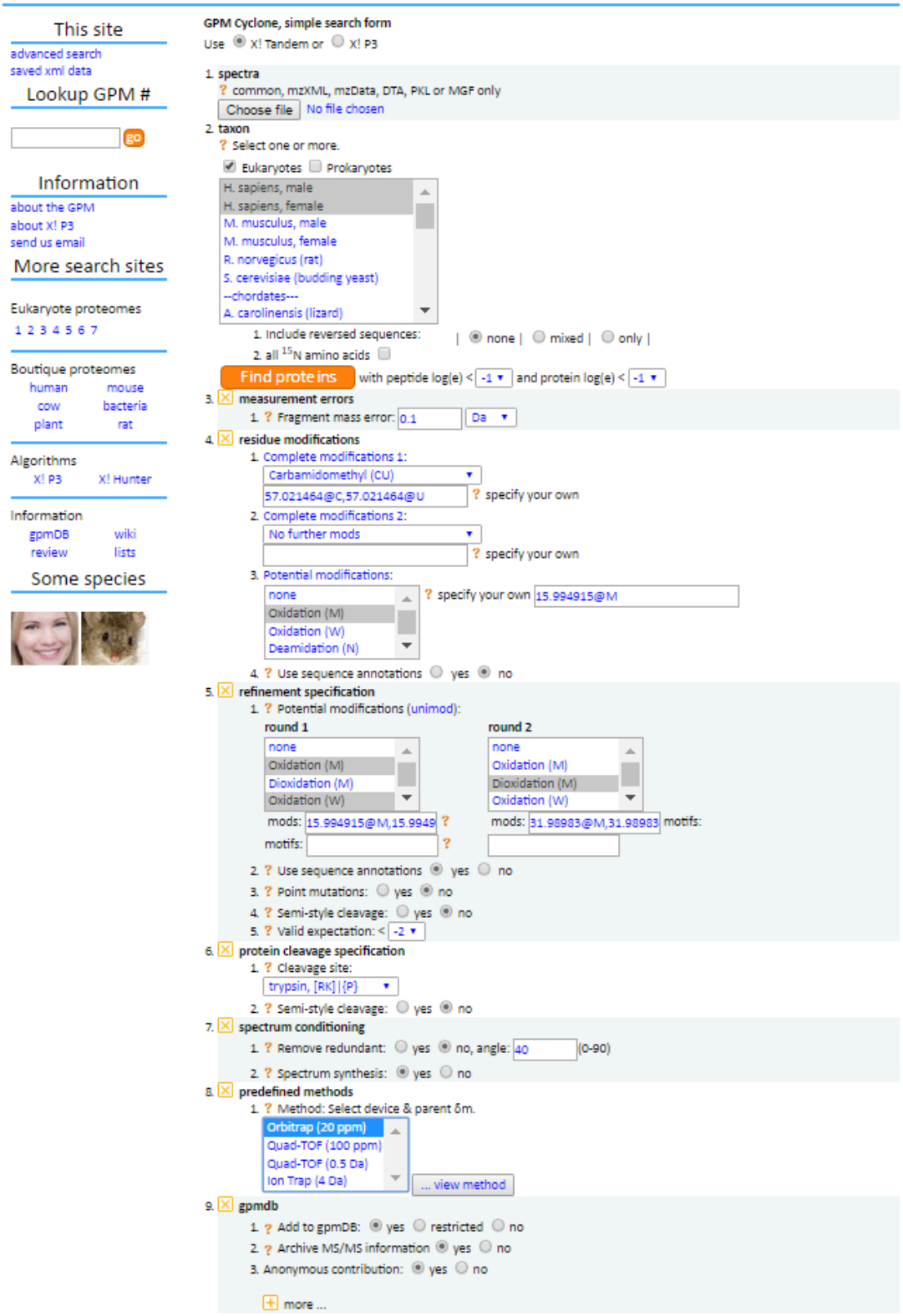

Appendix 8: MASCOT search parameters

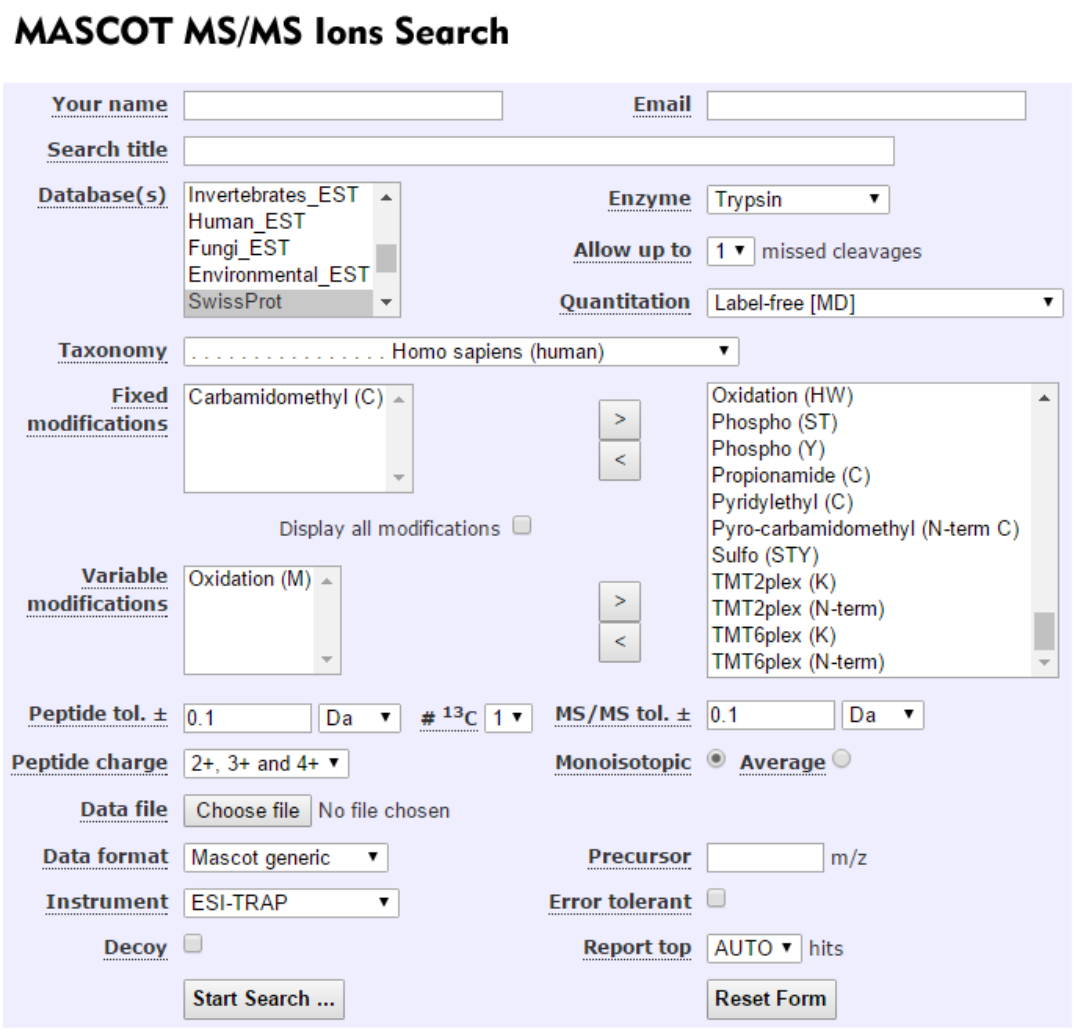

Appendix 9: Kinetic assays calculations

Interpretation of raw malachite green data (Cayman Chemicals)

For interpretation of malachite green raw data, the slope of the standard curve shown in Figure 4.2 (Chapter 4) was utilised, where the amount of phosphate produced in nMoL per 50µL at each time point was calculated as follows:

$$Phosphate\ (nM\ per\ 50\mu L) = \frac{(\mathrm{Abs635} + 0.0067)}{0.6712}$$

The value obtained was subsequently divided by 50 to obtain a value in nM. Conversion of values to µM was then undertaken by multiplying the value by 1 x 10^3. Finally, the relative blank value was taken away from this value, to give a true representation of the amount of phosphate produced by enzymatic hydrolysis.

Interpretation of raw data from PiColourLock™ Gold experiments

For interpretation of raw data from the PiColourLock™ Gold assays, the slope of the standard curve shown in Figure 4.3 (Chapter 4) was used. Here, µM of free inorganic phosphate could be derived immediately from the standard curve. Absorbance was read at discreet time points, as previously indicated in the literature, to produce bar charts representing µM phosphate produced per unit time.

Calculation of kinetic parameters

All kinetic parameters obtained were produced from the Lineweaver-Burke (LB) plots shown in Chpater 4. From these plots, the following kinetic parameters were derived:

V_{max} was derived from the y-intercept of each LB plot, which gave $1/V_{max}$

K_m was derived from multiplying the gradient of the respective LB plot by V_{max}

K_{cat} was derived from dividing V_{max} by the total concentration of enzyme used per well

K_{cat}/K_m was derived from dividing the value for K_{cat} with the value obtained for K_m

Appendix 10: Further xCELLigence information

Further information regarding the general set-up and system report generation for xCELLigence is given below.

Created By:	ADMINISTRATOR
Creation Date:	02/07/2016 14:05
File Name:	C:\Documents and Settings\RTCAOperator\My Documents\Rosemary projects\30Jun16migration.plt
Exp ID:	1606301736D2

System Information:

Software Version:	1.2.1.1002
Analyzer Model:	3x16
Analyzer SN:	3.21111E+11
FW Version:	V2.2
Station Model:	3x16
Station SN:	3.21111E+11
Station FW:	V2.2
Self Test Val:	99.9842

Seq.	Step	Step-Status	Sweep-Status	Sweeps	Interval	Unit	Total Time
1	Step_1	DONE	1	1	1	Minute	00:00:12
2	Step_2	DONE	100	100	15	Minute	25:36:45

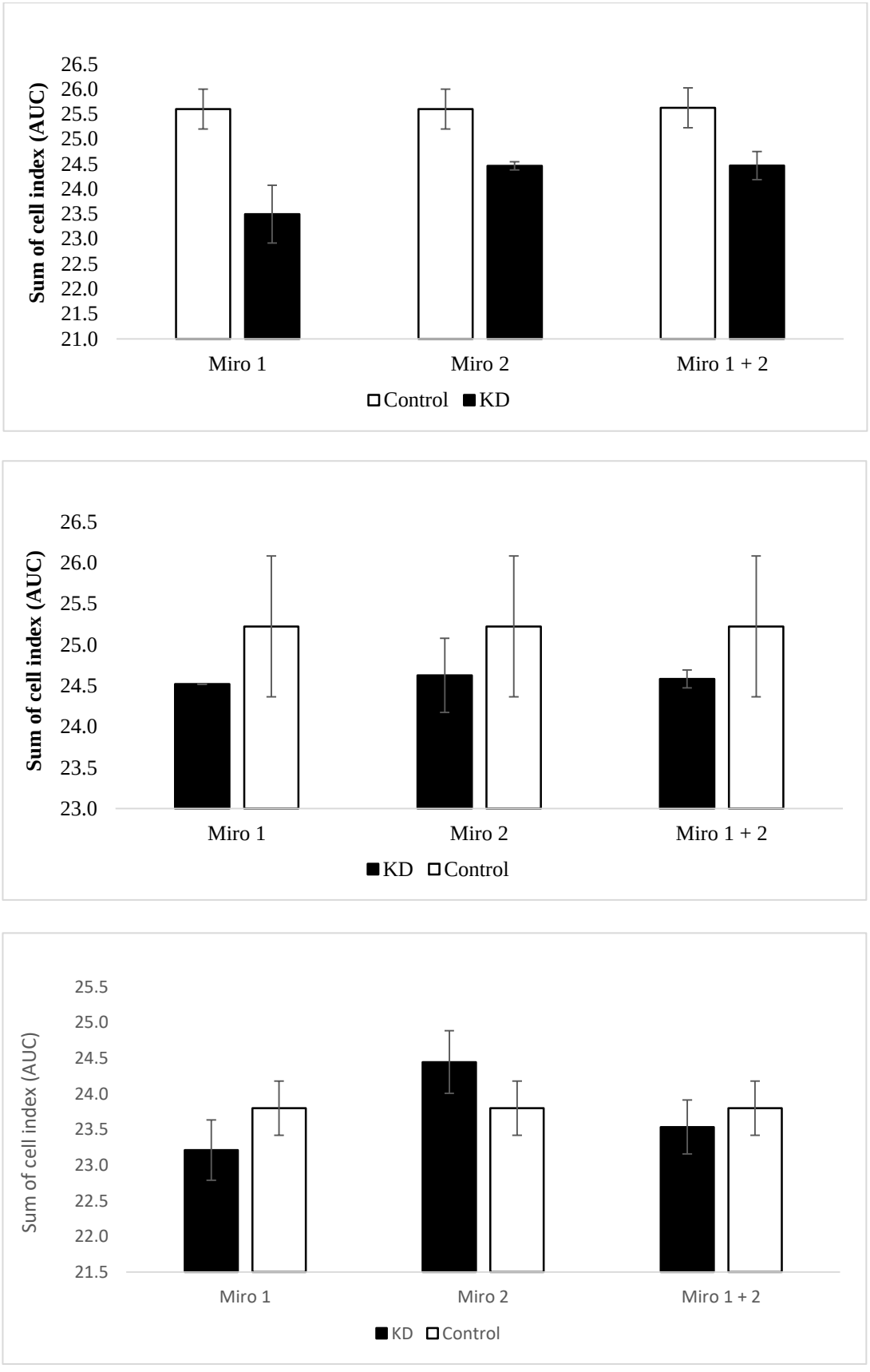

Figure A10.1. PC3 migration assays derived from each separate replicate set.

Appendix 11: STRING data example

Table A11.1 STRING data output example.

node1	node2	neighborhood	Gene fusion	Phylogenetic co-occurrence	homology	coexpression	experimental	Database annotated	Text-mining	Combined score
RPL31	RPL6	0	0	0	0	0.934	0.998	0.9	0.525	0.999
RPL31	RPS21	0	0	0	0	0.964	0.899	0.9	0.356	0.999
RPL39	RPL14	0	0	0	0	0.95	0.985	0.9	0.471	0.999
RBCK1	RNF31	0	0	0	0	0	0.999	0.9	0.974	0.999
RPL24	RPLP2	0	0	0	0	0.975	0.931	0.9	0.356	0.999
RPS19	RPS23	0	0	0	0	0.966	0.999	0.9	0.652	0.999
ITCH	UBE2L3	0	0	0	0	0	0.999	0	0.418	0.999
CDKN1B	CCND1	0	0	0	0	0	0.999	0.9	0.974	0.999
RPL36A	RPL30	0	0	0	0	0.975	0.982	0	0.778	0.999
RPL24	RPL19	0	0	0	0	0.975	0.999	0.9	0.558	0.999
RPS15A	RPL26	0.462	0	0	0	0.975	0.359	0.9	0.549	0.999
GNB2L1	IGF1R	0	0	0	0	0	0.922	0.9	0.879	0.999
RPL18	RPL18A	0	0	0	0	0.975	0.999	0.9	0.414	0.999
RPS6	RPL8	0	0	0	0	0.973	0.832	0.9	0.402	0.999
GRB2	CBL	0	0	0	0	0	0.999	0.9	0.901	0.999
RPL5	RPS7	0	0	0	0	0.975	0.779	0.9	0.667	0.999
SQSTM1	TRAF6	0	0	0	0	0	0.999	0.9	0.506	0.999
GRB2	BCR	0	0	0	0	0	0.999	0.9	0.701	0.999

Appendix 12: Proteomics data examples

Table A12.1. Sample of data from hMiro1N18 set.

Accession	Peptides	Score	Fractions	Description	Average Normalised Abundances
					Miro1N18
SPTN1_HUMAN	76 (74)	2223.03	12345678	Spectrin alpha chain, non-erythrocytic 1 OS=Homo sapiens GN=SPTAN1 PE=1 SV=3	5.17E+07
PLEC_HUMAN	66 (56)	2063.35	12345678	Plectin OS=Homo sapiens GN=PLEC PE=1 SV=3	1.37E+07
FLNA_HUMAN	57 (49)	1627.81	12345678	Filamin-A OS=Homo sapiens GN=FLNA PE=1 SV=4	4.64E+07
FLNC_HUMAN	49 (38)	1369.78	12345678	Filamin-C OS=Homo sapiens GN=FLNC PE=1 SV=3	4.93E+07
SPTB2_HUMAN	43 (40)	1220.9	12345678	Spectrin beta chain, non-erythrocytic 1 OS=Homo sapiens GN=SPTBN1 PE=1 SV=2	2.18E+07
FLNB_HUMAN	45 (36)	1043.61	12345678	Filamin-B OS=Homo sapiens GN=FLNB PE=1 SV=2	1.44E+07
HS90B_HUMAN	24 (16)	774.5	12345678	Heat shock protein HSP 90-beta OS=Homo sapiens GN=HSP90AB1 PE=1 SV=4	2.70E+07
HS90A_HUMAN	20 (8)	624.91	12345678	Heat shock protein HSP 90-alpha OS=Homo sapiens GN=HSP90AA1 PE=1 SV=5	1.01E+07
LMNA_HUMAN	10	599.01	12345678	Prelamin-A/C OS=Homo sapiens GN=LMNA PE=1 SV=1	1.40E+07

Table A12.2. Sample of data from hMiro1V13 set.

Accession	Peptides	Score	Fractions	Description	Average Normalised Abundances
					Miro1V13
SPTN1_HUMAN	17	897.03	12345678	Spectrin alpha chain, non-erythrocytic 1 OS=Homo sapiens GN=SPTAN1 PE=1 SV=3	6.62E+06
FLNC_HUMAN	12 (11)	653.53	12345678	Filamin-C OS=Homo sapiens GN=FLNC PE=1 SV=3	1.22E+07
HS90B_HUMAN	11 (9)	629.04	12345678	Heat shock protein HSP 90-beta OS=Homo sapiens GN=HSP90AB1 PE=1 SV=4	4.72E+07
K1C9_HUMAN	11	609.64	12345678	Keratin, type I cytoskeletal 9 OS=Homo sapiens GN=KRT9 PE=1 SV=3	2.64E+07
FLNA_HUMAN	11	585.1	12345678	Filamin-A OS=Homo sapiens GN=FLNA PE=1 SV=4	1.94E+07
HS90A_HUMAN	10	552.86	12345678	Heat shock protein HSP 90-alpha OS=Homo sapiens GN=HSP90AA1 PE=1 SV=5	6.04E+07
GANAB_MACFA	10	546.68	12345678	Neutral alpha-glucosidase AB OS=Macaca fascicularis GN=GANAB PE=2 SV=1	8.71E+06
LMNA_HUMAN	10	533.73	12345678	Prelamin-A/C OS=Homo sapiens GN=LMNA PE=1 SV=1	8.66E+06
SPTN1_HUMAN	17	897.03	12345678	Spectrin alpha chain, non-erythrocytic 1 OS=Homo sapiens GN=SPTAN1 PE=1 SV=3	6.62E+06

Table A12.3. Sample of data from hMiro2N18 set.

Accession	Peptides	Score	Fractions	Description	Average Normalised Abundances
					Miro2N18
FLNC_HUMAN	22 (21)	1187.45	12345678	Filamin-C OS=Homo sapiens GN=FLNC PE=1 SV=3	3.78E+07
SPTN1_HUMAN	19	996.59	12345678	Spectrin alpha chain, non-erythrocytic 1 OS=Homo sapiens GN=SPTAN1 PE=1 SV=3	2.34E+07
HSP7C_HUMAN	12 (10)	738.94	12345678	Heat shock cognate 71 kDa protein OS=Homo sapiens GN=HSPA8 PE=1 SV=1	2.45E+08
HS90A_HUMAN	13	732.06	12345678	Heat shock protein HSP 90-alpha OS=Homo sapiens GN=HSP90AA1 PE=1 SV=5	2.00E+08
K2C6C_HUMAN	10	721.34	12345678	Keratin, type II cytoskeletal 6C OS=Homo sapiens GN=KRT6C PE=1 SV=3	1.58E+08
K1C16_HUMAN	12 (11)	714.76	12345678	Keratin, type I cytoskeletal 16 OS=Homo sapiens GN=KRT16 PE=1 SV=4	1.69E+08
GRP78_HUMAN	14	714.28	12345678	78 kDa glucose-regulated protein OS=Homo sapiens GN=HSPA5 PE=1 SV=2	1.40E+08
VINC_HUMAN	12	697.62	12345678	Vinculin OS=Homo sapiens GN=VCL PE=1 SV=4	2.11E+07
FLNC_HUMAN	22 (21)	1187.45	12345678	Filamin-C OS=Homo sapiens GN=FLNC PE=1 SV=3	3.78E+07

Table A12.4. Sample of data from hMiro2V13 set.

Accession	Peptides	Score	Fractions	Description	Average Normalised Abundances
					Miro2V13
FLNC_HUMAN	11	630.67	12345678	Filamin-C OS=Homo sapiens GN=FLNC PE=1 SV=3	6.28E+06
HS90A_HUMAN	10 (6)	541.87	12345678	Heat shock protein HSP 90-alpha OS=Homo sapiens GN=HSP90AA1 PE=1 SV=5	1.17E+07
SPTN1_HUMAN	10	510.85	12345678	Spectrin alpha chain, non-erythrocytic 1 OS=Homo sapiens GN=SPTAN1 PE=1 SV=3	1.85E+06
HS90B_HUMAN	9 (3)	476.65	12345678	Heat shock protein HSP 90-beta OS=Homo sapiens GN=HSP90AB1 PE=1 SV=4	2.96E+06
LMNA_HUMAN	8	441.45	12345678	Prelamin-A/C OS=Homo sapiens GN=LMNA PE=1 SV=1	3.34E+06
ALDOA_HUMAN	7	429.86	12345678	Fructose-bisphosphate aldolase A OS=Homo sapiens GN=ALDOA PE=1 SV=2	9.95E+06
ACTB_CHLAE	7	417.23	12345678	Actin, cytoplasmic 1 OS=Chlorocebus aethiops GN=ACTB PE=2 SV=1	1.09E+08
K1C18_HUMAN	7 (5)	412.06	12345678	Keratin, type I cytoskeletal 18 OS=Homo sapiens GN=KRT18 PE=1 SV=2	4.29E+06
FLNC_HUMAN	11	630.67	12345678	Filamin-C OS=Homo sapiens GN=FLNC PE=1 SV=3	6.28E+06

Table A12.5. Sample of data from control set.

Accession	Peptides	Score	Fractions	Description	Average Normalised Abundances
					Control
SPTN1_HUMAN	24	1316.49	12345678	Spectrin alpha chain, non-erythrocytic 1 OS=Homo sapiens GN=SPTAN1 PE=1 SV=3	1.24E+07
K1C10_HUMAN	13 (11)	785.52	12345678	Keratin, type I cytoskeletal 10 OS=Homo sapiens GN=KRT10 PE=1 SV=6	3.37E+07
K1C9_HUMAN	13	753.14	12345678	Keratin, type I cytoskeletal 9 OS=Homo sapiens GN=KRT9 PE=1 SV=3	2.96E+07
LMNA_HUMAN	12	702.24	12345678	Prelamin-A/C OS=Homo sapiens GN=LMNA PE=1 SV=1	1.81E+07
K2C1_HUMAN	13	679.11	12345678	Keratin, type II cytoskeletal 1 OS=Homo sapiens GN=KRT1 PE=1 SV=6	5.32E+07
EF2_CALJA	12	665.73	12345678	Elongation factor 2 OS=Callithrix jacchus GN=EEF2 PE=2 SV=1	3.73E+07
HS90A_HUMAN	11	641.77	12345678	Heat shock protein HSP 90-alpha OS=Homo sapiens GN=HSP90AA1 PE=1 SV=5	9.50E+07
ENOA_HUMAN	10 (9)	620.33	12345678	Alpha-enolase OS=Homo sapiens GN=ENO1 PE=1 SV=2	1.40E+08
SPTN1_HUMAN	24	1316.49	12345678	Spectrin alpha chain, non-erythrocytic 1 OS=Homo sapiens GN=SPTAN1 PE=1 SV=3	1.24E+07

Appendix 13: RhoH DLS data

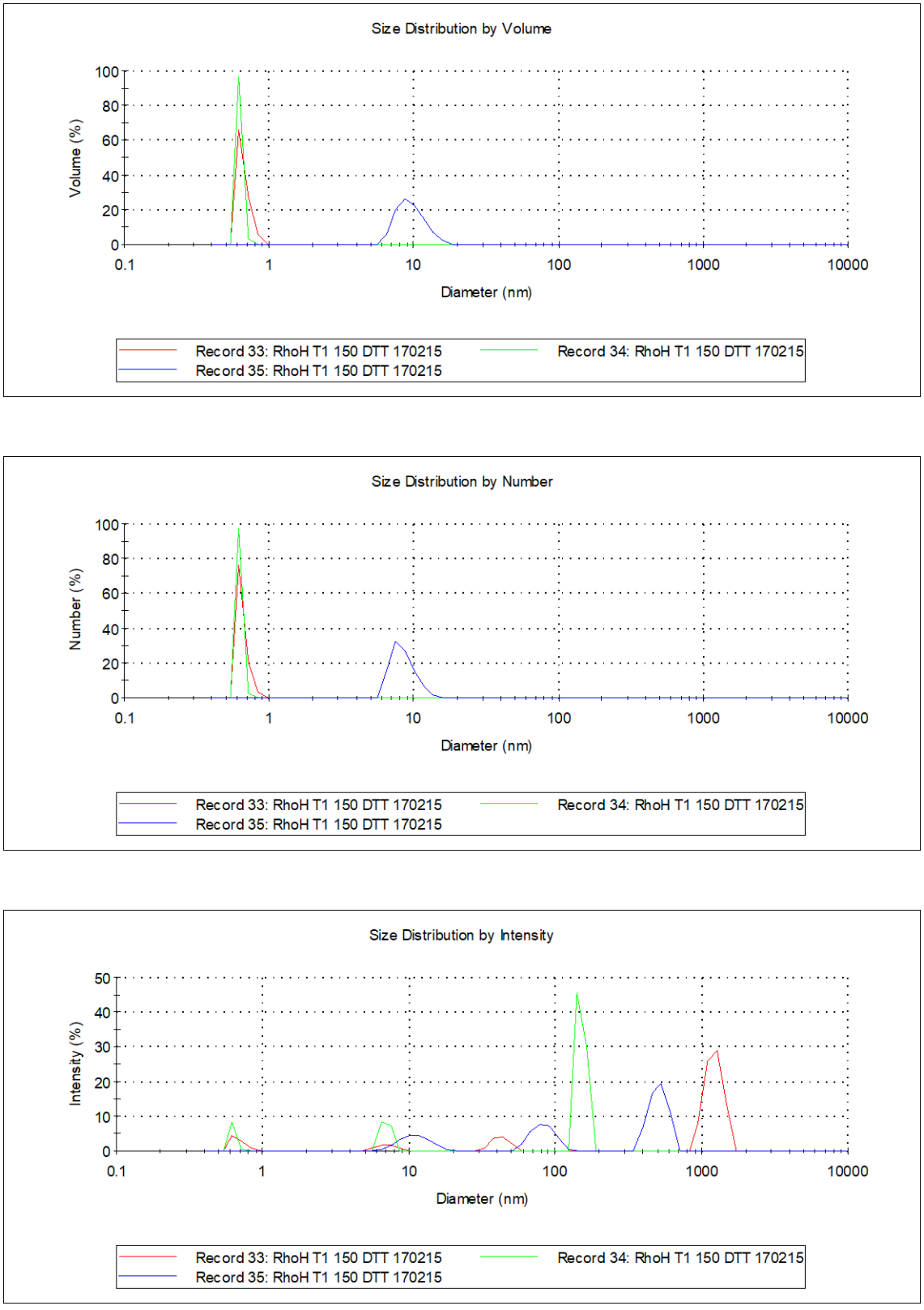

Figure A13.1 DLS results for $RhoH_{T1}$ showing size distribution by (a) volume, (b) number and (c) intensity. Triplicate set 1.

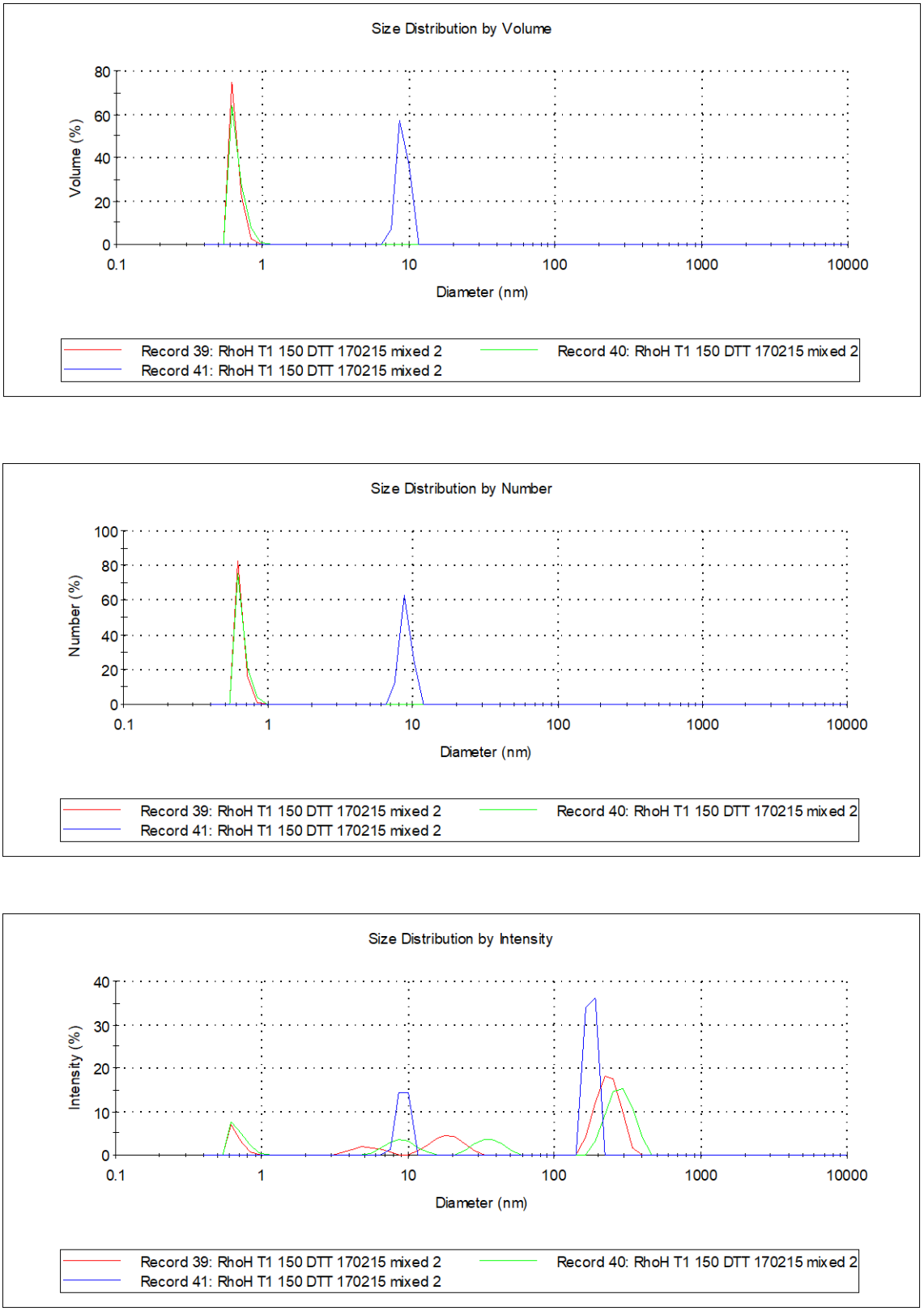

Figure A13.2 DLS results for $RhoH_{T1}$ showing size distribution by (a) volume, (b) number and (c) intensity. Triplicate set 2.

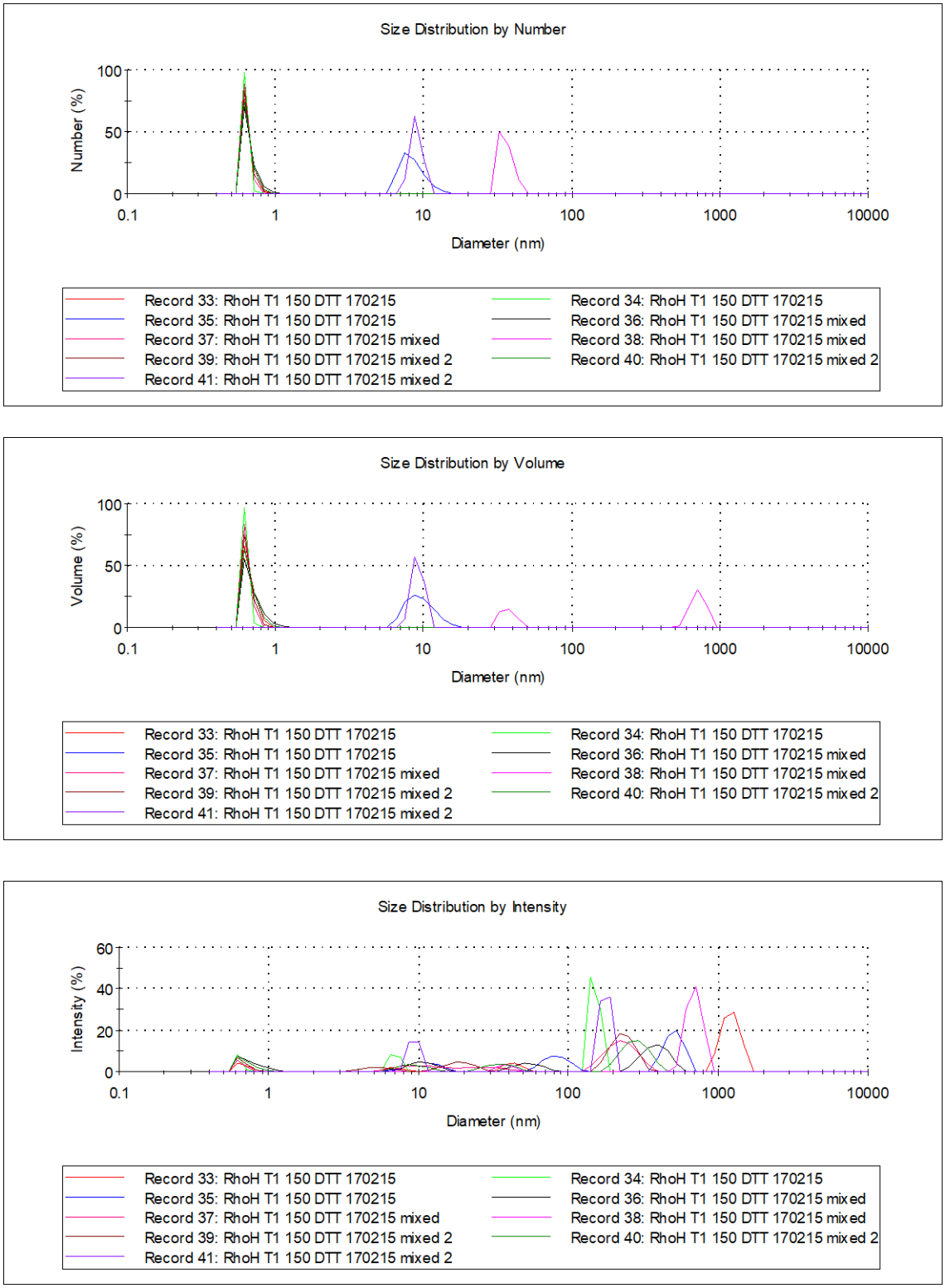

Figure A13.3 DLS results for $RhoH_{T1}$ showing size distribution by (a) volume, (b) number and (c) intensity. Triplicate set 3.

Appendix 14: Further LOMETS results

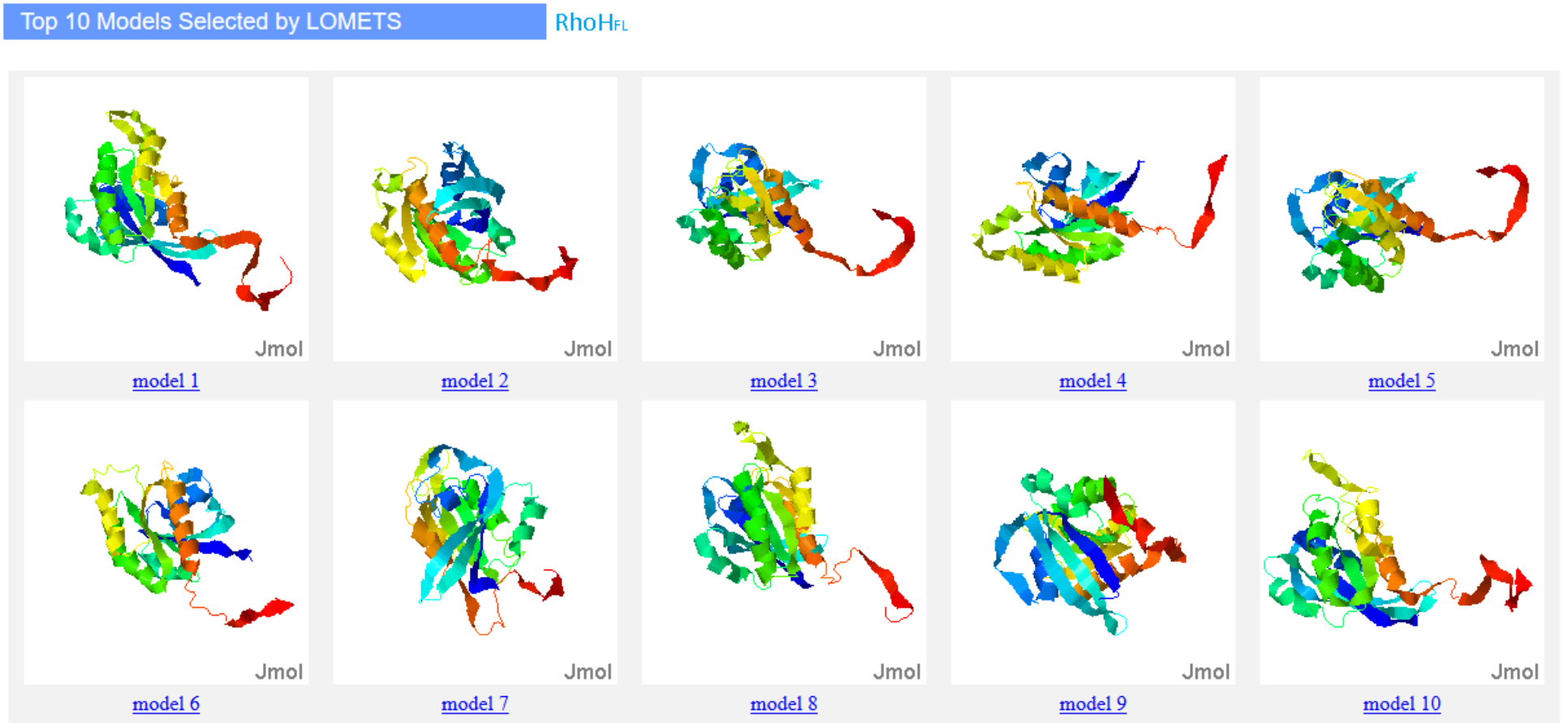

Figure A14.1 Top-scoring models for the prediction of $RhoH_{FL}$ according to the the LOcal MEta-Threading-Server (LOMETS) online server.

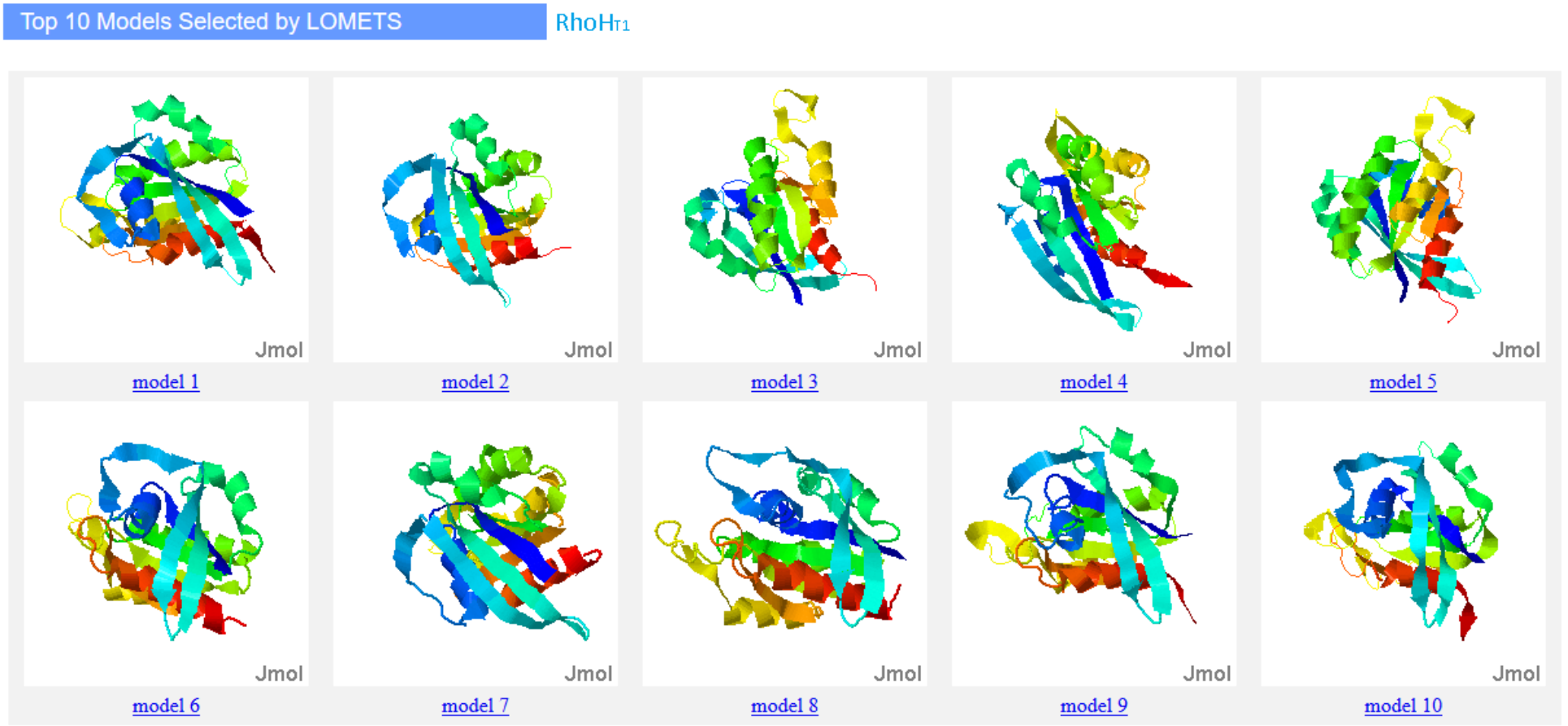

Figure A14.2 Top-scoring models for the prediction of RhoHFL according to the the LOcal MEta-Threading-Server (LOMETS) online server.